Self-organization in heterogeneous biological systems

How geometric and biochemical cues control pattern formation

Laeschkir Lukman Würthner

Munich 2022

Self-organization in heterogeneous biological systems

How geometric and biochemical cues control pattern formation

Laeschkir Lukman Würthner

A dissertation submitted to the Faculty of Physics
at the Ludwig–Maximilians–Universität München for the degree of
Doctor rerum naturalium

Munich, 26th July 2022

First referee: Prof. Dr. Erwin Frey
Second referee: Prof. Dr. Ulrich Gerland
Day of the oral examination: 17th October 2022

Zusammenfassung (Summary in German)

Selbstorganisation ist ein allgegenwärtiger und fundamentaler Prozess, der allen lebenden Systemen zugrunde liegt. In zellulären Organismen werden viele lebenswichtige Prozesse, wie zum Beispiel Zellteilung und Zellwachstum, räumlich und zeitlich durch Proteine – die Bausteine des Lebens – reguliert. Um das zu erreichen, bilden Proteine selbstorganisiert räumliche und zeitliche Muster. Im Allgemeinen reagieren Proteinmuster auf eine Vielzahl von internen und externen Stimuli, so wie beispielsweise Zellform oder Inhomogenitäten in der Aktivität von Proteinen. Aus diesem Grund erstreckt sich die Dynamik intrazellulärer Musterbildung über mehrere räumliche und zeitliche Skalen. Meine Doktorarbeit behandelt die zugrunde liegenden Mechanismen, die zur Entstehung von heterogenen Mustern führen. Die Hauptthemen dieser Arbeit sind in drei Teile organisiert und werden unten zusammengefasst.

I Musterbildung in heterogenen Systemen
Der erste Teil befasst sich mit der Dynamik Masse-erhaltender Reaktions-Diffusions-Systeme unter räumlich inhomogenen Bedingungen. In Abschnitt 1, Kapitel II untersuchen wir die Dynamik des *E. coli* Min-Protein-Systems – ein paradigmatisches Modell für Musterbildung. Dabei betrachten wir einen Aufbau mit einer festen räumlichen Heterogenität in einem Kontrollparameter und zeigen, dass das zu komplexen Multiskalen-Mustern führt. Wir entwickeln eine Vergröberungsmethode, welche es uns zum einen ermöglicht, die Dynamik zu erklären und zum anderen, auf die "hydrodynamischen Variablen" auf großen Längen-und Zeitskalen zu reduzieren. In einem weiteren Projekt betrachten wir ein System, in dem räumliche Heterogenitäten nicht von außen bestimmt werden, sondern dynamisch aufgrund einer mechano-chemischen Rückkopplungsschleife zwischen Geometrie und Reaktions-Diffusions-System erzeugt werden (Abschnitt 2, Kapitel II). Wir zeigen, dass die daraus resultierende Dynamik durch die Geometrie des Phasenraums des Reaktions-Diffusions-Systems erklärt werden kann.

II Geometrieerkennung und biochemische Vorlagen für Musterbildung
Der zweite Teil fokussiert sich auf die Frage, wie Muster in realistischen Zellgeometrien durch Form und biochemische Signale kontrolliert werden. Wir untersuchen Achsenselektion von PAR-Polaritätsmustern in *C. elegans* und zeigen, dass räumliche Variationen im Volumen-zu-Oberfläche-Verhältnis sowie eine Tendenz des Systems, die Mustergrenzfläche zu minimieren, zu einer robusten Langachsenpolarisation von PAR-Proteinmustern führen (Abschnitt 1, Kapitel III). In einem

weiteren Projekt entwickeln wir ein theoretisches Modell, das die Lokalisation des Min-Protein-Systems in *B. subtilis* erklärt (Abschnitt 2, Kapitel III). Wir zeigen des Weiteren, dass ein biochemische Vorlage – welches als Schablone für Musterbildung dient – Min-Protein-Muster führt sowie stabilisiert.

III Krümmungsinduzierte Instabilitäten von Protein-Lipid-Grenzflächen

Im dritten Teil studieren wir die Dynamik zwischen Lipidmembranen und Proteinen die Krümmungen generieren können. Wir demonstrieren, dass das Motorprotein Myosin-VI kooperativ an die Stellen von Lipidmembranen bindet, welche eine sattelförmige Krümmung aufweisen (Abschnitt 1, Kapitel IV). Dadurch induzieren die Motorproteine eine großflächige Umgestaltung der Membran. Um die Dynamik zu verstehen, entwickeln wir ein vergröbertes geometrisches Modell und zeigen, dass die Entstehung von regulären räumlichen Strukturen durch einen “Push-Pull”-Mechanismus erklärt werden kann: Proteinbindung destabilisiert die Membranform auf allen Längenskalen, und dieser Deformierung wird durch die Linienspannung der Grenzfläche entgegengewirkt. Inspiriert durch dieses Modellsystem untersuchen wir dann in einem weiteren Projekt ein allgemeines Modell, welches die Dynamik wachsender Protein-Lipid-Grenzflächen beschreibt (Abschnitt 2, Kapitel IV). Ein wesentliches Merkmal des Modells ist, dass die Bindekinetik der Proteine explizit an die Morphologie der Grenzfläche gekoppelt ist. Wir zeigen, dass solch eine Kopplung zu turbulenter Dynamik sowie zu einer Aufrauhung der Grenzfläche führt, was durch ein universelles Skalenverhalten gekennzeichnet ist.

Projects and contributions

Self-organization is an ubiquitous and fundamental process that underlies all living systems. In cellular organisms, many vital processes, such as cell division and growth, are spatially and temporally regulated by proteins – the building blocks of life. To achieve this, proteins self-organize and form spatiotemporal patterns. In general, protein patterns respond to a variety of internal and external stimuli, such as cell shape or inhomogeneities in protein activity. As a result, the dynamics of intracellular pattern formation generally span multiple spatial and temporal scales. This thesis addresses the underlying mechanisms that lead to the formation of heterogeneous patterns. The main themes of this work are organized into three parts, which are summarized below.

I Pattern formation in heterogeneous systems
with *F. Brauns, A. Goychuk, J. Halatek, G. Pawlik, J. Kerssemakers, C. Dekker, and E. Frey.*
The first part deals with the general problem of mass-conserving reaction-diffusion dynamics in spatially non-uniform systems. In section 1 of chapter II, we study the dynamics of the *E. coli* Min protein system – a paradigmatic model for pattern formation. More specifically, we consider a setup with a fixed spatial heterogeneity in a control parameter, and show that this leads to complex multiscale pattern formation. We develop a coarse-graining approach that enables us to explain and reduce the dynamics to the "hydrodynamic variables" at large length and time scales. In another project, we consider a system where spatial heterogeneities are not imposed externally, but self-generated by the dynamics via a mechanochemical feedback loop between geometry and reaction-diffusion system (section 2 of chapter II). We show that the resulting dynamics can be explained from the phase-space geometry of the reaction-diffusion system.

II Geometry-sensing and biochemical templates for pattern formation
with *R. Geßele, H. Feddersen, J. Halatek, M. Bramkamp, and E. Frey.*
The second part focuses on how patterns in realistic cell geometries are controlled by shape and biochemical cues. We examine axis selection of PAR polarity patterns in *C. elegans*, where we show that spatial variations in the bulk-surface ratio and a tendency of the system to minimize the pattern interface yield robust long-axis polarization of PAR protein patterns (section 1 of chapter III). In a second project, we develop a theoretical model that explains the localization of the *B. subtilis* Min

protein system (section 2 of chapter III). We show that a biochemical cue – which acts as a template for pattern formation – guides and stabilizes Min patterns.

III Curvature-induced instabilities of protein-lipid interfaces

B. Rogez, A. B. Petrova, F. B. Zierhut, D. Saczko-Brack, M. Huergo, C. Batters, E. Frey, and C. Veigel

In the third part, we study the coupling between lipid membranes and curvature-generating proteins. We demonstrate that myosin-VI motor proteins cooperatively bind to saddle-shaped regions of lipid membranes, and thereby induce large-scale membrane remodeling (section 1 of chapter IV). To understand the dynamics, we develop a coarse-grained geometric model and show that the emergence of regular spatial structures can be explained by a "push-pull" mechanism: protein binding destabilizes the membrane shape at all length scales, and this is counteracted by line tension. Inspired by this system, we then investigate a general model for the dynamics of growing protein-lipid interfaces (section 2 of chapter IV). A key feature of the model is that the protein binding kinetics is explicitly coupled to the morphology of the interface. We show that such a coupling leads to turbulent dynamics and a roughening transition of the interface that is characterized by universal scaling behaviour.

List of publications

Publications directly relevant to this thesis

* Indicates shared first authorship

1. L. Würthner*, A. Goychuk*, and E. Frey (2022). *Geometry-induced patterns through mechanochemical coupling*. **arXiv:** 2205.02820

2. T. Burkart*, M. C. Wigbers*, L. Würthner*, and E. Frey (2022). *Control of protein-based pattern formation via guiding cues*. ***Nature Reviews Physics***. DOI: 10.1038/s42254-022-00461-3

3. L. Würthner*, F. Brauns*, G. Pawlik, J. Halatek, J. Kerssemakers, C. Dekker, and E. Frey (2021). *Bridging scales in a multiscale pattern-forming system*. **arXiv:** 2111.12043

4. H. Feddersen, L. Würthner, E. Frey, and M. Bramkamp (2021). *Dynamics of the Bacillus subtilis Min system*. ***mBio*** **12 (2), e00296-21**. DOI: 10.1128/mBio.00296-21

5. R. Geßele, J. Halatek, L. Würthner, and E. Frey (2020). *Geometric cues stabilise long-axis polarisation of PAR protein patterns in C. elegans*. ***Nature Communications*** **11, 539**. DOI: 10.1038/s41467-020-14317-w

6. B. Rogez*, L. Würthner*, A. B. Petrova, F. B. Zierhut, D. Saczko-Brack, M. Huergo, C. Batters, E. Frey, and C. Veigel (2019). *Reconstitution reveals how myosin-VI self-organises to generate a dynamic mechanism of membrane sculpting*. Published in ***Nature Communications*** **10, 3305**. DOI: 10.1038/s41467-019-11268-9

Other publications

7. L. Würthner*, F. Gartner*, D. Muramatsu*, and E. Frey (2022). *Anomalous roughening of growing protein-lipid interfaces*. In preparation.

8. A. B. Petrova*, T. Burkart*, L. Würthner*, E. Frey, and C. Veigel (2022). *Myosin-VI self-organizes lipid segregation to enable cell-like membrane reshaping and scission*. In preparation.

9. A. Ren*, H. Weyer*,L. Würthner*, E. Frey, and S. Jun (2022). *A two-step detachment process explains the robustness of Min protein patterns in vivo*. In preparation.

10. A. Goychuk*, L. Würthner*, and E. Frey (2022). *Mechanics shapes chemical patterns*. In preparation.

11. L. Würthner*, J. Guerrero*, A. Goychuk*, and E. Frey (2022). *Pattern-controlled shape oscillations of lipid vesicles*. In preparation.

12. N. Ziereis*, F. Brauns*, L. Würthner*, and E. Frey (2022). *Universal mechanisms of spontaneous cell polarization*. In preparation.

Contents

I Intracellular pattern formation

1 Introduction

One of the key processes underlying the development of living organisms is *self-organization*. It is a process in which the small constituents of a system spontaneously form large-scale spatiotemporal structures. The emergence of such large-scale order is governed by interaction rules between the constituents, and is referred to as *pattern formation*. Many phenomena in nature arise from self-organization, such as cloud formation [1], dune fields [2], the shape of cells [3], and even we as humans [4]. In this thesis, we address diverse aspects of self-organized protein patterns in cellular organisms.

Proteins are the basic building blocks of life and regulate many cellular processes that are vital for cell survival and functioning [5]. These include, for instance, cell metabolism [6], division [7], motility [8, 9], and growth [10, 11]. Proteins reliably coordinate these processes in space and time by forming robust spatiotemporal patterns [5, 12–14]. For example, Min oscillations precisely regulate cytokinesis in the rod-shaped bacteria *Escherichia coli* (*E. coli*). Here, the proteins MinD, MinC, and MinE oscillate from pole-to-pole of the cell and thereby guide the division machinery (ftsZ proteins) to midcell, where the time-averaged concentrations of Min proteins are lowest [15–17]. Other representative examples include polarity pattern of PAR proteins in the *Caenorhabditis elegans* (*C. elegans*) worm embryo, whose function is to define the anterior and posterior of the animal [18–20], and Rho-GTPase waves that control the activity of the cytoskeleton in starfish and frog oocytes [21–23].

On a mechanistic level, patterns in biological systems generally emerge through the combined effect of (nonlinear) biomolecular interactions and transport processes (such as diffusive and advective redistribution of particles) [5, 13, 14]. The mathematical framework for pattern formation was first established by Alan Turing more than seven decades ago. In his seminal work, he showed that the interplay between local chemical reactions and diffusive redistribution can destabilize a (stable) homogeneous steady state, and thus lead to the formation of spatial patterns [24]. Such reaction-diffusion models have been successfully used to address pattern formation in various systems and across different length and time scales, ranging from intracellular protein patterns [5, 12, 13, 22, 25], to shape formation in developmental biology [26], and vegetation patterns [27]. The traditional (diffu-

sion driven) *Turing instability* outlined above has been derived on the basis of two crucial assumptions: (i) The system is spatially and temporally uniform (or more precisely, translationally invariant). This implies the existence of a homogeneous steady state, around which the dynamics of spatial perturbations is linearized. (ii) The spatial domain, on which the dynamics of chemicals is considered, is assumed to have a static shape and therefore does not evolve over time. This point also entails that chemical species do not interact with, e.g. , the boundaries of the domain and consequently cannot shape their environment through direct interactions with the geometry.

However, biological systems are intrinsically *heterogeneous systems*, meaning, for instance, that they generally do not exhibit homogeneous steady states, but rather spatially inhomogeneous *base states*. Alan Turing was well aware of this fact and came to the conclusion himself that *"Most of an organism, most of the time, is developing from one pattern into another, rather than from homogeneity into a pattern"* [24]. Moreover, in the particular context of intracellular organization, protein patterns usually do not emerge in the bulk solution (cytosol) of cells, but rather at the cell boundary, i.e. at the cell membrane. The underlying reason for this is that the membrane surface acts as a "catalyst" for biochemical reactions and hence promotes nonlinear interactions between protein species, such as cooperative membrane binding (recruitment) [5, 13, 14, 28] or mutual antagonistic interactions through phosphorylation [29, 30]. In addition, the shape of cells is not static, but highly dynamic and changes in response to a number of internal and external stimuli. Shape deformations are often controlled by protein patterns either through direct interactions with the membrane [31–35] or indirectly by regulating the cell cortex [21–23, 36–38]. Thus, intracellular patterns generally emerge through an intricate feedback loop between biochemistry and cell shape, and this interplay can lead to inhomogeneities and additional phenomena which are not taken into account in idealized models.

The overarching aim of this work is to shed light on (protein-based) pattern formation in heterogeneous systems, where the origin of such heterogeneities can be either intrinsic to the system (i.e. self-generated by the dynamics) or caused by (fixed external) spatial gradients in control parameters. The main themes of this thesis are organized into three comprehensive chapters, which we briefly summarize in the following. In chapter II, we first investigate reaction-diffusion dynamics in a heterogeneous geometry. More precisely, we show that the dynamics of the Min protein system in a wedge-shaped geometry produces spatiotemporal patterns that span multiple spatial and temporal scales. To deal with the complex dynamics, we present a coarse-graining approach that enables us to reduce the multiscale dynamics to the relevant degrees of freedom at large length and time scales (or "hydrodynamic variables"). Then, we investigate reaction-diffusion systems on dynamically deforming membranes. It is shown that a feedback loop between

reaction-diffusion system and membrane shape leads to spatial inhomogeneities of the reaction-diffusion dynamics, causing a variety of different patterns that do not emerge in a static geometry. We show that the dynamics can be explained by a simple criterion that links the onset of (geometry-induced) patterns to the phase-space geometry of the reaction-diffusion system.

In chapter III we discuss how cell shape and biochemical cues affect protein patterns. We first explain how PAR polarity patterns in *C. elegans* robustly select the long-axis in ellipsoidal geometry. It is shown that axis-selection is guided by cell geometry, due to variations of the membrane area to volume ratio, which is largest at the cell poles. As a second example where geometry plays a decisive role in the correct formation of protein patterns, we study bipolar gradients of the *Bacillus subtilis* Min protein system. In addition to inhomogeneities in the membrane area to volume ratio, we show that a biochemical template stabilizes the Min proteins at the cell poles, or at midcell once a septum forms.

In chapter IV we present our work on the interplay between curvature and biochemical dynamics of protein-lipid interfaces. First, we show how curvature-dependent binding of the motor protein myosin-VI to lipid membranes generates curvature and thereby remodels the membrane. We derive a coarse-grained theoretical model that explains the underlying mechanism and show that curvature-sensitive binding of myosin-VI leads to pattern formation of the (growing) protein-lipid interface. Motivated by this instructive biological example, we then develop and study a general model of growing protein-lipid interfaces with a feedback loop between protein binding and interface morphology. We show that morphological coupling gives rise to inhomogeneous growth rates of the interface, and thus leads to interesting phenomena such as large-scale pattern-forming instabilities and turbulent dynamics. For the latter case, we show that the system exhibits universal scaling that is driven solely by the deterministic dynamics (as opposed to classical noise-driven interface growth models).

2 Guiding cues

Before we turn to the main topics of this work, we first provide a general overview of how protein patterns are controlled by spatial heterogeneities and guiding cues in cells. The following content is based on and uses parts of our review article [14] (in collaboration with *T. Burkart, M. Wigbers and E. Frey*) published in *Nature Reviews Physics*. A reprint of the article is provided in section 3.

As emphasized in the previous section, patterns rarely form out of homogeneity, but rather emerge through explicit or implicit interactions with other components and cell features. More specifically, intracellular protein patterns are reliably controlled by various guiding cues, including geometric features such as cell size and

shape, biochemicals or other (protein) patterns, as well as non-uniform mechanical properties of the cell (comprising the cell membrane and cytoskeleton). In the following, we briefly summarize how these guiding cues impact pattern formation.

2.1 Cell size

Size threshold. A pattern-forming instability arises when the base state becomes unstable to small spatial perturbations, hence resulting in a *band of unstable modes* modes (dispersion relation) [13, 39]. Since cells have a finite size, a pattern can only emerge if the cell size exceeds a critical value, such that the dominant or fastest growing mode "fits" into the system. This has been demonstrated experimentally for PAR polarity patterns [40].

Bulk-boundary ratio. On the relevant time scale of pattern formation, the total average protein concentration can be assumed to be constant. Protein-based patterns are therefore mathematically described by *mass-conserving reaction-diffusion systems* [12, 13, 28, 41]. Due to the limited number of resources available, the membrane and cytosolic concentrations depend on the ratio of membrane surface area to bulk volume, which are defined by the size of the cells. This means, for instance, that the membrane concentration will be higher in cells with a larger area to volume ratio because more space is available for cytosolic proteins to bind to the membrane (assuming a constant total average density).

Cytosolic gradients. Mass-conservation further implies that proteins are not created or degraded, but cycle between the cytosol and membrane due to attachment, detachment, recruitment, and antagonistic reactions. Therefore, mass-conservation requires that these biochemical processes must be balanced by cytosolic fluxes (diffusive and advective fluxes) at the membrane. These fluxes generically result in cytosolic protein gradients perpendicular to the membrane, where the characteristic penetration depth typically depends on the transport processes and reactions in the bulk. The relative value of this characteristic length scale and the cell size is critical to the phenomenology of protein patterns, as has been demonstrated theoretically and experimentally for the Min protein system [5, 17, 28, 42, 43].

2.2 Cell shape

Curvature sensing. Some proteins have an intrinsic shape (BAR domains) and therefore preferentially bind to membrane regions with the same curvature [32, 44–46]. To sense curvature across large scales (much larger than the typical size of a protein), these proteins often form oligomers through cooperative interactions to form large structures [32, 47]. BAR proteins are also able to induce membrane

curvature, which can give rise to a positive feedback loop between protein binding and membrane shape [48].

Collective curvature sensing. Proteins without an intrinsic shape can indirectly respond to cell shape by sensing spatial variations in the membrane surface to bulk volume ratio (or bulk-surface ratio). The underlying reason for this lies in the cytosolic gradients: if the characteristic length of cytosolic gradients is larger than the radius of curvature of the cell (but smaller than the typical length of the cell), then these gradients overlap at regions of negative curvature. Or in other words, proteins accumulate in regions where the membrane surface to bulk volume is largest, such as the poles of a bacterial cell (corresponding to Gaussian negative curvature).

2.3 Biochemical cues

Spatially heterogeneous reaction kinetics. The (local) reaction kinetics of one protein species can depend on the (local) concentration level of another protein. In particular, a spatially varying reaction kinetics can result in spatially non-uniform local equilibria as well as different stability properties of these equilibria in space [49]. To put it differently, we can also say that a protein species which alters the reaction kinetics of another protein species encodes *positional information*. Indeed, this principle is common in many biological systems [26, 50–57].

Diffusiophoresis. Protein patterns can also serve as templates and cause the formation of patterns of functionless molecules (cargo particles that do not interact with each other) through effective friction forces [58, 59]. Such friction forces are caused, for instance, by diffusive fluxes of "carrier particles" (here protein patterns) that collide with and transport larger cargo particles. This mechanism is also termed *phoretic transport* and the basic principle is encountered in a variety of physical systems [60–64].

2.4 Mechanochemical cues

Cytoplasmic flows. The cytoplasm of a cell can be basically viewed as an incompressible fluid. Deformations of the cell membrane generate high and low pressure regions in the cytoplasm, thereby inducing flows of the fluid. Such deformations originate, for example, from surface contraction waves along the cell membrane [65]. Cytoplasmic flows break the symmetry in the system and thereby guide cytosolic proteins via advective transport.

Cortical flows. Flows can be also generated by the actomyosin complex through frictional coupling with the surrounding cytosol. Spatial inhomogeneities of myosin activity [25] or anisotropies in the cortical tension [66] lead to stress gradients in the actomyosin network and consequently to the flow of components of the actomyosin cortex (cortical flows).

3 Publication: Control of protein-based pattern formation via guiding cues

Control of protein-based pattern formation via guiding cues

by

T. Burkart[1,*], M. C. Wigbers[1,*], L. Würthner[1,*], and E. Frey[1,2]

[1] Arnold Sommerfeld Center for Theoretical Physics (ASC) and Center for NanoScience (CeNS), Department of Physics, Ludwig-Maximilians-Universität München, Theresienstraße 37, D–80333 Munich, Germany,

[2]Max Planck School Matter to Life, Hofgartenstraße 8, D-80539 Munich, Germany

*These authors contributed equally to this work.

Published in ***Nature Reviews Physics*** **(2022)**

DOI: 10.1038/s42254-022-00461-3.

also available on BIORXIV: 10.1101/2022.02.11.480095.

BIORXIV version reprinted on pages 10–33,

Control of protein-based pattern formation via guiding cues

Tom Burkart,[1,*] Manon C. Wigbers,[1,*] Laeschkir Würthner,[1,*] and Erwin Frey[1,2,†]

[1] *Arnold Sommerfeld Center for Theoretical Physics (ASC) and Center for NanoScience (CeNS), Department of Physics, Ludwig-Maximilians-Universität München, Theresienstraße 37, D-80333 Munich, Germany*

[2] *Max Planck School Matter to Life, Hofgartenstraße 8, D-80539 Munich, Germany*

(Dated: February 11, 2022)

Proteins control many vital functions in living cells, such as cell growth and cell division. Reliable coordination of these functions requires the spatial and temporal organizaton of proteins inside cells, which encodes information about the cell's geometry and the cell-cycle stage. Such protein patterns arise from protein transport and reaction kinetics, and they can be controlled by various guiding cues within the cell. Here, we review how protein patterns are guided by cell size and shape, by other protein patterns that act as templates, and by the mechanical properties of the cell. The basic mechanisms of guided pattern formation are elucidated with reference to recent observations in various biological model organisms. We posit that understanding the controlled formation of protein patterns in cells will be an essential part of understanding information processing in living systems.

I. INTRODUCTION

To ensure their survival, cells must tightly regulate a wide range of cellular functions, such as cell migration, cell growth, DNA synthesis, and cell division. For example, in order to produce two viable daughter cells, a cell must precisely coordinate cell growth with the duplication and segregation of DNA, and with subsequent cell division. These cellular functions, in turn, are controlled and coordinated by proteins. Robust timing and reliable control of these functions requires cells to process *spatiotemporal information*, such as information about cell size and shape, cell cycle state, the cell's surroundings, and the current state of other cellular processes. Such spatiotemporal information is encoded in *protein patterns* – i.e., an inhomogeneous spatial distribution of proteins – that regulate these cellular functions, whereby each type of protein may perform distinct tasks.

How then are proteins spatially and temporally organized in a cell? The idea that the collective organization of interacting chemicals (chemical reactions) in an initially homogeneous medium can give rise to spatial patterns dates back to Turing's seminal work on spontaneous pattern formation in reaction-diffusion systems [1]. While this work has greatly advanced the understanding of pattern formation in biological systems, many aspects of protein patterns such as their positioning, timing, reliability, and controllability – which are essential for the viability of living organisms – remain poorly understood. Since protein patterns in cells serve a timed and targeted functional purpose, they must form in response to certain signals and control mechanisms rather than spontaneously emerging from an initially homogeneous distribution. Indeed, an increasing number of theoretical and experimental studies find that protein distributions can respond and adapt to cell shape, size, and mechanics, as well as to signals encoded in previously established protein patterns [2–8].

This response is, in fact, bidirectional. Cells are not static objects but rather an active material whose size, shape, and mechanical properties can be altered dynamically through protein interactions in response to the cell's environment and the current state of the cell cycle [9–12]. These dynamic interactions between protein patterns and cell architecture are the subject of a rapidly developing field of study at the interface between cell biology and theoretical physics that benefits from constantly improving experimental techniques, as well as insights from physics that allow one to model and understand the guided organization of proteins into patterns.

In this review, we summarize recent advances in our understanding of how protein patterns are controlled by geometric, mechanical, and biochemical cues. The basics of pattern formation will only be summarized briefly, as recent reviews have provided a comprehensive introduction to this subject. The interested reader is referred to an elementary course on the mathematical tools that are required to study the physics of protein interactions and pattern formation, in particular ordinary differential equations (ODEs) and nonlinear dynamics [13]. For an introduction to the theory of pattern-forming systems, we direct the reader to pertinent textbooks [14, 15], and to lecture notes for a review on quantitative modeling of pattern formation in mass-conserving systems [16]. Other recent reviews have focused on the theory of two specific aspects of pattern formation, namely the role of bistability for polarity [17] and the curvature-generating properties of proteins [18]. The relevance of protein patterns for cells has also been reviewed from a more biological perspective recently [19], in particular with respect to midcell localization [20], and current advances in understanding pattern formation at a molecular level [21] have been reviewed recently. We also want to highlight three recent reviews that emphasize the importance and role of modeling for understanding cell polarity [22, 23]

* These authors contributed equally.
† frey@lmu.de

and biological phenomena in general [24].

Here, we discuss several theoretical models that have been developed with a view to reproducing and accounting for pattern guidance, together with examples of well-studied biological model organisms in which pattern guidance has been observed to play a critical role in cell viability. In particular, we discuss how biophysical theory has been instrumental in clarifying the underlying physical concepts of pattern guidance in living cells. We start by giving an overview of the predominant types of protein transport and chemical reactions that are predominately involved in the formation of patterns in cells. We then discuss how these factors can be affected by cell shape and size, pre-existing protein patterns, and cell mechanics, and how these cues guide and control protein pattern formation. We conclude with an outlook on the future research directions in this field.

II. BASIC PRINCIPLES OF PATTERN FORMATION

Protein patterns arise from the interplay of biochemical reaction kinetics with different types of transport mechanisms. While the amounts of locally available proteins are regulated by chemical reactions, their spatial distribution is altered by transport processes including diffusion, active transport and fluid flow (see Fig. 1). Some of the most important reaction and transport processes involved are presented in the following.

A. Protein reaction networks

Protein reaction networks differ in their degree of complexity, e.g., with respect to the number of different proteins and their conformations, as well as the number and type of reactions between them. Some of the most common types relevant to protein pattern formation are briefly discussed in the following.

Conformational state changes – The intracellular organization of proteins is largely controlled by protein reaction networks that contain nucleoside triphosphate[a] (NTP)-dependent regulatory modules. In prokaryotic cells, P-loop (phosphate binding loop) ATPases[b] such as ParA and MinD take on this role, and give rise to self-organized dynamic patterns at cellular interfaces – ParA on the nucleoid and MinD on the cell membrane [20, 25, 26]. Similarly, small GTPases like Cdc42 and RhoA play an important role in establishing cell polarity in eukaryotic cells [27–29]. Basically, all these proteins serve as molecular switches that can cycle between an active and inactive state based on nucleotide binding and delayed hydrolysis, typically regulated by auxiliary proteins [30–32] (Fig. 1a). Similarly, proteins that are not NTPases can act as molecular switches if cycling between active and inactive states (phosphorylation[c] and dephosphorylation) is catalyzed by separate kinases and phosphatases, respectively [33, 34]. These cycles have two key features. First, they are non-equilibrium processes driven by the supply of chemical energy, e.g. through ATP hydrolysis [35]. As such, they are the core element of most protein reaction networks, enabling them to drive self-organization processes. Secondly, the switch between active and inactive states is associated with changes in their affinity for targets such as the cell membrane and the nucleoid [35, 36], as well as their specific binding affinity for other proteins or lipids. For example, MinD can only bind to the cell membrane in its ATP-bound, dimeric form and is released into the cytosol as an ADP-bound monomer upon ATP hydrolysis [37].

Binding and unbinding reactions – Many proteins can bind to different substrates in a cell, such as membranes. Typical residence times of proteins on membranes range from seconds to minutes [4, 38, 39]. In several biological model systems, the nonlinear binding kinetics of proteins to membranes plays a key role in the formation of spatiotemporal protein patterns.

One way to confer nonlinear binding kinetics is through limitation of binding sites on the membrane, which leads to saturated binding kinetics [40]. Another example is cooperative reactions that amplify or attenuate the attachment and detachment of other proteins to the membrane [41–44] (Fig. 1a). These feedback mechanisms were shown to be an integral part of the patterning mechanisms in the most important model organisms: In the MinDE system of *E. coli*, pole-to-pole oscillations of the Min proteins rely on recruitment of cytosolic MinD and MinE by membrane-bound, active MinD (positive feedback) and their release into the cytosol through MinE-induced hydrolysis and concomitant inactivation of MinD (negative feedback) [37, 45–47]. In budding yeast (*S. cervisiae*), the establishment of cell polarity via asymmetric distribution of Cdc42 involves multiple positive and negative feedback loops, which provide a high degree of robustness [32, 40, 48, 49]. Finally, the PAR polarity system in the early *C. elegans* embryo exploits various antagonistic reactions that play a key role in specifying the correct orientation of the polarity axis [34, 50–52].

Complex formation – Proteins can also form oligomers[d], in particular dimers (Fig. 1a). This can have

[a] Nucleoside tri-/diphosphate (NTP/NDP) – Nucleotide molecules with three (two) phosphate groups typically based on guanine (GTP), adenine (ATP) or cytosine (CTP), forming the main carriers of chemical energy in cells.

[b] NTPase – Enzymes that bind to NTP and hydrolize it to NDP, thereby releasing energy.

[c] Phosphorylation – Proteins can be (de-)phosphorylated by the addition of a phosphate group, as a means of storing (releasing) chemical energy.

[d] Oligomer – Complex made up of a few proteins of the same or

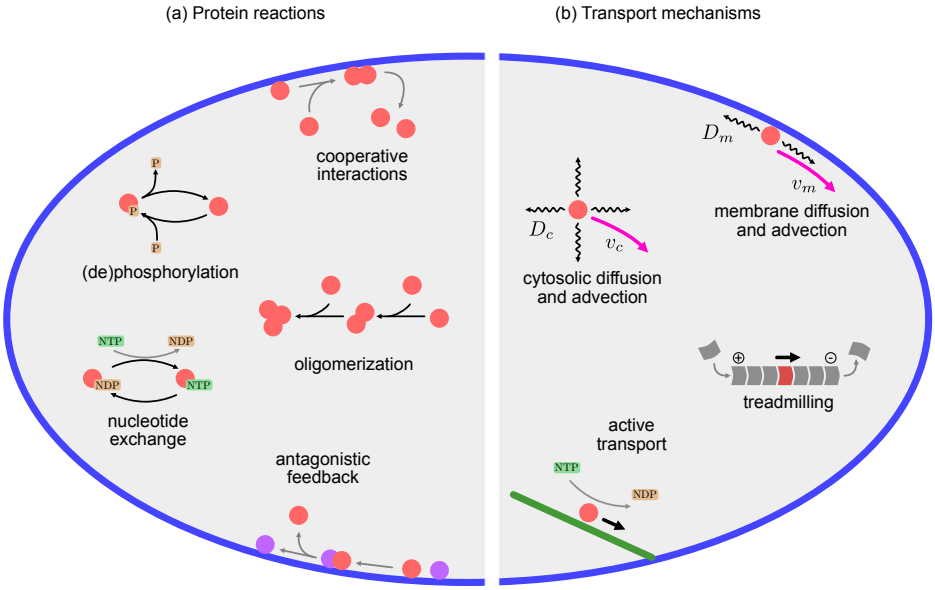

FIG. 1. **Reaction and transport processes involved in pattern formation:** (a) Protein reactions include binding to and detachment from the cell membrane or other intracellular structures, as well as conformational state changes due to (de-)phosphorylation or nucleotide exchange. Cooperative and antagonistic (nonlinear) reactions between multiple proteins can lead to assisted attachment (recruitment) or to detachment from the membrane. Multiple monomers can form oligomers with altered transport and reaction properties. (b) Proteins can be transported by diffusion (D_c, D_m, black arrows) and advection (v_c, v_m, pink) independently on surfaces – in particular cell cortex and membrane – and in the cytosol. In addition, directed protein transport can be established by subunit addition and disassembly of polymers, resulting in treadmilling of monomers, and by active transport along filamentous structures, mediated by energy-consuming motor proteins.

an impact on their ability to bind to cellular surfaces, as described above for active MinD dimers. The formation of higher-order protein aggregates leads to a change in Péclet number (see below), which in turn alters how they are affected by fluid flow as opposed to diffusion. Such an effect has been suggested to play a role in the transport of PAR-3 proteins in the *C. elegans* embryo. Here, diffusive transport may dominate for PAR-3 monomers (Pe < 1), whereas transport becomes dominated by flow (Pe > 1) upon cell-cycle-dependent aggregation of PAR-3 into complexes together with two other proteins – PAR-6 and aPKC [53]. Yet another process is the formation of higher-order oligomers, such as those observed for membrane-bound MinD [44, 46]. Similar to the nonlinear attachment kinetics discussed above, cooperative reactions have also been suggested to participate in protein complex formation, potentially allowing for feedback loops [34].

Theory – Mathematically, the dynamics of well-mixed protein reaction networks are described by sets of coupled nonlinear differential equations for the concentrations $u_i(t)$ of each of the different protein types and conformations $i \in \{1, \ldots, S\}$,

$$\partial_t u_i(t) = f_i(\{u_i\})\,. \tag{1}$$

In such *chemical rate equations*, the nonlinear reaction terms f_i (together with the reaction rates) must be inferred from the underlying reaction network using the law of mass action. An elaborate mathematical theory, called *dynamic system theory*, allows one to analyze systems of coupled nonlinear ordinary differential equations (ODEs). The basic idea of this theory, which goes back to the pioneering work of Poincaré [54], is to characterize the system dynamics in terms of certain geometric structures in the phase space spanned by the set of dynamical variables $u_i(t)$ [13, 14].

Of particular interest are the asymptotic dynamics of the system over large time scales, which are characterized by the *attractors* in phase space within the framework of dynamic system theory. These include fixed points corresponding to reactive equilibria (see Supplementary Information), limit cycles corresponding to nonlinear oscillators, and more intricate geometric objects [13, 14]. Importantly, the local properties of the fixed points (reactive equilibria), in particular their stability, can be

or a different type (homo- and hetero-oligomers, respectively).

determined using ODEs linearized around these fixed points [13, 14].

B. Protein transport

Transport mechanisms play a crucial role in the control of spatial variations in protein concentration. In the following, we provide an overview of the most important modes of intracellular protein transport involved in pattern formation (Fig. 1b).

Diffusion – Perhaps the most basic means of protein transport is diffusion. It is a consequence of Brownian motion and is directed from regions of high to regions of low protein concentration $u(\mathbf{x}, t)$ with a diffusive current $-D\nabla u(\mathbf{x}, t)$ (Fick's law). For spherical particles of radius r, the diffusion constant is given by the Stokes-Einstein relation $D = k_B T/(6\pi\eta r)$, where η is the viscosity of the surrounding cytosol [55]; a qualitatively similar relation holds for transmembrane proteins [56, 57]. This implies that the diffusive transport of proteins depends on their size and on the local properties of the surrounding medium.

Importantly, both the membrane and the cytoplasm[e] are highly heterogeneous environments crowded with macromolecular structures that interact with proteins, for example by temporarily binding or by taking up space [58]. For the purpose of studying pattern formation, however, one often disregards inhomogeneities and instead assumes an effective diffusion constant that takes into account such interactions that are not explicitly modeled. Hence, the diffusion constant is a mesoscopic quantity representing the mobility of proteins in a homogeneous, dilute fluid environment. In essence, the complex cytoplasmic environment is reduced to an effective cytosol for many applications in protein pattern formation, and similarly, the heterogeneous membrane is considered as an effective (dilute) fluid [59]. This simplification is justified since the length scale of patterns is typically larger than the length scale of heterogeneities in the cytoplasm or on the membrane, to which we will refer as substrates in the following. As a rough estimate, the diffusion coefficients of membrane-bound proteins are generically at least two orders of magnitude lower than those of their cytosolic counterparts: While characteristic values for membrane diffusion are $D_m \sim 0.01\,\mu m^2/s$, one observes $D_c \sim 10\,\mu m^2/s$ in the cytosol [60]. Although the models discussed in this review suggest that the heterogeneous character of the cellular substrates are of minor importance for protein pattern formation, it would be interesting to explicitly probe the robustness of these models against more realistic substrates. For example, this could be incorporated into models via time- and space-dependent diffusion constants.

Active transport – Proteins can also be transported via active processes driven by the chemical energy of ATP, GTP or CTP at the molecular level. Of particular biological relevance are translational molecular motors[f] [61–63]. An important subclass of these motors is comprised of kinesins and dyneins that bind to, and 'walk' on microtubules[g]. In this way, cargo – such as other proteins – can be transported along the microtubules [61, 62]. Depending on the type of motor and, in some cases, other factors such as external forces [64], this form of active transport is directed to either the plus or minus end of the microtubules [65]. Certain classes of myosin motors perform similar tasks by transporting cargo along actin filaments. Such active cargo transport is known to be involved in the polarization process of budding yeast. Here, the actin filaments are anchored to the polarity site, so that the myosin motors can deliver protein-coated vesicles towards the polarity site [66, 67].

Another class of active transport processes is mediated by the directed polymerization of cytoskeletal filaments such as F-actin [68] and microtubules [69], which is driven by ATP and GTP hydrolysis, respectively. For instance, tubulin-like FtsZ filaments are particularly important active structures in bacterial cell division. These filaments exhibit treadmilling dynamics (see the segmented structure in Fig. 1b), as FtsZ monomers can only bind to the plus end and detach from the minus end [70, 71]. By consuming GTP, this treadmilling allows FtsZ filaments to translocate directionally along the cell membrane, coordinating the activity of downstream cell division processes [72]. Similarly, treadmilling of actin filaments was shown to play a key role in cell migration, in particular for the extrusion of lamellipodia [73].

Both *in vivo* and *in vitro* experiments have shown how important these active transport processes are for the polarization of cells [74–78]. For example, during cell growth in fission yeast microtubules are aligned along the long axis of the cell, and direct the active transport of the tip factors Tea1 and Tea4 towards the cell poles in a two-fold manner [78–81]: The kinesin-like motor Tea2 mediates the transport of Tea1/Tea4 complexes along microtubules that emanate from the nucleus [82, 83]. In addition, these complexes bind to microtubule tips assisted by Mal3, a tip-binding protein. Therefore, due to the directed microtubule polymerization along the long cell axis, the tip factors are transported to the cell poles [83]. At the poles, they then serve as a spatial cue for cell growth, and therefore facilitate the elongation of the cell along its long axis [84].

[e] Cytoplasm – Heterogeneous material making up most of the volume of a cell (excluding the nucleus), mainly consisting of the cytosol and macromolecular organelles.

[f] Molecular motors – Enzymes that use energy released by NTP hydrolysis to perform mechanical work and that are generally associated with cytoskeletal filaments.

[g] Microtubules and actin filaments – Protein filaments comprised of tubulin and actin proteins, respectively, which form an integral part of the cytoskeleton.

Advective transport – In the fluid environment of a cell, proteins can also be transported by cytoplasmic [85, 86], cortical [51], and membrane flows [87, 88], whose effect on protein transport through friction strongly depends – like diffusion – on the viscosity of the respective environment. An important force-generating active structure is the actin cortex[h]. In addition to actin filaments, it includes cross-linker proteins and myosin motors that cause cortical contractions which, in turn, can induce flows [89, 90]. The cortical contractions that occur in the *C. elegans* zygote are a prominent example [4, 91, 92]. Here, local depletion of the concentration of the motor protein myosin at the cell cortex leads to a gradient of contractile stress, such that the cell cortex flows from the anterior to the posterior pole [93].

Cortical contractions can also lead to flows in the cytoplasm or membrane due to hydrodynamic coupling between membrane, cortex and cytoplasm [92]. In addition, they can also induce cell-shape changes that lead to flows in the cytoplasm. For example, surface contraction waves during the maturation of starfish oocytes have recently been shown to induce such flows [94, 95]. Similarly, shape changes resulting from blebbing incidents coincide with intracellular flows [96].

The Péclet number – The relative impact of diffusion and flow on protein transport is quantified by the Péclet number $\mathrm{Pe} = \xi \cdot v/D$, where v is the typical protein advection velocity and ξ a characteristic length scale. Large values of the Péclet number correspond to protein transport that is dominated by flow rather than diffusion. Hence, small proteins with large diffusion constants are less affected by flow than large proteins or protein assemblies. In addition, the detailed chemical interactions of proteins with other biomolecules and cellular structures can affect the effective diffusivity and advection velocity [97]. As for diffusive transport, the advection velocity – and hence the Péclet number – is a mesoscopic quantity that disregards the heterogeneous structure of the environment. This approximation is justified since variations in the mobility coefficients within a given substrate are usually much smaller than the variations between different substrates, such as the cytoplasm and the membrane. In general, a protein that diffuses in the cytoplasm is less affected by flows than it is when bound to the more viscous membrane.

Theory – The spatiotemporal transport of, and reactions between proteins are mathematically described by nonlinear partial differential equations (PDEs) [16]. The protein dynamics in terms of their cytosolic (volume) concentrations $\mathbf{c}(\mathbf{r}, t)$ and membrane (area) concentrations $\mathbf{m}(\boldsymbol{\sigma}, t)$ generally take the form of *general transport equations* with flux and source terms

$$\partial_t \mathbf{c}(\mathbf{r}, t) = -\nabla \cdot \mathbf{J}_c + \mathbf{f}_{\mathrm{cyt}}(\mathbf{c})\,, \tag{2}$$

$$\partial_t \mathbf{m}(\boldsymbol{\sigma}, t) = -\nabla_{\mathcal{S}} \cdot \mathbf{J}_m + \mathbf{f}_{\mathrm{mem}}(\mathbf{m}, \mathbf{c}|_{\mathcal{S}})\,, \tag{3}$$

which represent a broad and general class of interesting dynamic systems far from thermodynamic equilibrium. The divergence of the cytosolic and membrane fluxes $\mathbf{J}_{c/m}$ accounts for the (mass-conserving) spatial transport of proteins, and generally contains both diffusive and advective contributions. Here $\nabla_{\mathcal{S}}$ denotes the *covariant derivative* for the *curvilinear coordinates* $\boldsymbol{\sigma} \in \mathcal{S}$ on the membrane surface $\mathcal{S}$. The membrane is often considered as a static object for simplicity, however models can in general be extended to dynamic surfaces. In particular, this requires to extend the dynamics by an explicit expression for the time evolution of the membrane geometry, $\mathcal{S} \to \mathcal{S}(t)$ [18, 98–102]. The source terms $\mathbf{f}_{\mathrm{cyt}}$ and $\mathbf{f}_{\mathrm{mem}}$ result from the chemical reactions of the underlying protein networks, as discussed above. Note that membrane-bound proteins not only react with each other, but membrane reactions also involve interactions with cytosolic proteins in close proximity to the membrane ($\mathbf{c}|_{\mathcal{S}}$).

The set of nonlinear PDEs (Eqs. (2) and (3)) is closed by *reactive boundary conditions* at the membrane

$$\mathbf{J}_c \cdot \hat{\mathbf{n}}|_{\mathcal{S}} = \mathbf{g}(\mathbf{m}, \mathbf{c}|_{\mathcal{S}})\,, \tag{4}$$

which ensures local mass conservation: cytosolic fluxes normal to the membrane ($\hat{\mathbf{n}}$ denotes the outward normal vector) must be balanced by reactive fluxes $\mathbf{g}(\mathbf{m}, \mathbf{c}|_{\mathcal{S}})$ at the membrane [16]. An additional constraint for many models of protein pattern formation is the global conservation of protein mass, i.e., the assumption that no proteins are produced or degraded on the time scale of pattern formation. This assumption is violated on longer time scales, where protein production and degradation processes – in particular gene expression – need to be taken into account [23].

C. Lateral instabilities and trigger waves

This set of general transport equations provides the theoretical framework for studying the spatiotemporal dynamics of protein patterns. The interested reader may consult recent lecture notes [16] for an introduction to their analysis. Here, to conclude our introduction to the basic principles of pattern formation, we briefly introduce two particularly interesting phenomena: pattern-forming instabilities and trigger waves.

A *pattern-forming instability* arises when a spatially uniform steady state becomes unstable against spatially inhomogeneous perturbations (Fig. 2d). One example of such a pattern-forming instability is a mass-redistribution instability (see Supplementary Information), which amplifies spatial variations in protein number, thus leading to a protein concentration pattern [103].

[h] Actin cortex – Thin and dynamic network that acts as a scaffold that determines the cell's shape and which is comprised of actin filaments, motor proteins, and other associated proteins.

The dynamics and length scale of these patterns on short time scales are determined by the growth rate and wavelength of the unstable modes, termed *dispersion relation* (see Supplementary Information). The growth rate of the unstable modes depends on the specific reaction kinetics and transport properties of the dynamics. The wavelength of the fastest growing unstable mode determines the characteristic length scale of the initially growing pattern. While the initial pattern is dominated by the dynamics of the unstable modes, the dynamics on longer timescales may be dominated by other processes, such as coarsening [104] and non-linear interactions of the unstable modes far away from the linear regime.

In addition, nonlinear protein reaction kinetics can give rise to several reactive equilibria at the same total protein concentration, which is a necessary requirement for *trigger waves*. This phenomenon is best exemplified by systems that show bistability (see Supplementary Information) [105]. In this case, the system can be at different reactive equilibria at different regions in the cell, giving rise to front-like protein activity patterns. Such front-like patterns propagate with a finite velocity, whose magnitude and sign depend on the details of the reaction kinetics [94, 106]. This propagation is constrained by the limited abundance of proteins, which can result in localized wave fronts in cells [107–109]. Moreover, unstable reactive equilibria can give rise to spatially homogeneous oscillations and traveling spiral waves [103, 110, 111].

The spatiotemporal properties of these patterns, such as the orientation of static patterns or the direction of propagating wave fronts, need to be controlled tightly by the cell. This is achieved with the aid of guiding cues. In the following, we will discuss the most prominent types of guiding cues observed to play a role in pattern formation processes in cells.

III. GEOMETRIC GUIDING CUES

On the largest scales, cells are characterized by their size and shape, which together confine protein transport and protein reaction kinetics.

A. Cell size controls protein patterns

Experimental studies show that, in addition to reaction and transport properties of the cell, also the cell size affects protein patterns. Examples include the transition from pole-to-pole oscillatory patterns to stripe patterns of MinD in filamentous *E. coli* cells [112, 113], and the observation that the PAR proteins in *C. elegans* fail to polarize in small cells [8].

Bulk-boundary-ratio.– On the time scale of pattern formation and dynamics, the total concentration of proteins remains constant. As a consequence of these resource limitations, protein concentrations on the membrane and in the cytosol will in general depend on the ratio of membrane area to cell volume. Moreover, the number and stability of reactive equilibria, as well as pattern-forming instabilities, are controlled by the total concentration of proteins (see Supplementary Information), and variations in cell size can therefore qualitatively affect protein patterns. To understand the underlying idea, we assume for simplicity that the concentrations of cytosolic proteins c and membrane-bound proteins m, respectively, are uniformly distributed. The total number of proteins N is then given by $N = \mathcal{S} \cdot m + \mathcal{V} \cdot c$, where $\mathcal{S}$ and $\mathcal{V}$ denote the membrane (surface) area and the cytosolic (bulk) volume, respectively (Fig. 2a). Rewriting this mass-conservation relation in terms of the total protein density $\rho = N/\mathcal{V}$, one obtains $\rho = \mathcal{S}/\mathcal{V} \cdot m + c$. Thus, the protein concentrations on the membrane and in the cytosol depend on the ratio of membrane to volume $\mathcal{S}/\mathcal{V}$; for example, for a spherical cell with radius R, one finds $\rho = 3\,m/R + c$.

Cytosolic protein gradients.– Because the proteins of interest here are not permanently fixed to either the membrane or the cytosol, but circulate between these compartments due to various chemical processes such as membrane detachment, attachment, and recruitment, the cell membrane effectively acts both as a source and sink for cytosolic proteins. These chemical reactions need to be balanced by diffusive fluxes in the cytosol, otherwise local mass conservation would be violated. Hence, on these very general grounds, spatial gradients in the cytosolic protein density must be assumed [16, 103]. Strikingly, these gradients generally do not equilibrate over time, but are maintained by an interplay between diffusion and non-equilibrium reaction kinetics (see Supplementary Information).

Indeed, a good example is the case where proteins in the cytosol can have two different conformations, an *inactive* and an *active* state. Only proteins in the active state are able to bind to the membrane, and they typically undergo a conformational change to the inactive state upon detachment from the membrane (Fig. 2b). In the cytosol, inactive proteins can switch back to the active state with a rate λ. This reactivation step requires the consumption of energy and is a generic feature in NTPase or phosphorylation/dephosphorylation cycles [30–32]. Since detached proteins cannot immediately bind to the membrane again, a protein concentration gradient may form in the cytosol [114, 115]. The *penetration depth* ℓ of this gradient depends on the cytosolic diffusion constant D_c and the reactivation rate λ, and is given by $\ell = \sqrt{D_c/\lambda}$ [2].

If the cell size is much smaller than this penetration depth, the cytosolic protein concentration is effectively nearly homogeneous throughout the cell. Conversely, if the cell is much larger than the penetration depth, protein gradients can be established in the cytosol (Fig. 2b). The presence of such cytosolic gradients can fundamentally affect the formation of patterns on the membrane [103, 116, 117]. This is well exemplified in the

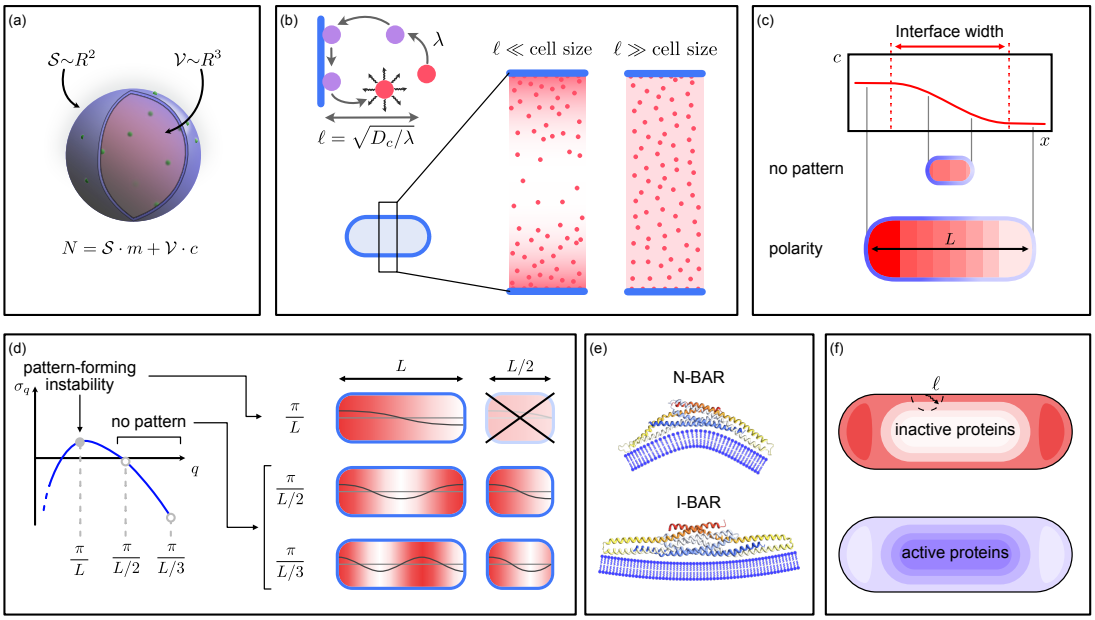

FIG. 2. **Size and shape as guiding cues:** (a) Schematic illustration of protein distribution in the cytosol and on the membrane: the cell volume scales with cell size R as R^3, whereas the cell surface scales as R^2, implying that both membrane and cytosolic protein concentration change with cell size. (b) Left: cytosolic gradients can emerge when proteins undergo a 'reacivation' step after detaching from the membrane. Inactive proteins (red) diffuse over a characteristic length scale ℓ before being reactivated (purple). Right: cytosolic gradients are established when the cell size is much larger than this characteristic length scale. (c) Cell size controls pattern formation: protein patterns cannot be established in cells smaller than the characteristic length scale of a pattern. (d) Only certain unstable modes with a wavelength limited by the cell size L can be realised. In a cell of size $L/2$, no pattern-forming instability arises. (e) Proteins including BAR domains preferentially bind to similarly curved membranes. (f) Characteristic distribution of proteins with delayed reactivation in elongated cells. Inactive proteins are reactivated after diffusing over a characteristic length scale ℓ. At the cell poles, this leads to the accumulation of inactive proteins, while they are diluted at the center of the cell. A complementary distribution of active proteins is established.

E.coli Min system, which shows standing wave patterns *in vivo*, but – strikingly – produces traveling and spiral wave patterns, among others, in reconstituted *in vitro* assays with large bulk volume [41, 113, 118].

Finite size effects.– In addition, cell size can affect pattern-forming instabilities. A pattern-forming instability arises when a spatially uniform steady state is unstable against spatially inhomogeneous perturbations (Fig. 2d). Due to the finite size of the cell, only particular unstable modes can grow, where the largest possible wavelength is constrained by the lateral length of the cell. Thus, while a reaction network can lead to a pattern-forming instability in large cells, it may result in a stable and spatially uniform steady state or a weak gradient in small cells (Fig. 2c,d). Indeed, this has been observed for the polarity pattern of PAR proteins in *C. elegans* (Fig. 2c) [8]. Similarly, cell size may not only limit the existence of a pattern, but also the type of protein pattern that can be established.

B. Cell shape and curvature sensing

For a wide range of cells, from bacteria [112, 119, 120] to migrating fibroblasts [121] to unicellular eukaryotes [122] and large zygotes [93], cell shape and local membrane curvature serve as important guiding cues for protein attachment to the membrane. The mechanisms underlying such curvature detection are based on the interaction of proteins with the membrane, in particular its membrane binding affinity (*curvature-sensing proteins*), and the probability that a protein will make contact with the membrane (*collective curvature sensing*). Both factors can be affected by cell shape (membrane curvature).

1. *Curvature-sensing proteins*

One prominent set of proteins that can individually sense membrane curvature are proteins containing a curved BAR domain[i] [123–126]. These proteins pref-

[i] BAR domain – A curved protein domain that binds to curved membranes, named after three proteins that contain this domain:

erentially bind to membrane regions that have a curvature comparable to that of the BAR domain itself (Fig. 2e). For example, during persistent cell motion, the curvature-sensitive protein BAIAP2, which contains such a BAR domain, accumulates at curved membrane patches at the cell front, inducing the formation of lamellipodia [121]. Since BAR domains have a length of about 20 nm, the sensitivity of individual proteins to weakly curved surfaces is limited [124, 127]. However, membrane curvature can facilitate the oligomerization of proteins into extended curved structures, which are capable of sensing membrane curvature on length scales larger than that of the individual protein [128]. Other important examples for such joint curvature sensing are dynamin, which forms helical collars around the thin neck during budding in yeast [129, 130], and MreB, which assembles into filaments that orient along the highest membrane curvature [131, 132].

Furthermore, some proteins recognize membrane curvature via defects in membrane structure. This mechanism is well exemplified by proteins with so-called *ALPS motifs*. ALPS motifs do not have a defined structure in solution, but insert into lipid bilayers by folding into an α-helix[j]. It has been shown that ALPS motifs bind preferably to regions with low lipid packing density [133]. Such low-density packing can arise from membrane curvature, where one sheet of the lipid bilayer is stretched compared to a flat membrane. In experiments, ALPS motifs were found to bind strongly to liposomes with sufficiently strong positive curvature ($R < 50$ nm), and to weakly curved liposomes with a high concentration of conically shaped lipids [133]. Thus, curvature-dependent binding affinity can lead to predominant accumulation of proteins at curved membrane regions.

It has been reported that proteins that sense curvature can also deform the membrane: The helical structure of dynamin oligomers induces membrane curvature during scission of the yeast bud [129, 134, 135]. Proteins with BAR domains play a curvature-sensing role at low concentrations, but stabilize membrane curvature at high protein concentrations [123, 124]. Such a dual role can lead to a positive feedback loop, when a slightly curved membrane leads to the accumulation of curvature-sensitive proteins. These proteins, in turn, deform the membrane, leading to a further increase in the binding affinity. This has been proposed as a general mechanochemical mechanism for protein recruitment [7]. However, the formulation of a mechanistic theory for such curvature-regulating feedback loops remains an open and highly interesting challenge to this day.

Bin, Amphiphysin, and Rvs.

[j] α-helix – Prevalent helical-like protein structure, which is highly stable due to hydrogen bonds.

2. *Collective curvature sensing*

It has recently been shown that the distribution of proteins on the membrane and in the cytosol can depend on the cell geometry, even when the binding affinity of proteins is independent of membrane curvature [2, 3, 136]. The underlying mechanism is based on the aforementioned cytosolic gradients of proteins that switch between an inactive and an active state in the cytosol. As the required reactivation step is a non-equilibrium process that consumes energy, these gradients are maintained by a constant cycling of such proteins between the membrane and the cytosol, and therefore do not equilibrate by cytosolic diffusion. Since cytosolic gradients from opposing membrane points overlap at curved regions, one generally expects accumulation of inactive proteins in regions of high curvature (e.g., near the cell poles of elongated cells, including the rod-shaped *E. coli* [2], the *C. elegans* zygote [3], and *Bacillus subtilis* [128]) and a corresponding depletion of active proteins (Fig. 2f). Moreover, the effect of such a cytosolic gradient on the protein distributions in curved geometries depends in particular on the characteristic length ℓ of the cytosolic gradient relative to the local membrane curvature [2, 3].

While this explains where proteins are most likely to encounter the membrane, its effect on the ensuing protein pattern depends on the protein reaction kinetics. For proteins that exhibit a simple attachment-detachment dynamics with the membrane, the increased encounter probability leads directly to an increase in protein concentration at the poles, which is further enhanced if the protein autocatalytically promotes its own binding [2]. In contrast, if two proteins mutually inhibit each others binding, an increased encounter probability leads to the formation of an interface between two protein domains on the membrane [3].

IV. BIOCHEMICAL GUIDING CUES

For spatially homogeneous systems, several theoretical and experimental studies have identified biochemical circuits that are able to perform logic operations [138], generate pulses [139, 140], act as noise-reduction filters [141], or process biochemical signals in other ways [142–146]. Here the information from an input signal – typically encoded in the concentration of a protein – is processed and an output signal is generated.

In general, however, protein concentrations tend to be spatially inhomogeneous, so that a locally varying input can lead to a locally varying output protein concentration in the cell. In this way, an input pattern can serve as a template or *biochemical guiding cue* for the formation of an output protein pattern. Such biochemical guidance has been observed in many biological processes and over widely varying scales, ranging from tissue development [147, 148] to the positioning of the cell-division site [41, 79, 115, 149–152]. In all these

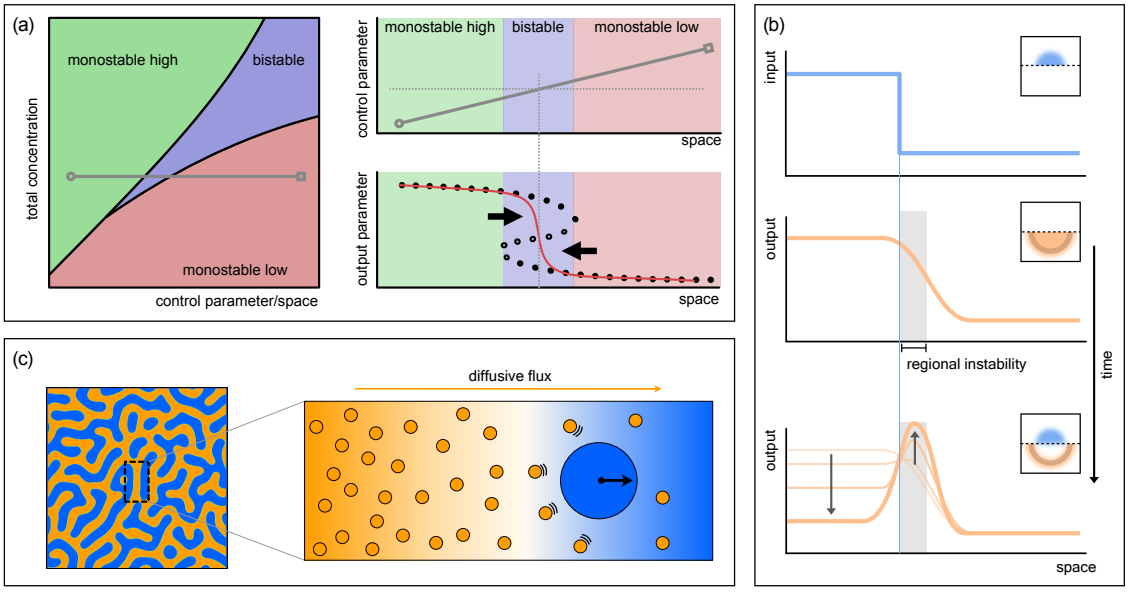

FIG. 3. **Principles of biochemical pattern guidance:** (a) Left: Characteristic bifurcation diagram for pattern-forming systems. For reaction kinetics where the concentration of the input protein is a control parameter, a spatially varying input protein concentration can serve as a map between space and varying reaction kinetics. Top right: an input protein concentration gradient corresponds to a cutline through the bifurcation diagram (gray line) laid out in space, which divides the cell into regions of distinct stability. Bottom right: for a system where the input concentration gradient connects two monostable regions via a bistable region, the resulting front pattern (red line) is pinned to a threshold concentration value of the input concentration. Fixed points of the protein reaction kinetics are indicated by filled (stable) and open (unstable) circles. (b) Edge detection: An input pattern (blue) spatially alters the reaction kinetics of the output protein, resulting in a regional instability of the output protein close to the input edge (gray filled area). This leads to a peak pattern of the output protein concentration (orange) that marks the position of the input edge. Insets show a possible realization of this edge-sensing process, leading to a ring around a template patch. The plots depict the concentration profiles along the black cutline. (c) Diffusiophoresis: Diffusive fluxes of pattern-forming proteins (carrier particles, shown in orange) are established at pattern interfaces. Carrier particles transport cargo particles (blue) via frictional interactions, resulting in a complementary pattern of cargo particles [137].

cases, the input patterns encode positional information, as each concentration marks a specific location or region in space [153]. In fact, there are several known instances in which protein patterns (input) control the formation of other patterns (output) [115, 154–157]. However, the physical mechanisms responsible for the processing of the positional information encoded in patterns, and the generation of a qualitatively different output pattern (e.g., gradient vs. step profile) are still largely unclear.

Such input/output relations are found, for example, in the polarity mechanism of budding yeast. Here, several so-called *landmark proteins* mark specific locations in the cell, such as the previous bud site. These landmark proteins (input) alter the kinetics of nucleotide exchange in the polarity factor Cdc42 (output), and thus contribute to the control of cell polarity in a symmetry-breaking manner [158, 159]. Another example is provided by the midcell localization machinery of *Caulobacter crescentus*. In these elongated cells, ParB-*parS* (input) complexes localized to the cell poles stimulate the ATP-dependent dimerization of MipZ (output), which results in the formation of a bipolar gradient of MipZ dimers with a minimum at midcell [114]. MipZ, in turn, inhibits the polymerization of FtsZ, which is a central component of the cell-division machinery. Thus, the bipolar MipZ gradient also acts as an input for the control and positioning of FtsZ (output) to midcell [160]. Such a hierarchy of pattern control through multiple stages of protein interaction is a common feature of many biochemical guidance mechanisms [94, 149, 159, 161].

In the following, we discuss some recent advances in this area, focusing on systems in which the concentration profile of an (input) protein is able to control the reaction kinetics of another (output) protein, such that one or more reaction rates become spatially inhomogeneous. This can result in an output protein pattern that is qualitatively different from the input pattern, which has been termed *spatial network computations* [162].

A. Spatially varying reaction kinetics

Since protein reaction kinetics can depend on the concentration of other proteins, a spatially varying input protein concentration can lead to locally varying reactive equilibria of the output protein. In particular, not only

can the protein concentration at each local reactive equilibrium be altered; also, the number and the stability of these equilibria can change in response to a varying input concentration (see Supplementary Information). Heuristically, this means that space itself serves as a control parameter[k] for the protein reaction kinetics. Hence, the input protein pattern encodes positional information.

The dynamics of the output protein depend crucially on its explicit biochemical interactions with the input proteins. For example, for a particular interaction between proteins, this can lead to bistability of the output protein over a limited range of input concentrations, as observed in starfish oocytes [94]. Due to the correspondence between input protein concentration and space, such a bistable parameter range maps to a region in space where the output protein reactions are bistable, which we refer to as *regional bistability*. In a similar way, a protein pattern can cause a pattern-forming instability in a specific spatial region, which has been termed *regional instability*[163, 164]. Thus, an input pattern can lead to a qualitatively different spatial concentration profile of the output protein, where the explicit output pattern strongly depends on the reaction kinetics (Fig. 3a). This fundamental property of protein interactions is likely to represent the mechanism that underlies many of the biochemically guided pattern-forming systems observed in experiments [156–160].

B. Wave localization by protein gradients

Biochemical trigger waves, consisting of a traveling front or pulse of biomolecule concentration, are a common means of long-ranged signal transmission in cells [105]. Prominent examples of such waves include calcium waves [165], the propagation of mitosis[l] [161] and apoptosis[m] [166] in *Xenopus* eggs, actin polymerization waves in *Dictyostelium* [167] and neutrophils [168], as well as intracellular signaling [169]. A key component of models for trigger waves, such as the FitzHugh-Nagumo model [170], are bistable reaction kinetics (see Supplementary Information). These bistable reaction kinetics, in addition to resulting in information transmission, allow trigger waves to serve as a readout for positional information encoded in other protein patterns.

To illustrate how spatially varying reactive equilibria allow proteins to read out this positional information, we now discuss how a protein gradient can lead to the localization of such a trigger wave, in particular a bistable front, to a specific position in the cell. We first consider a system with homogeneous bistable reaction kinetics forming a front pattern (see Supplementary Information). This front can propagate through the system at a speed and direction that depends on, among other factors, the concentration of the input protein [105, 171].

In the presence of an input pattern, the reaction kinetics are no longer homogeneous, so that a regional bistability can emerge. Since the front only propagates in a bistable parameter range, propagation is constrained to this regional bistability. In particular, since the direction of propagation depends on the input concentration, the front is pinned at a threshold input concentration (Fig. 3a) [105]. Due to the correspondence between input concentration and space, this means that the front is localized to a specific position within the regional bistability. Thus, the position of the front interface marks the location of the input threshold concentration, allowing the positional information encoded in the input pattern to be read out. Such a threshold-sensing mechanism has been proposed to play a role in the propagation of surface contraction waves during meiosis[n] in starfish oocytes [94] and during chemotaxis[o] in eukaryotes [172].

C. Edge-sensing and ring formation

Proteins also have been found to localize at the edges of spatial domains that exhibit a high concentration of other proteins or macromolecules. For example, during cellular wound healing, the Rho-GTPase Cdc42 and an associated GTPase regulator, Abr, accumulate locally to form two concentric rings [173]. Experimental evidence suggests that this structure is hierarchically organized, with the outer Cdc42 ring being dependent on the presence of an inner Abr zone. While it is not particularly surprising that a given spatial protein profile serves as a template for creating another protein profile with a similar shape, it is quite interesting that the downstream profile assumes a qualitatively different shape, with a peak localized right at the edge of the upstream profile (inner Abr ring, see insets in Fig. 3b). To account for such edge-sensing, a regional instability has been suggested [97, 164]. Here, the step-like Abr profile, acting as an input protein pattern, defines two spatial domains with qualitatively different reaction kinetics for Cdc42, which takes the role of the output protein. It was shown that the outer domain may effectively act as a stimulus that induces a lateral mass-redistribution instability in the inner domain, which leads to a concentration peak of the output protein at the template edge (Fig. 3b). Moreover, the formation of this output concentration ring can

[k] Control parameter – A parameter that alters the qualitative dynamics when it is changed, also referred to as a *bifurcation parameter* in nonlinear dynamics.

[l] Mitosis – Stage of the cell cycle during which chromosomes are segregated into the two daughter cells.

[m] Apoptosis – Cellular process leading to actively induced cell death.

[n] Meiosis – A type of cell division process that generates daughter cells that contain half as many chromosomes as the parent cell.

[o] Chemotaxis – Directed locomotion of cells along chemical gradients.

be controlled by both the magnitude of the input pattern step and the total amount of output protein. Thus, edge sensing is enabled by a regional mass-redistribution instability in a downstream protein pattern, which is itself triggered by an upstream protein pattern that acts as a step-like template.

Beyond the specific example discussed above, there are other biologically highly relevant processes that involve edge sensing. As in the case of wound healing, a ring of Rho forms around a patch of high Cdc42 concentration prior to polar body emission in *Xenopus* oocytes [174]. Another biological process in which protein templates appear to play an essential role is that of macropinocytosis, a form of endocytosis[P] associated with cell surface ruffling. Here, actin-recruiting proteins colocalize to high-density patches of PIP3 (a charged phospholipid) and a Ras-GTPase, forming a ring around the edge of the PIP3 domain, which in turn leads to the assembly of a conctractile actomyosin ring [175]. This whole process is invariably linked to the presence of PIP3 and Ras patches, suggesting that these biomolecules serve as a biochemical guiding cue for the actin-recruiting proteins. The specific physical mechanisms responsible for each of these edge-sensing processes have not yet been uncovered.

D. Tracking of moving patterns

In addition to varying in space, the input protein concentration can vary in time at a fixed location in the cell. Temporal changes of the input concentration can lead to sudden changes of the reactive equilibrium which, in turn, results in transient dynamics of the output concentration before the new reactive equilibrium is established – a phenomenon referred to as *excitability* in the field of nonlinear dynamics [14, 171]. Such transient dynamics can mark the position of local changes in the input concentration. For example, in the case of a traveling front pattern, the input concentration changes in time at a fixed position as the front passes by. Due to the transient output dynamics, this can lead to a traveling output concentration peak that closely follows the moving front. This has been observed in starfish oocytes, where a traveling front pattern leads to a moving concentration peak which, is ultimately responsible for the surface contraction waves observed during meiosis [94, 176, 177]. Similar observations have been made *in vitro* for an artificial cortex based on frog egg extracts [178].

E. Phoretic transport

A more intricate mechanism by which spatiotemporal protein patterns could serve as cues for the development of subsequent protein patterns are various types of phoretic transport processes. These are, in general, the result of an external field gradient acting on the protein [179, 180]. Examples include concentration gradients of carrier particles (*diffusiophoresis*) [137, 181], chemical potential gradients (*chemophoresis*) [182, 183], electric potential gradients (*electrophoresis*) [184], or temperature gradients (*thermophoresis*) [185], along which cargo can be transported. Thus, cargo particles can form a pattern guided by such gradients [179]. Notably, in phoretic transport mechanisms, energy is consumed to maintain the gradient, resulting in a flux of cargo particles. This is substantially different from other transport mechanisms such as active transport, where energy is consumed to fuel molecular motors that move cargo particles.

In the field of phoretic transport, research has long been focused on colloidal particles [179–181, 186]. Experimental evidence for phoretic transport in biological systems related to protein organisation and pattern formation has only recently been discovered [137, 182]. For example, *in-vitro* experiments have shown that diffusiophoresis can result in the spatial organization of DNA origami nanostructures in a concentration gradient of MinD [137]. Here, the Min proteins self-organize into a stationary pattern [187], resulting in diffusive fluxes at the domain edges (c.f. Fig. 3c). These diffusive fluxes are transferred to the DNA nanostructures via friction, leading to diffusiophoretic transport of the latter along the Min gradients. Thus, the movement of the DNA nanostructures mimics the movement of the Min proteins, resulting in the formation of an anti-correlated pattern of the DNA nanostructures. Such diffusiophretic transport has been suggested to play an important role for the distribution of large particles in cells in general [188].

In the context of plasmid segregation, chemophoresis has been suggested to drive the movement of plasmids on the nucleoid [182]. Here, ParA proteins on the nucleoid surface are thought to bind to large cargo, such as plasmids. Upon unbinding, ParA proteins are released from the nucleoid, resulting in a local depletion of ParA at the position of the cargo. The ParA concentration gradient at the edge of this depletion zone creates a chemical potential gradient for the cargo, which tends to bind more strongly at regions of high ParA concentration. Thus, the cargo moves along the chemical potential gradient away from the depletion zone [182, 183]. This chemophoretic movement is suggested to be sufficient to ensure a balanced distribution of plasmids on the nucleoid [182].

V. MECHANICAL GUIDING CUES

In addition to biochemical guiding and guidance by cell size and shape, also the mechanical properties of a cell can affect protein pattern formation by altering the transport and reaction kinetics of proteins.

Flows generally arise from stress gradients. In cells, such gradients can be generated via shape deformations

[P] Endocytosis – Cellular process that enables the uptake of biomolecules into the interior of the cell.

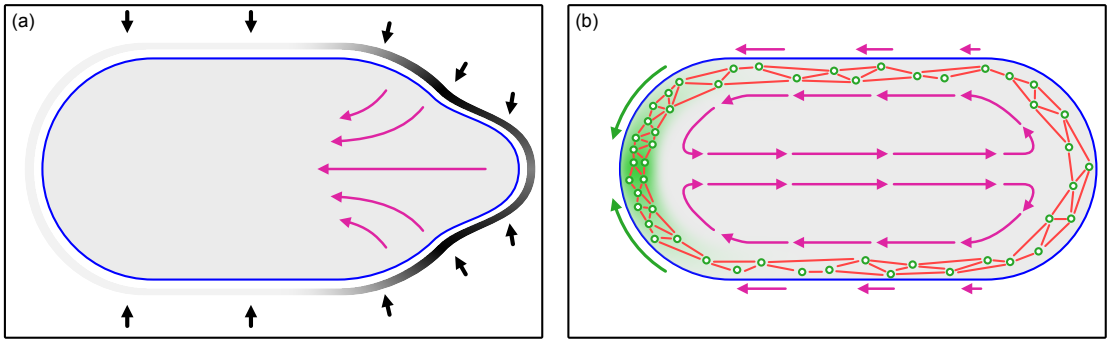

FIG. 4. **Principles of mechanical guidance by flow generation:** Stress gradients result in flows. (a) Heterogeneous cell deformations, as indicated by the grayscale outline, lead to pressure gradients in the cytosol, which in turn induce cytosolic flows towards regions of low pressure. (b) Heterogeneous actomyosin activity (green gradient; actin filaments shown in red, myosin shown as green circles), as observed in *C. elegans* zygotes [53], leads to polarized contractions of the actomyosin cortex and a flow of the entire cortex towards regions of high actomyosin activity. Hydrodynamic coupling results in cytosolic flows.

(Fig. 4a). For example, recent work has demonstrated the generation of flows in the cytoplasm due to shape deformations in starfish oocytes [95]. In these cells, a *surface contraction wave* travels across the membrane from the animal to the vegetal pole, which locally increases the pressure in the cytosol, and results in cytoplasmic flows along the oocyte's animal-vegetal axis[q]. Similar observations have been made for *Drosophila* embryos, where apical constrictions instead of surface contraction waves lead to cytoplasmic flows [189], and in *Drosophila* neuroblasts where cortical contractions induce flows in the cortex [190].

Next to deforming the cell shape, contractions of the actomyosin cortex can also lead to cortical flows, either as a consequence of spatially inhomogeneous actomyosin activity [4] or anisotropic cortical tension [191] (Fig. 4b). For example, cortical flows in *C. elegans* zygotes prior to PAR polarization arise due to nonuniform actomyosin activity [4]. Through hydrodynamic coupling, such flows may also induce cytoplasmic flows [53, 92].

How are protein patterns controlled by mechanical guiding cues? It has been suggested that a combination of pattern guidance by cortical flows and biochemical interactions may be ultimately responsible for the polarization mechanism in *C. elegans* zygotes [4]. Prior to polarization, a mechanical inhomogeneity in the cell cortex, induced by the symmetry-breaking introduction of a centrosome into the zygote, causes the cell cortex to contract asymmetrically. Here, the reduced actomyosin contractility at the posterior pole leads to anterior-directed cortical flow. Once symmetry is broken, the cortical flows and the associated anterior-directed cytoplasmic flows lead to a redistribution of PAR proteins, which in turn control and maintain the asymmetric actomyosin contractility of the cortex, thereby giving rise to a self-regulating polarization mechanism. These observations underline the key role of mechanical guiding cues in the process of protein pattern formation.

[q] Animal-vegetal axis – Symmetry axis in oocytes, along which the developmental activity varies, separating the cell into two distinct poles.

VI. UPCOMING CHALLENGES

In this review, we have focused on guidance mechanisms in model biological organisms that have been studied experimentally, and for which theoretical models exist. However, a much larger number of cellular processes rely on guiding cues and whose underlying biophysical mechanisms are still unknown. To conclude this review, we outline some promising recent developments in the field of protein pattern formation that build upon the recognition of the important role of guiding cues.

A. Robustness against guiding cues

Guiding cues can vary over time, as evidenced by cell size and shape, which change throughout the cell cycle. Moreover, these changes can affect the process of protein pattern formation in quite different ways: Protein patterns can either adapt to the changing guiding cues as discussed in this review, or they can be impervious to variations in geometric, mechanical, and biochemical factors. Pattern-forming mechanisms that are robust to changes in cell geometry or mechanics have recently been identified in various systems [94, 144], but a general understanding of robustness in pattern formation is still lacking. Future research on pattern formation mechanisms in living cells will reveal whether there are more examples where the formation of protein patterns adapts to be robust to the effects of cell mechanics and geometry.

B. Mechanochemical feedback loops

We discussed above how protein patterns can flexibly adjust to changes in the physical properties of cells. However, proteins can also actively modify the mechanical properties of the cell, resulting in a feedback loop between cell mechanics and protein patterns. Various theoretical studies showed that the coupling to cell mechanics in such mechanochemical feedback loops can lead to the formation of protein patterns [100, 192–197]. For example, coupling of a contractility-regulating chemical agent to an active fluid surface can result in shape deformations of axisymmetric surfaces, accompanied by polarization of the chemical agent [101]. This phenomenon shows similarities to the aforementioned self-reinforcing polarity mechanism of *C. elegans*, where cortical flows are created by asymmetric actomyosin activity [191]. In addition, a recent experimental study showed that the spatiotemporal patterning of the Min protein system can induce substantial shape deformations in GUVs[r] [198, 199]. This observation suggests a generic interplay between reaction-diffusion dynamics and membrane mechanics. We hypothesize that membrane properties, such as spontaneous curvature, may influence the kinetics of protein binding, and vice versa [7, 98, 102]. In combination with the hydrodynamic coupling of the cell membrane to the cortex and the cytosol, this can lead to a mutual feedback between the dynamics of protein patterns and cell shape.

A theoretical characterization of this two-way coupling between biochemical processes and cell mechanics is a promising avenue for future research [200]. Since such mechanochemical models need to account for protein reaction–diffusion dynamics as well as a dynamically varying three-dimensional cell shape, they are challenging to study both analytically and numerically [192, 196, 201, 202]. In future research, it will be important to further develop methods and, in particular, biologically realistic three-dimensional models, such that they can be compared to quantitative experimental data and contribute to the interpretation of experimental results in mechanochemical model systems.

Mechanochemical feedback loops are a special case of a general phenomenon that can be observed in many pattern-forming systems: may patterns in cells are not the result of a single guiding cue, but are the products of multiple interacting cues and processes [53, 75, 79, 203–205]. However, it is often difficult to separate all the processes involved in the robust formation of functional protein patterns in living cells, as the example of *C. elegans* polarisation shows [3, 8, 53, 93]. Recognizing and incorporating such interacting processes into the theoretical analysis of pattern-forming systems will therefore be a major task for future research on pattern formation.

[r] GUV – Giant unilamellar vesicle, an artificial spherical chamber bounded by a lipid bilayer that mimics the membrane of cells.

C. Perspectives for pattern guidance

At the conceptual level, we currently face three main challenges in the context of understanding the biophysical basis of pattern guidance. These relate to (i) progress in the study of fundamental aspects of processes in living systems far from thermal equilibrium, (ii) finding the right level of simplification for a given complex biological system, and (iii) improving both computational and experimental tools. In the long term, meeting these challenges will be vital to advancing our knowledge of pattern guidance, pattern formation, and information processing in biology in general.

1. *New frontiers in non-equilibrium physics*

Several interesting physics questions arise from the biological model systems we have discussed in this review. A central issue concerns how the dynamics of pattern-forming systems are mechanistically controlled by spatial and temporal gradients. These gradients lead to a variety of fascinating phenomena including information processing [147], templating [164], and hierarchies of different patterns [94]. Since these gradients can form for different physical quantities they can influence the formation of patterns in many ways. Among others, we have discussed spatially varying reaction kinetics which can lead to the localization of trigger waves in bistable media. But any gradient in an intensive thermodynamic variable, such as a chemical potential, can give rise to corresponding particle currents, as described by the laws of non-equilibrium thermodynamics [206]. Transport properties are also strongly influenced by spatial variations in kinetic coefficients such as diffusion constants. These processes lead to additional advection currents which we have not addressed in this review. Moreover, due to dynamic feedback between these particle currents and protein patterns, the gradients themselves may become part of the dynamics rather than acting solely as external guiding cues. This greatly expands the possibilities for future theoretical and experimental research on this topic.

2. *Levels of biological complexity*

Another crucial and actually quite general challenge is how to deal with the different levels of complexity in biological systems. For example, the full extents of interaction networks of proteins are generally unknown, and it is often unclear whether integrating all possible interaction pathways into a theoretical model is actually necessary to explain a particular phenomenon [207, 208]. Even in cases where networks are fully characterized, the information flow through the reaction network can be difficult to understand. Methods to analyse such information flows have been developed for well-mixed reaction

systems, such as the *modular response analysis* [209]. For spatially extended systems, where information is stored and processed by patterns, such methods have yet to be developed.

In addition, temporal regulatory mechanisms, such as cell-cycle-induced gene regulation, are often excluded from models of pattern forming system, even though the relevance of such regulatory mechanisms for pattern formation is not fully understood yet [140, 210]. Where such mechanisms are in place, global mass conservation – which is a cornerstone in many models of protein pattern formation – does not apply anymore, opening an avenue to additional concepts for pattern formation [104].

Avoiding the overfitting of models, and separating important components of interaction networks from irrelevant interactions (on the time scale of interest), are both difficult to achieve, and this presents major difficulties for theory and mathematical modeling. Ultimately, theoretical frameworks need to be developed that allow for a systematic coarse-graining that shows how the manifold components of a biological system can be reduced to its core elements. Such reductionism, at least for someone trained in physics, is the silver bullet to determining fundamental principles and improving our understanding.

3. *Finding the right level of geometric representation*

Similarly, the question of how theory should deal with the dimensionality and geometric form of biological systems needs careful consideration. For example, reducing the dimension of a specific system, e.g., to simplified one-dimensional models, may help to obtain an analytically more accessible representation. While such a simplification can be useful for gaining insight into the underlying dynamics and for guiding experiments, it may also obscure important aspects of pattern guidance. As pointed out in this review, certain phenomena, such as curvature sensing, only occur in realistic geometries and would therefore be erased in simplified one-dimensional models [2, 3]. In essence, the complexity of biological systems must be reduced in order to understand them better. However, the challenge for future models is to find the appropriate level of simplification without loss of crucial features.

4. *How to face the challenge of multiphysics problems*

In addition, many experimental results indicate that pattern formation, and pattern guidance in particular, are the result of a tight interplay between biochemical interactions, hydrodynamics of cellular substrates, and membrane mechanics [4, 121, 191, 211]. While numerous theoretical advances have been made in each of these areas (e.g., reaction-diffusion dynamics and non-equilibrium physics), there is so far no unified theoretical and computational approach that would allow a thorough analysis of such *multiphysics* problems. Therefore, in order to gain a deeper understanding of pattern guidance in realistic biological systems, a comprehensive theoretical framework that allows the study of the interplay between these different fields of physics must be developed.

5. *Improving experimental and computational methods*

Another roadblock that impedes progress is the limited availability of experimental, analytical and computational tools. On the experimental side, the current challenges, to name just a few examples, are to improve the spatial and temporal resolution of the quantities of interest (e.g., proteins) and to access quantitative information such as local densities, reaction rates, transport properties, and forces. In addition, conducting experiments under well controlled conditions, where only one or a few parameters are adjusted at a time, is often difficult owing to the associated technical demands, as well as the inherent complexity of biological systems. Future progress in this area would greatly enhance our ability to make more detailed comparisons with theory.

Concerning computational approaches, the simulation of multiphysics problems presents a major obstacle. In particular, the numerical implementation of bulk-boundary coupled reaction-diffusion systems in combination with hydrodynamics and deformable, time-evolving membranes, is an important task for future research. The primary difficulties here lie in the development of an efficient and stable numerical approach that allows one to solve multiphysics problems in which the numerical domain itself is part of the solution. In the case of reaction-diffusion dynamics on dynamic membranes without coupling to a bulk volume, this can be addressed by deriving the time-evolution of the surface from the (normal) variation of a free energy functional that describes the mechanical properties of the membrane [18, 98–102]. However, this does not account for dynamics in the bulk, such as intracellular flows and bulk-boundary coupling of protein reactions. Promising approaches that can cope with these problems in the future are the *level-set* and the *phase-field* methods [212, 213]. These strategies allow one to segregate the computational domain into different regions (e.g. interior and exterior of a cell), where the interface between these regions corresponds to a (smooth) boundary (that could represent, e.g., the cell membrane). In this way, one can define and solve a coupled set of partial differential equations between different regions, including the interface, and at the same time allow these regions to evolve over time by solving the level-set or phase-field equation. Most notably, the phase-field method is being used in current research to model cell migration [214], with applications to reaction-diffusion systems arising only recently [215–218]. At the same time, new methods are being developed [219]. In the long run, it will be a challenge to not only model a deformable domain, but also incorporate the biochemical

and mechanical details of membranes in computational approaches.

VII. SUMMARY

We have presented a summary of the recent progress in understanding the biophysical mechanisms underlying the guidance and control of protein patterns. In essence, one distinguishes between geometric, biochemical, and mechanical guidance cues.

First, geometric effects can control protein pattern formation, with the cell size affecting the bulk-boundary ratio and the relative penetration depth of cytosolic concentration gradients. In addition, pattern formation can be limited by finite-size effects. Geometric effects imposed by the cell shape – such as the local membrane curvature that controls the distribution of curvature-sensing proteins, and the overall cell shape, which affects the curvature-dependent probability that a protein will encounter the membrane – can also serve as guiding cues. Second, we reviewed how protein patterns can guide other protein patterns via biochemical interactions. Spatial information that is encoded in one protein pattern can be interpreted through protein-protein interactions, thereby transforming the spatial coordinate into a control parameter for downstream protein reactions. This gives rise to a wide range of different pattern guidance mechanisms, including threshold localization, edge-sensing, and phoretic transport. Third, mechanical guiding cues, among which flow and stress gradients are of particular relevance, can affect protein pattern formation. Finally, we outlined open questions and the associated experimental, theoretical, and numerical challenges that need to be faced to improve our understanding of guided pattern formation.

We believe that the mechanisms presented in this review can be applied to a wide range of processes in which spatial information is processed, such as cell migration, cytokinesis, and morphogenesis. To advance our understanding of the physical basis and biological relevance of pattern formation, further research on the concepts of pattern guidance will be required, as well as more refined methods to explain experimental observations. Taken together, this could ultimately contribute to the characterization of general biophysical principles of spatial information processing in living cells.

SUPPLEMENTARY INFORMATION

A. Methods of analysing pattern formation

1. Reactive equilibrium

Chemical reactions convert reactants to products and vice versa, thus resulting in fluxes. An equilibrium state is reached if the sum of all fluxes equals zero, which determines the equilibrium concentrations of constituents. This equilibrium state is commonly referred to as a *reactive equilibrium*, and is generally distinct from a thermodynamic chemical equilibrium because fluxes can originate from non-equilibrium processes (broken detailed balance) [220]. One example are NTPase cycles, in which proteins detach from the membrane and must undergo a conformational change before they can re-attach. The reactive equilibrium in this case is given by a balance between reactive fluxes onto and off the membrane.

Mathematically, the reaction kinetics of a well-mixed system are expressed by ordinary differential equations (ODEs)

$$\partial_t \mathbf{u}(t) = \mathbf{f}(\mathbf{u})\,, \tag{5}$$

where $\mathbf{f}(\mathbf{u})$ contains the (nonlinear) interactions between the components of $\mathbf{u}$ and therefore corresponds to the sum of individual reactive fluxes. Formally, a reactive equilibrium conforms to the steady state solution $\partial_t \mathbf{u} = 0$ of Eq. (5) and is termed the *fixed point* of the ODE system, i.e. $\mathbf{f}(\mathbf{u}^*) = 0$ for steady state solutions $\mathbf{u}^*$. In general, the long-term dynamics are governed by *attractors* of the nonlinear system, whose properties are the subject of the field of dynamical systems theory [13].

2. Phase space analysis

To assess the qualitative dynamics of nonlinear dynamics systems, one must often resort to geometric *phase space* analysis (Fig. 5b). In phase space, each point corresponds to a specific state of the system, with the *phase space flow* tracing out the time evolution of the system. Next to the flow lines, fixed points ($\mathbf{f}(\mathbf{u}^*) = 0$) and nullclines ($f_i(\mathbf{u}) = 0$) are characteristic features which reflect the topology of phase space. In particular, this representation allows one to identify important features of the system, such as steady states or limit cycles.

As a characteristic example, consider the phase space diagram shown in Fig. 5b, for a two-component system whose dynamics are given by $\partial_t u_1 = -u_1 + u_1^2 u_2$ and $\partial_t u_2 = u_1 - u_2$. Intersections of the nullclines correspond to fixed points, whose stability can be determined by visualizing the phase space flow. The system at hand possesses one stable fixed point and one saddle fixed point. Given a specific initial state, the time evolution of this state can be determined by following the flow line, which provides qualitative information about the system's dynamics.

3. Dispersion relation

In spatially extended systems, patterns typically form when a (spatially homogeneous) steady state is unstable against random spatial perturbations. The formal way to

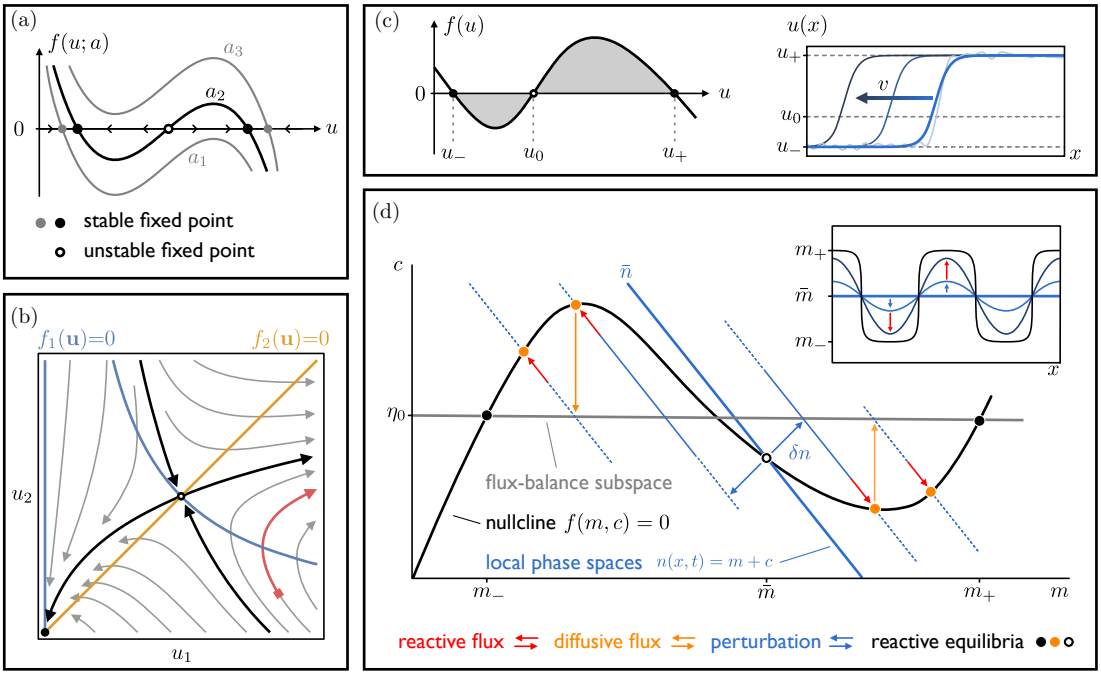

FIG. 5. **Geometric analysis of nonlinear dynamics:** (a) The number and stability of reactive equilibria (fixed points) depends, in general, on the reaction kinetics $f(u;a)$, where a is a control parameter. (b) Characteristic phase space diagram showing the system's fixed points, which can be derived from the nullclines (blue, orange); the separatrices (black) divide the phase space into qualitatively distinct areas. The time evolution of a given initial state (red square) is represented by the flow line associated with this state (red line). (c) Front propagation. Left: The reaction kinetics $f(u)$ determine the speed v of the wave. Right: For noisy initial conditions interpolating between the two stable plateaus $u_\pm$, the reaction kinetics first lead to a smoothening of the perturbation and then result in directed front propagation at velocity v. (d) Illustration of the mass-redistribution instability in phase-space for the biologically relevant limit $D_c \gg D_m$. The homogeneous steady state (black open circle) is determined from the intersection between the local phase space of the total average mass $\bar{n}$ (thick blue line) and the reactive nullcline $f(m,c)=0$ (thick black line). A spatial perturbation δn around this homogeneous state causes spatial gradients of the local total density in real space (inset top right). In phase space, the perturbation is represented by local phase spaces (thin blue lines) that contain masses that differ from the homogeneous state, and therefore lead to reactive fluxes (red arrows) towards the reactive equilibria (orange filled circles). This leads to a growing inhomogeneous density distribution in real space, which is further amplified by diffusive fluxes (orange arrows). Note that, since cytosolic diffusion is much faster than membrane diffusion $D_c \gg D_m$, diffusive fluxes must point along the vertical direction. The steady state density distribution in real space is represented by the flux-balance subspace in phase space (thick gray line) [163]. The constant η_0 determines the vertical position of the flux-balance subspace in phase space and can be interpreted as the (spatial) average cytosolic density.

probe for instabilities is to perform a linear stability analysis: One first expands spatial perturbations in normal modes and then linearizes the dynamics around a spatially homogeneous steady state $\mathbf{u}^*$. From the linearized system, one can determine the *dispersion relation* $\sigma(q_n)$, which relates the growth rate σ of perturbations to their respective mode number q_n. A typical dispersion relation is shown in Fig. 2d. Positive values of the growth rate indicate that spatial perturbations are amplified and grow exponentially. Since the critical mode q_c with the highest growth rate is expected to dominate near onset, this unstable mode sets the characteristic wavelength of the initial pattern. However, in general, the dispersion relation only informs about the characteristic length scale of the pattern in the vicinity of the homogeneous steady state [1]; the dominant length scale of the final pattern can be quite different.

B. Nonlinear feedback in protein pattern formation

1. *Bistability and propagation of bistable fronts*

Feedback loops are ubiquitous in biological systems and essential for many cellular processes [105, 110, 142]. For instance, the calcium waves that follow fertilization of an egg are the result of a positive feedback loop in which cytosolic calcium promotes the flow of additional calcium into the cytoplasm [105]. In general, feedback loops lead to nonlinear dynamics that exhibit multiple (linearly stable) reactive equilibria [221]. A common case is bistability, where the dynamics $\partial_t u = f(u)$ has three reactive equilibria, two of which are (linearly) stable ($u_\pm$) and one of which is (linearly) unstable (u_0). Consider a spatially extended bistable system with spatially uniform reaction kinetics $f(u)$, described by the reaction-diffusion

equation

$$\partial_t u(x,t) = D\partial_x^2 u(x,t) + f(u(x,t))\,. \tag{6}$$

In such a system, a front-like profile, where an interface connects two plateaus at the two linearly stable fixed points u_- and u_+ (Fig. 5c), will propagate [106]: one plateau invades the other with a constant velocity $v \sim -\int_{u_-}^{u_+} \mathrm{d}u\, f(u)$. These fronts will come to a halt only for a certain choice of parameters, namely when the areas enclosed by $f(u)$ in the intervals $[u_-, u_0]$ and $[u_0, u_+]$ are equal [16].

2. *Mass-redistribution instability*

A general design feature of biochemical networks underlying protein self-assembly is that their dynamics (approximately) preserve the mass of each protein species; i.e., on the time scale of pattern formation, both protein production and protein degradation can be neglected. Some key features of the patterning dynamics can already be seen with a two-component, mass-conserving system consisting of a cytosolic (c) and a membrane (m) species in one spatial dimension [16, 163]:

$$\partial_t m(x,t) = D_m \partial_x^2 m + f(m,c), \tag{7a}$$
$$\partial_t c(x,t) = D_c \partial_x^2 c - f(m,c). \tag{7b}$$

It is instructive to consider the system's dynamics in (m,c) phase space. The *reactive nullcline* ($f(m,c)=0$) typically shows a N-shape. Since the reaction kinetics are mass-conserving, reactive flows tend to remain within the corresponding local phase spaces ($n(x,t) = m + c$), and point towards the reactive equilibria determined by the intersection points of these local phase spaces with the reactive nullcline [163]. Now consider a homogeneous steady state $\bar{n}$ in phase space that intersects the nullcline in a region of negative slope. Spatial perturbations δn around the homogeneous steady state lead to a shift of the local reactive equilibria. Due to the resulting reactive currents, an upward shift δn in total density leads to a decrease in cytosolic density and vice versa (Fig. 5d). This gives rise to cytosolic concentration gradients, which in turn lead to diffusive fluxes, creating a positive feedback loop. Eventually, a steady-state pattern is reached when the diffusion currents at the membrane and in the cytosol balance out. In phase space, the steady state is represented by a *flux-balance subspace* given by $\widetilde{c}(x) + D_m/D_c\, \widetilde{m}(x) = \eta_0$, where η_0 is a constant. In summary, this pattern formation mechanism involves an intricate coupling between mass-redistribution and local reaction kinetics [16, 163].

[1] Alan Mathison Turing. The chemical basis of morphogenesis. *Philosophical Transactions of the Royal Society of London. Series B, Biological Sciences*, 237(641):37–72, 1952.

[2] Dominik Thalmeier, Jacob Halatek, and Erwin Frey. Geometry-induced protein pattern formation. *Proceedings of the National Academy of Sciences*, 113(3):548–553, 2016.

[3] Raphaela Geßele, Jacob Halatek, Laeschkir Würthner, and Erwin Frey. Geometric cues stabilise long-axis polarisation of PAR protein patterns in C. elegans. *Nature Communications*, 11(1):539, 2020.

[4] Peter Gross, K. Vijay Kumar, Nathan W. Goehring, Justin S. Bois, Carsten Hoege, Frank Jülicher, and Stephan W. Grill. Guiding self-organized pattern formation in cell polarity establishment. *Nature Physics*, 15(3):293–300, 2019.

[5] Armin Haupt and Nicolas Minc. How cells sense their own shape – mechanisms to probe cell geometry and their implications in cellular organization and function. *J Cell Sci*, 131(6):jcs214015, 2018.

[6] James B. Moseley and Paul Nurse. Cell Division Intersects with Cell Geometry. *Cell*, 142(2):189–193, 2010.

[7] Andriy Goychuk and Erwin Frey. Protein recruitment through indirect mechanochemical interactions. *Physical Review Letters*, 123(17):178101, 2019.

[8] Lars Hubatsch, Florent Peglion, Jacob D Reich, Nelio T L Rodrigues, Nisha Hirani, Rukshala Illukkumbura, and Nathan W Goehring. A cell-size threshold limits cell polarity and asymmetric division potential. *Nature Physics*, 15(10):1078–1085, 2019.

[9] Karen E Kasza, Amy C Rowat, Jiayu Liu, Thomas E Angelini, Clifford P Brangwynne, Gijsje H Koenderink, and David A Weitz. The cell as a material. *Current Opinion in Cell Biology*, 19(1):101–107, 2007.

[10] Thomas Lecuit and Pierre-François Lenne. Cell surface mechanics and the control of cell shape, tissue patterns and morphogenesis. *Nature Reviews Molecular Cell Biology*, 8(8):633–644, 2007.

[11] Claudia Tanja Mierke. Cellular Mechanics and Biophysics, Structure and Function of Basic Cellular Components Regulating Cell Mechanics. *Biological and Medical Physics, Biomedical Engineering*, 2020.

[12] Clotilde Cadart, Larisa Venkova, Pierre Recho, Marco Cosentino Lagomarsino, and Matthieu Piel. The physics of cell-size regulation across timescales. *Nature Physics*, 15(10):993–1004, 2019.

[13] Steven H Strogatz. *Nonlinear Dynamics and Chaos: With Applications to Physics, Biology, Chemistry and Engineering*. Perseus Books, 1994.

[14] Michael Cross and Henry Greenside. *Pattern Formation and Dynamics in Nonequilibrium Systems*. Cambridge University Press, 2009.

[15] Rashmi C Desai and Raymond Kapral. *Dynamics of Self-Organized and Self-Assembled Structures*. Cambridge University Press, 3 2009.

[16] Erwin Frey and Fridtjof Brauns. Self-organisation of Protein Patterns. *arXiv*, 2020.

[17] Alan R. Champneys, Fahad Al Saadi, Victor F. Breña–Medina, Verônica A. Grieneisen, Athanasius F.M. Marée, Nicolas Verschueren, and Bert Wuyts. Bistability, wave pinning and localisation in natural reaction–diffusion systems. *Physica D: Nonlinear Phenomena*, 416:132735, 2021.

[18] Haleh Alimohamadi and Padmini Rangamani. Modeling Membrane Curvature Generation due to Membrane–Protein Interactions. *Biomolecules*, 8(4):120, 2018.

[19] L. Shapiro, H. H. McAdams, and R. Losick. Why and How Bacteria Localize Proteins. *Science*, 326(5957):1225–1228, 2009.

[20] Joe Lutkenhaus. The ParA/MinD family puts things in their place. *Trends in Microbiology*, 20(9):411–418, 2012.

[21] Simon Kretschmer, Leon Harrington, and Petra Schwille. Reverse and forward engineering of protein pattern formation. *Philosophical Transactions of the Royal Society B: Biological Sciences*, 373(1747):20170104, 2018.

[22] Leah Edelstein-Keshet, William R. Holmes, Mark Zajac, and Meghan Dutot. From simple to detailed models for cell polarization. *Philosophical Transactions of the Royal Society B: Biological Sciences*, 368(1629):20130003, 2013.

[23] Andrew B. Goryachev and Marcin Leda. Compete or Coexist? Why the Same Mechanisms of Symmetry Breaking Can Yield Distinct Outcomes. *Cells*, 9(9):2011, 2020.

[24] Wolfram Möbius and Liedewij Laan. Physical and Mathematical Modeling in Experimental Papers. *Cell*, 163(7):1577–1583, 2015.

[25] Gert Bange and Irmgard Sinning. SIMIBI twins in protein targeting and localization. *Nature Structural & Molecular Biology*, 20(7):776–780, 2013.

[26] Anthony G. Vecchiarelli, Kiyoshi Mizuuchi, and Barbara E. Funnell. Surfing biological surfaces: exploiting the nucleoid for partition and transport in bacteria. *Molecular Microbiology*, 86(3):513–523, 2012.

[27] Sandra Iden and John G. Collard. Crosstalk between small GTPases and polarity proteins in cell polarization. *Nature Reviews Molecular Cell Biology*, 9(11):846–859, 2008.

[28] Sandrine Etienne-Manneville. Cdc42 - the centre of polarity. *Journal of Cell Science*, 117(8):1291–1300, 2004.

[29] Pilar Perez and Sergio A Rincón. Rho GTPases: regulation of cell polarity and growth in yeasts. *Biochemical Journal*, 426(3):243–253, 2010.

[30] G M Bokoch, B P Bohl, and T H Chuang. Guanine nucleotide exchange regulates membrane translocation of Rac/Rho GTP-binding proteins. *Journal of Biological Chemistry*, 269(50):31674–31679, 1994.

[31] Jeffrey A. Ubersax and James E. Ferrell Jr. Mechanisms of specificity in protein phosphorylation. *Nature Reviews Molecular Cell Biology*, 8(7):530–541, 2007.

[32] Javier E. Irazoqui, Amy S. Gladfelter, and Daniel J. Lew. Scaffold-mediated symmetry breaking by Cdc42p. *Nature Cell Biology*, 5(12):1062–1070, 2003.

[33] Chun-Chen Kuo, Natasha S. Savage, Hsin Chen, Chi-Fang Wu, Trevin R. Zyla, and Daniel J. Lew. Inhibitory GEF Phosphorylation Provides Negative Feedback in the Yeast Polarity Circuit. *Current Biology*, 24(7):753–759, 2014.

[34] Carsten Hoege and Anthony A Hyman. Principles of PAR polarity in Caenorhabditis elegans embryos. *Nature Reviews Molecular Cell Biology*, 14(5):315–322, 2013.

[35] Bruce Alberts, Alexander D Johnson, Julian Lewis, David Morgan, Martin Raff, Keith Roberts, and Peter Walter. *Molecular Biology of the Cell*. Garland Science, New York, 4 edition, 2002.

[36] Manuel Osorio-Valeriano, Florian Altegoer, Wieland Steinchen, Svenja Urban, Ying Liu, Gert Bange, and Martin Thanbichler. ParB-type DNA Segregation Proteins Are CTP-Dependent Molecular Switches. *Cell*, 179(7):1512–1524.e15, 2019.

[37] Laura L. Lackner, David M. Raskin, and Piet A. J. de Boer. ATP-Dependent Interactions between Escherichia coli Min Proteins and the Phospholipid Membrane In Vitro. *Journal of Bacteriology*, 185(3):735–749, 2003.

[38] Nathan W. Goehring, Carsten Hoege, Stephan W. Grill, and Anthony A. Hyman. PAR proteins diffuse freely across the anterior–posterior boundary in polarized C. elegans embryos. *Journal of Cell Biology*, 193(3):583–594, 2011.

[39] François B Robin, William M McFadden, Baixue Yao, and Edwin M Munro. Single-molecule analysis of cell surface dynamics in Caenorhabditis elegans embryos. *Nature Methods*, 11(6):677–682, 2014.

[40] Andrew B Goryachev and Marcin Leda. Many roads to symmetry breaking: molecular mechanisms and theoretical models of yeast cell polarity. *Molecular Biology of the Cell*, 28(3):370–380, 2017.

[41] Beatrice Ramm, Tamara Heermann, and Petra Schwille. The E. coli MinCDE system in the regulation of protein patterns and gradients. *Cellular and Molecular Life Sciences*, 76(21):4245–4273, 2019.

[42] J. Halatek, F. Brauns, and E. Frey. Self-organization principles of intracellular pattern formation. *Philosophical Transactions of the Royal Society B: Biological Sciences*, 373(1747):20170107, 2018.

[43] Andrew B. Goryachev and Marcin Leda. Cell Polarity: Spot-On Cdc42 Polarization Achieved on Demand. *Current Biology*, 27(16):R810–R812, 2017.

[44] Tamara Heermann, Frederik Steiert, Beatrice Ramm, Nikolas Hundt, and Petra Schwille. Mass-sensitive particle tracking to elucidate the membrane-associated MinDE reaction cycle. *Nature Methods*, 18(10):1239–1246, 2021.

[45] Zonglin Hu and Joe Lutkenhaus. Topological Regulation of Cell Division in E. coli Spatiotemporal Oscillation of MinD Requires Stimulation of Its ATPase by MinE and Phospholipid. *Molecular Cell*, 7(6):1337–1343, 2001.

[46] Atsushi Miyagi, Beatrice Ramm, Petra Schwille, and Simon Scheuring. High-Speed Atomic Force Microscopy Reveals the Inner Workings of the MinDE Protein Oscillator. *Nano Letters*, 18(1):288–296, 2018.

[47] Jacob Halatek and Erwin Frey. Highly Canalized MinD Transfer and MinE Sequestration Explain the Origin of Robust MinCDE-Protein Dynamics. *Cell Reports*, 1(6):741–752, 2012.

[48] Audrey S. Howell, Meng Jin, Chi-Fang Wu, Trevin R. Zyla, Timothy C. Elston, and Daniel J. Lew. Negative Feedback Enhances Robustness in the Yeast Polarity

Establishment Circuit. *Cell*, 149(2):322–333, 2012.

[49] Fridtjof Brauns, Leila M. Iñigo de la Cruz, Werner K.-G. Daalman, Ilse de Bruin, Jacob Halatek, Liedewij Laan, and Erwin Frey. Adaptability and evolution of the cell polarization machinery in budding yeast. *bioRxiv*, page 2020.09.09.290510, 2020.

[50] Fumio Motegi, Seth Zonies, Yingsong Hao, Adrian A. Cuenca, Erik Griffin, and Geraldine Seydoux. Microtubules induce self-organization of polarized PAR domains in Caenorhabditis elegans zygotes. *Nature Cell Biology*, 13(11):1361–1367, 2011.

[51] Edwin Munro, Jeremy Nance, and James R Priess. Cortical Flows Powered by Asymmetrical Contraction Transport PAR Proteins to Establish and Maintain Anterior-Posterior Polarity in the Early C. elegans Embryo. *Developmental Cell*, 7(3):413–424, 2004.

[52] Yingsong Hao, Lynn Boyd, and Geraldine Seydoux. Stabilization of Cell Polarity by the C. elegans RING Protein PAR-2. *Developmental Cell*, 10(2):199–208, 2006.

[53] Alicia G Gubieda, John R Packer, Iolo Squires, Jack Martin, and Josana Rodriguez. Going with the flow: insights from Caenorhabditis elegans zygote polarization. *Philosophical Transactions of the Royal Society B: Biological Sciences*, 375(1809):20190555, 2020.

[54] Henri Poincaré. *Periodic and asymptotic solutions*, volume 1 of *New Methods of Celestial Mechanics*. American Institute of Physics, New York, 1993.

[55] E. Frey and K. Kroy. Brownian motion: a paradigm of soft matter and biological physics. *Annalen der Physik*, 14(1-3):20–50, 2005.

[56] P G Saffman and M Delbrück. Brownian motion in biological membranes. *Proceedings of the National Academy of Sciences*, 72(8):3111–3113, 1975.

[57] Eugene P. Petrov and Petra Schwille. Translational Diffusion in Lipid Membranes beyond the Saffman-Delbrück Approximation. *Biophysical Journal*, 94(5):L41–L43, 2008.

[58] Anamika Agrawal, Zubenelgenubi C. Scott, and Elena F. Koslover. Morphology and Transport in Eukaryotic Cells. *Annual Review of Biophysics*, 51(1):1–20, 2022.

[59] Felix Höfling and Thomas Franosch. Anomalous transport in the crowded world of biological cells. *Reports on Progress in Physics*, 76(4):046602, 2013.

[60] G Meacci, J Ries, E Fischer-Friedrich, N Kahya, P Schwille, and K Kruse. Mobility of Min-proteins in Escherichia coli measured by fluorescence correlation spectroscopy. *Physical Biology*, 3(4):255, 2006.

[61] Ronald D Vale. The Molecular Motor Toolbox for Intracellular Transport. *Cell*, 112(4):467–480, 2003.

[62] Manfred Schliwa and Günther Woehlke. Molecular motors. *Nature*, 422(6933):759–765, 2003.

[63] Anatoly B. Kolomeisky. *Motor Proteins and Molecular Motors*. CRC Press, Boca Raton, 2015.

[64] Himanshu Pandey, Emanuel Reithmann, Alina Goldstein-Levitin, Jawdat Al-Bassam, Erwin Frey, and Larisa Gheber. Drag-induced directionality switching of kinesin-5 Cin8 revealed by cluster-motility analysis. *Science Advances*, 7(6):eabc1687, 2021.

[65] Günther Woehlke and Manfred Schliwa. Walking on two heads: the many talents of kinesin. *Nature Reviews Molecular Cell Biology*, 1(1):50–58, 2000.

[66] Yui Jin, Azmiri Sultana, Pallavi Gandhi, Edward Franklin, Susan Hamamoto, Amir R. Khan, Mary Munson, Randy Schekman, and Lois S. Weisman. Myosin V Transports Secretory Vesicles via a Rab GTPase Cascade and Interaction with the Exocyst Complex. *Developmental Cell*, 21(6):1156–1170, 2011.

[67] Marie Evangelista, David Pruyne, David C. Amberg, Charles Boone, and Anthony Bretscher. Formins direct Arp2/3-independent actin filament assembly to polarize cell growth in yeast. *Nature Cell Biology*, 4(1):32–41, 2002.

[68] Alex Mogilner and George Oster. Force Generation by Actin Polymerization II: The Elastic Ratchet and Tethered Filaments. *Biophysical Journal*, 84(3):1591–1605, 2003.

[69] Arshad Desai and Timothy J. Mitchison. Microtubule Polymerization Dynamics. *Annual Review of Cell and Developmental Biology*, 13(1):83–117, 1997.

[70] Jesse Stricker, Paul Maddox, E. D. Salmon, and Harold P. Erickson. Rapid assembly dynamics of the Escherichia coli FtsZ-ring demonstrated by fluorescence recovery after photobleaching. *Proceedings of the National Academy of Sciences*, 99(5):3171–3175, 2002.

[71] Martin Loose and Timothy J. Mitchison. The bacterial cell division proteins FtsA and FtsZ self-organize into dynamic cytoskeletal patterns. *Nature Cell Biology*, 16(1):38–46, 2014.

[72] Alexandre W. Bisson-Filho, Yen-Pang Hsu, Georgia R. Squyres, Erkin Kuru, Fabai Wu, Calum Jukes, Yingjie Sun, Cees Dekker, Seamus Holden, Michael S. VanNieuwenhze, Yves V. Brun, and Ethan C. Garner. Treadmilling by FtsZ filaments drives peptidoglycan synthesis and bacterial cell division. *Science*, 355(6326):739–743, 2017.

[73] Matthias Krause and Alexis Gautreau. Steering cell migration: lamellipodium dynamics and the regulation of directional persistence. *Nature Reviews Molecular Cell Biology*, 15(9):577–590, 2014.

[74] Hilary A Snaith, Itaru Samejima, and Kenneth E Sawin. Multistep and multimode cortical anchoring of tea1p at cell tips in fission yeast. *The EMBO Journal*, 24(21):3690–3699, 2005.

[75] Nicolas Minc, Scott V. Bratman, Roshni Basu, and Fred Chang. Establishing New Sites of Polarization by Microtubules. *Current Biology*, 19(2):83–94, 2009.

[76] Arne Gennerich and Ronald D Vale. Walking the walk: how kinesin and dynein coordinate their steps. *Current Opinion in Cell Biology*, 21(1):59–67, 2009.

[77] George M. Langford. Myosin-V, a Versatile Motor for Short-Range Vesicle Transport. *Traffic*, 3(12):859–865, 2002.

[78] Juan Mata and Paul Nurse. tea1 and the Microtubular Cytoskeleton Are Important for Generating Global Spatial Order within the Fission Yeast Cell. *Cell*, 89(6):939–949, 1997.

[79] Jian-geng Chiou, Mohan K. Balasubramanian, and Daniel J. Lew. Cell Polarity in Yeast. *Annual Review of Cell and Developmental Biology*, 33(1):1–25, 2016.

[80] Stephen M. Huisman and Damian Brunner. Cell polarity in fission yeast: A matter of confining, positioning, and switching growth zones. *Seminars in Cell & Developmental Biology*, 22(8):799–805, 2011.

[81] Hisashi Tatebe, Koichi Shimada, Satoru Uzawa, Susumu Morigasaki, and Kazuhiro Shiozaki. Wsh3/Tea4 Is a Novel Cell-End Factor Essential for Bipolar Distribution of Tea1 and Protects Cell

Polarity under Environmental Stress in S. pombe. *Current Biology*, 15(11):1006–1015, 2005.

[82] Heidi Browning, Jacqueline Hayles, Juan Mata, Lauren Aveline, Paul Nurse, and J. Richard McIntosh. Tea2p Is a Kinesin-like Protein Required to Generate Polarized Growth in Fission Yeast. *The Journal of Cell Biology*, 151(1):15–28, 2000.

[83] Kim J. A. Vendel, Sophie Tschirpke, Fayezeh Shamsi, Marileen Dogterom, and Liedewij Laan. Minimal in vitro systems shed light on cell polarity. *J Cell Sci*, 132(4):jcs217554, 2019.

[84] Ye Dee Tay, Marcin Leda, Andrew B. Goryachev, and Kenneth E. Sawin. Local and global Cdc42 guanine nucleotide exchange factors for fission yeast cell polarity are coordinated by microtubules and the Tea1–Tea4–Pom1 axis. *Journal of Cell Science*, 131(14):jcs216580, 2018.

[85] Raymond E. Goldstein and Jan-Willem van de Meent. A physical perspective on cytoplasmic streaming. *Interface Focus*, 5(4):20150030, 2015.

[86] Anthony G. Vecchiarelli, Min Li, Michiyo Mizuuchi, and Kiyoshi Mizuuchi. Differential affinities of MinD and MinE to anionic phospholipid influence Min patterning dynamics in vitro. *Molecular Microbiology*, 93(3):453–463, 2014.

[87] Veneta Gerganova, Iker Lamas, David M. Rutkowski, Aleksandar Vještica, Daniela Gallo Castro, Vincent Vincenzetti, Dimitrios Vavylonis, and Sophie G. Martin. Cell patterning by secretion-induced plasma membrane flows. *Science Advances*, 7(38):eabg6718, 9 2021.

[88] Anthony G. Vecchiarelli, Min Li, Michiyo Mizuuchi, Ling Chin Hwang, Yeonee Seol, Keir C. Neuman, and Kiyoshi Mizuuchi. Membrane-bound MinDE complex acts as a toggle switch that drives Min oscillation coupled to cytoplasmic depletion of MinD. *Proceedings of the National Academy of Sciences*, 113(11):E1479–E1488, 2016.

[89] Guillaume Salbreux, Guillaume Charras, and Ewa Paluch. Actin cortex mechanics and cellular morphogenesis. *Trends in Cell Biology*, 22(10):536–545, 2012.

[90] Priyamvada Chugh and Ewa K. Paluch. The actin cortex at a glance. *Journal of Cell Science*, 131(14):jcs186254, 2018.

[91] Nathan W. Goehring, Philipp Khuc Trong, Justin S. Bois, Debanjan Chowdhury, Ernesto M. Nicola, Anthony A. Hyman, and Stephan W. Grill. Polarization of PAR Proteins by Advective Triggering of a Pattern-Forming System. *Science*, 334(6059):1137–1141, 2011.

[92] Rukshala Illukkumbura, Tom Bland, and Nathan W. Goehring. Patterning and polarization of cells by intracellular flows. *Current Opinion in Cell Biology*, 62:123–134, 2020.

[93] Kerstin Klinkert, Nicolas Levernier, Peter Gross, Christian Gentili, Lukas von Tobel, Marie Pierron, Coralie Busso, Sarah Herrman, Stephan W Grill, Karsten Kruse, and Pierre Gönczy. Aurora A depletion reveals centrosome-independent polarization mechanism in Caenorhabditis elegans. *eLife*, 8:e44552, 2019.

[94] Manon C. Wigbers, Tzer Han Tan, Fridtjof Brauns, Jinghui Liu, S. Zachary Swartz, Erwin Frey, and Nikta Fakhri. A hierarchy of protein patterns robustly decodes cell shape information. *Nature Physics*, pages 1–7, 2021.

[95] Nils Klughammer, Johanna Bischof, Nikolas D Schnellbächer, Andrea Callegari, Péter Lénárt, and Ulrich S Schwarz. Cytoplasmic flows in starfish oocytes are fully determined by cortical contractions. *PLoS computational biology*, 14(11):e1006588, 2018.

[96] Guillaume Charras and Ewa Paluch. Blebs lead the way: how to migrate without lamellipodia. *Nature Reviews Molecular Cell Biology*, 9(9):730–736, 2008.

[97] Jaime Agudo-Canalejo, Pierre Illien, and Ramin Golestanian. Cooperatively enhanced reactivity and "stabilitaxis" of dissociating oligomeric proteins. *Proceedings of the National Academy of Sciences*, 117(22):11894–11900, 2020.

[98] Padmini Rangamani, Kranthi K. Mandadap, and George Oster. Protein-Induced Membrane Curvature Alters Local Membrane Tension. *Biophysical Journal*, 107(3):751–762, 2014.

[99] Zhanghan Wu, Maohan Su, Cheesan Tong, Min Wu, and Jian Liu. Membrane shape-mediated wave propagation of cortical protein dynamics. *Nature Communications*, 9(1):136, 2018.

[100] Alexander Mietke, Frank Jülicher, and Ivo F Sbalzarini. Self-organized shape dynamics of active surfaces. *Proceedings of the National Academy of Sciences*, 116(1):29–34, 2018.

[101] Alexander Mietke, V. Jemseena, K. Vijay Kumar, Ivo F. Sbalzarini, and Frank Jülicher. Minimal Model of Cellular Symmetry Breaking. *Physical Review Letters*, 123(18):188101, 2019.

[102] Arijit Mahapatra, David Saintillan, and Padmini Rangamani. Curvature-driven feedback on aggregation–diffusion of proteins in lipid bilayers. *Soft Matter*, 17(36):8373–8386, 2021.

[103] J. Halatek and E. Frey. Rethinking pattern formation in reaction–diffusion systems. *Nature Physics*, 14(5):507–514, 2018.

[104] Fridtjof Brauns, Henrik Weyer, Jacob Halatek, Junghoon Yoon, and Erwin Frey. Wavelength Selection by Interrupted Coarsening in Reaction-Diffusion Systems. *Physical Review Letters*, 126(10):104101, 2021.

[105] Lendert Gelens, Graham A. Anderson, and James E. Ferrell. Spatial trigger waves: positive feedback gets you a long way. *Molecular Biology of the Cell*, 25(22):3486–3493, 2014.

[106] Wim van Saarloos. Front propagation into unstable states. *Physics Reports*, 386(2-6):29–222, 2003.

[107] Yoichiro Mori, Alexandra Jilkine, and Leah Edelstein-Keshet. Wave-Pinning and Cell Polarity from a Bistable Reaction-Diffusion System. *Biophysical Journal*, 94(9):3684–3697, 2008.

[108] Georg R. Walther, Athanasius F. M. Marée, Leah Edelstein-Keshet, and Verônica A. Grieneisen. Deterministic Versus Stochastic Cell Polarisation Through Wave-Pinning. *Bulletin of Mathematical Biology*, 74(11):2570–2599, 2012.

[109] Steffen Rulands, Ben Klünder, and Erwin Frey. Stability of Localized Wave Fronts in Bistable Systems. *Physical Review Letters*, 110(3):038102, 2013.

[110] James E. Ferrell, Tony Yu-Chen Tsai, and Qiong Yang. Modeling the Cell Cycle: Why Do Certain Circuits Oscillate? *Cell*, 144(6):874–885, 2011.

[111] Frédéric Paquin-Lefebvre, Bin Xu, Kelsey L. DiPietro, Alan E. Lindsay, and Alexandra Jilkine. Pattern formation in a coupled membrane-bulk reaction-diffusion model for intracellular polarization and oscillations. *Journal of Theoretical Biology*, 497:110242, 2020.

[112] David M. Raskin and Piet A. J. de Boer. Rapid pole-to-pole oscillation of a protein required for directing division to the middle of Escherichia coli. *Proceedings of the National Academy of Sciences*, 96(9):4971–4976, 1999.

[113] Katja Zieske and Petra Schwille. Reconstitution of self-organizing protein gradients as spatial cues in cell-free systems. *eLife*, 3:e03949, 2014.

[114] Daniela Kiekebusch, Katharine A. Michie, Lars-Oliver Essen, Jan Löwe, and Martin Thanbichler. Localized Dimerization and Nucleoid Binding Drive Gradient Formation by the Bacterial Cell Division Inhibitor MipZ. *Molecular Cell*, 46(3):245–259, 2012.

[115] Daniela Kiekebusch and Martin Thanbichler. Spatiotemporal organization of microbial cells by protein concentration gradients. *Trends in Microbiology*, 22(2):65–73, 2014.

[116] Erwin Frey, Jacob Halatek, Simon Kretschmer, and Petra Schwille. Protein Pattern Formation. In Patricia Bassereau and Pierre Sens, editors, *Physics of Biological Membranes*, pages 229–260. Springer, Cham, 12 2018.

[117] Fridtjof Brauns, Grzegorz Pawlik, Jacob Halatek, Jacob Kerssemakers, Erwin Frey, and Cees Dekker. Bulk-surface coupling identifies the mechanistic connection between Min-protein patterns in vivo and in vitro. *Nature Communications*, 12(1):3312, 2021.

[118] Martin Loose, Elisabeth Fischer-Friedrich, Jonas Ries, Karsten Kruse, and Petra Schwille. Spatial Regulators for Bacterial Cell Division Self-Organize into Surface Waves in Vitro. *Science*, 320(5877):789–792, 2008.

[119] Fabai Wu, Jacob Halatek, Matthias Reiter, Enzo Kingma, Erwin Frey, and Cees Dekker. Multistability and dynamic transitions of intracellular Min protein patterns. *Molecular Systems Biology*, 12(6):873, 2016.

[120] Archana Varma, Kerwyn Casey Huang, and Kevin D. Young. The Min System as a General Cell Geometry Detection Mechanism: Branch Lengths in Y-Shaped Escherichia coli Cells Affect Min Oscillation Patterns and Division Dynamics. *Journal of Bacteriology*, 190(6):2106–2117, 2008.

[121] I. Begemann, T. Saha, L. Lamparter, I. Rathmann, D. Grill, L. Golbach, C. Rasch, U. Keller, B. Trappmann, M. Matis, V. Gerke, J. Klingauf, and M. Galic. Mechanochemical self-organization determines search pattern in migratory cells. *Nature Physics*, 15(8):848–857, 2019.

[122] Mithilesh Mishra, Yinyi Huang, Pragya Srivastava, Ramanujam Srinivasan, Mayalagu Sevugan, Roie Shlomovitz, Nir Gov, Madan Rao, and Mohan Balasubramanian. Cylindrical cellular geometry ensures fidelity of division site placement in fission yeast. *Journal of Cell Science*, 125(16):3850–3857, 2012.

[123] Carsten Mim and Vinzenz M. Unger. Membrane curvature and its generation by BAR proteins. *Trends in Biochemical Sciences*, 37(12):526–533, 2012.

[124] Mijo Simunovic, Gregory A. Voth, Andrew Callan-Jones, and Patricia Bassereau. When Physics Takes Over: BAR Proteins and Membrane Curvature. *Trends in Cell Biology*, 25(12):780–792, 2015.

[125] Brian J. Peter, Helen M. Kent, Ian G. Mills, Yvonne Vallis, P. Jonathan G. Butler, Philip R. Evans, and Harvey T. McMahon. BAR Domains as Sensors of Membrane Curvature: The Amphiphysin BAR Structure. *Science*, 303(5657):495–499, 2004.

[126] Barak Peleg, Andrea Disanza, Giorgio Scita, and Nir Gov. Propagating Cell-Membrane Waves Driven by Curved Activators of Actin Polymerization. *PLoS ONE*, 6(4):e18635, 2011.

[127] Britta Qualmann, Dennis Koch, and Michael Manfred Kessels. Let's go bananas: revisiting the endocytic BAR code. *The EMBO Journal*, 30(17):3501–3515, 2011.

[128] Helge Feddersen, Laeschkir Würthner, Erwin Frey, and Marc Bramkamp. Dynamics of the Bacillus subtilis Min System. *mBio*, 12(2), 2021.

[129] Katja Faelber, Martin Held, Song Gao, York Posor, Volker Haucke, Frank Noé, and Oliver Daumke. Structural Insights into Dynamin-Mediated Membrane Fission. *Structure*, 20(10):1621–1628, 2012.

[130] R Shlomovitz, N S Gov, and A Roux. Membrane-mediated interactions and the dynamics of dynamin oligomers on membrane tubes. *New Journal of Physics*, 13(6):065008, 2011.

[131] Saman Hussain, Carl N Wivagg, Piotr Szwedziak, Felix Wong, Kaitlin Schaefer, Thierry Izoré, Lars D Renner, Matthew J Holmes, Yingjie Sun, Alexandre W Bisson-Filho, Suzanne Walker, Ariel Amir, Jan Löwe, and Ethan C Garner. MreB filaments align along greatest principal membrane curvature to orient cell wall synthesis. *eLife*, 7:e32471, 2018.

[132] Felix Wong, Ethan C Garner, and Ariel Amir. Mechanics and dynamics of translocating MreB filaments on curved membranes. *eLife*, 8:e40472, 2019.

[133] Bruno Antonny. Mechanisms of Membrane Curvature Sensing. *Annual Review of Biochemistry*, 80(1):101–123, 2011.

[134] Shawn M. Ferguson and Pietro De Camilli. Dynamin, a membrane-remodelling GTPase. *Nature Reviews Molecular Cell Biology*, 13(2):75–88, 2012.

[135] Aurélien Roux, Gerbrand Koster, Martin Lenz, Benoît Sorre, Jean-Baptiste Manneville, Pierre Nassoy, and Patricia Bassereau. Membrane curvature controls dynamin polymerization. *Proceedings of the National Academy of Sciences*, 107(9):4141–4146, 2010.

[136] K. Eroumé, A. Vasilevich, S. Vermeulen, J. de Boer, and A. Carlier. On the influence of cell shape on dynamic reaction-diffusion polarization patterns. *PLOS ONE*, 16(3):e0248293, 2021.

[137] Beatrice Ramm, Andriy Goychuk, Alena Khmelinskaia, Philipp Blumhardt, Hiromune Eto, Kristina A. Ganzinger, Erwin Frey, and Petra Schwille. A diffusiophoretic mechanism for ATP-driven transport without motor proteins. *Nature Physics*, pages 1–9, 2021.

[138] Uri Alon. Network motifs: theory and experimental approaches. *Nature Reviews Genetics*, 8(6):450–461, 2007.

[139] Subhayu Basu, Rishabh Mehreja, Stephan Thiberge, Ming-Tang Chen, and Ron Weiss. Spatiotemporal control of gene expression with pulse-generating networks. *Proceedings of the National Academy of Sciences of the United States of America*, 101(17):6355–6360, 2004.

[140] Shuji Ishihara, Koichi Fujimoto, and Tatsuo Shibata. Cross talking of network motifs in gene regulation that generates temporal pulses and spatial stripes. *Genes to Cells*, 10(11):1025–1038, 2005.

[141] N. Barkai and S. Leibler. Robustness in simple biochemical networks. *Nature*, 387(6636):913–917, 1997.

[142] John J. Tyson and Béla Novák. Functional Motifs in Biochemical Reaction Networks. *Physical Chemistry*, 61(1):219–240, 2010.

[143] Yaakov Benenson. Biomolecular computing systems:

principles, progress and potential. *Nature Reviews Genetics*, 13(7):455–468, 2012.

[144] Uri Alon. *An Introduction to Systems Biology: Design Principles of Biological Circuits*. Chapman \& Hall/CRC Computational Biology Series. CRC Press, 7 2019.

[145] Dennis Bray. Protein molecules as computational elements in living cells. *Nature*, 376(6538):307–312, 1995.

[146] Jeremy E. Purvis and Galit Lahav. Encoding and Decoding Cellular Information through Signaling Dynamics. *Cell*, 152(5):945–956, 2013.

[147] Thomas Gregor, David W. Tank, Eric F. Wieschaus, and William Bialek. Probing the Limits to Positional Information. *Cell*, 130(1):153–164, 2007.

[148] Maura Strigini and Stephen M. Cohen. Wingless gradient formation in the Drosophila wing. *Current Biology*, 10(6):293–300, 2000.

[149] Sophie G. Martin and Martine Berthelot-Grosjean. Polar gradients of the DYRK-family kinase Pom1 couple cell length with the cell cycle. *Nature*, 459(7248):852–856, 2009.

[150] Dominik Schumacher, Silke Bergeler, Andrea Harms, Janet Vonck, Sabrina Huneke-Vogt, Erwin Frey, and Lotte Søgaard-Andersen. The PomXYZ Proteins Self-Organize on the Bacterial Nucleoid to Stimulate Cell Division. *Developmental Cell*, 41(3):299–314.e13, 2017.

[151] Joe Lutkenhaus. Assembly Dynamics of the Bacterial MinCDE System and Spatial Regulation of the Z Ring. *Biochemistry*, 76(1):539–562, 2007.

[152] Zongtian Tong, Xiang-Dong Gao, Audrey S. Howell, Indrani Bose, Daniel J. Lew, and Erfei Bi. Adjacent positioning of cellular structures enabled by a Cdc42 GTPase-activating protein–mediated zone of inhibition. *The Journal of Cell Biology*, 179(7):1375–1384, 2007.

[153] L. Wolpert. Positional information and the spatial pattern of cellular differentiation. *Journal of Theoretical Biology*, 25(1):1–47, 1969.

[154] Erik E. Griffin, David J. Odde, and Geraldine Seydoux. Regulation of the MEX-5 Gradient by a Spatially Segregated Kinase/Phosphatase Cycle. *Cell*, 146(6):955–968, 2011.

[155] Josana Rodriguez, Florent Peglion, Jack Martin, Lars Hubatsch, Jacob Reich, Nisha Hirani, Alicia G. Gubieda, Jon Roffey, Artur Ribeiro Fernandes, Daniel St Johnston, Julie Ahringer, and Nathan W. Goehring. aPKC Cycles between Functionally Distinct PAR Protein Assemblies to Drive Cell Polarity. *Developmental Cell*, 42(4):400–415.e9, 2017.

[156] Joseph O. Magliozzi, Jack Sears, Lauren Cressey, Marielle Brady, Hannah E. Opalko, Arminja N. Kettenbach, and James B. Moseley. Fission yeast Pak1 phosphorylates anillin-like Mid1 for spatial control of cytokinesis. *Journal of Cell Biology*, 219(8):e201908017, 2020.

[157] Bryant E. Walker, Jaana Männik, and Jaan Männik. Transient Membrane-Linked FtsZ Assemblies Precede Z-Ring Formation in Escherichia coli. *Current Biology*, 30(3):499–508.e6, 2020.

[158] Franz Meitinger, Anton Khmelinskii, Sandrine Morlot, Bahtiyar Kurtulmus, Saravanan Palani, Amparo Andres-Pons, Birgit Hub, Michael Knop, Gilles Charvin, and Gislene Pereira. A Memory System of Negative Polarity Cues Prevents Replicative Aging. *Cell*, 159(5):1056–1069, 2014.

[159] Erfei Bi and Hay-Oak Park. Cell Polarization and Cytokinesis in Budding Yeast. *Genetics*, 191(2):347–387, 2012.

[160] Martin Thanbichler and Lucy Shapiro. MipZ, a Spatial Regulator Coordinating Chromosome Segregation with Cell Division in Caulobacter. *Cell*, 126(1):147–162, 2006.

[161] Jeremy B. Chang and James E. Ferrell Jr. Mitotic trigger waves and the spatial coordination of the Xenopus cell cycle. *Nature*, 500(7464):603–607, 2013.

[162] Ali Kinkhabwala and Philippe IH Bastiaens. Spatial aspects of intracellular information processing. *Current Opinion in Genetics & Development*, 20(1):31–40, 2010.

[163] Fridtjof Brauns, Jacob Halatek, and Erwin Frey. Phase-Space Geometry of Mass-Conserving Reaction-Diffusion Dynamics. *Physical Review X*, 10(4):041036, 2020.

[164] Manon C. Wigbers, Fridtjof Brauns, Tobias Hermann, and Erwin Frey. Pattern localization to a domain edge. *Physical Review E*, 101(2):022414, 2020.

[165] Martin Falcke. Reading the patterns in living cells —the physics of Ca2+ signaling. *Advances in Physics*, 53(3):255–440, 2007.

[166] Xianrui Cheng and James E. Ferrell. Apoptosis propagates through the cytoplasm as trigger waves. *Science*, 361(6402):607–612, 2018.

[167] Till Bretschneider, Stefan Diez, Kurt Anderson, John Heuser, Margaret Clarke, Annette Müller-Taubenberger, Jana Köhler, and Günther Gerisch. Dynamic Actin Patterns and Arp2/3 Assembly at the Substrate-Attached Surface of Motile Cells. *Current Biology*, 14(1):1–10, 2004.

[168] Andrew R. Houk, Alexandra Jilkine, Cecile O. Mejean, Rostislav Boltyanskiy, Eric R. Dufresne, Sigurd B. Angenent, Steven J. Altschuler, Lani F. Wu, and Orion D. Weiner. Membrane Tension Maintains Cell Polarity by Confining Signals to the Leading Edge during Neutrophil Migration. *Cell*, 148(1-2):175–188, 2012.

[169] Urban Bezeljak, Hrushikesh Loya, Beata Kaczmarek, Timothy E. Saunders, and Martin Loose. Stochastic activation and bistability in a Rab GTPase regulatory network. *Proceedings of the National Academy of Sciences*, 117(12):6540–6549, 2020.

[170] Richard FitzHugh. Impulses and Physiological States in Theoretical Models of Nerve Membrane. *Biophysical Journal*, 1(6):445–466, 1961.

[171] Alexander S. Mikhailov. Foundations of Synergetics I, Distributed Active Systems. *Springer Series in Synergetics*, 1994.

[172] C Beta, G Amselem, and E Bodenschatz. A bistable mechanism for directional sensing. *New Journal of Physics*, 10(8):083015, 2008.

[173] Emily M. Vaughan, Ann L. Miller, Hoi-Ying E. Yu, and William M. Bement. Control of Local Rho GTPase Crosstalk by Abr. *Current Biology*, 21(4):270–277, 2011.

[174] Xuan Zhang, Chunqi Ma, Ann L. Miller, Hadia Arabi Katbi, William M. Bement, and X. Johné Liu. Polar Body Emission Requires a RhoA Contractile Ring and Cdc42-Mediated Membrane Protrusion. *Developmental Cell*, 15(3):386–400, 2008.

[175] Douwe M Veltman, Thomas D Williams, Gareth Bloomfield, Bi-Chang Chen, Eric Betzig, Robert H Insall, and Robert R Kay. A plasma membrane template for macropinocytic cups. *eLife*, 5:e20085, 2016.

[176] William M. Bement, Marcin Leda, Alison M. Moe, Angela M. Kita, Matthew E. Larson, Adriana E. Golding, Courtney Pfeuti, Kuan-Chung Su, Ann L. Miller, Andrew B. Goryachev, and George von Dassow. Activator–inhibitor coupling between Rho signalling and actin assembly makes the cell cortex an excitable medium. *Nature Cell Biology*, 17(11):1471–1483, 2015.

[177] Johanna Bischof, Christoph A. Brand, Kálmán Somogyi, Imre Májer, Sarah Thome, Masashi Mori, Ulrich S. Schwarz, and Péter Lénárt. A cdk1 gradient guides surface contraction waves in oocytes. *Nature Communications*, 8(1):849, 2017.

[178] Jennifer Landino, Marcin Leda, Ani Michaud, Zachary Swider, Mariah Prom, Christine Field, William Bement, Anthony G Vecchiarelli, Andrew Goryachev, and Ann L Miller. Rho and F-Actin Self-Organize within an Artificial Cell Cortex. *SSRN Electronic Journal*, 2021.

[179] Sophie Marbach and Lydéric Bocquet. Osmosis, from molecular insights to large-scale applications. *Chemical Society Reviews*, 48(11):3102–3144, 2019.

[180] J L Anderson. Colloid Transport by Interfacial Forces. *Annual Review of Fluid Mechanics*, 21(1):61–99, 1989.

[181] B.V. Derjaguin, S.S. Dukhin, and A.A. Korotkova. Diffusiophoresis in electrolyte solutions and its role in the Mechanism of the formation of films from caoutchouc latexes by the ionic deposition method. *Progress in Surface Science*, 43(1-4):153–158, 1993.

[182] Anthony G. Vecchiarelli, Keir C. Neuman, and Kiyoshi Mizuuchi. A propagating ATPase gradient drives transport of surface-confined cellular cargo. *Proceedings of the National Academy of Sciences*, 111(13):4880–4885, 2014.

[183] Takeshi Sugawara and Kunihiko Kaneko. Chemophoresis as a driving force for intracellular organization: Theory and application to plasmid partitioning. *BIOPHYSICS*, 7:77–88, 2011.

[184] Greg M. Allen, Alex Mogilner, and Julie A. Theriot. Electrophoresis of Cellular Membrane Components Creates the Directional Cue Guiding Keratocyte Galvanotaxis. *Current Biology*, 23(7):560–568, 2013.

[185] S. Iacopini and R. Piazza. Thermophoresis in protein solutions. *Europhysics Letters*, 63(2):247–253, 2003.

[186] Jérémie Palacci, Cécile Cottin-Bizonne, Christophe Ybert, and Lydéric Bocquet. Osmotic traps for colloids and macromolecules based on logarithmic sensing in salt taxis. *Soft Matter*, 8(4):980–994, 2011.

[187] Philipp Glock, Beatrice Ramm, Tamara Heermann, Simon Kretschmer, Jakob Schweizer, Jonas Mücksch, Gökberk Alagöz, and Petra Schwille. Stationary Patterns in a Two-Protein Reaction-Diffusion System. *ACS Synthetic Biology*, 8(1):148–157, 2019.

[188] Richard P. Sear. Diffusiophoresis in Cells: A General Nonequilibrium, Nonmotor Mechanism for the Metabolism-Dependent Transport of Particles in Cells. *Physical Review Letters*, 122(12):128101, 3 2019.

[189] Sebastian J Streichan, Matthew F Lefebvre, Nicholas Noll, Eric F Wieschaus, and Boris I Shraiman. Global morphogenetic flow is accurately predicted by the spatial distribution of myosin motors. *eLife*, 7:e27454, 2018.

[190] Chet Huan Oon and Kenneth E Prehoda. Asymmetric recruitment and actin-dependent cortical flows drive the neuroblast polarity cycle. *eLife*, 8:e45815, 2019.

[191] Mirjam Mayer, Martin Depken, Justin S Bois, Frank Jülicher, and Stephan W Grill. Anisotropies in cortical tension reveal the physical basis of polarizing cortical flows. *Nature*, 467(7315):617–621, 2010.

[192] Felix Brinkmann, Moritz Mercker, Thomas Richter, and Anna Marciniak-Czochra. Post-Turing tissue pattern formation: Advent of mechanochemistry. *PLOS Computational Biology*, 14(7):e1006259, 2018.

[193] Pearson W. Miller, Norbert Stoop, and Jörn Dunkel. Geometry of Wave Propagation on Active Deformable Surfaces. *Physical Review Letters*, 120(26):268001, 2018.

[194] F. Cagnetta, M. R. Evans, and D. Marenduzzo. Active Growth and Pattern Formation in Membrane-Protein Systems. *Physical Review Letters*, 120(25):258001, 2018.

[195] N. S. Gov. Guided by curvature: shaping cells by coupling curved membrane proteins and cytoskeletal forces. *Philosophical Transactions of the Royal Society B: Biological Sciences*, 373(1747):20170115, 2018.

[196] Caterina Tozzi, Nikhil Walani, and Marino Arroyo. Out-of-equilibrium mechanochemistry and self-organization of fluid membranes interacting with curved proteins. *New Journal of Physics*, 21(9):093004, 2019.

[197] Justin S Bois, Frank Jülicher, and Stephan W Grill. Pattern Formation in Active Fluids. *Physical Review Letters*, 106(2):028103, 2011.

[198] Simon Christ, Thomas Litschel, Petra Schwille, and Reinhard Lipowsky. Active shape oscillations of giant vesicles with cyclic closure and opening of membrane necks. *Soft Matter*, 17(2):319–330, 2020.

[199] Thomas Litschel, Beatrice Ramm, Roel Maas, Michael Heymann, and Petra Schwille. Beating Vesicles: Encapsulated Protein Oscillations Cause Dynamic Membrane Deformations. *Angewandte Chemie International Edition*, 57(50):16286–16290, 2018.

[200] Manon C. Wigbers, Fridtjof Brauns, Ching Yee Leung, and Erwin Frey. Flow Induced Symmetry Breaking in a Conceptual Polarity Model. *Cells*, 9(6):1524, 2020.

[201] Marcel Hörning and Tatsuo Shibata. Three-Dimensional Cell Geometry Controls Excitable Membrane Signaling in Dictyostelium Cells. *Biophysical Journal*, 116(2):372–382, 2019.

[202] Guillaume Salbreux and Frank Jülicher. Mechanics of active surfaces. *Physical Review E*, 96(3):032404, 2017.

[203] Athanasius F. M. Marée, Verônica A. Grieneisen, and Leah Edelstein-Keshet. How Cells Integrate Complex Stimuli: The Effect of Feedback from Phosphoinositides and Cell Shape on Cell Polarization and Motility. *PLoS Computational Biology*, 8(3):e1002402, 2012.

[204] Benoit Rogez, Laeschkir Würthner, Anastasiia B. Petrova, Felix B. Zierhut, Dario Saczko-Brack, Maria-Ana Huergo, Christopher Batters, Erwin Frey, and Claudia Veigel. Reconstitution reveals how myosin-VI self-organises to generate a dynamic mechanism of membrane sculpting. *Nature Communications*, 10(1):3305, 2019.

[205] Kiersten Elizabeth Scott, Stephanie I. Fraley, and Padmini Rangamani. A spatial model of YAP/TAZ signaling reveals how stiffness, dimensionality, and shape contribute to emergent outcomes. *Proceedings of the National Academy of Sciences*, 118(20):e2021571118, 2021.

[206] Sybren Ruurds de Groot and Peter Mazur. *Non-equilibrium thermodynamics*. Courier Corporation, 2013.

[207] Fumio Motegi and Geraldine Seydoux. The PAR network: redundancy and robustness in a symmetry-breaking system. *Philosophical Transac-*

tions of the Royal Society B: Biological Sciences, 368(1629):20130010, 2013.

[208] Ryan N Gutenkunst, Joshua J Waterfall, Fergal P Casey, Kevin S Brown, Christopher R Myers, and James P Sethna. Universally Sloppy Parameter Sensitivities in Systems Biology Models. *PLoS Computational Biology*, 3(10):e189, 2007.

[209] Frank J. Bruggeman, Hans V. Westerhoff, Jan B. Hoek, and Boris N. Kholodenko. Modular Response Analysis of Cellular Regulatory Networks. *Journal of Theoretical Biology*, 218(4):507–520, 2002.

[210] Jacob D. Reich, Lars Hubatsch, Rukshala Illukkumbura, Florent Peglion, Tom Bland, Nisha Hirani, and Nathan W. Goehring. Regulated Activation of the PAR Polarity Network Ensures a Timely and Specific Response to Spatial Cues. *Current Biology*, 29(12):1911–1923.e5, 2019.

[211] Tzer Han Tan, Maya Malik-Garbi, Enas Abu-Shah, Junang Li, Abhinav Sharma, Fred C. MacKintosh, Kinneret Keren, Christoph F. Schmidt, and Nikta Fakhri. Self-organized stress patterns drive state transitions in actin cortices. *Science Advances*, 4(6):eaar2847, 2018.

[212] A.J. Bray. Theory of phase-ordering kinetics. *Advances in Physics*, 43(3):357–459, 1994.

[213] Andreas Rätz and Axel Voigt. PDE's on surfaces — a diffusive interface approach. *Communications in Mathematical Sciences*, 4(3):575–590, 2006.

[214] Benjamin Winkler, Igor S. Aranson, and Falko Ziebert. Confinement and substrate topography control cell migration in a 3D computational model. *Communications Physics*, 2(1):82, 2019.

[215] Wieland Marth and Axel Voigt. Signaling networks and cell motility: a computational approach using a phase field description. *Journal of Mathematical Biology*, 69(1):91–112, 2014.

[216] Brian A. Camley, Yanxiang Zhao, Bo Li, Herbert Levine, and Wouter-Jan Rappel. Crawling and turning in a minimal reaction-diffusion cell motility model: Coupling cell shape and biochemistry. *Physical Review E*, 95(1):012401, 2017.

[217] Weikang Wang, Kuan Tao, Jing Wang, Gen Yang, Qi Ouyang, Yugang Wang, Lei Zhang, and Feng Liu. Exploring the inhibitory effect of membrane tension on cell polarization. *PLoS Computational Biology*, 13(1):e1005354, 2017.

[218] Wanda Strychalski, David Adalsteinsson, and Timothy C Elston. Simulating Biochemical Signaling Networks in Complex Moving Geometries. *SIAM Journal on Scientific Computing*, 32(5):3039–3070, 2010.

[219] Brian Drawert, Stefan Hellander, Michael Trogdon, Tau-Mu Yi, and Linda Petzold. A framework for discrete stochastic simulation on 3D moving boundary domains. *The Journal of Chemical Physics*, 145(18):184113, 2016.

[220] Daniel A Beard and Hong Qian. *Chemical Biophysics*. Cambridge University Press, 2008.

[221] Olivier Cinquin and Jacques Demongeot. Positive and Negative Feedback: Striking a Balance Between Necessary Antagonists. *Journal of Theoretical Biology*, 216(2):229–241, 2002.

God made the bulk; the surface was invented by the devil.
— Wolfgang Pauli

II Pattern formation in heterogeneous systems

1 Multiscale patterns

In this section we show how one can deal with spatiotemporal patterns that span multiple length and time scales. The following content is based on and uses parts of our submitted paper [67]. We provide a reprint of the paper in section 1.7.

1.1 Background

Although commonly assumed in theoretical approaches, biological systems are generally not uniform but rather inhomogeneous systems. This naturally implies that patterns do not emerge from homogeneity, but rather transition from one pattern to another over time and across different spatial regions, as Turing pointed out in his seminal paper [24]. One intriguing example of multiscale patterns in an intracellular context are the surface contraction waves in the starfish oocyte [21], which form in hierarchies of protein patterns that span multiple scales [22]. The question that then arises is: how should one deal with such complex multiscale systems?

The general procedure is to use systematic coarse-graining techniques that allow to reduce the dynamics to the relevant degrees of freedom at the length and time scales of interest. The best established and most widely used technique is the *renormalization group theory* (RG), which has considerably advanced the understanding of critical phenomena in equilibrium [68] and non-equilibrium [69] statistical physics. The basic idea is to iteratively integrate out degrees of freedom at small length scales, resulting in modified coupling parameters at large length scales. This way, flow equations can be derived for the model parameters as the system is viewed at larger and larger scales, and the fixed points of these flow equations remarkably expose the macroscopic state of the system. Unfortunately, one shortcoming of the RG method that impedes its application for pattern-forming systems is that it is restricted to narrow regions in parameter space (critical points). Another crucial drawback is that information about the small scale features, that have been integrated out, are lost and cannot be reconstructed from the dynamics at large scales. However, for pattern-forming systems, we are mainly interested in the patterns at small scales, as they regulate intracellular processes and therefore have important functions. Thus, what one requires is a general method that allows to reduce the complicated multiscale dynamics to simplified “hydrodynamic

variables" at large scales, from which one desires to reconstruct the small-scale features (patterns) of the system.

The *amplitude equation* formalism is one such approach that allows, in principle, to reconstruct patterns from a reduced dynamics at large scales. One way to derive amplitude equations is to perform a multiple scale analysis to separate the slow and fast variables in the dynamics [39, 70]. In the context of reaction-diffusion systems, for instance, this entails to write the solution $\boldsymbol{c}(\boldsymbol{x}, t)$ in terms of the dominant unstable mode $\boldsymbol{q}^*$ at onset (the mode corresponding to the largest growth rate σ^* in the dispersion relation) in the form:

$$\boldsymbol{c}(\boldsymbol{x}, t) = \tilde{\boldsymbol{c}}_{\boldsymbol{q}^*} A(x, y, t) e^{i\boldsymbol{q}^* \boldsymbol{x} + i\omega^* t} + c.c., \tag{II.1}$$

where $\tilde{\boldsymbol{c}}_{\boldsymbol{q}^*}$ denotes the eigenvector and ω^* the imaginary part of the growth rate that corresponds to the unstable mode (obtained from a linear stability analysis), $A(x, y, t)$ is a complex valued (slowly varying) amplitude, and $c.c.$ refers to the complex conjugate. In essence, Eq. (II.1) describes the evolution of an initially homogeneous solution near onset in terms of a fast spatial modulation (plane wave, given by the exponential or Fourier mode) and the slowly varying amplitude $A(x, y, t)$, which one may interpret as an envelope. Applying the aforementioned multiple scale analysis, one can reduce the dynamics and derive a single evolution equation (to leading order) for the amplitude that describes the (weakly) nonlinear behaviour of the system at large scales. For oscillatory systems, the amplitude equation typically takes the following form, also known as the *complex Ginzburg-Landau equation* (CGLE) [71]:

$$\frac{\partial}{\partial t} A(x, y, t) = A + (1 + i\alpha)\Delta A - (1 + i\beta)|A|^2 A\,. \tag{II.2}$$

Interestingly, the form of Eq. (II.2) is universal and does not depend on model details, but it reflects the underlying symmetries of the system. This permits to derive amplitude equations phenomenologically by exploiting the symmetries of the system [39, 71]. For example, it is straightforward to verify that Eq. (II.2) is invariant under translation, i.e. the mapping $A \to Ae^{i\boldsymbol{\phi}}$. Amplitude equations have been also studied for systems that exhibit conservation laws, including non-oscillatory [72, 73], and oscillatory [74, 75] systems. In such systems, it is required to derive an additional equation for the large-scale dynamics of the conserved field, which is coupled to the amplitude equation and therefore complicates the analysis.

To sum up, the amplitude equation formalism is a powerful method that enables one to reduce the dynamics of complicated pattern-forming systems to its essential "hydrodynamic variables" at large scales. From the spatiotemporal solution of the amplitude equation, one can in principle reconstruct the patterns at small scales via Eq. (II.1). However, there are also some serious limitations of this approach that

hinder its applicability. In general, and as can be inferred from Eq. (II.1), amplitude equations describe the (weakly) nonlinear behaviour of the (linearly unstable) homogeneous state close to a supercritical bifurcation point. The requirement of a supercritical bifurcation (including weakly subcritical systems) is an important one, since it would otherwise not be possible to expand the amplitude equation to leading order. In other words, this approach generally cannot be applied to subcritical systems that exhibit large amplitude patterns at onset, such as the Min protein system [28] or mass-conserving reaction-diffusion systems in general [41]. Another point is that the formalism requires to analytically determine (orthogonal) eigenfunctions of the operators that fulfil all boundary conditions. In complex geometries, and in particular for bulk-surface coupled system, this is in general not possible. Moreover, as outlined in the introduction of the thesis (section 1 of chapter I), heterogeneous systems often do not exhibit homogeneous steady states, but rather spatially non-uniform base states due to, e.g., spatial gradients in model parameters.

To overcome these restrictions, we follow here a different strategy and propose a new approach that enables us to characterize multiscale patterns in mass-conserving systems. The basic idea is to first partition the domain into distinct regions and to calculate instantaneous spatial averages of the total masses in each region. The coarse-grained spatial averages of the masses can then be used to calculate *instantaneous regional dispersion relations*, which ultimately inform about patterns in each region. Besides the conceptual simplicity of this method as compared to amplitude equation, it does not dependent on global orthogonal eigenfunctions of the considered geometry, because here we partition the geometry into simpler subdomains for which the regional eigenfunctions can be determined.

We demonstrate this approach in the context of multiscale patterns of the Min protein system in a three-dimensional wedge-shaped geometry. The specific geometry that we chose here induces a (fixed) spatial heterogeneity in the bulk height, which is an important control parameter for pattern formation [28, 76]. We show numerically that the Min dynamics produces a variety of complex patterns along the membrane and that these patterns transition to other patterns over time. Our theoretical findings are confirmed experimentally by reconstituting the Min system in a wedge-shaped microfluidic chamber. Applying the local equilibria theory for mass-conserving systems [41], we then derive mass-redistribution equations for the diffusively redistributed total protein masses, and show that these masses are the relevant degrees of freedom at large length and time scales. Based on an empirically obtained correlation between regional dispersion relations and established patterns in the highly nonlinear regime [28], we then show that one can reconstruct and even predict the dynamics from the reduced equations at large scales (mass-redistribution dynamics).

1.2 Min protein dynamics in a wedge-shaped geometry

Our starting point is the dynamics of the Min skeleton model [77] in a wedge-shaped setup, where the bottom surface represents the membrane (Fig. II.1a, top). On a mathematical level, the type of equations that we study here are bulk-surface coupled mass-conserving reaction-diffusion systems [67]. The dynamics of the cytosolic or bulk species $\boldsymbol{c}(\boldsymbol{x}, t)$ is given by a diffusion equation with linear source and degradation terms that account for conformational changes of MinD in the bulk:

$$\frac{\partial}{\partial t}\boldsymbol{c}(\boldsymbol{x}, t) = D_c \nabla^2 \boldsymbol{c} + \Lambda \mathbf{c} \,. \tag{II.3}$$

The dynamics of membrane components $\boldsymbol{m}(x, y, t)$ is constrained to the bottom surface $\mathcal{S}$ of the wedge and contains nonlinear membrane reactions $\boldsymbol{r}$ which account for attachment, detachment, and recruitment processes of proteins:

$$\frac{\partial}{\partial t}\boldsymbol{m}(x, y, t) = D_m \nabla_{\mathcal{S}}^2 \boldsymbol{m} + \boldsymbol{r}(\boldsymbol{c}|_{z=0}, \boldsymbol{m}) \,. \tag{II.4}$$

The bulk and membrane dynamics are coupled through reactive boundary conditions that describe a balance of the attachment and detachment processes by diffusive bulk fluxes:

$$-D_c \frac{\partial}{\partial z}\boldsymbol{c}|_{z=0} = \boldsymbol{f}(\boldsymbol{c}|_{z=0}, \boldsymbol{m}) \,. \tag{II.5}$$

Since proteins cycle between the bulk and membrane, the total average masses $\bar{n}_{\mathrm{D,E}}$ of MinD and MinE are conserved by the dynamics:

$$\bar{n}_{\mathrm{D}} = \langle m_{\mathrm{d}} + m_{\mathrm{de}} \rangle_{\mathcal{S}} \frac{|\mathcal{S}|}{|\mathcal{V}|} + \langle c_{\mathrm{D}} \rangle_{\mathcal{V}} \,, \tag{II.6a}$$

$$\bar{n}_{\mathrm{E}} = \langle m_{\mathrm{de}} \rangle_{\mathcal{S}} \frac{|\mathcal{S}|}{|\mathcal{V}|} + \langle c_{\mathrm{E}} \rangle_{\mathcal{V}} \,, \tag{II.6b}$$

where $|\mathcal{S}|/|\mathcal{V}|$ denotes the membrane area to bulk volume ratio.

In a rectangular geometry (where the bottom edge represents the membrane), careful analysis has shown that the Min system produces a range of different patterns, such as chemical turbulence, standing waves, and traveling waves, depending on the bulk height and the total average densities in the system [28]. Here, the (fixed) linear gradient in the bulk height $H(x)$ in the wedge-shape geometry introduces a spatial heterogeneity that leads to a complex phenomenology where different patterns form along the membrane (Fig. II.1a, bottom), and these patterns transition from one to another over time [67].

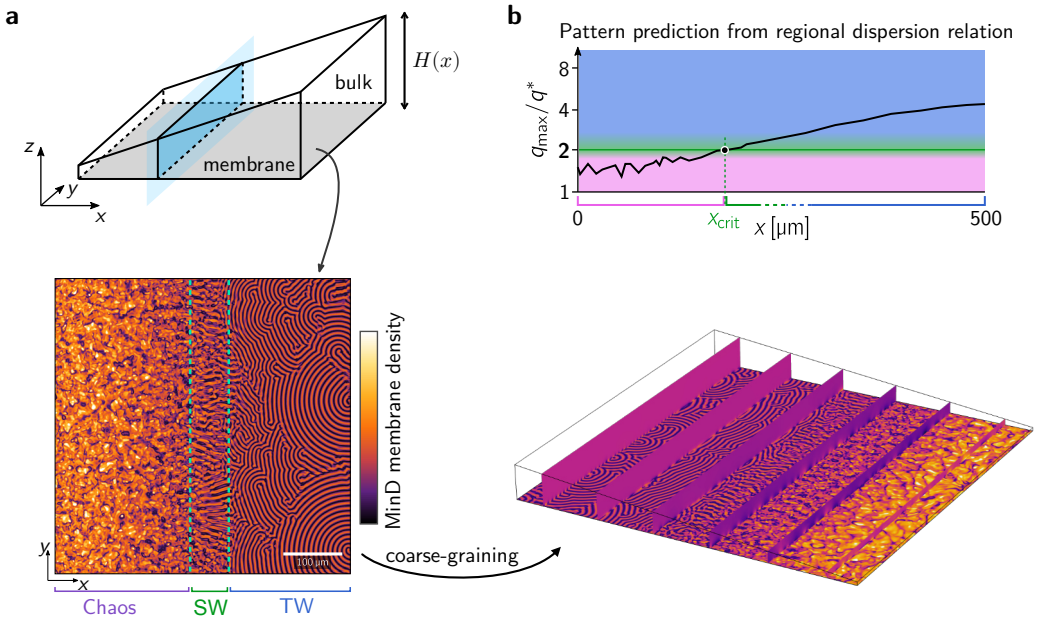

Figure II.1 Multiscale Min protein patterns in a wedge-shaped geometry and illustration of the coarse-graining procedure. a) Protein patterns (bottom) in a wedge-shaped geometry (top), where the bottom surface represents the membrane. One observes a variety of coexisting patterns along the membrane, and these patterns transition to one another over time [67]. b) The system is coarse-grained by slicing the wedge geometry into regions of constant bulk height (rectangular geometry, see bottom figure). In each of these slices, we determine the coarse-grained total masses $\langle \tilde{n}_{\mathrm{D,E}} \rangle_y (x,t)$ by averaging over the length of the slice. The slice-averaged total masses then serve as input for the regional dispersion relation in each slice, from which we predict the regional patterns by extracting the commensurability of modes (top). The figure is adopted from ref. [67].

1.3 Coarse-graining: Dynamic regional dispersion relations

To characterize the dynamics that play out on multiple scales, we first coarse-grain the system by partitioning the geometry into regions of constant bulk height (slices through the wedge, see Fig II.1b, bottom). In each of these slices, we calculate instantaneous average total densities $\langle \tilde{n}_{\mathrm{D,E}} \rangle_y (x,t)$ of MinD and MinE. Since slices represent rectangular geometries, the orthogonal eigenfunctions of the diffusion operator and hence the dispersion relation can be determined with standard techniques [13, 28, 43, 78]. Thus, we obtain the *regional dispersion relation* for each slice:

$$\sigma \left(q; H(x), \langle \tilde{n}_{\mathrm{D,E}} \rangle_y (x,t) \right) , \tag{II.7}$$

where q denotes the mode number of spatial perturbations. Note that Eq. (II.7) takes the spatially non-uniform bulk height as well as the dynamic slice-averaged

densities as input parameters. We therefore find that the regional dispersion relation is space and time dependent $\sigma(q; x, t)$.

1.4 Reconstructing patterns: Commensurability criterion

The question that remains is whether we can reconstruct information about the patterns solely from the dispersion relation? In general, the dispersion relation only informs about the onset of lateral instabilities and the wavelength of the unstable mode near onset, but not the exact pattern type deep in the nonlinear regime. However, for the Min system, recent work has identified a strong correlation between the dispersion relation and fully established patterns in the nonlinear regime [28]. In short, a *commensurability criterion* between the largest unstable mode $q_{\max}$ and the fastest growing mode q^* in the dispersion relation has been found: (i) For $q_{\max}/q^* < 2$ it has been shown that the system produces spatiotemporal chaos. (ii) In the vicinity of the commensurability criterion where $q_{\max}/q^* \gtrsim 2$, the system transitions to ordered standing wave patterns, and (iii) for $q_{\max}/q^* > 2$ one finds travelling wave patterns. This (empirically) obtained criterion together with the regional dispersion relation Eq. II.7 enables us to reconstruct the patterns in the system by extracting the slice-averaged densities from the numerical data. We find that this approach works remarkably well (see Fig. II.1b, top for a snapshot, more details are provided in our reprinted paper in chapter 1.6). Since the regional dispersion relation, as well as the commensurability criterion derived from it, depend on the slice-averaged densities $\langle \tilde{n}_{\mathrm{D,E}} \rangle_y (x, t)$, we conclude that the total masses are the relevant "hydrodynamic variables" at large length and time scales.

1.5 Reduced dynamics

This suggests that one can predict the entire dynamics independently of numerical simulations if one can establish an evolution equation for the total masses. We can derive such a reduced description of the dynamics by noting that the total masses between the slices are redistributed by diffusion due to concentration gradients. Moreover, since membrane diffusion is much slower compared to diffusion in the cytosol [5, 12, 14], we may neglect the former. In addition, applying the local equilibria theory for mass-conserving systems [28, 41], we can slave the cytosolic densities to their respective local equilibria

$$\langle c_i \rangle_{y,z}(x,t) \to c_i^* \left(H(x), \langle n_\mathrm{D} \rangle_{y,z}(x,t), \langle n_\mathrm{E} \rangle_{y,z}(x,t) \right) . \tag{II.8}$$

These approximations allow to derive a closed evolution equation for the mass-redistribution dynamics of MinD and MinE:

$$\frac{\partial}{\partial t}\langle n_i \rangle_{y,z}(x,t) \approx D_c \frac{\partial^2}{\partial x^2} c_i^*(x,t) + \frac{D_c}{H(x)} \frac{\partial}{\partial x} H(x) \frac{\partial}{\partial x} c_i^*(x,t) , \tag{II.9}$$

where $i \in \{D, E\}$. The solution of Eq. II.9 serves as input for the regional dispersion relation Eq. II.7 from which one can reconstruct patterns. Thus, given the initial condition $\langle n_i \rangle_{y,z}(x, 0)$ for the reduced dynamics, we can numerically propagate Eq. II.9 in time and thereby predict the entire multiscale dynamics. The results we obtain from solving the reduced dynamics agrees very well with the reconstruction obtained from the full numerical data (see section 1.7 for details).

1.6 Key points and outlook

In this section, we summarize the key findings of this research project. We also discuss generalization of our analysis beyond the Min system, and how one could include additional physics to the model.

- We proposed a new coarse-graining method for multiscale pattern-forming systems that is based on space and time dependent regional dispersion relations. The method is conceptually and technically simple to apply as it is effectively based on a linear theory. Importantly, and in contrast to traditional methods like amplitude equations, the approach is not restricted by the complexity of the geometry considered, since one can partition the full geometry into smaller convenient regions, for which the orthogonal eigenfunctions of the operators can be determined.

- One may view regional dispersion relations as a generalization of classical dispersion relations, which are by definition uniform and thus independent

of space and time. The space and time dependency of regional dispersion relations reflect the multiscale characteristics of the system. Using an empirically obtained commensurability criterion, we have shown that one can reconstruct the patterns in the system by extracting the densities from the full numerical simulation. Furthermore, we identified the redistribution of the total masses as the hydrodynamic variables that drive the dynamics at large length and time scales.

- On the basis of local equilibria theory for mass-conserving reaction-diffusion systems, we derived a reduced description for the hydrodynamics variables (redistributed total masses). From the reduced dynamics, one can reconstruct and even predict the entire dynamics from the initial conditions. Notably, the reconstruction from the reduced dynamics is by several orders of magnitude (minutes) faster than numerically solving the full dynamics (weeks).

- One striking feature of the system is that the total masses play a dual role: They are dynamic control variables (due to diffusive mass-redistribution) and at the same time control parameters [13, 28, 41] (which determine the local equilibria).

We assumed that the spatial heterogeneity (gradient in the bulk-boundary ratio) is static and hence does not change over time. One interesting extension of our model would be therefore to assume a dynamic bulk height $H(x,t)$. This can be realized in two ways: In the simplest case, one may assume that the bulk height is externally driven on a time scale much slower than the typical time of pattern formation (adiabatic deformations). A particularly interesting choice would be to let the (linear) bulk height gradient oscillate according to the following periodic function:

$$H(x,t) = \frac{H_0 + H_1}{2} + \cos\left(\frac{2\pi t}{T}\right)\frac{H_1 - H_0}{L}\left(x - \frac{L}{2}\right), \tag{II.10}$$

where H_0 denotes the smallest and H_1 the largest bulk height, respectively. The definition Eq. II.10 corresponds to a wedge geometry with lateral length L and where the bulk slope oscillates and changes its sign on a large time scale T. In the adiabatic limit, one can predict the dynamics from the solution of Eq. II.9 (and the replacement $H(x) \to H(x,t)$). We expect that the system does not reach a steady state in this case, but rather undergoes an intricate oscillatory dynamics in which multiscale patterns swap from one side of the wedge to the other.

Instead of controlling the bulk-surface ratio externally, another more natural and realistic scenario would be to couple the pattern-forming dynamics to the shape of the geometry. Thus, in this case, the bulk height parameter becomes part of the solution, and one needs to derive a separate equation that describes its time evolution. The general question of how one can describe reaction-diffusion systems

on deforming membranes and how membrane shape affects protein patterns is addressed in section 2.

We classified patterns in our analysis by the empirically obtained commensurability condition. Our approach can be generalized beyond the Min system by applying machine learning methods. This can be achieved as follows: First, one needs to collect a number of training data by numerically solving the full dynamics for smaller system sizes and times. The set of small-scale simulations can then be used to train, for instance, *physics-informed neural networks* (PINNs), from which one can then infer a mapping between control parameters (total masses) and the small-scale patterns. PINNs are very fast deep neural networks that take as input information about the underlying physical laws [79–81]. The major advantage of PINNs is that it reduces the solution space (since the physical laws are known) and therefore shortens the training time considerably.

1.7 Publication: Bridging scales in a multiscale pattern-forming system

Bridging scales in a multiscale pattern-forming system

by

L. Würthner[1,*], F. Brauns[1,2,*], G. Pawlik[3], J. Halatek[1,4], J. Kerssemakers[3], C. Dekker[3], and E. Frey[1,5]

[1]Arnold Sommerfeld Center for Theoretical Physics (ASC) and Center for NanoScience (CeNS), Department of Physics, Ludwig-Maximilians-Universität München, Theresienstraße 37, D–80333 Munich, Germany,

[2]Present address: Kavli Institute for Theoretical Physics, University of California Santa Barbara, Santa Barbara, CA 93106, USA

[3]Department of Bionanoscience, Kavli Institute of Nanoscience Delft, Delft University of Technology, Van der Maasweg 9, 2629 HZ Delft, the Netherlands

[4]Research Department, Oxford BioMedica Ltd., Windrush Court, Transport Way, Oxford, OX4 6LT, UK

[5]Max Planck School Matter to Life, Hofgartenstraße 8, D-80539 Munich, Germany

*These authors contributed equally to this work.

Preprint submitted for publication,

arXiv:2111.12043.

Reprinted on pages 46–71,

Supplemental Material reproduced on pages 72–85.

Bridging scales in a multiscale pattern-forming system

Laeschkir Würthner[1,*], Fridtjof Brauns[1,2,*], Grzegorz Pawlik[3], Jacob Halatek[1,4], Jacob Kerssemakers[3], Cees Dekker[3,†], and Erwin Frey[1,5,†]

[1]Arnold Sommerfeld Center for Theoretical Physics and Center for NanoScience, Department of Physics, Ludwig-Maximilians-Universität München, Theresienstraße 37, D-80333 München, Germany

[2]Present address: Kavli Institute for Theoretical Physics, University of California Santa Barbara, Santa Barbara, CA 93106, USA

[3]Department of Bionanoscience, Kavli Institute of Nanoscience Delft, Delft University of Technology, Van der Maasweg 9, 2629 HZ Delft, the Netherlands

[4]Research Department, Oxford BioMedica Ltd., Windrush Court, Transport Way, Oxford, OX4 6LT, UK

[5]Max Planck School Matter to Life, Hofgartenstraße 8, D-80539 Munich, Germany

[*]L.W. and F.B. contributed equally to this work.
[†]Corresponding authors. Email: frey@lmu.de or c.dekker@tudelft.nl

Abstract

Self-organized pattern formation is vital for many biological processes. Reaction-diffusion models have advanced our understanding of how biological systems develop spatial structures, starting from homogeneity. However, biological processes inherently involve multiple spatial and temporal scales and transition from one pattern to another over time, rather than progressing from homogeneity to a pattern. To deal with such multiscale systems, coarse-graining methods are needed that allow the dynamics to be reduced to the relevant degrees of freedom at large scales, but without losing information about the patterns at the small scales. Here, we present a semi-phenomenological approach which exploits mass-conservation in pattern formation, and enables to reconstruct information about patterns from the large-scale dynamics. The basic idea is to partition the domain into distinct regions (coarse-grain) and determine instantaneous dispersion relations in each region, which ultimately inform about local pattern-forming instabilities. We illustrate our approach by studying the Min system, a paradigmatic model for protein pattern formation. By performing simulations, we first show that the Min system produces multiscale patterns in a spatially heterogeneous geometry. This prediction is confirmed experimentally by in vitro reconstitution of the Min system. Using a recently developed theoretical framework for mass-conserving reaction-diffusion systems, we show that the spatiotemporal evolution of the total protein densities on large-scales reliably predicts the pattern-forming dynamics. Our approach provides an alternative and versatile theoretical framework for complex systems where analytical coarse-graining methods are not applicable, and can in principle be applied to a wide range of systems with an underlying conservation law.

Introduction

Pattern formation is fundamental for the spatiotemporal organization of biological processes, such as cell division, chemotaxis, and morphogenesis. More than half a century ago, Turing showed theoretically how local interactions (chemical reactions) and diffusion of chemical species can lead to spontaneous spatial patterns [1]. Such reaction–diffusion systems have been successfully used to explain pattern formation phenomena in nature that arise self-organized from a stable homogeneous steady state [2–5]. The analysis proposed by Turing allows to predict the emergence of patterns with a characteristic length scale as long as the entire dynamics remains in the vicinity of the homogeneous steady state [6]. The validity of Turing's approach has been also tested experimentally for coupled chemical oscillators, and was found to reliably predict the experimental observations, provided that the model parameters are spatially and temporally uniform [7]. Pattern-forming systems, however, are generally heterogeneous and therefore far from homogeneity, and involve multiple spatial and temporal scales. An intriguing example of biological pattern formation is morphogenesis, in which the spatiotemporal patterns of morphogens dictate the future shape of an organism that is orders of magnitude larger than its constituents [4]. On a smaller scale, protein concentration patterns in cells are essential for the spatiotemporal control of cellular processes such as cell division and motility [5, 8, 9]. Protein patterns can exhibit fascinating multiscale characteristics [10] and form in hierarchies of patterns on several scales that affect one another [11].

Such complex multiscale biological processes involve many degrees of freedom at multiple scales, rendering it difficult to analyze them and gain insight into the underlying principles. To make progress on this issue, one needs to use systematic coarse-graining schemes that allow the dynamics to be reduced to the essential degrees of freedom at the relevant time and length scales. For instance, a well-known and powerful method is the renormalization group theory [12]. Unfortunately, this method is restricted to the vicinity of critical points. The Mori-Zwanzig formalism [13] is another important approach which allows to decompose the dynamics of a system into 'fast' and 'slow' variables by means of projection operators. One arrives at a closed set of equations for the slow variables, while the fast variables are treated as noise. One property that these methods have in common is that the scales that have been integrated out or eliminated are not *resolved*, and cannot be recovered from the coarse-grained level of description. This is most apparent in the Mori-Zwanzig formalism, where the eliminated degrees of freedom appear effectively as noise terms on the resolved scales. For pattern-forming systems, one is however interested in the patterns on the *unresolved scales*[1] as they usually have a specific function in biological systems. This raises the question of whether it is possible to reconstruct information about the unresolved scales from the dynamics at the resolved scales? Indeed, amplitude equations describe the long-wavelength amplitude modulations of an underlying short-wavelength base pattern and therefore resolve both the small and the large scales. Unfortunately, however, they are limited to the vicinity

[1] We adapt the term unresolved scales from the computational fluid dynamics literature to refer to the (small) scales that have been integrated out in the coarse-grained description.

of the supercritical onset of pattern formation [6] (including weakly subcritical cases) and only feasible in simple geometries where the orthonormal basis functions of the diffusion operator can be found in closed analytical form. Hence, to fill these gaps, one relies on new concepts to deal with multiscale systems.

Here, we propose a semi-phenomenological approach to overcome these mathematical limitations in the concrete context of mass–conserving reaction–diffusion (MCRD) systems. Recently, a new theoretical framework for MCRD systems has been introduced [14, 15] that allows one to characterize their dynamics in the highly nonlinear regime. The basic idea is to consider reaction–diffusion system as decomposed into a set of reactive compartments which are spatially coupled by diffusion. For an isolated compartment, one can determine the steady state (*local equilibrium*) and its stability properties which both depend on the total densities within that compartment. Since diffusion causes the lateral redistribution of these total densities, these local equilibria will change over time. This concept of *moving local equilibria* enables one to study the physical mechanisms underlying pattern formation and characterize the dynamics far away from the homogeneous steady state. The fact that one is able to characterize the dynamics far from homogeneity suggests that the *local equilibria theory* may be a promising approach to study heterogeneous systems. We therefore asked whether the ideas from local equilibria theory would be applicable to investigate multiscale patterns?

To pursue this question, we use the Min protein system of *E. coli* which has emerged as a paradigmatic model system for the study of pattern formation in cell biology [16–20]. Its dynamics is driven by two proteins, MinD and MinE, which cycle between cytosolic and membrane–bound states and interact nonlinearly on the membrane (Fig. 1A). In *E. coli*, these proteins oscillate from cell pole to cell pole and thereby position the cell division machinery to midcell [16, 17]. Studying the Min dynamics in various reconstituted systems has led to the discovery of a rich set of patterns including traveling waves and spirals [18], chaotic patterns [10, 21–23], "homogeneous pulsing" [24–26], as well as quasi-stationary labyrinths, spots, and mesh-like patterns [10, 27]. Theoretical analysis of mathematical models has lead to the key insight — and experimentally confirmed prediction — that the average total densities of MinD and MinE and the bulk height are key control parameters for pattern formation in the reconstituted Min system [5, 28]. The rich set of patterns, experimental accessibility *in vitro* and theoretical understanding make the Min-system an ideal candidate to investigate the role of spatial heterogeneity on pattern formation.

Since varying the bulk height affects the local equilibrium state and is a key control parameter for pattern formation [5, 28], we study the Min dynamics in a wedge–shaped geometry with a membrane placed on the bottom surface (Fig. 1B). While there are many distinct ways to introduce large–scale spatial heterogeneities into the system, e.g. by introducing space-dependent kinetic rates, we chose to use a wedge geometry because it is relatively easy to implement experimentally. In numerical simulations, we find that the system exhibits a striking range of transient patterns, that coexist in different spatial regions along the membrane (Movie S1 and Fig. 1C). As time progresses, patterns in different regions change and transition to other patterns.

To characterize these complex dynamics that play out on multiple spatial and temporal scales, we generalize the concept of dispersion relations (obtained from a linear stability analysis) by applying it to sections of the domain, which we term *regional dispersion relations*. Combining this approach with the local equilibria theory [8, 14, 15], we show that one can reconstruct the type and characteristics of patterns on small scales from the local protein mass densities, which we identify as the essential degrees of freedom on large spatial and temporal scales, i.e. the "hydrodynamic variables" of the system. The key to this reconstruction are correlations between the regional pattern characteristics and instantaneous, regional dispersion relations, calculated from the instantaneous regional mass densities. Over time, these masses change due to diffusive redistribution, resulting in qualitatively different regional dispersion relations that indicate the local pattern type in the

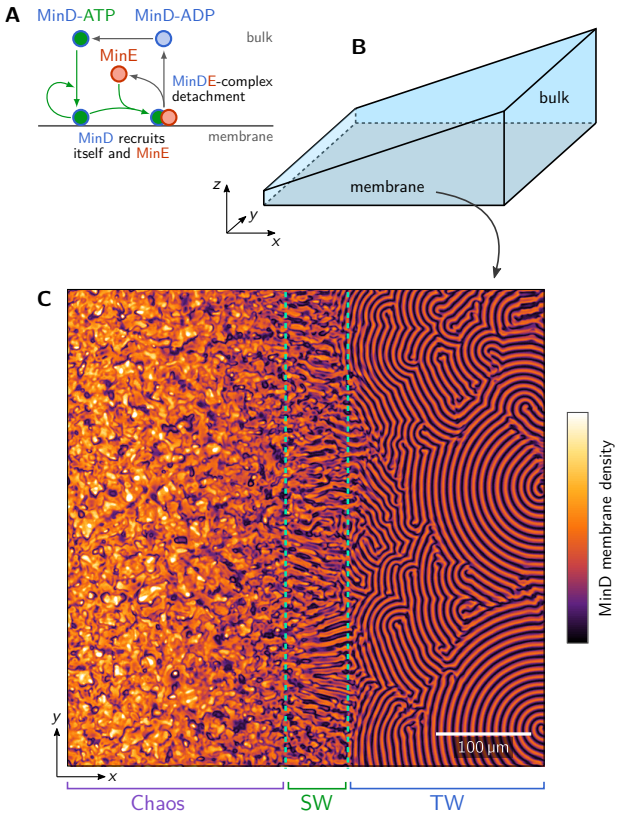

Fig. 1. (*A*) Schematic illustration of the Min-protein reaction network. (*B*) Wedge-geometry with a membrane surface at the bottom plane ($z = 0$) and bulk height $H(x)$ increasing linearly along the x direction. (*C*) Snapshot of the membrane-density of MinD, obtained by numerically simulating the Min dynamics Eqs. 1–3 in the geometry shown in (*B*). One observes regions with chaotic patterns, standing waves (SW, dashed green outline) and traveling waves (TW) along the membrane and at different bulk heights; see Movie S1.

system. This reconstruction of small-scale features (on *unresolved scales*), together with a coarse-grained description for the mass-redistribution dynamics on large scales allows us to understand and predict the long–term temporal evolution of the system. A major advantage of our approach is that it is based on a linear theory and therefore conceptually and technically simple to apply.

A key prediction from our numerical simulations and theoretical analysis is that different pattern types form at different positions along the wedge shaped geometry. To test this prediction experimentally, we performed experiments with a reconstituted Min system in wedge-shaped microfluidic cells. In agreement with the theoretical prediction, we find a range of transient patterns coexisting in different spatial regions along the membrane.

Results

The Min protein system in wedge geometry

Mathematically, the Min-protein dynamics is described by bulk-surface coupled reaction–diffusion equations, which describe the concentrations of cytosolic proteins MinD-ATP, MinD-ADP, and MinE, $\mathbf{c} = (c_{\mathrm{DD}}, c_{\mathrm{DT}}, c_{\mathrm{E}})$, in the bulk volume $\mathcal{V}$, and the concentrations of membrane-bound MinD and MinDE complexes, $\mathbf{m} = (m_{\mathrm{d}}, m_{\mathrm{de}})$, on the surface $\mathcal{S}$. For the wedge geometry, in spatial coordinates $\mathbf{x} = (x, y, z)$, we place the membrane surface (with lateral dimensions $L \times L$) in the $x-y$ plane at $z = 0$ and let the bulk height vary as a linear ramp from H_0 to H_1 along the x-direction (see Fig. 1B).

The dynamics of bulk components $\mathbf{c}(\mathbf{x}, t)$ is governed by the equation

$$\partial_t \mathbf{c}(\mathbf{x}, t) = D_c \nabla^2 \mathbf{c} + \Lambda \mathbf{c}, \tag{1}$$

where D_c denotes the bulk diffusion constant and the matrix $\Lambda = \mathrm{diag}(-\lambda, \lambda, 0)$ describes nucleotide exchange of MinD in the bulk. The dynamics of membrane components $\mathbf{m}(x, y, t)$ is constrained to the membrane surface and takes the form:

$$\partial_t \mathbf{m}(x, y, t) = D_m \nabla_{\mathcal{S}}^2 \mathbf{m} + \mathbf{r}(\mathbf{c}|_{z=0}, \mathbf{m}), \tag{2}$$

where D_m is the membrane diffusion constant and $\nabla_{\mathcal{S}}^2 = \partial_x^2 + \partial_y^2$ is the surface Laplacian. The membrane reactions $\mathbf{r}$, which comprise attachment, detachment, and recruitment processes of Min proteins, are specified in the Materials and Methods section.

The dynamics in the bulk and on the surface are coupled by reactive boundary conditions,

$$-D_c \partial_z \mathbf{c}|_{z=0} = \boldsymbol{f}(\mathbf{c}|_{z=0}, \mathbf{m}), \tag{3}$$

that describe the bulk fluxes induced by attachment and detachment of proteins at the membrane (see Materials and Methods). At the remaining boundaries, no-flux boundary conditions are imposed such that the system is closed. Together, the above dynamics conserve the average mass densities of MinD and MinE:

$$\bar{n}_{\mathrm{D}} \, |\mathcal{V}| = \langle m_{\mathrm{d}} + m_{\mathrm{de}} \rangle_{\mathcal{S}} \, |\mathcal{S}| + \langle c_{\mathrm{D}} \rangle_{\mathcal{V}} |\mathcal{V}| \,, \tag{4a}$$

$$\bar{n}_{\mathrm{E}} \, |\mathcal{V}| = \langle m_{\mathrm{de}} \rangle_{\mathcal{S}} \, |\mathcal{S}| + \langle c_{\mathrm{E}} \rangle_{\mathcal{V}} \, |\mathcal{V}| \,, \tag{4b}$$

where $c_D = c_{DD} + c_{DT}$ is the total cytosolic MinD concentration; $\langle\cdot\rangle_{\mathcal{S}}$ and $\langle\cdot\rangle_{\mathcal{V}}$ denote the mean on the surface and in the bulk respectively; $|\mathcal{S}|$ and $|\mathcal{V}|$ are the total surface area and bulk volume (see Materials and Methods).

Using finite element (FEM) simulations we investigated the spatiotemporal dynamics of the Min system in wedge geometry. Our simulations show a broad range of different patterns — including traveling waves, standing waves and chaotic patterns — coexisting in different spatial regions of the membrane (see Movie S1 and Fig. 1C). Interestingly, the regions where these patterns are found change over time as the patterns transition from one type to another. For long simulation times, we observe that patterns transition to standing waves, such that the entire domain is covered by a single pattern type in the final steady state. The pattern in steady state depends on the specific choice of parameters, and therefore can be altered by changing the model parameters (Fig. S1 and Movie S2).

Experimental implementation

We tested our theoretical prediction on this multi-scale dynamics in an experimental system consisting of a wedge-shaped microfluidic flow chamber (Fig. 2A). The bottom and top surface of the wedge were covered with a supported lipid bilayer consisting of DOPG:DOPC (30:70 %) which mimics the natural membrane composition of E. coli [29]. The length of the wedge was typically about $8 - 14\,\text{mm}$ and the width about $3 - 4\,\text{mm}$. The bulk height range was approximately $2 - 50\,\mu\text{m}$ (Fig. 2B). Min proteins were distributed in the chamber by rapid injection of a solution containing $1\,\mu\text{M}$ MinD and $1\,\mu\text{M}$ MinE (including 10 % fluorescently labelled MinD and MinE proteins for visualization), together with $5\,\text{mM}$ ATP and an ATP-regeneration system [28].

Figure 2C shows a snapshot of Min protein patterns along the bottom surface of the wedge geometry 30 minutes after injection. The experiments exhibit the same essential hallmarks of multiscale Min protein patterns that we observed in our numerical simulations. In particular, consistent with our simulations, we observe a sequence of distinct spatiotemporal patterns coexisting in different spatial regions of the membrane (Fig. 2C and Movie S3): At regions of low bulk height (approximately between $2 - 10\,\mu\text{m}$), one typically observes chaotic patterns and standing waves, whereas traveling wave patterns emerge at regions of large bulk height ($> 10\,\mu\text{m}$). Furthermore, as in the simulation, we observe a sharp boundary between regions that contain traveling wave patterns and regions that contain rather chaotic and standing wave patterns, and this boundary establishes quickly within a few minutes (Fig. S2 and Movie S4). Overall, the observations provide a striking verification of the height-dependent patterns predicted in the simulations.

There are also some differences between the patterns in the experiment and in our numerical simulations. First, while we observed occasional transitions from one pattern into another in our experiments (Fig. S3 and Movie S5), these transitions occurred frequently and were more pronounced in the simulations. This is explained by the lateral length of the experimental setup, that is about an order of magnitude larger as compared to the simulation setup, which is the main reason why we observe more frequent transitions between different patterns in the simulations, as will become clear later. Second, in contrast

to the simulations, we noticed some homogeneous oscillations in the experiments, which are characterized by large (homogeneous) density patches on the membrane (typically few hundred micrometers in size) that oscillate with time (Figs. S3– S4 and Movies S5– S7). We attribute this difference to the following: Due to the fabrication method of the microfluidic flow chamber, both the bottom and top surface of the wedge were covered with a supported lipid bilayer. In recent work, it has been shown that membrane-to-membrane crosstalk (i.e., between top and bottom surface) is responsible for the emergence of homogeneous oscillations [28]. In our simulations, however, we assume that Min proteins can only bind to the bottom membrane, which explains why we do not observe homogeneous oscillations.

Taken together, we have a system that exhibits a fascinatingly rich transient dynamics and involves patterns and transitions between them on multiple spatial and temporal scales. We are therefore left with the key question: Can we explain the cause why different patterns form in different spatial regions and how they transition from one to another over time? Moreover, is it possible to identify and reduce the system to its essential degrees of freedom? A standard way to address these questions mathematically would be to perform a multiscale

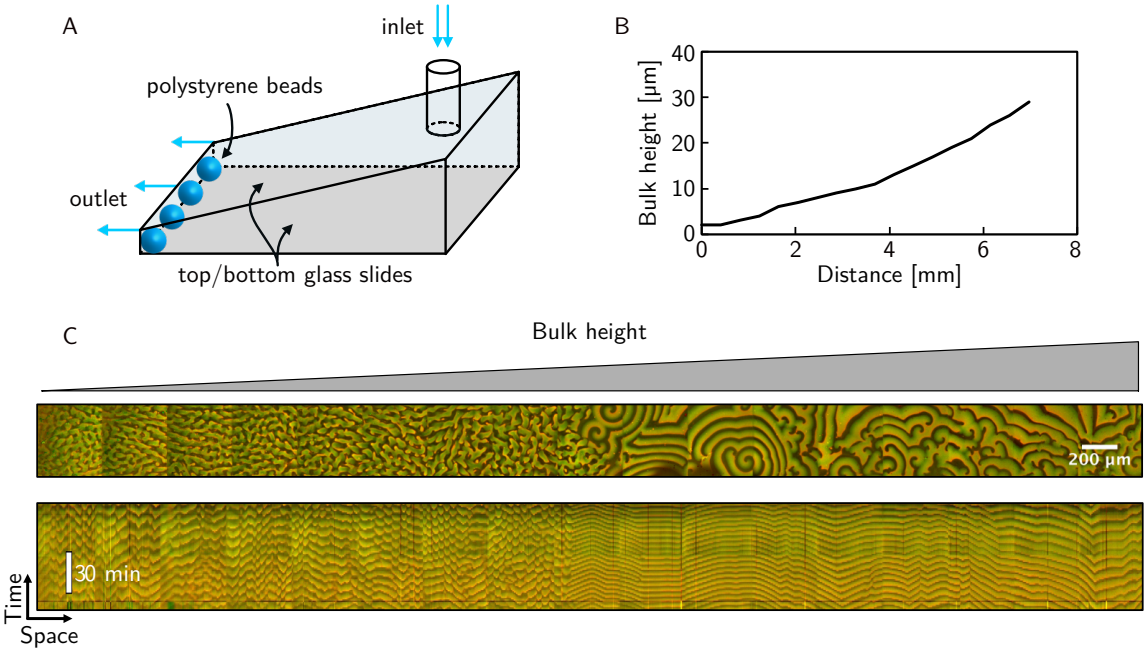

Fig. 2. Experimentally observed Min patterns in a wedge flow cell. (*A*) Schematic presentation of the experimental setup. Both, the bottom and the top surface (glass slides) are covered with a lipid bilayer. (*B*) Measurement of the bulk height profile of the flow cell versus distance along the lateral length of the wedge. The height was measured microscopically by z-stacks at multiple spots. (*C*) Snapshot of the Min pattern along the wedge, the picture was obtained by stitching individual adjacent images. Shown is a merge of MinD (green) and MinE (red) channels. The bottom figure shows a kymograph for intensities taken along the center line in the top figure.

analysis and to derive amplitude equations that describe the large-scale spatiotemporal evolution of the pattern amplitudes [6]. This would greatly simplify the problem as it allows to obtain a quantitative relationship between the small-scale patterns and the large-scale dynamics (slowly varying pattern amplitudes), thus ultimately enabling one to reconstruct the patterns from the reduced dynamics at large length and time scales [30–33]. Carrying out this analysis requires determining the set of orthogonal eigenmodes for the diffusion operator that satisfy the boundary conditions. In a one-dimensional domain, these eigenmodes are simply Fourier modes. Unfortunately, in the wedge geometry with bulk-surface coupling, the eigenmodes can not be found analytically, thus precluding the use of the amplitude equation framework. Moreover, amplitude equations are restricted to the vicinity of supercritical and weakly subcritical bifurcations [6, 34]. The Min patterns we observe here, however, are generically subcritical [15] and exhibit large amplitudes [14, 28]. We therefore aim to develop a new approach that overcomes these restrictions.

Instantaneous, regional dispersion relations predict patterns

The analysis of pattern-forming systems usually starts with calculating the homogeneous steady state (HSS) solutions and performing a linear stability analysis around these states. This yields a *dispersion relation* that informs about the growth rate $\sigma(q)$ of small spatial perturbations with a certain wavenumber q. However, the dispersion relation is generally only informative in the vicinity of the homogeneous steady state [1, 6], and thus unreliable for large amplitude patterns. Moreover, the spatial variation of parameters even precludes the existence of a global HSS, so that a global dispersion relation can no longer be determined. To overcome these limitations, we adopt a semi-phenomenological approach where we generalize the concept of dispersion relations.

Let us consider the wedge as dissected into a collection of two-dimensional slices along the direction of constant bulk height. Each slice corresponds to a rectangular geometry with a bulk height that depends on the position of the slice in the wedge (see Fig. 3A,B). Next, for each slice and at each point in time, we calculate instantaneous total densities of MinD and MinE, averaged over the slice length $\langle \tilde{n}_{\mathrm{D,E}} \rangle_y(t,x)$ (Materials and Methods). The average total densities, together with the local bulk height $H(x)$, then serve as parameters for the *regional dispersion relation* in each slice

$$\sigma\left(q; H(x), \langle \tilde{n}_{\mathrm{D,E}} \rangle_y(t,x)\right), \tag{5}$$

which is straightforward to determine because the slice represents a rectangular geometry [14, 23, 28] (see Fig. 3A,B and Supplementary Information). While the bulk height $H(x)$ varies linearly in space, the average total densities $\langle \tilde{n}_{\mathrm{D,E}} \rangle_y(t,x)$ are dynamic quantities and depend on the slice position x as well as on time t, since the diffusive coupling between the slices redistributes mass. It follows that the regional dispersion relation depends on the spatial position and is dynamic: $\sigma(q;x,t)$. This generalizes classical dispersion relations, which are by definition independent of space and time.

How does this spatially and temporally varying dispersion relation inform about the system's dynamics? As in uniform systems that exhibit homogeneous steady states, it serves

as a criterion for the onset of pattern formation and for estimating the characteristic wavelength of the initial pattern that is formed. While these insights are generally limited to the linear regime [1, 6], recent theoretical findings for the Min system in a two-dimensional rectangular geometry (representing a slice geometry) have shown that the dispersion relation reliably predicts the pattern type in the fully nonlinear regime [5]. In particular, it was shown that depending on the total densities of Min proteins, $\bar{n}_{\mathrm{D}}$ and $\bar{n}_{\mathrm{E}}$, and the bulk height H, the system exhibits a variety of different patterns on the membrane, such as chaos, standing waves, and traveling waves [14, 28]. Moreover, a careful analysis of numerical simulations has interestingly revealed a strong one-to-one correlation between the dispersion relation and the fully developed patterns in the highly nonlinear regime [14]: A *commensurability criterion* between the unstable mode with the shortest wavelength $q_{\max}$ and the fastest growing mode q^* has been found that determines the pattern type (Fig. 3C–E). In short, it has been shown that $q_{\max}/q^* < 2$ coincides with the regime of chemical

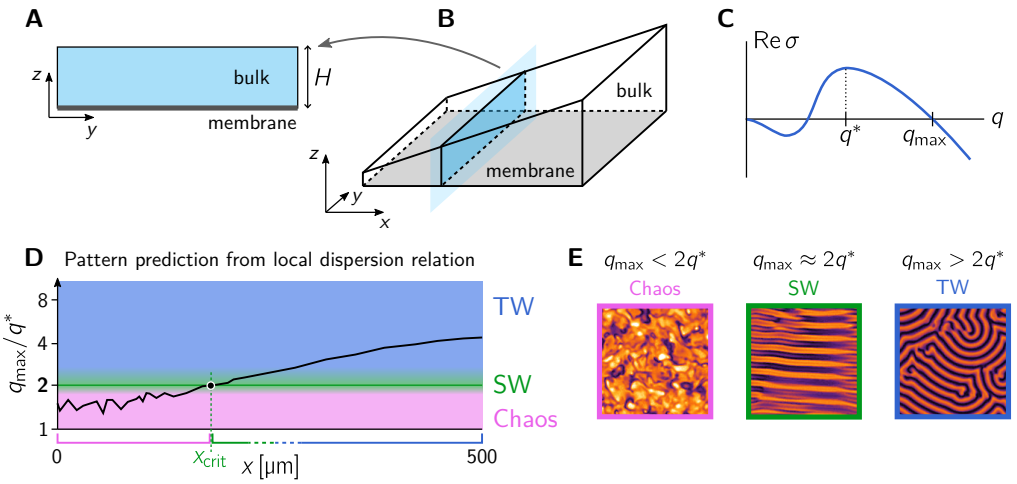

Fig. 3. (*A*) Rectangular geometry with membrane at the bottom edge representing a slice through the three-dimensional in vitro system. (*B*) A slice through the wedge geometry. For each such slice, at a given instance in time, we calculate the instantaneous total densities, averaged along its length $\langle \tilde{n}_{\mathrm{D,E}} \rangle_y(t, x)$, from the numerical simulation data. From these slice-averaged total densities, we can then calculate the corresponding local homogeneous steady state and its dispersion relation. (*C*) *Dispersion relation* with fastest growing mode q^* and right edge of the band of unstable modes $q_{\max}$ indicated. The ratio $q_{\max}/q^*$ has been empirically found to correlate with the type of the fully developed pattern, with a sharp transition from chaotic patterns for $q_{\max}/q^* < 2$ to ordered patterns for $q_{\max}/q^* > 2$. Close to the transition, standing waves are found, while travelling waves form for larger ratios $q_{\max}/q^*$ [14]. (*D*) Mode ratio $q_{\max}/q^*$ as a function of the slice position x for a given instance in time. The background shading indicates the type of pattern expected from the "commensurability criterion." (*E*) Representative snapshots of the three distinct pattern types: spatiotemporal chaos, standing waves (SW) and traveling waves (TW).

turbulence (spatiotemporal chaos), whereas for $q_{\max}/q^* > 2$ the system exhibits ordered patterns (standing/traveling waves). Standing wave patterns are found close to the commensurability transition $q_{\max}/q^* \gtrsim 2$, while traveling waves are found further away from the threshold. In the following, we use this observed one-to-one correspondence between the dispersion relation and the fully developed patterns to reconstruct the small scale pattern types from coarse grained densities.

To that end, we extracted the average total densities in each slice as a function of time from the numerical simulation. Based on these densities we then calculated the instantaneous regional dispersion relation in each slice and extracted the ratio $q_{\max}/q^*$ as a function of slice position x and time t (Fig. 3C–E). The resulting pattern-type prediction is shown in the space-time plot (kymograph) in Fig. 4A. Figure 4B shows the ratio $q_{\max}/q^*$ as a function of slice position x for a set of representative times (cf. Fig. 3D). The pattern-type prediction Fig. 4A is then obtained from these ratios via the mapping shown in Fig. 3D,E.

We find that this prediction correlates well with the patterns observed in the full numerical simulation (Fig. 4C,D and Movie S8). In particular, the temporally changing position $x_{\text{crit}}(t)$, marking regions where $q_{\max}/q^* = 2$ (indicated by the green arrows and dashed lines in Fig. 4B and C), agrees with the position along the wedge where traveling wave patterns transition to chaotic patterns. In the vicinity of $x_{\text{crit}}(t)$ we observe a band of standing waves as expected from the "commensurability criterion" [14]. Since the ratio $q_{\max}/q^*$ and with it $x_{\text{crit}}(t)$ are entirely determined by the slice-averaged masses $\langle \tilde{n}_{\text{D,E}} \rangle_y(x,t)$, we conclude that these masses are the essential degrees of freedom of the system at large scales.

Notably, we find that there are slight differences between the predictions and the actual patterns for large times (see Fig. 4A–C). The reason for these deviations lies in the model parameters, which were chosen such that the entire domain is near the critical mode ratio $q_{\max}/q^* = 2$ for large times. This renders the dynamics, and the prediction from the regional dispersion relation highly sensitive to slight variations of the regional total masses. Hence, the fact that our method is still able to qualitatively predict the dynamics in this case underscores the robustness of our approach. In the Supplemental Information, we provide additional results where the parameters were chosen such that the mode ratio is deep in the traveling wave regime ($q_{\max}/q^* > 2$) for late times. In this case, we obtain an excellent agreement between our predictions and the patterns observed in the numerical simulations (see Fig. S1).

Next, we ask whether one can find an approximate coarse-grained dynamics for these redistributed masses. Such a description would enable us to predict the time evolution of the redistributed masses independently from the full numerical simulations. One can then use the commensurability criterion to predict the pattern types that will form in different spatial regions as a function of the redistributed masses. In the next section we will show how one can find such a description.

Large-scale dynamics is driven by redistribution of mass

In general, mass redistribution between different spatial regions of the wedge is caused by diffusive fluxes due to concentration gradients. Similar as in the previous section, we

consider here the redistribution of mass between slices along the wedge (Fig. 3B). Since membrane diffusion is by two orders of magnitude slower than bulk diffusion it may be neglected, such that redistribution of protein mass between slices is governed by bulk diffusion alone (Materials and Methods)

$$\partial_t \langle n_i \rangle_{y,z}(x,t) \approx D_c \langle \partial_x^2 c_i \rangle_{y,z} + D_c \frac{\partial_x H(x)}{H(x)} \langle \partial_x c_i \rangle_{y,z}, \tag{6}$$

for $i = \mathrm{D}, \mathrm{E}$. Here, the second term accounts for the spatial variation of the bulk height, and thus the different volumes of neighboring slices between which the diffusive flux $D_c \langle \partial_x c_i \rangle_{y,z}$ redistributes mass. This can be seen by rewriting Eq. (6) in the form of a continuity equation

$$\partial_t \big[H(x) \cdot \langle n_i \rangle_{y,z}(x,t) \big] \approx -\partial_x \big[H(x) \cdot J_i^{\mathrm{diff}} \big] \tag{7}$$

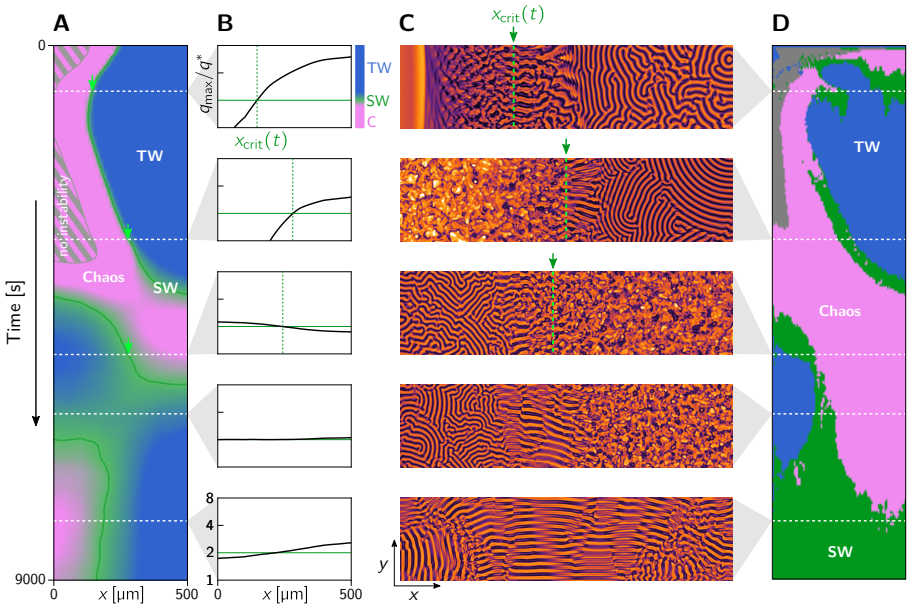

Fig. 4. (*A*) Kymograph showing the pattern-type prediction from the commensurability criterion (cf. Fig. 3D). The green line shows $x_{\mathrm{crit}}(t)$ where $q_{\mathsf{max}}/q^* = 2$, indicating the transition from chaotic to ordered patterns. Green arrows mark the position $x_{\mathrm{crit}}(t)$ for the times indicated by dashed white lines. (*B*) Plots of the mode ratio q_{max}/q^*, determined from the local dispersion relation, as a function of spatial position x for several representative times (dashed white lines in (A)). In the second to last row, the entire domain is near the critical ratio $q_{\mathsf{max}}/q^* = 2$, predicting the global emergence of standing waves (see last row). (*C*) Snapshots of the membrane patterns (MinD density, cf. Fig. 1) from the full numerical simulation. The green dashed line indicates $x_{\mathrm{crit}}(t)$. Note the standing wave patterns found near $x_{\mathrm{crit}}(t)$. Their fronts are aligned along the bulk height gradient such that the sequence of wavenodes lies on lines of constant bulk height. (*D*) Machine-learning based pattern classification using *ilastik* [35] (see Materials and Methods).

with the diffusive fluxes given by $J_i^{\mathrm{diff}} := -D_c\langle\partial_x c_i\rangle_{y,z}$. Since the area of slices increases along the positive $x-$direction, the diffusive fluxes J_i^{diff} on the right-hand side of Eq. (7) are rescaled by the bulk height $H(x)$. These equations seem to be simple, but unfortunately they are not closed, since the slice-averaged cytosolic densities $\langle c_i\rangle_{y,z}(x,t)$ appear on the right hand side.

We are interested in the dynamics of $\langle n_i\rangle_{y,z}$ on timescales much longer than typical oscillation periods of the patterns. Therefore, following the intuition gained from previous works on MCRD systems [15, 36], we assume that one can approximate the slice-averaged cytosol concentrations by the homogeneous steady-state concentration in each slice

$$\langle c_i\rangle_{y,z}(x,t) \approx c_i^*(x,t) := c_i^*\big(H(x), \langle n_{\mathrm{D}}\rangle_{y,z}, \langle n_{\mathrm{E}}\rangle_{y,z}\big). \tag{8}$$

This assumes that the spatial average over many wavelengths in y-direction is well approximated by the instantaneous homogeneous steady state in a slice. These steady state concentrations only depend on the slices bulk height $H(x)$ and the slice-averaged total densities $\langle n_i\rangle_{y,z}(x,t)$. Thus, the above approximation yields a closed set of equations for the mass-densities

$$\partial_t\langle n_i\rangle_{y,z}(x,t) \approx D_c\partial_x^2 c_i^*(x,t) + D_c\tfrac{\partial_x H(x)}{H(x)}\partial_x c_i^*(x,t). \tag{9}$$

We will call this the *reduced dynamics* in the following. Since the homogeneous steady

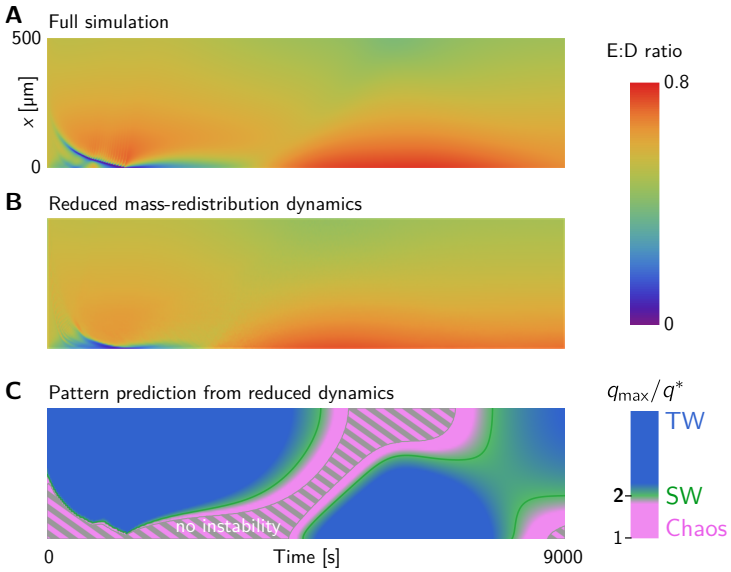

Fig. 5. (*A*,*B*) Kymographs showing the total-density ratio of MinE to MinD (E:D ratio) from the full numerical simulation (*A*) and from local-equilibria based reduced dynamics (*B*). (*C*) Kymograph showing the pattern-type prediction using the commensurability criterion based on the total densities from the reduced dynamics. Note the excellent qualitative agreement to the pattern-type prediction based on total densities from the full numerical simulation in Fig. 4A.

states may also undergo a saddle-node bifurcation, characterized by the emergence of three steady states (two stable, one unstable), this may lead to discontinuities in c_i^*. To regularize the dynamics, c_i is not set identical to c_i^* but relaxes towards it on a fast timescale (see SI for details).

Given the initial densities $\langle n_i \rangle_{y,z}(x, 0)$, one can numerically solve the reduced dynamics Eq. (9) to predict the entire time evolution of the slice-averaged masses and hence the dispersion relation at each point along the $x-$direction. Figure 5C shows the regional pattern types predicted from the reduced dynamics. We find good qualitative agreement for the distribution and transition of patterns as observed in the numerical simulations (cf. Fig. 4A). The main difference to the full numerical simulations is a slight quantitative deviation in the timescale, where the dynamics predicted by Eq. (9) is slightly slower compared to the full numerical simulation. We also note that the reduced dynamics predicts a larger region of no instabilities as compared to the numerical simulations (cf. Figs. 4A and 5C). This is because the chaotic regime is rather narrow and close to the regime for which the dispersion relation predicts no instability (cf. Figs. 3D and 4B). In addition, since the patterns emerge from a subcritical bifurcation [14] (a generic property of mass-conserving systems [15]), large amplitude patterns can be excited and maintained even below the instability threshold.

Figure 5A,B compare the time evolution of the slice-averaged total densities from the full numerical simulation and the solution obtained from the reduced dynamics. The colors in the kymographs indicate the total density ratio of MinE and MinD (short, E:D ratio), which is a key control parameter in the Min-protein dynamics [14].

Discussion

Multiscale patterns in biological systems often emerge from hierarchical systems, which are organized in a modular fashion. Each level of the hierarchy instructs dynamics on the next level which operates on a smaller spatial scale. For instance, along developmental trajectories of many organisms, upstream patterns such as maternal gradients instruct downstream gene-expression patterns on increasingly smaller scales [11, 37]. Importantly, on each level of the hierarchy, there is a clean separation between (spatially varying) control parameters and dynamical variables.

In contrast, in the system we have studied here, there is no such separation as the globally conserved total densities play a dual role: they are both dynamical variables and act as control parameters [14, 15]. Building on this key feature has allowed us to explain and predict the intriguingly complex patterns found in large-scale numerical simulations. The values of the total densities of MinD and MinE locally control the pattern type: we showed that a "regional dispersion relation" calculated from the regional average densities reliably predicts the pattern type. At the same time, concentration gradients in the bulk drive mass redistribution of MinD and MinE. Therefore, the total densities are hydrodynamic variables on large scales which control pattern formation on small scales. This separation of scales enabled us to derive a reduced dynamics for the total densities on large spatial and temporal scales which predicts the long-term dynamics of the system.

Notably, the dual role of total densities as dynamic variables and control parameters also plays out at the small scale of the patterns themselves [14, 15]. Here, instantaneous *local* total densities control *local* equilibria and their stability, which serve as proxies for the local dynamics. The local dynamics cause gradients, which drive diffusive redistribution of the total densities—in turn causing changes in the local dynamics. In the Min system, this point of view has led to a detailed understanding of the emergence of chaos near onset and of the transition to standing and traveling waves [14]. From a general perspective, the concept of local equilibria controlled by total local densities is at the core of a number of recent theoretical advances in the field of mass-conserving, pattern-forming systems [8, 15, 36, 38].

In addition to the dynamically changing total densities, the bulk height is also a (fixed) heterogeneous control parameter in our system. The bulk height (or more generally volume-to-surface ratio) is an important control parameter for bulk-surface coupled pattern-forming systems [14, 28]. Here, the bulk height gradient of the wedge serves to induce spatiotemporal heterogeneities in the total densities. Alternatively, one could induce heterogeneities in the total densities via spatial gradients of the kinetic rates or by imposing a heterogeneous initial condition in the total densities. However, these alternatives are difficult to realize experimentally in a reproducible and controlled manner, which is the main reason why we chose the wedge setup in this work. In a third scenario, large-scale gradients in the densities may also emerge spontaneously and be maintained in the absence of "external" heterogeneities.

An example for this third scenario is the Aranson–Tsimring model for pattern formation in vibrated granular media [39] (see Materials and Methods for details). In the following, we briefly discuss this model to put our approach into a broader context. In particular, this model has been extensively studied using amplitude equations allowing us to connect this mathematical approach to the regional dispersion relations introduced here. The Aranson–Tsimring model considers a system with a complex order parameter ψ (describing the surface modulation of a vibrated granular layer) which is coupled to a conservation law for the grain density ρ (see Eq. (24) in Materials and Methods). Near the onset of pattern formation, this coupling gives rise to localized patterns that have been studied using amplitude equations [30, 32, 33]. Figure 6 and Movie S9 illustrate how these patterns can be understood in terms of regional dispersion relations. For high densities, there are no unstable modes and no patterns form. Below a critical density ρ_c, a band of unstable modes appears, giving rise to patterns through a supercritical bifurcation. Indeed, localized patterns appear only where the average regional density is below ρ_c (see Fig. 6B). This demonstrates the idea of regional dispersion relations in a nutshell. Moreover, it shows that this approach gives rise to qualitatively similar insights as the technically much more involved amplitude equation formalism. The conceptual and technical simplicity of regional dispersion relations make this approach readily applicable. The caveat is that this approach lacks the mathematical rigor of the amplitude equation formalism and requires numerical solutions of the dynamics as a basis.

Since conservation laws are ubiquitous in many physical systems, we believe that our approach can be generalized to a broad class of multiscale pattern-forming systems. For

instance, mass conservation is inherent to particle–based active matter systems. The local particle density controls emergent orientational order, i.e. local symmetry breaking [40–42]. In turn, orientational order controls mass redistribution due to the particles' self-propulsion. Thus, the particle density again plays a dual role as a control parameter and a dynamic variable [42–44]. The dynamic interplay of mass redistribution and orientational order has been shown to give rise to coexistence of different macroscopic order (polar flocks, nematic lanes) and the interconversion between them [42], not unlike the coexistence and interconversion of different patterns we found for the reaction–diffusion system studied in this work. One way to induce spatial heterogeneities in these systems is to introduce a gradient of signaling chemicals (chemoattractants) that affect the local velocity of active particles. This would dynamically lead to redistribution of the particle densities on large scales. Since the particle densities, in turn, are themselves control parameters locally, non-trivial multiscale dynamics may emerge in such a setup. Exploring the effects of such gradients in active matter systems could be therefore an exciting task for future research.

On a broader perspective, our work shows how a linear analysis on small scales, combined with a reduced description for non-linear large scale dynamics (mass redistribution) can be employed to study complex multiscale phenomena. We believe that our approach can be generalized and applied to other multiscale systems with an underlying conservation law, such as transport processes in porous media, combustion, and cell migration, to name a few examples.

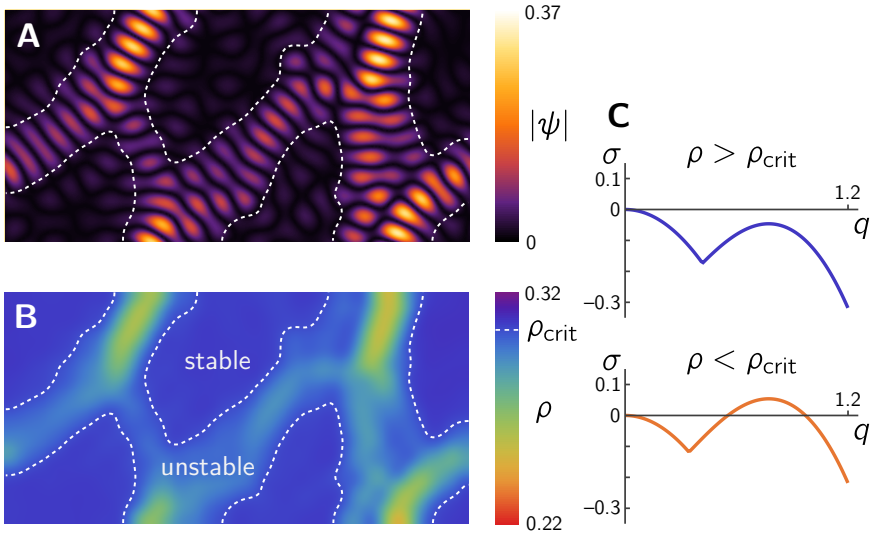

Fig. 6. Regional dispersion relations predict localized patterns in the Aranson–Tsimring model Eq. (24). (*A*) Snapshot of the order parameter magnitude ψ showing localized patterns. Dashed white line indicates the stability threshold determined from regional dispersion relations. (*B*) Coarse-grained density (Gaussian filter with standard deviation 10). (*C*) Representative dispersion relations in the stable and unstable regimes. Domain size: 100×50; see Materials and Methods for model details and remaining parmeters.

Acknowledgments. E.F. acknowledges support from the Deutsche Forschungsgemeinschaft (DFG, German Research Foundation) through the Collaborative Research Center (SFB) 1032 – Project-ID 201269156 – and the Excellence Cluster ORIGINS under Germany's Excellence Strategy – EXC-2094 – 390783311. C.D. acknowledges support from the NWO/OCW Gravitation program NanoFront and the ERC Advanced Grant 883684.

Materials and Methods

Mathematical model

We adopt the Min "skeleton model" introduced in Refs. [5, 45, 46] which is known to qualitatively reproduce Min patterns *in vivo* and *in vitro* [5, 28, 46]. The governing equations are given in the main text, Eqs. [1]–[3]. The membrane reactions are

$$\mathbf{r} = \left[r_{\mathrm{D}}^{\mathrm{on}} - r_{\mathrm{E}}^{\mathrm{on}}, r_{\mathrm{E}}^{\mathrm{on}} - r_{\mathrm{DE}}^{\mathrm{off}}\right]^{\top}, \tag{10}$$

with

$$r_{\mathrm{D}}^{\mathrm{on}} = (k_{\mathrm{D}} + k_{\mathrm{dD}} m_{\mathrm{d}}) c_{\mathrm{DT}}\,, \tag{11a}$$
$$r_{\mathrm{E}}^{\mathrm{on}} = k_{\mathrm{dE}} m_{\mathrm{d}} c_{\mathrm{E}}\,, \tag{11b}$$
$$r_{\mathrm{DE}}^{\mathrm{off}} = k_{\mathrm{de}} m_{\mathrm{de}}\,. \tag{11c}$$

The reaction terms account for MinD attachment and self-recruitment to the membrane, MinE recruitment by MinD, and dissociation of MinDE complexes with subsequent detachment of both proteins into the cytosol, respectively. Coupling between cytosol and membrane is established by reactive boundary conditions at the membrane [cf. Eq. (3)]. The boundary fluxes are given by

$$\boldsymbol{f} = \left[r_{\mathrm{DE}}^{\mathrm{off}}, -r_{\mathrm{D}}^{\mathrm{on}}, r_{\mathrm{DE}}^{\mathrm{off}} - r_{\mathrm{E}}^{\mathrm{on}}\right]^{\top}, \tag{12}$$

which follows from mass conservation. For analytical caclulations we adapt the following change of variables as it is more convenient: We describe the bulk dynamics of MinD in terms of the variables $c_{\mathrm{D}} = c_{\mathrm{DD}} + c_{\mathrm{DT}}$ and c_{DD}, i.e. in this case one defines the bulk concentration vector $\mathbf{c} = (c_{\mathrm{D}}, c_{\mathrm{DD}}, c_{\mathrm{E}})$. The membrane reaction in Eq. (11a) is then slightly modified by substituting $c_{\mathrm{DT}} = c_{\mathrm{D}} - c_{\mathrm{DD}}$, and the boundary fluxes are given by

$$\boldsymbol{f} = \left[-r_{\mathrm{D}}^{\mathrm{on}}, r_{\mathrm{DE}}^{\mathrm{off}}, r_{\mathrm{DE}}^{\mathrm{off}} - r_{\mathrm{E}}^{\mathrm{on}}\right]^{\top}. \tag{13}$$

The model parameters used in this study are summarized in Table 1.

Table 1. Min model parameters

Parameter	Symbol	Value
Bulk diffusion	D_c	$60\,\mu m^2\,s^{-1}$
Membrane diffusion	D_m	$0.013\,\mu m^2\,s^{-1}$
Average total MinD density	$\bar{n}_D$	$665\,\mu m^{-3}$
Aveage total MinE density	$\bar{n}_E$	$410\,\mu m^{-3}$
Attachment rate	k_D	$0.065\,\mu m\,s^{-1}$
MinD recruitment rate	k_{dD}	$0.098\,\mu m^3\,s^{-1}$
MinE recruitment rate	k_{dE}	$0.126\,\mu m^3\,s^{-1}$
MinDE dissociation rate	k_{de}	$0.34\,s^{-1}$
Nucleotide exchange	λ	$6\,s^{-1}$

Numerical simulations

To investigate the dynamics of the system, we performed 3D finite element (FEM) simulations using the commercially available software *COMSOL Multiphysics v5.6*. Numerical simulations were performed for a wedge geometry with lateral length $L = 500\,\mu m$ and bulk height $H(x)$ linearly increasing from $H_0 = 5\,\mu m$ to $H_1 = 50\,\mu m$. The simulation was initialized with the Min proteins uniformly distributed in the bulk and a small random spatial perturbation around this uniform state.

Homogeneous steady state and dispersion relation

The homogeneous steady state concentrations, $(\mathbf{c}^*|_{z=0}(H, \bar{n}_D, \bar{n}_E),\ \mathbf{m}^*(H, \bar{n}_D, \bar{n}_E))$ are obtained from the stationary solutions of Eqs. [1]–[3] together with the mass conservation condition Eq. (4):

$$\begin{cases} \mathbf{r}(\mathbf{c}^*|_{z=0}, \mathbf{m}^*) = \mathbf{0}, \\ \boldsymbol{f}\big(\mathbf{c}^*|_{z=0}, \mathbf{m}^*\big) = \boldsymbol{\Phi}, \\ c_D^*|_{z=0} + (m_d^* + m_{de}^*)/H = \bar{n}_D, \\ c_E^*|_{z=0} + m_{de}^*/H = \bar{n}_E, \end{cases} \tag{14}$$

where $\boldsymbol{\Phi}$ denotes the steady state fluxes at the membrane, given by:

$$\boldsymbol{\Phi} = [0, \phi, 0]^\top, \tag{15a}$$

$$\phi := \sqrt{D_c \lambda}\, \tanh\left(\sqrt{\lambda/D_c}\, H\right)\, c_{DD}^*|_{z=0}. \tag{15b}$$

A concise derivation of these equations and how they can be solved is provided in the Supplementary Information. For a thorough presentation of the linear stability analysis of the Min system in a 2D rectangular geometry we refer to the Supplementary Informations of Refs. [14] and [28].

Operators for spatial averaging

The operators used throughout this study to calculate mean values of densities on the membrane and in the cytosol are defined as follows:

$$\langle m\rangle_{\mathcal{S}} := |\mathcal{S}|^{-1}\int_{\mathcal{S}} \mathrm{d}x\mathrm{d}y\, m, \tag{16a}$$

$$\langle c\rangle_{\mathcal{V}} := |\mathcal{V}|^{-1}\int_{\mathcal{S}} \mathrm{d}x\mathrm{d}y \int_0^{H(x)} \mathrm{d}z\, c, \tag{16b}$$

$$\langle\cdot\rangle_y := \frac{1}{L}\int_0^L \mathrm{d}y\,(\cdot), \tag{16c}$$

$$\langle\cdot\rangle_{y,z} := \frac{1}{H(x)}\int_0^{H(x)} \mathrm{d}z\,\langle\cdot\rangle_y, \tag{16d}$$

where the membrane surface area and the bulk volume for the wedge geometry are explicitly given by $|\mathcal{S}| = L^2$ and $|\mathcal{V}| = L^2\,(H_0 + H_1)/2$.

Instantaneous total densities *at* the membrane

Since only cytosolic proteins in close proximity to the membrane participate in the nonlinear dynamics at the membrane, we define instantaneous total densities at the membrane:

$$\tilde{n}_{\mathrm{D}}(x,y,t) := \frac{1}{H(x)}(m_{\mathrm{d}} + m_{\mathrm{de}}) + c_{\mathrm{D}}|_{z=0}\,, \tag{17a}$$

$$\tilde{n}_{\mathrm{E}}(x,y,t) := \frac{1}{H(x)}m_{\mathrm{de}} + c_{\mathrm{E}}|_{z=0}\,. \tag{17b}$$

We further averaged these densities along the y–direction to obtain the the slice-averaged total densities $\langle\tilde{n}_{\mathrm{D,E}}\rangle_y(x,t)$. Note that the length of a slice is much larger than the typical pattern wavelength, which also permits to approximate the slice-averaged mass at the membrane by the vertically averaged mass: $\langle\tilde{n}_i\rangle_y(x,t) \approx \langle n_i\rangle_{y,z}(x,t)$ (see Ref. [14]). This is because the local deviations $\tilde{n}_i - \langle n_i\rangle_z$ largely cancel when averaging over the pattern wavelength.

Mass redistribution dynamics

Here, we provide more details on the derivation of the mass redistribution dynamics Eq. (7). For specificity, we present the calculation for MinD. The calculation for MinE works along the same lines. Our starting point is the slice averaged total MinD density:

$$\langle n_{\mathrm{D}}\rangle_{y,z}(x,t) := \frac{1}{H(x)}\left\langle m_{\mathrm{d}} + m_{\mathrm{de}} + \int_0^{H(x)} \mathrm{d}z\, c_{\mathrm{D}}\right\rangle_y. \tag{18}$$

The time evolution of this quantity then follows from Eq. (1) and Eq. (2):

$$H(x)\,\partial_t\langle n_{\mathrm{D}}\rangle_{y,z}(x,t) = D_m\partial_x^2\langle m_{\mathrm{d}} + m_{\mathrm{de}}\rangle_y + D_c\partial_z\langle c_{\mathrm{D}}\rangle_y\big|_{z=H(x)} + \int_0^{H(x)} \mathrm{d}z\, D_c\partial_x^2\langle c_{\mathrm{D}}\rangle_y, \quad (19)$$

where we used the reactive boundary condition Eq. (3) to rewrite the integral:

$$\begin{aligned}\int_0^{H(x)} \mathrm{d}z\, D_c\partial_z^2 c_{\mathrm{D}} &= D_c\partial_z c_{\mathrm{D}}\big|_{z=H(x)} - D_c\partial_z c_{\mathrm{D}}\big|_{z=0} \\ &= D_c\partial_z c_{\mathrm{D}}\big|_{z=H(x)} + r_{\mathrm{DE}}^{\mathrm{off}} - r_{\mathrm{D}}^{\mathrm{on}}. \end{aligned} \quad (20)$$

Note that due to mass-conservation the reaction terms at the membrane cancel.

Since the system is closed, the boundary condition at the inclined top surface of the wedge reads $\mathbf{n}\cdot\nabla c_{\mathrm{D}}|_{z=H(x)} = 0$, where $\mathbf{n} \propto (-\partial_x H, 0, 1)$ is the outward normal vector at the top surface. Writing out the boundary condition explicitly, we find that:

$$\partial_z c_{\mathrm{D}}|_{z=H(x)} = (\partial_x H)\,\partial_x c_{\mathrm{D}}|_{z=H(x)}. \quad (21)$$

To proceed, we substitute the relation above into Eq. (19) and slightly rewrite the resulting equation by applying the chain rule:

$$H(x)\,\partial_t\langle n_{\mathrm{D}}\rangle_{y,z}(x,t) = D_m\partial_x^2\langle m_{\mathrm{d}} + m_{\mathrm{de}}\rangle_y + \partial_x \underbrace{\int_0^{H(x)} \mathrm{d}z\, D_c\partial_x\langle c_{\mathrm{D}}\rangle_y}_{=:\,-H(x)J_{\mathrm{D}}(x)}. \quad (22)$$

Here, the first term describes diffusion of the averaged membrane concentrations. The integral on the right describes diffusion of the averaged cytosolic densities, where we defined the diffusive flux $J_{\mathrm{D}} = -D_c\langle\partial_x c_D\rangle_{y,z}$. The factor $H(x)$ in the cytosolic diffusion term accounts for the increasing area of the slice along the positive x–direction.

Since protein diffusion on the membrane is much smaller than cytosolic diffusion $D_m \ll D_c$ [47, 48], one can neglect membrane diffusion to arrive at the result shown in the main text (Eq. (7)). For completeness, note that Eq. (22) (without membrane diffusion) can be recast as

$$\begin{aligned}\partial_t\langle n_{\mathrm{D}}\rangle_{y,z}(x,t) &\approx \frac{1}{H(x)}\,\partial_x \int_0^{H(x)} \mathrm{d}z\, D_c\partial_x\langle c_{\mathrm{D}}\rangle_y, \\ &= D_c\partial_x\langle\partial_x c_{\mathrm{D}}\rangle_{y,z} + D_c\frac{\partial_x H(x)}{H(x)}\langle\partial_x c_{\mathrm{D}}\rangle_{y,z}, \end{aligned} \quad (23)$$

which is the form given in Eq. (6) in the main text.

Machine-learning based pattern classification

We used the pixel classifier provided by the software *ilastik* [35]. The classifier was trained based on a few representative snapshots, by manually marking areas where the pattern type (no pattern, chaos, standing wave, or traveling wave) is easily identified by visual inspection. The trained classifier then yields probabilities for each pattern type at each pixel. The classifier was applied to snapshots in 20 s intervals. This data was then downsampled and averaged over slices to yield an x–t space time map of pattern probabilities. To render the kymograph in Fig. 4D each pixel was colored based on the most probable pattern.

Aranson–Tsimring model

As a second example we briefly discuss a phenomenological model for pattern formation in vibrated granular media introduced in [39]. This model, which we call Aranson–Tsimring model in the following, couples a Ginzburg–Landau-type equation [34] for the complex order parameter ψ to a conservation law for the density ρ:

$$\partial_t \psi = \gamma\bar{\psi} - (1 - i\omega)\psi + (1 + ib)\nabla^2\psi - |\psi|^2\psi - \rho\psi, \tag{24a}$$

$$\partial_t \rho = \beta\nabla^2\rho + \alpha\nabla \cdot (\rho\nabla|\psi|^2), \tag{24b}$$

where $\bar{\psi}$ denotes the complex conjugate of ψ. The coupling is such that increasing the density ρ suppresses the instability in Eq. (24a) while gradients in the amplitude $|\psi|$ drive mass redistribution away from high amplitude regions (second term in Eq. (24b)). This feedback loop amplifies heterogeneities in the density and gives rise to localized patterns. These patterns have been studied in detail using amplitude equations in [32, 33]. Moreover, in Ref. [30] it was shown that the system Eq. (24) appears as the amplitude equation for a mass-conserving version of the classical Swift–Hohenberg–Turing equation [6, 49]. The reason for this is that the conserved density appears as a second hydrodynamic variable in addition to the pattern amplitude.

A linear stability analysis shows that the system Eq. (24) has a short wavelength instability when $b\omega - 1 - \rho_0 > 0$ and $\gamma > \gamma_c = (\omega + b(1+\rho_0))/\sqrt{1+b^2}$, where ρ_0 denotes the average density. Following Ref. [33], we set parameters $b = 1, \omega = 2.5, \alpha = 1.3, \beta = 0.3, \rho_0 = 0.3$. Localized patterns are found near the instability threshold, so we set $\gamma = 1.001\gamma_c$ for the simulation shown in Fig. 6 and Movie S9.

Preparation of the wedge flow cell

The microfluidic wedge chambers were prepared using two rectangular cover slips (bottom one of dimensions 22/50 mm, and top one of dimensions 5/30 mm). Close to one of the short edges of a top glass a tiny inlet hole was drilled using a sandblaster. Cover slips were cleaned in 1 M KOH for 1 h followed by a methanol bath for 10 min in a sonicator bath. Surfaces of the cover slips were activated with oxygen plasma for 20 s, using oxygen plasma PREEN I (Plasmatic System, Inc.) with a O2 flow rate of 1 SCFH. Furthermore, a small PDMS slab with a 0.3 mm hole was attached on to the top glass slide, such that it matches the

hole in the PDMS glass slide and a metal connector was inserted in the hole for connecting the syringe pump. Tilt of the top glass slide was achieved by placing a piece of aluminum foil between the top and bottom slide at the end, with the largest height between top and bottom at the side of the inlet. At the opposite side with the smallest distance between top and bottom slide, 2 µm polystyrene beads that were deposited on the bottom slide provided an outlet and prevent a collapse of the top and bottom slides (see Fig. 2). The lateral sides of the microchamber were sealed with a two-component epoxy resin leaving the short edge at the low height-side open for liquid flow (Fig. S4). The microfluidic cell was then filled with a solution of small unilamellar vesicles (SUVs) through an injection tube at the inlet of the PDMS slab and incubated for 30 min at 30 °C–yielding full lipid membrane coverage of the bottom and top slides. SUVs were prepared as described in Ref. [28]. Subsequently, the flow cell was thoroughly washed with a buffer to remove excess SUVs and Min protein experiments were started.

Observation of Min patterns

We purified the Min proteins based on the method proposed in Ref. [50]. Injection of Min proteins into the flow cells was performed through a syringe pump containing a solution of 0.8 M MinD, 0.2 mM MinD-Cy3, 0.8 mM MinE, 0.2 mM MinE-Cy5, 5 mM ATP, 4 mM phosphoenolpyruvate, 0.01 mg/ml pyruvate kinase, 25 mM Tris-HCl (pH 7.5), 150 mM KCl and 5 mM MgCl2. To ensure that all of the buffer solution in the microdevice is replaced by the protein solution, we chose a volume of the protein solution that was 50 times larger than the volume in the microdevice. During the filling process of the microdevice, the enire solution was rapidly injected (in 5 s) to prevent protein accumulation on the membrane.

For the generation of the fluorescence images, we used the following equipment: Olympus IX-81 inverted microscope equipped with an Andor Revolution XD spinning disk system with FRAPPA, illumination and detection system Andor Revolution and Yokogawa CSU X1, EM-CCD Andor iXon X3 DU897 camera, motorized x-y stage and a z-piezo stage, using a 20x objective (UPlansApo, NA 0.85, oil immersion). Imaging of MinD-Cy3 and MinE-Cy5 was performed with laser spectral lines at 561 nm and 640 nm, respectively, and we further used a 617/73 band-pass filter as well as a 690 long-pass filter. We imaged several uniformly sized regions at intervals of 30 s or 60 s along the lateral length of the wedge setup. To exclude membrane imperfections that may have arisen during preparation, we also imaged the membrane using the spectral line at 491 nm and a 525/50 band-pass filter.

Image sequence processing

We processed the fluorescence images using the following software packages: Andor iQ3 v3.1, ImageJ 1.52j, and custom written Matlab 2016a scripts. For better visualization, we additionally applied background correction and filtering of artifacts. In detail, these were carried out as follows: For the generation of the movies, each frame was first corrected for fluorescence bleaching (max. 20 % decay of the intensity for long movies) by normalizing to the mean intensity of the respective frame. Then, we generated two different modifications

of the images: First, we averaged out all transient features (i.e., patterns) in the frames to obtain 'static background'-images which we shall call `Imstat`. Second, we smoothed out the images, determined the average of all movie frames, and normalized the corresponding result with respect to its maximum. This way, we obtained an 'illumination correction' image `Imillum`. In the final step, each frame `Immovie` was corrected according to the rule `Imcorrected` = (`Immovie` - `Imstat`)/`Imillum`. On one hand, this ensures that irregularities in each image are suppressed, and on the other hand, the intensity amplitudes at the edges becomes comparable with the values at the center of the image.

References

[1] Alan M. Turing. The chemical basis of morphogenesis. *Philosophical Transactions of the Royal Society of London. Series B, Biological Sciences*, 237(641):37–72, 1952.

[2] Shigeru Kondo and Rihito Asai. A reaction–diffusion wave on the skin of the marine angelfish Pomacanthus. *Nature*, 376(6543):765–768, 1995.

[3] Christopher A. Klausmeier. Regular and irregular patterns in semiarid vegetation. *Science (New York, N.Y.)*, 284(5421):1826–1828, 1999.

[4] J. B. A. Green and J. Sharpe. Positional information and reaction-diffusion: Two big ideas in developmental biology combine. *Development (Cambridge, England)*, 142(7):1203–1211, 2015.

[5] Jacob Halatek, Fridtjof Brauns, and Erwin Frey. Self-organization principles of intracellular pattern formation. *Philosophical Transactions of the Royal Society B: Biological Sciences*, 373(1747):20170107, 2018.

[6] M. C. Cross and P. C. Hohenberg. Pattern formation outside of equilibrium. *Reviews of Modern Physics*, 65(3):851–1112, 1993.

[7] N. Tompkins, N. Li, C. Girabawe, M. Heymann, G. B. Ermentrout, I. R. Epstein, and S. Fraden. Testing Turing's theory of morphogenesis in chemical cells. *Proceedings of the National Academy of Sciences*, 111(12):4397–4402, 2014.

[8] Erwin Frey and Fridtjof Brauns. Self-organisation of protein patterns. *arXiv:2012.01797 [nlin, physics:physics]*, 2020.

[9] Andrew B. Goryachev and Marcin Leda. Many roads to symmetry breaking: Molecular mechanisms and theoretical models of yeast cell polarity. *Molecular Biology of the Cell*, 28(3):370–380, 2017.

[10] Philipp Glock, Fridtjof Brauns, Jacob Halatek, Erwin Frey, and Petra Schwille. Design of biochemical pattern forming systems from minimal motifs. *eLife*, 8:e48646, 2019.

[11] Manon C. Wigbers, Tzer Han Tan, Fridtjof Brauns, Jinghui Liu, S. Zachary Swartz, Erwin Frey, and Nikta Fakhri. A hierarchy of protein patterns robustly decodes cell shape information. *Nature Physics*, pages 1–7, 2021.

[12] Uwe C. Täuber. *Critical Dynamics: A Field Theory Approach to Equilibrium and Non-Equilibrium Scaling Behavior*. 2014.

[13] Robert Zwanzig. *Nonequilibrium Statistical Mechanics*. Oxford University Press, Oxford ; New York, 2001.

[14] J. Halatek and E. Frey. Rethinking pattern formation in reaction–diffusion systems. *Nature Physics*, 14(5):507, 2018.

[15] Fridtjof Brauns, Jacob Halatek, and Erwin Frey. Phase-space geometry of mass-conserving reaction-diffusion dynamics. *Physical Review X*, 10(4):041036, 2020.

[16] H. I. Adler, W. D. Fisher, A. Cohen, and A. A. Hardigree. Miniature escherichia coli cells deficient in DNA. *Proceedings of the National Academy of Sciences*, 57(2):321–326, 1967.

[17] Piet A. J. de Boer, Robin E. Crossley, and Lawrence I. Rothfield. A division inhibitor and a topological specificity factor coded for by the minicell locus determine proper placement of the division septum in E. coli. *Cell*, 56(4):641–649, 1989.

[18] M. Loose, E. Fischer-Friedrich, J. Ries, K. Kruse, and P. Schwille. Spatial regulators for bacterial cell division self-organize into surface waves in vitro. *Science (New York, N.Y.)*, 320(5877):789–792, 2008.

[19] Erwin Frey, Jacob Halatek, Simon Kretschmer, and Petra Schwille. Protein pattern formation. In Patricia Bassereau and Pierre Sens, editors, *Physics of Biological Membranes*, pages 229–260. Springer International Publishing, Cham, 2018.

[20] Beatrice Ramm, Tamara Heermann, and Petra Schwille. The E. coli MinCDE system in the regulation of protein patterns and gradients. *Cellular and Molecular Life Sciences*, 76(21):4245–4273, 2019.

[21] V. Ivanov and K. Mizuuchi. Multiple modes of interconverting dynamic pattern formation by bacterial cell division proteins. *Proceedings of the National Academy of Sciences*, 107(18):8071–8078, 2010.

[22] Anthony G. Vecchiarelli, Min Li, Michiyo Mizuuchi, Ling Chin Hwang, Yeonee Seol, Keir C. Neuman, and Kiyoshi Mizuuchi. Membrane-bound MinDE complex acts as a toggle switch that drives Min oscillation coupled to cytoplasmic depletion of MinD. *Proceedings of the National Academy of Sciences*, 113(11):E1479–E1488, 2016.

[23] Jonas Denk, Simon Kretschmer, Jacob Halatek, Caroline Hartl, Petra Schwille, and Erwin Frey. MinE conformational switching confers robustness on self-organized Min protein patterns. *Proceedings of the National Academy of Sciences*, 115(18):4553–4558, 2018.

[24] Thomas Litschel, Beatrice Ramm, Roel Maas, Michael Heymann, and Petra Schwille. Beating vesicles: Encapsulated protein oscillations cause dynamic membrane deformations. *Angewandte Chemie International Edition*, 57(50):16286–16290, 2018.

[25] Elisa Godino, Jonás Noguera López, David Foschepoth, Céline Cleij, Anne Doerr, Clara Ferrer Castellà, and Christophe Danelon. De novo synthesized Min proteins drive oscillatory liposome deformation and regulate FtsA-FtsZ cytoskeletal patterns. *Nature Communications*, 10(1):4969, 2019.

[26] Shunshi Kohyama, Natsuhiko Yoshinaga, Miho Yanagisawa, Kei Fujiwara, and Nobuhide Doi. Cell-sized confinement controls generation and stability of a protein wave for spatiotemporal regulation in cells. *eLife*, 8:e44591, 2019.

[27] Philipp Glock, Beatrice Ramm, Tamara Heermann, Simon Kretschmer, Jakob Schweizer, Jonas Mücksch, Gökberk Alagöz, and Petra Schwille. Stationary patterns in a two-protein reaction-diffusion system. *ACS Synthetic Biology*, 8(1):148–157, 2019.

[28] Fridtjof Brauns, Grzegorz Pawlik, Jacob Halatek, Jacob Kerssemakers, Erwin Frey, and Cees Dekker. Bulk-surface coupling identifies the mechanistic connection between Min-protein patterns in vivo and in vitro. *Nature Communications*, 12(1), 2021.

[29] Anthony G. Vecchiarelli, Min Li, Michiyo Mizuuchi, and Kiyoshi Mizuuchi. Differential affinities of MinD and MinE to anionic phospholipid influence Min patterning dynamicsin vitro. *Molecular Microbiology*, 93(3):453–463, 2014.

[30] P. C. Matthews and S. M. Cox. Pattern formation with a conservation law. *Nonlinearity*, 13(4):1293–1320, 2000.

[31] S. M. Cox and P. C. Matthews. Instability and localisation of patterns due to a conserved quantity. *Physica D: Nonlinear Phenomena*, 175(3-4):196–219, 2003.

[32] D. M. Winterbottom, P. C. Matthews, and S. M. Cox. Oscillatory pattern formation with a conserved quantity. *Nonlinearity*, 18(3):1031–1056, 2005.

[33] D. M. Winterbottom, S. M. Cox, and P. C. Matthews. Pattern formation in a model of a vibrated granular layer. *SIAM Journal on Applied Dynamical Systems*, 7(1):63–78, 2008.

[34] Igor S. Aranson and Lorenz Kramer. The world of the complex Ginzburg-Landau equation. *Reviews of Modern Physics*, 74(1):99–143, 2002.

[35] Stuart Berg, Dominik Kutra, Thorben Kroeger, Christoph N. Straehle, Bernhard X. Kausler, Carsten Haubold, Martin Schiegg, Janez Ales, Thorsten Beier, Markus Rudy, Kemal Eren, Jaime I. Cervantes, Buote Xu, Fynn Beuttenmueller, Adrian Wolny, Chong Zhang, Ullrich Koethe, Fred A. Hamprecht, and Anna Kreshuk. Ilastik: Interactive machine learning for (bio)image analysis. *Nature Methods*, 16(12):1226–1232, 2019.

[36] Fridtjof Brauns, Jacob Halatek, and Erwin Frey. Diffusive coupling of two well-mixed compartments elucidates elementary principles of protein-based pattern formation. *Physical Review Research*, 3(1), 2021.

[37] Mariela D. Petkova, Gašper Tkačik, William Bialek, Eric F. Wieschaus, and Thomas Gregor. Optimal decoding of cellular identities in a genetic network. *Cell*, 176(4):844–855.e15, 2019.

[38] Fridtjof Brauns, Henrik Weyer, Jacob Halatek, Junghoon Yoon, and Erwin Frey. Wavelength selection by interrupted coarsening in reaction-diffusion systems. *Physical Review Letters*, 126(10), 2021.

[39] Lev S. Tsimring and Igor S. Aranson. Localized and cellular patterns in a vibrated granular layer. *Physical Review Letters*, 79(2):213–216, 1997.

[40] M. C. Marchetti, J. F. Joanny, S. Ramaswamy, T. B. Liverpool, J. Prost, Madan Rao, and R. Aditi Simha. Hydrodynamics of soft active matter. *Reviews of Modern Physics*, 85(3):1143–1189, 2013.

[41] Markus Bär, Robert Großmann, Sebastian Heidenreich, and Fernando Peruani. Self-propelled rods: Insights and perspectives for active matter. *Annual Review of Condensed Matter Physics*, 11(1):441–466, 2020.

[42] Jonas Denk and Erwin Frey. Pattern-induced local symmetry breaking in active-matter systems. *Proceedings of the National Academy of Sciences*, 117(50):31623–31630, 2020.

[43] Olivier Dauchot and Hartmut Löwen. Chemical physics of active matter. *The Journal of Chemical Physics*, 151(11), 2019.

[44] Robert Großmann, Igor S. Aranson, and Fernando Peruani. A particle-field approach bridges phase separation and collective motion in active matter. *Nature Communications*, 11(1), 2020.

[45] K. C. Huang, Y. Meir, and N. S. Wingreen. Dynamic structures in Escherichia coli: Spontaneous formation of MinE rings and MinD polar zones. *Proceedings of the National Academy of Sciences*, 100(22):12724–12728, 2003.

[46] Jacob Halatek and Erwin Frey. Highly canalized MinD transfer and MinE sequestration explain the origin of robust MinCDE-Protein dynamics. *Cell Reports*, 1(6):741–752, 2012.

[47] Martin Loose, Karsten Kruse, and Petra Schwille. Protein self-organization: Lessons from the min system. *Annual Review of Biophysics*, 40(1):315–336, 2011.

[48] G. Meacci, J. Ries, E. Fischer-Friedrich, N. Kahya, P. Schwille, and K. Kruse. Mobility of Min-proteins in ¡i¿Escherichia coli¡/i¿ measured by fluorescence correlation spectroscopy. *Physical Biology*, 3(4):255–263, 2006.

[49] Jonathan H. P. Dawes. After 1952: The later development of Alan Turing's ideas on the mathematics of pattern formation. *Historia Mathematica*, 43(1):49–64, 2016.

[50] Yaron Caspi and Cees Dekker. Mapping out Min protein patterns in fully confined fluidic chambers. *eLife*, 5, 2016.

Supplementary Information for

Bridging scales in a multiscale pattern-forming system

Laeschkir Würthner*, Fridtjof Brauns*, Grzegorz Pawlik,
Jacob Halatek, Jacob Kerssemakers, Cees Dekker†, and Erwin Frey†

*L.W. and F.B. contributed equally to this work.
†Correspondence to: frey@lmu.de or c.dekker@tudelft.nl

Linear stability analysis

As outlined in the main text, we performed a linear stability analysis to determine the instantaneous dispersion relation in each slice of the wedge geometry. The dispersion relation, from which we determine the commensurability of unstable modes, then informs about the pattern type in the slice. The general procedure for the linear stability analysis is as follows: First, one determines a homogeneous steady state and linearizes the dynamics around this steady state. The linearized system can be solved by a *normal mode expansion*, which yields a relation between the growth rate of modes σ and the mode number q. The relationship $\sigma(q)$ is the dispersion relation, and indicates whether spatial perturbations with mode number q decay to the homogeneous steady state ($\sigma < 0$) or are amplified and growth exponentially with time ($\sigma > 0$). In the following, we briefly explain the linear stability analysis procedure for the Min dynamics in rectangular geometry and refer for an in-depth analysis to Refs. [1, 2]

Homogeneous steady states at the membrane

To obtain the homogeneous steady state solution along the membrane, we first determine the the steady state concentration profiles in the cytosol $\mathbf{c}^* = [c^*_\mathrm{D}, c^*_\mathrm{DD}, c^*_\mathrm{E}]^\top$:

$$\mathbf{0} = D_c(\partial_x^2 + \partial_z^2)\mathbf{c}^* - \beta\mathbf{c}^*, \tag{S1}$$

where $\beta = \mathrm{diag}(0, \lambda, 0)$. These equations can be solved by a separation of variables and yield the following solution:

$$c^*_\mathrm{D}(z) = c^*_\mathrm{D}|_{z=0} = \text{const.}, \tag{S2a}$$

$$c^*_\mathrm{DD}(z) = c^*_\mathrm{DD}|_{z=0}\frac{\cosh\left((H-z)/\ell\right)}{\cosh\left(H/\ell\right)}, \tag{S2b}$$

$$c^*_\mathrm{E}(z) = c^*_\mathrm{E}|_{z=0} = \text{const.}, \tag{S2c}$$

where $c^*|_{z=0} = c^*_i(z=0)$ ($i \in \{\mathrm{D}, \mathrm{DD}, \mathrm{E}\}$) denote the steady state homogeneous cytosolic concentrations at the membrane, and $\ell = \sqrt{D_c/\lambda}$ defines the characteristic length scale of cytosolic gradients into the bulk. Note that $\partial_x\mathbf{c}^* = 0$, because we are interested in homogeneous solutions along the membrane. Plugging these solutions into the membrane reactions and bulk-membrane coupling (cf. Eq. [2] and [3] in the main text) one finds the following set of equations:

$$\boldsymbol{f}\left(\mathbf{c}^*|_{z=0}, \mathbf{m}^*\right) = \boldsymbol{\Phi}, \tag{S3a}$$

$$\mathbf{r}(\mathbf{c}^*|_{z=0}, \mathbf{m}) = \mathbf{0}, \tag{S3b}$$

where

$$\mathbf{\Phi} = \begin{bmatrix} 0 \\ D_c/\ell \tanh\left(H/\ell\right) c^*_{\mathrm{DD}}|_{z=0} \\ 0 \end{bmatrix}. \tag{S4}$$

Together with the mass-conservation constraint:

$$\overline{n}_{\mathrm{D}} = c^*_{\mathrm{D}}|_{z=0} + \frac{1}{H}(m^*_{\mathrm{d}} + m^*_{\mathrm{de}}), \tag{S5a}$$

$$\overline{n}_{\mathrm{E}} = c^*_{\mathrm{E}}|_{z=0} + \frac{1}{H} m^*_{\mathrm{de}}, \tag{S5b}$$

the solution of the nonlinear system (S3) and (S5) determines the homogeneous steady state solutions at the membrane. This nonlinear system of equations can be solved numerically by root-finding algorithms such as the *Newton algorithm*. Here, we used the built-in function `NSolve[]` in Mathematica 12 to numerically determine the homogeneous steady states.

The linearized dynamics and growth rates for small spatial perturbations

Next, we ask for the stability of the homogeneous steady state against small spatial perturbations. To this end, we linearize the dynamics around the homogeneous steady state and determine the time evolution of perturbations $\delta\mathbf{m}(x,t) = \mathbf{m}(x,t) - \mathbf{m}^*$ and $\delta\mathbf{c}(x,z,t) = \mathbf{c}(x,z,t) - \mathbf{c}^*|_{z=0}$:

$$\partial_t \delta\mathbf{c} = D_c(\partial_x^2 + \partial_z^2)\delta\mathbf{c} - \beta\delta\mathbf{c}, \tag{S6a}$$

$$-D_c \partial_z \delta\mathbf{c}|_{z=0} = \partial_{\mathbf{u}}\mathbf{f}\, \delta\mathbf{u}, \tag{S6b}$$

$$\partial_t \delta\mathbf{m} = D_m \partial_x^2 \delta\mathbf{m} + \partial_{\mathbf{u}}\mathbf{r}\delta\mathbf{u}, \tag{S6c}$$

where $\mathbf{u} = [\mathbf{c}, \mathbf{m}]^\top$ denotes the concentration vector and $\delta\mathbf{u} = [\delta\mathbf{c}|_{z=0}, \delta\mathbf{m}]^\top$ the perturbation vector at the membrane. The Jacobian matrices of the bulk-boundary coupling and membrane reactions $\partial_{\mathbf{u}}\mathbf{f} \equiv \partial_{\mathbf{u}}\mathbf{f}|_{(\mathbf{c}^*|_{z=0}, \mathbf{m}^*)}$ and $\partial_{\mathbf{u}}\mathbf{r} \equiv \partial_{\mathbf{u}}\mathbf{r}|_{(\mathbf{c}^*|_{z=0}, \mathbf{m}^*)}$ are evaluated at the homogeneous steady state at the membrane. The linearized system (S6) can be solved by a normal mode expansion of the form:

$$\delta c_i(x,z,t) = \sum_q e^{\sigma_q t} \cos(qx) Z_i(z;\sigma_q,q)\delta\hat{c}_{i,q}, \tag{S7a}$$

$$\delta\mathbf{m}(x,t) = \sum_q e^{\sigma_q t} \cos(qx)\delta\hat{\mathbf{m}}_q, , \tag{S7b}$$

here σ_q defines the growth rate of perturbations with respective mode number q. The Fourier coefficients are given by $\delta\hat{\mathbf{c}}_q$ and $\delta\hat{\mathbf{m}}_q$, respectively, and the bulk modes $Z_i(z;\sigma_q,q)$ have a similiar form as for the homogeneous steady states:

$$Z_i(z;\sigma_q,q) \sim \frac{\cosh\left(\gamma_q^i(z-H)\right)}{\cosh\left(\gamma_q^i H\right)}, \tag{S8}$$

where the parameters γ_q^i take different values dependent on whether the bulk dynamics is purely diffusive or contains linear reactions (i.e. nucleotide exchange), therefore $\gamma_q^{\mathrm{D}} = \gamma_q^{\mathrm{E}} = \sqrt{\sigma_q/D_c + q^2}$ and $\gamma_q^{\mathrm{DD}} = \sqrt{(\sigma_q+\lambda)/D_c + q^2}$, respectively. Plugging the normal mode expansions (S7) into the linearized bulk-boundary coupling and membrane dynamics (S6) yields an eigenvalue problem for the growth rates σ_q as a function of the modes q. This transcendental eigenvalue problem is given in compact form by:

$$\underbrace{\begin{pmatrix} -D_c\,\mathbf{\Gamma}(\sigma_q,q) + \mathbf{f_c} & \mathbf{f_m} \\ \mathbf{r_c} & -(\sigma_q + q^2 D_m) I_2 + \mathbf{r_m} \end{pmatrix}}_{=:\,\mathbf{M}(\sigma_q,q)} \begin{bmatrix} \delta\hat{\mathbf{c}}_q \\ \delta\hat{\mathbf{m}}_q \end{bmatrix} = \mathbf{0} \tag{S9}$$

where I_2 denotes the 2x2 identity matrix, and $\mathbf{\Gamma} := \mathrm{diag}\left(\Gamma(\gamma_q^{\mathrm{D}}), \Gamma(\gamma_q^{\mathrm{DD}}), \Gamma(\gamma_q^{\mathrm{E}})\right)$ is a coupling matrix due to bulk-coupling, where

$$\Gamma(\gamma_q^i) = D_c \gamma_q^i \tanh\left(\gamma_q^i H\right). \tag{S10}$$

The growth rates σ_q are then determined by solving the transcendental characteristic equation:

$$\det\left(\mathbf{M}(\sigma_q,q)\right) = 0. \tag{S11}$$

The dispersion relation is given by the largest real solution (fastest growing mode) of (S11). We solved (S11) numerically using the built-in function `FindRoot[]` in Mathematica 12.

Pattern prediction from local dispersion relations

Here, we provide more details on how we technically predict the patterns in each slice from the simulation data. Specifically, we explain the steps required to generate the kymographs in the main text (Figs. 4 and 5)

Computation of the total densities in the slices from numerical data

To determine the slice averaged densities at each position x along the wedge geometry, we first exported the membrane concentration profiles of MinD and MinE from the simulation data as a *grid data file*. We exported the grid file for each time step $\delta t = 2\,\mathrm{s}$, where the grid file consists of 400×400 spatial points (400 data points in each spatial direction), which is equivalent to a spatial discretization of $\delta x = \delta y = 1.25\,\mu\mathrm{m}$.

To obtain the slice-averaged densities, we imported the simulation data to *Mathematica 12* and averaged the total densities of MinD and MinE along the $y-$direction, thereby reducing the data to a one-column grid file which contains 400 points, corresponding to the slice-averaged densities along the $x-$direction. To reduce the computational effort for the calculations of the dispersion relations and to smooth the data, we additionally averaged the slice densities over 4 points in space (i.e. resulting in a new step size $\delta x_{\mathrm{avg}} = 4\delta x$) and 10 steps in time (i.e. obtaining the new time step $\delta t_{\mathrm{avg}} = 10\delta t$) using the Mathematica built-in functions `Partition[]` and `Mean[]`. This way we reduced the number of points in the grid file to 100 spatial points and 450 points in time, respectively.

Determination of the instantaneous dispersion relations and commensurability condition

The total average densities in each slice (see above) are then plugged into (S11) to determine the dispersion relation at each point in time. From the disperion relation we determine the commensurability of unstable modes, whose value informs about the pattern in the slices as explained in the main text. To illustrate how the commensurability condition varies with time and space, we generated the kymographs (Figs. 4A and 5C) in the main text, where the commensurability condition is color coded as shown in the figure.

Since the transition in the commensurability condition from standing wave to traveling wave patterns is not sharp, but rather occurs around the onset for $q_{\mathrm{max}}/q^* = 2$, we additionally applied a color gradient for standing

waves (green) to make this point clear.

Regularization of the local-equilibrium approximation

In the main text, we use a local-equilibrium approximation to obtain the reduced dynamics for the (slice-averaged) total densities. This reduced dynamics is well-defined as long as the local equilibria c_i^* do not undergo saddle-node bifurcations (where a stable and an unstable equilibrium annihilate). If a saddle-node bifurcation occurs at some point in the spatial domain, $c_i^*(x)$ will be discontinuous at this point as it jumps from one branch of equilibria (which is annihilated) to another one. To regularize the dynamics, we introduce auxiliary fields $\tilde{c}_i(x,t)$ which relax to the equilibrium concentrations $c_i^*(x,t)$ on a fast timescale compared to the large scale mass-redistribution. In the limit of fast relaxation, the concrete implementation of the relaxation dynamics is irrelevant. An intuitive choice for the relaxation dynamics would be, for example, $\partial_t \tilde{c}_i(x,t) = -\alpha[\tilde{c}_i(x,t) - c_i^*(x,t)]$, where α denotes the relaxation rate. However, this choice requires explicit computation of the local equilibria $c_i^*(x,t)$ at each timestep which is computationally costly and complicates the numerical implementation.

In the following, we construct an auxiliary relaxation dynamics such that the equilibria c_i^* are implicit in the relaxation dynamics and don't need to be computed explicitly. We start by imposing the local equilibrium assumption on the vertical bulk profiles (cf. (S2)). Note that we do this at each lateral position x separately. For ease of notation, we do not denote the x-dependence explicitly below.

$$\tilde{c}_{\mathrm{D}}(z) = \tilde{c}_{\mathrm{D}} = \text{const.} \tag{S12a}$$

$$\tilde{c}_{\mathrm{DD}}(z) = \tilde{c}_{\mathrm{DD}}(0)\,\frac{\cosh\Big(\sqrt{\lambda/D_c}\,(H(x)-z)\Big)}{\cosh\Big(\sqrt{\lambda/D_c}\,H(x)\Big)}\,, \tag{S12b}$$

$$\tilde{c}_{\mathrm{E}}(z) = \tilde{c}_{\mathrm{E}} = \text{const.} \tag{S12c}$$

The dynamics for the total densities is now defined in terms of the auxiliary cytosolic densities (cf. Eq. [8] in the main text)

$$\partial_t \tilde{n}_{\mathrm{i}}(x,t) = D_c \partial_x^2 \tilde{c}_{\mathrm{i}} + D_c \tfrac{\partial_x H(x)}{H(x)}\,\partial_x \tilde{c}_{\mathrm{i}}\,. \tag{S13}$$

To construct the auxiliary relaxation dynamics for $\tilde{c}_{\mathrm{D}}$ and $\tilde{c}_{\mathrm{E}}$, we eliminate the membrane concentration variables m_{d}, m_{de} by using the mass conserva-

tion constraint (cf. 4a and 4b in the main text)

$$\tilde{m}_{\mathrm{d}} = H(x)\,\tilde{n}_{\mathrm{D}} - H(x)\,\tilde{c}_{\mathrm{D}} - \tilde{m}_{\mathrm{de}}, \tag{S14}$$

$$\tilde{m}_{\mathrm{de}} = H(x)\,\tilde{n}_{\mathrm{E}} - H(x)\,\tilde{c}_{\mathrm{E}}, \tag{S15}$$

Next, we eliminate $\tilde{c}_{\mathrm{DD}}(0)$ by imposing the boundary condition $\partial_z \tilde{c}_{\mathrm{DD}}|_{z=0} = k_{\mathrm{de}} m_{\mathrm{de}}$, which yields

$$\sqrt{\lambda/D_c}\,\tanh\Big(\sqrt{\lambda/D_c}\,H(x)\Big)\;\tilde{c}_{\mathrm{DD}}(0) = k_{\mathrm{de}}\tilde{m}_{\mathrm{de}}. \tag{S16}$$

Note that we do not enforce the boundary conditions for $\tilde{c}_{\mathrm{D}}$ and $\tilde{c}_{\mathrm{E}}$. Instead, we will use these boundary conditions to define auxiliary relaxation dynamics for $\tilde{c}_{\mathrm{D}}$ and $\tilde{c}_{\mathrm{E}}$ as follows

$$\partial_t \tilde{c}_{\mathrm{i}}(x,t) = D_c \partial_x^2 \tilde{c}_{\mathrm{i}} + D_c \tfrac{\partial_x H(x)}{H(x)}\,\partial_x \tilde{c}_{\mathrm{i}} + \alpha \tilde{f}_{\mathrm{i}}\big(\tilde{c}_{\mathrm{D}}, \tilde{c}_{\mathrm{E}}\big)\,, \tag{S17}$$

with the auxiliary reaction terms

$$\tilde{f}_{\mathrm{D}} = \frac{1}{H}\big(k_{\mathrm{de}}\tilde{m}_{\mathrm{de}} - (k_{\mathrm{D}} + k_{\mathrm{dD}}\tilde{m}_{\mathrm{d}})[\tilde{c}_{\mathrm{D}} - \tilde{c}_{\mathrm{DD}}(0)]\big), \tag{S18}$$

$$\tilde{f}_{\mathrm{E}} = \frac{1}{H}\big(k_{\mathrm{de}}\tilde{m}_{\mathrm{de}} - k_{\mathrm{dE}}\tilde{m}_{\mathrm{d}}\tilde{c}_{\mathrm{E}}\big) \tag{S19}$$

obtained by substituting the auxiliary variables into the boundary fluxes of c_i (see Eq. [11] in the main text). Observe that $\tilde{f}_{\mathrm{i}} = 0$ for $\tilde{c}_{\mathrm{i}} = c_{\mathrm{i}}^*$, i.e. the auxiliary reactions relax towards the local steady state concentrations, as required. The factor $1/H$ comes in because the auxiliary fields $\tilde{c}_i$ represent the uniform bulk concentrations whose rate of change is obtained by distributing the boundary flux f_i over the entire vertical column with height H. The relaxation rate factor α above can be used to adjust the relaxation rate to minimize the deviation from the local equilibria while avoiding the emergence of too sharp gradients. We performed simulations of the auxiliary dynamics for different values of α and found no noticeable changes in the results, when increasing α above 1.

We have numerically implemented the system of PDEs defined by (S13) and (S17) in *Mathematica 12.3* using a finite-difference discretization (first order central differences, 200 grid points). The resulting high-dimensional ODEs system is integrated using *Mathematica's* `NDSolve` function.

Average total densities control the final steady state pattern

In the main text, we have shown that a variety of different patterns emerge on the membrane, and that these patterns transition to other patterns over

time. For large times, however, we found that the system approaches a stable steady state that is characterized by standing wave patterns which emerge on the entire membrane. The underlying reason is that for large times the density profile in the bulk approaches a (heterogeneous) steady state distribution due to mass-redistribution (diffusive fluxes). At this steady state, the dispersion relation becomes insensitive to the local total densities and the bulk height, resulting in loss of heterogeneity and thus to the selection of one pattern type on the membrane. What determines the type of this pattern?

The final steady state profiles of the total densities depend on the average total densities in the system, which are set by the initial condition. For the simulation presented in the main text, we tuned these densities to achieve $q_{\max} \approx 2q^*$ (i.e. standing waves) in the final steady state. As the density profiles relax towards this steady state, they fluctuate (oscillate) around this critical mode ratio which leads to the intriguing sequence of transient patterns.

For comparison, we performed a second simulation with a lower average MinD density $\bar{n}_{\mathrm{D}} = 638\,\mu\mathrm{m}^{-3}$, such that the $q_{\max} > 2q^*$ in the final steady state. Accordingly, the system settles in traveling wave patterns after a considerably shorter transient (see Fig. 1 and Movie S1).

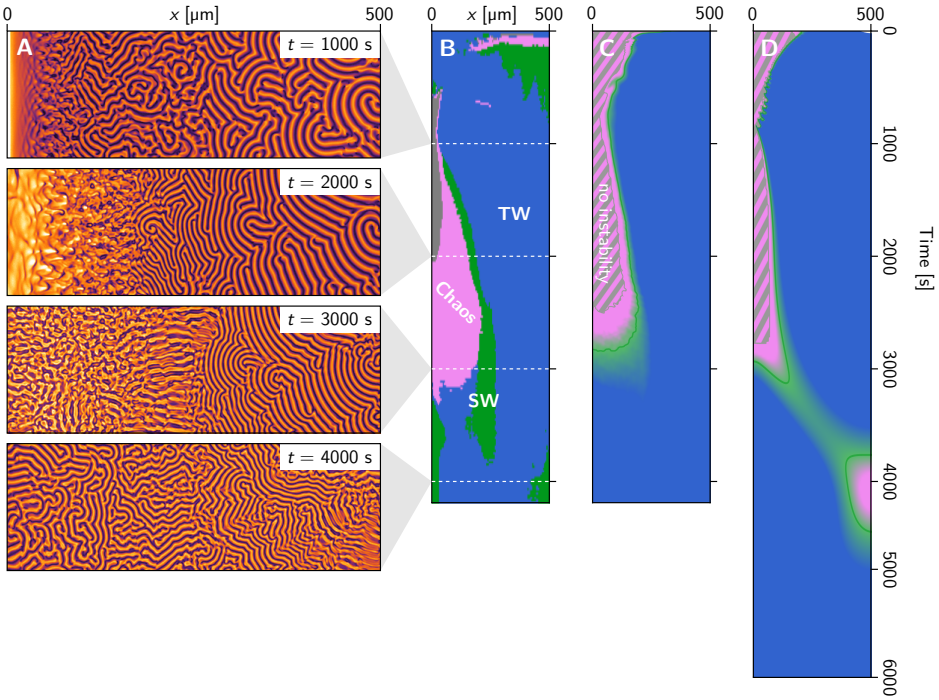

Fig. 1. Pattern type classification and prediction for a second parameter set which exhibits traveling waves in the entire domain in the steady state reached for large times ($t > 4000\,\mathrm{s}$). (A) Snapshots from the full numerical simulation (cf. Movie S1). Parameters: $\bar{n}_\mathrm{D} = 638\,\mu\mathrm{m}^{-3}$, all other parameters as in Tab. 1 in the main text. (B) Computer-based pattern classification from the full simulation using *ilastik* (compare to Fig. 4D). Note that the classifier is unreliable during the initial transient (first ∼500 s) where large scale trigger waves dominate. (C) Prediction based on slice-averaged total densities extracted from the full numerical simulation (analogous to Fig. 4A). (D) Prediction based on the reduced mass-redistribution dynamics Eq. [8] (analogous to Fig. 5C).

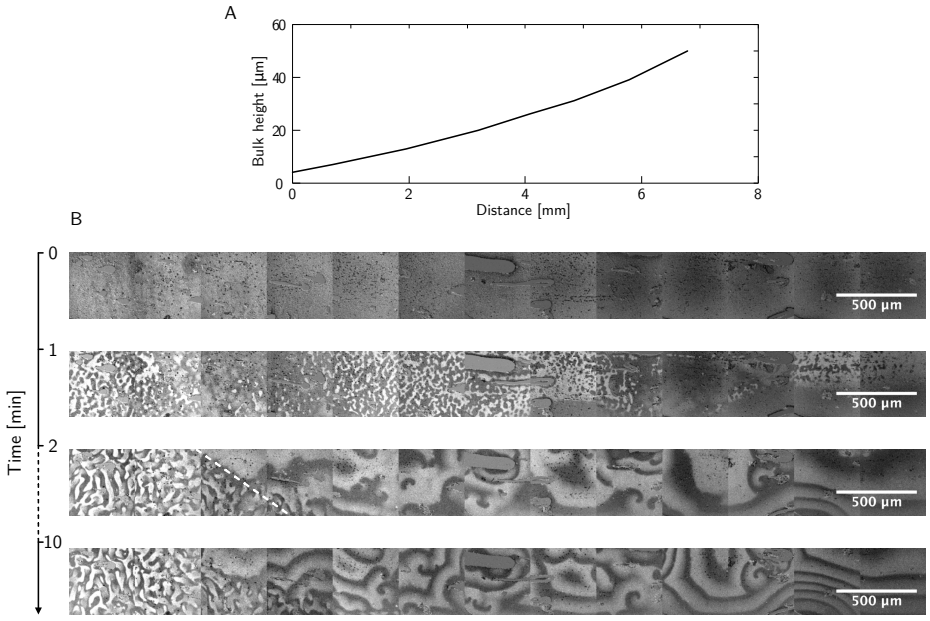

Fig. 2. Establishment of coexisting patterns in different spatial regions. (*A*) Measured bulk height profile versus lateral distance. (*B*) Spatial intensity profile of MinD along the wedge at different points in time, snapshots were taken at 0, 1, 2, and 10 minutes. White dashed line shows the approximate boundary line, where standing wave patterns transition to homogeneous oscillations.

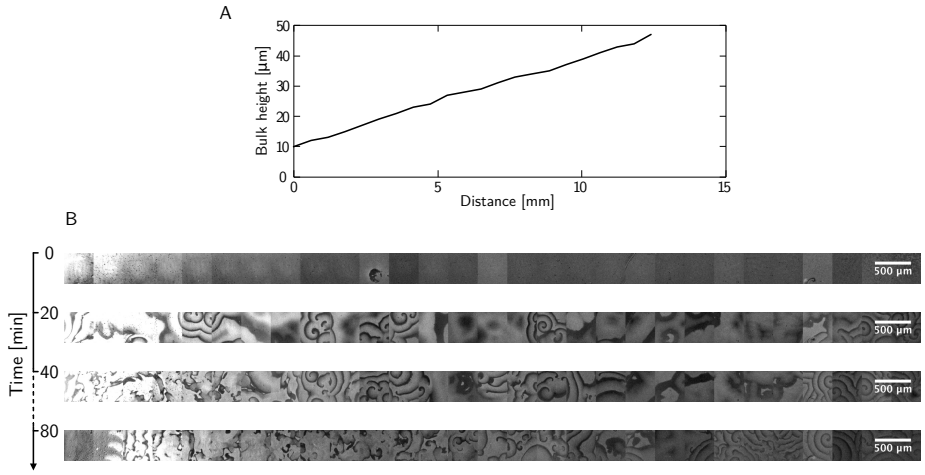

Fig. 3. Transition of homogeneous oscillations to traveling wave patterns. (*A*) Measured bulk height profile versus lateral distance. Snapshots along the wedge were taken at the time 0, 20, 40 and 80 minutes. (*B*) Spatial intensity profile of MinD along the wedge at different points in time, snapshots were taken at 0, 20, 40, and 80 minutes. At early times, homogenous oscillations turn into travelling waves at different regions. For long times, regions containing rather chaotic homogenous oscillations invade other regions (that contain different patterns) from low to high bulk heights.

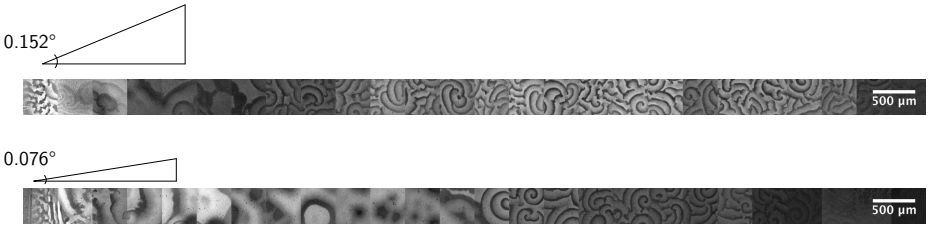

Fig. 4. The bulk height gradient affects patterns along the wedge. Shown are the Min patterns in two different flow cells that had a different tilt (angle between top and bottom membranes). In the setup with higher tilt (top), traveling wave patterns are more abundant than homogenous oscillations. For a smaller angle (bottom), one observes more regions that contain homogeneous oscillations. The snapshots were both taken 20 minutes after flushing in the Min proteins (MinD channel shown).

Movie S1. Numerical simulation of the Min dynamics in wedge geometry for total average densities $\bar{n}_{\mathrm{D}} = 665\,\mu\mathrm{m}^{-3}$ and $\bar{n}_{\mathrm{E}} = 410\,\mu\mathrm{m}^{-3}$. Shown is the MinD density along the membrane (bottom surface of the wedge, see Fig. 1B). For large times, the system approaches a steady state consisting of standing wave patterns on the entire membrane surface.

Movie S2. Numerical simulation for total average densities $\bar{n}_{\mathrm{D}} = 638\,\mu\mathrm{m}^{-3}$, $\bar{n}_{\mathrm{E}} = 410\,\mu\mathrm{m}^{-3}$. For these parameters, traveling wave patterns form in the entire wedge in the steady state reached for large times ($t > 4000\,\mathrm{s}$). Compare Fig. 1.

Movie S3. Experimentally observed Min patterns in a wedge-shaped microfluidic flow chamber. As in our numerical simulations, we observe coexisting spatiotemporal patterns along the membrane (as shown in Fig. 2C).

Movie S4. Experimentally observed establishment of a sharp boundary between regions containing traveling wave patterns and regions containing chaotic or standing wave patterns (as shown in Fig. 2).

Movie S5. Experiment showing emergence of homogeneous oscillations and transitions to traveling waves (corresponds to Fig. 3).

Movie S6. Experiments with steep bulk height gradients show the predominant emergence of traveling wave patterns (cf. Fig. 4, top).

Movie S7. Experiments with shallow bulk height gradients show more regions with nearly homogeneous oscillations/phase waves (cf. Fig. 4, bottom).

Movie S8. Pattern prediction from regional dispersion relations and coarse-grained densities (as illustrated in Fig. 3 and Fig. 4).

Movie S9. Numerical simulation of the Aranson–Tsimring model showing the order parameter amplitude $|\psi|$ (top) and coarse grained density (bottom). Dashed white line indicates the stability threshold determined from regional dispersion relations. See Fig. 6 for details.

References

[1] J. Halatek and E. Frey. Rethinking pattern formation in reaction–diffusion systems. *Nature Physics*, 14(5):507, 2018.

[2] Fridtjof Brauns, Grzegorz Pawlik, Jacob Halatek, Jacob Kerssemakers, Erwin Frey, and Cees Dekker. Bulk-surface coupling identifies the mechanistic connection between min-protein patterns in vivo and in vitro. *Nature Communications*, 12(1), 2021.

2 Pattern formation on dynamic manifolds

In this section we present our findings on how dynamic membrane deformations affect patterns along the membrane. The following content is based on and uses parts of our submitted paper [82]. We provide a reprint of the paper in section 2.6.

2.1 Background

In the specific context of intracellular patterns, the shape of cells dynamically adapts during many cellular processes such as growth, motility, and division. Such shape deformations are controlled by the cell cortex via a number of mechanisms, such as actin polymerization [83–85], or contractility gradients in the actomyosin complex (cortical flows) [38, 86]. Notably, shape deformations are not exclusively driven by cytoskeletal components. For example, proteins that contain BAR-domains can bind to the cell membrane in a curvature-dependent fashion and directly induce shape deformations [32, 33, 87–89]. In addition, as we will discuss in detail in chapter IV, it has been further shown that the motorprotein myosin-VI is capable of remodelling membranes by cooperatively binding to negatively curved regions of phospholipids [34]. Importantly, such shape changes are in general regulated by protein patterns, such as Rho-GTPases that control the spatiotemporal organization of the actomyosin complex [37]. Strikingly, it was recently shown that the reconstituted *E. coli* Min protein system is able to dynamically deform the shape of lipid membranes, including giant unilamellar vesicles (GUVs) [90–92].

The examples outlined above underscore that protein patterns are generally interlinked with cell shape, and this interplay gives rise to intricate *mechanochemical* feedback loops between shape and biochemical dynamics that lies at the heart of many cellular processes [93]. Many theoretical studies have been conducted to investigate mechanochemical pattern formation in biological systems [89, 94, 95]. For instance, in Refs. [96] the authors theoretically model the actomyosin cortex as an elastic active sheet, where the contractility is regulated by chemicals that bind to and are transported along the cortex (cortical flows). Other works studied computational models of classical reaction-diffusion equations on dynamic membrane surfaces [97, 98], or the impact of membrane curvature on the aggregation of transmembrane proteins [99]. In addition, recent studies theoretically investigated mechanochemical coupling between curved proteins (BAR proteins) and membrane shape [35, 100], as well as the coupled dynamics between morphogens and tissues [101]. Due to the inherent complexity of mechanochemical pattern formation, most of these works relied on linear stability analysis and numerical simulations, rendering it difficult to gain theoretical understanding of the underlying principles of such systems.

To elucidate some of the mechanisms that underlie such systems, we study here the dynamics of a two-component mass-conserving reaction-diffusion system (MCRD) coupled to the shape of a fluid-like one-dimensional manifold (which represents the cell membrane). We first derive the governing equations for general reaction-diffusion systems on time-evolving manifolds. By generalizing a recently developed framework for MCRD systems, termed *local equilibria theory* [13, 28, 41], we derive a criterion that allows to link the onset of lateral instabilities to the phase-space structure of the MCRD. Strikingly, our analytical results reveal that shape deformations generically induce inhomogeneities in the reaction kinetics, which may induce pattern-forming instabilities in parts of the geometry. We refer to this effect as *regional instabilities* and we identify the local conformation of the membrane as an important dynamical control parameter that drives these instabilities. In contrast to the system studied in section 1, the inhomogeneities here are self-generated by the dynamics. In addition, shape deformations may also suppress the establishment of patterns or spatially shift pre-existing patterns. Importantly, our work further shows that a mechanochemical feedback between the two-component MCRD system and the one-dimensional manifold leads to a variety of dynamic patterns, such as oscillations, traveling waves, and standing waves, that do not occur on a static geometry. We identify the local membrane conformation as an important degree of freedom in the dynamics (in addition to the local total masses).

2.2 Reaction-diffusion equations on time-evolving manifolds

We consider a two-component mass-conserving reaction-diffusion system defined on a dynamic, time-evolving geometry and ask for the general mathematical form of such a system. Moreover, to keep the discussion simple and concise, we restrict ourself to systems defined on a dynamic one-dimensional manifold. However, many of the ideas presented below can be readily generalized to higher dimensions.

The specific reaction-diffusion model that we consider here consists of one protein species that can cycle between a cytosolic state c and a membrane state m via (nonlinear) attachment and detachment processes described by the reaction function $f(m, c)$. This reaction-diffusion system has been proposed as a conceptual model for cell polarity[41, 102], and was extensively studied on a static straight line in the literature [41].

Applying tools from differential geometry, one can derive the following general form for a two-component system on a dynamic manifold:

$$\frac{d}{dt}m(\sigma,t) + \nabla_s(v_\tau m) = D_m\nabla_s^2 m + f(m,c) + \kappa\, v_n\, m\,, \tag{II.11a}$$

$$\frac{d}{dt}c(\sigma,t) + \nabla_s(v_\tau c) = D_c\nabla_s^2 c - f(m,c) + \kappa\, v_n\, c\,. \tag{II.11b}$$

The curve parameter $\sigma \in [0, \sigma_0]$ marks the *material points* along the manifold, and $\nabla_s \equiv d/ds$ denotes the arc-length derivative or surface gradient. The generalized Laplace operator ∇_s^2 in curved space (Laplace-Beltrami operator) is related to the curve parameter via the metric tensor $g(\sigma,t)$ (here scalar) or *first fundamental form*, which is induced by the parametrization

$$\nabla_s^2 = \frac{1}{\sqrt{g}}\frac{\partial}{\partial\sigma}\left(\frac{1}{\sqrt{g}}\frac{\partial}{\partial\sigma}\right)\,. \tag{II.12}$$

The role of the advective flux on the left-hand side in Eq. (II.11) is twofold: First, it describes dilution of particle concentrations in the co-moving frame by in-plane flows given by $\nabla_s v_\tau(\cdot)$, where v_τ denotes the tangential flow velocity. Such flows arise, for instance, naturally from dynamic in-plane stresses or contractility gradients along the manifold [96, 103]. Second, it accounts for the fact that manifold is advected relative to a reference frame, and this is described by the term $v_\tau\nabla_s(\cdot)$. The latter contribution strictly depends on the choice of parametrization, and can be interpreted as a reparametrization of the one-dimensional manifold [104, 105]. The last term $\kappa v_n(\cdot)$ on the right-hand side in Eq. (II.11) is a purely geometric contribution and accounts for dilution and accumulation of particle densities due to local length contraction and dilation, where κ describes the local (mean) curvature, and v_n the normal velocity of the manifold. As we will see below, this effect plays a significant role since it affects the local total protein density, which is an important control parameter for MCRD systems [13, 28, 41].

2.3 Material time-derivative and rescaled density fields

The two-component MRCD system Eq. (II.11) is complemented by the time-evolution of the *Lagrangian* position vector $\boldsymbol{r}(\sigma,t)$, that describes the temporal evolution of the manifold

$$\frac{d}{dt}\boldsymbol{r}(\sigma,t) = v_n\hat{\boldsymbol{n}} + v_\tau\hat{\boldsymbol{\tau}}\,, \tag{II.13}$$

where we decomposed the position vector along a direction normal and parallel to the manifold, given by the unit normal $\hat{\boldsymbol{n}}$ and tangential vector $\hat{\boldsymbol{\tau}}$ of the manifold, respectively. Since Eq. (II.11) is given in the Lagrangian frame, the time-derivative d/dt corresponds to the *material derivative* with respect to a stationary ambient frame, and this implies that the form of Eq. (II.11) depends explicitly on the parametrization. However, one can also define a time-derivative $\mathcal{D}_t$ that follows trajectories normal to the manifold and where the governing equations of scalar fields and tensor fields defined on the dynamic manifold become independent of the specific parametrization [105–107]. The definition of this operator is

$$\mathcal{D}_t := \frac{d}{dt} - v_\tau \frac{d}{ds} \,. \tag{II.14}$$

Using this operator, and assuming that proteins are mainly redistributed by diffusive fluxes, one can can rewrite Eq. (II.11) in the form:

$$\mathcal{D}_t m(\sigma, t) = D_m \nabla_s^2 m + f(m, c) + \kappa\, v_n\, m \,, \tag{II.15a}$$

$$\mathcal{D}_t c(\sigma, t) = D_c \nabla_s^2 c - f(m, c) + \kappa\, v_n\, c \,. \tag{II.15b}$$

Note that in the absence of tangential flows, the material derivative follows along trajectories normal to the manifold, i.e. $d/dt \equiv \mathcal{D}_t$ in this case.

To gain insight into the underlying dynamics of the system, we aim to apply the local equilibria theory for MCRD systems. Unfortunately, this appears to be challenging since the total average density $\langle n \rangle$ is generally not conserved by the dynamics, but the total particle N (as can be also inferred from the non-conservative form of Eq. (II.15)). However, we can bypass this issue by rescaling the cytosolic and membrane densities using the metric $\sqrt{g}$. Hence, to proceed, we define new variables $\widetilde{m} = m\sqrt{g}$ and $\tilde{c} = c\sqrt{g}$ and derive a time-evolution equation for the rescaled local total mass $\tilde{n} = \widetilde{m} + \tilde{c}$ from Eq. (II.15):

$$\mathcal{D}_t \tilde{n}(\sigma, t) = \frac{\partial}{\partial \sigma} \left[\frac{D_m}{\sqrt{g}} \frac{\partial}{\partial \sigma} \left(\frac{\widetilde{m}}{\sqrt{g}} \right) + \frac{D_c}{\sqrt{g}} \frac{\partial}{\partial \sigma} \left(\frac{\tilde{c}}{\sqrt{g}} \right) \right] . \tag{II.16}$$

From the equation above, one can see that the mass-redistribution dynamics of the rescaled local total mass $\tilde{n}$ corresponds to a nonlinear cross-diffusion equation, which is in addition coupled to the shape of the manifold via the metric. Importantly, we note that this equation is not closed, as it explicitly depends on the variables m and c. Equation (II.16) further reveals how shape deformations (effectively) affect transport processes along the manifold (here diffusion): one notes that the diffusion coefficients $D_{m/c}$ of the cytosolic and membrane components are rescaled by a factor $\sqrt{g}$. This rescaling accounts for the fact that diffusion from one point on the manifold to another point may take longer for curved regions

than for flat portions. Thus, the diffusion coefficients are (effectively) smaller for curved regions than for flat regions by a factor $\sqrt{g}$.

2.4 Regional instabilities

We can use Eq. (II.16) to derive a criterion that links the onset of lateral instabilities to the phase-space structure of the reaction-diffusion system. Following Ref. [41], we exploit the fact that the (stable) local reactive equilibria $\widetilde{m}^*$ and $\tilde{c}^*$ serve as scaffolds for patterns, and therefore replace the cytosolic and membrane densities by their local equilibria

$$(\widetilde{m}(\sigma,t),\tilde{c}(\sigma,t)) \to (\widetilde{m}^*(\tilde{n}(\sigma,t),\tilde{c}(\tilde{n}(\sigma,t)) \ . \tag{II.17}$$

Applying this approximation to Eq. (II.16), we find that the base state becomes laterally unstable if the slope of the reactive nullcline is steeper than the ratio of the membrane and cytosolic diffusion coefficients:

$$\frac{\partial}{\partial\widetilde{m}}\tilde{c}^*(\tilde{n}) < -\frac{D_m}{D_c} \ . \tag{II.18}$$

Due to dynamic shape changes of the manifold, and the rescaling defined above, the reactive nullcline $f(\sigma,t) = 0$ becomes space and time dependent. This entails that the instability criterion Eq. (II.18) is to be interpreted in a local sense. Thus, the heterogeneity in the reactive nullcline may lead to *regional lateral instabilities*, where the criterion above is fulfilled in parts of the geometry. Conversely, shape deformations may also suppress or shift existing patterns due to the inhomogeneity of the instability criterion. In particular, the instability criterion can be "propagated" in space and time by the dynamic of the manifold, resulting in rich dynamics such as travelling and standing wave patterns (see section 2.6).

Notably, our finding shows that the local total density as well as the local nullcline shape are important control variables, as the slope criterion Eq. (II.18) depends on these variables. This complements previous results on a static flat geometry, where the nullcline shape is uniform in space and time, thus leaving the local total density as the only relevant degree of freedom in the system [41]. Moreover, it is worth to mention that we have not specified details on how exactly the manifold shape is coupled to the chemical dynamics. Strikingly, the instability criterion Eq. (II.18) is quite generic and does not depend on the mechanical details of the manifold. The only relevant geometric quantity that contributes to Eq. (II.18) is the metric $\sqrt{g}$ (which encodes the local conformation). Thus, we conclude that, in addition to the local total mass, the metric is a relevant (dynamic) control parameter of the dynamics.

2.5 Key points and outlook

Below we summarize the key findings of this project and discuss possible extensions that could provide interesting tasks for future research.

- Mechanochemical coupling in mass-conserving reaction-diffusion systems leads to spatial inhomogeneities in the dynamics. These inhomogeneities are manifested in spatially and temporally non-uniform reaction kinetics, encoded by the nullcline shape of the MCRD.

- The onset of pattern-forming instabilities can be predicted by a simple analytical criterion, which is linked to the phase-space structure of the reaction-diffusion system. Importantly, the onset of instabilities is generic and does not depend on the exact details of the mechanical properties of the membrane or feedback loop between membrane shape and chemical dynamics.

- We identified the local total mass and the local conformation of the membrane (encoded by the metric) as the relevant degrees of freedom that drive the spatiotemporal dynamics. Strikingly, the metric plays the role of a dynamical control parameter for pattern formation.

Since the bulk-boundary ratio is an important control for pattern formation in MCRD systems [13, 28, 43], and interesting extension of our model would be to allow for cytosolic gradients perpendicular to the membrane. However, incorporating bulk-boundary coupling complicates the numerical simulations tremendously. The standard approach to solve the bulk dynamics is to first discretize both the bulk volume and membrane, and numerically determine the solution in the bulk. Given the bulk solution, one can advance the membrane shape and the dynamics of membrane components from one time point to another. This procedure, however, requires to adapt the mesh at each point in time (since the membrane shape is part of the solution), and is therefore highly susceptible to numerical instabilities.

To circumvent this issue, and to simplify the problem, we instead propose the following strategy: The bulk dynamics usually consists of a linear diffusion equation plus a linear degradation/creation term (accounting, e..g., for conformational changes of proteins). Under the assumption of linearity, one can analytically calculate the Green's function of the bulk dynamics, which can be used to reconstruct the bulk profile from its values at the membrane. This idea is known as the *boundary element method* (BEM), and is used extensively in other areas of physics, such as acoustics or structural mechanics [108, 109]. In essence, by using the BEM approach, one can eliminate the bulk dynamics and map the problem onto the membrane, hence preventing the numerical issues explained above and at the same time produce very similar equations as we have studied here.

One striking aspect of bulk-boundary coupling is that dynamic shape deformations of the membrane will cause spatiotemporal gradients in the bulk-boundary ratio, which conversely feeds back to the reaction-diffusion dynamics in a nontrivial way. We expect that this scenario leads to intricate multiscale protein patterns along the membrane. On a broader perspective, the idea of regional instabilities and the slope criterion determined in this work might help to characterize the dynamics in such systems.

2.6 Publication: Geometry-induced patterns through mechanochemical coupling

Geometry-induced patterns through mechanochemical coupling

by

L. Würthner[1,*], A. Goychuk[1,2,*], and E. Frey[1,3]

[1]Arnold Sommerfeld Center for Theoretical Physics (ASC) and Center for NanoScience (CeNS), Department of Physics, Ludwig-Maximilians-Universität München, Theresienstraße 37, D–80333 Munich, Germany,

[2]Present address: Institute for Medical Engineering and Science, Massachusetts Institute of Technology, Cambridge, MA 02139, United States

[3]Max Planck School Matter to Life, Hofgartenstraße 8, D-80539 Munich, Germany

*These authors contributed equally to this work.

Preprint submitted for publication,

arXiv: 2205.02820.

Reprinted on pages 96–119,

Geometry-induced patterns through mechanochemical coupling

Laeschkir Würthner,[1,*] Andriy Goychuk,[1,2,*] and Erwin Frey[1,3,†]

[1] *Arnold Sommerfeld Center for Theoretical Physics (ASC) and Center for NanoScience (CeNS), Department of Physics, Ludwig-Maximilians-Universität München, Theresienstraße 37, D–80333 Munich, Germany*

[2] *Present address: Institute for Medical Engineering and Science, Massachusetts Institute of Technology, Cambridge, MA 02139, United States*

[3] *Max Planck School Matter to Life, Hofgartenstraße 8, D-80539 Munich, Germany*

(Dated: May 6, 2022)

Intracellular protein patterns regulate a variety of vital cellular processes such as cell division and motility, which often involve dynamic changes of cell shape. These changes in cell shape may in turn affect the dynamics of pattern-forming proteins, hence leading to an intricate feedback loop between cell shape and chemical dynamics. While several computational studies have examined the resulting rich dynamics, the underlying mechanisms are not yet fully understood. To elucidate some of these mechanisms, we explore a conceptual model for cell polarity on a dynamic one-dimensional manifold. Using concepts from differential geometry, we derive the equations governing mass-conserving reaction–diffusion systems on time-evolving manifolds. Analyzing these equations mathematically, we show that dynamic shape changes of the membrane can induce pattern-forming instabilities in parts of the membrane, which we refer to as regional instabilities. Deformations of the local membrane geometry can also (regionally) suppress pattern formation and spatially shift already existing patterns. We explain our findings by applying and generalizing the local equilibria theory of mass-conserving reaction–diffusion systems. This allows us to determine a simple onset criterion for geometry-induced pattern-forming instabilities, which is linked to the phase-space structure of the reaction–diffusion system. The feedback loop between membrane shape deformations and reaction-diffusion dynamics then leads to a surprisingly rich phenomenology of patterns, including oscillations, traveling waves, and standing waves that do not occur in systems with a fixed membrane shape. Our work reveals that the local conformation of the membrane geometry acts as an important dynamical control parameter for pattern formation in mass-conserving reaction–diffusion systems.

I. INTRODUCTION

Many vital processes in living systems, such as cell division, motility, nutrient uptake, and growth, involve dynamic cell shape changes that are driven by forces produced by cytoskeletal structures and membrane-binding proteins. Mechanisms for cytoskeleton-induced deformation of the cell membrane are many, and include the polymerization of actin filaments [1, 2], guided by proteins that promote actin nucleation, polymerization and branching [3], or the generation of active stresses through myosin motor proteins in the actomyosin cortex [4, 5]. Remarkably, myosin–VI motor proteins can reshape membranes on their own by means of highly curvature-sensitive motor-protein–lipid interactions [6]. This molecular feature is akin to proteins containing BAR-domains that can directly induce shape deformations by binding to the cell membrane [7–11]. Cells coordinate these different processes by relying on regulatory signalling pathways and spatiotemporal protein organization involving, for example, the eukaryotic Rho family of GTPases which controls actomyosin polymerization and contractility [12]. In addition, spatiotemporal protein patterns arise from an interplay between localized biochemical reactions and diffusive transport [13–16], as well as possibly advective transport [17, 18]. All these processes show that intracellular reaction–diffusion systems are quite generally able to control cell shape, as was recently demonstrated in a minimal reconstituted setup where the *E. coli* MinDE protein system induced lipid vesicle deformations even in the absence of cytoskeletal proteins [19–21]. Since, conversely, cell geometry can guide protein pattern formation [22–27], this generically gives rise to mechanochemical feedback loops [28–31].

Such mechanochemical coupling implies an intricate interplay between dynamic shape deformations of the membrane, cytoskeletal dynamics, and chemical reaction kinetics. Theoretical investigations that address this rich topic range from computational models [32, 33] to models that place greater emphasis on the underlying molecular processes; for reviews see e.g. Refs. [11, 34, 35]. For example, recent studies have addressed the impact of curved proteins [36], phase separation of membrane-binding proteins [37], actin polymerization [38], and contractility of the actomyosin cortex [39] on membrane shape dynamics, as well as the interplay between morphogen and tissue dynamics [40]. While these studies have identified complex behavior such as membrane waves or complex three-dimensional shapes, they mostly rely on numerical simulations. Analytical methods like linear stability analysis have been employed to analyze the effect of mechanical and geometrical degrees of freedom on the onset of pattern formation in simple reaction-diffusion systems [33, 36, 39]. However, a comprehensive theoretical framework for studying the impact of geometric effects

* These authors contributed equally to this work.
† frey@lmu.de

on the resulting protein patterns in the fully nonlinear regime is currently lacking.

To further elucidate the theoretical understanding of systems with mechanochemical coupling, we here study a minimal model in the nonlinear regime employing analytical methods. Specifically, we consider a conceptual model of cell polarity given by a mass-conserving two-component reaction–diffusion system [41, 42] on a one-dimensional manifold, whose shape can evolve dynamically over time. Compared to a biologically realistic cell polarity model, the simplifications are twofold: (i) Instead of a complex protein reaction network for cell polarity [43, 44], we consider a reduced model with one protein species that can diffuse either in the cytosol or on the membrane. (ii) The cell membrane is considered as a deformable one-dimensional manifold. The membrane shape deformations cause inhomogeneous membrane compressions or dilations, leading to (local) accumulation or dilution of particle densities. Since protein densities are important control parameters in mass-conserving reaction–diffusion systems [26, 42, 45, 46], deformations of the one-dimensional manifold can qualitatively change the dynamics of protein pattern formation. In turn, if the local density of proteins also drives the dynamics of the one-dimensional manifold, then this leads to a feedback loop between shape changes of the manifold and reaction–diffusion dynamics. The goal of our analysis is to uncover important physical mechanisms underlying this intricate coupling between pattern formation and changes in membrane geometry—using a generic model.

We study this generic model by extending the *local equilibria theory*, a recently developed framework for analyzing mass-conserving reaction–diffusion systems [42, 45], to explicitly account for shape deformations of the manifold and the resulting changes in local geometry. In particular, we focus on two exemplary cases where (i) the shape is deformed adiabatically by some external agent, and (ii) the local concentration of proteins controls the dynamic shape changes of the membrane, for example by driving local outward growth through actin polymerization [47]. In the latter case, we consider the one-dimensional membrane as a fluid-like boundary under line tension. Specifically, our model could be interpreted as describing the dynamics of a small cell cortex section whose outward growth is (locally) driven by proteins. Therefore, to close our set of equations, we assume that proteins generate local forces that drive outward motion of the membrane along the direction of its normal vector.

We begin in Section II by reviewing the *local equilibria theory* in the context of a planar one-dimensional system with fixed geometry. In Sections III A and III B, we then apply concepts of differential geometry to describe the dynamics of a one-dimensional manifold, which sets the stage for coupling the manifold's geometry to the chemical degrees of freedom. By invoking the gauge invariance of the number of proteins enclosed in a given control volume with respect to deformations of the membrane geometry, we derive in Section III C how the number density of proteins responds to the shape dynamics of the one-dimensional manifold. We then show in Section III D how these general concepts apply to the specific case of a two-component mass-conserving reaction-diffusion system. In Section III E, we extend the local equilibria theory to systems that include shape deformation of the manifold and ensuing changes in their geometry. To test our theoretical results, in Sections IV A–IV C we study the response of a two-component mass-conserving reaction–diffusion system to shape deformations that are driven by an external agent. Finally in Sections IV D and IV E, we couple the conformational dynamics of the membrane to the local density of proteins, and study how such a system self-organizes in space and time.

II. LOCAL EQUILIBRIA THEORY

One of the main goals of this work is to find generic principles of pattern formation through reactions and diffusion on manifolds whose conformations change dynamically. To that end, we build on a recently developed framework for mass-conserving reaction–diffusion (MCRD) systems termed *local equilibria theory* [42, 45, 46]. With this framework, one can characterize the dynamics of MCRD systems by analyzing the phase portrait. However, since the local equilibria theory was originally developed in the context of a fixed spatial domain, it is not clear a priori how to apply it to a system where the patterns emerge on a manifold whose conformation and hence internal geometry changes over time. Interestingly, through our analysis we find that the main concepts of the local equilibria theory carry over to MCRD systems on dynamic manifolds without major modifications. Before we proceed with this main subject of our work, we first recapitulate the key points of local equilibria theory.

The basic idea is to think of a spatially extended system as being decomposed into a set of compartments that are coupled by diffusion. For an isolated compartment, one can determine the homogeneous steady state (*local reactive equilibrium*) and its stability, which both depend on the total particle densities within that compartment. Since diffusion redistributes these total densities, the local reactive equilibria will shift and change over time. The local reactive equilibria inside each compartment then serve as a scaffold for the spatially extended system, which allows one to study pattern formation by performing a phase portrait analysis.

To illustrate these ideas with a concrete example, consider a two-component MCRD system consisting of one protein species which can cycle between a membrane-bound state m and a cytosolic state c. On a static one-dimensional domain, e.g., an arbitrary curve in space, the dynamics is given by the following two-component

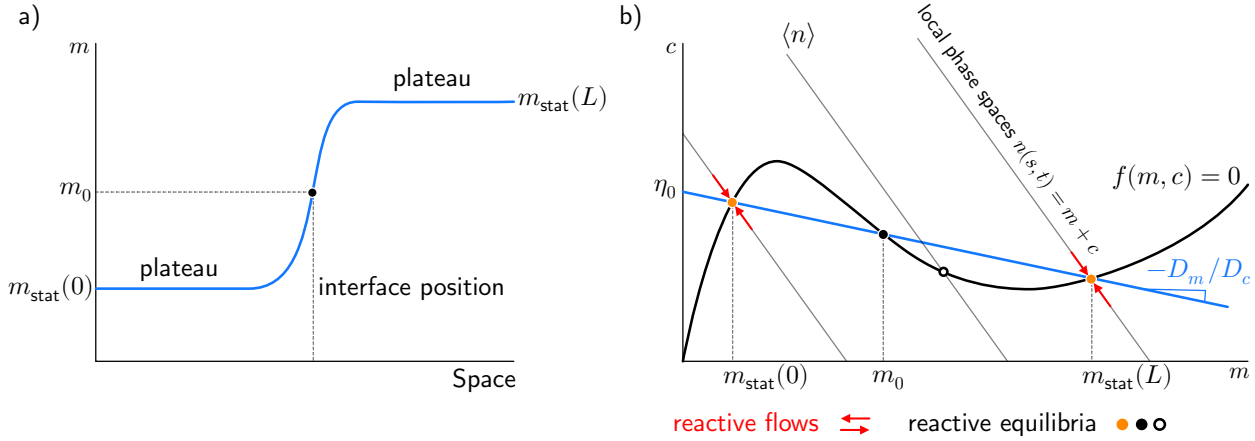

FIG. 1. Stationary pattern of a two-component mass-conserving reaction–diffusion system in phase-space. a) Stationary spatial profile shown for the membrane species m, consisting of two plateaus connected by an interface (mesa pattern). The interface position is defined by the inflection point of the pattern (black filled dot). b) Phase-space representation of the pattern shown in a). The stationary solution lies on a linear subspace (flux-balance subspace, blue line), and the slope of this line is given by the ratio of the diffusion coefficients (cf. Eq.(4)). The plateau values are determined by reactive flows (diffusive fluxes are zero in these regions). In phase-space, the reactive equilibria corresponding to the plateau values (orange filled dots) are given by intersections of local phase spaces (thin gray lines) with the reactive nullcline (black line), and $\langle n \rangle$ is the average total density. Note that due to mass-conservation, reactive flows (red arrows) are always parallel to the local phase spaces.

MCRD model:

$$\partial_t m(s,t) = D_m \partial_s^2 m + f(m,c)\,, \tag{1a}$$
$$\partial_t c(s,t) = D_c \partial_s^2 c - f(m,c)\,. \tag{1b}$$

Here, s denotes the arc length while the reaction term $f(m,c)$ describes the local attachment and detachment kinetics of the protein species. In Appendix A we provide the reaction kinetics that was used in this study. However, we emphasize that the main conclusions in this work do not depend on the specific choice of $f(m,c)$, as will become clear in the following sections [42, 46].

The dynamics of Eq. (1) conserves the total average density of proteins:

$$\langle n \rangle := \frac{1}{L}\int_0^L ds\, n(s,t)\,, \tag{2}$$

where $n(s,t) = m(s,t) + c(s,t)$ describes the local total protein density and L is the length of the line. Since the reaction kinetics conserves the total density, the reactive flow in phase space must point in the direction of *local reactive phase spaces* given by $n(s,t) = m(s,t) + c(s,t)$ (Fig. 1). The intersections between the local reactive phase spaces and the *reactive nullcline*, obtained from the equation $f(m,c) = 0$, determine the local reactive equilibria $(m^*(n), c^*(n))$. Hence, the values of the local reactive equilibria and how they change depend on the shape of the reactive nullcline and the total density n. This further implies that for a given system (specified by $f(m,c)$), the total density n plays the role of a control parameter for the local dynamics.

The dynamics of $n(s,t)$ is driven by diffusion, which can be shown by adding Eqs. (1a) and (1b):

$$\begin{aligned}\partial_t n(s,t) &= D_c\,\partial_s^2\left[c(s,t) + \frac{D_m}{D_c}\,m(s,t)\right] \\ &:= -\partial_s j(s,t)\,,\end{aligned} \tag{3}$$

where the diffusive density flux $j(s,t)$ is given by a combination of cytosolic and membrane density gradients $j(s,t) = -D_c\partial_s c(s,t) - D_m\partial_s m(s,t)$. From the dynamics of the total density, see Eq. (3), one directly infers that any stationary pattern, $m_{\text{stat}}(s)$ and $c_{\text{stat}}(s)$, must be constrained to a linear subspace in phase space that is (for no-flux or periodic boundary conditions) determined by:

$$c_{\text{stat}}(s) + \frac{D_m}{D_c}\,m_{\text{stat}}(s) = \eta_0\,, \tag{4}$$

where η_0 is a constant of integration. The linear subspace, given by Eq. (4), is termed the *flux-balance subspace* (FBS) and states that in steady state the diffusive fluxes in m and c must be balanced such that the net flux is zero (see Eq. (3)).

As shown in Ref. [42], the condition for the establishment of spatial density patterns is linked to the slope of the reactive nullcline by a simple geometric criterion in phase space: a homogeneous steady state becomes unstable to spatial perturbations (laterally unstable) when the slope of the reactive nullcline $s_{\text{nc}}(n)$ is steeper than the slope of the FBS:

$$s_{\text{nc}}(n) = \partial_m\, c^*(m)\big|_n < -\frac{D_m}{D_c}\,. \tag{5}$$

The underlying mechanism of this instability lies in a coupling between mass-redistribution and reactive flows:

regions with a high density of membrane-bound proteins act as a sink for cytosolic particles due to (nonlinear) attachment to the membrane, leading to depletion of cytosolic particles. Conversely, regions with a low density of membrane-bound proteins act as a source of cytosolic particles due to detachment from the membrane and hence increase the cytosolic density. Redistribution of mass through diffusion further amplifies this effect and leads to a feedback loop between mass-redistribution and reaction kinetics. This instability is hence termed the *mass-redistribution instability* and is generic to mass-conserving reaction-diffusion systems.

In Ref. [42] it was furthermore shown that the condition for a lateral instability, see Eq. (5), can be generalized to partitions of the geometry. In short, one can dissect a spatial pattern into spatially distinct regions, and associate each region with a regional phase space. Viewing these regions in isolation from the rest, one can repeat the same analysis for each region separately and thus reconstruct the global pattern by determining the *regional instability* from Eq. (5). For a comprehensive discussion of the local equilibria theory and the two-component MCRD model, we refer to Ref. [42].

III. REACTION–DIFFUSION DYNAMICS ON A DEFORMING MANIFOLD

Now that we have recapitulated local equilibria theory for pattern-forming systems on a given spatial domain, we will extend it towards systems on dynamic manifolds. To that end, we proceed with the following steps. We start by providing a generic description of a manifold in terms of curvilinear coordinates, where we restrict the discussion to a one-dimensional system (line). For a general review of differential geometry of surfaces, we refer to Ref. [48]. To determine the time evolution of patterns, we require that their dynamics is independent of the reference frame and that the dynamics of the manifold conserves the number of particles. By doing so, we derive a set of governing partial differential equations that describes mass-conserving reaction–diffusion systems on a deforming manifold in the laboratory frame. An important aspect of the dynamics is, that virtually every deformation of the manifold will inevitably change the local density of particles on the manifold.

A. Describing a deforming geometry

We begin with the general description of a one-dimensional time-dependent manifold (line). We parameterize the line by a time-dependent position vector $\boldsymbol{r}(\sigma, t) \in \mathbb{R}^2$, where σ is an arbitrary curve parameter that labels positions along the line (see Fig. 2). Given a specific parameterization of the position vector, one can then define further geometric features of the line. The

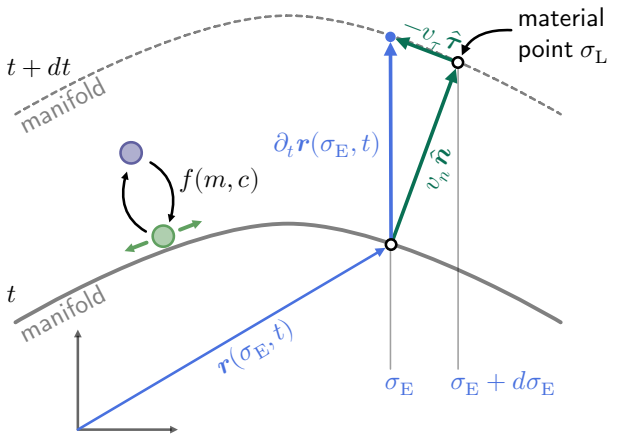

FIG. 2. Conceptual description of a time-evolving manifold. The line (solid thick gray) can be parameterized either with respect to a stationary ambient coordinate system (*Eulerian coordinates* σ_{E}, blue colors) or by using material coordinates σ_{L} (*Lagrangian coordinates* that label points traveling along trajectories normal to the line (black hollow dots). As illustrated, the coordinates σ_{E} change over time in the material frame, resulting in a flow $\sigma_{\mathrm{E}} \to \sigma_{\mathrm{E}} + d\sigma_{\mathrm{E}}$ of these coordinates that is directed along the tangential part of the velocity vector $\partial_t \boldsymbol{r}(\sigma_{\mathrm{E}}, t)$. We investigate a conceptual two-component mass-conserving reaction–diffusion system on such dynamic manifolds (schematically illustrated by the symbols in purple and green, which represent a cytosolic species c and a membrane species m, both diffusing along the line).

tangent vector of the curve is given by

$$\boldsymbol{\tau}(\sigma, t) = \partial_\sigma \boldsymbol{r}(\sigma, t)\,. \tag{6}$$

For calculations, it is convenient to consider the normalized tangent vector, which is given by

$$\hat{\boldsymbol{\tau}}(\sigma, t) = \frac{\boldsymbol{\tau}(\sigma, t)}{\sqrt{g(\sigma, t)}}\,, \quad \text{where} \quad g(\sigma, t) = \|\boldsymbol{\tau}(\sigma, t)\|^2 \tag{7}$$

refers to the *metric* or *first fundamental form*, which allows one to define arc distances along the curve:

$$s\,(\sigma, t) = \int_0^\sigma d\sigma'\,\sqrt{g(\sigma', t)}\,. \tag{8}$$

The conformation of the curve is described by the curvature κ and formally given by the definition

$$\partial_s \hat{\boldsymbol{\tau}} = \kappa\,\hat{\boldsymbol{n}}\,, \tag{9}$$

where $\hat{\boldsymbol{n}}$ is the unit normal vector on the curve. Note that the direction of the unit normal vector $\hat{\boldsymbol{n}}$ and the sign of the curvature are not uniquely defined but a matter of convention. Here, we choose the convention that the curvature is negative for a sphere (circle in two-dimensions). This means that the line *curves away from* its unit normal vector in the case of negative curvature, and towards its unit normal vector in the case of positive curvature (see Fig. 3).

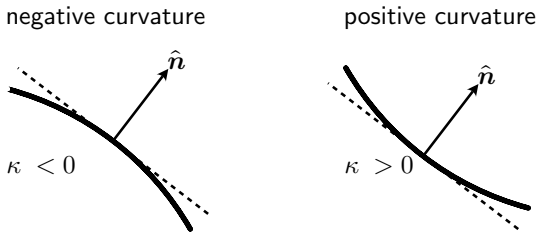

FIG. 3. Convention for the sign of the curvature. If the manifold (thick black line) curves away from its unit normal vector (black arrow), then the curvature is negative (left panel). If the geometry (thick black line) curves towards its unit normal vector (black arrow), then the curvature is positive (right panel). The dashed line represents a flat geometry with vanishing curvature.

The dynamics of the curve is determined by its velocity vector $\partial_t \boldsymbol{r}$ and can, in the most general case, be decomposed into parts normal and tangential to the curve:

$$\partial_t \boldsymbol{r}(\sigma, t) = v_n \hat{\boldsymbol{n}} + v_\tau \hat{\boldsymbol{\tau}}, \tag{10}$$

where v_n and v_τ refer to the normal velocity and tangential velocity, respectively. Note that only the normal velocity v_n affects the shape of the curve, while the shape is invariant to deformations in the tangential direction. In addition, the normal component of the velocity vector can generally be an arbitrarily complex function of the position vector, curvature, and other field variables. Hence, the exact form of the normal velocity must be determined by the specific physical system being studied. Conversely, as we will show in the next section, the tangential velocity strongly depends on the concrete choice of the curve parameterization and on the frame of reference.

B. Frame of reference

Up to this point, we have not specified the exact frame of reference for the parameterization of the geometry. In the following, by analogy with continuum mechanics, we distinguish between two different frames of reference, the *Lagrangian frame* and the *Eulerian frame*. In the Lagrangian frame, we exploit the fact that tangential motion, i.e., sliding of the curve along its own contour, does not change the shape of a line. Therefore, we specify the curve parameter σ_L to label material points with vanishing tangential velocity along the line. These material points then move with the line along the normal direction $\hat{\boldsymbol{n}}$ (Fig. 2). To further emphasize the special properties of the Lagrangian or co-moving frame, we define the *material derivative* $\mathcal{D}_t$. If any quantity, such as the position vector or some density field on the one-dimensional manifold, is parameterized by material coordinates σ_L, then the material derivative is identical to the (local) partial time derivative [49, 50]

$$\mathcal{D}_t \coloneqq \partial_t|_{\boldsymbol{r}(\sigma_\mathrm{L},t)} \,. \tag{11}$$

This further implies that the material coordinates σ_L are time-invariant in the Lagrangian frame of reference, as they should be.

In the *Eulerian frame*, one defines a curve parameter σ_E that labels points on the curve which do not move with the material coordinates, i.e., do not flow solely along the normal but also along the tangential direction of the moving line. The parameterization in this case is given with respect to an ambient coordinate system (*laboratory* frame) (Fig. 2) and therefore specifies a fixed coordinate for the position of the line over time (for fixed σ_E). Note, however, that while the material coordinates σ_L do not change in the Lagrangian frame, they do become time-dependent in the Eulerian frame $\sigma_\mathrm{L} = \sigma_\mathrm{L}(\sigma_\mathrm{E}, t)$ (see Fig. 2). This is analogous to fluid mechanics, where the coordinates of a fluid parcel in the material frame are fixed over time, while the fluid parcel moves at a certain velocity as seen by an observer in the laboratory frame.

Now, for a consistent physical description that is independent of the exact definition of the laboratory frame (i.e., parameterization in the Eulerian frame), the total time derivative of an arbitrary physical quantity in the laboratory frame must match the time derivative in the Lagrangian frame (i.e., using the operator $\mathcal{D}_t$). To understand this, we apply the material derivative $\mathcal{D}_t$ to the position vector field $\boldsymbol{r}(\sigma_\mathrm{E}(\sigma_\mathrm{L}, t), t)$ parameterized by Eulerian coordinates σ_E:

$$\begin{aligned} \mathcal{D}_t \boldsymbol{r}(\sigma_\mathrm{L}, t) &= \frac{d}{dt} \boldsymbol{r}(\sigma_\mathrm{E}(\sigma_\mathrm{L}, t), t) \,, \\ &= \partial_t \boldsymbol{r}(\sigma_\mathrm{E}, t) + \partial_{\sigma_\mathrm{E}} \boldsymbol{r}(\sigma_\mathrm{E}, t)\, \partial_t \sigma_\mathrm{E}(\sigma_\mathrm{L}, t) \,, \\ &= \partial_t \boldsymbol{r}(\sigma_\mathrm{E}, t) + \hat{\boldsymbol{\tau}}\, \sqrt{g}\, \partial_t \sigma_\mathrm{E}(\sigma_\mathrm{L}, t) \,, \end{aligned} \tag{12}$$

where $\partial_t \sigma_\mathrm{E}(\sigma_\mathrm{L}, t)$ denotes an ambient *coordinate flow* as seen by an observer in the material frame at σ_L (see Fig. 2). Note that, because we have chosen the material coordinates σ_L such that they label points with vanishing tangential velocity along the line, one finds that $\mathcal{D}_t \boldsymbol{r}(\sigma_\mathrm{L}, t) = v_n \hat{\boldsymbol{n}}$; i.e., the material derivative only contains a part normal to the line. The ambient coordinate flow can be determined by a simple geometric construction (see Fig. 2):

$$v_n dt\, \hat{\boldsymbol{n}} - \partial_t \boldsymbol{r}(\sigma_\mathrm{E}, t)\, dt = d\sigma_\mathrm{E} \boldsymbol{\tau} \,. \tag{13}$$

Inserting Eq. (10) into Eq. (13) one obtains $d\sigma_\mathrm{E}/dt = -v_\tau/\sqrt{g}$. With this result, one can rewrite Eq. (12) to obtain the equivalent form:

$$\mathcal{D}_t \boldsymbol{r}(\sigma_\mathrm{L}, t) = v_n \hat{\boldsymbol{n}} = \partial_t \boldsymbol{r}(\sigma_\mathrm{E}, t) - v_\tau\, \hat{\boldsymbol{\tau}} \,. \tag{14}$$

To conclude, by combining Eqs. (12) and (6), we find that the material derivative operator in the Eulerian frame is given by:

$$\mathcal{D}_t \equiv \partial_t - v_\tau\, \partial_s \,, \tag{15}$$

where we have also used $\partial_\sigma = \sqrt{g(\sigma,t)}\,\partial_s$ (cf. Eq. (8)). This operator serves as a link between the laboratory and material frames, and can be applied to any time-dependent quantity defined on the one-dimensional manifold.

C. Conformational dynamics of the line affects density fields

If the conformation of the line changes with time, then what is the time evolution of a density field that is defined on the one-dimensional manifold? We proceed by considering an arbitrary scalar field ϱ representing, for instance, the density fields of cytosolic and membrane-bound proteins. We first define the cumulative number of particles up to some coordinate σ along the line,

$$\begin{aligned} N_\varrho(\sigma,t) &\coloneqq \int_0^{s(\sigma,t)} ds'\,\varrho(s',t) \\ &= \int_0^{\sigma} d\sigma'\,\sqrt{g(\sigma',t)}\,\varrho(\sigma',t)\,, \end{aligned} \tag{16}$$

where for brevity of notation we have written $\varrho(\sigma,t) = \varrho(s(\sigma,t),t)$ using the same symbol for the function. For mass-conserving systems, the total number of particles remains constant over time, irrespective of any deformation of the line's shape that alters its total or local length. In contrast, the local density of particles can change as a result of shape deformations, since density fields are defined with respect to the local arc length, which is in general also a time-dependent quantity; see Eq. (8). To derive the time evolution of density fields, it is therefore useful to first look at the time evolution of the particle number. Consider the number of particles distributed on an infinitesimal line segment between coordinates σ and $\sigma + d\sigma$,

$$dN_\varrho(\sigma,t) = d\sigma\,\sqrt{g(\sigma,t)}\,\varrho(\sigma,t)\,, \tag{17}$$

and further assume that we have chosen a parameterization in the Lagrangian frame, i.e., we set $\sigma \equiv \sigma_\mathrm{L}$. The time evolution of the number of particles then follows by applying the material derivative to Eq. (17):

$$\mathcal{D}_t\big[dN_\varrho(\sigma_\mathrm{L},t)\big] = d\sigma_\mathrm{L}\,\sqrt{g}\,\left[\frac{\mathcal{D}_t g}{2g}\,\varrho + \mathcal{D}_t\varrho(\sigma_\mathrm{L},t)\right], \tag{18}$$

Since the left-hand side of Eq. (18) can only change due to local reactions, $f_\varrho(\sigma_\mathrm{L},t)$, and particle fluxes $j(\sigma_\mathrm{L},t)$ across the boundaries of the line segment $d\sigma_\mathrm{L}$, it must be given by the transport equation:

$$\begin{aligned} \mathcal{D}_t\big[dN_\varrho(\sigma_\mathrm{L},t)\big] &= j(\sigma_\mathrm{L},t) - j(\sigma_\mathrm{L}+d\sigma_\mathrm{L},t) \\ &\quad + d\sigma_\mathrm{L}\,\sqrt{g(\sigma_\mathrm{L},t)}\,f_\varrho(\sigma_\mathrm{L},t)\,. \end{aligned} \tag{19}$$

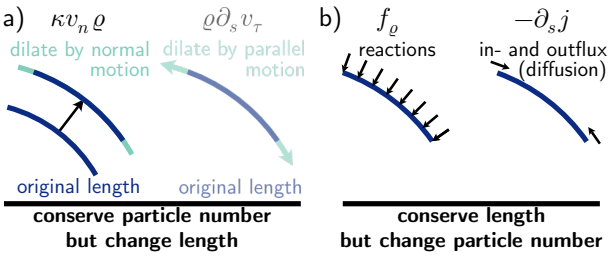

FIG. 4. The different physical contributions to a change in particle concentration on a deforming line. a) Mechanisms that conserve the local number of particles on a given line segment while changing the segment's length. Motion along the normal vector increases (decreases) the length of segments with negative (positive) curvature (cf. Fig. 3), thus reducing (increasing) the local concentration of particles. Since we here focus on exterior motion of the line (along a direction normal to the line), we do not consider changes in particle concentrations that would arise due to parallel (interior) motion (faded panel). However, one could also account for dilution and accumulation of particle densities due to parallel motion by incorporating a term $\varrho\,v_\tau$ into the density flux in Eq. (21). b) Reactions and diffusion are mechanisms that change the number of particles on a segment while conserving the segment's length.

The temporal evolution of the metric can be determined from the definition (7):

$$\begin{aligned} \mathcal{D}_t g(\sigma_\mathrm{L},t) &= \mathcal{D}_t\left[\partial_{\sigma_\mathrm{L}}\boldsymbol{r}\right]^2 = 2[\partial_{\sigma_\mathrm{L}}\mathcal{D}_t\boldsymbol{r}]\cdot[\partial_{\sigma_\mathrm{L}}\boldsymbol{r}] \\ &= 2g\,[\partial_s v_n\hat{\boldsymbol{n}} + v_n\partial_s\hat{\boldsymbol{n}}]\cdot\hat{\boldsymbol{\tau}} \\ &= -2\,g\,\kappa\,v_n\,, \end{aligned} \tag{20}$$

where we have used the relation $\partial_{\sigma_\mathrm{L}} = \sqrt{g}\,\partial_s$, see Eq. (8), and the fact that $\partial_s\hat{\boldsymbol{n}} = -\kappa\hat{\boldsymbol{\tau}}$. Combining Eqs. (18)–(20), we obtain the governing equation for the density field in the Lagrangian frame:

$$\mathcal{D}_t\varrho(\sigma_\mathrm{L},t) = -\partial_s j(\sigma_\mathrm{L},t) + f_\varrho(\sigma_\mathrm{L},t) + \kappa\,v_n\,\varrho(\sigma_\mathrm{L},t)\,. \tag{21}$$

The particle flux in Eq. (21) can in general include diffusive as well as advective fluxes along the one-dimensional manifold, $j(\sigma_\mathrm{L},t) = -D_\varrho\,\partial_s\varrho + v_\tau\,\varrho$, where D_ϱ and v_τ denote the diffusion coefficient and tangential advection velocity, respectively. Advective flows along the membrane may be caused, for instance, by spatial heterogeneities in actomyosin contractility [39] (cortical flows) or relaxation of in-plane elastic stresses of the membrane. In this work, we consider systems where the particles are transported only by diffusion and therefore disregard advective particle fluxes, in line with our choice of reference frame with a vanishing tangential velocity. The last term in Eq. (21) is a purely geometric contribution and accounts for local density variations due to local length extension and contraction. The various contributions to the local change of the particle density are summarized in Fig. 4.

While the Lagrangian frame is convenient for our analytic calculations, the choice of a specific parameteriza-

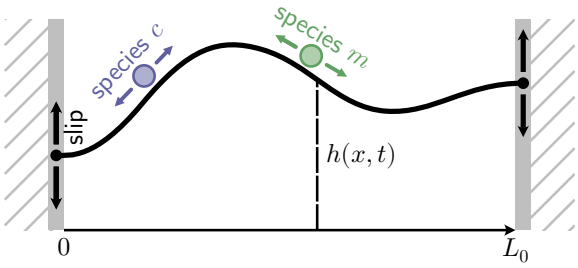

FIG. 5. Illustration of the Monge parameterization. The membrane (black solid line) is parameterized by its height relative to a flat line. The endpoints of the membrane can slip along two solid walls (grey), which are a distance L_0 apart.

tion in the Eulerian frame allows us to reduce the number of degrees of freedom in our numerical simulations. To that end, we choose a Monge parameterization of the line contour:

$$\boldsymbol{r}(x,t) = \begin{bmatrix} x \\ h(x,t) \end{bmatrix}, \tag{22}$$

where the height field $h(x,t)$ encodes the line conformations, and $x \in [0, L_0]$ is the curve parameter (here an Eulerian coordinate $\sigma_\mathrm{E} \equiv x$). Thus, by using a Monge parameterization, we eliminate the time evolution of one component of the position vector $\boldsymbol{r}(x,t)$, thus retaining only one degree of freedom. However, since the line is now represented by the graph $h(x,t)$, we explicitly exclude overhangs by using this parametrization. We further assume that the two opposing endpoints of the membrane are clamped, i.e., forced to a slope of zero, while allowing the line to slip vertically along the boundaries (Fig. 5). Since the line extends from $x = 0$ to L_0, we effectively introduce a length constraint, stating that the total length of the membrane may not fall below the minimum distance L_0 (Fig. 5).

One could generalize this choice to account for overhangs, at the expense of increased model complexity, by introducing additional degrees of freedom that allow the curve to freely move in space (for example described in the Lagrangian frame), and adding physical mechanisms such as stretching rigidity to constrain the total length of the curve. However, taking mechanical degrees of freedom into account would greatly complicate the dynamics, since stress propagation along lines exhibits a rather intricate dynamics, as was shown for polymers [51–55]. Here, we disregard these additional complexities and focus on the interplay between biochemical pattern formation and the shape deformation of the line.

Finally, using the definition of the material derivative in Eulerian coordinates, Eq. (15), the dynamics of density fields, Eq. (21), can be translated to the laboratory frame:

$$\begin{aligned}\partial_t \varrho(\sigma_\mathrm{E},t) = &-\partial_s j(\sigma_\mathrm{E},t) + f_\varrho(\sigma_\mathrm{E},t) \\ &+ \kappa\, v_n\, \varrho(\sigma_\mathrm{E},t) + v_\tau \partial_s \varrho(\sigma_\mathrm{E},t)\,. \end{aligned} \tag{23}$$

This reaction-diffusion equation on a deforming line taken together with the time evolution of the line's shape, Eq. (10), fully specify the dynamics of a density field on a manifold that changes its conformation. Next, our goal is to understand how shape deformations of a line affect protein pattern formation.

D. Two-component MCRD system on dynamically evolving manifolds

As we have now established the framework to study reaction–diffusion systems on lines exhibiting conformational dynamics, we proceed with the generic description of a two-component MCRD system on such a line in the laboratory frame. The governing equations that describe the dynamics of the density fields and the line conformation in Monge parameterization are then derived from Eqs. (10), (22), and (23):

$$\partial_t m(x,t) = D_m \partial_s^2 m + f + \kappa\, v_n\, m + v_\tau \partial_s m\,, \tag{24a}$$

$$\partial_t c(x,t) = D_c \partial_s^2 c - f + \kappa\, v_n\, c + v_\tau \partial_s c\,, \tag{24b}$$

$$\partial_t h(x,t) = \sqrt{g(x,t)}\, v_n\,, \tag{24c}$$

where $g(x,t) = 1 + [\partial_x h(x,t)]^2$ is the local metric and $v_\tau = v_n \partial_x h(x,t)$ denotes the tangential velocity in the Monge parameterization. Note that the tangential velocity follows from a geometric construction; see Eq. (13) and Fig. 2. The second spatial derivative ∂_s^2 along the curve corresponds to the (one-dimensional) *Laplace-Beltrami* operator and is explicitly given by:

$$\partial_s^2 \equiv \frac{1}{\sqrt{g}} \partial_x \left[\frac{1}{\sqrt{g}} \partial_x \right] = \frac{1}{g} \partial_x^2 - \frac{1}{2} \frac{\partial_x g}{g^2} \partial_x. \tag{25}$$

Unlike in the case of a fixed planar geometry, Eqs. (1a) and (1b), the two-component mass-conserving reaction–diffusion system on a deforming line, Eqs. (24a) and (24b), is not given in a form where mass-conservation is immediately apparent. This is due to the fact that the density fields are defined with respect to the local arc length, which is a dynamic quantity itself, as accounted for by the geometric terms $\kappa\, v_n\, m$ and $\kappa\, v_n\, c$ in Eqs. (24a) and (24b). Therefore, if one allows the conformation of the line to change over time, the total average density is not necessarily conserved by the dynamics. Instead, the quantity that must be conserved for a system with a mass-conserving reaction dynamics is the total particle number

$$N = \int_0^{L(t)} ds\, (m + c) = \int_0^{L_0} dx\, \sqrt{g(x,t)}\, n(x,t)\,. \tag{26}$$

This renders our analysis slightly more involved, since the local equilibria theory cannot be applied to the mathematical model, Eqs. (24a) and (24b), in their present form.

To get around this problem, we consider rescaled densities on the membrane $\widetilde{m}(x,t) := \sqrt{g(x,t)}\, m(x,t)$ and in

the cytosol $\tilde{c}(x,t) := \sqrt{g(x,t)}\, c(x,t)$. This mapping corresponds to a projection of the line densities along the curve, $m(x,t)$ and $c(x,t)$, onto the parameterization axis (in the case of a Monge representation the x-axis), so that

$$\begin{aligned} N &= \int_0^{L_0} dx\, \sqrt{g(x,t)}\, \big(m(x,t) + c(x,t)\big) \\ &= \int_0^{L_0} dx\, \big(\widetilde{m}(x,t) + \tilde{c}(x,t)\big) = \int_0^{L_0} dx\, \tilde{n}(x,t)\,. \end{aligned} \tag{27}$$

Thus, $\tilde{n}\, dx$ represents the total number of particles contained within an infinitesimal compartment dx. Using our mapping, one immediately sees that the mapped total average density $\langle \tilde{n} \rangle = N/L_0$ is conserved by the dynamics, thus allowing us to apply the local equilibria theory. The time evolution of the rescaled variables can be determined starting from:

$$\partial_t \widetilde{m}(x,t) = \sqrt{g}\, \partial_t m(x,t) + \frac{1}{2} \frac{\partial_t g(x,t)}{\sqrt{g(x,t)}}\, m(x,t)\,, \tag{28}$$

and an analogous equation for the cytosolic species $\tilde{c}$. In the following, only the derivation for the membrane species $\widetilde{m}$ is presented, since the calculations for the cytosolic species $\tilde{c}$ are completely analogous. The time evolution of the metric $\partial_t g(x,t)$ in the Eulerian frame can be determined similarly as shown in the previous section for $\mathcal{D}_t g(\sigma_{\mathrm{L}}, t)$:

$$\begin{aligned} \partial_t g(x,t) &= \partial_t \left[(\partial_x \boldsymbol{r}) \cdot (\partial_x \boldsymbol{r})\right] = 2\, (\partial_x \partial_t \boldsymbol{r}) \cdot (\partial_x \boldsymbol{r}), \\ &= 2\, g\, [\partial_s v_n \hat{\boldsymbol{n}} + v_n \partial_s \hat{\boldsymbol{n}} + \partial_s v_\tau \hat{\boldsymbol{\tau}} + v_\tau \partial_s \hat{\boldsymbol{\tau}}] \cdot \hat{\boldsymbol{\tau}}, \\ &= -2\, g\, \kappa\, v_n + 2\, g\, \partial_s v_\tau, \end{aligned} \tag{29}$$

where we used the general expression for the velocity vector Eq. (10), the definition Eq. (9), and the fact that $\partial_s \hat{\boldsymbol{n}} = -\kappa\, \hat{\boldsymbol{\tau}}$. Inserting Eqs. (24a) and (29) into Eq. (28), we obtain the continuity equation:

$$\partial_t \widetilde{m}(x,t) = -\partial_x\, j_{\widetilde{m}}(x,t) + \tilde{f}(x,t)\,, \tag{30}$$

where the flux $j_{\widetilde{m}}$ is given by:

$$j_{\widetilde{m}}(x,t) = -\left[\frac{D_m}{\sqrt{g}} \partial_x \left(\frac{\widetilde{m}(x,t)}{\sqrt{g}}\right) + v_\tau \frac{\widetilde{m}(x,t)}{\sqrt{g}}\right], \tag{31}$$

and the rescaled reaction term $\tilde{f}(x,t)$ is defined as:

$$\begin{aligned} \tilde{f}(x,t) &= \sqrt{g(x,t)}\, f(m,c) \\ &= \sqrt{g(x,t)}\, f\left(\frac{\widetilde{m}(x,t)}{\sqrt{g(x,t)}}, \frac{\tilde{c}(x,t)}{\sqrt{g(x,t)}}\right). \end{aligned} \tag{32}$$

Hence, the mass-conserving dynamics of the rescaled density fields are given by a reaction–diffusion system in conservative form:

$$\partial_t \widetilde{m}(x,t) = -\partial_x\, j_{\widetilde{m}}(x,t) + \tilde{f}(x,t)\,, \tag{33a}$$

$$\partial_t \tilde{c}(x,t) = -\partial_x\, j_{\tilde{c}}(x,t) - \tilde{f}(x,t)\,, \tag{33b}$$

$$\partial_t h(x,t) = \sqrt{g(x,t)}\, v_n\,. \tag{33c}$$

Note that the equations governing the dynamics of the rescaled fields are equivalent to a reaction–diffusion system defined on a fixed planar geometry of length L_0. The influence of shape deformations of the line on the reaction–diffusion dynamics is fully absorbed into the metric factor $\sqrt{g(x,t)}$, the conservative fluxes $j_{\widetilde{m}/\tilde{c}}$, and the rescaled reaction term $\tilde{f}(x,t)$. Strikingly, the reaction term becomes space- and time-dependent, in contrast to the case of a fixed planar geometry [42] where the reaction kinetics has the same form at each point in space and time. We will show in the following sections that this spatiotemporal inhomogeneity of the reaction term can lead to regional instabilities and thus deformation-induced protein pattern formation.

E. Lateral instability on a deforming manifold

In Sec. II we explained that the homogeneous steady state of the two-component MCRD system (on a fixed planar line) becomes unstable to spatial perturbations when the slope of the reactive nullcline is steeper than the slope of the flux-balance subspace; see Eq. (5). Here we ask whether it is possible to obtain an instability criterion when deformations of the line are considered.

To investigate this question, we start with the description of the two-component MCRD model in the Lagrangian frame, as this is more convenient for analytical calculations, and again project the density fields onto the parameterization axis (note that in this case the curve parameter is σ_{L}). The equations take the same form as for the laboratory frame, see Eq. (33), except that there is no tangential drift in the Lagrangian frame (cf. Eq. (31)):

$$\mathcal{D}_t \widetilde{m}(\sigma_{\mathrm{L}}, t) = \partial_{\sigma_{\mathrm{L}}} \left[\frac{D_m}{\sqrt{g}} \partial_{\sigma_{\mathrm{L}}} \left(\frac{\widetilde{m}}{\sqrt{g}}\right)\right] + \tilde{f}(\sigma_{\mathrm{L}}, t)\,, \tag{34a}$$

$$\mathcal{D}_t \tilde{c}(\sigma_{\mathrm{L}}, t) = \partial_{\sigma_{\mathrm{L}}} \left[\frac{D_c}{\sqrt{g}} \partial_{\sigma_{\mathrm{L}}} \left(\frac{\tilde{c}}{\sqrt{g}}\right)\right] - \tilde{f}(\sigma_{\mathrm{L}}, t)\,. \tag{34b}$$

The dynamics of the (rescaled) local total density $\tilde{n}(\sigma_{\mathrm{L}}, t)$ is obtained by summing Eqs. (34a) and (34b):

$$\mathcal{D}_t \tilde{n} = \partial_{\sigma_{\mathrm{L}}} \left[\frac{D_m}{\sqrt{g}} \partial_{\sigma_{\mathrm{L}}} \left(\frac{\widetilde{m}}{\sqrt{g}}\right) + \frac{D_c}{\sqrt{g}} \partial_{\sigma_{\mathrm{L}}} \left(\frac{\tilde{c}}{\sqrt{g}}\right)\right], \tag{35}$$

and resembles a nonlinear diffusion equation with cross-diffusion terms, which here result from concentration gradients and shape deformations of the line.

Now, since local reactive equilibria in mass-conserving reaction–diffusion systems serve as scaffolds for patterns [42, 45, 46], one can approximate the membrane and cytosolic densities by their respective (stable) local reactive equilibria

$$[\widetilde{m}(\sigma_{\mathrm{L}}, t), \tilde{c}(\sigma_{\mathrm{L}}, t)] \to [\widetilde{m}^*(\tilde{n}(\sigma_{\mathrm{L}}, t)), \tilde{c}^*(\tilde{n}(\sigma_{\mathrm{L}}, t))]\,. \tag{36}$$

In doing so, one finds that only the metric g and the (rescaled) local total density $\tilde{n}$ remain as the relevant

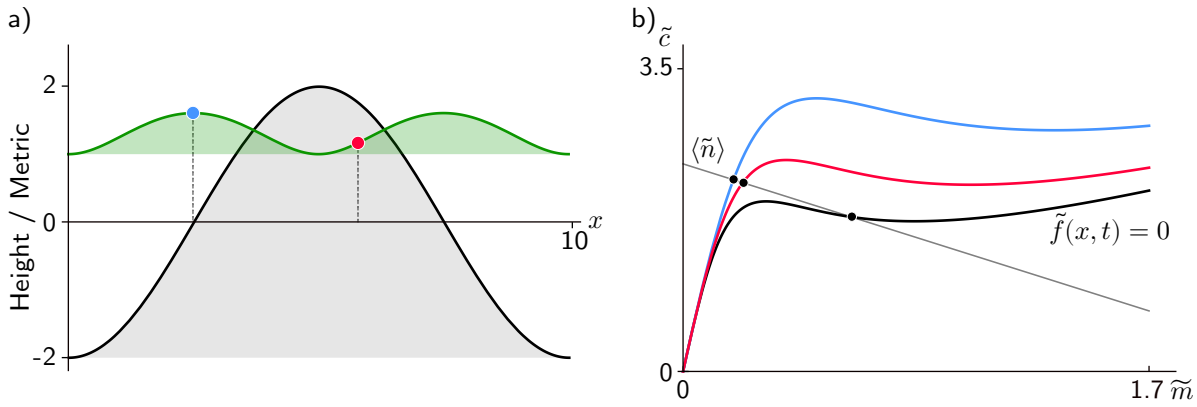

FIG. 6. Shape deformations of the manifold induce spatial inhomogeneities of the reactive nullcline. a) Height profile (black line) in Monge parametrization and the corresponding spatial profile of the metric (green line) for a given point in time. b) Phase space geometry for the rescaled variables $\tilde{c}$ and $\widetilde{m}$ at the same time point as in panel a). The differently colored lines show the reactive nullcline $f(x,t)=0$ at different positions in space (as depicted by the blue and red points in panel a)). The black line corresponds to the reactive nullcline for a planar geometry, i.e., for regions of the height profile where $\sqrt{g}\approx 1$. The thin gray line shows the local phase space for the (conserved) rescaled total average density $\langle\tilde{n}\rangle$. The intersections of this line with the reactive nullclines determines the local equilibria (black dots). Note that the local phase space intersects the black nullcline in a section where the slope is negative, hence fulfilling the instability criterion (38), while the intersections with the blue and red nullclines lie in sections where the slope is positive (laterally stable).

dynamic variables in Eq. (35). Evaluation of the spatial derivative inside the brackets in Eq. (35) results in:

$$\mathcal{D}_t\tilde{n} \approx \partial_{\sigma_\mathrm{L}}\left[\frac{D_m\partial_{\tilde{n}}\widetilde{m}^* + D_c\partial_{\tilde{n}}\tilde{c}^*}{g}\,\partial_{\sigma_\mathrm{L}}\tilde{n} - \frac{1}{2}\frac{D_m\widetilde{m}^* + D_c\tilde{c}^*}{g^2}\,\partial_{\sigma_\mathrm{L}}g\right]. \quad (37)$$

The first term inside the brackets in Eq. (37) describes diffusive mass-redistribution of $\tilde{n}$, and the second term contains higher-order nonlinear contributions to mass-redistribution originating from geometry deformations. To proceed, we consider several limiting cases. If g is independent of $\tilde{n}$, then Eq. (37) is an equation with a linear feedback (first term, linear order in $\tilde{n}$) together with a forcing term (second term, zeroth order in $\tilde{n}$). The stability of such equations is in general independent of the zeroth-order forcing term, and only depends on the linear-order feedback term. In contrast, if the normal velocity of the curve is an arbitrary function of the local total density $\tilde{n}$, then according to Eq. (20) the dynamics of the metric is governed by $\mathcal{D}_t g(\sigma_\mathrm{L},t) = -2\,g\,\kappa\,v_n(\tilde{n})$. If we expand around an initially flat configuration of the line, $g=1$ and $\kappa=0$, then gradients of the metric will always vanish to linear order in time, so that the second term in Eq. (37) still drops out. In the most general case, the metric g could be an arbitrary function of the local total density $\tilde{n}$. In that case, we need to assume that deformations are weakly varying near onset of pattern formation such that $\partial_{\sigma_\mathrm{L}}g \ll 1$, which, again, implies that instabilities are dominated by the first term in Eq. (37). Without this approximation, no statement about instabilities can be made from Eq. (37) and one would need to perform a (weakly) nonlinear analysis instead (assuming that the instability is supercritical) [56], which is a challenging task for our problem. Using this approximation, we find that the stability of the system against spatial perturbations is determined by the effective diffusion coefficient in the first term of Eq. (37). Since the metric g is always positive by definition, the effective diffusion coefficient of $\tilde{n}$ becomes negative (leading to anti-diffusion) if $D_m\partial_{\tilde{n}}\widetilde{m}^* + D_c\partial_{\tilde{n}}\tilde{c}^* < 0$. Hence, a homogeneous steady state becomes unstable to spatial perturbations if:

$$\frac{\partial_{\tilde{n}}\tilde{c}^*}{\partial_{\tilde{n}}\widetilde{m}^*} = \partial_{\widetilde{m}}\tilde{c}^*(\tilde{n}) < -\frac{D_m}{D_c}, \quad (38)$$

which, analogously to fixed planar geometries [42], shows that lateral instabilities occur if the slope of the reactive nullcline, $\partial_{\widetilde{m}}\tilde{c}^*(\tilde{n})$, is steeper than the ratio of diffusion coefficients on the membrane and in the cytosol, $-D_m/D_c$.

Our key finding here is that the generalized slope criterion, Eq. (38), depends explicitly on the local total densities $\tilde{n}$ as well as the shape of the reactive nullcline $\tilde{f}(\sigma_\mathrm{L},t)=0$, which is in general space and time dependent. This finding differs sharply from the case of a fixed planar geometry, where the same form of a slope criterion holds but with the shape of the nullcline fixed in both space and time, therefore leaving the local total density as the only control variable [42]. The space and time dependency of the reactive nullcline results in inhomogeneities, which suggests that the lateral stability of the system may vary between spatial regions and may also evolve over time, depending explicitly on the time evolution of the line conformation. This is illustrated in Fig. 6, where we show how spatial variations in the metric $\sqrt{g}$ (at a given point in time) induce spatial inhomogeneities

of the nullcline shape, which results in lateral instabilities in those segments of the line where the criterion given by Eq. (38) is fulfilled.

IV. PATTERN FORMATION ON DEFORMING MANIFOLDS

A. External control of manifold conformations

In the preceding sections, we established the theoretical framework to study reaction–diffusion systems on time-evolving one-dimensional manifolds. So far, the analysis has been general, and we have not further specified exactly how the shape of the line deforms over time, or whether and how protein dynamics can feed back onto these deformations.

To illustrate the key points of pattern formation on lines that can change their conformation, we analyze below simple examples where we assume that the conformation of the line is controlled externally, i.e., we explicitly specify the temporal evolution of the line shape and investigate how the reaction–diffusion dynamics responds to these perturbations. In detail, we consider the following scenario: we assume that the line shape is initially flat, and initialize the reaction–diffusion system such that the homogeneous steady state is stable against spatial perturbations (no pattern formation). In other words, the total density is chosen such that the slope criterion, Eq. (38), is not fulfilled. At time $t = T_0$, the shape of the line is then *adiabatically* deformed from a straight conformation to a cosine-shape (Fig. 7c):

$$h(x,t) = A(t)\cos\left(\frac{\pi x}{L}\right) , \tag{39}$$

where the amplitude $A(t)$ is chosen to increase linearly from 0 to A_0 during the time interval $[T_0, T_1]$ (ramp function):

$$A(t) = A_0 \times \begin{cases} 0, & t < T_0 \\ \frac{t-T_0}{T_1-T_0}, & T_0 \le t \le T_1 \\ 1, & t > T_1 \end{cases} . \tag{40}$$

The length of the time interval and the final amplitude A_0 are chosen such that the rate of line shape deformation is slow compared to the typical growth rate of unstable modes (small compared to $\sim D_c q^2$, where q denotes the mode number; see Ref. [42] for details). For clarity, we omit physical units in the following and specify typical length and time scales in an intracellular context in Appendix D. Note that in our numerical analysis we explicitly use a Monge parameterization to describe the line conformations, and perturb the line shape by directly increasing the height $h(x,t)$ instead of imposing motion along the normal vector of the line. This leads to a slight change in the equations, as the tangential velocity v_τ in Eq. (31) can be omitted.[1] To investigate the dynamics, we performed finite-element-method (FEM) simulations using the commercially available software *COMSOL Multiphysics v5.6*. The simulations show that the homogeneous steady state becomes laterally unstable for sufficiently large line shape deformations, and the concentration profile then gradually evolves into a mesa pattern along the spatial domain considered (Fig. 7b,c,d and Movie 1).

What is the mechanism underlying this lateral instability induced by the deformations that we impose on the line shape? To answer this question, we make use of the instability criterion for the rescaled densities, Eq. (38). Specifically, at each point in space and time, we determine the range of the (rescaled) total densities for which criterion (38) is fulfilled. To that end, we solve the equation $\partial_{\tilde{m}}\tilde{c}^*(\tilde{n}) = -D_m/D_c$ for the rescaled total density $\tilde{n}$, and thereby determine an upper threshold $\tilde{n}^+_{\mathrm{lat}}(x,t)$ and a lower threshold $\tilde{n}^-_{\mathrm{lat}}(x,t)$, for which the instability criterion is fulfilled, i.e., for total densities that obey the inequality $\tilde{n}^-_{\mathrm{lat}} < \tilde{n} < \tilde{n}^+_{\mathrm{lat}}$. Geometrically, these thresholds determine the points of the nullcline where the slope is equal to $-D_m/D_c$; see inset of Fig. 7a.

In contrast to the case of a fixed planar geometry, the existence and concentration range of a lateral instability here generally depends on space and time, since deformations cause spatial heterogeneities of the nullcline shape; see Eq. (32). This implies that shape deformations of the line may induce pattern-forming instabilities in regions of the line where the slope criterion (38) is fulfilled (regional instabilities, see Fig. 7a).

Figure 7b shows the spatiotemporal dynamics of the rescaled local total density $\tilde{n}$ (blue solid line) and the region of lateral instability (orange shaded region). For $t < T_0$, where the conformation of the line is flat, no pattern forms since $\tilde{n}$ lies outside the laterally unstable region. Note that the region of lateral instability is spatially uniform for $t < T_0$ since one has a flat geometry with a metric $g(x,t) = 1$. As the shape of the line is adiabatically deformed, the spatial profile of $\tilde{n}$ and the region of lateral instability also deform, eventually causing spatial sections of $\tilde{n}$ to enter the laterally unstable region. This event then induces a regional instability of the reaction–diffusion system and therefore leads to establishment of a pattern along the one-dimensional manifold considered (see Fig. 7a,b,d).

To conclude this section, we briefly summarize our key findings. Essentially, the impact of line shape deformations is reflected in the spatially inhomogeneous nullcline

[1] Consistent with our assumption of deformations along the normal direction, a tangential velocity only enters the equations if one chooses a parametrization in the Eulerian frame (as illustrated in Fig. 2). Here, to keep the analysis concise, we assume that the manifold is deformed along the vertical direction. Hence, since the direction of the deformations coincides with the coordinate system in this case, the tangential velocity v_τ can be disregarded.

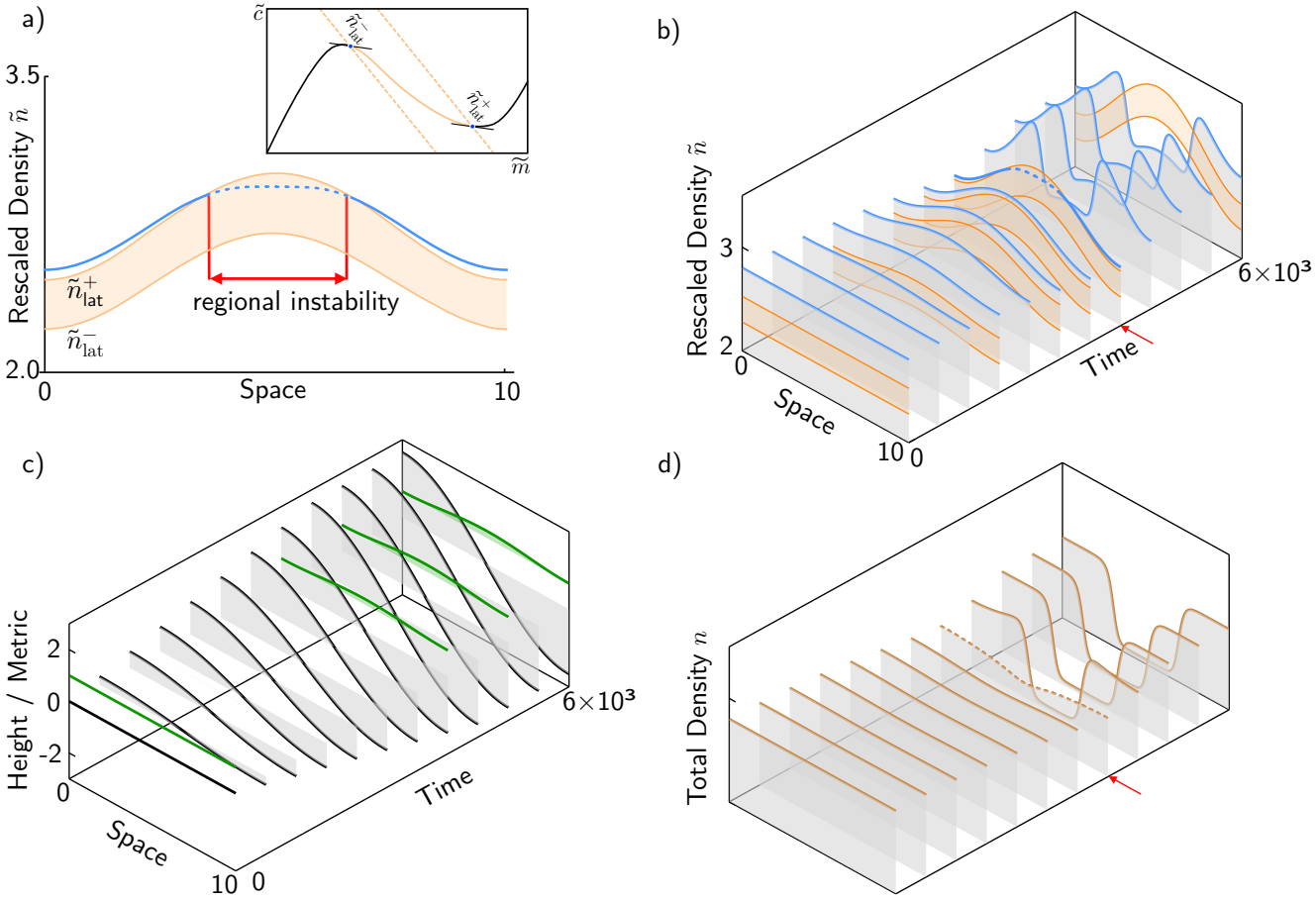

FIG. 7. Regional instability induced by line shape deformations. a) Snapshot of the rescaled local total density $\tilde{n}$ (blue solid line) and the region of lateral instability (orange area, the inset illustrates the definition of this area in phase space). The snapshot further shows the onset of the regional instability as $\tilde{n}$ enters the orange area (dashed blue line). b) Same as a), but for a set of time points (kymograph, where the grey shading visualizes the offset of the graph in the vertical direction). A pattern forms when $\tilde{n}$ enters the region of instability; the red arrow indicates the onset of the instability and corresponds to the graph shown in a). For clarity, the region of instability is only shown for selected time points. c) Time evolution of the line shape (black solid line) and metric (green solid line) as defined in Eq. (39). d) Actual local total density n; the red arrow indicates the onset of instability (same axes range as in b)).

shapes, which physically correspond to inhomogeneous reactive flows due to local length expansion and contraction and the corresponding changes in local particle concentrations. This heterogeneity in the nullcline shape (dictated by the conformation of the line) leads to a non-uniform region of instability, which may induce (regional) pattern-forming instabilities in the reaction–diffusion dynamics as explained above. We will in the following refer to this as a *geometry-induced instability*, since changes in the shape of the manifold lead to spatial variations of the metric, which in turn affect the stability of the reaction–diffusion dynamics.

B. Shape deformations act as a template for patterns

Above, we have shown that an externally controlled deformation of the line shape can induce lateral instabilities and thus lead to pattern formation. While we have chosen a specific way to gradually deform the geometry, the principle that we have found is general: the high-concentration plateaus of the emerging pattern form at characteristic locations along the line determined by geometric features, here extrema of the height profile; see Fig. 7c and Fig. 7d. Thus, the shape of the line acts as a kind of template for the patterns, with the low-concentration plateaus emerging in regions where the height profile has maximal slope. In these regions, the metric of the line is at its largest, thus maximizing the local depletion of particles due to dilation in the local

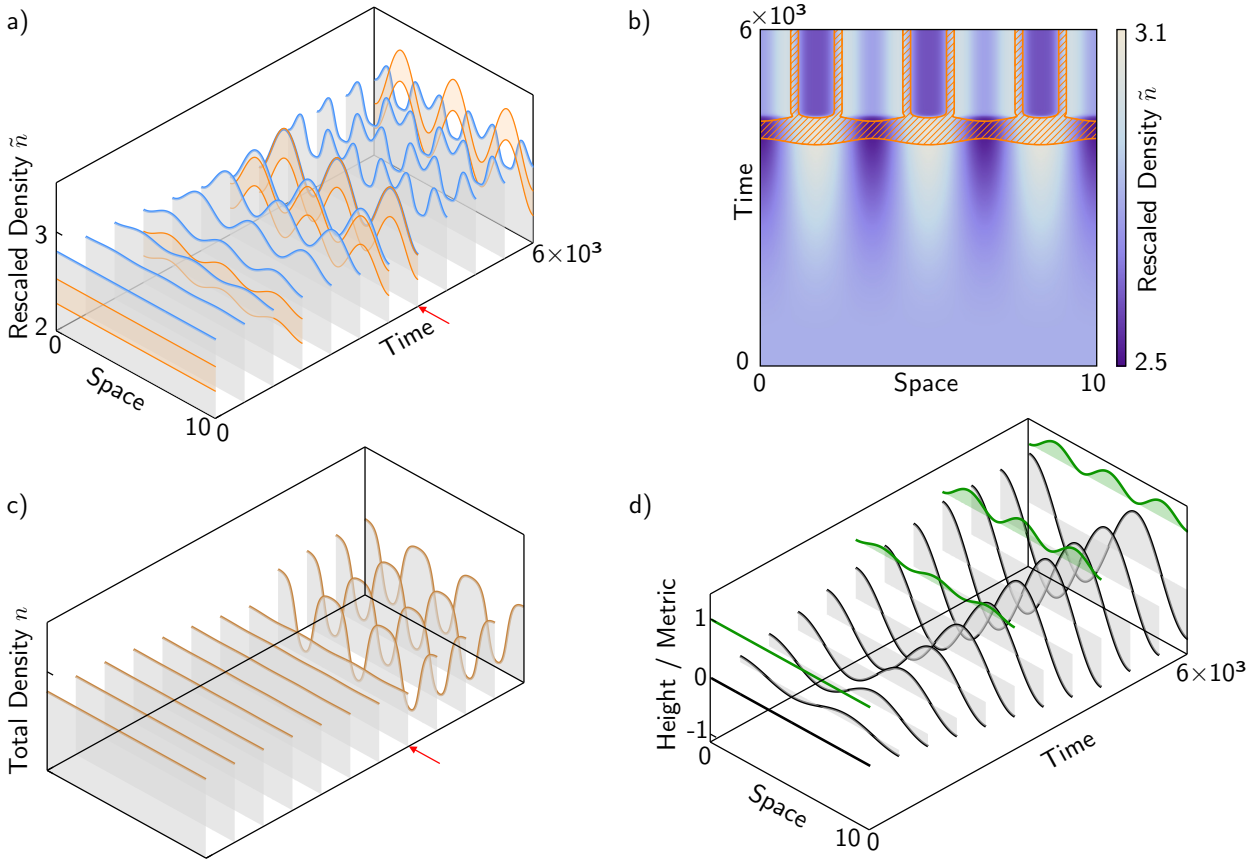

FIG. 8. The shape of the line acts as a template for patterns. a) A pattern-forming instability is triggered once the rescaled local total density $\tilde{n}$ (blue solid line) enters the region of instability (orange area). For clarity, the region of instability is only shown for selected time points. The red arrow indicates the onset of pattern formation. b) Same kymograph as shown in a), but projected onto the space–time plane with the color-coding indicating the rescaled local total density $\tilde{n}$. The orange hatched area indicates the values of $\tilde{n}$ which lie in the region of a lateral instability. Note that a pattern forms once the orange hatched area appears (after a short lag time). c) Actual local total density n (same axes range as in a)). Note that the rescaled density $\tilde{n}$ (shown in a) and b)) is non-uniform before the onset of a lateral instability (due to deformations), while the actual density initially remains nearly homogeneous and develops a spatial pattern once the system reaches the onset of instability. d) This panel shows the line conformation (black solid line) and metric (green solid line), corresponding to Eq. (41). Comparing with c) reveals that the high concentration regions of the pattern (plateaus) form precisely at the extrema of the height profile.

line geometry. This is a generic feature of the system, as we will explain in the following.

To elucidate this templating effect further, we repeat the analysis from the previous section, but this time consider a higher-harmonic shape deformation (Fig. 8c):

$$h(x,t) = A(t)\cos\left(\frac{3\pi x}{L}\right), \tag{41}$$

where the amplitude $A(t)$ is defined by Eq. (40) and the initial conditions are again chosen such that the homogeneous steady state is laterally stable. In agreement with our previous results, a pattern-forming instability is triggered as soon as the rescaled total density $\tilde{n}$ enters the region of lateral instability (see Fig. 8a,b,c and Movie 2). As we have chosen a higher-harmonic shape deformation for the line, multiple plateaus now form. As expected, the high-density plateaus are located at the extrema of the line height, while the low-density plateaus are located in regions where the height profile of the line is steepest; compare Fig. 8c and Fig. 8d.

This is effect is due to the non-uniform deformation of the line shape. In particular, while the total length of the height profile increases over time, the local length of individual line segments barely changes at the extrema of the height profile. Thus, the growth of the line's contour length occurs primarily in regions with a steep slope of the height profile, where the metric is largest. In these regions, where $\partial_t \sqrt{g(x,t)} > 0$, the concentration of particles will be diluted. Thus, even when starting from an initially homogeneous concentration profile, such geometric effects alone lead to a redistribution of particles and density inhomogeneities $n(x,t)$ along the line (Fig. 8c). If this effect is coupled to the onset of a lateral instability, then troughs in the density profile will further decrease,

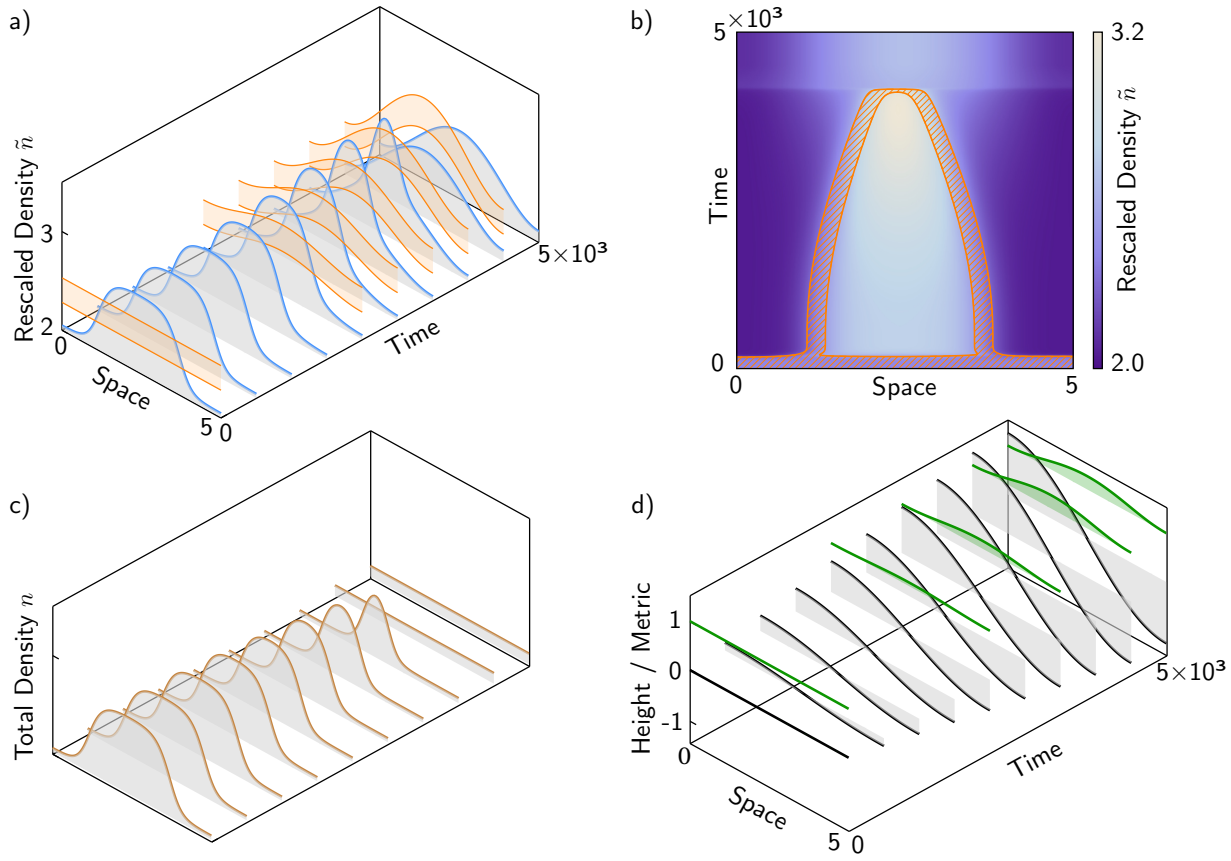

FIG. 9. Shape deformations shift the interface and suppress patterns. a) The total average density is chosen such, that initially a mesa pattern forms. Due to deformations of the line shape, the interface (connecting the lower and upper plateau) is shifted such that the plateau width decreases (see discussion in main text). For sufficiently large deformations, only a small region of the rescaled local total density $\tilde{n}$ (blue solid line) lies in the region of instability (orange area), which then leads to suppression of the pattern (see also c)). b) Same kymograph as shown in a), but projected onto the space–time plane with the color-coding indicating the rescaled local total density $\tilde{n}$. The orange hatched area indicates the values of $\tilde{n}$ which lie in the region of a lateral instability. Note that the interface is first shifted and then suppressed as the plateau width becomes too small. c) Actual local total density n (same axes range as in a)). d) Time evolution of the line shape (black solid line) and metric (green solid line), as defined in Eq. (42).

while hills (located at the extrema of the height profile where $\sqrt{g(x,t)} \approx 1$) will increase (Fig. 8a,b,d). In other words, the mass-redistribution instability [42] will further amplify geometry-induced density inhomogeneities.

C. Interface shift and pattern suppression

So far, we have investigated cases where the homogeneous steady state was laterally stable for a planar geometry, and we induced an instability only by deforming the line shape. We now ask how shape deformations affect already established patterns. To address this question, we choose the initial total density such that the homogeneous steady state is laterally unstable, thereby resulting in the formation of a mesa pattern (Fig. 9a,c and Movie 3).

We initialize the reaction–diffusion system and its steady-state pattern on an initially planar geometry (straight line). Then, following the same procedure as before, we deform the line shape adiabatically (Fig. 9d):

$$h(x,t) = A(t)\cos\left(\frac{\pi x}{L}\right), \tag{42}$$

where the amplitude $A(t)$ is defined by Eq. (40). We find that the deformation in the line's shape (Fig. 9d) gradually changes the pattern profile from a mesa to a narrow peak pattern, until eventually the peak disappears altogether (Fig. 9c). There are two major underlying reasons for these observations: First, for the two-component reaction–diffusion system that we study here, it has been shown that the interface position (which connects the lower and upper plateau of a mesa pattern) depends only on the average total density $\langle n \rangle$, as long as the system size is larger than the typical length scale of the pattern interface [42]. Thus, altering the average total density will shift the interface as a consequence

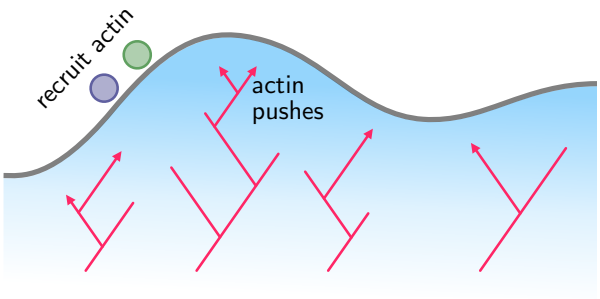

FIG. 10. Illustration of actin-driven membrane deformations. Membrane-bound and cytosolic proteins enhance the local polymerization of actin filaments, which in turn push the membrane outwards. These effects can most simply be modelled by an isotropic cytosolic pressure that drives membrane motion along its normal vector (see Eq. (43)).

of mass-conservation, where addition or removal of mass leads to a respective increase or decrease of the plateau width. Since deformations of the line shape effectively lead to a depletion of the total average density due to an increase in the total length of the spatial domain, this explains the shift of the pattern interface. Second, for large enough shape deformations, only a small part of the system lies in a region of lateral instability; see Fig. 9a and Fig. 9b. Once the size of this region becomes comparable or even smaller than the typical length scale of the interface, pattern formation is suppressed.

D. Self-organized mechanochemical coupling

In the previous sections, we have gained basic insights into how shape deformations affect the pattern formation of mass-conserving reaction–diffusion systems. We now consider a more intricate scenario where the dynamics of the conformation of the line is explicitly coupled to the density fields on the one-dimensional manifold. In other words, we incorporate a feedback loop between the line shape and the reaction–diffusion dynamics of the density fields. In general, there are many ways to implement such a coupling. For example, the local concentration of proteins can drive shape deformations as well as protein transport on and onto the manifold through local bending of the membrane [30, 37, 57], active stresses in the form of myosin contractility [39, 58, 59] or actin polymerization [47, 58].

Furthermore, there are many ways to account for the mechanical properties of an elastic (or viscoelastic) manifold. For example, consider a cell membrane; the line we have considered so far can be seen as a one-dimensional projection of such a membrane. The conformation of a membrane is characterized by an elastic energy that generally contains both a bending energy term and a surface tension term. Which of these contributions dominates depends on the system in question [60–62]. Here, we study a conceptually simple example where we assume that the line can be regarded as a fluid-like substrate, i.e., we disregard mechanical properties of the line such as bending rigidity. To further simplify our system, we additionally assume that the tension γ, cf. Eq. (43), is spatially uniform. The feedback loop between the particle density and the membrane conformation is implemented by assuming that shape deformations are locally driven by the local total density of proteins. Specifically, we consider the following form for the normal velocity v_n:

$$v_n = \mu \left[m(\sigma_\mathrm{E}, t) + c(\sigma_\mathrm{E}, t)\right] + \gamma\, \kappa(\sigma_\mathrm{E}, t)\,. \tag{43}$$

The parameter μ denotes the coupling strength between the local protein density and the normal velocity of the line. Physically, one may interpret this term as a protein-controlled recruitment and polymerization rate of actin filaments that drive outwards motion of the membrane through an effective pressure [47, 58, 63] (see Fig. 10 for an illustration). The second term accounts for the Laplace pressure caused by surface tension effects due to the local curvature $\kappa(\sigma_\mathrm{E}, t)$. Phenomenologically, the first term thus describes local growth of the membrane that is proportional to the local total density of proteins, while the second term counteracts this effect by minimizing the membrane area (which is a length in our case since we consider a one-dimensional projection of the membrane surface).

In the Monge representation of the line, and mapping to rescaled variables $\widetilde{m}$ and $\tilde{c}$ (Sec. III D), one can rewrite Eq. (43) as:

$$v_n = \mu\, \frac{1}{\sqrt{g}} \left[\widetilde{m}(x,t) + \tilde{c}(x,t)\right] + \gamma\, \frac{1}{g^{3/2}}\, \partial_x^2 h(x,t)\,. \tag{44}$$

The time evolution of the line conformation is then obtained from Eqs. (33c) and (44):

$$\begin{aligned} \partial_t h(x,t) &= \sqrt{g(x,t)}\, v_n \\ &= \mu \left[\widetilde{m}(x,t) + \tilde{c}(x,t)\right] + \gamma\, \frac{1}{g}\, \partial_x^2 h(x,t)\,. \end{aligned} \tag{45}$$

Eq. (45) for the height profile of the one-dimensional manifold, together with Eqs. (33a) and (33b) for the density profiles of the proteins, provide a closed set of equations governing the self-organized dynamics of a two-component MCRD system on a deforming manifold with mechanochemical coupling.

In general, the dynamics of the mechanochemically coupled system is expected to depend on the relative time scales of line shape deformation and protein pattern formation. The former is determined by the coupling strength μ and the total average density $\langle \tilde{n} \rangle$, and yields the characteristic time scale for the growth of the line's length, $t_\mathrm{G} = L_0/(\mu \langle \tilde{n} \rangle)$. The latter is dominated by cytosolic redistribution of particles and thus provides a typical time scale of diffusion $t_\mathrm{D} = L_0^2/D_c$. Hence, one

may define a dimensionless number that relates the time scales of diffusion and growth, which we call in analogy to fluid dynamics the Péclet number

$$\mathrm{Pe} := \mu\langle\tilde{n}\rangle L_0/D_c\,. \tag{46}$$

For small values of the Péclet number, $\mathrm{Pe} \ll 1$, diffusion is much faster than the dynamics of line shape deformations. In particular, in the limiting case of $\mathrm{Pe} \to 0$, the dynamics of shape deformations becomes infinitely slow on the time scales of diffusive mass redistribution. This is equivalent to abolishing mechanochemical coupling altogether, $\mu \to 0$, where the protein patterns approach a stationary state. We provide a systematic analysis of the impact of this parameter on the pattern-forming dynamics in Sec. IV E.

In the following, we will first explore the system's dynamics through FEM simulations, and find a broad variety of dynamic patterns.

1. *Oscillations*

First, we performed simulations of small confined systems with reflecting boundaries. The initial total average density was chosen such that the reaction–diffusion system is laterally unstable and therefore generates a mesa pattern. For the initial conformation of the line, we selected a flat state with $h(x,0) = 0$.

Interestingly, although the two-component reaction–diffusion system shows only stationary patterns for a static line shape, we here find self-organized oscillations. These spatiotemporal patterns must therefore clearly be due to the mechanochemical feedback between the protein pattern and the line shape (Fig. 11, Movie 4). However, the question remains as to how the mechanism driving these oscillations relates to the geometry effects discussed earlier (Secs. IV A–IV C).

From the first term in the equation for the normal velocity v_n, Eq. (43), we deduce that an initial pattern formed on a flat line destabilizes this line conformation by inducing faster growth of the height profile at the pattern's peaks than at its valleys. The resulting change in the line shape geometrically corresponds to local length dilations and contractions. Here, where we started from a flat line conformation, the slope of the height profile and thus the local contour length of the line grows fastest at the pattern's interfaces between two plateaus. To illustrate how these changes in the line's geometry affect the dynamics of the protein pattern, let us for now suppose that we initiate the system with a protein pattern consisting of two plateaus (mesa pattern) and a flat conformation of the line (see Fig. 12). Then, the growth of the local line length at the interface (connecting the lower and upper plateau) will locally dilute the density of proteins. As a consequence, the lower plateau will expand at the expense of the upper plateau, pushing the interface towards the upper plateau (see Fig. 12). Since line shape deformations also alter the region of instability of the

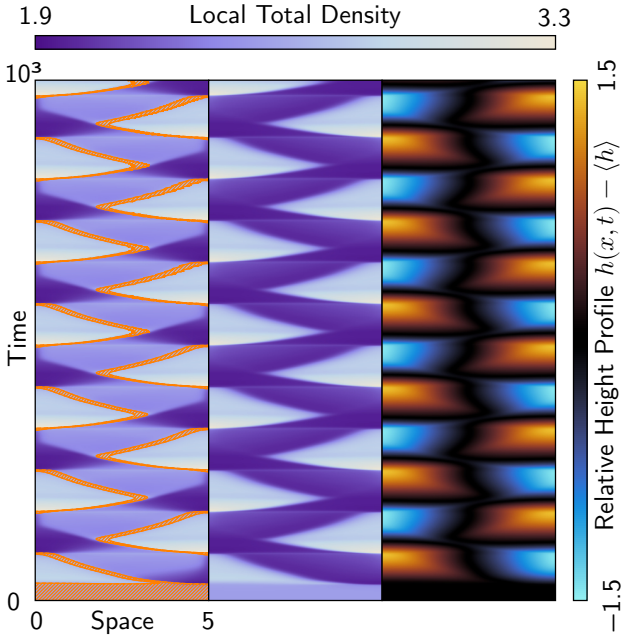

FIG. 11. Coupling the reaction–diffusion dynamics to the shape of the line leads to self-organized spatiotemporal patterns. The left panel shows a kymograph of the spatiotemporal dynamics of the rescaled total density $\tilde{n}$ and illustrates the emergence of oscillations. The orange shaded area corresponds to values of $\tilde{n}$ which fulfill the instability criterion Eq. (38). Note that, as the pattern amplitude on one boundary of the domain disappears (due to deformations of the line shape, see right panel), a regional instability is induced at the opposite boundary. This interplay between reaction–diffusion dynamics and line shape deformations drives the spatiotemporal dynamics. The middle panel shows the actual local total density n. The right panel illustrates the patterns in the relative height profile, defined as $h(x,t) - \langle h\rangle$, where the average height $\langle h\rangle$ is proportional to the average total density and time $\langle h\rangle \sim \langle\tilde{n}\rangle\, t$.

reaction–diffusion system, large enough deformations will suppress the initial pattern and trigger a regional instability at the opposite side of the geometry (see Fig. 11). As the upper plateau grows at the opposing side, it gradually restores the height profile to a flat conformation. After the plateau pattern is fully re-established at the opposing side and the conformation has returned to a flat conformation, the cycle repeats. This intricate interplay between the dynamics of the line shape and the reaction–diffusion system (mechanochemical feedback) is the key mechanism that leads to spatiotemporal oscillations.

2. *Traveling waves*

For spatial domains much larger than the wavelength λ_c of the fastest growing mode in the dispersion relation (Appendix F), the two-component mass-conserving

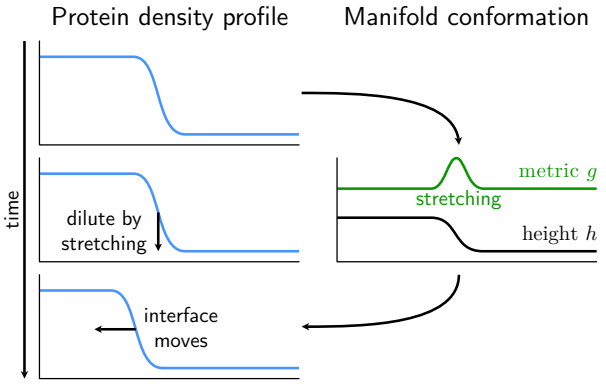

FIG. 12. Illustration of the mechanism that drives the motion of the protein pattern's interface. The one-dimensional manifold moves along its normal vector, with a velocity that is proportional to the local protein density. Therefore, gradients in protein density lead to gradients in the height profile, thus stretching the line at the location of the protein pattern's interface. Since local stretching of the line corresponds to local dilution of the protein density, the interface of the protein pattern moves.

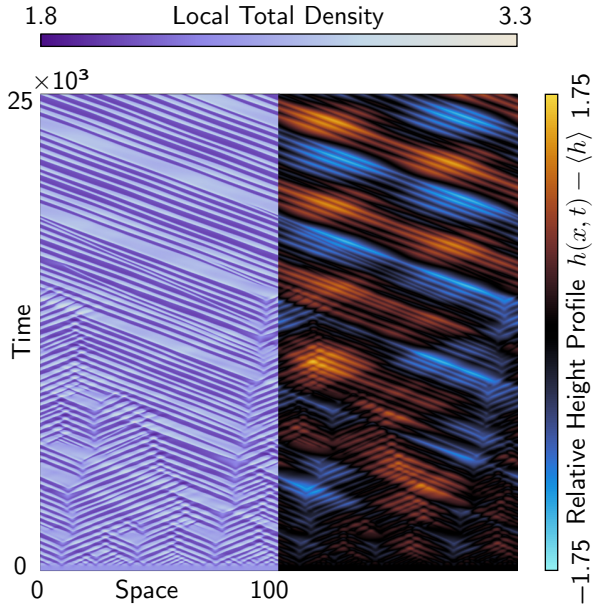

FIG. 13. Emergence of traveling wave patterns for Péclet numbers $\mathrm{Pe} < 0.6$. The left panel shows a kymograph of the spatiotemporal dynamics of the actual local total density n, and the right panel depicts the relative height difference $h(x,t) - \langle h \rangle$. Wave fronts emerge and vanish at specific points along the spatial domain considered. The positions of these events depend on the initial condition, which in our FEM simulations is a small random perturbation around the homogeneous steady state. For long times, the system self-organizes into periodic traveling wave fronts.

reaction–diffusion system initially leads to the formation of patterns consisting of multiple plateaus or peaks.[2] The wavelength of this initial pattern is well approximated by λ_c. However, this initial pattern is not stable and slowly coarsens to a single peak or interface [64–69].

Let us now again consider how the dynamics is changed when there is a mechanochemical coupling between the density profile emerging from the reaction–diffusion system and the conformation of the line. As in Sec. IV D 1, we choose a flat height profile $h(x,0) = 0$ for the initial line conformation, and a homogeneous concentration of proteins with a slight random perturbation around this state; however, we now impose periodic boundary conditions for both, the reaction–diffusion dynamics and the line's shape.

In our FEM simulations, we observe that propagating density waves and accompanying waves in the height profile arise at specific points in space ("sources") (Fig. 13, Movie 5). Each of these sources gives rise to two waves that travel in opposite directions and, given the periodic boundary conditions, mutually annihilate at specific points on the spatial domain considered ("sinks"). The position of these sources and sinks depend on the initial conditions, that is, the slight perturbations of the initially homogeneous density profiles. Furthermore, we observe that these sources and sinks slowly migrate in space, and eventually meet and annihilate for large times. The steady-state pattern then consists of periodic traveling wave fronts, as shown in Fig. 13. Importantly, we note that the system selects a typical wavelength for large times. Hence, our results suggest that the coarsening process is interrupted if the dynamics is explicitly coupled to the geometry.

[2] For the specific system that we consider here, these are always mesa patterns (see Appendix A).

3. *Standing waves*

Depending on the relative magnitude of the characteristic time scales of changes in the line shape and the mass redistribution—the Péclet number Eq. (46)—we observe a transition from traveling wave patterns to standing wave patterns (Fig. 14 and Movie 6).

For the parameter combination used in this study (Appendix D), the transition from traveling waves to standing waves occurs at a critical value of $\mathrm{Pe}_c \simeq 0.6$. This suggests that standing wave patterns emerge if the time scales of line shape dynamics and diffusive redistribution of proteins are comparable, whereas the emergence of traveling wave patterns requires that diffusive redistribution of proteins is the dominant (fastest) time scale. Moreover, as for the traveling waves in Sec. IV D 2, we find that the system selects a typical wavelength for large times (see Fig. 14a,b). Notably, for large domains, we observe that the pattern wavelength at small times is larger

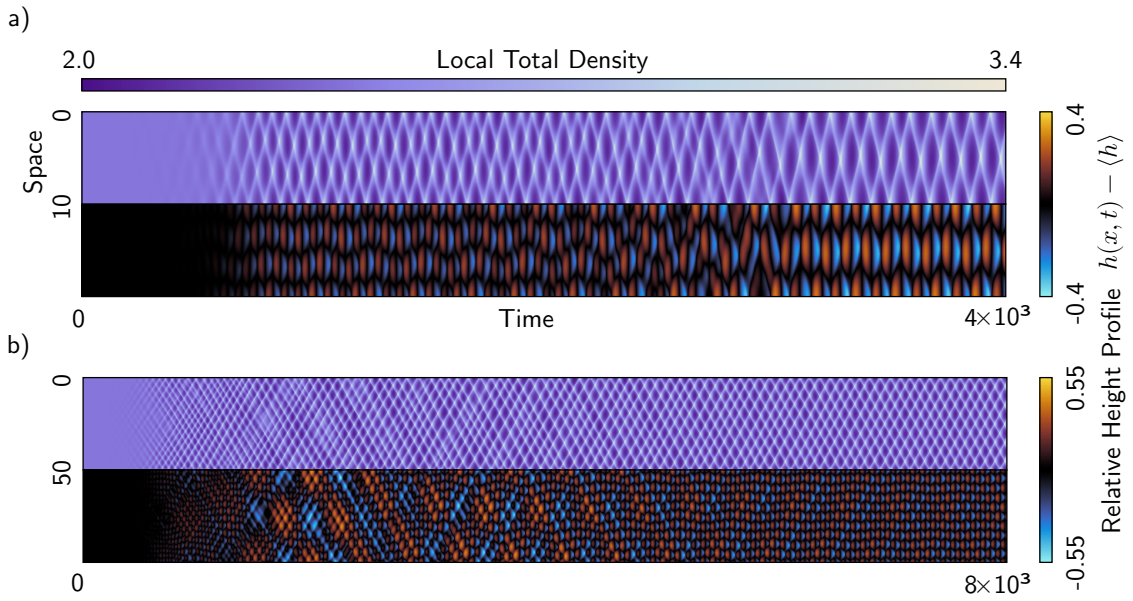

FIG. 14. Emergence of standing wave patterns for Pe > 0.6. a) Spatiotemporal dynamics of the actual local total density n and the relative height difference $h(x,t) - \langle h \rangle$ for system size $L_0 = 10$. As for traveling waves, the dynamics settles on a specific wavelength over long times. b) Same FEM simulation and parameters as shown in a), but for a larger system size $L_0 = 50$. The final wavelength at long times is identical to that shown in a).

than the final wavelength in steady state (see Fig. 14b). This again indicates that coarsening in the system seems to be interrupted.

E. Tuning the relative time scales of the conformational dynamics and diffusive transport

In the previous sections, we found that coupling a MCRD system on a one-dimensional manifold with deformations of this manifold can lead to rich spatiotemporal dynamics. In FEM simulations of the coupled system we have observed oscillations or traveling waves, even though the MCRD system on a static manifold would typically approach a stationary steady state through coarsening. As discussed above, such a mechanochemical coupling introduces an additional time scale that competes with the typical time that the MCRD system requires to generate a protein pattern, see Eq. (46).

But how in detail does the dynamics of shape deformations affect the formation of protein patterns through reactions and diffusion? Here, we answer this question by performing numerical parameter sweeps. For convenience, we first introduce dimensionless quantities by rescaling spatial coordinates and time,

$$\{x,\, h\} \to L_0 \times \{x',\, h'\}, \text{ and } \quad t \to D_c^{-1}\, L_0^2 \times t'\,, \quad \text{(47a)}$$

and thus also velocities, $v \to D_c\, L_0^{-1} \times v'$. Furthermore, we also rescale particle densities,

$$\{\tilde{n},\, \tilde{c},\, K_d\} \to L_0^{-1} \times \{\tilde{n}',\, \tilde{c}',\, K_d'\}\,, \quad \text{(47b)}$$

and all control parameters:

$$\{D_m,\, \mu,\, \gamma\} \to D_c \times \{D,\, \mu',\, \gamma'\}\,, \quad \text{(47c)}$$

$$\{k_{\text{on}},\, k_{\text{fb}},\, k_{\text{off}}\} \to D_c\, L_0^{-2} \times \{k'_{\text{on}},\, k'_{\text{fb}},\, k'_{\text{off}}\}\,. \quad \text{(47d)}$$

Here, we have grouped parameters with identical units of measurement and indicate their non-dimensionalized counterparts by the prime symbols on the right-hand side. The non-dimensionalized equations are shown in Appendix C, where we have dropped the primes to simplify notation. Due to the non-dimensionalization, all variables are scaled to the system size. Here $D = D_m/D_c$ denotes the ratio of diffusion constants, and the Péclet number relating the time scale of shape dynamics to the time scale of (cytosolic) diffusion is now given by $\text{Pe} = \mu' \langle n' \rangle$.

From our numerical parameter study, we find that the system can remain in a stationary state as long as the Péclet number is sufficiently small, below a finite critical value of $\text{Pe} \lesssim 0.2$. However, if we increase the Péclet number beyond this value, then we find a discontinuous onset of oscillations (Fig. 15). When further increasing the Péclet number, the oscillation frequency increases. When the line moves at a high velocity (corresponding to large oscillation frequencies), the coupling to the manifold quickly redistributes proteins and thus flattens out protein density gradients via an effective artificial diffusion. For example, regions with a high concentration of proteins grow faster, hence reducing the local concentration of proteins by virtue of mass conservation. Thus, above a large Péclet number of $\text{Pe} \gtrsim 50$, we find a suppression of both protein pattern formation and conse-

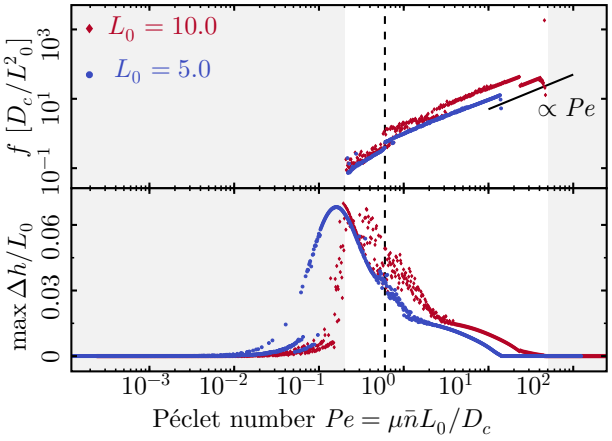

FIG. 15. Features of the oscillatory dynamics of the one-dimensional manifold in our simulations, as a function of the Péclet number. In our FEM simulations, we monitor the height difference, $h(L,t) - h(0,t)$, of the one-dimensional manifold as a function of time. We then determine the frequency of the oscillations (top) and the maximal amplitude of the oscillations (bottom). In the limit of small Péclet number, the height profile remains static, thus leading to stationary patterns that persist until a critical value of Pe ~ 0.2. For sufficiently large Péclet number, we observe an onset of oscillations, whose frequency increases (approximately) linearly. When the Péclet number exceeds a second critical value of $\mu/D_c \simeq 50$, all dynamics vanishes.

quently oscillations (Fig. 15). Interestingly, we find a doubling of the measured oscillation frequencies at intermediate Péclet numbers Pe ~ 0.6, which for large system sizes corresponds to the onset of standing wave patterns, as discussed in the previous section.

To conclude, through our numerical parameter study we have learned how the shape dynamics affects protein pattern formation on the one-dimensional manifold. The qualitative dynamics of protein pattern formation remains largely unaffected by the deformations as long as the Péclet number, which relates the time scale of the line's deformations to the time scale of protein diffusion, is sufficiently small. However, there are two qualitative changes with increasing Péclet number: First, one observes a discontinuous onset of oscillatory patterns, and second, at high Péclet numbers all patterns are gradually extinguished.

V. DISCUSSION

We investigated the dynamics of a two-component mass-conserving reaction–diffusion system on a dynamically deforming one-dimensional manifold embedded in two-dimensional space. To shed light on how deformations of the line influence pattern formation, we first studied a scenario where these shape deformations are externally controlled and occur on a time scale much larger than that of the intrinsic dynamics of the reaction–diffusion system (adiabatic deformations). Next, we considered a feedback loop between shape deformations and the reaction–diffusion dynamics. To keep the analysis simple and concise, we assumed a fluid-like substrate with a growth rate proportional to the local total protein density. We found that shape deformations induce spatially non-uniform pattern-forming instabilities, which we refer to as *regional instability*. Moreover, our analysis shows that the shape dynamics may also (regionally) suppress protein patterns and spatially shift already established protein pattern interfaces. Despite its simplicity, the model already shows a surprisingly wide range of dynamic patterns, such as oscillations and traveling waves. They emerge as a direct consequence of the interplay between shape deformations and reaction–diffusion dynamics.

Based on the local equilibria theory [42], we then derived a criterion that links the onset of instabilities to the slope of the reactive nullcline in phase-space. Specifically, we find that the nullcline shape becomes spatially non-uniform because the metric of the geometry enters the dynamics. This differs sharply from the case of a flat static geometry [42], where the nullcline shape is uniform in space and time. Our analysis shows that the interplay between the dynamics of the local total density, an important control parameter for pattern formation in mass-conserving reaction–diffusion systems [42, 45, 46], and the metric is key to understanding the phenomenology of the system. From a physical point of view, the underlying mechanism of the observed dynamics lies in the local dilution and enrichment of particle densities by local length contraction and extension, respectively, which occur concomitantly with dynamic changes in the shape of the line.

We further showed that the existence of dynamic patterns crucially depends on the characteristic time scales of shape deformations and (cytosolic) diffusive mass redistribution, which we quantified by defining a (dimensionless) Péclet number that describes the ratio between these two time scales. Depending on the Péclet number, we identified two distinct asymptotic limits: (i) for small values of the Péclet number, one finds quasi-stationary patterns as the line deforms on a time scale much larger than the typical time scale of mass redistribution (diffusion-dominated regime), and (ii) for large values of the Péclet number, pattern formation is suppressed due to an instantaneous and large deformation rate of the line, which prevents the establishment of gradients in the particle densities (growth-dominated regime). Between these two limiting regimes, the mechanochemical coupling yields a rich dynamics including oscillations and traveling wave patterns.

We found that the impact of deformations of the manifold is specified by a simple criterion, Eq. (38), which predicts the onset of regional instabilities. Strikingly, the only geometric information that enters this criterion is the metric of the manifold. This implies that the in-

stability criterion is generic for mass-conserving reaction-diffusion systems, regardless of the exact cause and the associated mechanical forces that lead to shape deformations. Here, we assumed a fluid-like manifold where shape deformations are driven by the local concentration of proteins. Additional mechanical properties, such as bending stiffness, in-plane elasticity, and volume or area constraints can be incorporated into our model by including further terms in the normal velocity. While these additional features do not affect the instability criterion Eq. (38), they will introduce further nonlinearities, which in general will lead to complex pattern-forming dynamics and wavelength selection in the highly nonlinear regime.

Turing systems on growing domains.— Our model shows conceptual differences when compared to classical Turing models on homogeneously growing domains, such as uniformly growing planar lines [70]. In such systems, which grow uniformly in length, each length segment of the domain grows at the same rate, so that the dynamics of the metric can be eliminated by being absorbed into the temporal change of the total length. For mass-conserving reaction-diffusion systems, this entails that the local total density is the only relevant degree of freedom in the system. The system considered here involves a dynamic interplay between the local total density and the metric, which leads to (self-organized) non-uniform growth rates and thereby rich pattern-forming dynamics. Classical Turing models have also been studied for non-uniformly growing lines [71], where, for example, one segment of the line is assumed to grow at a different rate from that of the remaining portion, which can effectively be described as a piecewise uniformly growing line. It was found that this leads to asymmetric pattern formation and peak-splitting of patterns, which can be interpreted as regional patterns in analogy to our work. However, the underlying mechanism leading to such regional Turing patterns is, again, substantially different from our model. In essence, Turing patterns in such systems occur (including peak-splitting) once the local line segment length exceeds a critical value, thus inducing (regional) Turing instabilities or frequency-doubling of the pattern.

Notably, these classical Turing models have been mainly studied in the quasi-stationary limit [70, 71], where one assumes that the pattern-forming dynamics unfolds on a much smaller time scale than domain growth. While such an assumption is reasonable at larger scales, such as in the context of morphogenesis, the time scales of growth and pattern formation are generally not far apart in an intracellular context. This is evidenced by recent *in vitro* experiments, which show that proteins are capable of dynamically deforming giant unilamellar vesicles (GUVs) [19], or reshaping supported lipid bilayers [6]. Therefore, here we have examined the full range of relative time scales (diffusive mass redistribution and shape deformations) by varying the Péclet number, and indeed found qualitative differences in the dynamics as a function of these time scales, such as a transition from traveling waves to standing waves. This underscores the relevance of the different time scales as an additional means by which mechanochemical patterns in cells may be controlled. For concentration-dependent growth, as we have considered here, cells may achieve such control by regulating the total density of proteins.

Bulk-boundary coupling.— Protein patterns in biological systems often emerge at surfaces, such as the cell membrane, where proteins cooperatively bind to and detach from the membrane. Consequently, proteins have to be transported from the bulk solution (cytosol) to the cell membrane, which is achieved by diffusive and advective fluxes in cells [27]. This leads to cytosolic protein density gradients perpendicular to the membrane, and these gradients have been shown to be crucial for pattern formation in mass-conserving reaction–diffusion systems [16, 26, 45, 72]. Another interesting extension of our work would be therefore to explicitly account for bulk-boundary coupling in the reaction–diffusion dynamics. Potentially, this might yield additional interesting geometric effects, since shape deformations would (locally) alter the bulk-boundary ratio, which is an important control parameter for protein pattern formation [22–24, 26, 45, 72].

Biologically realistic reaction networks.— We expect that our analysis can be transferred to more complex mass-conserving reaction–diffusion systems. One prominent example is the Min protein system in *E. coli*, which can generate a broad variety of self-organized patterns such as traveling waves, standing waves, chaos, and stationary patterns (for a review please refer to e.g. Ref. [73]). Recently, it was shown that the *in vitro* Min system in a heterogeneous setup (three-dimensional wedge-shaped geometry) leads to patterns on multiple length and time scales [26]. Importantly, these joint theoretical and experimental studies have shown that the large-scale dynamics can be characterized by diffusive redistribution of protein mass, which is the essential degree of freedom on large spatial and temporal scales. In the present work, we found that spatial heterogeneities generally also occur in systems that exhibit a feedback loop between shape deformations and reaction–diffusion dynamics. Then, in contrast to systems with (fixed) spatially varying geometry as in the wedge setup mentioned above or in the context of a fixed cell shape, spatial heterogeneities and complex geometries are generated by the dynamics. One might therefore wonder why we do not observe multiscale patterns here. The reason is that the two-component system has only one stable attractor (mesa or peak pattern) [42, 67, 69], which significantly limits the phenomenology. One could, however, readily apply our approach to the Min dynamics by replacing the reaction–diffusion component in our model with the biochemical reaction network of the Min system. Coupling Min patterns to shape deformations may lead to interesting dynamics that possibly span multiple spatial and temporal scales, and the concept of regional instabilities would enable one to characterize and explain such multiscale patterns on dynamic manifolds.

Moreover, this could provide a rich field of research if one, for example, considers placing an additional lipid bilayer membrane at some height above a supported lipid bilayer membrane [21]. Now, if this additional lipid bilayer is not supported by a solid surface but is free standing, it can be deformed by the Min proteins and thereby dynamically affect the cytosolic volume between the two membranes and thus the local volume-boundary ratio. That Min proteins are indeed capable of deforming giant unilamellar vesicles was recently demonstrated experimentally [19, 21]. We hypothesize that in such a system one could observe an intricate dynamic interplay between multiscale protein patterns and the dynamics of the free-standing membrane.

ACKNOWLEDGMENTS

We would like to thank A. Ziepke and T. Roth for critical reading of the manuscript. This work was funded by the Deutsche Forschungsgemeinschaft (DFG, German Research Foundation) through the Collaborative Research Center (SFB) 1032 – Project-ID 201269156 – and the Excellence Cluster ORIGINS under Germany's Excellence Strategy – EXC-2094 – 390783311. AG was supported by a DFG fellowship through the Graduate School of Quantitative Biosciences Munich (QBM). During his time at the Massachusetts Institute of Technology, AG was supported by the National Science Foundation (NSF) through grant number 2044895.

Appendix A: Reaction term

We adopted a reaction term that has been proposed as a conceptual model for cell polarization [41, 42]. The reaction kinetics are based on autocatalytic recruitment of membrane proteins and linear detachment:

$$f(m,c) = \left[k_{\mathrm{on}} + k_{\mathrm{fb}}\,\frac{m^2}{K_{\mathrm{d}}^2 + m^2}\right] c - k_{\mathrm{off}}\, m\,. \tag{A1}$$

For the specific parameters that we chose here (see Appendix D), we obtain an N-shaped nullcline, as qualitatively shown in Fig. 1b. Hence, for our choice of parameters, the reaction–diffusion model always produces mesa patterns (lower and upper plateau in the density profile which are connected by an interface, see Fig. 1a), because the flux-balance subspace intersects the reactive nullcline at three points [42, 67, 69] (see Fig. 1a,b).

The space- and time-dependent reaction term $\tilde{f}(x,t)$ for the rescaled densities $\widetilde{m}$ and $\tilde{c}$ then follows from Eq. (32) and takes the form:

$$\tilde{f}(x,t) = \left[k_{\mathrm{on}} + k_{\mathrm{fb}}\,\frac{\widetilde{m}^2}{K_{\mathrm{d}}^2\, g + \widetilde{m}^2}\right] \tilde{c} - k_{\mathrm{off}}\,\widetilde{m}\,. \tag{A2}$$

Appendix B: Time-evolution of the curvature

Instead of tracking the temporal change of the position vector, one may also study how the curvature at each point along the manifold evolves with time. Since the curvature characterizes the (local) conformation of the one-dimensional manifold, one could also reconstruct the position vector from the solution of the curvature alone (up to translation and rotation) [6]. Here, we present the derivation of the evolution equation for the curvature in the material frame $\mathcal{D}_t\kappa(\sigma_{\mathrm{L}},t)$.

To this end, we first determine the commutator of time and arc length derivatives along the manifold:

$$\begin{aligned}\mathcal{D}_t\partial_s &= \mathcal{D}_t\left[\frac{1}{\sqrt{g(\sigma_{\mathrm{L}},t)}}\partial_{\sigma_{\mathrm{L}}}\right]\\ &= \partial_s\mathcal{D}_t + v_n\kappa\,\partial_s,\end{aligned} \tag{B1}$$

where, after applying the chain rule, we used Eq. (20) to obtain the result above. To proceed, we now use Eq. (B1) to determine the temporal evolution of the unit tangent vector:

$$\begin{aligned}\mathcal{D}_t\hat{\boldsymbol{\tau}} &= \mathcal{D}_t\partial_s\boldsymbol{r} = \partial_s\mathcal{D}_t\boldsymbol{r} + v_n\kappa\,\partial_s\boldsymbol{r}\\ &= \partial_s[v_n\hat{\boldsymbol{n}}] + v_n\kappa\,\hat{\boldsymbol{\tau}}\\ &= \partial_s v_n\hat{\boldsymbol{n}},\end{aligned} \tag{B2}$$

where we used the definition $\mathcal{D}_t\boldsymbol{r}(\sigma_{\mathrm{L}},t) = v_n\hat{\boldsymbol{n}}$ and the fact that $\partial_s\hat{\boldsymbol{n}} = -\kappa\hat{\boldsymbol{\tau}}$. Finally, by using Eqs. (B1) and (B2) we compute the following expression:

$$\begin{aligned}\partial_s\mathcal{D}_t\hat{\boldsymbol{\tau}} &= \partial_s^2 v_n\hat{\boldsymbol{n}} + \partial_s v_n\partial_s\hat{\boldsymbol{n}}\\ &= \mathcal{D}_t\partial_s\hat{\boldsymbol{\tau}} - v_n\kappa\,\partial_s\hat{\boldsymbol{\tau}}\\ &= (\mathcal{D}_t\kappa - v_n\kappa^2)\hat{\boldsymbol{n}} + \kappa\,\mathcal{D}_t\hat{\boldsymbol{n}},\end{aligned} \tag{B3}$$

here, we used Eq. (9) to obtain the third line. Comparing the first and last lines in the equation above, one finds that

$$\mathcal{D}_t\kappa(\sigma_{\mathrm{L}},t) = \partial_s^2 v_n + \kappa^2\, v_n. \tag{B4}$$

Appendix C: Non-dimensionalized equations

After non-dimensionalization, we arrive at the following set of partial differential equations:

$$\partial_t \tilde{n}(x,t) = \partial_x \left[\frac{\partial_x h}{g}\, v_y\, \tilde{n} + \frac{D}{\sqrt{g}}\, \partial_x \left(\frac{\tilde{n}}{\sqrt{g}} \right) + \frac{1-D}{\sqrt{g}} \partial_x \left(\frac{\tilde{c}}{\sqrt{g}} \right) \right], \tag{C1a}$$

$$\partial_t \tilde{c}(x,t) = \partial_x \left[\frac{\partial_x h}{g}\, v_y\, \tilde{c} + \frac{1}{\sqrt{g}}\, \partial_x \left(\frac{\tilde{c}}{\sqrt{g}} \right) \right] - \left[k_{\mathrm{on}} + k_{\mathrm{fb}}\, \frac{(\tilde{n}-\tilde{c})^2}{K_{\mathrm{d}}^2\, g + (\tilde{n}-\tilde{c})^2} \right] \tilde{c} + k_{\mathrm{off}}\, (\tilde{n}-\tilde{c}), \tag{C1b}$$

$$\partial_t h(x,t) = v_y, \quad \text{where} \quad v_y = \tilde{\mu}\, \tilde{n} + \tilde{\gamma}\, \frac{1}{g}\, \partial_x^2 h. \tag{C1c}$$

Note that we solve here for the variables $\tilde{n}$ and $\tilde{c}$, instead of $\widetilde{m}$ and $\tilde{c}$ (which are related via local mass conservation $\tilde{n} = \widetilde{m} + \tilde{c}$, cf. Eq. (27)). We solved these equations numerically with FENICs, which allowed us to perform the parameter sweeps with greater efficiency. Furthermore, using two different softwares for solving the partial differential equations allowed us to further validate the accuracy and reliablity of our numerical results.

Appendix D: Parameters

For convenience, we have omitted physical units throughout the manuscript. Here, we provide the values of the model parameters, and give an estimate of the typical length and time scales of protein patterns in biological systems. The typical system size in an intracellular context is $L_0 \approx 10\,\mu\mathrm{m}$. The typical value for membrane diffusion is $D_m \sim 0.01\,\mu\mathrm{m}^2\,\mathrm{s}^{-1}$, while in the cytosol $D_c \sim 0.1 - 10\,\mu\mathrm{m}^2\,\mathrm{s}^{-1}$. The characteristic time scale of pattern formation is determined by the kinetic parameters as well as mass redistribution in the cytosol and on the membrane (via diffusion and possibly advection), and is typically on the order of minutes in an intracellular context [27]. In this work, length scales are given in units of $1\,\mu\mathrm{m}$, and time scales in units of $k_{\mathrm{off}} = 1.0\,\mathrm{s}^{-1}$ (see Table I).

TABLE I. Model parameters. If not otherwise specified, the parameter set below were used in this study.

Parameter	Symbol	Value
Cytosolic diffusion	D_c	$0.1\,\mu\mathrm{m}^2\,\mathrm{s}^{-1}$
Membrane diffusion	D_m	$0.01\,\mu\mathrm{m}^2\,\mathrm{s}^{-1}$
Average total density	$\langle n \rangle$	$2.4\,\mu\mathrm{m}^{-1}$
Attachment rate	k_{on}	$0.07\,\mathrm{s}^{-1}$
Detachment rate	k_{off}	$1.0\,\mathrm{s}^{-1}$
Recruitment rate	k_{fb}	$1.0\,\mathrm{s}^{-1}$
Carrying capacity	K_d	$1.0\,\mu\mathrm{m}^{-1}$
Coupling strength	μ	$0.05\,\mu\mathrm{m}^2\,\mathrm{s}^{-1}$
Line tension	γ	$0.001\,\mu\mathrm{m}^2\,\mathrm{s}^{-1}$

Appendix E: Linear stability analysis for a one-component system in the absence of chemical reactions

To gain further insight into how geometry deformations affect the relaxation of a single membrane-bound particle species to a homogeneous state via diffusion, we consider the following simplified model:

$$\mathcal{D}_t \varrho(\sigma_{\mathrm{L}},t) = \frac{1}{\sqrt{g}} \frac{\partial}{\partial \sigma_{\mathrm{L}}} \left[\frac{D}{\sqrt{g}} \frac{\partial \varrho}{\partial \sigma_{\mathrm{L}}} \right] + \kappa\, v_n\, \varrho, \tag{E1a}$$

$$\mathcal{D}_t \kappa(\sigma_{\mathrm{L}},t) = \kappa^2\, v_n + \frac{1}{\sqrt{g}} \frac{\partial}{\partial \sigma_{\mathrm{L}}} \left[\frac{1}{\sqrt{g}} \frac{\partial v_n}{\partial \sigma_{\mathrm{L}}} \right], \text{and} \tag{E1b}$$

$$\mathcal{D}_t g(\sigma_{\mathrm{L}},t) = -2\, g\, \kappa\, v_n, \quad \text{where} \quad v_n = \mu \varrho. \tag{E1c}$$

We perform a linear stability analysis around a homogeneous steady state, $\varrho = \varrho^* + \delta\varrho$, with a flat configuration of the interface, $\kappa = \delta\kappa$ and $g = g^* + \delta g$. Then, up to linear order, Eqs. (E1) further simplify to:

$$\mathcal{D}_t[\delta\varrho(\sigma_{\mathrm{L}},t)] = \frac{D}{g^*} \partial^2_{\sigma_{\mathrm{L}}}[\delta\varrho] + \mu\, \varrho^{*2}\, [\delta\kappa], \tag{E2a}$$

$$\mathcal{D}_t[\delta\kappa(\sigma_{\mathrm{L}},t)] = \frac{\mu}{g^*} \partial^2_{\sigma_{\mathrm{L}}}[\delta\varrho]. \tag{E2b}$$

Note that we have here omitted the dynamics of the metric g, since it decouples from the set of equations (E2) to linear order and is therefore not relevant. Taking the Fourier transform of the perturbations,

$$\delta\varrho(\sigma_{\mathrm{L}},t) = \frac{1}{2\pi} \int dq\, \delta\hat{\varrho}(q,t)\, \exp(i\, q\, \sigma_{\mathrm{L}}), \tag{E3a}$$

$$\delta\kappa(\sigma_{\mathrm{L}},t) = \frac{1}{2\pi} \int dq\, \delta\hat{\kappa}(q,t)\, \exp(i\, q\, \sigma_{\mathrm{L}}) \tag{E3b}$$

we thus arrive at:

$$\mathcal{D}_t \begin{bmatrix} \delta\hat{\varrho}(q,t) \\ \delta\hat{\kappa}(q,t) \end{bmatrix} = \begin{bmatrix} -Dq^2/g^* & \mu\varrho^{*2} \\ -\mu q^2/g^* & 0 \end{bmatrix} \cdot \begin{bmatrix} \delta\hat{\varrho}(q,t) \\ \delta\hat{\kappa}(q,t) \end{bmatrix} \coloneqq \boldsymbol{J} \cdot \begin{bmatrix} \delta\hat{\varrho}(q,t) \\ \delta\hat{\kappa}(q,t) \end{bmatrix}, \tag{E4}$$

where we have lastly defined the Jacobian $\boldsymbol{J}$ of the linearized system. Note that the trace of the Jacobian is always negative, $\mathrm{tr}\,\boldsymbol{J} = -Dq^2/g^* < 0$ while its determinant is always positive, $\det \boldsymbol{J} = \mu^2 q^2 \varrho^{*2}/g^* > 0$. Thus, the system is always stable. We find that all slow modes

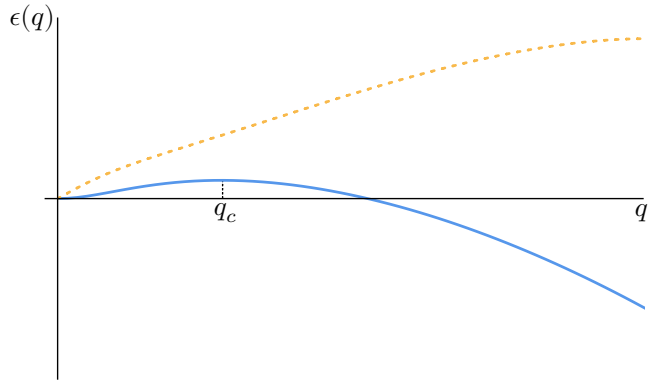

FIG. 16. Typical dispersion relation for the two-component model on a dynamic one-dimensional manifold. The blue solid line shows the real part of the growth rate $\epsilon(q)$, and the orange dashed line shows the imaginary part. The fact that the imaginary part is non-zero indicates local oscillations that lead to traveling wave patterns.

below a cricitcal wave number,

$$\frac{q^2}{g^*} < \frac{q_c^2}{g^*} := \left(2\frac{\mu\,\varrho^*}{D}\right)^2, \tag{E5}$$

are stable spirals, while all fast modes are stable nodes.

Appendix F: Linear stability analysis for the two-component system with mechanochemical coupling

We can now extend the analysis in Appendix E to the two-component system, where the Jacobian in this case is given by:

$$\boldsymbol{J} = \begin{bmatrix} -D_m q^2/g^* + \partial_m f & \partial_c f & \mu\, m^*(m^*+c^*) \\ -\partial_m f & -D_c q^2/g^* - \partial_c f & \mu\, c^*(m^*+c^*) \\ -\mu q^2/g^* & -\mu q^2/g^* & 0 \end{bmatrix}, \tag{F1}$$

with $\partial_{m/c} f := \partial_{m/c} f\big|_{[m^*,c^*]}$. From (F1) we determined the dispersion relation $\epsilon(q)$ which relates the growth rate of perturbations to the mode number q (Fig. 16). While the growth rate of the two-component model on a static planar geometry contains only a real part in the unstable regime [42], we find here that both the real and imaginary part of the growth rate can become positive. Hence, this suggests that the system exhibits traveling wave patterns, since a non-zero imaginary part indicates local oscillations, as confirmed by our simulations. From (F1) we further numerically determined the fastest growing mode q_c (which corresponds to the eigenvalue with the largest real part, see Fig. 16), from which we obtained an estimate for the initial pattern wavelength in our simulations $\lambda_c \approx 4\,\mu\text{m}$ (using the parameters provided in Table I).

[1] T. D. Pollard and G. G. Borisy, Cellular motility driven by assembly and disassembly of actin filaments, Cell **112**, 453 (2003), doi: 10.1016/S0092-8674(03)00120-X.

[2] T. D. Pollard and J. A. Cooper, Actin, a central player in cell shape and movement, Science **326**, 1208 (2009).

[3] M. D. Welch and R. D. Mullins, Cellular control of actin nucleation, Annual Review of Cell and Developmental Biology **18**, 247 (2002), doi: 10.1146/annurev.cellbio.18.040202.112133.

[4] Y.-L. Shih and L. Rothfield, The bacterial cytoskeleton, Microbiology and Molecular Biology Reviews **70**, 729 (2006).

[5] P. Chugh and E. K. Paluch, The actin cortex at a glance, Journal of Cell Science **131**, jcs186254 (2018).

[6] B. Rogez, L. Würthner, A. B. Petrova, F. B. Zierhut, D. Saczko-Brack, M.-A. Huergo, C. Batters, E. Frey, and C. Veigel, Reconstitution reveals how myosin-vi self-organises to generate a dynamic mechanism of membrane sculpting, Nature Communications **10**, 3305 (2019).

[7] J. Zimmerberg and M. M. Kozlov, How proteins produce cellular membrane curvature, Nature Reviews Molecular Cell Biology **7**, 9 (2006).

[8] W. A. Prinz and J. E. Hinshaw, Membrane-bending proteins, Critical Reviews in Biochemistry and Molecular Biology **44**, 278 (2009).

[9] M. Simunovic, G. A. Voth, A. Callan-Jones, and P. Bassereau, When physics takes over: Bar proteins and membrane curvature, Trends in Cell Biology **25**, 780 (2015).

[10] H. T. McMahon and E. Boucrot, Membrane curvature at a glance, Journal of Cell Science **128**, 1065 (2015).

[11] N. S. Gov, Guided by curvature: shaping cells by coupling curved membrane proteins and cytoskeletal forces, Philosophical Transactions of the Royal Society B: Biological Sciences **373**, 20170115 (2018).

[12] C. D. Lawson and A. J. Ridley, Rho gtpase signaling complexes in cell migration and invasion, Journal of Cell Biology **217**, 447 (2018).

[13] A. M. Turing, The chemical basis of morphogenesis, Philosophical Transactions of the Royal Society of Lon-

don. Series B, Biological Sciences **237**, 37 (1952).
[14] C. A. Klausmeier, Regular and irregular patterns in semiarid vegetation, Science **284**, 1826 (1999).
[15] J. B. A. Green and J. Sharpe, Positional information and reaction-diffusion: two big ideas in developmental biology combine, Development **142**, 1203 (2015).
[16] J. Halatek, F. Brauns, and E. Frey, Self-organization principles of intracellular pattern formation, Philosophical Transactions of the Royal Society B: Biological Sciences **373**, 10.1098/rstb.2017.0107 (2018).
[17] N. W. Goehring, P. K. Trong, J. S. Bois, D. Chowdhury, E. M. Nicola, A. A. Hyman, and S. W. Grill, Polarization of par proteins by advective triggering of a pattern-forming system, Science **334**, 1137 (2011).
[18] P. Gross, K. V. Kumar, N. W. Goehring, J. S. Bois, C. Hoege, F. Jülicher, and S. W. Grill, Guiding self-organized pattern formation in cell polarity establishment, Nature Physics **15**, 293 (2018).
[19] T. Litschel, B. Ramm, R. Maas, M. Heymann, and P. Schwille, Beating vesicles: Encapsulated protein oscillations cause dynamic membrane deformations, Angewandte Chemie International Edition **57**, 16286 (2018).
[20] S. Christ, T. Litschel, P. Schwille, and R. Lipowsky, Active shape oscillations of giant vesicles with cyclic closure and opening of membrane necks, Soft Matter **17**, 319 (2021).
[21] M. Fu, H. G. Franquelim, S. Kretschmer, and P. Schwille, Non-equilibrium large-scale membrane transformations driven by minde biochemical reaction cycles, Angewandte Chemie International Edition **60**, 6496 (2021).
[22] D. Thalmeier, J. Halatek, and E. Frey, Geometry-induced protein pattern formation, Proceedings of the National Academy of Sciences **113**, 548 (2016).
[23] R. Geßele, J. Halatek, L. Würthner, and E. Frey, Geometric cues stabilise long-axis polarisation of par protein patterns in c. elegans, Nature Communications **11**, 10.1038/s41467-020-14317-w (2020).
[24] H. Feddersen, L. Würthner, E. Frey, and M. Bramkamp, Dynamics of the bacillus subtilis min system, mBio **12**, e00296 (2021).
[25] M. C. Wigbers, T. H. Tan, F. Brauns, J. Liu, S. Z. Swartz, E. Frey, and N. Fakhri, A hierarchy of protein patterns robustly decodes cell shape information, Nature Physics , 1 (2021).
[26] L. Würthner, F. Brauns, G. Pawlik, J. Halatek, J. Kerssemakers, C. Dekker, and E. Frey, Bridging scales in a multiscale pattern-forming system, arXiv:2111.12043v2 (2021).
[27] T. Burkart, M. C. Wigbers, L. Würthner, and E. Frey, Control of protein-based pattern formation via guiding cues, bioRxiv:2022.02.11.480095 10.1101/2022.02.11.480095 (2022).
[28] N. W. Goehring and S. W. Grill, Cell polarity: mechanochemical patterning, Trends in Cell Biology **23**, 72 (2013).
[29] E. Hannezo and C.-P. Heisenberg, Mechanochemical feedback loops in development and disease, Cell **178**, 12 (2019).
[30] A. Goychuk and E. Frey, Protein recruitment through indirect mechanochemical interactions, Physical Review Letters **123**, 178101 (2019).
[31] A.-L. Le Roux, C. Tozzi, N. Walani, X. Quiroga, D. Zalvidea, X. Trepat, M. Staykova, M. Arroyo, and P. Roca-Cusachs, Dynamic mechanochemical feedback between curved membranes and bar protein self-organization, Nature Communications **12**, 6550 (2021).
[32] P. W. Miller, N. Stoop, and J. Dunkel, Geometry of wave propagation on active deformable surfaces, Physical Review Letters **120**, 268001 (2018), pRL.
[33] N. Tamemoto and H. Noguchi, Pattern formation in reaction–diffusion system on membrane with mechanochemical feedback, Scientific Reports **10**, 19582 (2020).
[34] H. Alimohamadi and P. Rangamani, Modeling membrane curvature generation due to membrane–protein interactions, Biomolecules **8**, 10.3390/biom8040120 (2018).
[35] F. Frey and T. Idema, More than just a barrier: using physical models to couple membrane shape to cell function, Soft Matter **17**, 3533 (2021).
[36] C. Tozzi, N. Walani, and M. Arroyo, Out-of-equilibrium mechanochemistry and self-organization of fluid membranes interacting with curved proteins, New Journal of Physics **21**, 093004 (2019).
[37] F. Yuan, H. Alimohamadi, B. Bakka, A. N. Trementozzi, K. J. Day, N. L. Fawzi, P. Rangamani, and J. C. Stachowiak, Membrane bending by protein phase separation, Proceedings of the National Academy of Sciences of the United States of America **118**, e2017435118 (2021).
[38] M. Fošnarič, S. Penič, A. Iglič, V. Kralj-Iglič, M. Drab, and N. S. Gov, Theoretical study of vesicle shapes driven by coupling curved proteins and active cytoskeletal forces, Soft Matter **15**, 5319 (2019).
[39] A. Mietke, F. Jülicher, and I. F. Sbalzarini, Self-organized shape dynamics of active surfaces, Proceedings of the National Academy of Sciences **116**, 29 (2019).
[40] M. Mercker, F. Brinkmann, A. Marciniak-Czochra, and T. Richter, Beyond turing: mechanochemical pattern formation in biological tissues, Biology Direct **11**, 10.1186/s13062-016-0124-7 (2016).
[41] Y. Mori, A. Jilkine, and L. Edelstein-Keshet, Asymptotic and bifurcation analysis of wave-pinning in a reaction-diffusion model for cell polarization, SIAM Journal on Applied Mathematics **71**, 1401 (2011).
[42] F. Brauns, J. Halatek, and E. Frey, Phase-space geometry of mass-conserving reaction-diffusion dynamics, Physical Review X **10**, 10.1103/PhysRevX.10.041036 (2020).
[43] A. B. Goryachev and M. Leda, Many roads to symmetry breaking: molecular mechanisms and theoretical models of yeast cell polarity, Molecular Biology of the Cell **28**, 370 (2017), doi: 10.1091/mbc.e16-10-0739.
[44] B. Klünder, T. Freisinger, R. Wedlich-Söldner, and E. Frey, Gdi-mediated cell polarization in yeast provides precise spatial and temporal control of cdc42 signaling, PLOS Computational Biology **9**, e1003396 (2013).
[45] J. Halatek and E. Frey, Rethinking pattern formation in reaction–diffusion systems, Nature Physics **14**, 507 (2018).
[46] E. Frey and F. Brauns, Self-organisation of protein patterns (2020).
[47] N. S. Gov and A. Gopinathan, Dynamics of membranes driven by actin polymerization, Biophysical Journal **90**, 454 (2006).
[48] M. Deserno, Fluid lipid membranes: From differential geometry to curvature stresses, Chemistry and Physics of Lipids **185**, 11 (2015).
[49] P. Grinfeld, Exact nonlinear equations for fluid films and proper adaptations of conservation theorems from classical hydrodynamics (2009).
[50] P. Grinfeld, A better calculus of moving surfaces (2012).

[51] O. Hallatschek, E. Frey, and K. Kroy, Propagation and relaxation of tension in stiff polymers, Physical Review Letters **94**, 077804 (2005), pRL.

[52] O. Hallatschek, E. Frey, and K. Kroy, Tension dynamics in semiflexible polymers. i. coarse-grained equations of motion, Physical Review E **75**, 031905 (2007), pRE.

[53] O. Hallatschek, E. Frey, and K. Kroy, Tension dynamics in semiflexible polymers. ii. scaling solutions and applications, Physical Review E **75**, 031906 (2007), pRE.

[54] B. Obermayer and O. Hallatschek, Coupling of transverse and longitudinal response in stiff polymers, Physical Review Letters **99**, 098302 (2007), pRL.

[55] B. Obermayer, O. Hallatschek, E. Frey, and K. Kroy, Stretching dynamics of semiflexible polymers, The European Physical Journal E **23**, 375 (2007).

[56] M. C. Cross and P. C. Hohenberg, Pattern formation outside of equilibrium, Reviews of Modern Physics **65**, 851 (1993).

[57] A. Mahapatra, D. Saintillan, and P. Rangamani, Curvature-driven feedback on aggregation–diffusion of proteins in lipid bilayers, Soft Matter **17**, 8373 (2021).

[58] R. Shlomovitz and N. S. Gov, Membrane waves driven by actin and myosin, Physical Review Letters **98**, 168103 (2007), pRL.

[59] A. Mietke, V. Jemseena, K. V. Kumar, I. F. Sbalzarini, and F. Jülicher, Minimal model of cellular symmetry breaking, Physical Review Letters **123**, 10.1103/PhysRevLett.123.188101 (2019).

[60] U. Seifert, Configurations of fluid membranes and vesicles, Advances in Physics **46**, 13 (1997).

[61] C. T. Lee, M. Akamatsu, and P. Rangamani, Value of models for membrane budding, Current Opinion in Cell Biology **71**, 38 (2021).

[62] R. Lipowsky, Remodeling of membrane shape and topology by curvature elasticity and membrane tension, Advanced Biology **6**, 2101020 (2022).

[63] A. Mogilner, Mathematics of cell motility: have we got its number?, Journal of Mathematical Biology **58**, 105 (2009).

[64] A. P. Arkin, M. Otsuji, S. Ishihara, C. Co, K. Kaibuchi, A. Mochizuki, and S. Kuroda, A mass conserved reaction–diffusion system captures properties of cell polarity, PLoS Computational Biology **3**, 10.1371/journal.pcbi.0030108 (2007).

[65] S. Ishihara, M. Otsuji, and A. Mochizuki, Transient and steady state of mass-conserved reaction-diffusion systems, Physical Review E **75**, 10.1103/PhysRevE.75.015203 (2007).

[66] Q. Nie, J.-G. Chiou, S. A. Ramirez, T. C. Elston, T. P. Witelski, D. G. Schaeffer, and D. J. Lew, Principles that govern competition or co-existence in rho-gtpase driven polarization, PLOS Computational Biology **14**, 10.1371/journal.pcbi.1006095 (2018).

[67] F. Brauns, H. Weyer, J. Halatek, J. Yoon, and E. Frey, Wavelength selection by interrupted coarsening in reaction-diffusion systems, Physical Review Letters **126**, 10.1103/PhysRevLett.126.104101 (2021).

[68] S. Subramanian and S. M. Murray, Pattern selection in reaction diffusion systems, Physical Review E **103**, 10.1103/PhysRevE.103.012215 (2021).

[69] H. Weyer, F. Brauns, and E. Frey, Coarsening and wavelength selection far from equilibrium: a unifying framework based on singular perturbation theory, arXiv:2203.03892 [nlin, physics:physics] 10.48550/arxiv.2203.03892 (2022).

[70] P. K. Maini, T. E. Woolley, R. E. Baker, E. A. Gaffney, and S. S. Lee, Turing's model for biological pattern formation and the robustness problem, Interface Focus **2**, 487 (2012).

[71] A. L. Krause, E. A. Gaffney, P. K. Maini, and V. Klika, Modern perspectives on near-equilibrium analysis of turing systems, Philosophical Transactions of the Royal Society A: Mathematical, Physical and Engineering Sciences **379**, 20200268 (2021).

[72] F. Brauns, G. Pawlik, J. Halatek, J. Kerssemakers, E. Frey, and C. Dekker, Bulk-surface coupling identifies the mechanistic connection between min-protein patterns in vivo and in vitro, Nature Communications **12**, 3312 (2021).

[73] B. Ramm, T. Heermann, and P. Schwille, The e. coli mincde system in the regulation of protein patterns and gradients, Cellular and Molecular Life Sciences **76**, 4245 (2019).

III Geometry-sensing and biochemical templates

1 Polarity axis selection in *C. elegans*

In this section, we discuss how PAR polarity patterns, based on a reaction-diffusion mechanism, are controlled by geometry. The following content is based on and uses parts of our paper [30] published in *Nature communications*. We provide a reprint of the paper in chapter 1.6.

1.1 Background

One of the most fundamental patterns by which cells spatially segregate (hierarchical) processes critical to their development is *cell polarity* [110]. Representative examples where cell polarity plays a decisive role includes regulation of cell division in budding and fission yeast, driven by the GTPase Cdc42 [111–113], and the selection of the anterior-posterior axis of the *Caenorhabditis elegans* zygote (*C. elegans*), which is controlled by a polarization pattern of *partitioning defective* proteins (PAR proteins) [18, 114–116]. The polarity pattern in *C. elegans* is established by anterior PARs (aPARs) and posterior PARs (pPARs), which both diffusive in the cytosol and bind to the cell membrane. At the membrane, aPAR and pPAR proteins form two separate domains (polarity pattern) which defines the anterior-posterior axis of the embryo. The establishment of these domains has been shown to be driven by antagonistic interactions between PAR proteins as well as by interactions of PAR proteins with the cell cortex [25, 117–121]. The mutual antagonistic interactions at the membrane cause both aPARs and pPARs to dissociate into the cytosol through phosphorylation [20, 29].

Open questions here are how the robust establishment of PAR polarity patterns depends, if at all, on mechanical interactions of PAR proteins with the actomyosin cortex, or whether biochemical interactions between PAR proteins alone (reaction-diffusion dynamics) are sufficient to explain robust polarization. The contractility of the actomyosin network has been shown to be dependent on PAR proteins [25], and it has been argued that the resulting cortical flows are required to guide the establishment of long-axis polarization [120], while biochemical interactions play a rather stabilizing role by maintaining PAR polarity after establishment [25]. However, several experimental studies have shown that PAR polarity does not

require advective flows [122–128]. Indeed, previous studies have demonstrated that PAR polarity can be in principle explained by a reaction-diffusion mechanism alone [25, 116, 120, 128, 129]. The question that then remains is whether a reaction-diffusion mechanism is sufficient for robust and correct selection of the long-axis of the embryo, or whether advective flows are required to push the reaction-diffusion dynamics towards the desired attractor. Previous studies for simplified one-dimensional geometries concluded that advective flows are necessary for reliable long-axis selection, as well as maintaining polarity [25, 116, 120]. However, these simplified models disregarded the impact of cell shape on the reaction-diffusion dynamics, and therefore erased geometric effects that might be relevant for axis selection and robust establishment of cell polarity [29, 30].

To shed light on the role of cell shape and geometry-sensing, we study a reaction-diffusion model for PAR polarity in realistic three-dimensional cell geometries. In contrast to previous studies [25, 116, 120], the model accounts for bulk-boundary coupling between cytosolic proteins and membrane-bound proteins, as well as delayed reattachment of cytosolic proteins due to dephosphorylation (reactivation of cytosolic proteins). This activation-deactivation cycle of cytosolic proteins is an important feature of the model, as it leads to cytosolic gradients perpendicular to the membrane which renders the dynamics sensitive to cell shape [30, 130, 131]. To disentangle different geometric effects, we first study PAR polarity in a two-dimensional elliptical geometry, and show that the reactivation-deactivation cycle is crucial for robust long-axis selection. Similar as in Ref. [130], we relate this effect to the (local) ratio of cytosolic volume to membrane surface (bulk-surface ratio), which is intrinsically non-uniform in curved geometries. We then show that polarity establishment in three-dimensional ellipsoidal geometries can be explained by the same effect. However, we also identify an additional effect in three-dimensional geometries. We find that long-axis polarization in ellipsoidal geometries is even more favoured, and we explain this by the tendency of the system to minimize the interface of the aPAR-pPAR pattern on the surface of the ellipsoid. Overall, our results suggest that a reaction-diffusion mechanism in realistic cell geometries is sufficient to explain robust PAR polarity in *C. elegans*.

1.2 PAR polarity in ellipsoidal geometry

The reaction kinetics in our model is derived from the current biological understanding of the PAR reaction network [114, 117, 132–136]. The dynamics of aPAR proteins is effectively accounted for by two protein species A_1 and A_2, where the former can be interpreted as a (membrane-binding) scaffold protein, which recruits cytosolic A_2 to the membrane. These processes effectively describe the formation of aPAR hetero-dimers A_{12} on the membrane, which then interact with and phosphorylate membrane-bound pPARs. Similarly, we effectively describe pPAR

proteins by a single protein species P which dephosphorylates both membrane-bound aPAR proteins A_1 and A_{12}. Mathematically, the set of equations take the form of bulk-boundary coupled mass-conserving reaction-diffusion systems, where phosphorylated proteins can only rebind the membrane after dephosphorylation with a rate λ (for details on the mathematical model please refer to the reprint in section 1.6). We consider the reaction-diffusion dynamics in a prolate spheroid, where the boundary of the spheroid represents the cell membrane and the enclosing volume the cytosol, respectively.

1.3 Geometric effect: The membrane to bulk ratio

The activation-deactivation cycle (in combination with bulk-boundary coupling) leads to cytosolic protein gradients with a characteristic (reactivation) length scale ℓ that is dictated by cytosolic diffusion D_{cyt} and the dephosphorylation rate λ [30, 130, 131]:

$$\ell = \sqrt{D_{\text{cyt}}/\lambda}\,. \tag{III.1}$$

These gradients result in interesting geometric effects, which can be best understood by considering the following cases for the reactivation length ℓ: (i) Let us assume that the reactivation rate is chosen such that ℓ is smaller compared to the typical length of the cell L, but larger than the typical radius of curvature R of the cell poles, i.e. $R < \ell < L$. In this case, detached cytosolic proteins travel a small distance before they become reactivated and rebind to the membrane. Importantly, proteins have a higher probability of membrane binding if they are close to the cell poles, where the membrane surface to cytosolic volume ratio is largest [130]. Hence, this naturally leads to protein accumulation at the cell poles, as attachment rates are effectively amplified by membrane curvature (the "hitting probability" is higher in curved regions). This effect is quite general for bulk-surface coupled mass-conserving reaction-diffusion systems, and entails important consequences: In curved geometries, the base state of the system will be always non-uniform. However, the final pattern for large times cannot be concluded from the base state and depends explicitly on the reaction kinetics considered. For the PAR system, one finds that aPARs initially accumulate at the cell poles (due to cooperative binding), which leads to the formation of an interface between aPARs and pPARs near the poles. Due to mutual antagonism, pPAR proteins are forced to bind near midcell, which ultimately leads to the formation of short-axis polarization for large times. (ii) For the biologically relevant case, however, where the reactivation length is comparable with the cell size $\ell \simeq L$, aPARs will preferentially bind the membrane near midcell, as they diffuse larger distances after phosphorylation. Consequently, one finds that the system selects the long-axis is in this case. (iii) In the limit where $\ell \ll L$ or $\ell \gg L$, the geometric effect outlined above is lost since cytosolic densities

approach a homogeneous concentration profile. Thus, the limit where $\ell \ll L$ or $\ell \gg L$ correspond to simplified one-dimensional models, where the geometric effect is wiped out. The heuristic arguments above can be quantitatively confirmed by a linear stability analysis (LSA), which we have performed for an ellipse, as the orthogonal eigenfunctions (Mathieu functions [137]) of the diffusion operator can be determined in elliptical coordinates [77]. From the LSA, one can determine the growth rates of the first even mode and the first odd mode, corresponding to long-axis and short-axis polarization, respectively. Consistent with the arguments above, the analysis reveals that long-axis polarization is favoured above a sufficient large value of the reactivation length ℓ^*, while the short-axis is selected below this threshold value.

1.4 Pattern interface minimization

The results that we obtained for a two-dimensional ellipse can be in principle transferred to prolate spheroids, where the same geometric effect determines axis-selection at onset. However, we identified another crucial physical effect that is related to the interface length of aPAR-pPAR domains. For parameters where one obtains short-axis polarization at early times, we observe that the pattern rotates to long-axis polarization for long times. In other words, long-axis polarization is even more favoured in realistic three-dimensional geometries. By quantifying the average net cytosolic protein flux towards the membrane, we found that the system tends to minimize this flux, which is achieved by minimizing the total length of the protein interface (which is simply a line for three-dimensional geometries). Indeed, for prolate spheroids the interface length is minimized for long-axis polarization, which explains why the pattern rotates from short-axis to long-axis. Note that this effect is absent in two-dimensional geometries, since the interface consists of just two points in two dimensions.

To quantitatively test and confirm the idea of interface length minimization, we consider PAR polarity in prolate and oblate spheroids that have the same volume, but different ratios of the interface length for long-axis and short axis polarization (perimeter ratio). For oblate spheroids, the perimeter ratio for short- and long-axis polarity remains close to unity and is therefore less sensitive to variations of the semi-major axis, while the perimeter ratio varies strongly with the semi-major axis in the case of prolate spheroids. This suggests that one should be able to stabilize short-axis polarization in oblate spheroids, because the effect resulting from interface minimization should be weaker in oblates based on the above considerations. We confirmed this intuition by extensive FEM parameter sweeps in the $\lambda - D_{\text{cyt}}$ parameter space, and indeed found a broad regime where short-axis polarization can be stabilized (for details please see reprint in section 1.6). Interestingly, the transition from short-axis to long-axis polarization is not sharp,

but varies smoothly from diagonal patterns to long-axis polarization. The idea outlined above does not exclude stable short-axis polarization in prolates, but rather suggests that axis selection should be independent of interface length minimization if the perimeter ratio is close to unity, which is for example the case for almost spherical prolate spheroids. We also performed extensive FEM parameter sweeps for nearly spherical prolate spheroids, and found a similar bifurcation diagram as for oblate spheroids. In conclusion, the perimeter ratio provides a reasonable estimate of which polarity axis dominates in ellipsoidal geometries.

1.5 Key points and outlook

We summarize the key findings of this research project in the following and further discuss additional open questions as well as interesting extensions of our approach for future research.

- We have shown that PAR polarity and axis selection can be explained by a reaction-diffusion mechanism alone. Cytosolic gradients perpendicular to the membrane cause collective "curvature-sensing" of proteins, and we explained this effect by the membrane surface to cytosolic volume ratio, which is largest at negatively curved regions (such as the cell poles). Our results highlight the importance of bulk-boundary coupling and realistic cell geometries, which control and stabilize long-axis polarization.

- Long-axis polarization is additionally favoured for three-dimensional ellipsoidal geometries, as the system tries to minimize the protein interface length. This effect can be physically, on a heuristical level, explained by the minimization of the average net cytosolic protein flux towards the membrane. The perimeter ratio of the geometry provides a reasonable estimate of which axis dominates.

- Notably, our analysis suggests that PAR polarization can be stabilized and controlled independently of mechanical guiding cues and cortical flows. From our perspective, advective flows are not required at all for stable long-axis polarization, and their exact role remains under debate. However, mechanical guiding cues might be relevant for the correct time scale of cell polarity, since advective flows provide additional means of timing pattern formation.

Our analysis in ellipsoidal geometry relied on computationally extensive FEM simulations. For future studies, it would be desirable to develop a theoretical tool that allows to perform a linear stability analysis in realistic three-dimensional geometries. The challenge here is to determine a set of orthogonal eigenfunctions of the Laplace operator that satisfy all boundary conditions. Unfortunately, this

is a complicated task in non-trivial geometries, and generally not possible. One way to overcome this limitation is to apply perturbation theory: One starts with a spherical geometry, for which the eigenfunctions can be determined by standard methods (spherical harmonics), and then considers a smooth small deformation of the sphere to an ellipsoid. The growth rates in ellipsoidal geometry are then given by the growth rate of the sphere plus additional correction terms (to first order), which account for the correction of the operators due to the smooth deformation. Moreover, the approach is not restricted to ellipsoidal geometries, but can be in principle applied to a range of different geometries, including modulated cylindrical geometries [138].

We provided a heuristic explanation for the minimization of interface length, but a rigorous quantitative explanation is still lacking. One interesting observation is that the protein interface somewhat acts as a liquid-gas interface and can therefore be viewed as a line on a curved surface under "surface tension". It is well known that surface tension leads to *mean curvature flow* that tends to minimize the interface length [139]. Hence, to gain understanding of the interface length minimization discovered here, it would be worthwhile to quantitatively investigate the dynamics of the protein interface, and compare it to classical systems that are known to behave similarly, such as pattern interfaces in the Cahn-Hilliard equation [140]. Interestingly, the Cahn-Hilliard equation evolves under the *Willmore flow* [141], and therefore can be interpreted as a volume-preserving version of the mean curvature flow.

1.6 Publication: Geometric cues stabilise long-axis polarisation of PAR protein patterns in *C. elegans*

Geometric cues stabilise long-axis polarisation of PAR protein patterns in *C. elegans*

by

R. Geßele[1], J. Halatek[1], L. Würthner[1], and E. Frey[1]

[1]Arnold Sommerfeld Center for Theoretical Physics (ASC) and Center for NanoScience (CeNS), Department of Physics, Ludwig-Maximilians-Universität München, Theresienstraße 37, D–80333 Munich, Germany

Published in ***Nature Communications*** **11, 539 (2020)**

DOI: 10.1038/s41467-020-14317-w.

also available on BIORXIV: 10.1101/451880 .

BIORXIV version reprinted on pages 129–177,

Supplemental Material reproduced on pages 178–199.

Geometric cues stabilise long-axis polarisation of PAR protein patterns in *C. elegans*

Raphaela Geßele[1], Jacob Halatek[1], Laeschkir Würthner[1] & Erwin Frey[1⋆]

[1]Arnold Sommerfeld Center for Theoretical Physics and Center for NanoScience,

Department of Physics, Ludwig-Maximilians-Universität München,

Theresienstraße 37, 80333 München, Germany.

⋆Correspondence and requests for materials should be addressed to E.F.: frey@lmu.de.

Abstract In the *Caenorhabditis elegans* zygote, PAR protein patterns, driven by mutual anatagonism, determine the anterior-posterior axis and facilitate the redistribution of proteins for the first cell division. Yet, the factors that determine the selection of the polarity axis remain unclear. We present a reaction-diffusion model in realistic cell geometry, based on biomolecular reactions and accounting for the coupling between membrane and cytosolic dynamics. We find that the kinetics of the phosphorylation-dephosphorylation cycle of PARs and the diffusive protein fluxes from the cytosol towards the membrane are crucial for the robust selection of the anterior-posterior axis for polarisation. The local ratio of membrane surface to cytosolic volume is the main geometric cue that initiates pattern formation, while the choice of the long-axis for polarisation is largely determined by the length of the aPAR-pPAR interface, and mediated by processes that minimise the diffusive fluxes of PAR proteins between cytosol and membrane.

Introduction

Cell polarisation is a crucial process in development[1]. Well studied examples include localisation of bud sites in *Saccharomyces cerevisiae*[2], apico-basal asymmetry in mammalian epithelial cells[3], and the asymmetric placement of the first cell division in the *Caenorhabditis elegans* zygote[4]. A key question in such systems is how the correct polarity axis is established and robustly maintained.

In *C. elegans*, the anterior-posterior axis of the embryo is determined in the fertilised egg by a polarised distribution of PAR (partitioning defective) proteins[4–6]. Immediately before the establishment of polarisation begins, the future anterior PARs (aPARs) cover the cell cortex uniformly, while posterior PARs (pPARs) are cytoplasmic[7]. After fertilisation, the sperm-donated centrosome induces contraction of the actomyosin network, which leads to cortical flows that displace cortical aPARs anteriorly, allowing cytoplasmic pPARs to bind in the posterior zone[8–11]; see Fig. 1*A*. Once these two PAR domains have formed (during the 'establishment phase') and have thereby established the anterior-posterior axis, they persist for several minutes through the 'maintenance' phase until cell division[5,7].

Several independent in vivo experiments on *C. elegans* have demonstrated that maintenance of PAR protein polarity is independent of an intact actomyosin network[7,11–15]. Rather, it appears that the entry of the sperm and the following contractions of the cortical actomyosin serve as a temporal trigger for the rapid establishment of the PAR protein pattern[9,13,16]. However, experimental observations also suggest that while the rapid establishment and perfect position of anterior-posterior PAR domains are the result of an interplay between mechanical, hydrodynamical

and biochemical mechanisms, polarisation is nevertheless robustly established (albeit with some delay) when various mechanical and hydrodynamical mechanisms are eliminated.[10,11,17–19]. To disentangle and understand these distinct mechanisms one needs to investigate the mechanism of self-organised polarisation by the biochemical PAR protein network. Based on the fact that aPAR and pPAR proteins mutually drive each other off the membrane by phosphorylation[20], and that this antagonism promotes formation of distinct domains on the membrane[10,21,22], previous studies have outlined how self-organisation of PAR proteins maintain polarisation until cell division[?,15,16]. These studies showed that basic features of PAR protein polarisation can be explained by minimal reaction-diffusion models. However, as these models used a simplified one-dimensional geometry and assumed that cytosolic proteins are homogeneously distributed, the effect of cell geometry was disregarded and the distinction between long and short axis was lost. Thus, how the long axis is selected for polarisation and subsequently maintained, and in a broader context, which features of a reaction-diffusion system are responsible for axis selection remain open questions.

To answer these questions we draw on previous studies of other intracellular pattern-forming protein systems which revealed that even the typically rather fast cytosolic diffusion does not eliminate protein gradients in the cytosol[23–26]. As a consequence, protein patterns are generically sensitive to cell geometry through coupling between processes in the cytosol and on the membrane. In particular, it was predicted[23,24] that delayed reattachment to the cell membrane (e.g., due to cytosolic nucleotide exchange) is key to geometry sensing. Indeed, recent experimental studies support the idea that axis selection depends on the interplay between reaction kinetics and cellular geometry[25].

These results suggest that the protein dynamics in the cytoplasm of the *C. elegans* embryo may also influence the selection of the long over the short axis during polarity maintenance. In order to investigate axis alignment, we developed a reaction-diffusion model of the PAR protein dynamics . As in previous studies[9,15,27], a central element in our model is mutual displacement of membrane-bound aPARs and pPARs by phosphorylation. However, in contrast to earlier models[9,28], we do not use effective nonlinearities but strictly biomolecular reactions based on mass-action law kinetics, e.g. by explicitly modelling the formation of PAR protein complexes. Importantly, we also account for the delay caused by the need for reactivation of detached PAR proteins by cytosolic dephosphorylation, thus introducing the generic feature of a biochemical activation-deactivation cycle.

Our extended reaction-diffusion model in realistic cell geometry reveals that the dynamics of the phosphorylation-dephosphorylation cycle of PAR proteins is crucial for long-axis polarisation. Without this additional feature, the biochemical network of PAR proteins would not lead to robust polarisation along the long axis but instead exhibit a strong tendency to first polarise along the short axis, and polarisation would not re-align within a time that corresponds to a typical time before cell division. Furthermore, the extended model enables us to characterise the roles of mutual antagonism (phosphorylation) and overall protein numbers in robust long-axis polarisation: while the phosphorylation rates determine how distinctively one polarisation axis is selected over the other, relative protein numbers primarily affect the robustness of pattern formation as a whole.

Most importantly, our analysis indicates that these findings can be generalised beyond the

specific model for the PAR system: axis selection is based on the generic dependence of intracellular pattern-forming processes on the local ratio of membrane surface to cytosolic volume and on the cell geometry via the length of the interface between the two different protein domains. Broadly speaking, the membrane-to-bulk ratio determines the likelihood that a given protein will reattach to the membrane quickly after detachment into the cytosol and the interface length affects both the establishment and maintenance of long-axis polarisation.

Results

Model The aPAR set of proteins comprises PAR-3, PAR-6, and the atypical protein kinase PKC-3. Only complexes containing PKC-3 can phosphorylate pPARs, thereby disabling their membrane--binding capacity[21,29]. How trimeric complexes consisting of PAR-3, PAR-6 and PKC-3 actually form is not fully understood. The evidence so far suggests that PAR-6 acts as a linker between PKC-3 and PAR-3, which can itself bind directly to the membrane[30–33]. In the absence of PAR-6, PKC-3 freely diffuses in the cytosol[34,35]. In the reaction network upon which our mathematical model is based, we simplify the formation of trimeric complexes to the formation of a complex consisting of two effective species of aPARs: A_1 and A_2 (Fig. 1*C*). The first species, A_1, models the membrane binding function of PAR-3, thus we also refer to it as a scaffold protein. The second species, A_2, corresponds to a complex of PAR-6 and PKC-3. It is assumed to be recruited by scaffold proteins A_1 that are already bound to the membrane, thereby forming hetero-dimers A_{12} on the membrane . These complexes can then phosphorylate membrane-bound pPARs, which initiates their release into the cytosol in a phosphorylated (inactive) state.

As with aPARs, there are different pPAR species, PAR-1 and PAR-2. While it is known that PAR-2 binds directly to the membrane, and PAR-1 phosphorylates PAR-3, it remains unclear whether PAR-2 also helps to maintain anterior-posterior polarity by excluding aPAR complexes from the membrane[7,20]. However, PAR-2 is required for posterior binding of PAR-1[36] and PAR-2 exclusion from the membrane by PKC-3 is essential for proper restriction of pPARs to the posterior[21]. In view of the remaining uncertainties we refrain from distinguishing between different species and effectively treat the pPARs as a single species P (Fig. 1*C*). P phosphorylates membrane-bound A_1 and A_{12}, which triggers their subsequent detachment as a phosphorylated (inactive) species into the cytosol.

Our model also accounts for protein dephosphorylation reactions in the cytosol. This creates deactivation-reactivation cycles, as proteins that were phosphorylated (deactivated) on the membrane are thereby reactivated for membrane binding (Fig. 1*B*, *C*). For simplicity, the reactivation (dephosphorylation) rate λ is assumed to be identical for cytosolic pPARs (P) and aPARs (only A_1). The ensuing reaction-diffusion equations are given in the Method section Equations (7-18).

We approximate the natural shape of a *C. elegans* embryo by a prolate spheroid with semi-axis lengths $a = 27\mu m$ and $b = 15\mu m$ (see Fig. 1 *D*) [9]. Here, a is the distance from centre to pole through a focus along the symmetry axis, also called the semi-major axis, while b is the equatorial radius of the spheroid, which is called the semi-minor axis. The boundary and interior of the ellipse represent the cell membrane and cytosolic volume, respectively.

Dephosphorylation plays a key role for axis determination For mutually antagonistic protein interactions , protein domains are separated by an interface at which mutually induced membrane detachment dominates[9,15,16]. For its maintenance proteins that have detached from the membrane must be replaced, otherwise the antagonistic interaction between the proteins would deplete either aPARs or pPARs from the membrane. As the protein interactions are mass-conserving, maintenance requires that detached proteins quickly rebind, unless the cytosolic reservoir of proteins is large enough for them to be replenished directly. This suggests that an interface can best be maintained locally in those membrane regions where rebinding to the membrane after detachment is most likely.

The likelihood of rebinding depends on the availability of cytosolic proteins for binding, which depends on the interplay between the local cell geometry and the time required for reactivation of detached proteins by dephosphorylation (Fig. 2). The ratio of available membrane surface to cytosolic volume is highest at cell poles and lowest at mid-cell. How this local cell geometry affects protein rebinding depends on the dephosphorylation time: a longer reactivation time implies that a protein that detached in a phosphorylated state from the membrane will on average diffuse farther away from the membrane before it can be reactivated and reattaches. The corresponding reactivation length is estimated as

$$\ell := \sqrt{D_{\text{cyt}}/\lambda}\,. \tag{1}$$

To see how this diffusion length affects protein dynamics, consider a protein with a short inactive (phosphorylated) phase, such that ℓ is significantly smaller than the cell length $L = 2a$

(Fig. 2*A*). Then, proteins are likely to be dephosphorylated fast and can therefore rebind very soon after phosphorylation-induced detachment. Since the local ratio of membrane surface to cytosolic volume at the cell poles is larger than at mid-cell, these proteins are more likely to reencounter the membrane in the polar zone which translates into higher polar reattachment (after reactivation), i.e. proteins remain caged at the cell poles (Fig. 2*A*). Conversely, proteins that detached from the membrane at mid-cell have more cytosolic volume available than those that detached at the poles and, thus, are less likely to re-encounter the membrane and rebind there (Fig. 2*A*). This heuristic picture suggests that for $\ell \ll L$ domain interfaces preferentially form at the cell poles and hence cell polarity will be established along the short-axis. If dephosphorylation requires more time, ℓ increases and the effect of local membrane curvature is attenuated (Fig. 2*B*). Ultimately, when $\ell > L$, proteins can be considered as uniformly distributed throughout the cytosol for the next attachment event (Fig. 2*D*). Therefore, reactivated proteins are more likely to attach at mid-cell, where the accumulated density along the long-axis (or, equivalently, the ratio of cytosolic volume to membrane area) is highest (Fig. 2*C*). This implies that an interface between different protein domains will establish itself at mid-cell and cells will become polarised along the long-axis for large enough reactivation length ℓ.

In summary, if cell polarisation is induced by antagonistic protein interaction , we expect long-axis polarisation to be favoured only if the delay resulting from the inactive phase is sufficiently long. Moreover, our analysis suggests that relative protein numbers affect axis selection, as the global availability of an abundant protein species attenuates the effect of cell geometry associated with the activation-deactivation cycle.

In the heuristic arguments outlined above, we tacitly considered a single position along the interface between the PAR domains. In general, however, the length of the interface may also play an important role in determining the orientation of the axis ultimately selected, as one expects energetic costs for interface establishment and maintenance to scale with its length. In the following we will analyse the system's dynamics in a two-dimensional as well as in a three-dimensional cell geometry; an analysis of a simplified rectangular geometry would actually be misleading (Supplementary Note 3). Furthermore, the analysis in two and three dimensions enables us to disentangle the effects due to the membrane-to-bulk ratio and interface length in polarisation establishment and maintenance. Note that in a two-dimensional ellipse the interface between the domains reduces to a point, such that all geometric effects can be solely attributed to the membrane-to-bulk ratio.

Growth rates of long versus short-axis polarisation To put the above heuristic reasoning concerning the role of membrane-to-bulk ratio on a firm basis , we first performed a mathematical analysis in two-dimensional elliptical geometry , building on previous investigations of intracellular pattern formation [23,24].

Importantly, in the bounded geometry of a cell, broken detailed balance due to the dephosphorylation-phosphorylation cycle implies that a uniform well-mixed state can no longer be a steady state of the system[24]. Instead, all steady states show cytosolic gradients with a density profile that is spatially non-uniform but unpolarised[24]. As the reactive dynamics in the PAR system is bistable, there are two such unpolarised states, one with aPAR and the other with pPAR being the more abundant membrane species. In the zygote, aPARs predominate on the membrane,

and we refer to this aPAR-dominant state as the unpolarised state.

To perform a linear stability analysis with respect to this unpolarised state, we use Fourier modes specific for elliptical geometry[23]. These modes are classified as even and odd by their symmetry with respect to reflections through a plane along the long axis, and correspond to patterns aligned along the long and short axes, respectively (Fig. 3*A*). If the real parts of the growth rates σ of all modes are negative, small spatial perturbations of the unpolarised state will decay and it will remain stable. In contrast, a positive real part of any growth rate ($\sigma > 0$) indicates that the unpolarised state is unstable , and initially a pattern will emerge corresponding to the mode with the highest growth rate (Fig. 3*B*). Hence, linear stability analysis can identify the parameter regime where patterns of a certain symmetry (short- vs. long-axis) form spontaneously. On very general grounds [26,38], we expect that bifurcations in mass-conserving reaction-diffusion systems are subcritical and hence these pattern attractors persist over some range outside the linear unstable parameter regime (see also details on FEM simulations in the Method section), where patterns do not form spontaneously but can be triggered by a finite perturbation – such as the fertilisation event.

For a typical cell size and cytosolic diffusion constants in the range of $D_{\text{cyt}} = 5 - 50\ \mu m^2 s^{-1}$, linear stability analysis shows that second- and higher-order modes are negligible compared to the first even and odd modes, σ_{e} and σ_{o}. In the parameter regime under consideration, those two growth rates exhibit similar magnitude and at least one of them is positive. To quantify the competition between the first even and odd modes (long- vs. short-axis), we define the relative difference in

their growth rates,

$$\delta\sigma := (\sigma_{\mathrm{e}} - \sigma_{\mathrm{o}})/\sqrt{\sigma_{\mathrm{e}}^2 + \sigma_{\mathrm{o}}^2}\,; \tag{2}$$

for an illustration see Fig. 3*B*.

Cytosolic reactivation length is crucial for axis selection We computed $\delta\sigma$ as a function of λ and D_{cyt}. As shown in Fig. 3*C*, the even mode dominates ($\delta\sigma > 0$) for large cytosolic diffusion constant and low reactivation rates (favouring long-axis polarisation), otherwise the odd mode dominates. This is consistent with the above heuristic reasoning suggesting that reactivation must be slow or cytosolic diffusion must be fast for the establishment of long-axis polarity. While linear stability analysis can elucidate the selection of the polarisation axis during the onset of pattern formation, it can not predict the final pattern as it neglects nonlinear effects in the diffusion-reaction equation. To determine the final stable polarisation axis we performed finite-element (FEM) simulations; see alslo details on FEM simulations in the Method Section. These simulations show that there is a threshold value for the reactivation length $\ell^\star = 11.4\ \mu m$ above/below which cells stably polarise along the long/short-axis (Fig. 3*C*). We conclude that in a two-dimensional cell geometry the reactivation length ℓ, which determines the spatial distribution of active proteins, is the decisive parameter that determines both initial axis selection and its long-term maintenance. How in full three-dimensional cell geometry this effect of the membrane-to-bulk ratio interacts with the role of the interface length will be discussed below.

Role of phosphorylation rates Whether there is a spatial separation between aPAR and pPAR domains, is known to depend on the relative magnitude of the phosphorylation rates k_{Ap} and k_{Pa}[9,16]: an interface between different domains exists and can be maintained only if these antagonistic phosphorylation processes are balanced. To determine the necessary conditions for this balance, we analysed the stability of the unpolarised state using linear stability analysis varying both phosphorylation rates over one order of magnitude. We fixed $D_{\mathrm{cyt}} = 30\,\mu m^2 s^{-1}$ and chose two representative reactivation rates, $\lambda = 0.3\,s^{-1}$ and $\lambda = 0.05\,s^{-1}$, corresponding to reactivation lengths, $\ell = 10\,\mu m$ and $\ell = 24.5\,\mu m$, respectively.

Our analysis in elliptical cell geometry shows that spontaneous polarisation starting from the unpolarised state arises only within a limited range of $k_{\mathrm{Pa}}/k_{\mathrm{Ap}}$ values (cones in Fig. 4), in accordance with previous studies using a one-dimensional model[9,28]. Strikingly, however, we find that the selection of the polarisation axis does not depend on the mutual antagonism but primarily on the activation-deactivation cycle. The ratio of the phosphorylation rates mainly determines the initial preference for a polarisation axis starting from an unpolarised state (Fig. 4*A* and *B*). Specifically, we find that for $\lambda = 0.3\,s^{-1}$, the first even mode grows more slowly than the first odd mode ($\delta\sigma < 0$), favouring short-axis polarisation. In contrast, for slower reactivation $\lambda = 0.05\ s^{-1}$, the first even mode grows faster than the first odd mode ($\delta\sigma > 0$). These respective preferences are most pronounced for large $k_{\mathrm{Pa}}/k_{\mathrm{Ap}}$. For the mid to low range of $k_{\mathrm{Pa}}/k_{\mathrm{Ap}}$, one finds $\delta\sigma \approx 0$, i.e. linear stability analysis does not predict a clear preference for either long- or short-axis polarisation. FEM simulations (for details on the FEM simulations see Method Section) show, however, that – irrespective of the ratio $k_{\mathrm{Pa}}/k_{\mathrm{Ap}}$ – long- and short-axis polarisation in the final steady state is

obtained for $\ell = 10\,\mu m$ and $\ell = 24.5\,\mu m$, respectively; see Supplementary Movies **M2d_1 – M2d_3** and Supplementary Tables 2, 3. These simulations confirm that the reactivation length ℓ is the deciding factor for axis selection in elliptical geometry.

The FEM simulations further show that outside of the parameter regime of linear instability there exist stable polarised states, showing that the system is excitable, i.e. that patterns can be triggered by a large enough finite perturbation ; see Supplementary Notes 1. This parameter regime is actually quite broad (see also Supplementary Fig. 1). As a generic example for an external stimulus, we have investigated how the PAR system reacts to initial concentration gradients on the membrane that were aligned along the final stable polarisation axes. We find that large enough gradients can indeed stimulate the formation of cell polarisation. It would be interesting to specify external cues more in detail experimentally and study how they affect pattern formation. In another work we recently showed that Turing instabilities and excitability (i.e. the ability to establish a pattern by applying a larger perturbation to the stable uniform steady state) are mechanistically linked in mass-conserving systems such as the PAR system [38]. Hence, even in systems where polarity is established by an external cue, identifying a Turing instability also locates regions where external stimulation leads to stable pattern formation.

The dependence of initial growth rates on the ratio of phosphorylation rates can be attributed to the fact that, in the unpolarised (aPAR-dominant state), the cytosolic concentration of aPARs increases with the rate at which aPARs are phosphorylated by pPARs, i.e. with a reduction in $k_{\mathrm{Pa}}/k_{\mathrm{Ap}}$ (Fig. 4*C*, *D*). If a protein species is abundant in the cytosol, recycling of recently detached

proteins can be compensated for by a protein of the same type in the cytosolic reservoir attaching to the membrane. Hence, effects due to different membrane-to-bulk ratios in the initial polarisation phase are dominant if the cytosolic pool of proteins undergoing an activation-deactivation cycle is low, explaining why $\delta\sigma$ depends on geometry for large values of $k_{\mathrm{Pa}}/k_{\mathrm{Ap}}$ (Fig. 4*C*, *D*).

Axis selection depends on relative protein densities After learning that the abundance of cytosolic proteins determines initial axis selection, we asked how changing the relative total protein densities affects cell polarisation. For all investigations up to this point the average densities were fixed to the order of magnitude determined experimentally by Gross et al.[?] (see Table 1 and see Supplementary Note 2). A linear stability analysis revealed that density variations alter several features: the range of ratios $k_{\mathrm{Pa}}/k_{\mathrm{Ap}}$ for which an interface between different PAR domains can be stably maintained, and the threshold value of reactivation length $\ell^\star$ that distinguishes between short- and long-axis polarisation. The effects were most prominent when the ratio of pPAR and aPAR proteins that phosphorylate each other ($[P]/[A_2]$), and the ratio of aPAR proteins ($[A_1]/[A_2]$) was varied.

As shown in Fig. 5, increasing the ratio of the antagonistic proteins ($[P]/[A_2]$) mainly shifts the regime of spontaneous cell polarisation up on the $k_{\mathrm{Pa}}/k_{\mathrm{Ap}}$ axis. This upward shift is easily explained, as the effective mutual phosphorylation rates are given by $k_{Ap}[P]$ and $k_{Pa}[A_{12}]$, respectively – where $[A_{12}]$ is mainly limited by the availability of $[A_2]$. Therefore, when the concentration of pPAR proteins ($[P]$) is increased relative to $[A_2]$, the per capita rate k_{Pa} has to be increased relative to k_{Ap} as well, in order to retain the balance between the mutual phosphorylation processes.

Changing the ratio between the different types of aPAR proteins has two effects. First, spontaneous polarisation is possible for a broader range of $k_{\mathrm{Pa}}/k_{\mathrm{Ap}}$. Increasing the concentration of the scaffold protein $[A_1]$ relative to $[A_2]$, which phosphorylates pPARs, decreases the lower bound of $k_{\mathrm{Pa}}/k_{\mathrm{Ap}}$ that allows for polarisation. This is a consequence of the increased reservoir size of A_1 which implies a higher rate of attachment of cytosolic A_1 to the membrane and hence a fast local redimerisation of A_2 (which lacks an inactive phase) right after the detachment of a hetero-dimer A_{12}. This newly formed hetero-dimer A_{12} is then competent to phosphorylate pPARs. Thus it is plausible that even for low $k_{\mathrm{Pa}}/k_{\mathrm{Ap}}$ one can achieve a balance of mutual antagonism, extending the lower bound of the polarisation regime. Second, changing the ratio $[A_1]/[A_2]$ also has a major effect on the threshold value of the reactivation length $\ell^\star$. We find that $\ell^\star$ increases with increasing concentration of the scaffold protein $[A_1]$ (Fig. 5). Again, this can be understood as a reservoir effect: globally abundant A_1 promotes immediate re-dimerisation of A_2 with any available A_1. Axis selection is then affected by the polar recycling of A_2.

Taken together, both of these findings emphasise the importance of the activation-deactivation cycle. A cell polarises more robustly when amounts of scaffold proteins are higher. However, at the same time, the cytosolic reactivation length has to increase significantly in order to also robustly maintain long-axis polarisation.

Role of interface length in three-dimensional cell geometry With the previous analysis in two-dimensional cell geometry we have built up a basic understanding of the role of the membrane-to-bulk ratio for the selection of the polarisation axis. In a nutshell, we concluded that sufficiently fast

diffusion and a sufficiently long inactive phase of the antagonistic proteins ensure that long-axis polarisation is established in a self-organised manner from homogeneous initial membrane concentrations. As the main parameter serving as a proxy for this effect we identified the reactivation length ℓ. Is this result directly transferable to a full three-dimensional cell geometry?

Since sensing of the local membrane-to-bulk ratio does not depend significantly on spatial dimension (see also Supplementary Note 4), one would at first sight expect the same conclusions to hold. However, there is a fundamental difference between a three- and a two-dimensional cell geometry. While for an ellipse the interface is always point-like , for a prolate spheroid the interface is longer for short-axis polarisation than for long-axis polarisation; in our case, we have $135\,\mu m$ and $94\,\mu m$, respectively (Fig. 1 D). This inherent difference between a two- and a three--dimensional cell geometry could significantly affect the protein dynamics on the membrane and in the cytosol. In the absence of an interface the only geometric effect is the membrane-to-bulk ratio. Therefore, as in the two-dimensional case, we expect this ratio to be the main factor that determines the initial formation of the protein domains and the interface between them. However, as soon as an interface has formed, its length is likely to affect the stability of the polarisation axis. The maintenance of the interface between protein domains is presumably energetically costly (protein fluxes sustaining antagonistic reactions, reactivation and rebinding have to be maintained). Therefore, since the interface is longer for short-axis than for long-axis polarisation, it is possible that even an initially favoured alignment of polarisation with the short-axis can become unstable.

To assess the protein dynamics of the system in full cell geometry we performed extensive

FEM simulations, restricting ourselves to parameter regimes that we identified as most relevant from the two-dimensional geometry (see Table 4 and compare with Table 1). Starting from a weakly perturbed unpolarised state we observe the following time evolution (Fig. 6 A,B); see the Method section on FEM simulations for 3d system and see our Supplementary Movies 4 and 5 (M3d_1.mp4 and M3d_2.mp4). During an initial time period T_{initial} a protein pattern forms that is either aligned along the short or long cell axis or somewhere in between. While long-axis polarisation is stable, any other polarisation is only metastable and after some persistence time T_{pers} transitions into stable long-axis polarisation during T_{trans}; as discussed in Supplementary Note 5 and Supplementary Figures 4-6 there are (unphysiological) cell geometries where short-axis polarisation is stable .

We observe that, as for the two-dimensional case, initial long-axis polarisation is favoured for large cytosolic diffusion constants D_{cyt} and low reactivation rates λ, while initial short-axis polarisation is favoured for the diametrically opposed case; compare Fig. 6 D with Fig. 3 D. This shows that the local membrane-to-bulk ratio is indeed the main factor that determines initial axis selection . Moreover, the persistence time T_{pers} (Fig. 6 C) and the transition time T_{trans} (Fig. 6 C,D) both depend strongly on D_{cyt} but only weakly on λ. In the regime with a clear preference for short-axis polarisation (below the dashed line in Fig. 6 D), T_{trans} becomes as large as several hours; for reference see Fig. 6 D with $\ell^\star \approx 7\mu m$; for further discussion and results on time scales see also Supplementary Note 8 and Supplementary Figure 8.

Finally, we wanted to investigate the main factors that determine the stability of long- versus

short-axis polarisation. As the essential novel feature of a three-dimensional cell geometry is the length of the interface between the PAR domains, we speculated that an additional mechanism relevant for axis polarisation is the minimisation of the interface length. To test this hypothesis, we performed FEM simulations in different prolate and oblate geometries ; see Supplementary Notes 5 and Supplementary Figures 4 to 6 , and Supplementary Movies 6 to 8 (M3d_3 to M3d_5) . We find that (for a given set of model parameters) the local diffusive protein fluxes from the cytosol to the membrane at the aPAR-pPAR interface are the same for short- and long-axis polarisation. Hence, the corresponding total fluxes scale with the length of the interface (see also Supplementary Note 6). This suggests that the mechanism responsible for long-axis stability is minimisation of protein fluxes. As a consequence, the transition times T_{trans} from short- to long-axis polarisation should also decrease with larger cytosolic protein fluxes as the maintenance of a larger interfaces becomes more costly. Indeed, FEM simulations show that changing the cytosolic diffusion constant leads to an increase in the associated cytosolic fluxes (see Supplementary Note 7 and Supplementary Figs. 7 and 8), and concomitantly to a significant decrease in the transition times T_{trans} (Fig. 6 C,D). Taken together, this shows that it is the interplay between membrane-to-bulk ratio and interface length minimisation due to flux (energy) minimisation that drives the selection of the polarisation axis and determines stability and robustness of this selection process.

Discussion

Here, we have addressed two linked questions concerning cell polarity in *C. elegans*: Under what conditions do cells polarise, and what determines the polarisation axis?

Polarisation in *C. elegans* is controlled by several mechanisms and their interplay: an initial polarisation cue of the centrosome, contraction of the actomyosin network and the PAR reaction-diffusion system which leads to polarisation in a self-organised manner but also interacts with the centrosome as well as with the actomyosin network. Recent research has further revealed some redundant pathways for the reaction-diffusion system depending on other proteins such as CHIN-1, LGL-1 and Cdc42 [11,17,39,40]. In view of this complexity, it is constructive to disentangle all individual building blocks, mechanical as well as kinetic, and investigate each separately in order to properly identify the underlying mechanisms which (i) leads to polarisation and (ii) aligns it with the long axis. With our work we could now shed light on polarisation and its alignment by the PAR reaction-diffusion system in 2d and in 3d. We expect the insights gained to be essential elements for a future three-dimensional model which combines the reaction-diffusion system with mechanical effects to quantitatively understand pattern formation in the *C. elegans* embryo.

Previous experiments supported by mathematical models in simplified cell geometry have indicated that balance between mutual phosphorylation of aPAR and pPAR proteins is a key mechanism responsible for cell polarisation [9,15,16,41]. Our theoretical results in realistic cell geometry support this finding. In addition, we have shown that robustness of cell polarity to variations in the phosphorylation rates increases if the scaffold protein PAR-3 is more abundant than PKC-3, which phosphorylates pPARs. Hence, low scaffold abundance is incompatible with robust biological function. This agrees with experimental findings that the scaffold function of PAR-3 is at least partially supported by other proteins (e.g. Cdc-42 [33]). Our results suggest that it would be worthwhile to experimentally search for other scaffold proteins and test their functional roles in

axis selection.

Most importantly, our theoretical analysis in realistic cell geometry reveals that the key processes for axis selection are cytosolic, specifically the cytosolic diffusion and an inactive (phosphorylated) phase of PAR-3 and PAR-2 after detachment from the membrane. The reactivation time (λ^{-1}) implies a cytosolic reactivation length $\ell = \sqrt{D_{\text{cyt}}/\lambda}$ which defines a cytosolic zone of inactive proteins close to the membrane. Proteins with a short reactivation length remain partially caged at the cell poles after membrane detachment, while those with a large reactivation length are uncaged and thereby become uniformly distributed in the cytosol before rebinding. Similarly, proteins lacking a delay, like the PAR-6 PKC-3 complex, are available for rebinding immediately after detachment from the membrane and are thus strongly caged to the cell poles.

Our theoretical analysis in a two-dimensional elliptical geometry shows that only for a sufficiently large cytosolic reactivation length ℓ does the long axis become the preferred polarisation axis, at onset as well as for the steady state. For the onset of polarisation, starting from a spatially homogeneous protein distribution, this result is fully transferable to a three-dimensional prolate spheroid. However, in such a realistic cell geometry, the length of the aPAR-pPAR interface also becomes important for the stability of the polarisation axis. Our simulation results suggest an (approximate) extremal principle: The dynamics tries to minimise the interface length such that for physiologically relevant geometries the long axis is always stable. Initial metastable short-axis polarisation is observed if the reactivation length ℓ is small (fast reactivation) such that proteins exhibit caging at the polar zones. In that regime, the transition times from short-axis to long-axis

polarisation can be of the order of several hours. In contrast, if $\ell/L \gtrapprox 0.3$ this time can be as short as 10min. This implies that without guiding cues the reaction-diffusion system requires a sufficiently slow phosphorylation-dephosphorylation cycle and a sufficiently large diffusion constant for fast and robust long-axis polarisation.

Furthermore, how slow reactivation and how fast cytosolic diffusion need to be in order to efficiently and robustly establish and maintain long-axis polarisation depends on the ratio of PAR-3 proteins to the PAR-6 PKC-3 complex: a larger cytosolic pool of PAR-3 attenuates the effect of selecting the interface at midplane and at the same time strengthens the tendency of PKC-3 to put the interface at the poles. Hence we predict that increasing the number of PAR-3 should destabilise long-axis polarisation in favour of short-axis polarisation.

On a broader perspective, these results show that selection of a characteristic wavelength for a pattern and selection of a polarity axis are distinct phenomena and are, in general, mediated by different underlying mechanisms. We expect the following findings to be generic for mass-conserved intracellular protein systems: local membrane-to-bulk ratio and the length of interfaces between different protein domains act as geometric cues for protein pattern formation, and an activation-deactivation as well as cytosolic protein reservoirs alter the sensitivity to cell geometry. Identifying the biochemical steps that are most relevant for axis selection in other intracellular pattern forming systems is an important theme for future research.

Methods

Model First we introduce and discuss the mathematical formulation and analysis of the reaction--diffusion model for PAR protein dynamics. To account for a realistic cell geometry we use, similar as in previous studies of the Min system[23], a two-dimensional elliptical geometry where the boundary of the ellipse ($\partial\Omega$) represents the membrane and the interior (Ω) represents the cytosol. Attachment-detachment processes are encoded by nonlinear reactive boundary conditions as introduced in Ref.[23]. Protein interactions are assumed to be bimolecular reactions that follow mass--action law kinetics. In the following a species identifies a mass- conserved protein type, whereas a component indicates the subgroup of proteins in a specific state, such as e.g. 'phosphorlyated' ('inactive') or 'membrane bound'.

Cytosolic dynamics Proteins in the cytosol are all assumed to diffuse with the same diffusion constant, $D_{\text{cyt}} = 30\,\mu m^2 s^{-1}$ (see also Table 1). In addition, we consider dephosphorylation (reactivation) of phosphorylated proteins with an activation (dephosphorylation) rate $\lambda = 0.05$/s (see also Table 1). The cytosolic concentration of each protein type X is denoted by c_X in its active form and by c_{X^*} in its inactive form (if applicable). The dynamics of the bulk components are thus given by the following set of reaction-diffusion equations:

$$\partial_t c_{A_1} = D_{\text{cyt}} \nabla^2 c_{A_1} + \lambda\, c_{A_1^*}\,, \tag{3}$$

$$\partial_t c_{A_1^*} = D_{\text{cyt}} \nabla^2 c_{A_1^*} - \lambda\, c_{A_1^*}\,, \tag{4}$$

$$\partial_t c_{A_2} = D_{\text{cyt}} \nabla^2 c_{A_2}\,, \tag{5}$$

$$\partial_t c_P = D_{\text{cyt}} \nabla^2 c_P + \lambda\, c_{P^*}\,, \tag{6}$$

$$\partial_t c_{P^*} = D_{\text{cyt}} \nabla^2 c_{P^*} - \lambda\, c_{P^*}\,, \tag{7}$$

where ∇^2 is the Laplacian in the two-dimensional bulk.

Membrane dynamics On the membrane all species are assumed to diffuse with the respective diffusion constant, $D^{\text{a}}_{\text{mem}} = 0.28\,\mu m^2 s^{-1}$ and $D^{\text{p}}_{\text{mem}} = 0.15\,\mu m^2 s^{-1}$ for aPARs and pPARs (see also Table 1). With m_X we denote the membrane-bound concentration of protein X. Then, the bimolecular reactions discussed above (see Fig. 1) translate into the following set of reaction-diffusion equations:

$$\partial_t m_{A_1} = D^{\text{a}}_{\text{mem}} \nabla^2_{||} m_{A_1} + k^{\text{on}}_{\text{a}}\, c_{A_1} - k^{\text{off}}_{\text{a}}\, m_{A_1} - k_{\text{Ap}}\, m_P\, m_{A_1} - k_{\text{d}}\, m_{A_1}\, c_{A_2}\,, \tag{8}$$

$$\partial_t m_{A_{12}} = D^{\text{a}}_{\text{mem}} \nabla^2_{||} m_{A_{12}} - k^{\text{off}}_{\text{a}}\, m_{A_{12}} + k_{\text{d}}\, m_{A_1}\, c_{A_2} - k_{\text{Ap}}\, m_P\, m_{A_{12}}\,, \tag{9}$$

$$\partial_t m_P = D^{\text{p}}_{\text{mem}} \nabla^2_{||} m_P + k^{\text{on}}_{\text{p}}\, c_P - k^{\text{off}}_{\text{p}}\, m_P - k_{\text{Pa}}\, m_{A_{12}} m_P\,, \tag{10}$$

where $\nabla^2_{||}$ is the Laplacian operator on the boundary $\partial\Omega$, i.e. on the membrane.

Reactive boundary conditions The membrane dynamics and cytosolic dynamics are coupled through reactive boundary conditions. These describe the balance between diffusive fluxes ($D_{\text{cyt}} \nabla_\perp$

acting on cytosolic concentration) and attachment and detachment processes between membrane and cytosol:

$$D_{\text{cyt}} \nabla_\perp c_{A_1} = k_{\text{a}}^{\text{off}} \left(m_{A_1} + m_{A_{12}} \right) - k_{\text{a}}^{\text{on}}\, c_{A_1} \tag{11}$$

$$D_{\text{cyt}} \nabla_\perp c_{A_2} = \left(k_{\text{Ap}} m_P + k_{\text{a}}^{\text{off}} \right) m_{A_{12}} - k_{\text{d}}\, c_{A_2} m_{A_1} \tag{12}$$

$$D_{\text{cyt}} \nabla_\perp c_P = k_{\text{p}}^{\text{off}} m_P - k_{\text{p}}^{\text{on}} c_P \tag{13}$$

$$D_{\text{cyt}} \nabla_\perp c_{A_1^*} = k_{\text{Ap}}\, m_P \left(m_{A_1} + m_{A_{12}} \right) \tag{14}$$

$$D_{\text{cyt}} \nabla_\perp c_{P^*} = k_{\text{Pa}}\, m_P m_{A_{12}} \tag{15}$$

where $\nabla_\perp$ is the Nabla operator perpendicular to the boundary, such that $D_{\text{cyt}} \nabla_\perp$ is the flux operator between cytosol and membrane.

Mass conservation On the time scale of establishment and maintenance of polarisation in *C. elegans*, PAR protein production and degradation are negligible. Hence, the total number N_X of each protein species $X \in \{A_1, A_2, P\}$ is conserved. It can be obtained by integrating the average densities over the whole space or by integrating the space-dependent cytoplasmic concentrations and membrane concentrations over Ω and $\partial\Omega$, respectively:

$$N_{A_1} = \int_\Omega \rho_{A_1} = \int_\Omega \left(c_{A_1} + c_{A_1^*} \right) + \int_{\partial\Omega} \left(m_{A_1} + m_{A_{12}} \right), \tag{16}$$

$$N_{A_2} = \int_\Omega \rho_{A_2} = \int_\Omega c_{A_2} + \int_{\partial\Omega} m_{A_{12}}\,, \tag{17}$$

$$N_P = \int_\Omega \rho_P = \int_\Omega \left(c_P + c_{P^*} \right) + \int_{\partial\Omega} m_P\,, \tag{18}$$

where $\int_\Omega$ and $\int_{\partial\Omega}$ denote integrals over the interior and the boundary of the ellipsoid, respectively.

Linear Stability Analysis In the following we outline the main steps required to perform a linear stability analysis (LSA) in elliptical geometry, emphasising the major differences relative to the well known stability analysis in planar system geometries with no bulk-boundary coupling (see e.g. a didactic derivation of linear stability analysis written by Cross and Greenside[42]). A detailed derivation of LSA in elliptical geometry can be found in the Supplementary Information of Halatek et al.[23].

Reaction-diffusion equations in elliptical geometry A LSA yields the initial dynamics of a system perturbed from any of its steady states. In the context of pattern formation in reaction-diffusion systems this is typically a uniform steady state. The eigenfunctions of the linearised system (around the steady state) serve as an orthogonal basis in which any perturbation can be expressed. In planar systems these are simply Fourier modes, e.g. $\sim \cos(qx)$ with spatial variable x and wavenumber q, where q is chosen such that boundary conditions are satisfied. The LSA then yields the temporal eigenvalues σ_q (growth rates) for each wavenumber that express exponential growth or decay, and possible oscillation (if the imaginary part $\Im[\sigma_q] \neq 0$) of the respective eigenfunction $\exp(\sigma_q t)\cos(qx)$. Hence, the main objective is (i) to derive the eigenfunctions for the linearised system in the corresponding geometry, and (ii) to calculate the associated growth rates (real parts $\Re[\sigma_q]$), where positive growth rates signify formation of patterns with wavelength $\sim 1/q$.

For reaction-diffusion systems with bulk-boundary coupling in elliptical geometry there are three major complications with this approach.

Due to bulk-boundary coupling, we are faced with two separate sets of reaction–diffusion equations. One set is defined in the bulk and accounts for the dynamics in the cytosol. Here reactions are assumed to be linear (first order kinetics) and typically account for nucleotide exchange or (de-)phosphorylation, Eq. (3) – Eq. (7). The second set is defined on the boundary and accounts for the dynamics on the membrane (or cell cortex) including diffusion and reaction, Eq. (8) – Eq. (10).

The first complication arises as follows: Given orthogonal elliptical coordinates

$$x = d\,\cosh\mu\,\cos\nu\,, \tag{19}$$

$$y = d\,\sinh\mu\,\sin\nu\,, \tag{20}$$

with 'radial' variable $\mu > 0$, 'angular' variable $0 \leq \nu < 2\pi$, and elliptical eccentricity $d = \sqrt{a^2 - b^2}$ (with long half-axis a and short half-axis b), the diffusion operator in the bulk $D_{\text{cyt}}\nabla^2$ reads:

$$D_{\text{cyt}}\,\frac{1}{d^2(\sinh^2\mu + \sin^2\nu)}\,(\partial_\mu^2 + \partial_\nu^2)\,. \tag{21}$$

On the boundary the diffusion operator $D_{\text{mem}}\nabla_{||}^2$ acts along constant $\mu = \mu_0 = \arctan(b/a)$ and reads:

$$D_{\text{mem}}\left(-\frac{\cos\nu\sin\nu}{d\,(\sinh^2\mu_0 + \sin^2\nu)^{3/2}}\,\partial_\nu + \frac{1}{d^2\,(\sinh^2\mu_0 + \sin^2\nu)}\,\partial_\nu^2\right). \tag{22}$$

Due to these different diffusion operators the sets of reaction–diffusion equations in the bulk and on the boundary do not share the same set of canonical eigenfunctions (i.e. eigenfunction obtained from separation of variables). To overcome this problem the diffusion on the membrane can be more conveniently expressed in arclength parametrisation $s(\nu)$:

$$s(\nu) = \int_0^\nu d\tilde{\nu}\,\sqrt{b^2 + (a^2 - b^2)\sin^2\tilde{\nu}}\,. \tag{23}$$

Then, the diffusion operator $D_{\text{mem}}\nabla^2_{||}$ simplifies to $D_{\text{mem}}\partial^2_s$, and the eigenfunctions are obtained as

$$\Psi^{\text{mem}}_{e,n}\left(\mu_0, s\left(\nu\right)\right) = \cos\left(\frac{2\pi n}{S} s\left(\nu\right)\right), \tag{24}$$

$$\Psi^{\text{mem}}_{o,n}\left(\mu_0, s\left(\nu\right)\right) = \sin\left(\frac{2\pi n}{S} s\left(\nu\right)\right), \tag{25}$$

with the circumference of the ellipse $S = 2\pi\, s$. The goal is then to express these functions in terms of the orthogonal eigenfunctions of the bulk problem — the Mathieu functions, here denoted by $\Psi(\nu)$ and $R(\mu)$ — which are obtained as solutions of the Mathieu equations:

$$0 = \partial^2_\nu \Psi(\nu) + \left[\alpha - 2q \cdot \cos(2\nu)\right]\Psi(\nu) \tag{26}$$

$$0 = \partial^2_\mu R(\mu) - \left[\alpha - 2q \cdot \cosh(2\mu)\right]R(\mu)\,. \tag{27}$$

Here α is a constant of separation, and

$$q = -(\sigma + \lambda)\frac{d^2}{4D_{\text{cyt}}} \tag{28}$$

denotes a dimensionless parameter (not to be confused with a wavenumber!). For small q, analytical approximations of the Mathieu functions can be obtained [?,?,23] and matched with the eigenfunctions $\Psi^{\text{mem}}_{e,n}$ and $\Psi^{\text{mem}}_{o,n}$ at the boundary $\mu = \mu_0$.

The second complication is a consequence of the coupling between bulk and boundary processes through the reactive boundary condition, see e.g. the model equations Eq. (11) – Eq. (15). This coupling introduces an explicit dependence of the linearised system on the (derivative of the) radial eigenfunctions $R(\mu)$ (see Ref.[23]), which, in turn, depends on the temporal eigenvalues σ in a non-algebraic fashion. Usually, the final step in any LSA is the solution of a characteristic equation

$0 = f(\sigma)$, which is typically polynomial in σ. Due to the bulk-boundary coupling this is no longer the case (irrespective of the geometry, see e.g. Ref.[26]; the characteristic equation is transcendental and can only be solved numerically for each parameter combination [23]. Therefore, it is not possible to derive a general stability criterion analogous to that known for planar systems without bulk-boundary coupling [42]. We further note that the boundary condition introduces a coupling between the angular eigenfunctions $\Psi(\nu)$, which, however, is small and can be neglected [23].

The final complication arrises as consequence of the cytosolic reactivation cycle. This cycle generically precludes the existence of a uniform steady state (including states uniform along the boundary). The origin of this symmetry adaption process has been discussed in Ref.[24]. Following Ref.[23] we approximate the near-uniform steady state with the eigenfunction that is constant along the boundary, i.e. $\Psi_{e,0}^{\mathrm{mem}}\left(\mu_0, s\left(\nu\right)\right)$. In this case nonlinearities (which are restricted to the boundary) do not induce mode coupling, which would otherwise complicate the LSA.

Finite Element Simulations (FEM) Linear stability analysis can only predict the onset of pattern formation. In order to understand the full nonlinear protein dynamics and to determine the steady states corresponding to given parameter sets we further performed finite element (FEM) simulations on a triangular mesh using Comsol Multiphysics 5.1 - 5.4 (updating versions).

Setup for FEM simulations As time-dependent solver in Comsol Multiphysics we chose PARDISO with a multithreaded nested dissection. The time stepping was performed with a relative tolerance of 10^{-6} between time steps and solved with a multistep method (BDF). In all simulations we used triangular meshing (setting 'finer') with additional refinement at the boundary, i.e. along

the membrane. As for the linear stability analysis, if not specified otherwise, the parameters for the FEM simulations can be found in Table 1. For the standard parameter sets given in Table 1, we ran the simulation up to $5 \cdot 10^6 s$. Since the system reached the steady state for most parameter sets at the latest after $5 \cdot 10^5 s$, we limited simulation times for large parameter sweeps at $10^6 s$.

The critical reactivation rate The 2d FEM sweep of λ versus D_{cyt} was initialised with a random initial perturbation of the stationary state with high aPAR concentration on the membrane. The initial perturbation was implemented by drawing a random number rand(x, y) from a normal distribution with zero mean and unit variance and multiplying the membrane concentration of aPARs by $(1 + 0.01 \cdot \text{rand}(x, y))$ and that of pPARs by $(1 - 0.01 \cdot \text{rand}(x, y))$, i.e. we perturbed the initial condition randomly by 1%. The parameter sweep was performed varying λ from $5 \cdot 10^{-3}\,\text{s}^{-1}$ to $0.3\,\text{s}^{-1}$ in steps of $5 \cdot 10^{-3}\,\text{s}^{-1}$ and varying D_{cyt} from $6\,\mu m^2 s^{-1}$ to $40\,\mu m^2 s^{-1}$ with a uniform spacing of $2\,\mu m^2 s^{-1}$.

We further performed two test simulations (sweeping λ and D_{cyt}) which were initialised with linear gradients. These implementations were intended to uncover dependencies of the final pattern on the initial perturbation. In the first sweep, the gradient was oriented along the long-axis, i.e. the aPAR concentrations were multiplied by $(1 + 0.1 \cdot x/a)$ and the pPAR concentrations by $(1 - 0.1 \cdot x/a)$. In the second sweep the gradient was oriented along the short-axis, i.e. the aPAR concentrations were multiplied by $(1 + 0.1 \cdot y/b)$ and the pPAR concentrations by $(1 - 0.1 \cdot y/b)$. We found that the steady state polarisation was the same as with small random perturbations. Initial linear gradients with the 'wrong? alignment only lead to a transient polarisation along the same axis as the initially imposed gradient but then turned to the same polarisation axis as with the

random initial perturbation.

Furthermore, we checked the linear stability analysis sweeps on k_{Ap} and k_{Pa} in Fig. 4 using FEM simulations. The explicit parameter sets k_{Ap} and k_{Pa} used for probing FEM simulations are shown in Tables 2 and 3. 2d FEM simulations confirm that there λ is the decisive parameter that determines the polarisation axis and not k_{Ap} and k_{Pa}.

In order to find ℓ^*/L in steady state for different combinations of density ratios shown in Fig. 5, we performed FEM sweeps of k_{Pa} (for fixed $k_{\text{Ap}} = 0.4\,\mu m s^{-1}$) and λ (for fixed $D_{\text{cyt}} = 30\,\mu m^2 s^{-1}$) at first in broad steps (the steps for λ were initiated with $5 \cdot 10^{-3}\,\text{s}^{-1}$ and those for k_{Pa} with $0.2\,\mu m s^{-1}$). As soon as we identified a regime of parameters for ℓ^*/L where long-axis polarisation turned to short-axis polarisation, we used finer steps, with the step size being chosen in accordance with the cone size of each of the $k_{\text{Pa}}/k_{\text{Ap}}$ versus ℓ^*/L cones in Fig. 5.

FEM simulations for 3d system In 3d FEM simulations for all sweeps were initiated with an initial *aPAR*-dominant concentration on the membrane and 1% random perturbation thereof. All parameters are shown in Table 4. For the sweep of λ versus D_{cyt} resulting in the data discussed in the main text and Fig. 6 the parameter range was set to $D_{\text{cyt}} = 2 - 32\,\mu m^2 s^{-1}$ in steps of $2\,\mu m^2 s^{-1}$, and reactivation rate $\lambda = 0.03 - 0.3\,s^{-1}$ in steps of $0.03\,s^{-1}$. The full region of the formation of any pattern can be found by using the feature that the absolute value of membrane gradients is zero for a homogeneous distribution on the membrane and a positive number for inhomogeneous (patterned) protein distributions on the membrane. To distinguish between long and short axis patterns the FEM simulations were analysed by investigating (i) the angle of the concentration maxima

on the membrane in ellipsoidal coordinates (which is $90°$ for perfect short axis polarisation and $0/180°$ for perfect long axis polarisation) and additionally (ii) the distance between the concentration maximum of P and A_1 on the membrane (which is $2{\cdot}\text{a}= 54\mu m$ for long axis polarisation and $2{\cdot}\text{b}= 30\mu m$ for short axis polarisation). For a final check, the pattern dynamics was sampled by eye to ensure that these criteria work. In order to numerically investigate the onset of long axis polarisation - which is very sensitive to λ - a finer sweep was additionally performed with $D_{\text{cyt}} = 2 - 32\,\mu m^2 s^{-1}$ in steps of $2\,\mu m^2 s^{-1}$, and reactivation rate $\lambda = 0.015 - 0.01\,s^{-1}$ in steps of $0.005\,s^{-1}$. To find the boundary for a polarity onset with long axis alignment we filtered for a short axis and a diagonal onset.

Data availability Data supporting the findings of this manuscript are available from the corresponding authors upon reasonable request. A reporting summary for this Article is available as a Supplementary Information file.

Code availability Custom written codes used in this study are available from the corresponding author upon reasonable request.

1. Campanale, J. P., Sun, T. Y. & Montell, D. J. Development and dynamics of cell polarity at a glance. *J Cell Sci* **130**, 1201–1207 (2017).

2. Chiou, J.-g., Balasubramanian, M. K. & Lew, D. J. Cell polarity in yeast. *Annu Rev Cell Dev Biol* **15**, 365–391 (2017).

3. Roignot, J., Peng, X. & Mostov, K. Polarity in mammalian epithelial morphogenesis. *Cold Spring Harb Protoc* **33** (2013).

4. Goehring, N. W. PAR polarity: from complexity to design principles. *Exp Cell Res* **328**, 258–266 (2014).

5. Goldstein, B. & Macara, I. G. The PAR proteins: fundamental players in animal cell polarization. *Dev Cell* **13**, 609–622 (2007).

6. Gönczy, P. Asymmetric cell division and axis formation in the embryo. *WormBook* 1–20 (2005).

7. Cuenca, A. A., Schetter, A., Aceto, D., Kemphues, K. & Seydoux, G. Polarization of the C. elegans zygote proceeds via distinct establishment and maintenance phases. *Development* **130**, 1255–1265 (2003).

8. Munro, E., Nance, J. & Priess, J. R. Cortical flows powered by asymmetrical contraction transport PAR proteins to establish and maintain anterior-posterior polarity in the early C. elegans embryo. *Dev Cell* **7**, 413–424 (2004).

9. Goehring, N. W. *et al.* Polarization of PAR proteins by advective triggering of a pattern-forming system. *Science* **334**, 1137–1141 (2011).

10. Motegi, F. *et al.* Microtubules induce self-organization of polarized PAR domains in Caenorhabditis elegans zygotes. *Nat Cell Biol* **13**, 1361–7 (2011).

11. Motegi, F. & Seydoux, G. The PAR network: redundancy and robustness in a symmetry-breaking system. *Philos Trans R Soc Lond B Biol Sci* **368**, 20130010 (2013).

12. Hill, D. P. & Strome, S. An analysis of the role of microfilaments in the establishment and maintenance of asymmetry in Caenorhabditis elegans zygotes. *Dev Biol* **125**, 75–84 (1988).

13. Cowan, C. R. & Cowan, A. A. Centrosomes direct cell polarity independently of microtubule assembly in C. elegans embryos. *Nature* **431**, 92–96 (2004).

14. Petrásek, Z. *et al.* Characterization of protein dynamics in asymmetric cell division by scanning fluorescence correlation spectroscopy. *Biophys J* **95**, 5476–5486 (2008).

15. Dawes, A. T. & Munro, E. M. PAR-3 oligomerization may provide an actin-independent mechanism to maintain distinct par protein domains in the early Caenorhabditis elegans embryo. *Biophys J* **101**, 1412–1422 (2011).

16. Goehring, N. W., Hoege, C., Grill, S. W. & Hyman, A. PAR proteins diffuse freely across the anterior-posterior boundary in polarized C. elegans embryos. *J Cell Biol* **193**, 583–594 (2011).

17. Schonegg, S. & Hyman, A. A. Cdc-42 and rho-1 coordinate acto-myosin contractility and par protein localization during polarity establishment in c. elegans embryos. *Development* **133**, 3507–3516 (2006).

18. Schonegg, S., Constantinescu, A. T., Hoege, C. & Hyman, A. A. The Rho GTPase-activating proteins RGA-3 and RGA-4 are required to set the initial size of PAR domains in Caenorhabditis elegans one-cell embryos. *Proc Natl Acad Sci USA* **104**, 14976–14981 (2007).

19. Schenk, C., Bringmann, H., Hyman, A. A. & Cowan, C. R. Cortical domain correction repositions the polarity boundary to match the cytokinesis furrow in C. elegans embryos. *Development* **137**, 1743–1753 (2010).

20. Hoege, C. & Hyman, A. A. Principles of PAR polarity in Caenorhabditis elegans embryos. *Nat Rev Mol Cell Biol* **14**, 315–322 (2013).

21. Hao, Y., Boyd, L. & Seydoux, G. Stabilization of cell polarity by the c. elegans ring protein par-2. *Dev Cell* **10**, 199–208 (2006).

22. Zonies, S., Motegi, F., Hao, Y. & Seydoux, G. Symmetry breaking and polarization of the C. elegans zygote by the polarity protein PAR-2. *Development* **137**, 1669–1677 (2010).

23. Halatek, J. & Frey, E. Highly canalized MinD transfer and MinE sequestration explain the origin of robust MinCDE-protein dynamics. *Cell Rep* **1**, 741–752 (2012).

24. Thalmeier, D., Halatek, J. & Frey, E. Geometry-induced protein pattern formation. *Proc Natl Acad Sci USA* **113**, 548–553 (2016).

25. Wu, F., Halatek, J., Reiter, M., Kingma, E. & Frey, E. Multistability and dynamic transitions of intracellular Min protein patterns. *Mol Syst Biol* **12**, 873 (2016).

26. Halatek, J. & Frey, E. Rethinking pattern formation in reaction-diffusion systems. *Nat Phys* **14**, 507–514 (2018).

27. Dawes, A. T. & Iron, D. Cortical geometry may influence placement of interface between Par protein domains in early Caenorhabditis elegans embryos. *J Theor Biol* **333**, 27–37 (2013).

28. Trong, P. K., Nicola, E. M., Goehring, N. W., Kumar, K. V. & Grill, S. W. Parameter-space topology of models for cell polarity. *New J Phys* **16**, 65009 (2014).

29. Tabuse, Y. *et al.* Atypical protein kinase C cooperates with PAR-3 to establish embryonic polarity in Caenorhabditis elegans. *Development* **125**, 3607–3614 (1998).

30. Etemad-Moghadam, B., Guo, S. & Kemphues, K. Asymmetrically distributed PAR-3 protein contributes to cell polarity and spindle alignment in early C. elegans embryos. *Cell* **83**, 743–752 (1995).

31. Watts, J. L. *et al.* par-6, a gene involved in the establishment of asymmetry in early C. elegans embryos, mediates the asymmetric localization of PAR-3. *Development* **122**, 3133–3140 (1996).

32. Hung, T.-J. & Kemphues, K. J. PAR-6 is a conserved PDZ domain-containing protein that colocalizes with PAR-3 in Caenorhabditis elegans embryos. *Development* **126**, 127–135 (1999).

33. Rodriguez, J. *et al.* aPKC cycles between functionally distinct PAR protein assemblies to drive cell polarity. *Dev Cell* **42**, 400–415.e9 (2017).

34. Li, J. *et al.* Binding to PKC-3, but not to PAR-3 or to a conventional PDZ domain ligand, is required for PAR-6 function in C. elegans. *Dev Biol* **340**, 88–98 (2010).

35. Li, B., Kim, H., Beers, M. & Kemphues, K. Different domains of C. elegans PAR-3 are required at different times in development. *Dev Biol* **344**, 745–757 (2010).

36. Boyd, L., Guo, S., Levitan, D., Stinchcomb, D. T. & Kemphues, K. J. PAR-2 is asymmetrically distributed and promotes association of P granules and PAR-1 with the cortex in C. elegans embryos. *Development* **122**, 3075–3084 (1996).

37. Driever, W. & Nüsslein-Volhard, C. A gradient of bicoid protein in Drosophila embryos. *Cell* **54**, 83–93 (1988).

38. Brauns, F., Halatek, J. & Frey, E. Phase-space geometry of reaction–diffusion dynamics. Preprint at arXiv:1812.08684 (2018).

39. Sailer, A., Anneken, A., Li, Y., Lee, S. & Munro, E. Dynamic Opposition of Clustered Proteins Stabilizes Cortical Polarity in the C.elegans Zygote. *Dev Cell* **35**, 131–142 (2015).

40. Beatty, A., Morton, D. G. & Kemphues, K. PAR-2, LGL-1 and the CDC-42 GAP CHIN-1 act in distinct pathways to maintain polarity in the C. elegans embryo. *Development* **140**, 2005–2014 (2013).

41. Tostevin, F. & Howard, M. Modeling the establishment of PAR protein polarity in the one-cell C. elegans embryo. *Biophys J* **95**, 4512–4522 (2008).

42. Cross, M. & Greenside, H. *Pattern Formation and Dynamics in Nonequilibrium Systems* (Cambridge University Press, 2009).

Acknowledgements We would like to thank T. Fehm and T. Meinhardt who were involved at early, preliminary stages of this project, and F. Brauns and B. Osberg for critical reading of the manuscript and for providing valuable feedback. E.F. acknowledges support from the Deutsche Forschungsgemeinschaft (DFG) via project B02 within the Collaborative Research Center Deutsche Forschungsgemeinschaft (DFG, German Research Foundation) - Project-ID 201269156 - SFB 1032. R.G. is supported by a DFG fellowship through the Graduate School 'Quantitative Bioscience Munich' (QBM).

Author contributions R.G., J.H., L.W., and E.F. designed research, performed research, and wrote the paper.

Competing interests The authors declare no conflict of interest.

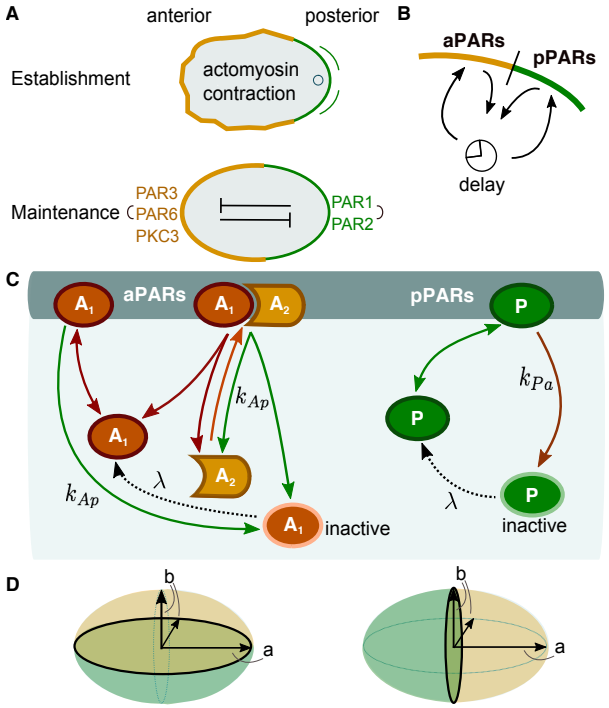

Figure 1:

Figure 1: Biological background and model network (*A*) Cell polarisation in the *C. elegans* embryo during the establishment (top) and maintenance (bottom) phases; sketch adapted from Ref.[5]. (*B*) Illustration of protein flux between cytosol and membrane. As proteins detach from the membrane when phosphorylated, they cannot immediately rebind to the membrane. There is therefore an intrinsic delay before dephosphorylation permits rebinding. (*C*) The biochemical reaction network is comprised of two mutually antagonistic sets of proteins, aPARs and pPARs. Dephosphorylated (active) A_1 and P attach to the membrane with rates $k_{\mathrm{a}}^{\mathrm{on}}$ and $k_{\mathrm{p}}^{\mathrm{on}}$, respectively. Both active proteins may also detach spontaneously from the membrane with rates $k_{\mathrm{a}}^{\mathrm{off}}$ and $k_{\mathrm{p}}^{\mathrm{off}}$, respectively. A_1 acts as a scaffold protein: Once bound to the membrane it recruits A_2 with rate k_{d} and forms a membrane-bound hetero-dimeric aPAR complex A_{12}. The hetero-dimer A_{12} may

itself spontaneously detach from the membrane with rate $k_{\mathrm{a}}^{\mathrm{off}}$ and dissociate into A_2 and active A_1. Membrane-bound A_1 and A_{12} can also be phosphorylated by P with rate $k_{\mathrm{Ap}}[P]$, thereby initiating dissociation of the aPAR complex and release of aPAR proteins into the cytosol. While reattachment of the scaffold protein A_1 is delayed by the requirement for dephosphorylation (reactivation), detached A_2 can be recruited to the membrane by membrane-bound A_1 immediately. Similarly, P is phosphorylated by the hetero-dimer A_{12} at rate $k_{\mathrm{Pa}}[A_{12}]$, and is consequently released as inactive P into the cytosol. In the same way as A_1, also P must be dephosphorylated before it can bind again to the membrane. For simplicity, we take identical dephosphorylation (reactivation) rates λ for inactive A_1 and P. The ensuing reaction-diffusion equations are provided in the Method section and a table listing the values of the rate constants can be found in 1. (*D*) Sketch of the cell's geometry: Prolate spheroid with long axis a and short axis b, and with short- (left) and long-axis (right) polarisation.

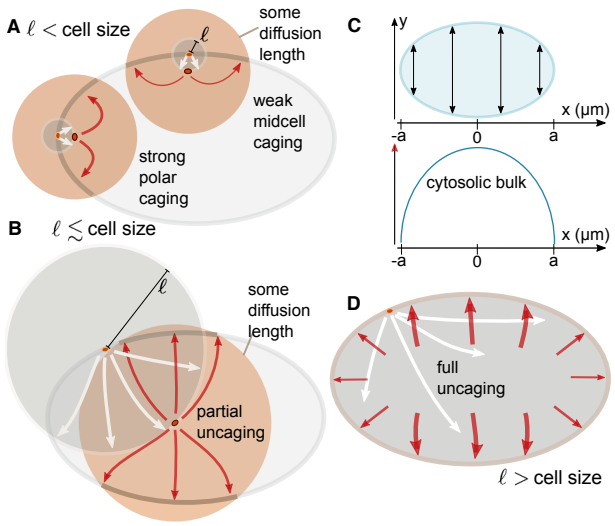

Figure 2:

Figure 2: Role of dephosphorylation in axis determination. (*A*, *B*, and *D*): A protein is shown in the elliptical cell firstly at its phosphorylation and detachment site on the membrane and then at the point of its reactivation. The reactivation length gives an average radius (gray circles) how far from the detachment point a protein travels before reactivation. The orange circles around the reactivated protein and the associated arrows sketch some diffusion distance corresponding to a time interval Δt following reactivation, i.e. during this time interval the protein can reattach to the membrane. (*A*) If the reactivation length ℓ (radius of gray circle) is small compared to the cell size, the local membrane surface to cytosolic volume ratio strongly affects the position at which detached proteins reattach. Due to the reactivation occurring close to the membrane, within some time interval Δt following reactivation a protein that detaches from a cell pole is more likely to reattach near that same cell pole than a protein detaching from mid-cell is to reattach at mid-cell. Hence, dynamics that are based on membrane-cytosol cycling (such as antagonistic

reactions that maintain an interface) are enhanced at the cell poles. (*B*) As the reactivation length ℓ approaches the length of the cell, this effect of geometry becomes weaker, and detaching proteins become increasingly unconstrained by the position of detachment (uncaged). (*C*) Illustration of the distribution of cytosolic bulk proteins along the long-axis. The elliptical cell and the cytosol height is depicted as a function of x, where the x-axis aligns with the long axis (top). The amount of cytosolic bulk proteins for each x varies from the poles to mid-cell as illustrated (bottom). (*D*) This effect of cell geometry is completely lost if the reactivation length ℓ exceeds the length of the cell. Hence, detached proteins become uniformly distributed throughout the cell before reactivation occurs. In that case, most will re-encounter the membrane near mid-cell after reactivation, since a delocalised protein will most likely be found in the mid-cell area.

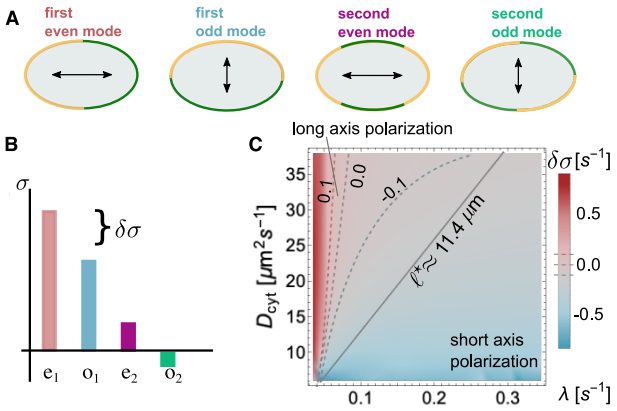

Figure 3:

Figure 3: Mode selection and polarity. (*A*) Illustration of the protein distribution on the membrane and the ensuing polarity axis for the lowest-order even and odd modes. (*B*) Illustration of the mode spectrum for these lowest-order modes and the gap $\delta\sigma$ in the growth rates between the first even and odd modes. (*C*) Relative difference in the growth rates of the first even and odd modes (linear stability analysis in colour code with dashed threshold lines $\delta\sigma = 0s^{-1}$, $\delta\sigma = \pm 0.1s^{-1}$), $\delta\sigma$, as a function of D_{cyt} and λ. For small λ and large D_{cyt}, $\delta\sigma$ is clearly greater than zero (red, long-axis polarisation), whereas for large λ and small D_{cyt}, $\delta\sigma$ lies below zero (blue, short-axis polarisation). These findings are validated using FEM simulations. FEM sweeps in D_{cyt} and λ were run until the steady state was reached. These simulations yielded a straight-line interface (black-solid line in (*C*)) in the λ-D_{cyt} parameter space which divides long- (above) from short-axis (below) polarisation in steady state. The line corresponds to a constant threshold reactivation length $\ell^\star$. All other parameters can be found in Table 1.

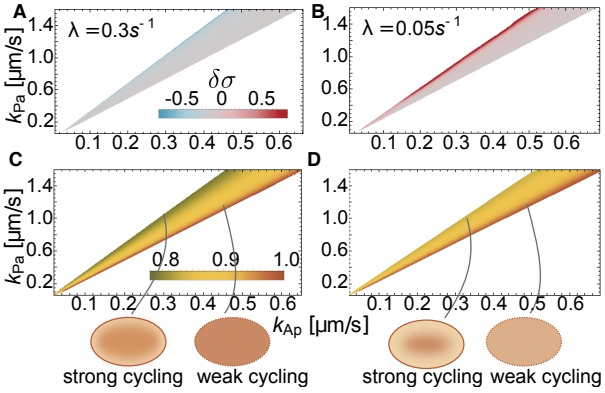

Figure 4:

Figure 4: Role of phosphorylation rates in polarisation and axis selection. Linear stability analysis shows that spontaneous polarisation is possible only within a range of ratios of the phosphorylation rates, $k_{\mathrm{Pa}}/k_{\mathrm{Ap}}$ (cone-shaped regions): The relative difference in the growth rates of even and odd modes ($\delta\sigma$) is shown in (*A*) for $\lambda = 0.3\,s^{-1}$, and (*B*) for $\lambda = 0.05\,s^{-1}$ in colour code (indicated in the graph). Panels (*C*) and (*D*) show the corresponding cytosolic concentration of A_1 in the aPAR dominant unpolarised state (A_2 has a quantitatively similar concentration gradient to A_1 within the cone, not shown), normalised with respect to the maximal concentration of A_1 obtained within the respective cone. Cartoons at the bottom of the figure schematically depict the cytosolic distribution of aPARs throughout the cell.

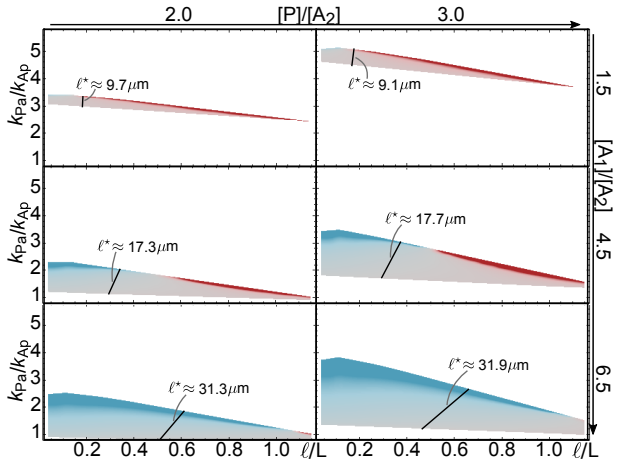

Figure 5:

Figure 5: Relative protein numbers determine robustness of cell polarity. Linear stability analysis for a range of density ratios $[P]/[A_2]$ and $[A_1]/[A_2]$; $[A_2]$ was kept constant. Each graph shows the range of phosphorylation ratios ($k_{\mathrm{Pa}}/k_{\mathrm{Ap}}$) and relative reactivation lengths (ℓ/L) where the base state is linearly unstable, with $\delta\sigma$ given by the same colour code as in Fig. 4*A*; fixed parameters are $k_{\mathrm{Ap}} = 0.4\,\mu\mathrm{m}\ s^{-1}$ and $D_{\mathrm{cyt}} = 30\,\mu m^2 s^{-1}$, and further parameters not varied can be found in Table 1. FEM parameter sweeps of k_{Pa} and λ, with fixed parameters $k_{\mathrm{Ap}} = 0.4\,\mu\mathrm{m}\ s^{-1}$ and $D_{\mathrm{cyt}} = 30\,\mu m^2 s^{-1}$, for each density set show that the steady state polarisation axis also depends strongly on the ratio $[A_1]/[A_2]$. The steady state switches from short- to long-axis polarisation at the black line in each graph, indicating $\ell^\star$.

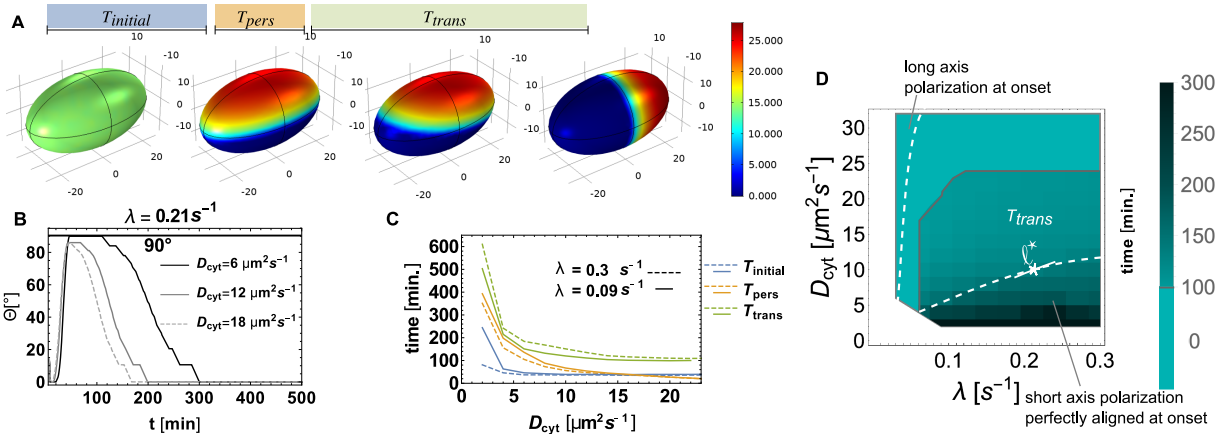

Figure 6:

Figure 6: Cell polarisation in three dimensions. (*A*) Image series from FEM (Comsol) simulation for $D_{\text{cyt}} = 6\,\mu m^2 s^{-1}$, and reactivation rate $\lambda = 0.21\,s^{-1}$. The series illustrates the different times which are further analysed: The time from the initial aPAR-dominated unpolarised state to the initial short-axis polarisation, T_{initial}; the time duration of persistent short-axis polarisation, T_{pers}; and the time the pattern takes to turn from short- to long-axis polarisation, T_{trans}. (*B*) The angle Θ of the concentration maximum of membrane-bound A_1 is plotted against simulation time for different D_{cyt} indicated in the graph. (*C*) T_{initial}, T_{pers}, T_{trans} plotted as a function of D_{cyt} for $\lambda = 0.09\,s^{-1}$ and $\lambda = 0.3\,s^{-1}$. (*D*) The magnitude of the transition time from short- to long-axis polarisation, T_{trans}, in D_{cyt}-λ parameter space; a cell was considered to be polarised along the short axis if $90° - 10° \leq \Theta \leq 90° + 10°$. The monochrome cyan-coloured region above the gray line corresponds to a parameter region where there is no short-axis polarisation, but the polarisation axis is aligned along the diagonal or long axis from the beginning. The dashed lines demarcate parameter regimes where the initial polarisation is aligned perfectly with the short axis ($\Theta = 90°$) or with the long-axis, as indicated in the graph.

Parameters:	$a[\mu m]$	$b[\mu m]$	$D_{\text{cyt}}[\mu m^2 s^{-1}]$	$k^{\text{on}}_{\text{a/p}}[\mu m s^{-1}]$	$k^{\text{off}}_{\text{a/p}}[\,s^{-1}]$	$k_{\text{Ap}}[\mu m s^{-1}]$	$k_{\text{Pa}}[\mu m s^{-1}]$
	27	15	30	0.1	0.005	0.4	1.2

Parameters:	$k_{\text{d}}[\mu m^2 s^{-1}]$	$D^{\text{a}}_{\text{mem}}[\mu m^2 s^{-1}]$	$D^{\text{p}}_{\text{mem}}[\mu m^2 s^{-1}]$	$\lambda[\,s^{-1}]$	$\rho_{A_1}[\mu m^{-2}]$	$\rho_{A_2}[\mu m^{-2}]$	$\rho_P[\mu m^{-2}]$
	0.034	0.28	0.15	0.3	8.0	2.5	8.0

Table 1: Parameters used to create Fig. 3-5.

Fig. 3: For the sweep using linear stability analysis in Fig. 3 **C** all parameters but λ and D_{cyt} were chosen as shown in this Table. λ was varied between $5 \cdot 10^{-3}\, s^{-1}$ and $0.35\, s^{-1}$ with a uniform spacing of $5 \cdot 10^{-3}\, s^{-1}$. D_{cyt} was varied from $6\, \mu m^2 s^{-1}$ to $38\, \mu m^2 s^{-1}$ with a uniform spacing of $2\, \mu m^2 s^{-1}$. **Fig. 4**: For the linear stability analysis sweep in Fig. 4 **A,B** all parameters but λ and k_{Ap} and k_{Pa} were chosen as above. k_{Ap} was varied between $0.02 \mu m s^{-1}$ and $0.8 \mu m s^{-1}$ and k_{Pa} was varied between $0.06 \mu m s^{-1}$ and $1.6 \mu m s^{-1}$; for both parameters values were uniformly spaced with distance $0.02 \mu m s^{-1}$. **Fig. 5**: For the linear stability analysis sweeps in Fig. 5 all parameters but the densities ρ_{A_1}, ρ_{A_2} and ρ_P, λ and k_{Ap} were set as shown above. For all triples of densities $\rho_{A_2} = [\mu m^{-2}]$ while ρ_{A_1} and ρ_P were varied accordingly. The simultaneous sweep of ℓ and $k_{\text{Pa}}/k_{\text{Ap}}$ was obtained by varying λ and k_{Pa} for fixed $D_{\text{cyt}} = 30\, \mu m^2 s^{-1}$ and $k_{\text{Ap}} = 0.4 \mu m s^{-1}$.The values of ℓ were uniformly spaced from $2 \mu m$ to $62 \mu m$ with distance $2 \mu m$. The ratio $k_{\text{Pa}}/k_{\text{Ap}}$ was varied from 0.7 to 8.0 with uniform steps of 0.05.

k_{Ap}	k_{Pa}	steady state	onset
0.44	1.68	no pattern	no pattern
0.46	1.62	no pattern	no pattern
0.48	1.56	no pattern	no pattern
0.5	1.5	short-axis polarisation	short-axis
0.52	1.44	short-axis polarisation	short-axis
0.54	1.38	short-axis polarisation	short-axis
0.56	1.32	short-axis polarisation	long-axis
0.58	1.26	short-axis polarisation	long-axis
0.6	1.2	no pattern	no pattern

Table 2: FEM sample sweeps of k_{Ap}, k_{Pa} with small initial perturbation (1%) for $\lambda = 0.3s^{-1}$.

k_{Ap}	k_{Pa}	steady state	onset
0.44	1.68	no pattern	no pattern
0.46	1.62	no pattern	no pattern
0.48	1.56	no pattern	no pattern
0.5	1.5	long-axis polarisation	long-axis
0.52	1.44	long-axis polarisation	long-axis
0.54	1.38	long-axis polarisation	short-axis
0.56	1.32	long-axis polarisation	short-axis
0.58	1.26	long-axis polarisation	short-axis
0.6	1.2	no pattern	no pattern

Table 3: FEM sample sweeps of k_{Ap}, k_{Pa} with small initial perturbation (1%) for $\lambda = 0.05s^{-1}$

Parameters:	$a[\mu m]$	$b[\mu m]$	$D_{\text{cyt}}[\mu m^2 s^{-1}]$	$k^{\text{on}}_{\text{a/p}}[\mu m s^{-1}]$	$k^{\text{off}}_{\text{a/p}}[\,s^{-1}]$	$k_{\text{Ap}}[\mu m^2 s^{-1}]$	$k_{\text{Pa}}[\mu m^2 s^{-1}]$
	27	15	30	0.1	0.005	0.4	1.2

Parameters:	$k_{\text{d}}[\mu m^3 s^{-1}]$	$D^{\text{a}}_{\text{mem}}[\mu m^2 s^{-1}]$	$D^{\text{p}}_{\text{mem}}[\mu m^2 s^{-1}]$	$\lambda[\,s^{-1}]$	$\rho_{A_1}[\mu m^{-3}]$	$\rho_{A_2}[\mu m^{-3}]$	$\rho_P[\mu m^{-3}]$
	0.034	0.28	0.15	0.3	8.0	2.5	8.0

Table 4: Parameters for three-dimensional FEM simulations. For the sweeps shown in Fig. 6 all parameters but λ and D_{cyt} were chosen as shown in this Table. λ was varied between $3 \cdot 10^{-2}\,s^{-1}$ and $0.3\,s^{-1}$ with a uniform spacing of $3 \cdot 10^{-2}\,s^{-1}$. D_{cyt} was varied from $2\,\mu m^2 s^{-1}$ to $32\,\mu m^2 s^{-1}$ with a uniform spacing of $2\,\mu m^2 s^{-1}$.

Geometric cues stabilise long-axis polarisation of PAR protein patterns in *C. elegans*

– Supplementary Document –

Raphaela Geßele, Jacob Halatek, Laeschkir Würthner & Erwin Frey*
Arnold Sommerfeld Center for Theoretical Physics
and Center for NanoScience, Department of Physics,
Ludwig-Maximilians-Universität München,
Theresienstraße 37, 80333 München, Germany.

SUPPLEMENTARY NOTES

Following the structure of the main text, Supplementary Note 1 discusses further aspects of cell polarisation in two-dimensional elliptical geometry using finite element simulations: excitable region in parameter space, and time evolution of the polarisation axis. Supplementary Note 2 summarises experimental information on protein numbers. In Supplementary Note 3 we show why it is not sufficient to use a planar geometry in order to learn about the selection of the polarisation axis. The membrane-to-bulk ratio in two-dimensional elliptical and three-dimensional ellipsoidal geometry is summarised in Supplementary Note 4. In order to challenge the hypothesis of interface minimisation, in Supplementary Note 5 the results on axis selection in oblate and prolate geometries are discussed. To understand the relative role of the activation-deactivation cycle and interface minimisation an extensive set of finite element simulations was performed and the results are discussed. Supplementary Note 6 and 7 show that interface minimisation arises from flux minimisation. Finally, in Supplementary Note 8 patterning time scales are provided and discussed.

Supplementary Note 1

Stimulus-induced polarisation and transient polarisation alignment. In the wild type *C. elegans* embryo polarisation is established by an interplay between mechanical cues (forces of the centrosome after male sperm entry and actomyosin contraction towards the anterior) and the PAR reaction diffusion system. In the main text we focused on spontaneous pattern formation facilitated by a Turing instability. Here, we investigate whether the Turing instability is subcritical, i.e. whether patterns can be induced (stimulated) by large perturbations outside the Turing unstable region, such as the fertilization event. To this end, we performed FEM simulations that were initiated with linear concentration gradients along the membrane as initial conditions. The gradient was chosen to favor selection of a pattern aligned with the same polarisation axis as predicted by linear stability analysis.

Specifically, for $\lambda = 1s^{-1}$ (fast reactivation) shown in Supplementary Figure 1(**A**) top row, the gradient was chosen along the short axis, i.e. the aPAR concentrations were multiplied by $(1 + y/b)$ and the pPAR concentrations by $(1 - y/b)$, where $2b$ is the length of the short axis. For $\lambda = 0.05s^{-1}$ (slow reactivation) shown in Supplementary Figure 1**(B)** top row, the gradient was aligned along the long axis, i.e. the aPAR concentrations was multiplied with $(1 + x/a)$ and the pPAR concentrations with $(1 - x/a)$, where $2a$ is the length of the long axis. Indeed, in both cases we found a large parameter domain outside the regime of spontaneous polarisation where pattern formation can be triggered by finite perturbations. The specific sets $(k_{\mathrm{Ap}}, k_{\mathrm{Pa}})$ for which the system was tested for stimulus-induced pattern formation are provided in the Tables 1, 2 and 3. In Supplementary Figure 1 we extrapolated from this data to find an outer cone of the excitable region (dashed lines in the k_{Ap}-k_{Pa} diagrams).

Furthermore, in the Turing unstable regime we tested alignment of polarisation when the initial condition in the FEM simulation was chosen to select for the pattern orthogonal to the polarisation axis predicted by linear stability analysis. For all sets of parameters

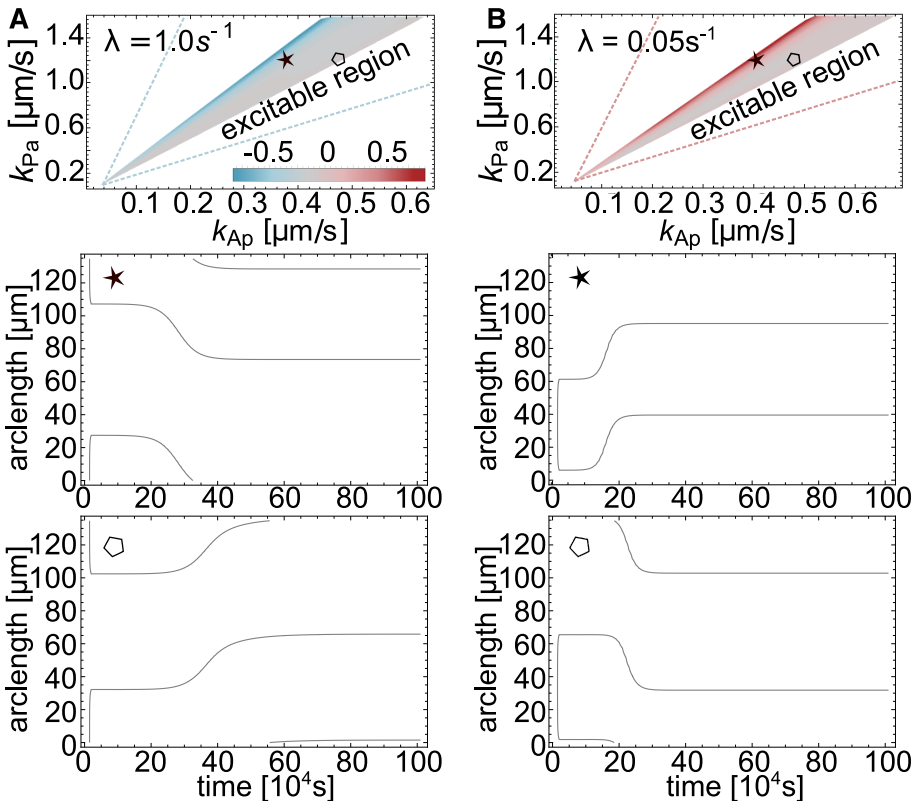

Supplementary Figure 1. Testing the steady state polarity axis with initial gradients. (**A,B**) top row: Investigation of excitable region. The cones show the results of a linear stability analysis in the 2d ellipse as a function of k_{Ap} and k_{Pa} with the color code indicating the normalized difference of the first even and odd growth rate, $\delta\sigma$ (same color code as in Fig. 4 of the main text, i.e. even mode grows faster: red, odd mode grows faster: blue, $\delta\sigma \approx 0s^{-1}$: gray). These Turing-unstable regions are flanked by parameter regimes (bounded by dashed lines), where patterns can only be induced by a large enough stimulus acting on the uniform state; we call this the excitable region. Parameters as in Table 1 of the main text. (**A,B**) Middle and bottom row: Investigation of polarisation re-alignment. The black lines indicate the interface position between aPAR and pPAR domain. Shown are sample interface trajectories from FEM simulations for parameters at the upper (star) and lower (hexagon) bound of the Turing-unstable regime. In contrast to the top row of the Figure, here the FEM simulations were initialised with gradients aligned perpendicularly to the predicted pattern orientation (gradients as above, but orthogonal to predicted polarisation alignment, for mathematical definition see text). We find that the initial polarisation axis is aligned with the initial gradient while the final pattern is dictated by the reactivation cycle. k_{Ap} and k_{Pa} do not impact this qualitatively but only the transition time from one to the other polarisation axis.

$(k_{\mathrm{Ap}}, k_{\mathrm{Pa}})$ which we tested we found that the final steady state was the same as the one predicted by linear stability analysis (at the upper bound of $(k_{\mathrm{Pa}}, k_{\mathrm{Ap}})$ where $\delta\sigma$ is decisively above or below zero). However, a transiently lasting polarisation along the axis of the initial gradient was observed (see Supplementary Figure 1 middle and bottom row). In detail, for fast $\lambda = s^{-1}$ the initial gradient is aligned with the long axis, i.e. the original

aPAR concentrations were multiplied with $(1+x/a)$ and the pPAR concentrations with $(1-x/a)$. Polarisation establishes along the long axis first (for both pairs of (k_{Ap}, k_{Pa}) in Supplementary Figure 1, "star" and "hexagon"), and then transitions to align with the short axis where it then finds its steady state. This turning of the polarisation axis starts later for lower k_{Pa}/k_{Ap} ratios (compare Supplementary Figure 1, bottom row). For slow $\lambda = 0.05 s^{-1}$ we find just the opposite behaviour: Initial short axis polarisation establishes aligned with the gradient but then turns towards steady state long axis polarisation. The time of turning again depends on the ratio k_{Pa}/k_{Ap}.

Supplementary Note 2

Total and relative protein numbers. For the PAR protein system in *C. elegans*, many parameters have been measured including relative and total protein numbers, binding and unbinding rates, and diffusion constants of proteins on the membrane [1–4]. However, measurements of the PAR protein density were reported with a relatively large uncertainty; according to the Supplementary Material in Ref. [1] with a relative error larger than 20%. Most recent experiments report total PAR protein densities between 2 and 6 proteins per μm^3 if all proteins were evenly distributed in the cytosol (depending on the specific PAR protein) [4]. We used the corresponding order of magnitude of total protein numbers (see Table 1 of the main text) for our studies and further investigated relative abundances of proteins (see the relative density variations $[P]/[A_2]$ and $[A_1]/[A_2]$ discussed in Section "Robustness of polarisation as well as axis selection depend on the relative protein densities") and Fig. 5 in the main text).

Supplementary Note 3

Planar geometry: the characteristic lengthscale does not select the axis. Is it possible to simplify the geometry of a cell in order to answer the question of axis selection for cell polarisation? A heuristic argument in favor of a positive answer would be: Let's simplify to a planar geometry as illustrated in Fig 2 A, and perform a linear stability analysis. This will yield a fastest growing mode at some characteristic wavelength. Intuitively, one may now expect that in elliptical geometry those axis is selected which length fits this characteristic wavelength best. Is this intuition correct?

To answer this question, we investigated the PAR model in planar geometry and compared it with the results that we obtained in elliptical and ellipsoidal geometry (main text). The linear stability analysis was performed in a rectangular two-dimensional geometry (x, z) with variable width and fixed height h that matches the short half-axis b of the ellipsoidal cell; see Supplementary Figure 2 A. The membrane is at the bottom, $z = 0$, where we assume reactive boundary conditions. For symmetry reasons we assume no-flux boundary conditions at $z = b$. The details of the linear stability analysis can be found in Ref. [5]. The

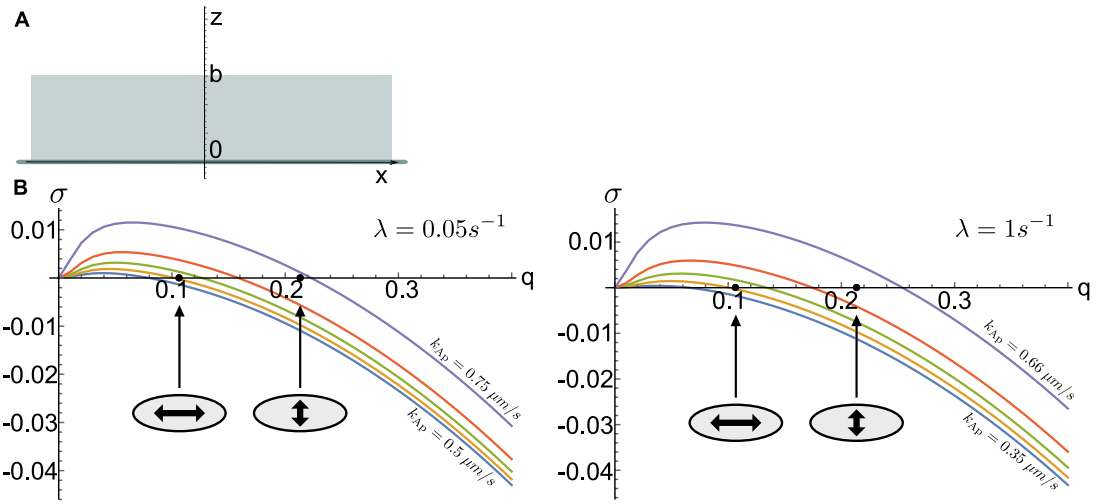

Supplementary Figure 2. Linear stability analysis in planar geometry. (**A**) Illustration of a planar geometry with membrane at the bottom, $z=0$, and cytosol of height $h=b$. (**B**) Dispersion relations in rectangular geometry for $\lambda=0.05\,\mathrm{s}^{-1}$ (left, long-axis selection in the ellipse) and $\lambda=1\,\mathrm{s}^{-1}$ (right, short-axis selection in the ellipse), showing that the fastest growing mode depends sensitively on k_{Ap}. The filled black circles highlight the length scales corresponding to long axis polarity $q=\pi/(2a)$ and short axis polarity $q=\pi/(2b)$. Naively, the stability analysis in rectangular geometry suggests that modes with large length scale (long axis polarity) are always preferred, contradicting the correct results from the simulations and linear stability analysis in elliptical geometry.

numerical values of all parameters are unchanged (i.e. as in Table 1 in the main text), except the attachment rates $k^{\mathrm{on}}_{\mathrm{a/p}}$ which we rescaled to $0.3\mu m s^{-1}$] to recover the lateral (Turing) instability of the unpolarised aPAR state. A parameter sweep of the phosphorylation rate constant k_{Ap} for $\lambda=0.05\,\mathrm{s}^{-1}$ (long axis selection in the ellipse) and $\lambda=1\,\mathrm{s}^{-1}$ (short axis selection in the ellipse) shows that the band of unstable modes and the *fastest growing mode* (the mode which determines the *characteristic length scale* at onset) sensitively depend on k_{Ap} but not on λ. Furthermore, we find that the *fastest growing mode* corresponds to a *characteristic length scale* which is always longer than the short axis of the cell, $2b$, and can be tuned to fit the long axis, $2a$ (see also marks in the dispersion relation in Supplementary Figure 2 B). Following the heuristic argument one would conclude that the long axis is chosen for polarisation because it fits better into the cell. However, our results in the main text demonstrate that axis selection in cellular geometry is determined by cytosolic parameters such as λ and D_{cyt}, but effects by k_{Ap} are negligible. Hence, we conclude that the *characteristic length scale* determined by linear stability in planar geometry does neither inform about axis selection in elliptical nor ellipsoidal geometry.

We find that pattern alignment is a process which strongly depends on the distribution of binding active proteins in the cytosol. For our model pattern alignment is not dictated by the wavelength of a pattern but rather by the reactivation length ℓ^* and the topology of the domain interfaces.

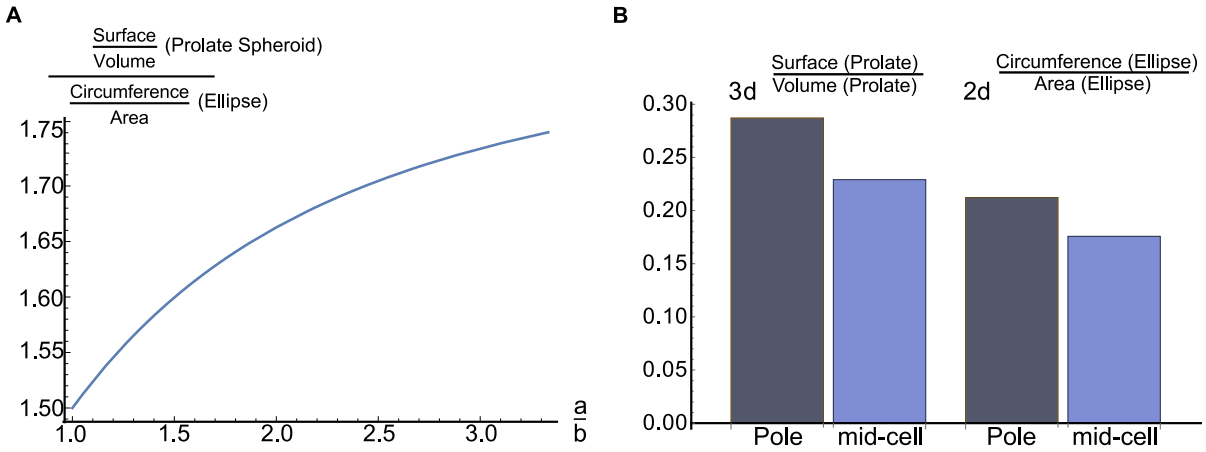

Supplementary Figure 3. Membrane-to-bulk ratio for a two-dimensional (2d) ellipse and a three--dimensional (3d) prolate spheroid. (**A**) The *overall* membrane-to-bulk ratio (integrated over the whole cell boundary) of a prolate spheroid is compared to that of an ellipse with the same minor and major axes as a function of the aspect ratio a/b. (**B**) The *local* membrane-to-bulk ratio (as defined in the main text of the supplement) of a prolate spheroid and an ellipse, both at the cell poles and at midcell. The membrane-to-bulk ratio was calculated for some sample diffusion length $\ell_D = 7.5 \mu m$.

Supplementary Note 4

Membrane-to-bulk ratio for ellipses and prolate spheroids. In the main text we showed that the membrane-to-bulk ratio is a key factor for axis selection, especially during the initial phase of pattern formation. How does this ratio depend on the dimensionality of the system? Figure 3**A** compares the *overall* membrane-to-bulk ratio — the ratio of area/circumference of the membrane to volume/area of the cytosol ('bulk') — for a two-dimensional ellipse and a three-dimensional prolate spheroid (ellipsoid). One observes that this ratio is in general larger for a prolate spheroid, and the surplus is increasing with the aspect ratio a/b.

The *local* membrane-to-bulk ratio varies qualitatively in a similar fashion for the two- and three-dimensional case: it is maximal at the poles and decreases monotonously towards midcell where it reaches its minimum. In order to see this quantitatively we have calculated the membrane-to-bulk ratio for a sample diffusion length ($\ell_D = 7.5\,\mu m$) at the poles and at midcell for an ellipse and a prolate spheroid; see Supplementary Figure 3**B**. To determine the membrane-to-bulk ratio at the poles, we defined a sphere with the sample diffusion length $\ell_D = 7.5\,\mu m$ as radius and center at the cell pole. Then we calculated the membrane region of the ellipse (2d) or ellipsoid (3d) which lies within this sphere. This gives the membrane part of the membrane-to-bulk ratio. The bulk part was calculated by the intersecting region of the ellipse (2d) or ellipsoid (3d) with the sphere. Similarly, we defined the membrane to bulk ratio at midcell with the help of a sphere with radius ℓ_D and center at the midcell membrane. We find that quantitatively, the change in the local membrane-to-bulk ratio from midcell to pole is more pronounced in a three-dimensional prolate spheroid than in a

two-dimensional ellipse.

Supplementary Note 5

The role of interface length for the selection of the polarity axis. We argued in the main text, that axis selection during cell polarisation is determined by an interplay between two effects: The higher membrane-to-bulk ratio at the cell poles favors short-axis selection for small enough reactivation lengths ℓ. Otherwise, long-axis polarisation is favored. This is confirmed by our studies for two-dimensional ellipses; see also Method Section *The critical reactivation rate to switch steady state polarity*. On the other hand, we have argued in the main text that there is a tendency of the dynamics to minimize the length of the interface between aPAR and pPAR domains, which would always favor long-axis polarisation.

In this section we give a detailed account of FEM simulations Comsol Multiphysics 5.4 for various three-dimensional ellipsoidal geometries including both prolate and oblate spheroids; see Tables 4, 5. The goal is to clarify the relative role of the membrane-to-bulk ratio and the interface length in the axis selection process.

a. ***Perimeter ratio for long- and short-axis polarisation in prolate and oblate spheroid geometries.*** The interface length for short-axis polarisation, L_{short}, and long-axis polarisation, L_{long} are different for an ellipsoidal geometry. There is a difference between prolate and oblate geometries insofar as the ratio of the interface length for long- and short-axis polarisation, $L_{\text{long}}/L_{\text{short}}$ (short: perimeter ratio), differs; for an illustration see Supplementary Figure 4.

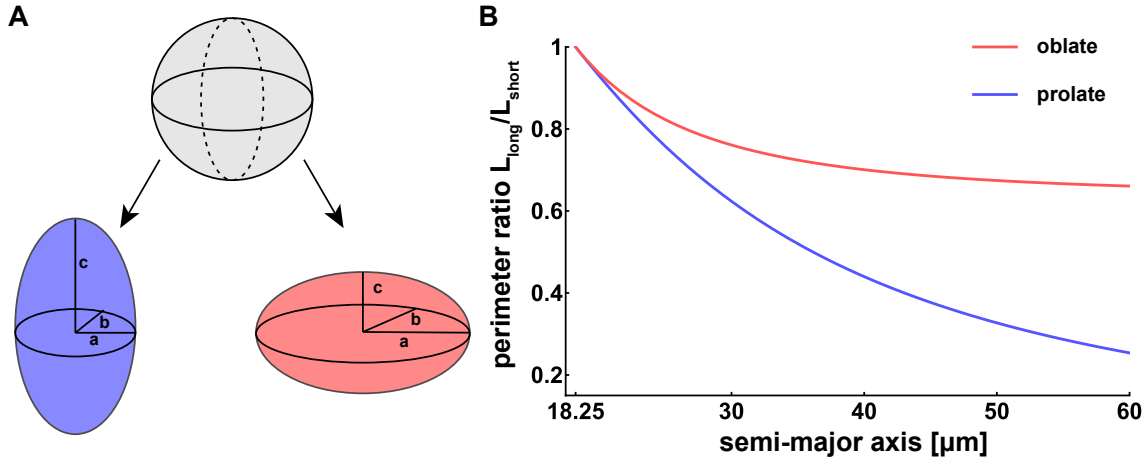

Supplementary Figure 4. Perimeter ratio for an oblate and a prolate spheroid. **(A)** Smooth deformation of a sphere (top) to a prolate spheroid (bottom, left) or to an oblate spheroid (bottom, right) with the same volume as the sphere. Note that for a prolate $a = b < c$ while for an oblate $a = b > c$. **(B)** The perimeter ratio, $L_{\text{long}}/L_{\text{short}}$, as a function of the length of the semi-major axis for an oblate (red curve) and a prolate spheroid (blue curve) with the same volume as a sphere of radius $R = 18.25\,\mu m$

We compare the perimeter ratio $L_{\text{long}}/L_{\text{short}}$ for three-dimensional ellipsoids of the same volume. As our reference system we us a prolate spheroid with axes $15\,\mu m - 15\,\mu m - 27\,\mu m$, i.e. $a = b = 15\mu m$ (semi-minor axis) and $c = 27\,\mu m$ (semi-major axis). This is the same geometry that has been used to generate the results shown in the main text. The volume of an ellipsoid is $V_{\text{ellipsoid}} = \frac{4\pi}{3}a^2c$, corresponding to a sphere of same volume with radius $R = (a^2c)^{1/3} = 18.25\,\mu m$. Note that in contrast to a prolate spheroid, for an oblate spheroid a and c correspond to the semi-major and semi-minor axis, respectively; for an illustration see Supplementary Figure 4A.

Figure 4B shows the perimeter ratio for prolate (blue) and oblate (red) spheroids as a function of the semi-major axis (c for prolate and a for oblate). Due to spherical symmetry, the perimeter ratio between long- and short-axis polarisation is equal to 1 for a sphere. For small deviations from spherical geometry (semi-major axis comparable with the radius of the sphere $R = 18.25\mu m$), the perimeter ratios in the prolate and oblate geometries are nearly the same. For larger deviations, however, the perimeter ratio for a prolate geometry becomes significantly smaller than for an oblate geometry. This difference suggests that long-axis polarisation is more favourable for a prolate spheroid than for an oblate spheroid.

b. ***Axis selection for an oblate spheroid.*** As a representative example we analyzed pattern formation in an oblate spheroid with axes $35\,\mu m - 35\,\mu m - 13.2\,\mu m$ and the same volume as a sphere with radius $R = 18.25\,\mu m$ corresponding to a perimeter ratio of 0.72; note the smaller perimeter ratio 0.52 for a prolate spheroid with the same volume and semi-major axis $35\,\mu m$. We performed an extensive set of FEM simulations sweeping both λ and D_{cyt} in a range between $0.01\,s^{-1} - 0.3\,s^{-1}$ (with step size $0.01\,s^{-1}$) and $1.0\,\mu m^2 s^{-1} - 20\,\mu m^2 s^{-1}$ (with step size $1\,\mu m^2 s^{-1}$), respectively, and determined the steady state solution of the reaction-diffusion model. Figure 5A shows a "phase diagram" indicating the parameter regimes where the polarisation axis is oriented along the long or short axis or along some intermediate axis (diagonal). We find that there is indeed a parameter regime where short-axis polarisation is stable, namely for D_{cyt} smaller than approximately $5\,\mu m^2 s^{-1}$ and independent of the value of λ. This suggests that weak cytosolic flows are required for stable short-axis polarisation. Interestingly, there is no direct transition between stable short-axis and stable long-axis polarisation but an intermediary regime where the stable polarisation axis is aligned at an intermediate orientation. This indicates a subtle interplay between interface length minimisation and effects due to bulk-to-boundary ratios in this region of the $\lambda - D_{\text{cyt}}$ parameter space.

c. ***Axis selection for a prolate spheroid.*** We have just learned that for a large perimeter ratio in an oblate spheroid one can find parameter regimes where short-axis polarisation is stable. However, for the prolate spheroid with the same volume (axes $15\mu m - 15\mu m - 27\mu m$) we only find metastable short-axis polarisation (see section *three-dimensional cell geometry and the role of interface length* and Fig. 6 in the main text). We hypothesize that this is due to the smaller perimeter ratio if compared to an oblate with the same volume (see Supplementary Figure 4).

It is, however, not clear whether short-axis polarisation is always metastable in any prolate spheroids. If the perimeter ratio is indeed an important factor, it should be possible to find

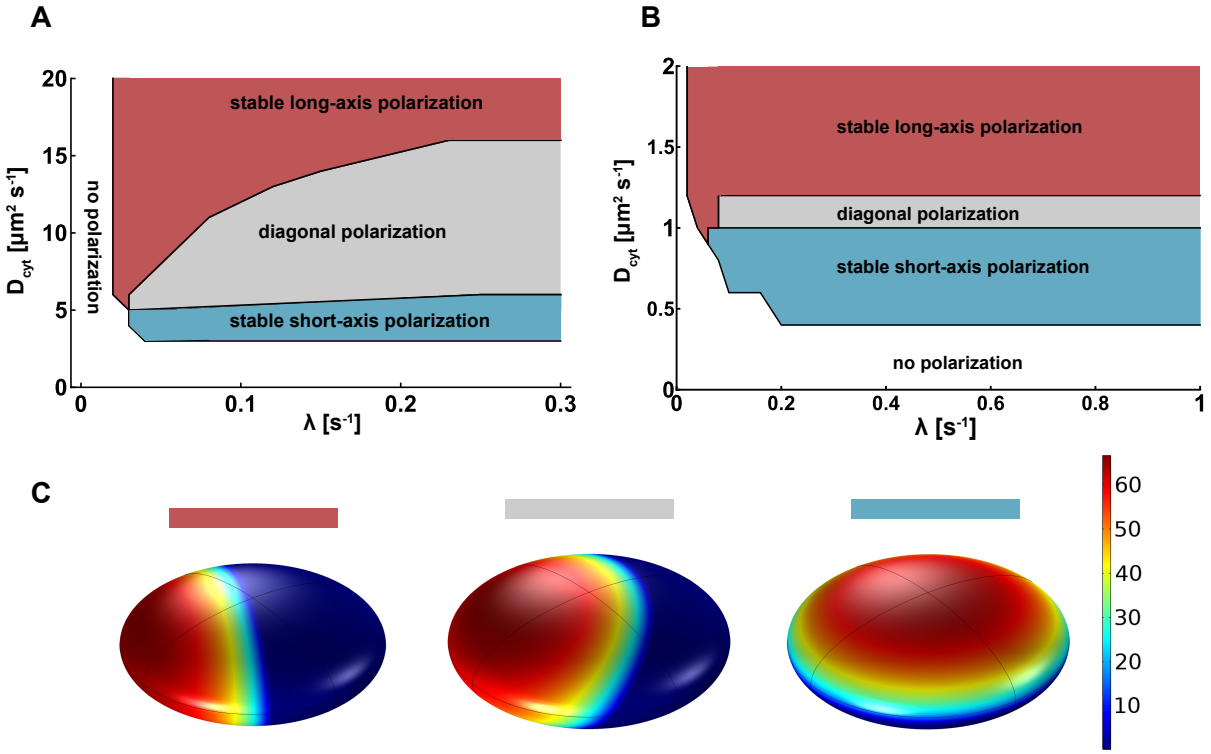

Supplementary Figure 5. Axis selection for oblate and prolate spheroids. Stable polarisation axis in steady state as obtained from FEM simulations for an oblate (**A**) and a prolate spheroid (**B**) in the $\lambda - D_{\text{cyt}}$ parameter space. For an oblate spheroid (**A**), we find that short-axis polarisation is stable for small values of D_{cyt} (shaded cyan region) quite independent of the value for λ, while long-axis polarisation is stable for sufficiently large D_{cyt} and small λ (shaded red region), similar to our findings for two-dimensional ellipses (Fig. 3 in the main text). The transition from stable short-axis polarisation to long-axis polarisation is not abrupt but there is an intermediary region where the pattern aligns along the diagonal (shaded grey region). For a prolate spheroid (**B**), we find similar results but for different parameter regimes. Long-axis polarisation is stable for sufficiently large D_{cyt} (shaded red region), and the regime with diagonal polarisation is less pronounced. (**C**) Typical steady state patterns as obtained from the corresponding parameter combinations in **(A)** and **(B)** (red, grey, and cyan shaded area) shown for an oblate spheroid.

stable short-axis polarisation for a prolate spheroid that has a perimeter ratio comparable with an oblate spheroid (as is the case for prolate spheroids that are almost spherical, cf. Supplementary Figure 4B). To test this, we performed an extensive set of FEM simulations for a prolate spheroid with axes $16.6\,\mu m - 16.6\,\mu m - 22\,\mu m$, corresponding to a perimeter ratio of 0.86; note that an oblate with the same volume and semi-major axis $22\,\mu m$ gives a perimeter ratio of 0.88. We used parameter for λ and D_{cyt} ranging between $0.01 s^{-1} - 1.0 s^{-1}$ (with step size $0.01 s^{-1}$) and $0.4 \mu m^2 s^{-1} - 3 \mu m^2 s^{-1}$ (with step size $0.2 \mu m^2 s^{-1}$). Similar to the oblate case we indeed find that short-axis polarisation can be stabilized for a small parameter region in the $\lambda - D_{\text{cyt}}$ space and that the two regions (stable long- and short--axis polarisation) are connected by a regime where the pattern aligns along the diagonal (Supplementary Figure 5B). The parameter range for such an intermediate polarisation is,

however, significantly smaller as for the oblate case.

Supplementary Note 6

Minimisation of the average net cytosolic protein flux onto the membrane explains interface minimisation. To shed more light on the observed interface minimisation in three-dimensional ellipsoidal geometries we analysed the net cytosolic protein fluxes onto the membrane for the different pPAR and aPAR protein species:

$$J_{\rm net}^{(\rm P)} = D_{\rm cyt}\nabla_\perp c_P + D_{\rm cyt}\nabla_\perp c_{P^*} = k_p^{\rm off}\, m_P - k_p^{\rm on}\, c_P + k_{Pa}\, m_P\, m_{A_{12}}\,, \tag{1}$$

$$\begin{aligned} J_{\rm net}^{(\rm A_1)} &= D_{\rm cyt}\nabla_\perp c_{A_1} + D_{\rm cyt}\nabla_\perp c_{A_1^*} \\ &= k_a^{\rm off}\,(m_{A_1} + m_{A_{12}}) - k_a^{\rm on} c_{A_1} + k_{Ap}\, m_P\,(m_{A_1} + m_{A_{12}})\,, \end{aligned} \tag{2}$$

$$J_{\rm net}^{\rm A_2} = D_{\rm cyt}\nabla_\perp c_{A_2} = \left(k_{Ap}\, m_P + k_a^{\rm off}\right) m_{A_{12}} - k_d c_{A_2} m_{A_1}\,, \tag{3}$$

see also in the Methods Section the paragraph on reactive boundary conditions.

Strikingly, we find that all of the local net protein fluxes $J_{\rm net}^{(\rm P/A_{1,2})}$ remain constant as the pattern rotates from short- to long-axis polarisation; as an example the pPAR flux is shown in Supplementary Figure 6. Hence, one expects that the averages of the absolute values of the net membrane fluxes integrated over the whole membrane area $\partial\Omega$

$$\overline{J}^{(\rm P/A_{1,2})} = \int_{\partial\Omega} |J_{\rm net}^{(\rm P/A_{1,2})}|\,{\rm d}S \,/ \int_{\partial\Omega} {\rm d}S \tag{4}$$

are expected to be larger for short-axis polarisation than for long-axis polarisation, simply due to the larger interface perimeter. This is indeed the case: for the pPAR flux shown in Supplementary Figure 6, we find that the average absolute net flux ratio between long- and short-axis polarisation is $\overline{J}^{(\rm P)}_{\rm long}/\overline{J}^{(\rm P)}_{\rm short} = 0.66$. This indicates that long-axis polarisation is maintained by a smaller total protein flux and is therefore more favourable.

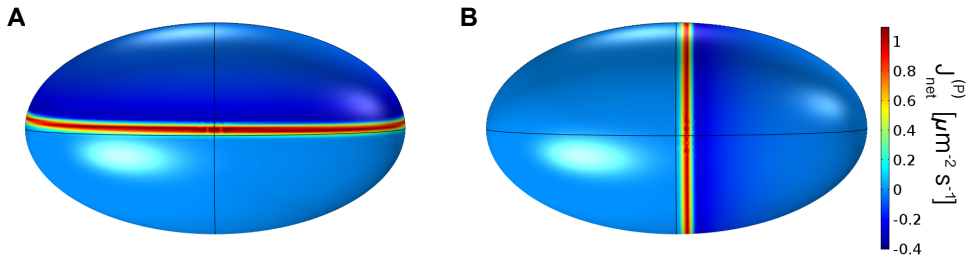

Supplementary Figure 6. Illustration of protein fluxes onto the membrane. (**A**) A snapshot of the net flux $J_{\rm net}^{(\rm P)}$ of pPAR proteins where the system is polarised in a metastable state (short-axis polarisation) is shown. (**B**) A snapshot of the net flux $J_{\rm net}^{(\rm P)}$ of pPAR proteins where the system is polarised in a long-axis polarised is shown. The net flux of pPAR proteins along the interface has the same local magnitude for the steady state with long-axis polarisation as for the metastable short-axis polarisation. All parameters are set as in Table 6.

Supplementary Note 7

Cytosolic fluxes depend on the cytosolic diffusion and dictate the transition time from short to long axis polarisation. As discussed in the main text and shown there in Fig. 6, the transition time from short- to long-axis polarisation (for a 3d prolate spheroid) depends on both the reactivation rate λ and the cytosolic diffusion D_{cyt}. However, this dependence is not simply explained by the reactivation length ℓ alone, since our results show that actually the dependence on the cytosolic diffusion constant D_{cyt} is decisively stronger than that on λ. Because the transition from short- to long-axis polarisation (interface minimisation) is driven by protein fluxes, we investigated the cytosolic protein flux for different cytosolic diffusion constants D_{cyt}.

Figure 7A shows the magnitude of the cytosolic flux of species A_1 after the steady state (long-axis polarisation) has been reached. We defined the magnitude of the cytosolic flux as its Euclidean norm:

$$||\mathbf{J}_{A_1}|| = D_{\mathrm{cyt}}\,||\big(\partial_x c_{A_1}, \partial_y c_{A_1}, \partial_z c_{A_1}\big)||\,. \tag{5}$$

This flux decreases with increasing distance from the membrane. Moreover, the lower the

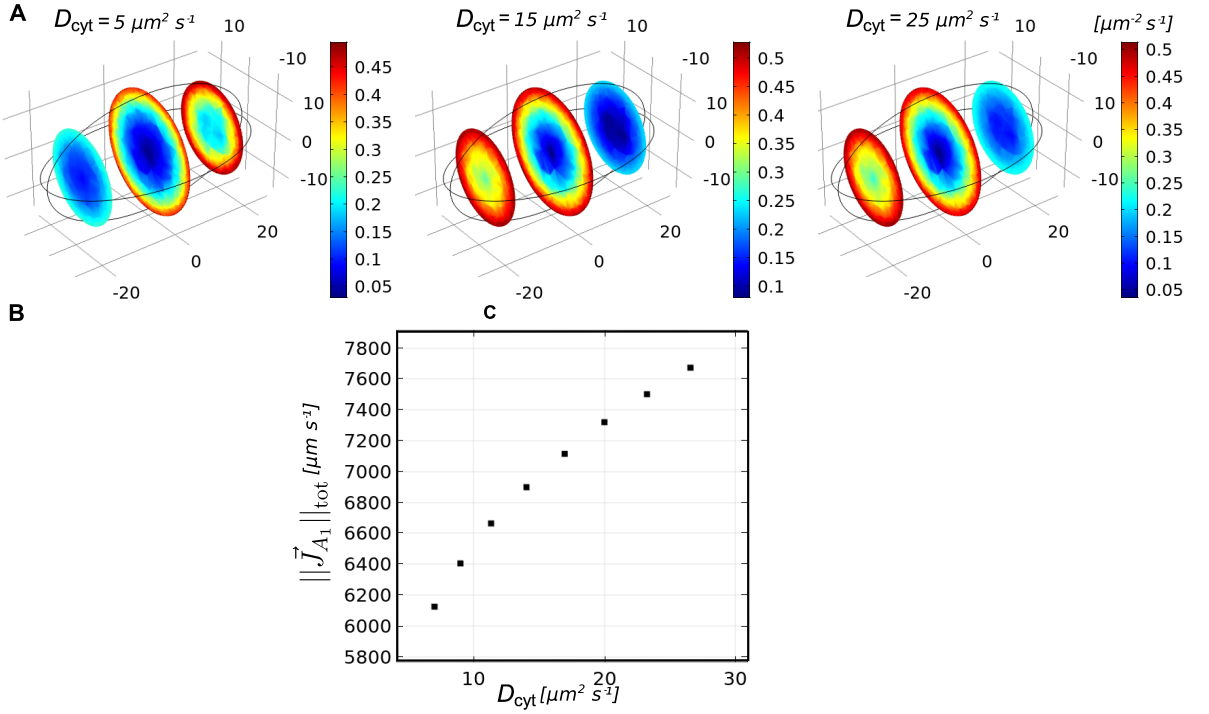

Supplementary Figure 7. Illustration of cytosolic fluxes. (**A**) The magnitudes of cytosolic fluxes of species A_1 for three different cytosolic diffusion constants (indicated in the graph) are shown for three slices through the cytosol at $x = 0\mu m$ and $x = \pm 18\,\mu m$. The reactivation rate was set to $\lambda = 0.15 s^{-1}$ and all other parameters were set as given in the main text table 4. (**B**) The overall cytosolic flux (absolute value of flux integrated over the full cytosolic volume) is shown as a function of the cytosolic diffusion constant.

cytosolic diffusion the steeper are the flux gradients, i.e. the shorter is the penetration depth of the flux from the membrane into the cytosol; the width of the red domains (at midcell) in Supplementary Figure 7A decreases with lowering the diffusion constant from $D_{\rm cyt} = 25\,\mu m^2 s^{-1}$ to $5\,\mu m^2 s^{-1}$. We also notice that the polar cytosolic region shows high cytosolic fluxes on the pPAR-side of the cell, i.e. where the P domain is on the membrane. In contrast, the cytosolic flux of A_1 is very low (blue in Supplementary Figure 7A) in the polar region where A_1 builds the domain on the membrane. Figure 7B shows the magnitude of the cytosolic flux of species A_1 integrated over the whole cytosol (total flux)

$$||\mathbf{J}_{A_1}||_{\rm tot} = D_{\rm cyt} \int_\Omega ||(\partial_x c_{A_1}, \partial_y c_{A_1}, \partial_z c_{A_1})|| \tag{6}$$

as a function of the cytosolic diffusion constant. Clearly, with increasing cytosolic diffusion constant, the overall cytosolic flux is increasing. Together with the observation that the transition times become shorter with increasing cytosolic diffusion constant (see Fig. 6D in the main text) this shows that there is a correlation between faster transition times and higher cytosolic fluxes.

Supplementary Note 8

Time scales for the formation of cell polarisation. In order to determine the time required for the formation of long-axis polarisation, we consider an idealised situation where this is achieved by the PAR reaction-diffusion system alone. For the cell polarisation process in *C. elegans* there is experimental evidence that the localisation of the centrosome as well as the successive actomyosin contraction play an important role in polarity establishment and support its alignment with the long axis ([4, 6, 7]). However, how the PAR reaction-diffusion system acts in concert with actomyosin contraction is not understood in realistic three--dimensional cell geometry. Previous work uses a simplified one-dimensional cell geometry ([1, 4, 8]). Here, we focus (as a first and important step) on the reaction-diffusion pathway alone disregarding any effects due to the PAR interaction with the centrosome or actomyosin contraction and ensuing cytoplasmic flows. This way one can learn how robust and fast reaction-diffusion dynamics on its own can establish long-axis polarisation and what the relative role of other effects like cytoplasmic flow may be. In the actual C. elegans embryo polarisation has to be stable along the long axis for $\approx 15\,$min until the first cell division. Therefore, the time of a possibly existing short- axis polarisation and the transition to the long axis is an important observable for the real system. Hence we ask: How fast is the long axis selected as the stable polarisation axis driven solely by a reaction-diffusion dynamics?

We find that the time scales for the selection and maintenance of different polarisation axes depend on the reactivation rate λ and the cytosolic diffusion $D_{\rm cyt}$ both in a two-dimensional elliptical geometry and in an three-dimensional ellipsoidal geometry (see Fig. 6 in the main text and Supplementary Figure 8). Strikingly, the transition time from short to long axis polarisation is extremely slow in 2d compared to 3d ($\approx 1000\,$min in 2d compared to $\approx 100\,$min for 3d data: compare Supplementary Figure 8 with Fig.6 in the main text). The

transition time from any transient polarisation pattern to a steady state long-axis polarisation pattern may be taken as a proxy for the expected typical time scales of polarisation re-alignment in case of an initially non-aligned cue (e.g. this happens if the centrosome does not localise at the poles initially). Hence, we conclude that for physiological parameters in 2d these times are far too long: a wrong alignment induced by cues or flows can not be corrected by a mechanism based on reaction and diffusion alone. In contrast, our simulations in 3d show that these transition times are short in a broad region of parameter space; compare Supplementary Figure 8 with Fig. 6 in the main text. Therefore, we conclude, that all geometry-sensitive mechanisms of the reaction-diffusion system, as well as the activation--deactivation cycle and interface minimisation, play an important role for cell polarisation in *C. elegans*. Antagonism (of aPARs and pPARs) and recruitment (among aPARs) enables polarisation, fast cytosolic diffusion and the activation-deactivation cycle enable the cell to polarise along the long axis from the beginning on, and interface minimisation always leads to long axis polarisation in the long term. Furthermore, cytosolic diffusion, as it determines the magnitude of fluxes, decisively influences perfect polarity establishment along the long axis on a biologically reasonable time scale. E.g. if the centrosome was originally localised close to mid-cell and would induce an initial polarity alignment with the long axis, fast cytosolic diffusion would rescue such an embryo and polarisation would align with the long axis before cell division.

In contrast to the transition time from any initial polarisation to well aligned long-axis polarisation, the establishment time of the initial polarisation from a homogenous aPAR dominated state on the membrane is strongly dependent on the type of initial perturbations. Take Supplementary Figure1 middle and bottom row as an example in 2d, where polarisation is quickly established with initial gradients (despite of misalignment). The establishment time of any polarisation from a homogenous aPAR dominated state with only a small random initial perturbation is of the order of 30 minutes in 3d and is approximately three times slower in 2d. Therefore, with only a small random initial perturbation the reaction-diffusion system alone does still lead to stable polarisation, but on a time scale that is too slow for the real embryo (see Fig. 8 A for 2d and 3d times).

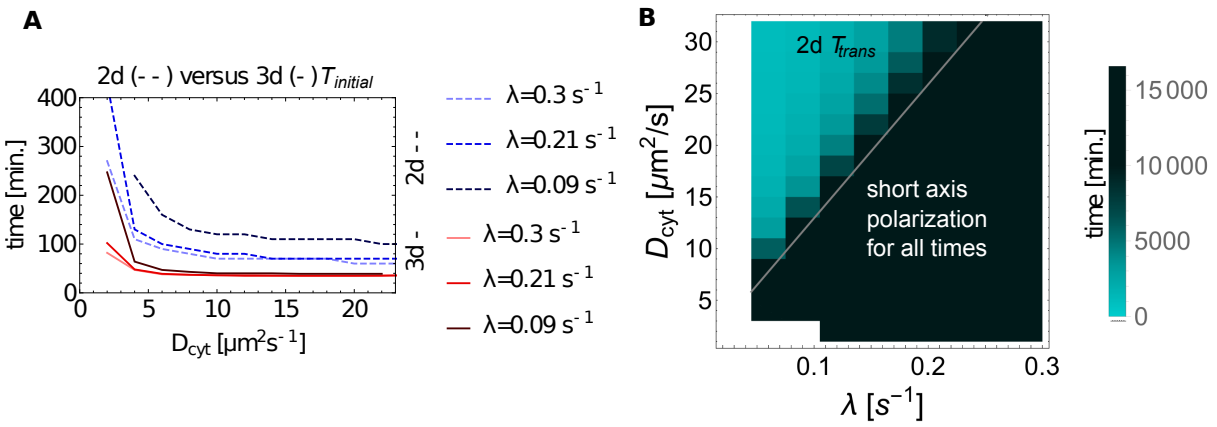

Supplementary Figure 8. **Times in 2d versus 3d**. (**A**) The initial time of polarisation T_{initial} is plotted against the cytosolic diffusion for various reactivation rates in 2d as well as in 3d. (**B**) T_{trans} is shown in cyan color code in the D_{cyt}-λ parameter space. The gray line shows the line of constant reactivation length, which divides steady state long- and short-axis polarisation $\ell^\star$. It was interpolated as a linear function with zero offset.

SUPPLEMENTARY TABLES

k_{Ap}	k_{Pa}	steady state	onset
0.24	2.28	no pattern	transient long axis pol.
0.28	2.16	long axis polarisation	long axis
0.32	2.04	long axis polarisation	long axis
0.36	1.92	long axis polarisation	long axis
0.4	1.8	long axis polarisation	long axis
0.44	1.1.68	long axis polarisation	long axis
0.48	1.56	long axis polarisation	long axis
0.5	1.5	long axis polarisation	long axis
0.52	1.44	long axis polarisation	long axis
0.54	1.38	long axis polarisation	long axis
0.56	1.32	long axis polarisation	long axis
0.58	1.26	long axis polarisation	long axis
0.6	1.2	long axis polarisation	long axis
0.64	1.08	long axis polarisation	long axis
0.68	0.96	long axis polarisation	long axis
0.72	0.84	no pattern	transient long axis pol.
0.76	0.72	no pattern	transient long axis pol.

Supplementary Table 1. **Sweep of antagonistic rates to investigate the excitable region with initial gradients for slow reactivation.** FEM sample sweeps of k_{Ap}, k_{Pa} with initial linear gradient for $\lambda = 0.05 s^{-1}$ (for more details see supplementary section A). The sweep shows that also outside of the spontaneously polarizing region the system can be excited into stable long axis polarisation. All other parameters were set as in the standard parameter set shown in Table 1 of the main text.

k_{Ap}	k_{Pa}	steady state	onset
0.2	2.4	no pattern	transient short axis p.
0.24	2.28	short axis polarisation	short axis
0.28	2.16	short axis polarisation	short axis
0.32	2.04	short axis polarisation	short axis
0.36	1.92	short axis polarisation	short axis
0.4	1.8	short axis polarisation	short axis
0.44	1.1.68	short axis polarisation	short axis
0.48	1.56	short axis polarisation	short axis
0.5	1.5	short axis polarisation	short axis
0.52	1.44	short axis polarisation	short axis
0.54	1.38	short axis polarisation	short axis
0.56	1.32	short axis polarisation	short axis
0.58	1.26	short axis polarisation	short axis
0.6	1.2	short axis polarisation	short axis
0.64	1.08	short axis polarisation	short axis
0.68	0.96	short axis polarisation	short axis
0.72	0.84	no pattern	transient short axis p.
0.76	0.72	no pattern	transient short axis p.

Supplementary Table 2. **Sweep of antagonistic rates to investigate the excitable region with initial gradients for fast reactivation.** FEM sample sweeps of k_{Ap}, k_{Pa} with initial linear gradient for $\lambda = 0.3s^{-1}$ (for more details see supplementary section A). The sweep shows that also outside of the spontaneously polarizing region the system can be excited into stable short axis polarisation. All other parameters were set as in the standard parameter set shown in Table 1 of the main text.

k_{Ap}	k_{Pa}	steady state	onset
0.2	2.4	no pattern	transient short axis p.
0.24	2.28	short axis polarisation	short axis
0.28	2.16	short axis polarisation	short axis
0.32	2.04	short axis polarisation	short axis
0.36	1.92	short axis polarisation	short axis
0.4	1.8	short axis polarisation	short axis
0.44	1.1.68	short axis polarisation	short axis
0.48	1.56	short axis polarisation	short axis
0.5	1.5	short axis polarisation	short axis
0.52	1.44	short axis polarisation	short axis
0.54	1.38	short axis polarisation	short axis
0.56	1.32	short axis polarisation	short axis
0.58	1.26	short axis polarisation	short axis
0.6	1.2	short axis polarisation	short axis
0.64	1.08	short axis polarisation	short axis
0.68	0.96	short axis polarisation	short axis
0.72	0.84	no pattern	transient short axis p.
0.76	0.72	no pattern	transient short axis p.

Supplementary Table 3. **Sweep of antagonistic rates to investigate the excitable region with initial gradients for fast reactivation.** FEM sample sweeps of k_{Ap}, k_{Pa} with initial linear gradient for $\lambda = 1.s^{-1}$ (for more details see supplementary section A). The sweep shows that also outside of the spontaneously polarizing region the system can be excited into stable short axis polarisation. All other parameters were set as in the standard parameter set shown in Table 1 of the main text.

Parameter	Value
a	$13.2\,\mu m$
b	$13.2\,\mu m$
c	$35\,\mu m$
$k_{a/p}^{on}$	$0.1\,\mu m \cdot s^{-1}$
$k_{a/p}^{off}$	$0.005\,s^{-1}$
k_{Ap}	$0.4\,\mu m^2 \cdot s^{-1}$
k_{Pa}	$1.2\,\mu m^2 \cdot s^{-1}$
k_d	$0.15\,\mu m^3 \cdot s^{-1}$
D_{mem}^a	$0.28\,\mu m^2 \cdot s^{-1}$
D_{mem}^p	$0.15\,\mu m^2 \cdot s^{-1}$
ρ_{A1}	$10.5\,\mu m^{-3}$
ρ_{A2}	$2.5\,\mu m^{-3}$
ρ_P	$12.0\,\mu m^{-3}$

Supplementary Table 4. Parameter set for the oblate 3d FEM sweep in Fig. 5. All parameters were fixed to the values shown above except for D_{cyt} and λ. The cytosolic difffusion constant D_{cyt} was varied between $1.0\,\mu m^2 \cdot s^{-1} - 20\,\mu m^2 \cdot s^{-1}$ (with step size of $1\,\mu m^2 \cdot s^{-1}$) and the reactivation rate λ was varied between $0.01\,s^{-1} - 0.3\,s^{-1}$ (with step size of $0.01\,s^{-1}$) to generate the result shown in Fig 5.

Parameter	Value
a	$22\,\mu m$
b	$22\,\mu m$
c	$16.6\,\mu m$
$k_{a/p}^{on}$	$0.1\,\mu m \cdot s^{-1}$
$k_{a/p}^{off}$	$0.005\,s^{-1}$
k_{Ap}	$0.4\,\mu m^2 \cdot s^{-1}$
k_{Pa}	$1.2\,\mu m^2 \cdot s^{-1}$
k_d	$0.15\,\mu m^3 \cdot s^{-1}$
D_{mem}^a	$0.28\,\mu m^2 \cdot s^{-1}$
D_{mem}^p	$0.15\,\mu m^2 \cdot s^{-1}$
ρ_{A1}	$10.5\,\mu m^{-3}$
ρ_{A2}	$2.5\,\mu m^{-3}$
ρ_P	$18.0\,\mu m^{-3}$

Supplementary Table 5. Parameter set for the prolate 3d FEM sweep in Fig. 5. All parameters were fixed to the values shown above except for D_{cyt} and λ. The cytosolic diffusion constant D_{cyt} was varied between $0.4\,\mu m^2 \cdot s^{-1} - 3.0\,\mu m^2 \cdot s^{-1}$ (with step size of $0.2\,\mu m^2 \cdot s^{-1}$) and the reactivation rate λ was varied between $0.01\,s^{-1} - 1.0\,s^{-1}$ (with step size of $0.01\,s^{-1}$) to generate the result shown in Fig 5.

Parameter	Value
a	$27\,\mu m$
b	$15\,\mu m$
c	$15\,\mu m$
D_{cyt}	$10\,\mu m^2 s^{-1}$
λ	$0.2\,s^{-1}$
$k_{a/p}^{on}$	$0.1\,\mu m \cdot s^{-1}$
$k_{a/p}^{off}$	$0.005\,s^{-1}$
k_{Ap}	$0.4\,\mu m^2 \cdot s^{-1}$
k_{Pa}	$1.2\,\mu m^2 \cdot s^{-1}$
k_d	$0.034\,\mu m^3 \cdot s^{-1}$
D_{mem}^a	$0.28\,\mu m^2 \cdot s^{-1}$
D_{mem}^p	$0.15\,\mu m^2 \cdot s^{-1}$
ρ_{A1}	$10.5\,\mu m^{-3}$
ρ_{A2}	$2.5\,\mu m^{-3}$
ρ_P	$8.0\,\mu m^{-3}$

Supplementary Table 6. Parameter set for the pPAR average net membrane flux shown in Fig. 6.

SUPPLEMENTARY REFERENCES

[1] Goehring, N. W. *et al.* Polarization of PAR proteins by advective triggering of a pattern-forming system. *Science* **334**, 1137–1141 (2011).

[2] Goehring, N. W., Hoege, C., Grill, S. W. & Hyman, A. PAR proteins diffuse freely across the anterior-posterior boundary in polarized C. elegans embryos. *J Cell Biol* **193**, 583–594 (2011).

[3] Robin, F. B., McFadden, W. M., Yao, B. & Munro, E. M. Single-molecule analysis of cell surface dynamics in Caenorhabditis elegans embryos. *Nat Methods* **11**, 677–682 (2014).

[4] Gross, P. *et al.* Guiding self-organized pattern formation in cell polarity establishment. *Nat Phys* **15**, 293–300 (2019).

[5] Halatek, J. & Frey, E. Rethinking pattern formation in reaction-diffusion systems. *Nat Phys* **14**, 507–514 (2018).

[6] Nance, J. & Zallen, J. Elaborating polarity: PAR proteins and the cytoskeleton. *Development* 799–809 (2011).

[7] Motegi, F. & Seydoux, G. The PAR network: redundancy and robustness in a symmetry-breaking system. *Philos Trans R Soc Lond B Biol Sci* **368**, 20130010 (2013).

[8] Dawes, A. T. & Munro, E. M. PAR-3 oligomerization may provide an actin-independent mechanism to maintain distinct par protein domains in the early Caenorhabditis elegans embryo. *Biophys J* **101**, 1412–1422 (2011).

2 Localization of Min proteins in *B. subtilis*

In this section, we explain how the localization of the Min protein system in the rod-shaped bacteria *Bacillus subtilis* (*B. subtilis*) is controlled by cell shape and a biochemical template. The following content is based on and uses parts of our paper [131] published in *mBio*. We provide a reprint of the paper in section 2.6.

2.1 Background

Similar as *E. coli*, the rod-shaped Gram-positive bacteria *B. subtilis* also divides precisely at midcell [142]. The machinery that orchestrates binary fission (once assembled at the desired location) is the Z-ring, which consists of self-assembled FtsZ proteins. The Z-ring is a tubulin homologue, and is actually conserved in many different bacteria [143]. The assembly of the Z-ring is precisely guided to midcell by the *B. subtilis* Min protein system, similarly as in *E. coli*. However, the Min system in *B. subtilis* does not oscillate from pole to pole, but rather forms a stationary bipolar gradient that decreases towards midcell [143, 144], and thereby restricts FtsZ assembly to midplane of the cell.

The reason for the absence of oscillations is due to fact that *B. subtilis* lacks MinE. Instead, the Min system consists of the proteins MinD, MinC, MinJ, and DivIVA, where MinC (and the MinCD complex) is the primary FtsZ antagonist and therefore inhibits its assembly [145, 146] (again, analogous as in *E. coli* [147, 148]). The protein DivIVA is known to cooperatively bind to negatively curved membrane regions (such as the cell poles) [149, 150], where it then recruits MinCD and MinJ via as yet unknown pathways. The exact mechanism by which DivIVA targets negatively curved membrane shape is not fully understood. However, since DivIVA can assemble into very large (micrometer-sized) oligomers [151, 152], one possible explanation of curvature-sensing is via "molecular bridging", as proposed in Ref. [150]: DivIVA proteins bound to negatively shaped regions can self-stabilize by forming wire-like structures that touch two opposite points on the (curved) membrane.

MinD does not directly interact with DivIVA, but its localization is controlled by the transmembrane protein MinJ, which acts as an intermediary between MinD and DivIVA [131, 153–155]. Prior to septum formation, the Min system localizes to the poles of the cell [131, 143, 144, 156, 157], where DivIVA seems to act as a biochemical template (spatial cue) for the process. At the onset of cytokinesis, the Min system surprisingly redistributes from the cell poles to the septum, and this redistribution is, again, believed to be initiated by DivIVA, because the local curvature at the septum is greater than at the cell poles [149, 158]. These observations raise two important open questions: (i) What exactly is the role of the Min system in *B. subtilis*? Clearly, Min proteins do not seem to just inhibit

the division machinery at the cell poles, but they also possibly act downstream by preventing FtsZ assembly at former sites of cytokinesis [131, 153–155]. (ii) What is the underlying mechanism that drives Min localization and, in particular, its redistribution from the cell poles to midcell? Theoretical approaches that address the localization of the *B. subtilis* Min system are lacking, mainly because the biochemical reaction network of the Min system remains largely elusive. To the best of our knowledge, there exists only one theoretical work that addresses this question [159]. This work explained Min localization by a reaction-diffusion mechanism and laid an important foundation for the theoretical investigation of protein localization in *B. subtilis*. However, after further experimental studies were conducted, some of the model assumptions turned out to be invalid. Moreover, the Min dynamics was investigated by a simplified one-dimensional model, which certainly erases important geometric effects as we have shown in section 1, especially since DivIVA senses cell shape and accumulates at negatively curved regions.

We therefore developed a minimal theoretical model that addresses Min dynamics in *B. subtilis* in realistic three-dimensional cell geometries (spherocylinder). The model consists of a reaction-diffusion system with spatially inhomogeneous reaction kinetics: motivated by the experimental observations outlined above, we assume that DivIVA acts as a biochemical spatial template for MinD membrane binding. The impact of DivIVA-MinJ complexes on MinD is implicitly accounted for in the model by assuming spatially non-uniform attachment and detachment rates of MinD. Specifically, we assume that MinD binding is enhanced in the presence of DivIVA-MinJ (enhanced recruitment rate) and that DivIVA-MinJ stabilize membrane-bound MinD (reduced detachment rate). Our model correctly reproduces the experimental observations, and shows that Min localization corresponds to a stationary steady state (non-uniform base state of the reaction-diffusion model). We show that the redistribution of MinD from the cell poles to midcell is guided by the same geometric effect as discussed in the previous section for the PAR system. Our results highlight the importance of realistic cell geometries, and further show that the Min dynamics in *B. subtilis* is governed by a highly dynamic process.

2.2 Reaction-diffusion model with non-uniform rates

Similar as for the dynamics in *E. coli*, we assume that MinD diffuses in the cytosol and on the membrane with diffusion coefficients D_{D} and D_{d}, respectively. Cytosolic MinD can only bind to the membrane in its active MinD-ATP state c_{DT} , and detachment from the membrane is facilitated by hydrolysis with basal rate $\tilde{k}_{\mathrm{H}}$ (in the absence of DivIVA). After detachment, MinD is in an inactive MinD-ADP state c_{DD} and can only rebind the membrane after nucleotide exchange with rate

λ. The reaction-diffusion system therefore reads:

$$\frac{\partial}{\partial_t} c_{\mathrm{DD}} = D_{\mathrm{c}} \nabla^2 c_{\mathrm{DD}} - \lambda c_{\mathrm{DD}}\,, \tag{III.2}$$

$$\frac{\partial}{\partial_t} c_{\mathrm{DT}} = D_{\mathrm{c}} \nabla^2 c_{\mathrm{DT}} + \lambda c_{\mathrm{DD}} \tag{III.3}$$

$$\frac{\partial}{\partial_t} m_{\mathrm{d}} = D_{\mathrm{m}} \nabla_{\mathcal{S}}^2 m_{\mathrm{d}} + \left(k_{\mathrm{D}} + \tilde{k}_{\mathrm{dD}}\, m_{\mathrm{d}} \right) c_{\mathrm{DT}} - \tilde{k}_{\mathrm{H}}\, m_{\mathrm{d}}\,. \tag{III.4}$$

$$\tag{III.5}$$

Here, m_d denotes membrane-bound MinD-ATP proteins, and the parameters k_{D} and k_{dD} describe attachment and the basal rate of MinD recruitment to the membrane, respectively. The operator $\nabla_{\mathcal{S}}^2$ is the surface diffusion operator (Laplace-Beltrami operator). These equations are complemented by reactive boundary conditions (flux conditions) at the membrane surface:

$$D_{\mathrm{D}} \nabla_{\hat{\boldsymbol{n}}} c_{\mathrm{DD}} = \tilde{k}_{\mathrm{H}}\, m_{\mathrm{d}}\,, \tag{III.6}$$

$$D_{\mathrm{D}} \nabla_{\hat{\boldsymbol{n}}} c_{\mathrm{DT}} = -\left(k_{\mathrm{D}} + \tilde{k}_{\mathrm{dD}}\, m_{\mathrm{d}} \right) c_{\mathrm{DT}}\,, \tag{III.7}$$

$$\tag{III.8}$$

where $\hat{\boldsymbol{n}}$ denotes the (outward) unit normal vector of the membrane surface.

The impact of DivIVA-MinJ complexes on the MinD kinetics is implicitly accounted for by employing spatially non-uniform attachment and detachment rates, i.e. we assume that $k_{\mathrm{dD}}(\boldsymbol{r})$ and $k_{\mathrm{H}}(\boldsymbol{r})$, where $\boldsymbol{r}$ denotes a position vector that marks each point in the spherocylinder.

2.3 Polar localization

Before septum formation, DivIVA accumulates at the cell poles, and we may therefore assume that the rates are exclusively altered at those regions of the cell, while assuming uniform rates elsewhere. Hence, $\tilde{k}_{\mathrm{dD}}$ is enhanced by a factor α, and we assume that $\tilde{k}_{\mathrm{H}}$ is reduced by a factor β (since DivIVA-MinJ stabilizes MinD proteins on the membrane), i.e. we set $k_{\mathrm{dD}} = \alpha \tilde{k}_{\mathrm{dD}}$ and $k_{\mathrm{H}} = \tilde{k}_{\mathrm{H}}/\beta$ at the spherical caps of the geometry. For specificity, we set here $\alpha = 4$ and $\beta = 3$, but our results are not sensitive to the exact values of these parameters (as long as they are larger than one). Consistent with experimental observations [131], our numerical simulations (FEM simulations) show that MinD localizes to the cell poles. It is important to note here that the stationary bipolar gradient corresponds to a non-uniform base state, for which the spatially heterogeneous parameters are the cause.

2.4 Redistribution to the septum

Next, we test whether our model correctly reproduces the redistribution of Min proteins to midcell, once DivIVA looses its affinity to the cell poles (which is the case once a septum forms). We first consider the case where the rates are spatially uniform, i.e. we set $\alpha = 1$ and $\beta = 1$. Intuitively, one would expect that MinD is uniformly distributed on the membrane in this case. However, our numerical simulations show that the MinD concentration profile is non-uniform with a broad maxima at midcell. The underlying reason for this counter-intuitive result is the geometric effect outlined in section 1.2: MinD-ATP is depleted at the cell poles, since the membrane surface to cytosolic volume ratio is largest at the poles. Hence, MinD-ADP is (on average) reactivated near midcell, where it can rebind the membrane. Note that this effect alone explains the redistribution of MinD to midcell once DivIVA looses its affinity to the poles.

To additionally reproduce the sharp peak of MinD at the septum (i.e. accounting for the accumulation of DivIVA at the septum), we may now, again, employ non-uniform kinetic rates. Thus, we define a small region at midcell, and set $\alpha = 4$ and $\beta = 3$ at that region. Consistent with experimental findings, our numerical simulations show that MinD sharply accumulates at the septum of the bacteria.

2.5 Key points and outlook

In the following, we summarize the key findings of this research project and provide a brief outlook.

- We developed a minimal reaction-diffusion model in realistic cell geometry that correctly explains the localization of Min proteins in *B. subtilis*. The key assumption of our model is that the MinD reaction kinetics is spatially heterogeneous, which is biochemically attributed to the actions of DivIVA that serves as a biochemical template for MinD and MinJ binding.

- We have shown that the non-uniform reaction rates of MinD explain its localization to the cell poles and to the septum. Importantly, the redistribution of MinD from the cell poles towards midcell can be solely explained by a geometric effect: once DivIVA loses its affinity to the poles (when a septum forms), MinD-ATP will be depleted from the poles and flows towards midplane of the cell.

- Beside the key assumption of spatially non-uniform reaction rates, our results highlight the importance of realistic cell geometries. The redistribution of MinD from the cell poles to the septum cannot be correctly reproduced in simplified one-dimensional models. In such models, one would need to

artificially alter kinetic rates to account for the impact of geometry on the reaction-diffusion dynamics.

The theoretical model contains the assumption that MinD can spontaneously detach from the membrane through hydrolysis. While it is well established that MinE stimulates hydrolysis of MinD in *E. coli*, the biochemical origin of this (hypothetical) reaction is not known in *B. subtilis*. However, we have two guesses: One possibility is that MinJ induces MinD hydrolysis, since MinJ has been shown to directly interact with MinD [131, 153, 155]. Since MinD is an ATPase [160, 161], yet another hypothesis is that MinD does not rely on other proteins to stimulate its hydrolysis, but might be well able to induce self-hydrolysis just by interacting with phospholipids. The exact mechanism driving the dissociation of MinD from the membrane is an important component for theoretical modeling and is thus required for a thorough understanding of the Min dynamics in *B. subtilis*. Identification of these biochemical pathways requires thorough experimental investigations in the future.

2.6 Publication: Dynamics of the *Bacillus subtilis* Min system

Dynamics of the *Bacillus subtilis* Min system

by

H. Feddersen[1], L. Würthner[2], E. Frey[2], and M. Bramkamp[1,3]

[1]Institute for General Microbiology, Christian-Albrechts-University Kiel, Am Botanischen Garten 1-9, 24118 Kiel, Germany,

[2]Arnold Sommerfeld Center for Theoretical Physics (ASC) and Center for NanoScience (CeNS), Department of Physics, Ludwig-Maximilians-Universität München, Theresienstraße 37, D–80333 Munich, Germany,

[3]Central Imaging Facility, Christian-Albrechts-University Kiel, Kiel, Germany

Published in **textitmBio 12 (2), e00296-21 (2021)**

DOI: 10.1128/mBio.00296-21.

also available on BIORXIV: 10.1101/2020.04.29.068676 .

reprinted on pages 208–229,

Supplemental Material reproduced on pages 230–245.

AMERICAN SOCIETY FOR MICROBIOLOGY | mBio®

RESEARCH ARTICLE

Dynamics of the *Bacillus subtilis* Min System

Helge Feddersen,[a] Laeschkir Würthner,[b] Erwin Frey,[b] Marc Bramkamp[a,c]

[a]Institute for General Microbiology, Christian-Albrechts-University Kiel, Kiel, Germany
[b]Arnold-Sommerfeld-Center for Theoretical Physics and Center for NanoScience, Ludwig-Maximilians-Universität München, Munich, Germany
[c]Central Imaging Facility, Christian-Albrechts-University Kiel, Kiel, Germany

ABSTRACT Division site selection is a vital process to ensure generation of viable offspring. In many rod-shaped bacteria, a dynamic protein system, termed the Min system, acts as a central regulator of division site placement. The Min system is best studied in *Escherichia coli,* where it shows a remarkable oscillation from pole to pole with a time-averaged density minimum at midcell. Several components of the Min system are conserved in the Gram-positive model organism *Bacillus subtilis*. However, in *B. subtilis,* it is commonly believed that the system forms a stationary bipolar gradient from the cell poles to midcell. Here, we show that the Min system of *B. subtilis* localizes dynamically to active sites of division, often organized in clusters. We provide physical modeling using measured diffusion constants that describe the observed enrichment of the Min system at the septum. Mathematical modeling suggests that the observed localization pattern of Min proteins corresponds to a dynamic equilibrium state. Our data provide evidence for the importance of ongoing septation for the Min dynamics, consistent with a major role of the Min system in controlling active division sites but not cell pole areas.

IMPORTANCE The molecular mechanisms that help to place the division septum in bacteria is of fundamental importance to ensure cell proliferation and maintenance of cell shape and size. The Min protein system, found in many rod-shaped bacteria, is thought to play a major role in division site selection. It was assumed that there are strong differences in the functioning and in the dynamics of the Min system in *E. coli* and *B. subtilis*. Most previous attempts to address Min protein dynamics in *B. subtilis* have been hampered by the use of overexpression constructs. Here, functional fusions to Min proteins have been constructed by allelic exchange and state-of-the-art imaging techniques allowed to unravel an unexpected fast dynamic behavior of the *B. subtilis* Min system. Our data show that the molecular mechanisms leading to Min protein dynamics are not fundamentally different in *E. coli* and *B. subtilis*.

KEYWORDS *B. subtilis*, Min system, cell division, FRAP, PALM, super resolution microscopy, protein patterns, reaction diffusion equations

The spatiotemporal regulation of cell division in bacteria is an essential mechanism ensuring correct partitioning of DNA to produce viable daughter cells upon division. The best-studied model organisms in this aspect are the rod-shaped Gram-positive and Gram-negative bacteria *Bacillus subtilis* and *Escherichia coli*, respectively. Both species divide precisely at the geometric middle via binary fission. The earliest observed event in this process is the formation of the Z-ring, a ring-like structure consisting of polymerized FtsZ proteins, a highly conserved homologue of eukaryotic tubulin (1–5). Once assembled, FtsZ acts as a dynamic scaffold and recruits a diverse set of proteins forming the divisome, a complex that mediates cytokinesis (6–8). Recently, treadmilling of FtsZ filaments was shown to drive circumferential

Citation Feddersen H, Würthner L, Frey E, Bramkamp M. 2021. Dynamics of the *Bacillus subtilis* Min system. mBio 12:e00296-21. https://doi.org/10.1128/mBio.00296-21.

Editor Houra Merrikh, Vanderbilt University

Address correspondence to Marc Bramkamp, bramkamp@ifam.uni-kiel.de.

Received 9 February 2021
Accepted 4 March 2021
Published 13 April 2021

peptidoglycan (PG) synthesis (9–11). However, it is still not fully understood how FtsZ finds the precise midplane of the cell. In *E. coli* and *B. subtilis,* the nucleoid occlusion (NO) and the Min system, two negative FtsZ regulators, have been shown to confine its action spatially to the center of the cell. Noc in *B. subtilis* and SlmA in *E. coli* bind to DNA and inhibit FtsZ polymerization across the nucleoid (12–16).

The Min system in *E. coli* consists of the three proteins MinC, MinD, and MinE (17, 18) and has been studied extensively both experimentally (19–31) and theoretically (31–37). MinC is the inhibitor of Z-ring formation, inhibiting the bundling of FtsZ filaments (24, 38–41). MinC is localized through MinD, a protein that belongs to the WACA (Walker A cytomotive ATPase) family (42, 43). Upon binding ATP, MinD dimerizes and associates with the membrane through a conserved C-terminal membrane targeting sequence (MTS) (3, 44, 45). MinC and MinD have been described to form large ATP-dependent alternating polymers that assemble cooperatively and locally inhibit FtsZ bundling (46, 47). In the absence of MinCD, cells frequently produce the name-giving anucleate minicells (48, 49). The *E. coli* MinCD complexes are disassembled and detached from the membrane by MinE, a protein that forms a ring-like density profile at the rim of MinD assemblies (50, 51) and binds to the membrane via an amphipathic helix serving as MTS (52, 53). MinE triggers ATPase activity of MinD, leading to membrane detachment of MinCD (29). Cytosolic MinD rebinds ATP and binds the membrane again, thereby leading to a remarkably robust oscillation of the Min system in *E. coli* (27, 29, 54, 55). Min protein dynamics are a paradigmatic example of cellular self-organization (56). Due to the simplicity of the system, it has been subject to several molecular modeling studies and *in vitro* reconstructions (28–37).

The Min system in *B. subtilis* lacks MinE as the essential factor that is responsible for Min oscillation in *E. coli*, and therefore the Min proteins do not oscillate in *B. subtilis*. Even though the original publications only vaguely suggest this (57, 58), the *B. subtilis* Min proteins are often described to form a stationary bipolar gradient decreasing toward midcell (3, 8), therefore restricting assembly of a functional FtsZ ring to the midplane of the cell. The spatial cue for a gradient in *B. subtilis* is provided by DivIVA (59, 60). DivIVA targets and localizes to negatively curved membrane regions (61). MinJ acts as a molecular bridge between MinD and DivIVA (62, 63). MinJ contains six predicted transmembrane helices and a PDZ domain, which often participate in protein-protein interactions (64). Due to the polar targeting of DivIVA, MinCDJ should form a stationary polar gradient decreasing toward midcell, restricting FtsZ polymerization spatially (57, 58). However, several studies suggest that the *B. subtilis* Min system may rather act downstream of FtsZ ring formation by preventing reinitiation of division at former sites of cytokinesis (62, 63, 65), including some of the very early work (58).

We have recently analyzed DivIVA dynamics in *B. subtilis* and found that Min proteins redistribute from the cell poles to midcell as soon as a septum is formed (66), which prompted us to reanalyze Min protein dynamics in this organism. To this end, we generated a set of new fusions to DivIVA, MinD and MinJ. To avoid overexpression artifacts that would corrupt protein dynamics studies, we generated strains where the native gene copies were replaced by functional fluorescent fusions. These allelic replacements were used to determine precise molecule counts per cell. Using fluorescent recovery after photobleaching (FRAP), we determined the protein dynamics of the individual Min proteins. We then calculated protein diffusion coefficients that were further used for modeling and simulations of the observed Min dynamics. We finally analyzed the nanoscale spatial distribution of the Min proteins in *B. subtilis* by single-molecule localization microscopy (SMLM). Our data are consistent with a dynamic turnover of MinD between membrane and cytosol. Moreover, our SMLM data support a model in which the Min complex is in a dynamic steady state that is able to relocalize from the cell pole to the septum facilitated by a geometric cue, namely, the invagination of the membrane at the septum. Based on our experimental data, we propose a minimal theoretical model for the Min dynamics in *B. subtilis* in realistic three-dimensional (3D) cell geometry. The model is based on a reaction-diffusion system for MinD and incorporates the effects of DivIVA and MinJ implicitly through space-dependent recruitment

TABLE 1 Phenotypic characterization of relevant strains[a]

Strain	Description of strain	Mean growth rate constant (μ) ± SD	Mean cell length (μm) ± SD	% Minicells
168	Wild type	0.53 ± 0.004	3.11 ± 0.77	0.3
3309	Δ*minCD*	0.45 ± 0.021	7.64 ± 2.70	45.8
RD021	Δ*minJ*	0.51 ± 0.049	6.65 ± 2.02	13.8
4041	Δ*divIVA*	0.46 ± 0.020	8.13 ± 3.40	29.6
BHF011	Dendra2-MinD	0.49 ± 0.004	2.67 ± 0.61	0.9
BHF017	msfGFP-MinD	0.55 ± 0.004	4.22 ± 1.04	9.1
JB38	MinJ-Dendra2	0.51 ± 0.006	3.44 ± 1.06	0
BHF007	MinJ-msfGFP	0.57 ± 0.013	3.38 ± 0.76	0.3
JB40	MinJ-mNeonGreen	0.57 ± 0.002	3.16 ± 0.67	0
JB36	DivIVA-Dendra2	0.50 ± 0.007	4.33 ± 0.92	8.0
1803	DivIVA-GFP	0.45 ± 0.021	3.31 ± 0.73	1.1
BHF028	DivIVA-mNeonGreen	0.54 ± 0.029	5.42 ± 1.35	5.3
JB37	DivIVA-PAmCherry	0.51 ± 0.019	4.35 ± 1.11	3.3

[a]For determination of the growth rate constant, μ, the optical density at 600 nm of exponentially growing cells was measured. Cell length and the percentage of minicells were determined microscopically using Fiji, with $n \geq 200$. Strains were grown in independent triplicates, with differences reflected in the standard deviation (SD).

and detachment processes. Our computational analysis of the mathematical model reproduces qualitative features of the Min dynamics in *B. subtilis* and shows that localization of MinD to the poles or septum corresponds to a dynamic equilibrium state. Furthermore, our model suggests that a geometric effect alone could explain septum localization of MinD once DivIVA is recruited to the growing septum, therefore highlighting the importance of geometry effects that cannot be captured in a simplified one-dimensional (1D) model.

RESULTS

Construction of fluorescent fusions with native expression level. Even though the Min system in *B. subtilis* has been extensively investigated before, most studies were conducted using strains that overexpress fluorescent fusions from ectopic locations upon artificial induction (57, 58), leading to nonnative expression levels that can alter the native behavior of fine-tuned systems like the Min system. Additionally, even small populations of a protein from overexpression make it difficult to identify a dynamic fraction through diffraction-limited microscopy (67). Hence, we aimed to recharacterize the dynamics of the Min components in *B. subtilis* by using strains that avoid or minimize overexpression artifacts and, hence, created a set of allelic replacements (see Fig. S1a in the supplemental material).

Dysfunctionality or deletion of Min components in *B. subtilis* manifests in an easily observable phenotype of increased cell length and DNA-free minicells (Table 1). This allows rapid evaluation of the functionality of fluorescent fusions in the constructed strains by comparing cell length and number of minicells between mutant and wild-type strains (Table 1).

Here, we generated functional fusions to MinD (Dendra2 [68]) and MinJ (monomeric superfolder GFP [msfGFP] [69] and mNeonGreen [70]), as judged by cell length, number of minicells, and subcellular protein localization (Fig. S1b; Table 1). Dendra2-MinD displayed a phenotype comparable to that of the wild type. Unfortunately, Dendra2-MinD could not be used for FRAP studies, because excitation at 488 nm leads to a significant green-to-red conversion during the course of the experiment. When all proteins were converted from green to red prior to the FRAP experiment with UV light (405 nm), the red fluorescent signal was poor and bleaching of most proteins occurred during the first image acquisitions, prohibiting reliable quantification. Upon converting protein locally at one of the poles or a septum with a short laser pulse at 405 nm and subsequent imaging in the red channel, very fast diffusion of converted Dendra2-MinD throughout the cell could be observed (data not shown). However, the signal was too dim to be quantified satisfactorily.

Therefore, another strain expressing msfGFP fused to MinD was created. This fusion protein was at least partially functional according to cell length and number of

TABLE 2 Relative quantification of Min proteins fused to Dendra2[a]

Protein	Relative amount (%)	Total no. of copies/cell
MinD	100 ± 2.51	3,544 ± 89
MinJ	16.25 ± 4.36	576 ± 25
DivIVA	47.70 ± 3.51	1,690 ± 59

[a]Relative amounts of protein were determined via in-gel fluorescence of biological triplicates of cell lysates (see Fig. S4 in the supplemental material). Absolute protein quantities were determined relative to MinD, which was quantified in another publication (75) under similar conditions. Values are shown with standard deviations (SD).

minicells (Fig. S1b; Table 1). When *msfGFP-minD* was transformed in a genetic background of a Δ*minJ* or Δ*divIVA* mutant, the fluorescent signal was, as expected, distributed in the cytosol, sometimes forming small foci. MinJ-msfGFP also lost its polar and septal localization upon deletion of *divIVA*, as reported previously (62). These strains were not used for further analysis of protein dynamics, because without protein interaction, a merely diffusive behavior will dominate and no further insight into Min protein dynamics and interaction will be gained. We also aimed at constructing membrane-binding mutants in which the MTS of MinD was altered. However, we were not able to create viable strains with allelic replacement of the native *minD* gene.

When DivIVA fluorescent fusions were constructed, several different fluorophores (FPs) were successfully fused to DivIVA, namely, mCherry2, mNeonGreen, Dendra2, PAmCherry, mGeosM, and Dronpa (68, 70–74), with linkers of between 2 and 15 amino acids. Unfortunately, all of them showed a mild or strong phenotype, some even severe protein mislocalization, hinting toward limited functionality of these DivIVA fusion proteins (75; and data not shown). Since this did not meet the set standards for this study, we turned toward strain 1803 (76), carrying a *divIVA-GFP* copy with its native promoter in the ectopic *amyE* locus. While DivIVA-green fluorescent protein (GFP) has been shown to not fully complement a Δ*divIVA* strain (76, 77), it still localizes correctly and can be used for studies of DivIVA dynamics (66, 77). Additionally, we performed FRAP on DivIVA-mNeonGreen, which shows only a mild phenotype (Table 1), in wild-type and Min knockout backgrounds to be able to compare it with the effect of the extra copy of DivIVA in strain 1803 (Fig. S2).

All fluorescent fusions were analyzed via SDS-PAGE with subsequent visualization through in-gel fluorescence or Western blotting (Fig. S3). We used in-gel fluorescence to obtain estimations about the number of molecules of the Min proteins during mid-exponential phase. We calculated protein numbers relative to the total amount of MinD that was quantified under the same growth conditions using mass spectrometry described previously (78) (Table 2; Fig. S4). MinD proteins are highly abundant (3,544 proteins per cell), while DivIVA numbers are less than 50% of that (1,690 proteins per cell). MinJ has only 16% of MinD abundancy (576 proteins per cell).

The Min system in *B. subtilis* is in a dynamic steady state. Strains expressing functional Min fusions were then used for microscopic analysis of protein dynamics using fluorescent recovery after photobleaching (FRAP) experiments. All three components of the Min system showed relatively fast diffusion in FRAP (Fig. 1 and 2; Table 3). A strain expressing msfGFP-MinD (BHF017) was used for FRAP analysis of MinD dynamics. We observed a fast fluorescence recovery (time when fluorescence recovery reaches half of total recovery [$T_{1/2}$] = 7.55 s), indicating rapid exchange of MinD molecules around the division septum, similar to what was previously reported for MinC (67). Bleaching of MinD at a septum was very efficient (Fig. 1a, upper panel), and the exchange of MinD molecules at the bleached spot appeared to include proteins localized distant from the bleached septum as well as in the vicinity, since the fluorescent signal in the cell decreased evenly over the whole cell length during recovery. Furthermore, around 79% of the msfGFP-MinD population appeared to be mobile (Fig. 1; Table 3). Next, we investigated MinJ-msfGFP fluorescence recovery, which was considerably slower than that of msfGFP-MinD but still indicating protein diffusion

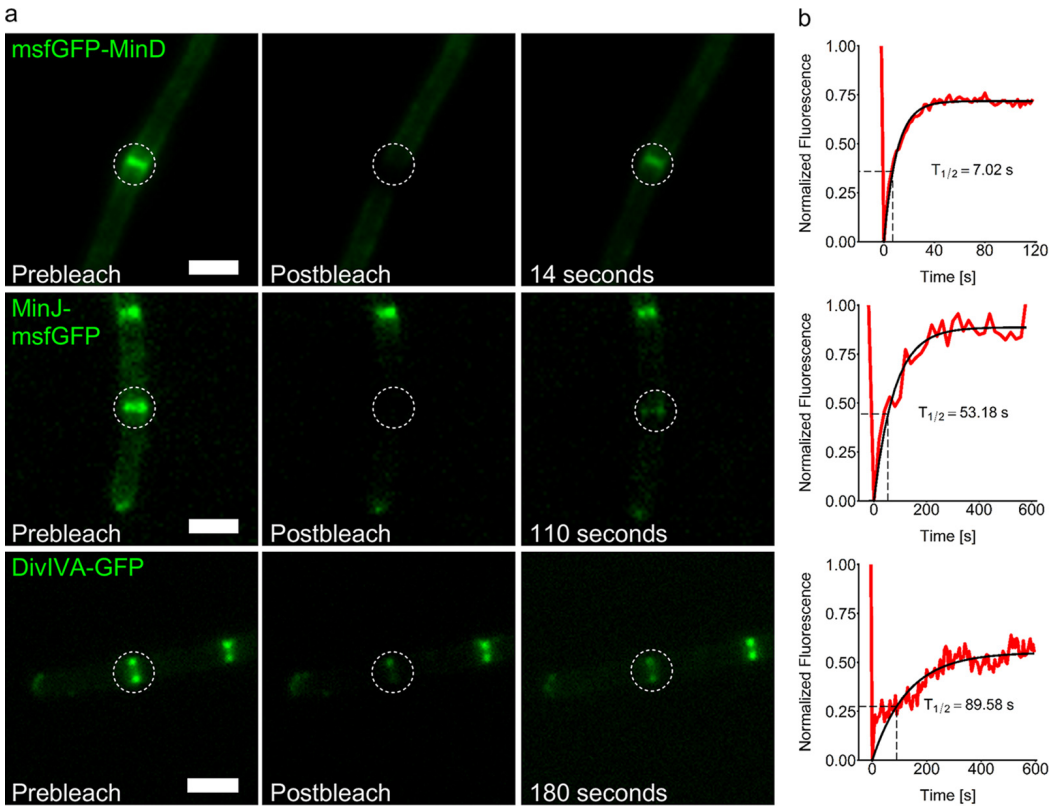

FIG 1 FRAP experiments in growing *B. subtilis* cells reveal Min protein dynamics. (a) Representative microscopy images of msfGFP-MinD (BHF017), MinJ-msfGFP (BHF007), and DivIVA-GFP (1803) before bleaching of the indicated spot with a 488-nm laser pulse, directly after bleaching, and after recovery of fluorescence. Scale bars, 2 μm. (b) Representation of the normalized fluorescence recovery in the green channel over time. $T_{1/2}$ = time when fluorescence recovery reaches half height of total recovery; the shown value corresponds to the displayed cell, indicated on the graph with a dashed square. The red line represents measured values of the displayed cell, and the black line represents the fitted values. Values were obtained as described in Materials and Methods (equations 1 to 3).

($T_{1/2}$ = 62.4 s). MinJ contains six predicted transmembrane helices, and therefore, a slower recovery was expected. Again, most of the MinJ-msfGFP protein pool appeared to participate in the fluorescence recovery (77%). When we measured DivIVA-GFP and DivIVA-mNeonGreen dynamics at septal localizations using FRAP, we observed similar mobilities (DivIVA GFP $T_{1/2}$ = 128 s; DivIVA-mNeonGreen $T_{1/2}$ = 60.3 s). Since the DivIVA-GFP-expressing strain has an extra copy of *divIVA*, it seems logical that the recovery time roughly doubles compared to the DivIVA-mNeonGreen-expressing strain with only one copy of the gene. DivIVA has previously been reported as static (77); however,

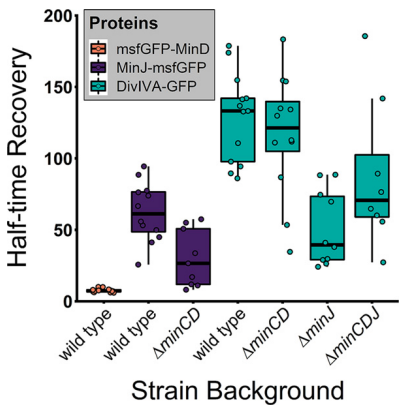

FIG 2 *B. subtilis* Min proteins form dynamic complexes. Shown are median half-time recovery values, indicated by the black bar inside each box. Each box represents a different strain; see also Table 3 for mean values. Every dot represents a single FRAP experiment ($n \geq 8$).

TABLE 3 Results of FRAP analysis for Min proteins in different genetic backgrounds

Protein and genetic background	Fluorophore	Diffusion coefficient ($\mu m^2 \cdot 10^{-3} \cdot s^{-1}$)	Half-time recovery (s)	Mobile fraction
MinD in wild type	msfGFP	57.8 ± 10.1	7.55 ± 1.31	0.79
MinJ in wild type	msfGFP	7.19 ± 2.27	62.4 ± 19.7	0.77
MinJ in Δ*minCD* mutant	msfGFP	14.5 ± 9.54	30.2 ± 19.9	0.75
DivIVA in wild type	GFP	3.39 ± 0.82	128 ± 30.9	0.65
DivIVA in Δ*minCD* mutant	GFP	3.74 ± 1.36	116 ± 42.4	0.68
DivIVA in Δ*minJ* mutant	GFP	8.57 ± 4.43	50.9 ± 26.4	0.49
DivIVA in Δ*minCDJ* mutant	GFP	4.98 ± 2.93	87.7 ± 51.6	0.61
DivIVA in wild type	mNeonGreen	7.23 ± 1.99	60.3 ± 16.6	0.64
DivIVA in Δ*minCD* mutant	mNeonGreen	6.88 ± 2.76	63.4 ± 25.4	0.67
DivIVA in Δ*minJ* mutant	mNeonGreen	18.0 ± 3.22	24.4 ± 4.33	0.39
DivIVA in Δ*minCDJ* mutant	mNeonGreen	9.47 ± 4.26	46.1 ± 20.7	0.66

those FRAP experiments were carried out using overexpression strains and a much shorter time frame than here. Earlier observations from our own lab using a merodiploid strain have already suggested that DivIVA is dynamic (66). Roughly two-thirds of DivIVA molecules were participating in dynamics. Since DivIVA is cytosolic while MinJ is a membrane protein, it was surprising that both proteins presented similar fluorescence recovery speeds. To test if the comparatively slow recovery of DivIVA can be explained only by its ability to oligomerize, we made use of a previously described oligomerization mutant, DivIVAΔ34 (79). Despite still being able to dimerize and bind the plasma membrane, this mutant is unable to form larger DivIVA multimers (79), and a corresponding strain expressing DivIVAΔ34-mNeonGreen was constructed (BHF067). Fluorescent imaging of this strain revealed a loss in polar and septal stabilization and localization of DivIVA (Fig. S2a to c). Instead, DivIVAΔ34-mNeonGreen was observed inhomogeneously distributed in the cytosol, with no apparent tendency for membrane binding (Fig. S2c). In FRAP experiments, recovery of DivIVAΔ34-mNeonGreen was almost instantaneous (Fig. S2a). It is, however, difficult to measure diffusion coefficients of freely diffusing proteins accurately by FRAP in bacteria, because of the small cellular volume (80). The observed result confirmed the prediction that DivIVA mobility is affected mainly by its ability to oligomerize, which not only stabilizes the protein but also affects its ability to sense negative curvature (79).

Interaction of Min proteins influences their dynamics. To obtain a better understanding of the interactions between Min proteins and to find an explanation for the observed dynamics, we performed FRAP experiments in various genetic knockout backgrounds of Min genes. The Min system is hierarchically assembled, with DivIVA recruiting MinJ, which then recruits MinD (62). In agreement with that, we saw a loss of polar and septal msfGFP-MinD localization (BHF025 and BHF026) when we knocked out *minJ* or *divIVA*, which we show in a Δ*minJ* background (BHF069) in Fig. S5, where *minC* was also knocked out to achieve comparable cell length distributions. Instead, loss of DivIVA or MinJ leads to a dispersed MinD localization with a weak enrichment of MinD around the cell center and a depletion at the cell poles in short cells (Fig. S5). Loss of polar and septal localization was also observed for MinJ-msfGFP upon knocking out *divIVA* (BHF032), further corroborating that DivIVA/MinJ complexes are required for controlled MinD localization. Therefore, we did not include these strains in the FRAP analysis. When *minCD* was knocked out in a strain expressing MinJ-msfGFP, the half-time recovery in FRAP dropped from 62 s to 30 s (Fig. 2; Table 3; Fig. S6). This behavior is in line with a direct interaction between the two proteins. We cannot exclude that the phenotype itself impacts the dynamic behavior of MinJ, since cells are elongated and often redivide after successful cytokinesis (65). When *minCD* was knocked out in a DivIVA-GFP-expressing strain (BHF040), however, we could not see any significant difference in fluorescence recovery. Since there is no direct interaction, DivIVA dynamics do not seem to be affected by MinCD directly or indirectly, which includes the effects

of the phenotype of elongated cells. In contrast to that, knocking out *minJ* sped up recovery of DivIVA-GFP (BHF041) significantly, with a recovery time less than half of the wild type, which was also true for DivIVA-mNeonGreen (BHF027) (Table 3; Fig. S6). This result is consistent with a direct interaction. Interestingly, there was also an impact on the mobile fraction, which decreased from around two-thirds to roughly 40% to 50% in both strains. Thus, dynamics are modulated by complex formation reflecting the expected protein hierarchy. MinD recruitment to midcell is fully dependent on DivIVA/MinJ. Since these proteins are relocating only to late stages of septum development, e.g., after a cross wall has started to form, we argue that this geometric change in the cell is important to redistribute MinD from the poles to midcell and establish a new dynamic steady state at the septum/new pole. This localization of MinD at midcell is lost if either DivIVA or MinJ is deleted, or MinD ATPase activity is abolished, as it can be observed in the G12V and K16A ATPase mutants of MinD (81). Thus, maintenance of a steady gradient requires ATPase activity and is therefore similar to the *E. coli* system. Therefore, we aimed to support this hypothesis by mathematical modeling to further understand the observed dynamics.

Theoretical model for MinD dynamics in *B. subtilis*. Previous theoretical analyses of the Min system in *B. subtilis* using quantitative mathematical models are sparse. To our knowledge, there is actually only a single theoretical study that has investigated a mechanism for the polar localization of proteins (82). In this work, the coupled dynamics of DivIVA and MinD are modeled by a reaction-diffusion system in one spatial dimension. Both MinD and DivIVA are considered to diffuse on the membrane and in the cytosol and cycle between these two compartments by attachment and detachment processes. Membrane-bound MinD is assumed to be stabilized through DivIVA, and hence its role is quite different from that of MinE, which destabilizes membrane-bound MinD. Moreover, it was argued that DivIVA requires the presence of MinD for membrane binding (82), specifically, that DivIVA binds to and then stabilizes the edges of MinD clusters. Note that this assumption is no longer valid, as more recent studies have shown that DivIVA can directly bind the membrane. Since the model was studied in one spatial dimension, the author accounted for geometric effects only implicitly by reducing the MinD attachment rate near the cell poles. The importance of ATP binding and hydrolysis on MinD activity has been discussed but was disregarded in the model, as explicit coupling between cytosol and membrane (bulk-boundary coupling) was not considered. In summary, the model was a first and important theoretical analysis dissecting the relative roles of MinD and DivIVA as well as their interplay in shaping protein localization in *B. subtilis*.

Here, on the basis of previous theoretical studies of intracellular protein dynamics (32, 34, 36, 83), we propose a minimal reaction-diffusion system to model Min localization in *B. subtilis*. Building on the idea of geometry sensing put forward previously (83), our model provides a possible mechanism for how proteins sense cell geometry. This mathematical analysis shows that Min polarization and localization are established through a highly dynamic process driven by the ATPase activity of MinD. This implies that Min protein gradients are maintained by genuine nonequilibrium processes and not by thermodynamic binding (chemical equilibrium) of Min proteins to a DivIVA template at the cell poles (3, 8).

We study protein dynamics in realistic three-dimensional (3D) cellular geometry, where proteins cycle between cytosol and membrane, and MinD diffuses with diffusion constants $D_D = 16 \ \ \mu m^2/s$ and $D_d = 0.06 \ \ \mu m^2/s$ in the cytosol and on the membrane, respectively. We consider fully resolved dynamics of MinD (including its ATPase cycle). The biochemical reaction scheme, illustrated in Fig. 3a and b, is based on the following molecular processes: (i) attachment to and detachment from the membrane with rates $k_D = 0.068 \ \ \mu m/s$ and $\tilde{k}_H = 0.1 \ \ s^{-1}$ respectively; (ii) a nonlinear recruitment process of cytosolic MinD by membrane-bound MinD with rate $\tilde{k}_{dD} = 0.04 \ \ \mu m^2/s$; (iii) after detachment from the membrane, MinD is in an ADP-bound state and can rebind to the membrane only after nucleotide exchange, which occurs at rate

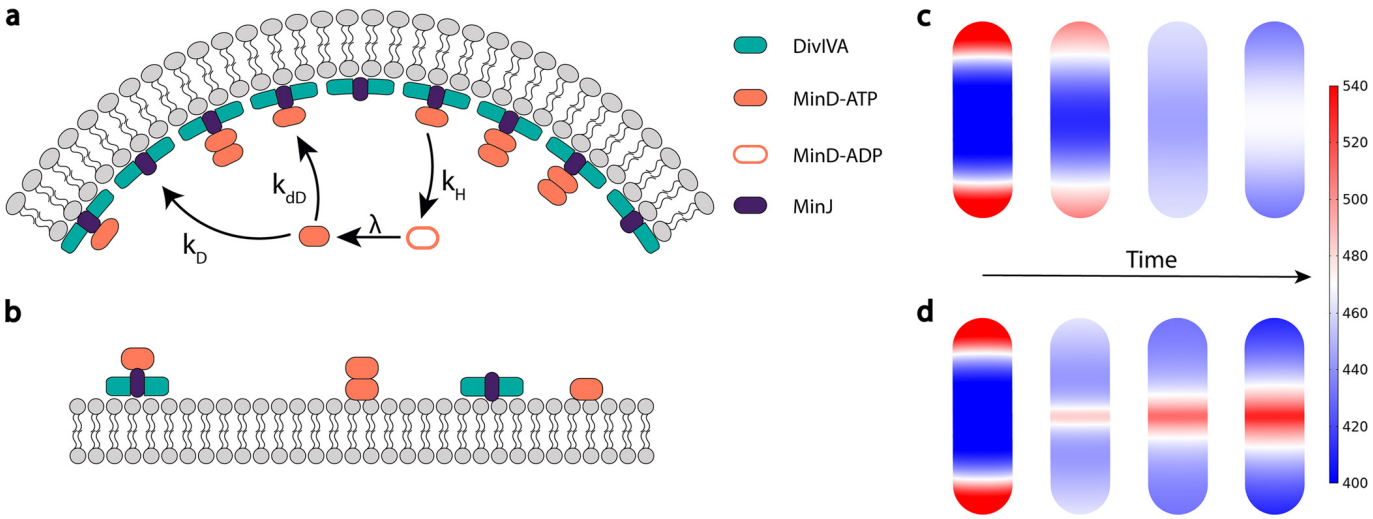

FIG 3 Model and simulation of the Min system in *B. subtilis*. (a) The geometry sensing protein DivIVA (green) preferentially localizes to regions of highest negative curvature and stabilizes MinJ (purple) to these regions. Membrane-bound DivIVA acts as a template for MinD recruitment of cytosolic MinD-ATP (orange) facilitated through MinJ. MinD-ATP binds to the membrane with a rate, k_D, and recruits cytosolic MinD-ATP with a (space-dependent) recruitment rate, k_{dD}, to the membrane. Membrane-bound MinD is stabilized by MinJ-DivIVA complexes, which is reflected in a space-dependent detachment rate, k_{det}. After detachment, MinD is in a hydrolyzed state, MinD-ADP, and can rebind to the membrane only after nucleotide exchange with a rate λ. (b) MinD binds to flat membrane regions as well and recruits MinD-ATP from the cytosol. Binding to flat regions is, however, less favored, due to the lower concentration of MinJ-DivIVA complexes. (c) Simulation of the reaction-diffusion model in a 3D rod-shaped cell; shown is the membrane-bound MinD density distribution. As the initial condition, we take the steady-state distribution of the scenario where DivIVA is localized at the poles (left figure). At simulation start, we assume that MinD is losing its affinity to the poles by making the recruitment and detachment rate uniform on the entire cell membrane (this is, for example, the case at the onset of septum formation). From left to right, the time evolution of membrane-bound MinD is shown, where the far-right side shows the final steady-state density distribution. We find that polar localization of MinD becomes unstable and that the proteins preferentially localize at the cell center. (d) To test whether MinD can be localized at midplane through MinJ-DivIVA complexes after septum formation, we took the same initial condition as described for panel c and enhanced recruitment and decreased detachment near midcell. We find that MinD can sharply localize at the septum.

$\lambda = 6\ \ s^{-1}$. The protein numbers and membrane diffusion of MinD were extracted from our measurements (Tables 2 and 3; see Table S1 in the supplemental material), and the values for the kinetic parameters (rate constants) were estimated from previous work on protein pattern formation (32, 34, 36, 83).

Since the above reaction scheme contains only the attachment and detachment kinetics of MinD, one would intuitively expect that the steady-state MinD membrane density distribution is spatially uniform. Interestingly, from finite element simulations (see Materials and Methods), we find that the steady-state density distribution of membrane-bound MinD is not homogeneous but is nonuniform along the whole cell body and with a weak maximum at midcell (Fig. 3c, right figure), comparable to our observations *in vivo* (Fig. S5). The reason for this unexpected spatial localization of MinD is a purely geometric effect suggested previously (83). For a better understanding of our following arguments, let us briefly summarize the core results of this study. Due to the curvature at the poles, the effective "hitting frequency" (attachment rate) of active MinD-ATP becomes larger in these regions, which initially leads to an accumulation of MinD-ATP at the poles. However, upon detachment, MinD is in an inactive MinD-ADP state and first needs to exchange its nucleotide in order to rebind to the membrane. Hence, during this time, one can define a characteristic length scale of $l = \sqrt{D_D/\lambda}$ (see Materials and Methods), during which inactive proteins travel in the cytosol until they become able to rebind to the membrane. For our parameter choice, we have $l \approx 1.6\ \mu$m, which corresponds roughly to half the typical size of a *B. subtilis* cell (Table S1; and see Materials and Methods). Therefore, due to the curved cell geometry, MinD-ATP is depleted at the poles, resulting in an accumulation of MinD-ATP near midcell. To test this prediction, a strain expressing msfGFP-MinD in a *minJ* background was created (BHF069). Furthermore, we knocked out *minC* in this strain to partially account for the shifted cell length distribution of a *minJ* background. As predicted through the model, we found a clear maximum of msfGFP-MinD at midcell, when cells did not yet

start to form a septum (Fig. S5), indicated by their size ($<5\,\mu$m). Longer cells ($>5\,\mu$m) often start to divide at midcell, thereby creating a membrane curvature that affects distribution of msfGFP-MinD. In these cells, the concentration is highest in the center of both cell halfs (Fig. S5). This finding also highlights the importance of realistic 3D simulations, as geometric sensing would be absent in simplified 1D systems.

As already outlined in the previous sections, experimental studies have shown that DivIVA binds preferentially to regions of high negative membrane curvature and that MinJ localization is dependent on the presence of DivIVA (61, 62). MinD does not interact with DivIVA directly but through MinJ, which is known to act as an intermediary between DivIVA and MinD (62). Furthermore, our experiments suggest that DivIVA-MinJ complexes act as a spatial template for MinD binding. This suggests that the effective role of DivIVA and MinJ on MinD binding can be summarized in spatially varying values of the MinD recruitment and detachment rate, where the recruitment rate is larger in the presence of DivIVA-MinJ complexes (cell poles and septum) and smaller in the remaining part of the cell. Similarly, the detachment rate is lower in the presence of DivIVA-MinJ complexes (cell poles and septum) and higher otherwise. Intuitively, one would then expect that MinD localizes to those regions where the recruitment and detachment rate are altered, as this would effectively result in a higher binding rate of MinD.

To put this idea into test, we first incorporated space-dependent recruitment and detachment rates of MinD at membrane areas with a negative curvature; for details, see Materials and Methods (Fig. S7). Under the above conditions, MinD accumulates at both cell poles in a dynamic equilibrium state, with proteins constantly cycling between cytosol and membrane (Fig. 3c, left figure). In contrast, in the absence of preferential attachment at the cell poles facilitated by DivIVA-MinJ complexes (i.e., by employing uniform rates), polar localization of MinD becomes unstable and the proteins become preferentially localized in the cell center (again in a dynamic equilibrium state). The underlying reason is the geometric effect as explained above. To appreciate this result, note that this effect alone could explain the redistribution of MinD from the cell poles to midcell at the onset of cytokinesis (initiated by the redistribution of DivIVA to the septum, which would have a higher curvature than the cell poles).

Next, we tested whether MinD can be localized at midplane in the presence of DivIVA-MinJ complexes once a septum has formed there. Indeed, emulating the presence of these complexes by an enhanced recruitment and detachment rate localized at the septum, our simulations show that MinD becomes sharply localized at midplane following the transfer of DivIVA-MinJ complexes from the poles to the septum (Fig. 3d). The width of the MinD distribution at midcell is determined by the interplay between membrane diffusion and localized recruitment of MinD at the septum (see Materials and Methods).

Single-molecule resolution of the Min system reveals cluster formation. Next, we wanted to test these theoretical predictions concerning a dynamic steady state of MinD proteins experimentally, using single-molecule resolution microscopy. In contrast to a stationary bipolar gradient of Min proteins from the cell poles, as described before (3, 8, 57, 58) based on a simple thermodynamic binding of Min proteins to a DivIVA/MinJ template, we expect a dynamic relocalization of Min proteins from the cell pole to the septum. This dynamic steady state would reveal Min components along the entire membrane, including the lateral sites at any time. To achieve the highest possible resolution, we used photoactivated light microscopy (PALM). Accordingly, strains expressing Dendra2-MinD (BHF011), MinJ-mNeonGreen (JB40), and DivIVA-PAmCherry (JB37) were utilized. While Dendra2 and PAmCherry are photoswitchable or photactivatable FPs that can be converted from green to red or activated with UV light, respectively, and are hence well suited for PALM (68), mNeonGreen can be used for PALM because of its innate capability to photoswitch (70). However, mNeonGreen presents some challenges in comparison to classical photoactivatable FPs, as it cannot be prebleached and therefore requires more postprocessing to reach satisfying artifact-free molecule localizations (75).

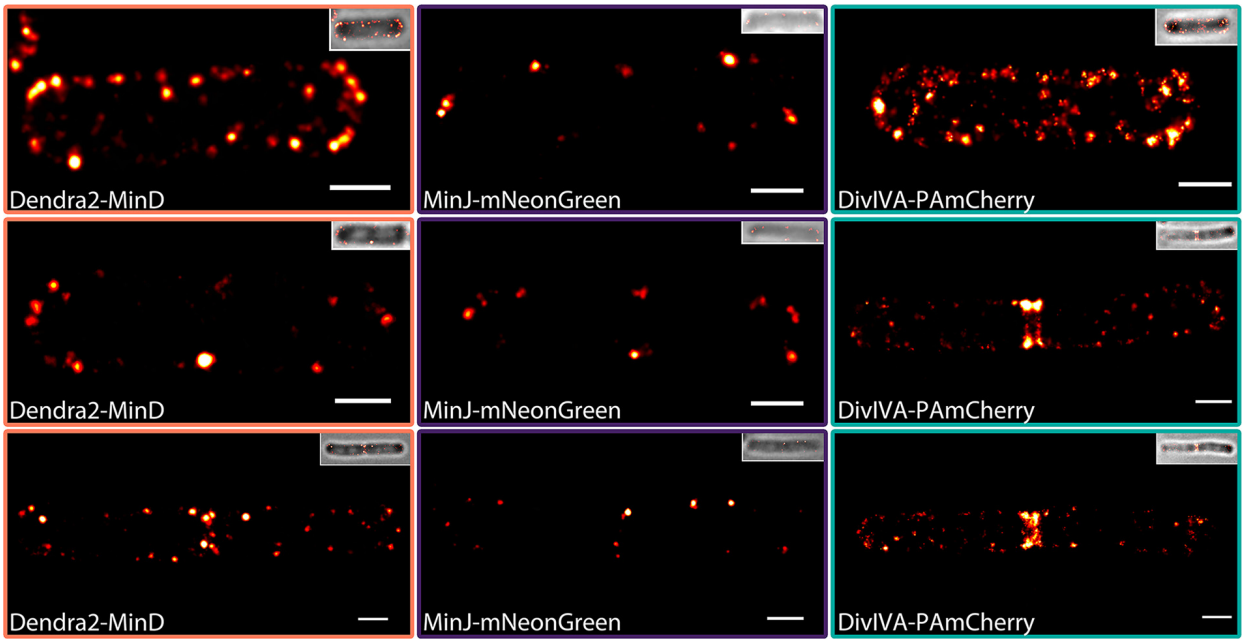

FIG 4 PALM imaging of strains expressing Dendra2-MinD, MinJ-mNeonGreen, and DivIVA-PAmCherry. Representative PALM images of Dendra2-MinD (BHF011), MinJ-mNeonGreen (JB40), and DivIVA-PAmCherry (JB37) expressing cells at different divisional states are shown. Upon formation of a division site, DivIVA, MinJ, and MinD partially relocalize from the poles to the division septum, where they reside after successful cytokinesis. Samples were fixed prior to imaging; every image represents a different cell. Scale bar, 500 nm.

Nevertheless, all three strains could be successfully imaged in fixed cells with average precisions of 25 to 30 nm (Fig. 4) using appropriate filter settings (see Table 7).

Importantly, we observed that all Min proteins not only localized to the cell poles but also as clusters along the membrane and with some apparent cytoplasmic localizations. These protein accumulations were mainly seen along the membrane for MinJ (Fig. 4, middle panels), while a fraction of MinD and DivIVA could be observed in the cytosol (Fig. 4, left and right panels). The high abundance of these protein accumulations indicates that recruitment of MinD and DivIVA by existing clusters progresses at higher rates than individual membrane binding, which is also reflected in the proposed mathematical model. Double rings of MinJ and DivIVA have been reported previously in 3D structured illumination microscopy (77), which could be observed in late divisional cells in PALM as well (Fig. 4, middle and bottom panels). The active enrichment at the young cell pole is consistent with the theoretical model described above and with a role of the Min system in regulation of cell division rather than protection of cell poles from aberrant cell division (65).

To get a deeper insight into the structure and distribution of the imaged proteins and to confirm clustering, a single-molecule point-based cluster analysis was performed for MinD and DivIVA (Fig. 5; Fig. S8). Unfortunately, MinJ-mNeonGreen imaging did not produce a sufficient number of events to be analyzed robustly (Fig. S8a), as MinJ expression levels are low in comparison and only a small fraction of mNeonGreen molecules blink reliably (75).

In total, we recorded 151,887 events in 48 cells for Dendra2-MinD, while 52,377 events of DivIVA-PAmCherry were recorded in 37 cells. When clusters with at least 10 molecules per cluster were identified, 55.61% (84,470) of all Dendra2-MinD events were organized in clusters, while 52.27% (27,379) of events of DivIVA-PAmCherry could be assigned to clusters. Thus, the average prevalence of clusters per cell was higher for MinD (24 clusters per cell) than for DivIVA (15 clusters per cell) (Fig. 5c). The size of these clusters varied greatly (Fig. 5d): an average number of 72 MinD proteins per cluster was determined, while the average number of DivIVA proteins per cluster was 47. However, we also observed some very large clusters with up to 1,390 MinD proteins and 1,198 DivIVA proteins, respectively. Analysis of the relative position of all clusters per cell revealed a high tendency for clusters to form around poles and septa (Fig. 5e), where around two-thirds of DivIVA clusters (66%) and more than half of MinD clusters

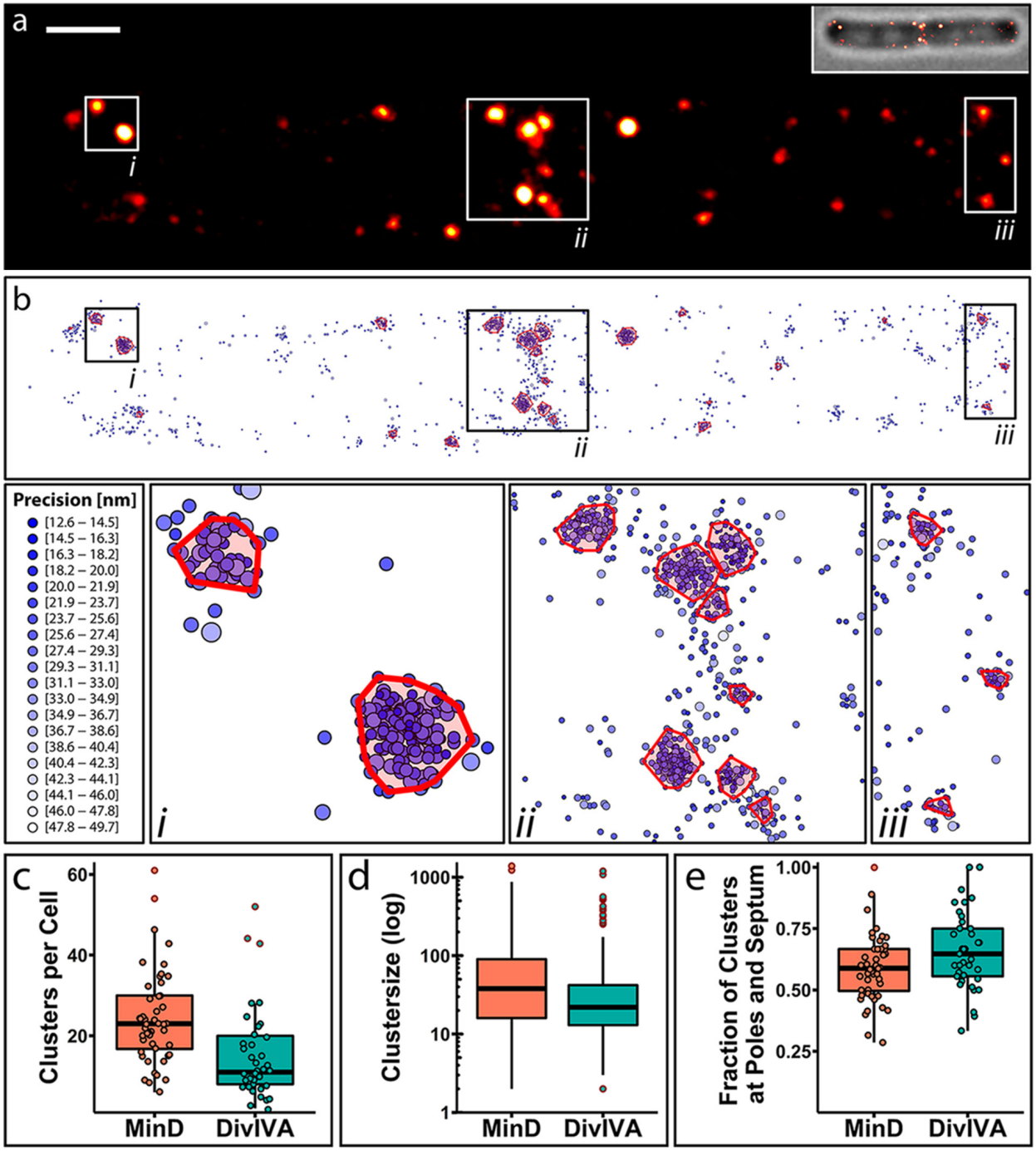

FIG 5 PALM imaging and representative cluster analysis of Dendra2-MinD and DivIVA-PAmCherry. (a) Representative PALM image of Dendra2-MinD (BHF011) in a cell in a late division state. Scale bar, 500 nm. (b) Cluster analysis of the same PALM data as shown in panel a with three highlighted regions (i, ii, and iii). Cluster analysis was performed in R using the OPTICS algorithm from the DBSCAN package. Every point indicates a single event and thus a Dendra2-MinD/DivIVA-PAmCherry protein, and precision is indicated by color and size of the circle. (c) Box plot of the number of clusters of Dendra2-MinD and DivIVA-PAmCherry per cell (MinD, n_{cells} = 48; DivIVA, n_{cells} = 37). (d) Box plot of the number of proteins per cluster; no jitter is shown due to the high sample number (Dendra2-MinD, $n_{clusters}$ = 1,171; DivIVA-PAmCherry, $n_{clusters}$ = 586). (e) Box plot of fraction of clusters localized at poles and septa per cell (MinD, n_{cells} = 48; DivIVA, n_{cells} = 37). Outliers in box plots are indicated by a red outline.

(59%) were observed, while the rest was found along the lateral membrane or in the cytosol. This correlates well with the idea that most of MinD is recruited to negative membrane curvature (poles and septum) by DivIVA via MinJ. MinD also binds to flat membrane areas, where it recruits more MinD from the cytosol. This is less favored due to the lower concentration of MinJ-DivIVA complexes, which is reflected in our

simulations and data. Our data also reveal that MinD and DivIVA seem to accumulate, and cytosolic proteins therefore have a higher tendency to bind to existing clusters than to free membrane surfaces. We did not observe a large proportion of MinD dimers and also no homogeneous binding of MinD or DivIVA to the membrane.

DISCUSSION

The Min reaction network has been extensively studied in various organisms (8, 84). In *E. coli*, it was found to be a highly dynamic and self-organizing system capable of pole-to-pole oscillation, a prime example for intracellular protein pattern formation (36). The two core components in this network, MinE and MinD, cycle between membrane and cytosol and are sufficient to induce robust protein patterns both *in vivo* and *in vitro* (19, 20, 29, 85, 86). Therefore, it has been puzzling that the Min system in *B. subtilis* was described to form a rather stationary bipolar gradient from poles to midcell, although MinC and MinD are well conserved. The differences are mainly accredited to the absence of MinE, which stimulates ATP hydrolysis and thus membrane detachment of MinD. Instead, the curvature-sensing DivIVA was found to recruit MinCDJ to the negatively curved poles. However, MinC has been shown to dynamically relocalize to midcell prior to division in fluorescence microscopy (67), and the same study highlights open questions in the current Min model for *B. subtilis*, pointing out that earlier studies were conducted using strains that artificially overexpress Min network components, thereby possibly masking dynamic populations.

In this study, we analyzed protein dynamics of the *B. subtilis* Min system based on experiments conducted with native expression levels of fluorescently labeled Min components. First, we found all components to be highly dynamic. MinD had the shortest recovery time of the three investigated proteins, while MinJ and DivIVA both had considerably slower recovery times than MinD but in a similar range when compared to each other (Table 3). Similar tendencies were detected when mobile and immobile fractions were compared, where MinD had the highest mobile fraction, with almost 80% of the protein taking part in the recovery. With diffusion coefficients between 0.057 $\mu m^2/s$ and 0.0034 $\mu m^2/s$, the three proteins were found in an expected range for membrane (-associating) proteins in bacteria (87). Considering the nature of DivIVA, which binds to the membrane and stabilizes itself at negative curvature, and MinJ as an integral membrane protein, it is not surprising that the cytosolic MinD is around 10-fold faster in recovery. This observation leads to the speculation of a relatively fast exchange of membrane-bound MinD proteins at the division septum, considering relatively high total protein quantities (Table 2) in combination with a large mobile fraction and fast recovery when bleaching these sites. DivIVA total protein numbers were found to be around half of MinD, while MinJ was by far the least abundant Min component. These findings correlate with the corresponding fluorescence intensity and appearance when imaging the respective Min proteins tagged with the same fluorophore during mid-exponential growth (for examples, see Fig. S1 in the supplemental material).

Moreover, knocking out single or multiple components had an impact on the dynamics of the respective upstream recruiting factor, validating interactions between MinD and MinJ and between MinJ and DivIVA, respectively, that were observed in genetic studies previously (62, 63). Based on this interaction network and the respective protein behaviors in combination with the knowledge gained from the *E. coli* Min system, a mathematical model was designed.

We propose a minimal reaction-diffusion model that correctly reproduces qualitative features of MinD localization in *B. subtilis*. We extracted the parameters for the model from our measurements (protein numbers and diffusion coefficients) (Tables 2 and 3) and from previous work on intracellular protein pattern formation (32, 34, 36, 83). The basic assumption of the model is that DivIVA acts as a spatial template for MinJ and MinD, which we accounted for implicitly through a space-dependent recruitment and detachment rate for MinD. From the computational analysis of the model (finite element method [FEM] simulations), we found that localization of MinD to the

poles or the division site corresponds to a dynamic equilibrium state of the reaction-diffusion equation. Further, our results show that a geometric effect alone is sufficient to guide MinD to the division site, therefore highlighting the importance of realistic 3D models.

Our model can be straightforwardly extended to include the explicit dynamics of DivIVA and MinJ. As the exact reaction network of the Min system in *B. subtilis* remains elusive, a theoretical model could help in identifying the essential components of Min dynamics. By following the same approach as for the *E. coli* Min system, reconstitution of the Min system *in vitro* would also help to dissect the complexity of the system and to make the comparison between experiments and theory even more feasible. We believe that our theoretical approach may serve as a basis for future studies addressing protein dynamics in *B. subtilis*.

We note that the observed dynamics are not compatible with a division site selection system, because ongoing division is needed for correct localization and dynamics of the Min system in *B. subtilis*. This is in line with data obtained by Elizabeth Harrýs lab showing that deletion of Min proteins does not abolish midcell positioning of the Z-ring in *B. subtilis* (88) and our own data describing reduced disassembly of Z-rings in the absence of the Min system (65). The model we propose includes a yet unknown protein or mechanism that stimulates MinD-ATP hydrolysis. The uniform hydrolysis rate k_H in our model was predicted to be similar to that of the closely related MinD in *E. coli*, which is stimulated by MinE (25, 29). The responsible protein or mechanism has yet to be elucidated, but the presence of cytosolic and membrane-bound MinD fractions and their respective dynamics as well as the well-conserved ATPase domain argue very convincingly for its existence.

Additionally, we investigated the Min components with single-molecule resolution, revealing a strong tendency for cluster formation, and these clusters are also found at the lateral sides of the cell membrane. The lateral Min assemblies have not been resolved by conventional light microscopy images, and hence the idea of an exclusive polar Min assembly was manifested. Clusters of MinD and DivIVA are indeed frequently observed close to poles and midcell. In accordance with the mathematical model, we hence hypothesize that a fraction of MinD will diffuse away from these primary binding sites after recruitment. Most of this fraction will quickly unbind the membrane due to the lack of stabilization and will be recruited again by DivIVA-MinJ to either pole or septum clusters. Proteins that are part of a cluster will show less exchange or dynamic behavior, further decreasing toward the center, as is typically observed in protein clusters (89). This mechanism could tightly regulate spatiotemporal localization of MinCD and, likewise, aid in transitioning from polar localization to septal localization rapidly upon septum formation, as DivIVA and MinJ would transition to the septum first. Since the current view on the task of the Min system in *B. subtilis* proposes a role downstream of cell division, all components need to be concentrated at the septum in time to inhibit a second round of division by promoting the disassembly of the division apparatus (65).

This study provides a model of the Min protein dynamics in *B. subtilis* that makes testable predictions. It emerges that the Min systems in *B. subtilis* and *E. coli* are not so fundamentally different as initially thought. Future research will therefore address the unsolved question of how MinD ATPase activity is triggered in *B. subtilis*. Furthermore, the influence of membrane binding of DivIVA and MinD requires a closer look to gain quantitative data for a refined mathematical model.

MATERIALS AND METHODS

Bacterial strains, plasmids, and oligonucleotides. The oligonucleotides, plasmids, and strains used in this study are listed in Tables 4 to 6, respectively. *E. coli* NEB Turbo was used to amplify and maintain plasmids.

Strain construction: Golden Gate assembly. Fragments for Golden Gate assembly were amplified from *B. subtilis* 168 (*trpC2*) genomic DNA or template plasmids via PCR with the respective primers containing directional overhangs (Table 4). The vector pUC18mut was also amplified via PCR to introduce BsaI restriction sites and allow subsequent digestion of circular PCR template with DpnI, which cuts only methylated DNA. Plasmid construction was verified via individual control digestion and DNA

TABLE 4 Oligonucleotides used in this study

Oligonucleotide name	Sequence (5′ to 3′)
bsarem1	TTTGGTCTCAGGTTCTCGCGGTATCATTGCAGC
bsarem2	TTTGGTCTCAAACCACGCTCACCGGCTCCAG
HF0061	GTCGGTCTCAACTAGAATTCGTAATCATGGTCATAGCTG
HF0062	CTCGGTCTCATCGGAAGCTTGGCACTGGC
HF0037	TATGGTCTCCCCGAGTTCATTCTATTGACAGTGAAGTC
HF0038	CTAGGTCTCTCTCCTTCACATTCCTCCCTCAAG
HF0040	AATGGTCTCTGGAGGGGTGAAAGGATGTACTTA
HF0041	TTTGGTCTCGCGAATAATTGAGAGAAGTTTCTATAG
HF0042	GGAGGTCTCTTTCGATGAACACCCCGGGAATTAAC
HF0043	CACGGTCTCCCATTCCACACCTGGCTGGGCAGG
HF0044	ACGGGTCTCAAATGGGTTGGGTGAGGCTATCGTAATAAC
HF0045	CGGGGTCTCTTAGTCAATATTTTCCTCTTGCTCCAGC
HF0065	GGAGGTCTCTTTCGATGGGTACCCTGCAGATG
HF0066	CACGGTCTCCCATTTTTGTAGAGCTCATCCATGC
G40	CTAGGTCTCTCCGATGTCGGATTTGGACA
G41	TATGGTCTCCCTCCTGATCCCGAAGCGAC
HF0029	AATGGTCTCTGGAGGGATGGGTACCCTGCAGATG
HF0030	TTTGGTCTCGCGAATTTGTAGAGCTCATCCATGC
G20	AATGGTCTCTGGAGGGATGAACACCCCGGGAATTAAC
G21	TTTGGTCTCGCGAATTACCACACCTGGCT
G36	GGAGGTCTCTTTCGGGGTGAAAGGATGTACTTA
G37	CACGGTCTCCCATTTAATTGAGAGAAGTT
G42	ACGGGTCTCAAATGGGAAGGCAGCCCGGCACCGCAGG
G43	CGGGGTCTCTTAGTCCATGATGGCTGGTG
HF0077	AATGGTCTCTGGAGGGATGGTGAGCAAGGGCG
HF0078	TTTGGTCTCGCGAATTACTTGTACAGCTCGTCCATG
G32	ACGGGTCTCAAATGGGATTCTCTGATTATCT
G33	CGGGGTCTCTTAGTATCGGGAAATCTGTT
G34	CTAGGTCTCTCCGAGAATTCCTAGCCCAAGTCAG
G35	TATGGTCTCCCTCCTTCCTTTTCCTCAAA
HF0206	TATGGTCTCCCCGAGTTAACCGTGACGTGC
HF0207	CTAGGTCTCTCTCCAATATTCACCTCAACAACATAC
HF0203	AATGGTCTCTGGAGTACCGTTCGTATAGCATAC
HF0204	TTTGGTCTCGCGAATCTACCGTTCGTATAATG

sequencing. Correct plasmids were transformed into *B. subtilis* 168 with the respective genetic background (Table 6) and selected for the introduced resistance (Table 5). Resistant candidates were confirmed by PCR and microscopy.

pHF01 (pUC18mut-*minDup-aad9-Dendra2-minD*) was created by a Golden Gate assembly of 5 fragments: (i) PCR with primers HF0061 and HF0062 with pUC18mut as the template (yielding a linear pUC18mut); (ii) PCR with primers HF0037 and HF0038 and 168 genomic DNA (containing the region upstream of *minD*); (iii) PCR with primers HF0040 and HF0041 and JB40 genomic DNA (containing the spectinomycin adenyltransferase gene *aad9*); (iv) PCR with primers HF0042 and HF0043 and pDendra2-N plasmid DNA (containing the *Dendra2* gene); (v) PCR with primers HF0044 and HF0045 and 168 genomic DNA (containing the N-terminal region of *minD*).

pHF02 (pUC18mut-*minDup-aad9-msfGFP-minD*) was created by a Golden Gate assembly of 5 fragments: (i) PCR with primers HF0061 and HF0062 with pUC18mut as the template (yielding a linear pUC18mut); (ii) PCR with primers HF0037 and HF0038 and 168 genomic DNA (containing the region upstream of *minD*); (iii) PCR with primers HF0040 and HF0041 and JB40 genomic DNA (containing the spectinomycin adenyltransferase gene *aad9*); (iv) PCR with primers HF0065 and HF0066 and pHJS105 (containing the *msfGFP* gene); (v) PCR with primers HF0044 and HF0045 and 168 genomic DNA (containing the N-terminal region of *minD*).

pHF03 (pUC18mut-*minJ-msfGFP-aad9-minJdown*) was created by a Golden Gate assembly of 5 fragments: (i) PCR with primers HF0061 and HF0062 with pUC18mut as the template (yielding a linear pUC18mut); (ii) PCR with primers G40 and G41 and 168 genomic DNA (containing the C-terminal region of *minJ*); (iii) PCR with primers HF0029 and HF0030 and pHJS105 (containing the *msfGFP* gene); (iv) PCR with primers G36 and G37 and JB40 genomic DNA (containing the spectinomycin adenyltransferase gene *aad9*); (v) PCR with primers G42 and G43 and 168 genomic DNA (containing the region downstream of *minJ*).

pHF04 (pUC18mut-*minJ-mNG-aad9-minJdown*) was created by a Golden Gate assembly of 5 fragments: (i) PCR with primers HF0061 and HF0062 with pUC18mut as the template (yielding a linear pUC18mut); (ii) PCR with primers G40 and G41 and 168 genomic DNA (containing the C-terminal region

TABLE 5 Plasmids used in this study

Plasmid	Characteristics	Reference or source
pUC18	*lacZα*, pMB1 *ori*, *bla* (Ap^r)	99
pUC18mut	pUC18 with mutated BsaI site in *bla*	Laboratory collection
pDendra2-N	pUC *ori,* SV40 *ori*, PCMVIE, *aph3-A3*	Evrogen
pNCS-mNeonGreen	pUC *ori,* SV40 *ori, bla* (Ap^r)	Allele Biotechnology
pUC57-DivIVAd34-mNG	pUC57-BsaI-free*, bla* (Ap^r), *divIVAΔ34-mNeonGreen*	Synthesized by Biocat
pHJS105	*amyE* integration vector containing P*xyl-msfGFP-MCS, spc bla*	100
pHF01	pUC18mut-*minDup-aad9-Dendra2-minD*	This study
pHF02	pUC18mut-*minDup-aad9-msfGFP-minD*	This study
pHF03	pUC18mut-*minJ-msfGFP-aad9-minJdown*	This study
pHF04	pUC18mut-*minJ-mNG-aad9-minJdown*	This study
pHF05	pUC18mut-*divIVA-mNG-aad9-divIVAdown*	This study
pHF06	pUC18mut-*minJ-Dendra2-aad9-minJdown*	This study
pHF07	pUC18mut-*divIVA-Dendra2-aad9-divIVAdown*	This study
pHF08	pUC18mut-*divIVAΔ34-mNG-aad9-divIVAdown*	This study
pHF09	pUC18mut-*minCup-aph3-A3—aad9*	This study

of *minJ*); (iii) PCR with primers HF0077 and HF0078 and pNCS-mNeonGreen DNA (containing the *mNeonGreen* gene); (iv) PCR with primers G36 and G37 and JB40 genomic DNA (containing the spectinomycin adenyltransferase gene *aad9*); (v) PCR with primers G42 and G43 and 168 genomic DNA (containing the region downstream of *minJ*).

pHF05 (pUC18mut-*divIVA-mNG-aad9-divIVAdown*) was created by a Golden Gate assembly of 5 fragments: (i) PCR with primers HF0061 and HF0062 with pUC18mut as the template (yielding a linear

TABLE 6 Strains used in this study

Strain	Relevant features or genotype	Reference or source
B. subtilis		
168	*trpC2*	Laboratory collection
3309	*minCD*::*aph3-A3*	Wu and Errington, 2004 (12)
RD021	*minJ*::*tet*	Bramkamp et al., 2008 (62)
4041	*divIVA*::*tet*	Bramkamp et al., 2008 (62)
SB075	*minCD*::*erm minJ*::*tet*	Laboratory collection
BHF011	*minD*::*aad9-Dendra2-minD*	This study, pHF01→168
BHF017	*minD*::*aad9-msfGFP-minD*	This study, pHF02→168
BHF025	*minD*::*aad9-msfGFP-minD minJ*::*tet*	This study, pHF02→RD021
BHF026	*minD*::*aad9-msfGFP-minD divIVA*::*tet*	This study, pHF02→4041
JB038	*minJ*::*minJ-Dendra2-aad9*	This study, pHF06→168
BHF007	*minJ*::*minJ-msfGFP-aad9*	This study, pHF03→168
BHF015	*minJ*::*minJ-msfGFP-aad9 minCD*::*aph3-A3*	This study, pHF03→3309
BHF032	*minJ*::*minJ-msfGFP-aad9 divIVA*::*tet*	This study, pHF03→4041
JB40	*minJ*::*minJ-mNeonGreen-aad9*	This study, pHF04→168
JB36	*divIVA*::*divIVA-Dendra2-aad9*	This study, pHF07→168
BHF028	*divIVA*::*divIVA-mNeonGreen-aad9*	This study, pHF05→168
BHF036	*divIVA*::*divIVA-mNeonGreen-aad9 minCD*::*aph3-A3*	This study, pHF05→3309
BHF027	*divIVA*::*divIVA-mNeonGreen-aad9 minJ*::*tet*	This study, pHF05→RD021
BHF037	*divIVA*::*divIVA-mNeonGreen-aad9 minCD*::*erm minJ*::*tet*	This study, pHF05→SB075
1803	*divIVA*::*divIVA-GFP-cat*	Thomaides et al., 2001 (76)
BHF040	*divIVA*::*divIVA-GFP-cat minCD*::*aph3-A3*	This study, 1803→3309
BHF041	*divIVA*::*divIVA-GFP-cat minJ*::*tet*	This study, 1803→RD021
BHF042	*divIVA*::*divIVA-GFP-cat minCD*::*erm minJ*::*tet*	This study, 1803→SB075
BHF067	*divIVA*::*divIVAΔ34-mNG-aad9*	This study, pHF08→168
BHF069	*minD*::*aad9-msfGFP-minD minC*::*aph3-A3 minJ*::*tet*	This study, pHF09→BHF025
JB37	*divIVA*::*divIVA-PAmCherry-aad9*	Stockmar et al., 2018 (75)
E. coli		
NEB Turbo	F′ *proA*$^+$*B*$^+$ *lacI*^{q} Δ*lacZM15/fhuA2* Δ(*lac-proAB*) *glnV galK16 galE15* R(*zgb-210*::Tn*10*)Tet^s *endA1 thi-1* Δ(*hsdS-mcrB*)*5*	New England Biolabs

pUC18mut); (ii) PCR with primers G34 and G35 and 168 genomic DNA (containing the C-terminal region of *divIVA*); (iii) PCR with primers HF0077 and HF0078 and pNCS-mNeonGreen DNA (containing the *mNeonGreen* gene); (iv) PCR with primers G36 and G37 and JB40 genomic DNA (containing the spectinomycin adenyltransferase gene *aad9*); (v) PCR with primers G32 and G33 and 168 genomic DNA (containing the region downstream of *divIVA*).

pHF06 (pUC18mut-*minJ-Dendra2-aad9-minJdown*) was created by a Golden Gate assembly of 5 fragments: (i) PCR with primers HF0061 and HF0062 with pUC18mut as the template (yielding a linear pUC18mut); (ii) PCR with primers G40 and G41 and 168 genomic DNA (containing the C-terminal region of *minJ*); (iii) PCR with primers G20 and G21 and pDendra2-N plasmid DNA (containing the *Dendra2* gene); (iv) PCR with primers G36 and G37 and JB40 genomic DNA (containing the spectinomycin adenyltransferase gene *aad9*); (v) PCR with primers G42 and G43 and 168 genomic DNA (containing the region downstream of *minJ*).

pHF07 (pUC18mut-*divIVA-Dendra2-aad9-divIVAdown*) was created by a Golden Gate assembly of 5 fragments: (i) PCR with primers HF0061 and HF0062 with pUC18mut as the template (yielding a linear pUC18mut); (ii) PCR with primers G34 and G35 and 168 genomic DNA (containing the C-terminal region of *divIVA*); (iii) PCR with primers G20 and G21 and pDendra2-N plasmid DNA (containing the *Dendra2* gene); (iv) PCR with primers G36 and G37 and JB40 genomic DNA (containing the spectinomycin adenyltransferase gene *aad9*); (v) PCR with primers G32 and G33 and 168 genomic DNA (containing the region downstream of *divIVA*).

pHF08 (pUC18mut-*divIVAΔ34-mNG-aad9-divIVAdown*) was created by a Golden Gate assembly of 4 fragments: (i) PCR with primers HF0061 and HF0062 with pUC18mut as the template (yielding a linear pUC18mut); (ii) PCR with primers G34 and HF0078 and pUC57-DivIVAd34-mNG plasmid DNA (containing *divIVAΔ34-mNeonGreen*); (iii) PCR with primers G36 and G37 and JB40 genomic DNA (containing the spectinomycin adenyltransferase gene *aad9*); (iv) PCR with primers G32 and G33 and 168 genomic DNA (containing the region downstream of *divIVA*).

pHF09 (pUC18mut-*minCup-aph3-A3-aad9*) was created by a Golden Gate assembly of 4 fragments: (i) PCR with primers HF0061 and HF0062 with pUC18mut as the template (yielding a linear pUC18mut; (ii) PCR with primers HF0206 and HF0207 and 168 genomic DNA (containing the region upstream of *minC*); (iii) PCR with primers HF0203 and HF0204 and 3309 genomic DNA (containing the aminoglycoside-3′-phosphotransferase gene *aph3-A3*, conferring resistance to kanamycin); (iv) PCR with primers G36 and G37 and JB40 genomic DNA (containing the spectinomycin adenyltransferase gene *aad9*).

Media and growth conditions. *B. subtilis* was grown on nutrient agar plates using commercial nutrient broth and 1.5% (wt/vol) agar at 37°C overnight. To reduce inhibitory effects, antibiotics were used only for transformations and when indicated, since allelic replacement is stable after integration (chloramphenicol, 5 μg ml^{-1}; tetracycline, 10 μg ml^{-1}; kanamycin, 5 μg ml^{-1}; spectinomycin, 100 μg ml^{-1}; erythromycin, 1 μg ml^{-1}).

For growth curves, *B. subtilis* was inoculated to an optical density at 600 nm (OD_{600}) of 0.05 from a fresh overnight culture and grown in LB (lysogeny broth) (10 g liter^{-1} tryptone, 10 g liter^{-1} NaCl, and 5 g liter^{-1} yeast extract) at 37°C with aeration in baffled shaking flasks (200 rpm) to an OD_{600} of 1. Subsequently, cultures were diluted to an OD_{600} of 0.1 in fresh LB and measured every hour for at least 6 h.

For microscopy, *B. subtilis* was inoculated to an OD_{600} of 0.05 from a fresh overnight culture and grown in MD medium, a modified version of Spizizen minimal medium (90), at 37°C with aeration in baffled shaking flasks (200 rpm) to an OD_{600} of 1. MD medium contains 10.7 mg ml^{-1} K_2HPO_4, 6 mg ml^{-1} KH_2PO_4, 1 mg ml^{-1} Na_3 citrate, 20 mg ml^{-1} glucose, 20 mg ml^{-1} L-tryptophan, 20 mg ml^{-1} ferric ammonium citrate, 25 mg ml^{-1} L-aspartate, and 0.36 mg ml^{-1} $MgSO_4$ and was always supplemented with 1 mg ml^{-1} Casamino Acids. Subsequently, cultures were diluted to an OD_{600} of 0.1 in fresh MD medium and grown to an OD_{600} of 0.5 (exponential phase).

For epifluorescence and time-lapse imaging (e.g., FRAP), *B. subtilis* cells were mounted on prewarmed 1.5% MD agarose pads, sealed with paraffin, and incubated for 10 min at 37°C before microscopic analysis. When used, FM4-64 dye or Nile red was added to the agarose pad before polymerization (1 μM final concentration).

For PALM imaging, a 0.5-ml portion of *B. subtilis* cells was fixed by addition of formaldehyde (1.5% [wt/vol] final concentration) and incubated for 20 min at 37°C. Subsequently, cells were washed (1 min, 2,300 relative centrifugal force [rcf]), resuspended in fresh MD medium supplemented with 10 mM glycine to stop the cross-linking reaction, and incubated for 10 min at 37°C. Cells were then washed 2 more times with MD medium containing 10 mM glycine. In a final washing step, the pellet was resuspended in 50 μl of MD medium with 10 mM glycine to reach a higher cell density. Cells were mounted on chambered coverslips (μ-slide 8 well; Ibidi) containing 200 μl MD medium with 10 mM glycine, which were pretreated for 30 to 60 min with 0.1% poly-L-lysine and successively washed 3 times with MD medium containing 10 mM glycine. Furthermore, TetraSpeck microspheres (100 nm; ThermoFisher) were added at a dilution that results in about 3 to 10 beads per field of view. To help sedimentation of cells and beads and to reach a uniform attachment to the glass surface, the chambered coverslip was centrifuged at 3,400 rcf for 10 min in a bucket-swing rotor (Eppendorf).

Typhoon imaging and Western blot analysis. To confirm the presence of full-length protein fusions and for quantitative analysis, *B. subtilis* strains were inoculated from an overnight culture to an OD_{600} of 0.05 in the morning and grown to an OD_{600} of 0.5 in 10 ml LB medium (MD medium for quantitative studies) at 37°C. Cells were then diluted 1/10 and grown again to mid-exponential phase (OD_{600}, 0.5). Cultures were centrifuged at 15,700 rcf for 1 min, washed once with lysis buffer (10 mM Tris, pH 7.5, 150 mM NaCl, 500 μM EDTA, 1 mM phenylmethylsulfonyl fluoride [PMSF]), and resuspended in lysis buffer with additional 10 mg/ml lysozyme (Sigma-Aldrich), 10 μg/ml DNase I (Roche), and 100 μg/ml

RNase A (Roche), concentrating the sample to an OD_{600} of 30. After incubation at 37°C for 20 min, the sample was briefly vortexed to crack the remaining intact cells. Thirty microliters of sample was then mixed with 10 μl of 4× SDS-PAGE loading buffer (200 mM Tris-HCl [pH 6.8], 400 mM dithiothreitol [DTT], 8% SDS, 0.4% bromophenol blue, and 40% glycerol). For Typhoon imaging and subsequent Western blotting, either samples were incubated for 20 min at room temperature or, for some samples meant exclusively for Western blotting, they were incubated at 95°C for 10 min for full denaturation (indicated in Fig. S3 in the supplemental material). Ten or 20 μl of sample was then separated by SDS-PAGE in 12% Bis-Tris gels. For visualization of green fluorescent fusions, gels were imaged in a Typhoon Trio (GE Healthcare; photomultiplier voltage [PMT], 600 to 800; excitation, 488 nm; emission, 526 short pass filter [SP]). For Western blotting, proteins were blotted onto 0.2-μm-pore-size polyvinylidene difluoride (PVDF) membranes. Proteins were visualized via anti-mCherry (polyclonal), anti-mNG (monoclonal), or anti-Dendra (polyclonal) antibodies, respectively.

To quantify Dendra2 fusions of MinD, MinJ, and DivIVA via in-gel fluorescence, three biological triplicates were prepared and imaged as described above, while avoiding oversaturation. The total number of MinD molecules was taken from a publication that utilized targeted mass spectrometry to determine absolute protein amounts of *B. subtilis* at mid-exponential phase in minimal medium with glucose (78). Relative quantification was then performed using ImageJ by measuring and comparing intensities of the bands.

Fluorescence microscopy. For strain characterization, microscopy images were taken with a Zeiss Axio Observer Z1 microscope equipped with a Hamamatsu OrcaR^2 camera using a Plan-Apochromat 100×/1.4 oil Ph3 objective (Zeiss). Dendra2, GFP, msfGFP, and mNeonGreen fluorescence was visualized with a 38 HE eGFP shift-free filter set (Zeiss), and FM4-64 membrane dye was visualized with a 63 HE mCherry filter set (Zeiss). The microscope was equipped with an environmental chamber set to 37°C. Digital images were acquired with Zen software (Zeiss).

For FRAP experiments, a Delta Vision Elite imaging system (GE Healthcare, Applied Precision) equipped with an InsightSSI illumination unit, an X4 laser module, and a CoolSnap HQ2 charge-coupled device (CCD) camera was used. Images were taken with a 100× oil PSF U-Plan S-Apo 1.4 numerical aperture objective. A four-color standard set InsightSSI unit was used with the following: excitation wavelengths for DAPI (4′,6-diamidino-2-phenylindole), 390/18 nm; FITC (fluorescein isothiocyanate), 475/28 nm; TRITC (tetramethyl rhodamine isocyanate), 542/27 nm; and Cy5, 632/22 nm; single band pass emission wavelengths for DAPI, 435/48 nm; FITC, 525/48 nm; TRITC, 597/45 nm; and Cy5, 679/34 nm; and a suitable polychroic for DAPI/FITC/TRITC/Cy5. GFP, msfGFP, and mNeonGreen were visualized using FITC settings and exposure times between 0.1 s (msfGFP, GFP) and 0.2 s (mNeonGreen). Bleaching was performed using a 488-nm laser (50 mW) with 10% power and a 0.005- to 0.01-s pulse. Frequency of acquisition and total amount of images were chosen according to the individual recovery times after initial testing with various settings.

Analysis of the images was performed using ImageJ 1.51 s. The corrected total cell fluorescence (CTCF) was calculated according to following formula: CTCF = integrated density − (area of selected cell × mean fluorescence of unspecific background readings) (91). For FRAP experiments, unspecific background was subtracted for every region of interest (ROI) (see above). The CTCF of the septa was divided by the CTCF of the whole cell to account for photobleaching during acquisition. The respective quotient of the unbleached spot was always set as 1 for normalization. Since *B. subtilis* keeps growing during time-lapse experiments like FRAP, the bleached spot moves in the field of view as cells elongate. Therefore, a macro in Fiji was created to dynamically follow and center the bleached spot through the frames of acquisition without any bias, which resulted in more precise FRAP curves. To determine halftime recovery and mobile/immobile fractions, the FRAP curve from the normalized recovery values was fitted to an exponential equation:

$$I(t) = A(1 - e^{-\tau t}) \tag{1}$$

where $I(t)$ is the normalized FRAP curve, A is the final value of the recovery, τ is the fitted parameter, and t is the time after the bleaching event. After determination of the fitted coefficients, they can be used to determine mobile (A) and immobile ($1 - A$) fractions, while the following equation was used to determine halftime recovery (equation 2):

$$T_{1/2} = \frac{\ln 0.5}{-\tau} \tag{2}$$

where $T_{1/2}$ is the halftime recovery and τ is the fitted parameter. Diffusion coefficients were then calculated with the following formula:

$$D = (w^2/4T_{1/2}) \times 0.88 \tag{3}$$

according to Axelrod et al. (92), where D is the diffusion coefficient, w is the radius of the circular laser beam, and $T_{1/2}$ is the time when fluorescence recovery reaches half height of total recovery. To estimate the bleaching spot radius, cells expressing cytosolic GFP were fixed with 1.5% (vol/vol) formaldehyde as described above, mounted on agarose pads, bleached at laser powers of 10% to 100% in increments of 10%, and imaged right after bleaching. The radius was measured in ImageJ and averaged per triplicate to calculate the function of bleach radius over laser power. Graphs and statistics were created in R 3.3.1 (93) utilizing the packages ggplot2 (94) and nlstools (95). For measuring cell profiles, Fiji (ImageJ) was

used, and a segmented line of width 5 was drawn through the longitudinal axis of the cells and subsequently measured. Analysis and demographs were created in R.

Reaction-diffusion equations. The setup of our mathematical model is based on previous approaches for intracellular protein dynamics (32, 34, 36, 83). Specifically, we present a minimal model to account for DivIVA-mediated MinD localization. The model includes the following set of biochemical reactions: (i) attachment of MinD-ATP (with volume concentration u_{DT}) from the bulk to the membrane with constant rate k_D; (ii) recruitment of bulk MinD-ATP to the membrane by membrane-bound MinD (with areal concentration u_d) with rate $\tilde{k}_{dD}$; (iii) hydrolysis and detachment of membrane-bound MinD into bulk MinD-ADP (u_{DD}) with rate $\tilde{k}_H$; (iv) reactivation of bulk MinD-ADP by nucleotide exchange to MinD-ATP with rate λ. The system of ensuing reaction-diffusion equations reads as follows:

$$\partial_t u_{DD} = D_D \nabla_c^2 u_{DD} - \lambda u_{DD} \tag{4a}$$

$$\partial_t u_{DT} = D_D \nabla_c^2 u_{DT} + \lambda u_{DD} \tag{4b}$$

$$\partial_t u_d = D_d \nabla_m^2 u_d + \left(k_D + \tilde{k}_{dD} u_d\right) u_{DT} - \tilde{k}_H u_d \tag{4c}$$

where the subscript *c* or *m* denotes that the nabla operator acts in the bulk or on the membrane, respectively. These equations are coupled through nonlinear reactive boundary conditions at the membrane surface, stating that the biochemical reactions involving both membrane-bound and bulk proteins equal the diffusive flux onto and off the membrane:

$$D_D \nabla_n u_{DD}|_m = \tilde{k}_H u_d \tag{5a}$$

$$D_D \nabla_n u_{DT}|_m = -(k_D + \tilde{k}_{dD} u_d) u_{DT} \tag{5b}$$

Here, the subscript *n* denotes that we take the nabla operator acting along the outward normal vector of the boundary (membrane). The set of reaction-diffusion equations conserve the total mass of MinD. Hence, the total particle number, N_D, of MinD obeys the relation

$$N_D = \int_\Omega (u_{DD} + u_{DT})\, dV + \int_{\partial\Omega} u_d dS \tag{6}$$

We simulated the set of reaction-diffusion equations in a spherocylindrical geometry in three-dimensional space (3D) using the finite-element software COMSOL v5.4a; for an illustration of the geometry used, see Fig. S7. The length (L) and height (h) were set to typical values known for *B. subtilis* cells, $L = 2.8\ \mu$m and $h = 0.85\ \mu$m, respectively. The mean total density of MinD was set to $[\text{MinD}] = 2,450\ \mu\text{m}^{-3}$ for all simulations (Table S1). We assume that in addition to MinD self-recruitment, MinJ recruits MinD-ATP from the bulk to the membrane and that membrane-bound MinD is stabilized by DivIVA-MinJ complexes on the membrane. We model the interaction of MinD with MinJ and DivIVA implicitly through space-dependent recruitment and detachment rates. To this end, we assume that the recruitment rate is amplified by a factor α and that the detachment rate is reduced by a factor β at regions of high negative curvature (such as the poles or the septum). This assumption is motivated by experiments which suggest that MinD localization is dependent on MinJ and that DivIVA acts as a scaffold that stabilizes MinJ and MinD (see Discussion). We therefore set the recruitment and detachment rates to $k_{dD} = \alpha \tilde{k}_{dD}$ and $k_H = \tilde{k}_H/\beta$ at regions of high negative curvature (Fig. S7), where α and β denote dimensionless amplification and reduction prefactors, respectively. The parameters $\tilde{k}_{dD}$ and $\tilde{k}_H$ denote the uniform recruitment and detachment rates that one would obtain if interactions between MinD and DivIVA-MinJ complexes were neglected, i.e., if $\alpha = \beta = 1$ (see below).

Simulation of the model: polar localization. In a cell with no preexisting division apparatus, the Min system localizes at the poles of the bacteria (see Discussion). We model this case by setting $\alpha = 4$ and $\beta = 3$ at the polar caps and $\alpha = \beta = 1$ for the remaining part of the rod-shaped geometry (Fig. S7b). The uniform rates were set to $\tilde{k}_{dD} = 0.04\ \mu\text{m}^2/\text{s}$ and $\tilde{k}_H = 0.1\ \mu\text{m}^2/\text{s}$ as given above. Simulations show that MinD can be pinned to the cell poles for nonuniform kinetic parameters (Fig. 3c, left).

Depletion of MinD at the poles. Next, we tested if the polar distribution of MinD decays to a homogeneous protein distribution along the membrane when the rates are uniform over the whole cell body. To this end, we used the steady-state polar distribution of MinD (as obtained above) as the initial condition for a simulation with uniform rates in the entire geometry, i.e., $\alpha = 1,\ \beta = 1$. We found that for uniform rates, MinD proteins preferentially localize near the cell center (Fig. 3c, left to right). The reason for this unexpected inhomogeneous protein distribution is a purely geometric effect (see Discussion).

Localization at septum. The curvature-sensing protein DivIVA targets the division site and guides MinJ and MinD to the septum (see Discussion). Above, we showed that MinD localizes to the cell poles if the recruitment and detachment rate of MinD are altered at the poles due to interactions with MinJ and DivIVA. For uniform rates, however, the MinD density distribution is spread around midcell but not sharply localized at the septum as observed in experiments. Sharp localization of MinD at midcell requires interaction with DivIVA and MinJ, and we therefore model this case in the same way as for polar

TABLE 7 Filter parameters for PALM imaging of the different strains[a]

Strain or FP	point spread function (PSF) at half maximum [nm]	No. of photons
Dendra2-MinD	70–160	70–250
MinJ-mNeonGreen	70–160	70–300
DivIVA-PAmCherry	60–170	50–500

[a]Filters were chosen according to the fluorophore (FP) behavior in PALM to eliminate background and signal of fluorescent beads from the results.

localization. First, we define a narrow region with width $s_w = 0.14\ \mu$m at midcell, which represents the septum (Fig. S7c). We set again $\alpha = 4$ and $\beta = 3$ at this geometric region to model the interactions of MinD with MinJ and DivIVA implicitly through a modified recruitment and detachment rate. Simulations of the model show that MinD localizes sharply at the septum (Fig. 3d, left to right).

Parameter dependence of the simulation results. Since we consider steady-state solutions of the reaction-diffusion system in equations 4 and 5, our qualitative results are not sensitive against variations of the kinetic parameters (Table S1). Changing the values of the kinetic parameters would only shift the dynamic equilibrium state, without affecting the protein distributions qualitatively. There is only one exception, which is the nucleotide exchange rate, λ, or, more precisely, the reactivation length scale $l = \sqrt{D_D/\lambda}$.

Since nucleotide exchange and diffusion are the main reasons for the geometric effect discussed above, the qualitative steady-state density distributions may depend on l. We will discuss two relevant limits which affect the redistribution of MinD to midcell. (i) Let us assume that the reactivation of detached MinD-ADP to MinD-ATP is instantaneous and hence λ is very large. In this case, the reactivation length would be much smaller than the radius of curvature at the poles R, i.e., $l \ll R$. A very small value of l implies that detached proteins can rebind the membrane without delay. Therefore, in this case, there is no geometric effect and the steady-state density distribution of MinD would be homogeneous. (ii) Next, let us assume that λ is very small, such that the reactivation length becomes much larger than the length of the bacteria L, i.e., $l \gg L$. This would imply that proteins detaching from the membrane diffuse a long distance until they exchange their nucleotide and become able to rebind the membrane again. In this case, the MinD density distribution would be also homogeneous. However, due to the small value of λ, inactive MinD-ADP proteins are abundant in the cytosol and only few MinD-ATP proteins attach to the membrane, resulting in low membrane densities.

The geometric effect (see above) is present if the value of l lies between the radius of curvature at the poles and the length of the bacteria, i.e., $R<l<L$. Therefore, our qualitative results are not sensitive to the exact choice of l as long as the inequality above is fulfilled. For our parameters, we have $R \approx 0.42\ \mu$m, $L = 2.8\ \mu$m, and $l = \sqrt{D_D/\lambda} \approx 1.6\ \mu$m. In summary, this geometric effect is quite robust and does not require the fine-tuning of parameters. For an in-depth discussion of the geometric effect and its dependence on various system parameters, see reference 83.

PALM and cluster analysis. Photoactivated localization microscopy (PALM) imaging was performed with the microscope system ELYRA P.1 (Zeiss) and the accompanying Zen software. It is equipped with a 405-nm diode-laser (50 mW), a 488-nm laser (200 mW), a 561-nm laser (200 mW), and a 640-nm laser (150 mW). Furthermore, an alpha Plan-Apochromat 100×/1.46 oil differential inference contrast (DIC) M27 objective (Zeiss) was used, in combination with a 1.6× Optovar. The filter sets were the following: a 77 HE GFP+mRFP+Alexa 633 shift-free (EX TBP 483 + 564 + 642, BS TFT 506 + 582 + 659, EM TBP 526 + 601 + 688), a 49 DAPI shift-free (EX G 365, BS FT 395, EM BP 445/50), a BP 420–480/LP 750, a BP 495–550/LP 750, an LP 570, and an LP 655 filter set. Images were recorded with an Andor EMCCD camera iXon DU 897. Samples expressing mNeonGreen were illuminated with the 488-nm laser at 7.4 mW. Samples expressing Dendra2 or PAmCherry were illuminated with an excitation laser (561 nm, 5.3 mW) and an activation laser (405 nm). To avoid cooccurrence of multiple events in the same spot, the power of the activation laser was increased stepwise from 0.008 mW to 1.6 mW. MinJ-mNeonGreen was illuminated in pseudo-TIRF (total internal reflection fluorescence) mode and recorded at 20 Hz with 200 camera gain, while Dendra2-MinD and DivIVA-PAmCherry were imaged with the same camera settings in regular wide field. Analysis was performed in the Zen Black (Zeiss) software. Detection of single emitters was performed with a peak mask size of 9 pixels and a minimum peak intensity-to-noise ratio of 6.0; overlapping emitters were discarded. Localization was extrapolated via a 2D Gaussian fitting, and images were drift corrected utilizing a fiducial-based mode with at least 3 beads in focus. Filtering was used to minimize noise, background, and out-of-focus emitters and to exclude beads from the evaluation, according to Table 7, which were different for each respective fluorophore.

Cluster analysis was performed in R 3.3.1 (93) utilizing the DBSCAN package (96, 97) including OPTICS (98). Clusters were determined by applying the OPTICS algorithm to the respective molecule tables generated via PALM. The minimal number of points that define a cluster (minPts) was defined as 10, reflecting apparent clusters seen in rendered PALM imaging, and a minimum distance between cluster edge points (epsCl) of 20 and 30 nm for MinD and DivIVA, respectively, according to the observed density of protein localization.

SUPPLEMENTAL MATERIAL

Supplemental material is available online only.

FIG S1, TIF file, 2.5 MB.
FIG S2, TIF file, 1.1 MB.
FIG S3, TIF file, 1 MB.
FIG S4, TIF file, 2.3 MB.
FIG S5, TIF file, 0.6 MB.
FIG S6, TIF file, 2.4 MB.
FIG S7, TIF file, 0.2 MB.
FIG S8, TIF file, 1.2 MB.
TABLE S1, DOCX file, 0.02 MB.

ACKNOWLEDGMENTS

This research was supported by the Deutsche Forschungsgemeinschaft within the Transregio Collaborative Research Center (TRR 174) Spatiotemporal Dynamics of Bacterial Cells (project P03 to E.F. and project P05 to M.B.).

We thank Abigail Savietto for help with the phenotypic characterization and the other members of the M.B. lab for discussions, feedback, and comments on the manuscript.

M.B. and E.F. conceived the study, H.F. constructed the strains, performed the *in vivo* experiments, including microscopy, and analyzed the data, and L.W. and E.F. developed the theoretical model and performed the mathematical analysis. All authors wrote the manuscript.

We declare no competing interests.

REFERENCES

1. Bi EF, Lutkenhaus J. 1991. FtsZ ring structure associated with division in *Escherichia coli*. Nature 354:161–164. https://doi.org/10.1038/354161a0.
2. Margolin W. 2005. FtsZ and the division of prokaryotic cells and organelles. Nat Rev Mol Cell Biol 6:862–871. https://doi.org/10.1038/nrm1745.
3. Rowlett VW, Margolin W. 2015. The Min system and other nucleoid-independent regulators of Z ring positioning. Front Microbiol 6:478. https://doi.org/10.3389/fmicb.2015.00478.
4. Shih YL, Rothfield L. 2006. The bacterial cytoskeleton. Microbiol Mol Biol Rev 70:729–754. https://doi.org/10.1128/MMBR.00017-06.
5. Lutkenhaus J, Pichoff S, Du S. 2012. Bacterial cytokinesis: from Z ring to divisome. Cytoskeleton (Hoboken) 69:778–790. https://doi.org/10.1002/cm.21054.
6. Ortiz C, Natale P, Cueto L, Vicente M. 2016. The keepers of the ring: regulators of FtsZ assembly. FEMS Microbiol Rev 40:57–67. https://doi.org/10.1093/femsre/fuv040.
7. Errington J, Wu LJ. 2017. Cell cycle machinery in *Bacillus subtilis*. Subcell Biochem 84:67–101. https://doi.org/10.1007/978-3-319-53047-5_3.
8. Haeusser DP, Margolin W. 2016. Splitsville: structural and functional insights into the dynamic bacterial Z ring. Nat Rev Microbiol 14:305–319. https://doi.org/10.1038/nrmicro.2016.26.
9. Bisson-Filho AW, Hsu YP, Squyres GR, Kuru E, Wu F, Jukes C, Sun Y, Dekker C, Holden S, VanNieuwenhze MS, Brun YV, Garner EC. 2017. Treadmilling by FtsZ filaments drives peptidoglycan synthesis and bacterial cell division. Science 355:739–743. https://doi.org/10.1126/science.aak9973.
10. Yang X, Lyu Z, Miguel A, McQuillen R, Huang KC, Xiao J. 2017. GTPase activity-coupled treadmilling of the bacterial tubulin FtsZ organizes septal cell wall synthesis. Science 355:744–747. https://doi.org/10.1126/science.aak9995.
11. Wagstaff JM, Tsim M, Oliva MA, Garcia-Sanchez A, Kureisaite-Ciziene D, Andreu JM, Löwe J. 2017. A polymerization-associated structural switch in FtsZ that enables treadmilling of model filaments. mBio 8:e00254-17. https://doi.org/10.1128/mBio.00254-17.
12. Wu LJ, Errington J. 2004. Coordination of cell division and chromosome segregation by a nucleoid occlusion protein in Bacillus subtilis. Cell 117:915–925. https://doi.org/10.1016/j.cell.2004.06.002.
13. Bernhardt TG, de Boer PA. 2005. SlmA, a nucleoid-associated, FtsZ binding protein required for blocking septal ring assembly over chromosomes in *E. coli*. Mol Cell 18:555–564. https://doi.org/10.1016/j.molcel.2005.04.012.
14. Tonthat NK, Arold ST, Pickering BF, Van Dyke MW, Liang S, Lu Y, Beuria TK, Margolin W, Schumacher MA. 2011. Molecular mechanism by which the nucleoid occlusion factor, SlmA, keeps cytokinesis in check. EMBO J 30:154–164. https://doi.org/10.1038/emboj.2010.288.
15. Tonthat NK, Milam SL, Chinnam N, Whitfill T, Margolin W, Schumacher MA. 2013. SlmA forms a higher-order structure on DNA that inhibits cytokinetic Z-ring formation over the nucleoid. Proc Natl Acad Sci U S A 110:10586–10591. https://doi.org/10.1073/pnas.1221036110.
16. Adams DW, Wu LJ, Errington J. 2015. Nucleoid occlusion protein Noc recruits DNA to the bacterial cell membrane. EMBO J 34:491–501. https://doi.org/10.15252/embj.201490177.
17. de Boer PA, Crossley RE, Rothfield LI. 1988. Isolation and properties of *minB*, a complex genetic locus involved in correct placement of the division site in *Escherichia coli*. J Bacteriol 170:2106–2112. https://doi.org/10.1128/jb.170.5.2106-2112.1988.
18. de Boer PA, Crossley RE, Rothfield LI. 1992. Roles of MinC and MinD in the site-specific septation block mediated by the MinCDE system of *Escherichia coli*. J Bacteriol 174:63–70. https://doi.org/10.1128/jb.174.1.63-70.1992.
19. Hu Z, Lutkenhaus J. 1999. Topological regulation of cell division in *Escherichia coli* involves rapid pole to pole oscillation of the division inhibitor MinC under the control of MinD and MinE. Mol Microbiol 34:82–90. https://doi.org/10.1046/j.1365-2958.1999.01575.x.
20. Hu Z, Gogol EP, Lutkenhaus J. 2002. Dynamic assembly of MinD on phospholipid vesicles regulated by ATP and MinE. Proc Natl Acad Sci U S A 99:6761–6766. https://doi.org/10.1073/pnas.102059099.
21. Szeto TH, Rowland SL, Rothfield LI, King GF. 2002. Membrane localization of MinD is mediated by a C-terminal motif that is conserved across eubacteria, archaea, and chloroplasts. Proc Natl Acad Sci U S A 99:15693–15698. https://doi.org/10.1073/pnas.232590599.
22. Lackner LL, Raskin DM, de Boer PA. 2003. ATP-dependent interactions between *Escherichia coli* Min proteins and the phospholipid membrane in vitro. J Bacteriol 185:735–749. https://doi.org/10.1128/jb.185.3.735-749.2003.
23. Mileykovskaya E, Fishov I, Fu X, Corbin BD, Margolin W, Dowhan W. 2003. Effects of phospholipid composition on MinD-membrane interactions in vitro and in vivo. J Biol Chem 278:22193–22198. https://doi.org/10.1074/jbc.M302603200.
24. Hu Z, Mukherjee A, Pichoff S, Lutkenhaus J. 1999. The MinC component of the division site selection system in *Escherichia coli* interacts with FtsZ

to prevent polymerization. Proc Natl Acad Sci U S A 96:14819–14824. https://doi.org/10.1073/pnas.96.26.14819.
25. Hu Z, Lutkenhaus J. 2001. Topological regulation of cell division in *E. coli*: spatiotemporal oscillation of MinD requires stimulation of its ATPase by MinE and phospholipid. Mol Cell 7:1337–1343. https://doi.org/10.1016/S1097-2765(01)00273-8.
26. Touhami A, Jericho M, Rutenberg AD. 2006. Temperature dependence of MinD oscillation in *Escherichia coli*: running hot and fast. J Bacteriol 188:7661–7667. https://doi.org/10.1128/JB.00911-06.
27. Park KT, Wu W, Battaile KP, Lovell S, Holyoak T, Lutkenhaus J. 2011. The Min oscillator uses MinD-dependent conformational changes in MinE to spatially regulate cytokinesis. Cell 146:396–407. https://doi.org/10.1016/j.cell.2011.06.042.
28. Schweizer J, Loose M, Bonny M, Kruse K, Monch I, Schwille P. 2012. Geometry sensing by self-organized protein patterns. Proc Natl Acad Sci U S A 109:15283–15288. https://doi.org/10.1073/pnas.1206953109.
29. Loose M, Fischer-Friedrich E, Ries J, Kruse K, Schwille P. 2008. Spatial regulators for bacterial cell division self-organize into surface waves in vitro. Science 320:789–792. https://doi.org/10.1126/science.1154413.
30. Wu F, van Schie BG, Keymer JE, Dekker C. 2015. Symmetry and scale orient Min protein patterns in shaped bacterial sculptures. Nat Nanotechnol 10:719–726. https://doi.org/10.1038/nnano.2015.126.
31. Wu F, Halatek J, Reiter M, Kingma E, Frey E, Dekker C. 2016. Multistability and dynamic transitions of intracellular Min protein patterns. Mol Syst Biol 12:873. https://doi.org/10.15252/msb.20156724.
32. Huang KC, Meir Y, Wingreen NS. 2003. Dynamic structures in *Escherichia coli*: spontaneous formation of MinE rings and MinD polar zones. Proc Natl Acad Sci U S A 100:12724–12728. https://doi.org/10.1073/pnas.2135445100.
33. Fange D, Elf J. 2006. Noise-induced Min phenotypes in E. coli. PLoS Comput Biol 2:e80. https://doi.org/10.1371/journal.pcbi.0020080.
34. Halatek J, Frey E. 2012. Highly canalized MinD transfer and MinE sequestration explain the origin of robust MinCDE-protein dynamics. Cell Rep 1:741–752. https://doi.org/10.1016/j.celrep.2012.04.005.
35. Halatek J, Frey E. 2018. Rethinking pattern formation in reaction-diffusion systems. Nature Phys 14:507–514. https://doi.org/10.1038/s41567-017-0040-5.
36. Denk J, Kretschmer S, Halatek J, Hartl C, Schwille P, Frey E. 2018. MinE conformational switching confers robustness on self-organized Min protein patterns. Proc Natl Acad Sci U S A 115:4553–4558. https://doi.org/10.1073/pnas.1719801115.
37. Hoffmann M, Schwarz US. 2014. Oscillations of Min-proteins in micropatterned environments: a three-dimensional particle-based stochastic simulation approach. Soft Matter 10:2388–2396. https://doi.org/10.1039/c3sm52251b.
38. Shen B, Lutkenhaus J. 2010. Examination of the interaction between FtsZ and MinCN in *E. coli* suggests how MinC disrupts Z rings. Mol Microbiol 75:1285–1298. https://doi.org/10.1111/j.1365-2958.2010.07055.x.
39. Shen B, Lutkenhaus J. 2009. The conserved C-terminal tail of FtsZ is required for the septal localization and division inhibitory activity of MinC(C)/MinD. Mol Microbiol 72:410–424. https://doi.org/10.1111/j.1365-2958.2009.06651.x.
40. Dajkovic A, Lan G, Sun SX, Wirtz D, Lutkenhaus J. 2008. MinC spatially controls bacterial cytokinesis by antagonizing the scaffolding function of FtsZ. Curr Biol 18:235–244. https://doi.org/10.1016/j.cub.2008.01.042.
41. Blasios V, Bisson-Filho AW, Castellen P, Nogueira ML, Bettini J, Portugal RV, Zeri AC, Gueiros-Filho FJ. 2013. Genetic and biochemical characterization of the MinC-FtsZ interaction in Bacillus subtilis. PLoS One 8:e60690. https://doi.org/10.1371/journal.pone.0060690.
42. Ebersbach G, Gerdes K. 2005. Plasmid segregation mechanisms. Annu Rev Genet 39:453–479. https://doi.org/10.1146/annurev.genet.38.072902.091252.
43. Gitai Z. 2006. Plasmid segregation: a new class of cytoskeletal proteins emerges. Curr Biol 16:R133–R136. https://doi.org/10.1016/j.cub.2006.02.007.
44. Hu Z, Lutkenhaus J. 2003. A conserved sequence at the C-terminus of MinD is required for binding to the membrane and targeting MinC to the septum. Mol Microbiol 47:345–355. https://doi.org/10.1046/j.1365-2958.2003.03321.x.
45. de Boer PA, Crossley RE, Hand AR, Rothfield LI. 1991. The MinD protein is a membrane ATPase required for the correct placement of the *Escherichia coli* division site. EMBO J 10:4371–4380. https://doi.org/10.1002/j.1460-2075.1991.tb05015.x.
46. Conti J, Viola MG, Camberg JL. 2015. The bacterial cell division regulators MinD and MinC form polymers in the presence of nucleotide. FEBS Lett 589:201–206. https://doi.org/10.1016/j.febslet.2014.11.047.
47. Ghosal D, Trambaiolo D, Amos LA, Löwe J. 2014. MinCD cell division proteins form alternating copolymeric cytomotive filaments. Nat Commun 5:5341. https://doi.org/10.1038/ncomms6341.
48. Reeve JN, Mendelson NH, Coyne SI, Hallock LL, Cole RM. 1973. Minicells of *Bacillus subtilis*. J Bacteriol 114:860–873. https://doi.org/10.1128/JB.114.2.860-873.1973.
49. de Boer PA, Crossley RE, Rothfield LI. 1990. Central role for the Escherichia coli *minC* gene product in two different cell division-inhibition systems. Proc Natl Acad Sci U S A 87:1129–1133. https://doi.org/10.1073/pnas.87.3.1129.
50. Raskin DM, de Boer PA. 1997. The MinE ring: an FtsZ-independent cell structure required for selection of the correct division site in *E. coli*. Cell 91:685–694. https://doi.org/10.1016/S0092-8674(00)80455-9.
51. Hale CA, Meinhardt H, de Boer PA. 2001. Dynamic localization cycle of the cell division regulator MinE in *Escherichia coli*. EMBO J 20:1563–1572. https://doi.org/10.1093/emboj/20.7.1563.
52. Ma LY, King G, Rothfield L. 2003. Mapping the MinE site involved in interaction with the MinD division site selection protein of *Escherichia coli*. J Bacteriol 185:4948–4955. https://doi.org/10.1128/jb.185.16.4948-4955.2003.
53. Hsieh CW, Lin TY, Lai HM, Lin CC, Hsieh TS, Shih YL. 2010. Direct MinE-membrane interaction contributes to the proper localization of MinDE in *E. coli*. Mol Microbiol 75:499–512. https://doi.org/10.1111/j.1365-2958.2009.07006.x.
54. Loose M, Fischer-Friedrich E, Herold C, Kruse K, Schwille P. 2011. Min protein patterns emerge from rapid rebinding and membrane interaction of MinE. Nat Struct Mol Biol 18:577–583. https://doi.org/10.1038/nsmb.2037.
55. Vecchiarelli AG, Li M, Mizuuchi M, Hwang LC, Seol Y, Neuman KC, Mizuuchi K. 2016. Membrane-bound MinDE complex acts as a toggle switch that drives Min oscillation coupled to cytoplasmic depletion of MinD. Proc Natl Acad Sci U S A 113:E1479–E1488. https://doi.org/10.1073/pnas.1600644113.
56. Halatek J, Brauns F, Frey E. 2018. Self-organization principles of intracellular pattern formation. Philos Trans R Soc Lond B Biol Sci 373:20170107. https://doi.org/10.1098/rstb.2017.0107.
57. Marston AL, Errington J. 1999. Selection of the midcell division site in *Bacillus subtilis* through MinD-dependent polar localization and activation of MinC. Mol Microbiol 33:84–96. https://doi.org/10.1046/j.1365-2958.1999.01450.x.
58. Marston AL, Thomaides HB, Edwards DH, Sharpe ME, Errington J. 1998. Polar localization of the MinD protein of *Bacillus subtilis* and its role in selection of the mid-cell division site. Genes Dev 12:3419–3430. https://doi.org/10.1101/gad.12.21.3419.
59. Cha JH, Stewart GC. 1997. The *divIVA* minicell locus of *Bacillus subtilis*. J Bacteriol 179:1671–1683. https://doi.org/10.1128/jb.179.5.1671-1683.1997.
60. Edwards DH, Errington J. 1997. The *Bacillus subtilis* DivIVA protein targets to the division septum and controls the site specificity of cell division. Mol Microbiol 24:905–915. https://doi.org/10.1046/j.1365-2958.1997.3811764.x.
61. Lenarcic R, Halbedel S, Visser L, Shaw M, Wu LJ, Errington J, Marenduzzo D, Hamoen LW. 2009. Localisation of DivIVA by targeting to negatively curved membranes. EMBO J 28:2272–2282. https://doi.org/10.1038/emboj.2009.129.
62. Bramkamp M, Emmins R, Weston L, Donovan C, Daniel RA, Errington J. 2008. A novel component of the division-site selection system of *Bacillus subtilis* and a new mode of action for the division inhibitor MinCD. Mol Microbiol 70:1556–1569. https://doi.org/10.1111/j.1365-2958.2008.06501.x.
63. Patrick JE, Kearns DB. 2008. MinJ (YvjD) is a topological determinant of cell division in *Bacillus subtilis*. Mol Microbiol 70:1166–1179. https://doi.org/10.1111/j.1365-2958.2008.06469.x.
64. Jemth P, Gianni S. 2007. PDZ domains: folding and binding. Biochemistry 46:8701–8708. https://doi.org/10.1021/bi7008618.
65. van Baarle S, Bramkamp M. 2010. The MinCDJ system in *Bacillus subtilis* prevents minicell formation by promoting divisome disassembly. PLoS One 5:e9850. https://doi.org/10.1371/journal.pone.0009850.
66. Bach JN, Albrecht N, Bramkamp M. 2014. Imaging DivIVA dynamics using photo-convertible and activatable fluorophores in *Bacillus subtilis*. Front Microbiol 5:59. https://doi.org/10.3389/fmicb.2014.00059.

67. Gregory JA, Becker EC, Pogliano K. 2008. *Bacillus subtilis* MinC destabilizes FtsZ-rings at new cell poles and contributes to the timing of cell division. Genes Dev 22:3475–3488. https://doi.org/10.1101/gad.1732408.
68. Gurskaya NG, Verkhusha VV, Shcheglov AS, Staroverov DB, Chepurnykh TV, Fradkov AF, Lukyanov S, Lukyanov KA. 2006. Engineering of a monomeric green-to-red photoactivatable fluorescent protein induced by blue light. Nat Biotechnol 24:461–465. https://doi.org/10.1038/nbt1191.
69. Pedelacq JD, Cabantous S, Tran T, Terwilliger TC, Waldo GS. 2006. Engineering and characterization of a superfolder green fluorescent protein. Nat Biotechnol 24:79–88. https://doi.org/10.1038/nbt1172.
70. Shaner NC, Lambert GG, Chammas A, Ni Y, Cranfill PJ, Baird MA, Sell BR, Allen JR, Day RN, Israelsson M, Davidson MW, Wang J. 2013. A bright monomeric green fluorescent protein derived from *Branchiostoma lanceolatum*. Nat Methods 10:407–409. https://doi.org/10.1038/nmeth.2413.
71. Shaner NC, Campbell RE, Steinbach PA, Giepmans BN, Palmer AE, Tsien RY. 2004. Improved monomeric red, orange and yellow fluorescent proteins derived from *Discosoma* sp. red fluorescent protein. Nat Biotechnol 22:1567–1572. https://doi.org/10.1038/nbt1037.
72. Subach FV, Patterson GH, Manley S, Gillette JM, Lippincott-Schwartz J, Verkhusha VV. 2009. Photoactivatable mCherry for high-resolution two-color fluorescence microscopy. Nat Methods 6:153–159. https://doi.org/10.1038/nmeth.1298.
73. Ando R, Mizuno H, Miyawaki A. 2004. Regulated fast nucleocytoplasmic shuttling observed by reversible protein highlighting. Science 306:1370–1373. https://doi.org/10.1126/science.1102506.
74. Chang H, Zhang M, Ji W, Chen J, Zhang Y, Liu B, Lu J, Zhang J, Xu P, Xu T. 2012. A unique series of reversibly switchable fluorescent proteins with beneficial properties for various applications. Proc Natl Acad Sci U S A 109:4455–4460. https://doi.org/10.1073/pnas.1113770109.
75. Stockmar I, Feddersen H, Cramer K, Gruber S, Jung K, Bramkamp M, Shin JY. 2018. Optimization of sample preparation and green color imaging using the mNeonGreen fluorescent protein in bacterial cells for photoactivated localization microscopy. Sci Rep 8:10137. https://doi.org/10.1038/s41598-018-28472-0.
76. Thomaides HB, Freeman M, El Karoui M, Errington J. 2001. Division site selection protein DivIVA of *Bacillus subtilis* has a second distinct function in chromosome segregation during sporulation. Genes Dev 15:1662–1673. https://doi.org/10.1101/gad.197501.
77. Eswaramoorthy P, Erb ML, Gregory JA, Silverman J, Pogliano K, Pogliano J, Ramamurthi KS. 2011. Cellular architecture mediates DivIVA ultrastructure and regulates min activity in *Bacillus subtilis*. mBio 2:e00257-11. https://doi.org/10.1128/mBio.00257-11.
78. Maass S, Sievers S, Zuhlke D, Kuzinski J, Sappa PK, Muntel J, Hessling B, Bernhardt J, Sietmann R, Volker U, Hecker M, Becher D. 2011. Efficient, global-scale quantification of absolute protein amounts by integration of targeted mass spectrometry and two-dimensional gel-based proteomics. Anal Chem 83:2677–2684. https://doi.org/10.1021/ac1031836.
79. van Baarle S, Celik IN, Kaval KG, Bramkamp M, Hamoen LW, Halbedel S. 2013. Protein-protein interaction domains of *Bacillus subtilis* DivIVA. J Bacteriol 195:1012–1021. https://doi.org/10.1128/JB.02171-12.
80. Montero Llopis P, Sliusarenko O, Heinritz J, Jacobs-Wagner C. 2012. In vivo biochemistry in bacterial cells using FRAP: insight into the translation cycle. Biophys J 103:1848–1859. https://doi.org/10.1016/j.bpj.2012.09.035.
81. Karoui ME, Errington J. 2001. Isolation and characterization of topological specificity mutants of *minD* in *Bacillus subtilis*. Mol Microbiol 42:1211–1221. https://doi.org/10.1046/j.1365-2958.2001.02710.x.
82. Howard M. 2004. A mechanism for polar protein localization in bacteria. J Mol Biol 335:655–663. https://doi.org/10.1016/j.jmb.2003.10.058.
83. Thalmeier D, Halatek J, Frey E. 2016. Geometry-induced protein pattern formation. Proc Natl Acad Sci U S A 113:548–553. https://doi.org/10.1073/pnas.1515191113.
84. Eswara PJ, Ramamurthi KS. 2017. Bacterial cell division: nonmodels poised to take the spotlight. Annu Rev Microbiol 71:393–411. https://doi.org/10.1146/annurev-micro-102215-095657.
85. Kretschmer S, Schwille P. 2016. Pattern formation on membranes and its role in bacterial cell division. Curr Opin Cell Biol 38:52–59. https://doi.org/10.1016/j.ceb.2016.02.005.
86. Vecchiarelli AG, Li M, Mizuuchi M, Mizuuchi K. 2014. Differential affinities of MinD and MinE to anionic phospholipid influence Min patterning dynamics in vitro. Mol Microbiol 93:453–463. https://doi.org/10.1111/mmi.12669.
87. Kumar M, Mommer MS, Sourjik V. 2010. Mobility of cytoplasmic, membrane, and DNA-binding proteins in *Escherichia coli*. Biophys J 98:552–559. https://doi.org/10.1016/j.bpj.2009.11.002.
88. Rodrigues CD, Harry EJ. 2012. The Min system and nucleoid occlusion are not required for identifying the division site in *Bacillus subtilis* but ensure its efficient utilization. PLoS Genet 8:e1002561. https://doi.org/10.1371/journal.pgen.1002561.
89. Sieber JJ, Willig KI, Kutzner C, Gerding-Reimers C, Harke B, Donnert G, Rammner B, Eggeling C, Hell SW, Grubmuller H, Lang T. 2007. Anatomy and dynamics of a supramolecular membrane protein cluster. Science 317:1072–1076. https://doi.org/10.1126/science.1141727.
90. Anagnostopoulos C, Spizizen J. 1961. Requirements for transformation in *Bacillus subtilis*. J Bacteriol 81:741–746. https://doi.org/10.1128/JB.81.5.741-746.1961.
91. Gavet O, Pines J. 2010. Activation of cyclin B1-Cdk1 synchronizes events in the nucleus and the cytoplasm at mitosis. J Cell Biol 189:247–259. https://doi.org/10.1083/jcb.200909144.
92. Axelrod D, Koppel DE, Schlessinger J, Elson E, Webb WW. 1976. Mobility measurement by analysis of fluorescence photobleaching recovery kinetics. Biophys J 16:1055–1069. https://doi.org/10.1016/S0006-3495(76)85755-4.
93. Team RC. 2016. R: a language and environment for statistical computing. R Foundation for Statistical Computing, Vienna, Austria.
94. Wickham H. 2009. ggplot2: elegant graphics for data analysis. Springer-Verlag, New York, NY.
95. Baty F, Ritz C, Charles S, Brutsche M, Flandrois J-P, Delignette-Muller M-L. 2015. A toolbox for nonlinear regression in R: the package nlstools. J Stat Soft 66:1–21. https://doi.org/10.18637/jss.v066.i05.
96. Ester MK, Kriegel HP, Sander J, Xu X. 1996. A density-based algorithm for discovering clusters in large spatial databases with noise, p 226–231. *In* KDD'96 Proceedings of the Second International Conference on Knowledge Discovery and Data Mining.
97. Hahsler M, Piekenbrock M, Doran D. 2019. dbscan: fast density-based clustering with R. J Stat Softw 91:1–30.
98. Ankerst M, Breunig MM, Kriegel HP, Sander J. 1999. OPTICS: ordering points to identify the clustering structure. SIGMOD Rec 28:49–60. https://doi.org/10.1145/304181.304187.
99. Jahn H, Brantl S, Strahl H. 2015. Against the mainstream: the membrane-associated type I toxin BsrG from *Bacillus subtilis* interferes with cell envelope biosynthesis without increasing membrane permeability. Mol Microbiol 98:651–666. https://doi.org/10.1111/mmi.13146.
100. Norrander J, Kempe T, Messing J. 1983. Construction of improved M13 vectors using oligodeoxynucleotide-directed mutagenesis. Gene 26:101–106. https://doi.org/10.1016/0378-1119(83)90040-9.

Supplemental Information

Dynamics of the *Bacillus subtilis* Min system

Helge Feddersen[1,3], Laeschkir Würthner[2], Erwin Frey[2] and Marc Bramkamp[1,3]*

[1] *Institute for General Microbiology, Christian-Albrechts-University Kiel, Am Botanischen Garten* 1-9, 24118 Kiel, Germany

[2]*Arnold-Sommerfeld-Center for Theoretical Physics and Center for NanoScience, Ludwig-Maximilians-University Munich,* Theresienstr. 37, 80333 Munich, Germany

[3]*Ludwig-Maximilians-University Munich, Faculty of Biology, Großhaderner Straße 2-4, 82152 Planegg-Martinsried, Germany*

*To whom correspondence should be addressed: Marc Bramkamp, Christian-Albrechts-University Kiel, Institute for General Microbiology, Am Botanischen Garten 1-9, 24118 Kiel, Germany, Email: bramkamp@ifam.uni-kiel.de; Phone: +49 (0)431-880-4341; Telefax: +49(0)431-880-2198
Twitter: @BramkampLab

Supplementary Tables

Tab. S1: Relative quantification of Min proteins fused to Dendra2. Relative amounts of protein were determined via in-gel fluorescence of biological triplicates of cell lysates (see Fig. S5). Absolute protein quantities were determined relative to MinD, which was quantified in another publication [75] in similar conditions. Values are shown with standard deviation.

Protein	Relative amount	Total copies per cell
MinD	100% ± 2.51%	**3544 ± 89**
MinJ	16.25% ± 4.36%	**576 ± 25**
DivIVA	47.70% ± 3.51%	**1690 ± 59**

Tab. S2: Kinetic rate constants for the MinD dynamics. The membrane diffusion coefficient, MinD protein density, cell length and cell width are chosen in accordance with our experimental data. The bulk diffusion coefficient, attachment rate, hydrolysis rate and nucleotide exchange rate were estimated from previous approaches for intracellular protein dynamics.

Parameter	Symbol	Value
Bulk Diffusion	D_D	$16\ \mu m^2 \cdot s^{-1}$
Membrane Diffusion	D_d	$0.06\ \mu m^2 \cdot s^{-1}$
Mean total density	$[MinD]$	$2450\ \mu m^{-3}$
Attachment rate	k_D	$0.068\ \mu m \cdot s^{-1}$
Uniform recruitment rate	$\tilde{k}_{dD}$	$0.04\ \mu^2 \cdot s^{-1}$
Uniform hydrolysis rate	$\tilde{k}_H$	$0.1\ s^{-1}$
Recruitment rate amplification factor	α	4
Hydrolysis rate reduction factor	β	3
Nucleotide exchange rate	λ	$6\ s^{-1}$
Cell length	L	$2.8\ \mu m$
Cell width	h	$0.85\ \mu m$

Supplementary Figure legends

Fig. S1: Cartoon of strain construction strategy for allelic replacement in *B. subtilis*. All strains in this study were created to express fluorophore-fusions from their native promoter to sustain native protein levels. Furthermore, they were tested for functionality**. (a)** Construction of plasmids was performed with golden-gate cloning, yielding a plasmid that can directly be transformed into *B. subtilis*. **(b)** After transformation, genes for a fluorophore and an antibiotic resistance cassette are integrated into the genomic locus of interest via homologous recombination

Fig. S2: Microscopic images of a selection of strains used in this study. Columns from left to right: Phase contrast, red fluorescent channel using membrane dye (FM4-64), green fluorescent channel depicting the indicated fluorophore and composite of all three channels. Scale bars 2µm.

Fig. S3: Representative microscopy images of FRAP analysis of DivIVA-mNeonGreen. (a) DivIVA-mNeonGreen expressed in wild type background (BHF028). Images taken before bleaching the indicated spot with a 488 nm laser pulse, directly after bleaching and after recovery of fluorescence. Scale bars 2 µm. **(b)** Representation of the normalized fluorescence recovery in the green channel over time. $T_{1/2}$ = time when fluorescence recovery reaches half height of total recovery, indicated on the graph with a dashed square. The red line represents measured values, black the fitted values.

Fig. S4: Western blots or in-gel fluorescence of native Min protein fusions. To control for full-length of fluorescent protein fusions with MinD, MinJ or DivIVA, cell lysates were either fully (96°C for 10 min, **d**) or partially (room temperature for 20 min, **a**, **b**, **c** and **e**) denatured and separated via SDS-PAGE. Protein bands were then visualized either directly via in-gel fluorescence **(c, e)** with excitation and emission at 488/526 nm, respectively, or colorimetrically via western-blot with the respective

indicated antibody (**a**: polyclonal anti-Dendra2, **b**: monoclonal anti-mNeonGreen, **d**: polyclonal anti-mCherry).

Fig. S5: Relative quantification of native Dendra2 fusions assayed by in-gel fluorescence of SDS-PAGE gels. Biological triplicates indicated by top right number **(1-3)**. Lysates of the respective strain were partially denatured with SDS loading dye at room temperature for 20 min, loaded in different relative amounts (left 1x, right 2x) and separated via SDS-PAGE. (**a**) Visualization via Typhoon Trio scanner, with excitation at 488 nm and an emission filter of 526 nm. (**b**) Coomassie stain of the respective image as loading control. Results of quantification can be found in **Tab. S1**.

Fig. S6: Representative microscopy images of FRAP analysis of Min proteins in different knockout backgrounds.(a) MinJ-msfGFP expressed in ΔminCD background (BHF015), and DivIVA-GFP expressed in ΔminCD (BHF040), ΔminJ (BHF041) and ΔminCDJ (BHF042) backgrounds. Images taken before bleaching the indicated spot with a 488 nm laser pulse, directly after bleaching and after recovery of fluorescence. Scale bars 2 µm. **(b)** Representation of the normalized fluorescence recovery in the green channel over time. $T_{1/2}$ = time when fluorescence recovery reaches half height of total recovery, indicated on the graph with a dashed square. The red line represents measured values, black the fitted values.

Fig. S7: Geometry for the simulation of the model. (a) Sketch of the simulation geometry (spherocylinder). **(b)** Polar localization is achieved by setting $\alpha = 4$ and $\beta = 3$ at the poles (green area), and $\alpha = \beta = 1$ for the remaining part of the geometry. (**c**) Localization at the septum is achieved by setting $\alpha = 4$ and $\beta = 3$ in a narrow region at mid cell (green) and else $\alpha = \beta = 1$.

Fig. S8: PALM imaging and representative cluster analysis of strain JB40 expressing MinJ-mNeonGreen. (a) PALM image of MinJ-mNeonGreen in a cell in late division state. Scale bar 500 nm. **(b)** Cluster analysis of the same PALM data with three highlighted regions *(**i, ii** and **iii**).* Cluster analysis was performed in R using the OPTICS algorithm from the DBSCAN package. Every point indicates a single event and thus a MinJ-mNeonGreen protein, precision is indicated by colour and size of the circle.

Fig. S9: PALM imaging and representative cluster analysis of strain JB37 expressing DivIVA-PAmCherry. (a) PALM image of DivIVA-PAmCherry in a cell in late division state. Scale bar 500 nm. **(b)** Cluster analysis of the same PALM data with three highlighted regions (***i, ii*** and ***iii***). Cluster analysis was performed in R using the OPTICS algorithm from the DBSCAN package. Every point indicates a single event and thus a DivIVA-PAmCherry protein, precision is indicated by colour and size of the circle.

Fig. S10: Visualization of longitudinal Dendra2-MinD gradients with different microscopy techniques. Comparison of Dendra2-MinD fluorescent signal (**left**) and longitudinal relative fluorescence intensity (**right**) between conventional live-cell light microscopy **(a)**, live-cell PALM **(b)** and live-cell PALM with a rendered point-spread function of 200 nm **(c)**, resembling conventional light microscopy resolution. While **(b)** reveals a very sharp gradient with strong peaks at poles and geometric mid-cell, **(a)** and **(c)** appear to have a smoother Dendra2-MinD gradient, likely due to the lower localization precision.

Supplementary Figures

Figure S1

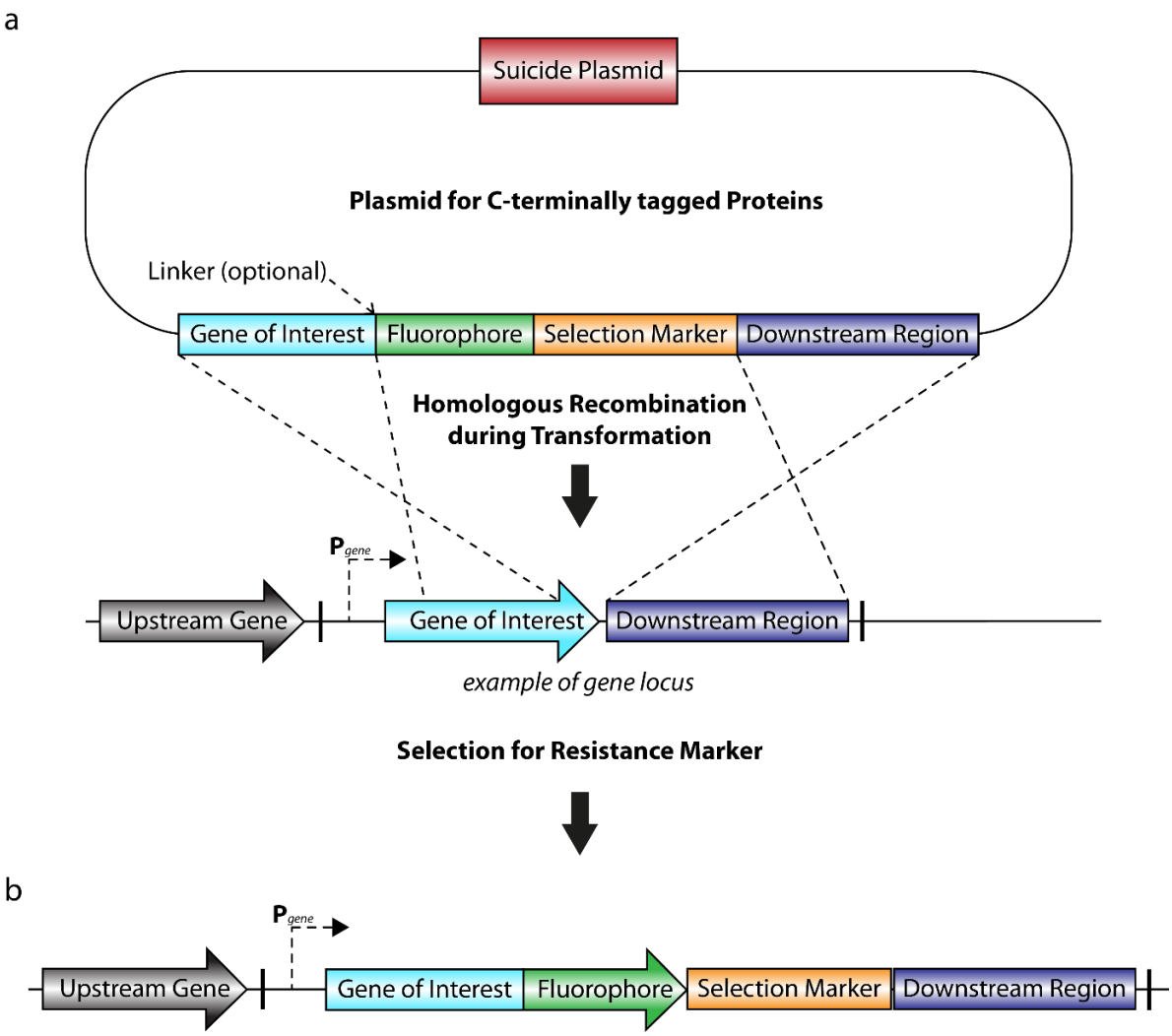

Figure S2

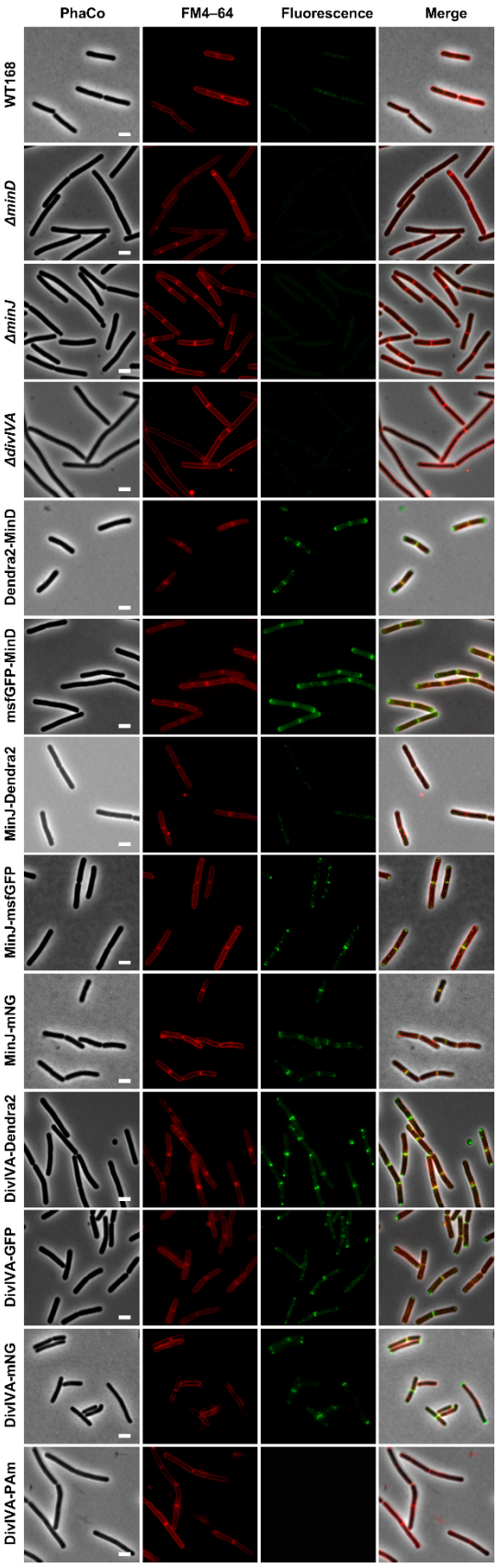
PhaCo
FM4–64
Fluorescence
Merge
WT168
ΔminD
ΔminJ
ΔdivIVA
Dendra2-MinD
msfGFP-MinD
MinJ-Dendra2
MinJ-msfGFP
MinJ-mNG
DivIVA-Dendra2
DivIVA-GFP
DivIVA-mNG
DivIVA-PAm

Figure S3

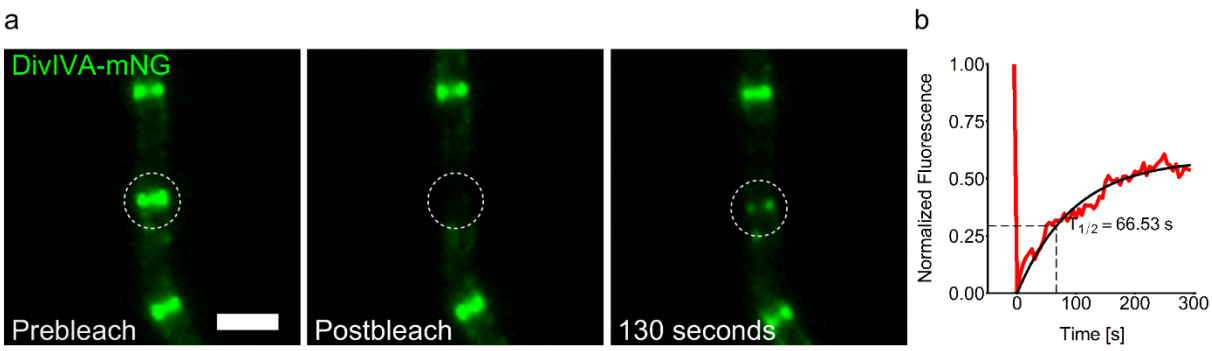
a
b
DivIVA-mNG
Prebleach
Postbleach
130 seconds
Normalized Fluorescence
1.00
0.75
0.50
0.25
0.00
0
100
200
300
Time [s]
$T_{1/2}$ = 66.53 s

Figure S4

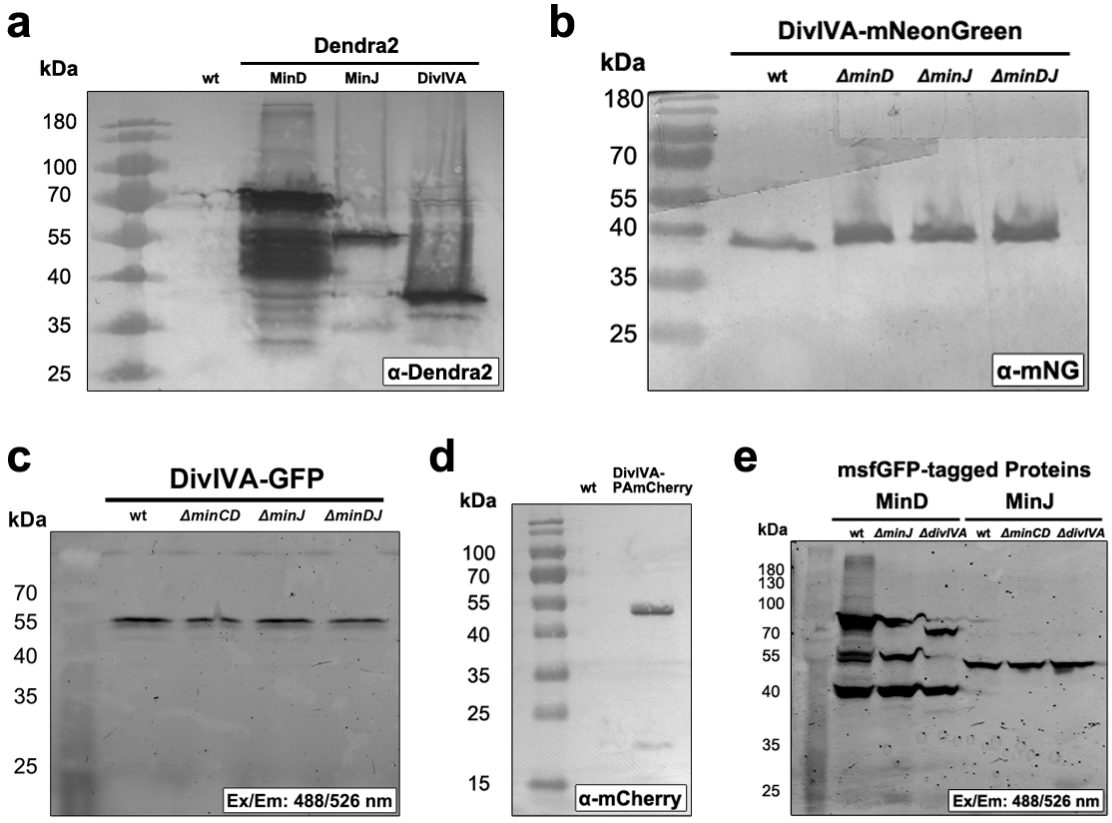
a
Dendra2
kDa
wt
MinD
MinJ
DivIVA
180
100
70
55
40
35
25
α-Dendra2
b
DivIVA-mNeonGreen
kDa
wt
ΔminD
ΔminJ
ΔminDJ
180
70
55
40
35
25
α-mNG
c
DivIVA-GFP
kDa
wt
ΔminCD
ΔminJ
ΔminDJ
70
55
40
35
25
Ex/Em: 488/526 nm
d
kDa
wt
DivIVA-PAmCherry
100
70
55
40
35
25
15
α-mCherry
e
msfGFP-tagged Proteins
MinD
MinJ
kDa
wt
ΔminJ
ΔdivIVA
wt
ΔminCD
ΔdivIVA
180
130
100
70
55
40
35
25
Ex/Em: 488/526 nm

Figure S5

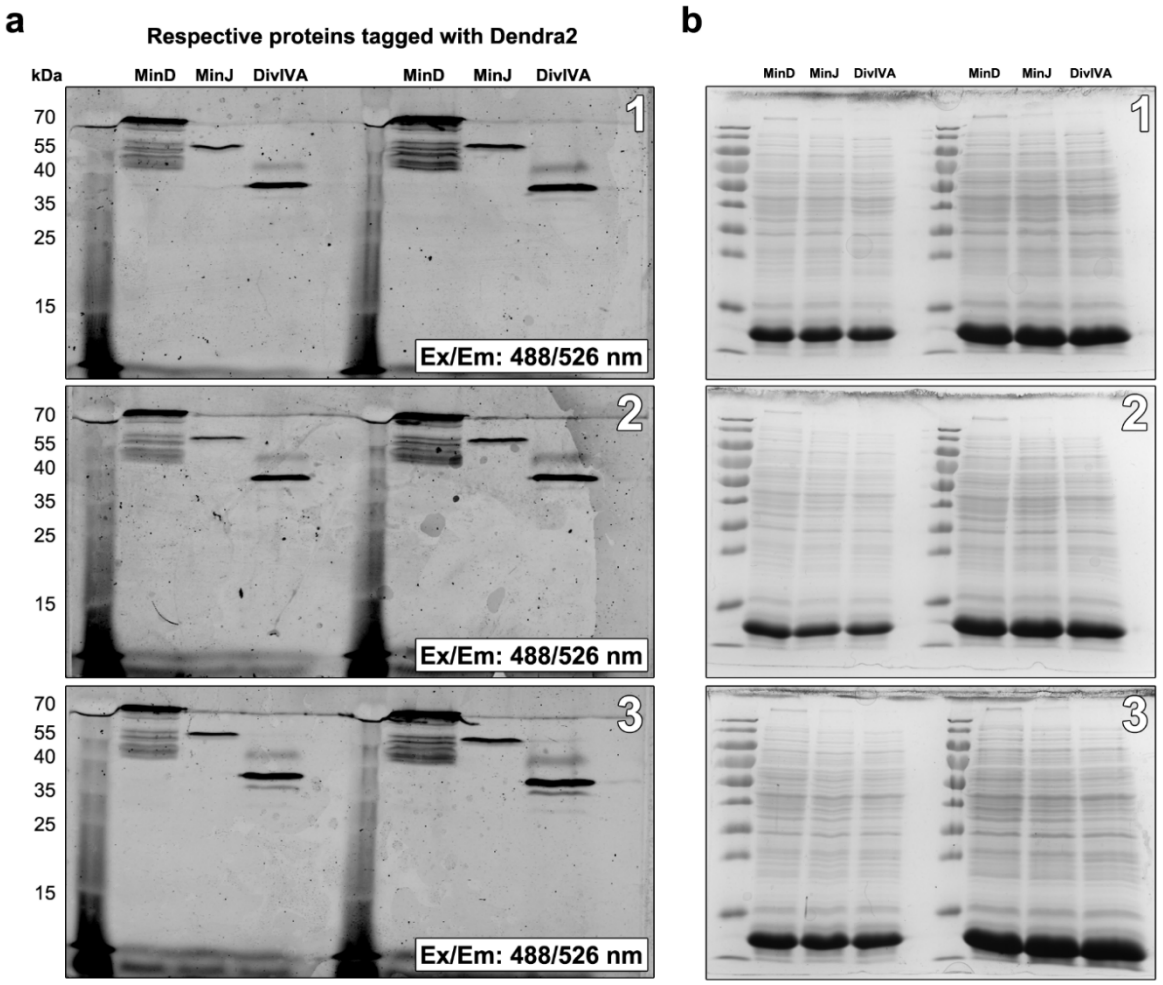
a
Respective proteins tagged with Dendra2
kDa
MinD MinJ DivIVA MinD MinJ DivIVA
70
55
40
35
25
15
1
Ex/Em: 488/526 nm
2
Ex/Em: 488/526 nm
3
Ex/Em: 488/526 nm
b
MinD MinJ DivIVA MinD MinJ DivIVA
1
2
3

Figure S6

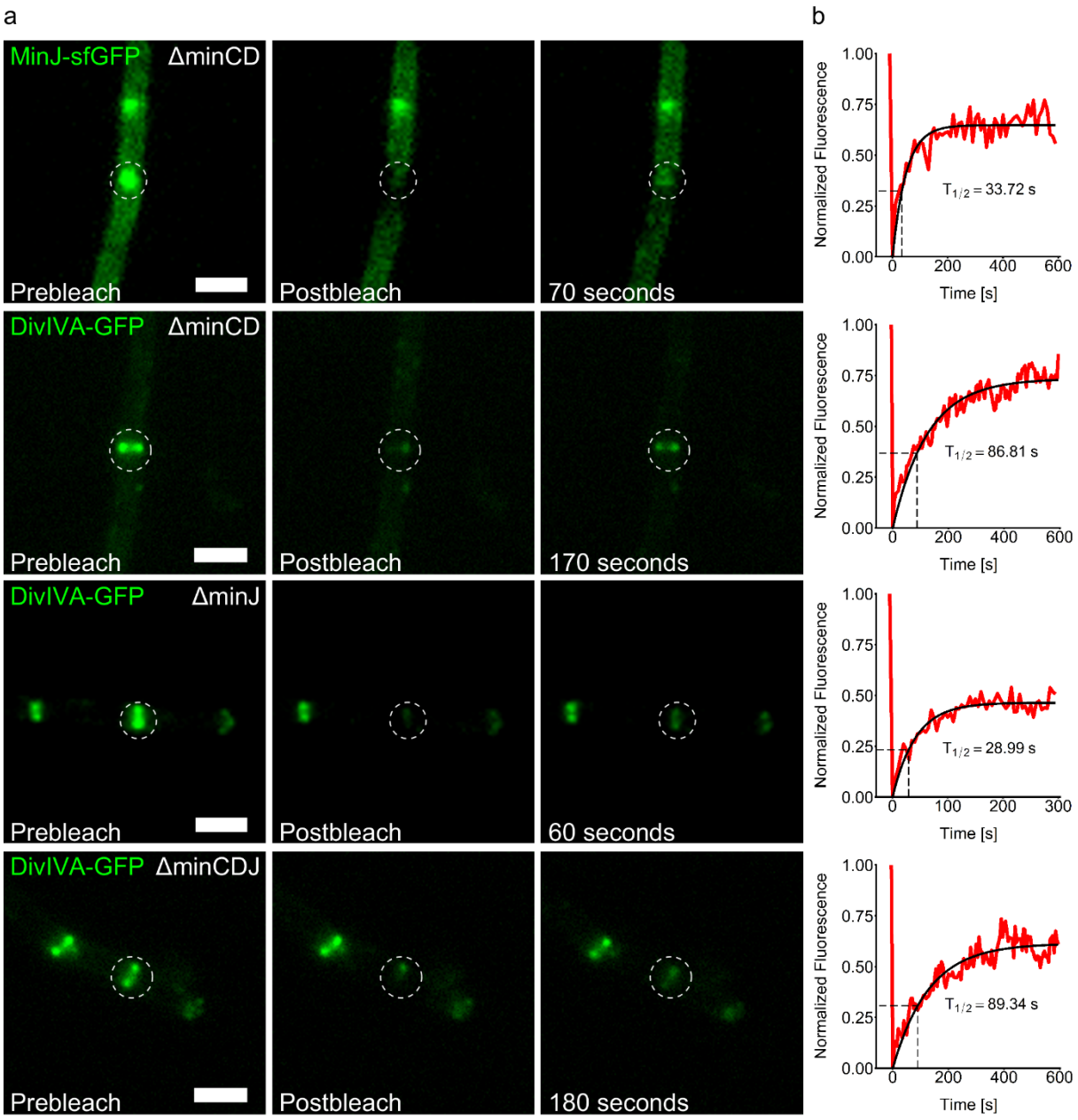
a
b
MinJ-sfGFP ΔminCD
Prebleach
Postbleach
70 seconds
DivIVA-GFP ΔminCD
Prebleach
Postbleach
170 seconds
DivIVA-GFP ΔminJ
Prebleach
Postbleach
60 seconds
DivIVA-GFP ΔminCDJ
Prebleach
Postbleach
180 seconds
Normalized Fluorescence
Time [s]
T1/2 = 33.72 s
T1/2 = 86.81 s
T1/2 = 28.99 s
T1/2 = 89.34 s

Figure S7

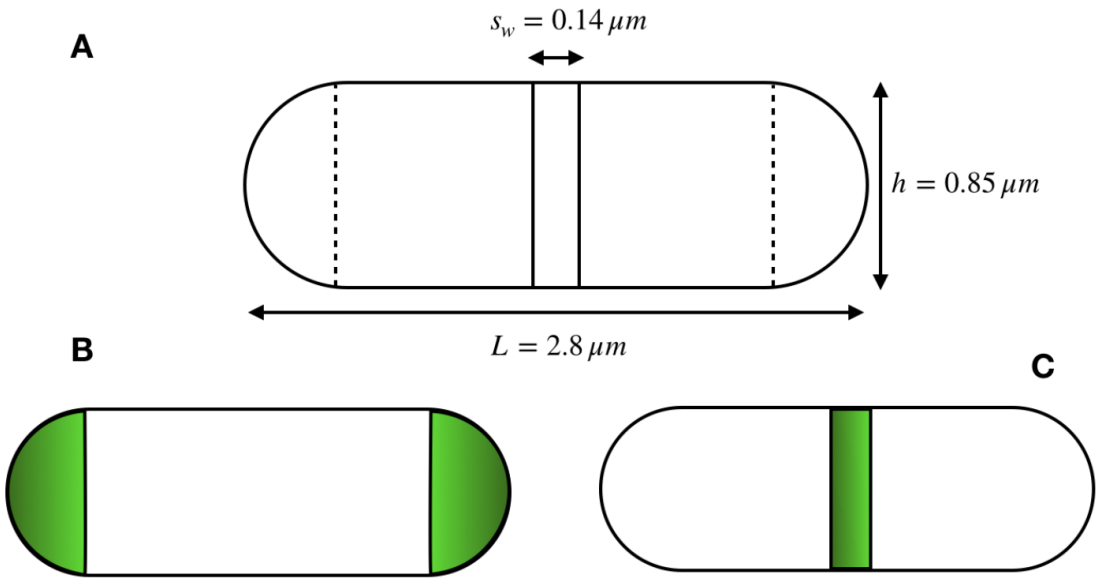

Figure S8

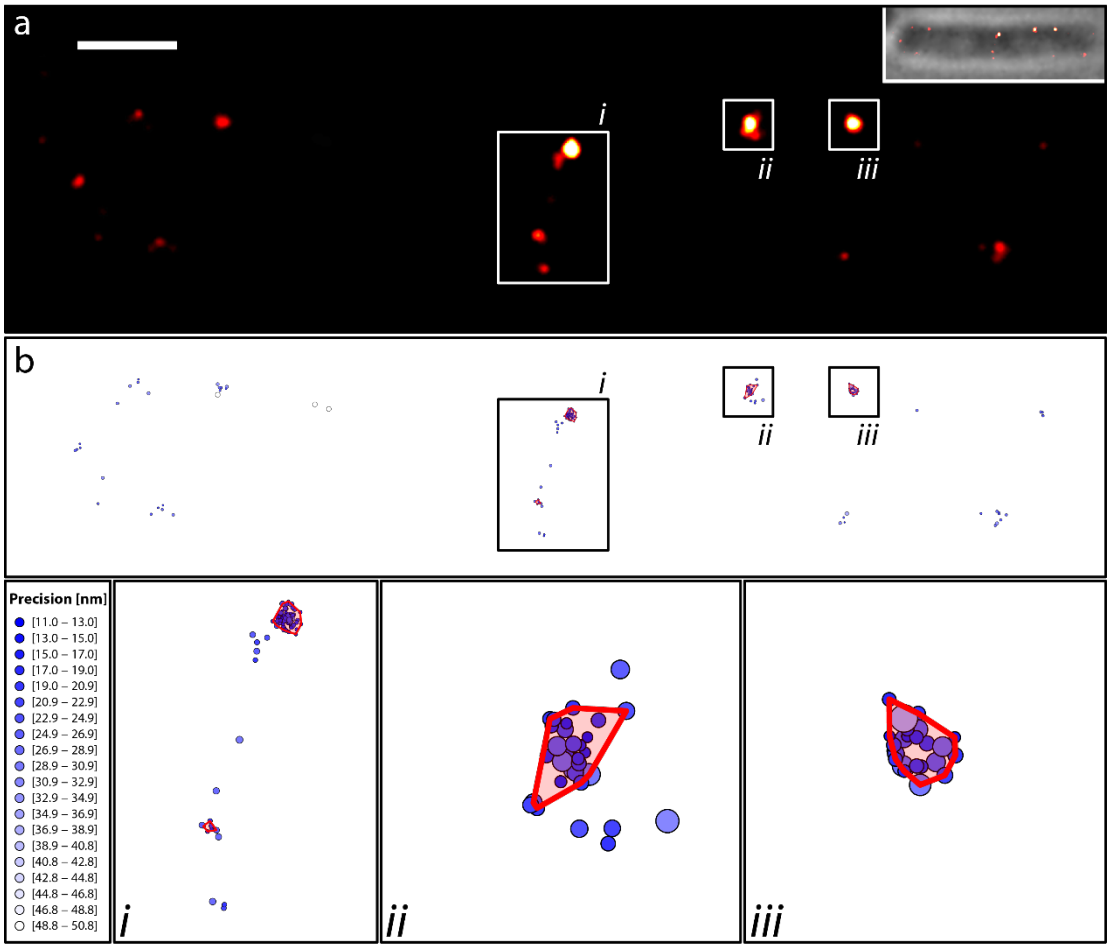
a
i
ii
iii
b
i
ii
iii
Precision [nm]
[11.0 – 13.0]
[13.0 – 15.0]
[15.0 – 17.0]
[17.0 – 19.0]
[19.0 – 20.9]
[20.9 – 22.9]
[22.9 – 24.9]
[24.9 – 26.9]
[26.9 – 28.9]
[28.9 – 30.9]
[30.9 – 32.9]
[32.9 – 34.9]
[34.9 – 36.9]
[36.9 – 38.9]
[38.9 – 40.8]
[40.8 – 42.8]
[42.8 – 44.8]
[44.8 – 46.8]
[46.8 – 48.8]
[48.8 – 50.8]
i
ii
iii

Figure S9

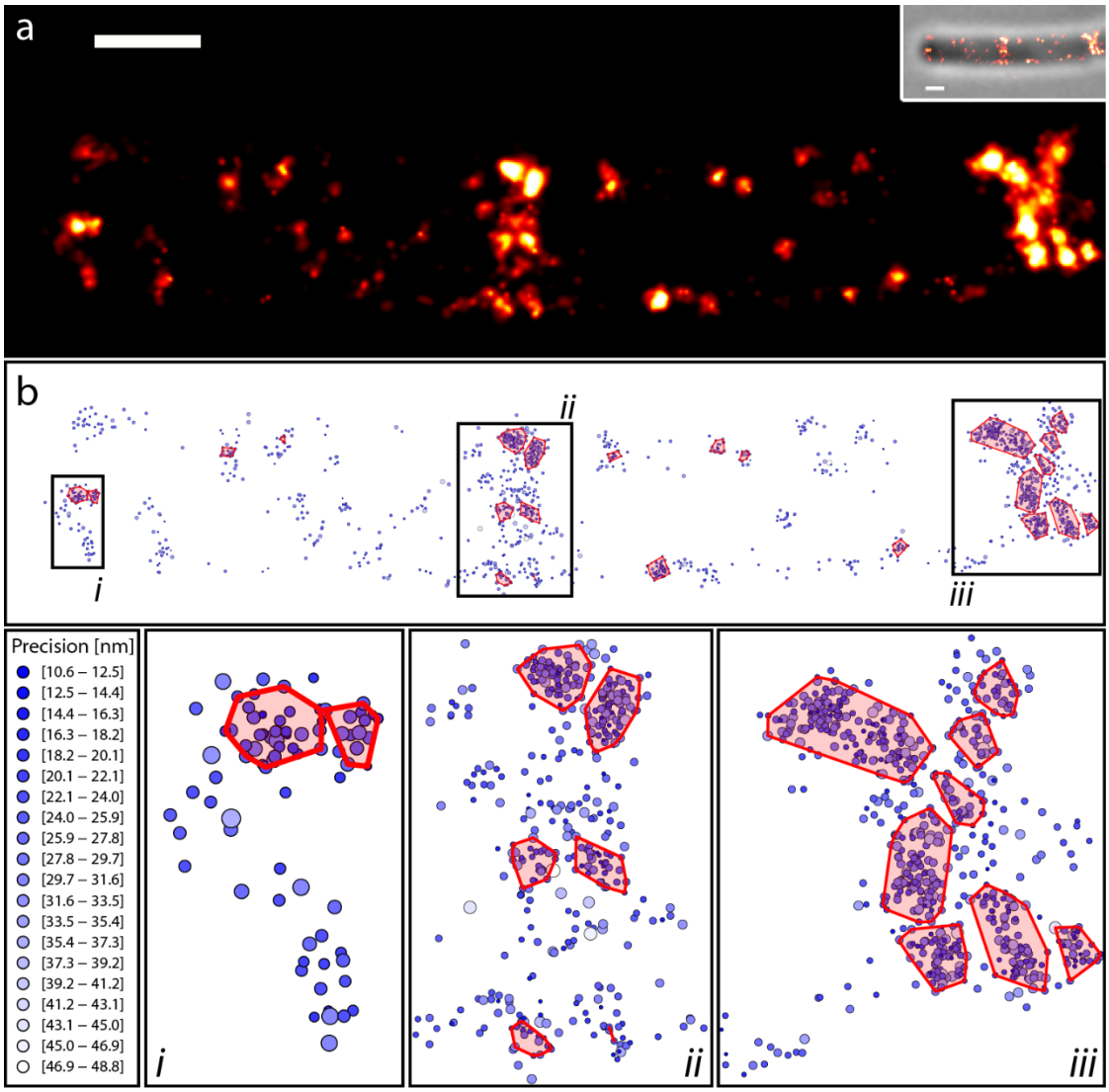
a
b
i
ii
iii
Precision [nm]
[10.6 – 12.5]
[12.5 – 14.4]
[14.4 – 16.3]
[16.3 – 18.2]
[18.2 – 20.1]
[20.1 – 22.1]
[22.1 – 24.0]
[24.0 – 25.9]
[25.9 – 27.8]
[27.8 – 29.7]
[29.7 – 31.6]
[31.6 – 33.5]
[33.5 – 35.4]
[35.4 – 37.3]
[37.3 – 39.2]
[39.2 – 41.2]
[41.2 – 43.1]
[43.1 – 45.0]
[45.0 – 46.9]
[46.9 – 48.8]
i
ii
iii

Figure S10

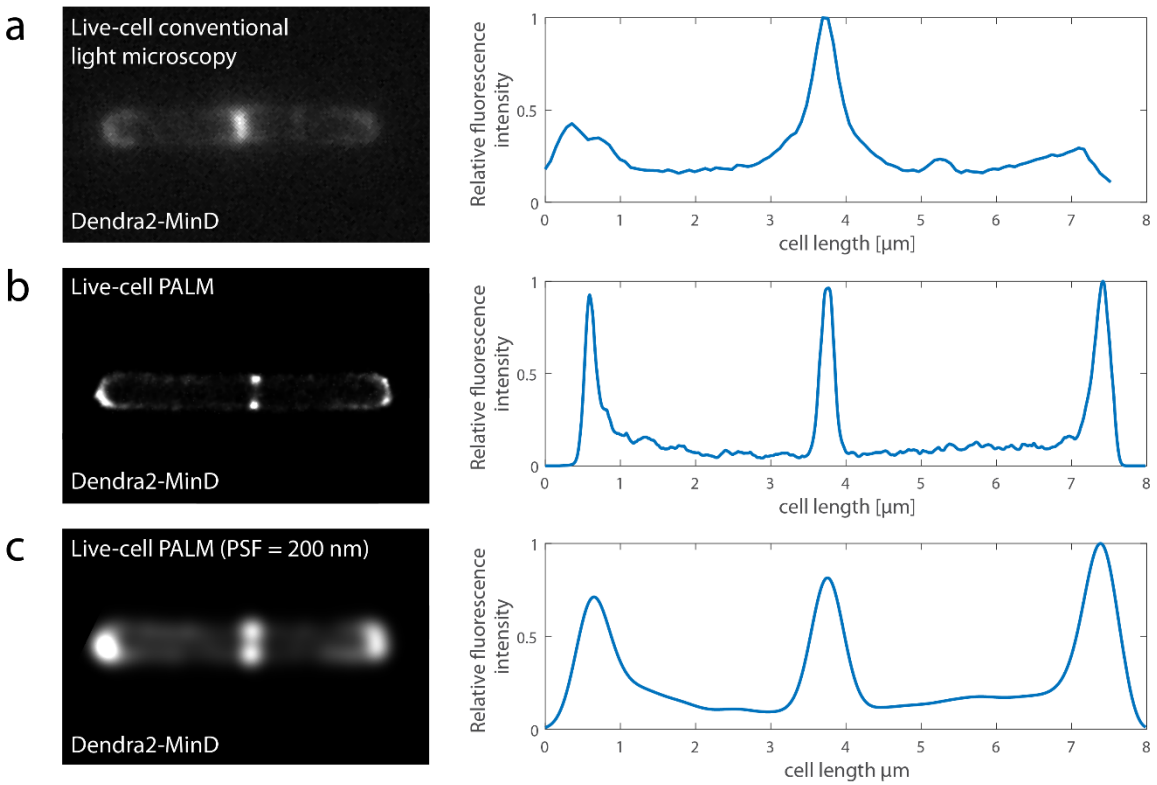
a
Live-cell conventional light microscopy
Dendra2-MinD
Relative fluorescence intensity
cell length [µm]
b
Live-cell PALM
Dendra2-MinD
Relative fluorescence intensity
cell length [µm]
c
Live-cell PALM (PSF = 200 nm)
Dendra2-MinD
Relative fluorescence intensity
cell length µm

Matter tells space how to curve; space tells matter how to move.
— John Archibald Wheeler

IV Curvature-induced instabilities of protein-lipid interfaces.

1 Membrane remodeling by motor proteins

In this section, we dive into the topic of membrane curvature generation via motorprotein-lipid interactions. The following is based on and uses parts of our paper [34] published in *Nature Communications*. We provide a reprint of the paper in section 1.6.

1.1 Background

In section 2 of chapter II, we discussed that the cytoplasmic membrane of cells is not a static but rather a highly dynamic object that undergoes shape changes in response to many stimuli. Membrane adaptation is crucial for cells, since many functions rely on dynamic reshaping of the cell membrane. Representative examples where membrane remodeling is critical includes cell motility, cell division, and also intracellular transport such as endocytosis [31, 32, 162].

It is widely accepted that membrane curvature is generated and controlled by the cytoskeleton (including all its components, such as motor proteins, actin filaments, microtubules etc.) [162–164]. The basic pathways by which cytoskeletal components induce curvature may be categorized as follows: (i) Some proteins, including transmembrane proteins, have a characteristic conical or inverted conical shape and can thus induce curvature by direct insertion between the lipid heads [33]. Here, curvature generation is caused by elastic tension gradients between the inner and outer leaflets of the lipid bilayer, which results effectively in a different spontaneous curvature of the membrane [165–168]. (ii) Other proteins have intrinsic shapes, such as proteins with BAR domains, or so-called ALPS motifs (amphipathic helices), which can explicitly induce curvature by binding or insertion, respectively [33, 169]. (iii) Membrane curvature may be also generated via scaffolding, such as the ATP-dependent clathrin-coat [33], and oligomerization of BAR-domains on membranes [32, 33]. (iv) The actomyosin complex, as well as microtubule polymerization, can induce curvature by directly exerting mechanical forces to the membrane [33, 162]. Here, myosin motor proteins act as crosslinkers between actin filaments, and therefore orchestrate these processes, provided that energy is supplied to the system in the form of ATP. While it has been shown

that motor proteins are in principle able to bind to lipid membranes [170–173], it remained unclear whether interactions between motor proteins and membranes alone can also generate curvature (i.e. without actin filaments or microtubules). For example, the atypical motor protein myosin-VI, the only motor protein that has been shown to walk towards the minus end of actin filaments [174, 175], is able to directly bind to lipid membranes [171].

In this project, using a reconstituted *in vitro* system, we investigated the interactions of the motor protein myosin-VI with supported lipid bilayers. To our surprise, we found that myosin-VI, on its own, reshapes the membrane by generating pores that grow over time and form regular, flower-like, spatial structures [34]. Interestingly, the binding of myosin-VI to the membrane is highly curvature-dependent, and does not require the supply of ATP. We developed a quantitative theoretical model that explains and correctly reproduces the experimental observations. The basic mechanism leading to pattern formation of the motorprotein-lipid interface is based on a "push-pull" mechanism: The curvature-sensitive membrane binding of myosin-VI acts as a destabilizing driving force, which is counteracted by line tension of the protein-lipid interface (short wavelength cut-off), thus resulting in a band of unstable modes.

1.2 Growing pores in supported lipid membranes

Before we dive into the theoretical details, we briefly recapitulate the phenomenology of the system. By reconstituting myosin-VI in a box-like *in vitro* setup, where the bottom surface of the box is coated with a supported lipid bilayer, we observe by fluorescence microscopy that GFP-tagged myosin-VI generates micrometer sized holes in the lipid membrane (see Fig. IV.1a). These pores grow over time, and sometimes also fuse with other holes if they overlap during the grow process. Notably, the circumference of the motorprotein-lipid interface is not perfectly circular but rather appears to be rough. Using super resolution microscopy (STORM) [176], we observe that pores are initially nearly circular, but for sufficiently long times exhibit regular spatial structures with a characteristic wavelength (Fig. IV.1b). In other words, the initially circular shape of the interface seems to undergo a pattern-forming instability. Interestingly, we find that most binding events of bulk myosin-VI to the membrane occurs at regions of the interface which exhibit a Gaussian negative curvature [34] (outward bulges, see Fig. IV.1b).

1.3 Theoretical model with bulk-surface coupling

What drives the pattern-forming instability of the motorprotein-lipid interface? To address this question, we develop a theoretical model that describes the grow of the interface. We assume that the circumference of the pore can be described by

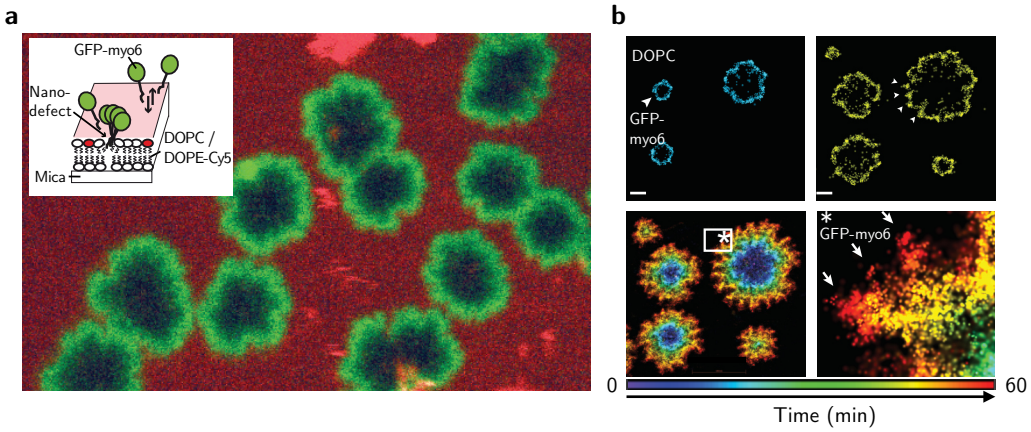

Figure IV.1 Myosin-VI mediated remodeling of supported lipid bilayers. a) Using fluorescence microscopy, we find that myosin-VI generates holes in the membrane that grow over time. The main solution is contains abundant myosin-VI. b) Super resolution microscopy reveals that the pores grow and eventually form flower-like shapes, and that myosin-VI preferentially binds to regions of the interface which exhibit a Gaussian negative curvature (arrows). The figure is adopted from ref. [34].

a periodic, one-dimensional line $\Gamma(t)$, which should be a reasonable assumption since the thickness of the lipid bilayer is much smaller than the typical size of the pores. This assumption also requires to map diffusion of myosin-VI in the three-dimensional bulk onto the bottom surface. What, then, drives the grow of the protein-lipid interface? From a physical point of view, grow is driven by diffusive fluxes of myosin-VI mass towards the interface, i.e. by conservation of mass, we obtain a governing equation for the normal velocity v_n of the interface in terms of the bulk concentration $c(\boldsymbol{r}, t)$ of myosin-VI

$$v_n = \frac{D_c}{c_\mathrm{I}} \nabla_{\hat{\boldsymbol{n}}} c|_{\Gamma(t)} \ . \tag{IV.1}$$

Here, c_I denotes the myosin-VI concentration at the interface, and D_c is the bulk diffusion coefficient. The key point now is that the concentration of myosin-VI at the interface must be a function the local curvature, since negatively curved regions "create space" for more myosin proteins from the bulk to bind to the interface. This feature can be described by a *Gibbs-Thomson relation*, which links the interface concentration of myosin-VI to the local morphology

$$c|_{\Gamma(t)} = c_0 \left(1 + \tau\kappa\right) \ , \tag{IV.2}$$

where c_0 denotes the bulk concentration at the interface, τ the line-tension coefficient, and κ the local curvature. Equation (IV.2) states that the concentration

at the interface is shifted relative to the value c_0 for flat regions. This is a general phenomenon that underlies many physical systems, including the Laplace pressure of fluid interfaces, temperature shift of solid-liquid interfaces [177], and the concentration offset of active droplets [178]. To complete the description, we assume that myosin proteins diffuse freely in the bulk, where we view the bulk volume as a very large reservoir (which should be a reasonable assumption as the size of a pore is much smaller than the bulk volume). Hence, we may assume that the bulk concentration sufficiently far away from the interface $r \to \infty$ is given by the constant value $c(\boldsymbol{r}, t) = c_\infty$. We therefore obtain the following set of equations that describe the dynamics of the protein-lipid interface:

$$c|_{\Gamma(t)} = c_0 \left(1 + \tau\kappa\right) , \tag{IV.3a}$$

$$\frac{\partial}{\partial t} c(\boldsymbol{r}) = D_c \nabla^2 c(\boldsymbol{r}) , \tag{IV.3b}$$

$$v_n = \frac{D_c}{c_\mathrm{I}} \nabla_{\hat{\boldsymbol{n}}} c|_{\Gamma(t)} . \tag{IV.3c}$$

These equations are seemingly simple, but they are, unfortunately, very difficult to solve (analytically and numerically), because they link the bulk dynamics of proteins to the morphology of the protein-lipid interface $\Gamma(t)$. The main difficulty arises here from the fact that the boundary $\Gamma(t)$ itself is a time-dependent, unknown variable, which must be solved together with the bulk dynamics and the Gibbs-Thomson boundary condition at the interface.

1.4 Coarse-grained geometric model

However, we may simplify the problem by deriving a phenomenological model that reproduces the qualitative features outlined above. As before, we parametrize the protein-lipid interface by a position vector $\boldsymbol{r}(t, \sigma)$ which is related to the normal velocity as follows:

$$\boldsymbol{r} \cdot \hat{\boldsymbol{n}} = v_n , \tag{IV.4}$$

where $\hat{\boldsymbol{n}}$ describes as usual the outward normal vector of the interface. Instead of relating v_n to the bulk dynamics, we now implicitly incorporate the bulk dynamics by assuming that the normal velocity is an arbitrary complex function of the local shape $v_n = v_n\left(\kappa, \nabla_s^2\kappa, \ldots\right)$, where ∇_s^2 denotes the second derivative with respect to the arc length of the interface. Note that we assume that the lipid membrane is uniform in its properties, which excludes dependencies on the position vector $\boldsymbol{r}$ as well as gradients in the curvature $\nabla_s\kappa$, (which requires that the system is invariant under parity transformation $s \to -s$). Similar as for crystal growth

processes [177, 179–184] or combustion [185–187] (among others), we may now perform a gradient expansion of the normal velocity to leading order

$$v_n \approx \epsilon_0 - \epsilon_1(\kappa - \kappa_0) + \epsilon_2(\kappa - \kappa_0)^2 - \epsilon_3(\kappa - \kappa_0)^3 - \alpha\,\nabla_s^2\kappa\,, \tag{IV.5a}$$

$$\equiv f(\kappa) - \alpha\,\nabla_s^2\kappa\,. \tag{IV.5b}$$

Here, the parameters ϵ_i are phenomenological parameters that (effectively) describe myosin-VI attachment and recruitment to negatively curved shapes. The (coarse-grained) curvature-dependent binding kinetics is therefore contained in the function $f(\kappa)$, which drives the growth of the protein-lipid interface at all length scales. The second term proportional to $\nabla_s^2\kappa$ penalizes gradients in the curvature, and therefore tries to stabilize the interface by smoothing out gradients – similar to diffusion. One may therefore interpret the phenomenological parameter α as a line tension coefficient. This can be also seen by rewriting Eq. (IV.5) as the gradient flow of a free energy functional:

$$\mathcal{F} = \int_\Gamma \left(F(\kappa) + \frac{\gamma}{2}(\nabla_s\kappa)^2\right) ds\,, \tag{IV.6}$$

where the normal velocity is obtained by the first variation of this functional with respect to curvature

$$v_n = \mu\frac{\delta\mathcal{F}}{\delta\kappa}\,. \tag{IV.7}$$

The stiffness parameter γ is related to the phenomenological parameter α through the mobility μ, i.e. $\alpha = \mu\gamma$, and the function $F(\kappa) \propto \int f(\kappa)d\kappa$ can be interpreted as an effective curvature potential. The alternative formulation above underlines that the phenomenological approach used here is very similar to Ginzburg-Landau equations for equilibrium thermodynamics.

The coarse-grained model Eq. (IV.5) considerably simplifies the problem, since it reduces the complicated set of (non-local) bulk-surface coupled equations to a local geometric evolution law for the position vector $\boldsymbol{r}$, which is the only unknown degree of freedom in the system. Importantly, we can immediately identify the mechanism that drives pattern formation: The curvature-dependent driving force $f(\kappa)$ destabilizes the interface at all length scales, and this is counteracted by line tension $\nabla_s^2\kappa$, which ultimately results in a band of unstable modes – very similar to the famous *Mullins-Sekerka instability* for solidification fronts [179]. We fitted the phenomenological parameters in Eq. (IV.5) to the experimental data, and numerically solved the equation. Our results reproduce the experimental patterns very well, and also show that the system selects a final wavelength for long times via a sequence of tip-splitting.

1.5 Key points and outlook

In the following we summarize the key findings of this research project and provide an outlook.

- By reconstituting myosin-VI *in vitro*, we have shown that the motor protein myosin-VI induces micrometer sized growing holes in supported lipid membranes. Using super resolution microscopy, we further identified that myosin-VI reshapes membrane pores into regular spatial structures that exhibit a characteristic wavelength. Importantly, we have shown that binding of myosin-VI to the lipid membrane is highly curvature-sensitive: proteins are recruited to regions with a Gaussian negative curvature (corresponding to outward bulges).

- We developed a quantitative theoretical model that explains the morphological instability. From a physical point of view, grow of pores is driven by a diffusive mass flux of proteins from the bulk solution towards the motorprotein-lipid interface. This flux is coupled to the local shape (curvature) of the pore through a Gibbs-Thomson relation. We then developed a coarse-grained model that effectively describes the growth dynamics of the protein-lipid interface. The model captures the curvature-dependent grow of the interface, and correctly reproduces the experimental observations.

- The origin of the morphological instability is reminiscent to unstable solidifications fronts [177, 179], or fingering instabilities of multiphase flows in Hele-Shaw cells [177, 188]: A driving force that destabilizes the morphology of the interface at all length scales is counteracted by line tension, which tries to stabilize the interface by smoothing out gradients in the curvature. Here, we identified the curvature-dependent recruitment of myosin-VI to the lipid membrane as the “driving force” that destabilizes the interface. This force is counteracted by line tension of the motorprotein-lipid interface, which then results in a band of unstable modes that leads to pattern formation of the protein-lipid interface. Thus, the underlying mechanism driving pattern formation is, from a physical point of view, analogous as pattern formation in growing solidification fronts or instabilities in multiphase flows.

We have considered here the dynamics of protein-lipid interfaces on flat supported lipid bilayers. In cells, lipid membranes are rarely flat, but usually curved. In fact, myosin-VI proteins are often found at curved membrane regions, such as the invagination region during endocytosis [189]. An exiting extension of our theoretical model would be therefore to study interface grow on curved lipid surfaces. Due to bending rigidity (which is irrelevant in flat lipid surfaces), we expect that the out-of-plane curvature of the lipid membrane might be an important

control parameter for wavelength selection. Besides theoretical modeling, one may also investigate such systems experimentally. For instance, one could study the dynamics of myosin-VI on the surface of giant unilamellar vesicles (GUVs), or on the surface of cylindrical membrane shapes. Such shapes can be generated experimentally by a number of techniques, such as micropipette aspiration or via hydrodynamic shear flows [190–192].

Since NTPases are ubiquitous in cells and play an important role for protein pattern formation, another interesting extension of our model would be to consider an activation-reactivation cycle for myosin-VI. In general, such a cycle leads to non-trivial geometric effects as we have shown in section 1 of chapter III. However, the incorporation of nucleotide exchange requires to explicitly account for bulk-surface coupling, and one therefore must solve the non-local model Eq. (IV.3a). Assuming a time scale separation between the diffusive dynamics in the bulk and grow of the interface, one may simplify the problem by considering an adiabatic bulk dynamics, i.e. one can omit the time-dependency of the bulk species. This is a reasonable assumption, because the interface grows on a much longer time scale than the typical time scale of diffusive protein redistribution in the bulk [34, 193]. In this case, one can analytically solve the (linear) bulk dynamics by using the Green's function formalism, which would ultimately allow to reduce the complexity of the problem by mapping the bulk equations to the boundary. We expect that the dynamics of such a non-local model will be much richer in its phenomenology, and therefore possibly yield a variety of different interesting morphological patterns.

1.6 Publication: Reconstitution reveals how myosin-VI self-organises to generate a dynamic mechanism of membrane sculpting

Reconstitution reveals how myosin-VI self-organises to generate a dynamic mechanism of membrane sculpting

by

B. Rogez[1,2,*], L. Würthner[2,3,*], A. B. Petrova[1,2], F. B. Zierhut[1,2], D. Saczko-Brack[1,2], M. Huergo[4], C. Batters[1,2], E. Frey[2,3], and C. Veigel[1,2]

[1]Department of Cellular Physiology, Biomedical Center (BMC), Ludwig-Maximilians-Universität München, Grosshadernerstrasse 9, 82152 Planegg- Martinsried, Germany,

[2]Center for Nanosciences (CeNS), Ludwig-Maximilians-Universität München, Schellingstrasse 4, 80799 München, Germany,

[3]Arnold-Sommerfeld-Center for Theoretical Physics (ASC), Department of Physics, Ludwig-Maximilians-Universität München, Theresienstrasse 37, 80333 München, Germany,

[4]Theoretical and Applied Physical Chemistry Research Institute (INIFTA), National University of La Plata, Diagonal 113, 1900 La Plata, Argentina

*These authors contributed equally to this work.

Published in ***Nature Communications*** **10, 3305 (2019)**

DOI: 10.1038/s41467-019-11268-9.

reprinted on pages 256–266,

Supplemental Material reproduced on pages 267–275.

nature COMMUNICATIONS

ARTICLE

https://doi.org/10.1038/s41467-019-11268-9 OPEN

Reconstitution reveals how myosin-VI self-organises to generate a dynamic mechanism of membrane sculpting

Benoit Rogez[1,2,5], Laeschkir Würthner[2,3,5], Anastasiia B. Petrova[1,2], Felix B. Zierhut[1,2], Dario Saczko-Brack[1,2], Maria-Ana Huergo[4], Christopher Batters[1,2], Erwin Frey[2,3] & Claudia Veigel[1,2]

One enigma in biology is the generation, sensing and maintenance of membrane curvature. Curvature-mediating proteins have been shown to induce specific membrane shapes by direct insertion and nanoscopic scaffolding, while the cytoskeletal motors exert forces indirectly through microtubule and actin networks. It remains unclear, whether the manifold direct motorprotein–lipid interactions themselves constitute another fundamental route to remodel the membrane shape. Here we show, combining super-resolution-fluorescence microscopy and membrane-reshaping nanoparticles, that curvature-dependent lipid interactions of myosin-VI on its own, remarkably remodel the membrane geometry into dynamic spatial patterns on the nano- to micrometer scale. We propose a quantitative theoretical model that explains this dynamic membrane sculpting mechanism. The emerging route of motorprotein–lipid interactions reshaping membrane morphology by a mechanism of feedback and instability opens up hitherto unexplored avenues of membrane remodelling and links cytoskeletal motors to early events in the sequence of membrane sculpting in eukaryotic cell biology.

[1] Department of Cellular Physiology, Biomedical Center (BMC), Ludwig-Maximilians-Universität München, Grosshadernerstrasse 9, 82152 Planegg-Martinsried, Germany. [2] Center for Nanosciences (CeNS), Ludwig-Maximilians-Universität München, Schellingstrasse 4, 80799 München, Germany. [3] Arnold-Sommerfeld-Center for Theoretical Physics (ASC), Department of Physics, Ludwig-Maximilians-Universität München, Theresienstrasse 37, 80333 München, Germany. [4] Theoretical and Applied Physical Chemistry Research Institute (INIFTA), National University of La Plata, Diagonal 113, 1900 La Plata, Argentina. [5] These authors contributed equally: Benoit Rogez, Laeschkir Würthner. Correspondence and requests for materials should be addressed to E.F. (email: frey@lmu.de) or to C.V. (email: claudia.veigel@med.lmu.de)

In eukaryotes, the morphology of cells, organelles and membrane domains is critically dependent on the membrane curvature. Active remodelling of the membrane curvature is the key to cellular motile processes, including endocytosis, cell migration and polarisation in morphogenesis and development[1,2]. Curvature-mediating proteins have been shown to induce specific membrane shapes by direct insertion and nanoscopic scaffolding[3–5]. Since fundamental concepts and the biological relevance of membrane curvature were first recognised over 40 years ago[6,7], it was understood that the cytoskeleton plays a more indirect role by generating a macroscopic scaffold to exert forces onto the plasma membrane and intracellular membrane systems via actin and microtubule polymerisation and motor protein activity[8]. It remained unexplored, however, whether the manifold direct interactions between lipid-binding motor proteins and the target membranes themselves affect the membrane curvature[9–11], and if so, how? The lipid-binding molecular motor myosin-VI (myo6) functions in a wide range of cellular processes that involve not only dramatic changes in local membrane shape, including endocytosis, polarized secretion, Golgi re-organisation and autophagy[9,12–14], but also cell migration and invasion in numerous cancers[15–17]. Myo6, the only myosin class that has been shown to move towards the minus end of actin filaments, has been reported to bind directly to lipid membranes via its C-terminal tail domain[9]. The molecular mechanisms of this protein–lipid interaction remained unclear[9,18].

Using reconstituted, fluid supported lipid bilayers, super-resolution fluorescence microscopy and membrane-reshaping gold nano-particles, we show that myo6 on its own remarkably remodels the membrane to form rugged, flower-shaped membrane pores. We find that the curvature-dependent and cooperative binding kinetics of the myosin favour saddle-shaped membrane geometries, which leads to characteristic and growing spatial patterns. We propose a quantitative theoretical model that describes this innovative route of protein–membrane interaction and ensuing membrane morphology, which we call a dynamic membrane sculpting mechanism. Our findings highlight a previously unnoticed basic feature of protein–lipid interactions that opens up unexplored avenues for the shaping of the plasma membrane and intracellular organelle systems in eukaryotes.

Results

Myosin-VI reshapes the protein–lipid interface. We investigated the effect of fluorescently labelled myo6 in solution on the shape of a reconstituted fluid model membrane consisting of a phosphatidylcholine lipid bilayer, a major constituent of the plasma and organelle membranes in animals and plants[19,20], and a well-characterised model system[21] (Fig. 1a). The lipid diffusion coefficient $D \sim 1.15-1.8\,\mu m^2\,s^{-1}$, determined by fluorescence recovery after photobleaching (FRAP) in the absence and presence of myo6 (Supplementary Fig. 1a, b), confirmed the fluidity of the solid supported and intrinsically flat 1,2-dioleoyl-sn-glycero-3-phosphocholine (DOPC) bilayer[22,23]. Unexpectedly, we found that the myosin-binding events to the bilayer were very sparse but highly cooperative, consistent with the motor molecules binding to a small number of spontaneously and transiently forming nanometre-sized membrane defects or transversal membrane pores[24,25]. The binding process caused the pores to grow into rugged flower shapes, reaching several microns in diameter after about 30 min (at 150 nM myo6 in solution). The lipids displaced from the perimeter of the pores to accommodate myosin binding were redeposited onto the membrane as micelles or small vesicles (double asterisks (**) in Fig. 1a), revealing a heretofore unknown process of motor protein–lipid interaction. Using a quantitative analysis of the total internal reflection fluorescence microscopy (TIRFM) data (Fig. 1b and Supplementary Fig. 1c, d) and a 10:1 ratio of myo6:green fluorescent protein (GFP)-myo6 to ensure the fluorescence signal measured for each flower was within the linear range of the EMCCD camera, we estimated the density of the myo6 motors at the protein–lipid interface. By measuring the perimeter of the flowers, their total fluorescence intensity and the fluorescence signal of single GFP-myo6 molecules in TIRF mode, we estimated an average distance of $\langle dx \rangle \sim 3.74 \pm 0.64$ nm (mean ± s.d.) between neighbouring myosin molecules along the perimeter of the growing flowers (see 'Methods'). The value dx was independent of the actual perimeter of the pore and indicated a dense packing, given the physical size of the myosin molecules (diameter ~ 3–5 nm[18,26]). The myo6 molecules might well interact with each other and arrange themselves in a more complex geometry than in a monolayer. We then investigated the mechanical properties of these ensembles of densely packed myosin and found that they were mechanically fully functional. They translocated Alexa 488-labelled actin filaments at $365 \pm 125\,nm\,s^{-1}$ (mean ± s.d., $n = 153$ filaments) at saturating ATP concentrations (Fig. 1c, actin in yellow, 2 mM ATP, 22 °C), at least as fast as myo6 monomers and dimeric constructs in vitro and in cells[27–29]. The propensity to self-organise to generate membrane pores was also observed on giant unilamellar DOPC vesicles (Supplementary Fig. 1e), which confirmed that this cooperative membrane interaction of myo6 was not restricted to the flat supported bilayer but an intrinsic property of the motor–lipid interaction.

Myosin-VI binding to a lipid bilayer is curvature sensitive. To uncover the mechanisms underlying pore growth and the emergent flower-like morphology of the motor–lipid interface, we applied super-resolution microscopy (SRM) and localised single GFP-myo6 molecules at ~ 25nm spatial resolution ('Methods'). The colour-coded time stamps in Fig. 2a, b obtained from SRM images integrated over 1 min time periods showed the new appearance and growth of myo6 flowers during a 60-min time interval (150 nM myo6 in solution, 10% GFP-myo6). The perimeter of the flowers grew at a roughly constant rate, directly proportional to the myo6 concentration in solution (Fig. 2c). Combined with the constant density of myo6 along the growing perimeter (Fig. 1b), this result indicated a mechanism with an—on average—constant rate of myosin binding to and lipid displacement from the protein–lipid interface. Strikingly, the SRM images also exposed local hotspots of myo6 attachment (arrow heads), which formed a quite regular spatial pattern along the growing perimeter of the flowers in the time stamp overlay. Inspection of the hotspots in the zoomed-in image indicated that the freshly bound GFP-myo6 molecules (red, arrows) were incorporated preferentially at regions where the membrane was bulging outward, away from the centre of the flower; there the membrane geometry is saddle-shaped (negative Gaussian curvature). Superposition of all GFP-myo6 molecules, detected during different time stamps, over the respective perimeter of the flower (Fig. 2b) demonstrated that the hotspots indeed co-localised with the protrusions of the perimeter (arrows heads). This showed that the process of myosin binding was cooperative and strongly sensitive to the membrane curvature. The curvature dependence of the myosin binding was also reflected in the roughness of the perimeter, so that the ratio of flower area vs perimeter deviated slightly from a perfect circle growing over time (Fig. 2c, black curve).

Myosin-VI favours a saddle-shaped membrane geometry. Next, we set out to characterise the morphology of the motor–lipid interface by SRM (Fig. 3a) using an intensity threshold to separate

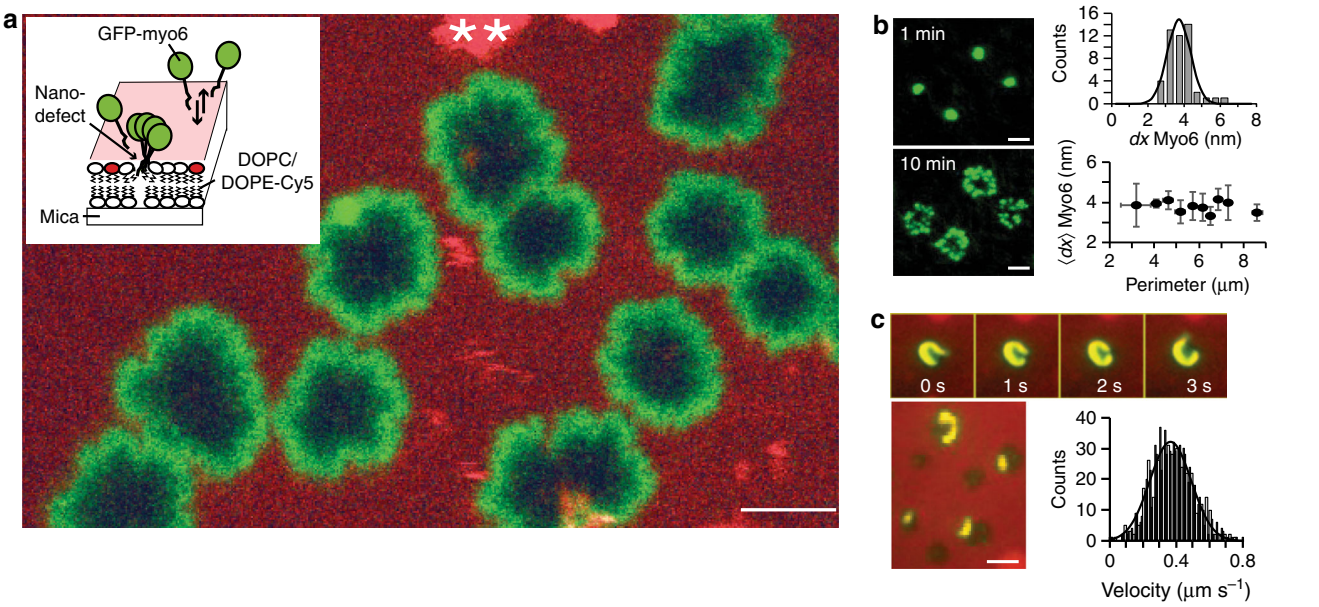

Fig. 1 Myo6 reshapes transient membrane defects into growing pores. **a** Schematic of the in vitro assay with 150 nM green fluorescent protein (GFP)-myo6 (green) in solution interacting with a 1,2-dioleoyl-sn-glycero-3-phosphocholine (DOPC):1,2-dioleoyl-sn-glycero-phosphoethanolamine-*N*-Cyanine 5 (DOPE-Cy5) (red) fluid lipid bilayer (4000:1 ratio) imaged using confocal microscopy; image after 30 min; scale bar 5 μm. **b** Growth of flower-shaped membrane pores 1 and 10 min after addition of 150 nM myo6, with a GFP-myo6 (green):myo6 ratio of 1:10 and the DOPC bilayer unlabelled; scale bars 2 μm. Average distance between myo6 molecules lining the flower ⟨dx⟩ ~ 3.74 ± 0.64 nm (mean ± s.d., $R^2 = 0.92$, $n = 48$ flowers, perimeters 2–9 μm), independent of the perimeter of the flower (total internal reflection fluorescence microscopy). Same data plotted as a single distribution and sorted by perimeter (mean ± s.d.). **c** Myo6 motors (unlabelled) bound to a DOPC:DOPE-Cy5 (red) fluid lipid bilayer (4000:1 ratio) translocate Alexa 488-labelled actin filaments (yellow) at an average velocity 365 ± 125 nm s^{-1} (mean ± s.d., $n = 153$ filaments) along the perimeter of the flower (2 mM ATP); scale bar 3 μm. Source data are provided as a Source Data file

the hotspots of myosin binding from the surrounding fluorescence signal (Supplementary Fig. 2). The distances *dz* between the hotspots were determined for different myo6 concentrations in solution. At 10 nM myo6, the speed of flower growth was slow enough to resolve the early stages of hotspot formation (Fig. 3b). As for all different myo6 concentrations and speeds of flower growth, the hotspots were almost equally spaced with an average distance $\langle dz \rangle$ saturating at ~900 nm (Fig. 3c), we concluded that this regular myosin pattern is likely an intrinsic feature of the process underlying membrane reshaping by myo6 in our two-component model system (myo6, DOPC). In particular, these observations hinted at a feedback between myosin binding and membrane curvature.

To address (and quantify) this possible feedback, we studied how the shape of the initial nano-pore affected the myo6 binding. To this end, we used gold nano-triangles[30] with a side length of 60–80 nm and a height of ~8 nm (Fig. 3d, transmission electron microscopy (TEM)), which were deposited on the mica surface before the bilayer was applied. With their sufficiently small aspect ratio, the nano-triangles were not covered by the bilayer surrounding them[31]. FRAP studies confirmed bilayer fluidity in their presence (Supplementary Fig. 3). The nano-triangles acted as seeds for myosin insertion into the bilayer, as shown in the three-colour confocal fluorescence experiment (Fig. 3d nano-triangles T, white arrows). During the first 5 min following addition of 10 nM myo6, the triangular binding pattern intriguingly indicated that myo6 inserted nearly exclusively near the tips of the gold nano-triangles (Fig. 3e). The smallest distances of ~100 nm between the earliest myo6 hotspots (Fig. 3e) forming a triangular shape indicated that initially the proximity between bilayer and nano-triangle (60–80 nm side length) must have been ≤20 nm. Over ~20 min, the triangular shape and orientation of the pattern was preserved, as the flower diameter expanded (Fig. 3c inset), until additional myo6 hotspots emerged and the 'memory' of the initial pore shape was lost. The experiments confirmed that myo6 strongly favoured the saddle-shaped membrane geometry (negative Gaussian curvature)[5] at the tips of the triangular pore over the sides of the pore (cartoon). Importantly, the final characteristic distance between the hotspots was similar to the one observed in the absence of the triangles (Fig. 3c).

A quantitative model explains the dynamic membrane sculpting. We integrated the above experimental observation to propose a quantitative theoretical model for this emerging form of dynamic membrane sculpting. The model describes the dynamics of the experimentally determined protein–lipid interface (Fig. 4a, b) as the time evolution of a closed (planar) curve $\Gamma(t)$ (Fig. 4c, d), which we represent by the position vector $\vec{\mathbf{x}}(t,\sigma) = (x(t,\sigma), y(t,\sigma))$ ('Methods', Supplementary Fig. 4), where t denotes time and σ parametrises the position along the curve $\Gamma(t)$. Our basic assumption is that the dynamics of the interface is determined by the normal velocity V_n,

$$\partial_t \vec{\mathbf{x}} \cdot \hat{\mathbf{n}} = V_n, \qquad (1)$$

where $\hat{\mathbf{n}}$ is the outward unit normal vector on $\Gamma(t)$ ('Methods', Supplementary Fig. 4). The growth velocity V_n is determined by the interface morphology, i.e. the local interface curvature κ and its spatial modulation: $V_n = f(\kappa) - \alpha\nabla^2\kappa$ (see 'Methods' section for a detailed derivation). The observed feedback between interface curvature and myosin binding is accounted for by a curvature-dependent growth rate $f(\kappa)$, shown in Fig. 4e, which we obtained by (systematically) fitting the measured time dependence of the average flower radius to our theoretical description (Fig. 2c, 'Methods', Supplementary Fig. 6). As in the experiments,

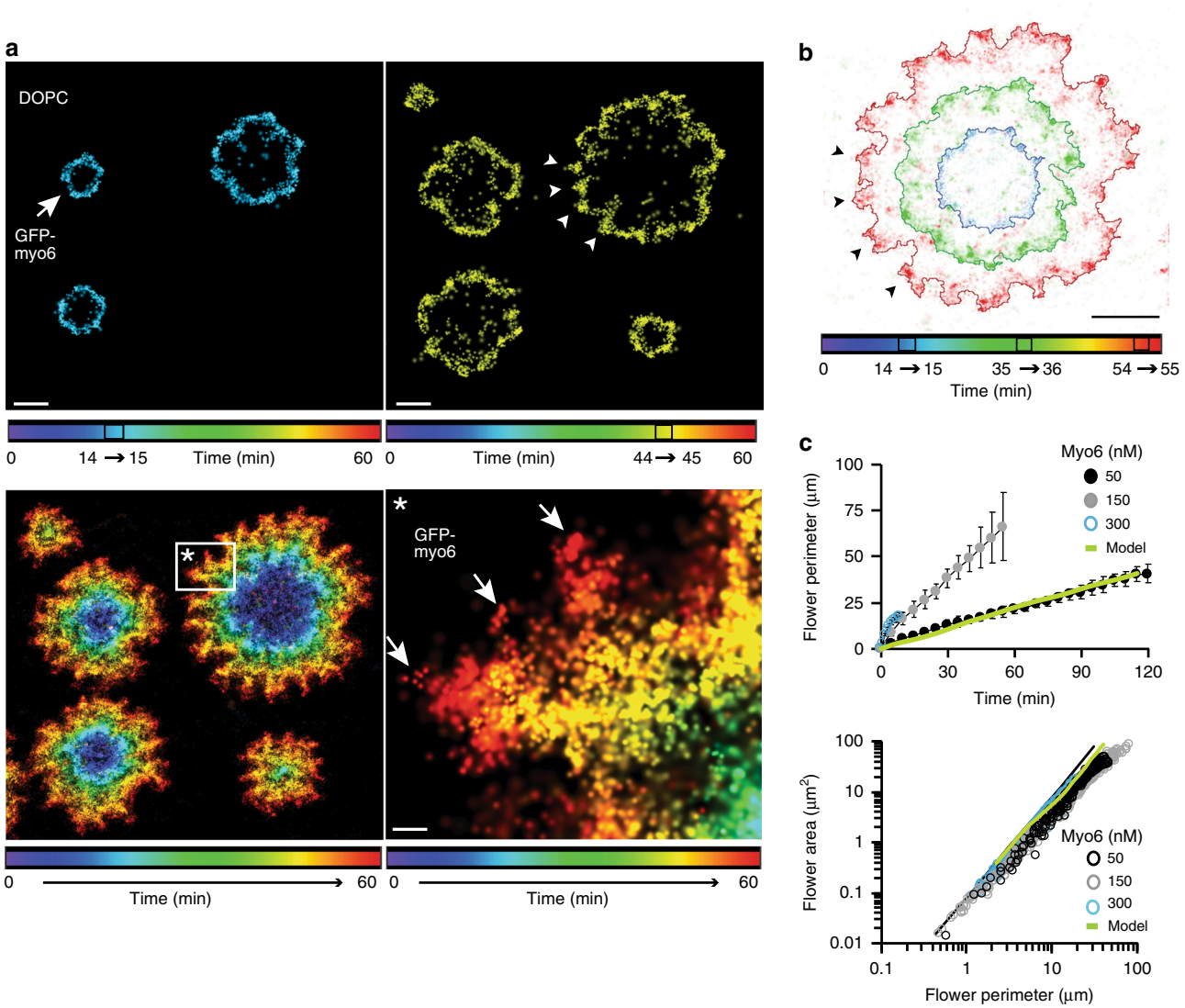

Fig. 2 Myo6 binding to a lipid bilayer is curvature sensitive. **a** Super-resolution microscopy (SRM) of myo6 flowers growing over 60 min (150 nM myo6, 10% green fluorescent protein (GFP)-myo6; bilayer unlabelled). The colour-coded time stamps were obtained from SRM images integrated over 1 min time periods (14–15 and 44–45 min, respectively), bilayer unlabelled. Arrow heads mark hotspots of GFP-myo6 binding. The SRM image integrated over 60 min shows the new appearance and growth of the myo6 flowers with the colour encoding the progress in time. Zoomed-in image shows freshly bound myo6 (red) at hotspots (arrows) where the membrane border bulges outward, away from the pore centre; scale bars 1 μm; scale bar in inset (*) 200 nm. **b** GFP-myo6 detected during three colour-coded, 1 min time intervals superimposed onto the respective perimeter of the flowers (solid lines, 'Methods'). Hotspots of GFP-myo6 marked by arrow heads; scale bar 1000 nm. **c** Perimeter determined by integrating SRM data over time *t*; $n = 253$, 561 and 948 measurements in total for 50 (black filled circles), 150 (grey filled circles) and 300 nM myo6 (blue unfilled circles) from 20 to 70 flowers in each condition. Same data shown as scatter plot (area vs perimeter) and as mean perimeter (mean ± s.d.) sorted by time *t*. Green line, theoretical model (see below). Source data are provided as a Source Data file

the interface growth speed is enhanced at negative and reduced at positive curvatures with respect to the average value. This theoretical approach for the dynamics of the protein–lipid interface is different from force balance arguments used to describe the dynamics of pore nucleation and growth in giant unilamellar vesicles (GUVs) or lipid membranes[32–34]. The main difference arises from the positive feedback of myo6 binding to regions of negative curvature (recruitment), which is the major driving force of the dynamics. Dynamics based on this feedback alone would lead to rough protein–lipid interfaces with no emerging characteristic length scale. This roughening tendency is counteracted by molecular processes including myosin rearrangement on the membrane and line tension of the lipid bilayer that smoothen the interfaces similar to models for crystal growth[35–38]; for a more detailed discussion and an illustration, see 'Methods' section and Supplementary Fig. 5a, b. We effectively account for these processes by a term, $\alpha \nabla^2 \kappa$, which is acting as an effective line tension term penalising changes in the interface curvature. This can be seen by rewriting the growth law in 'potential form',

$$V_n = \mu \frac{\delta \mathcal{F}}{\delta \kappa}, \qquad (2)$$

where μ denotes an interface mobility. The effective free energy functional is given by

$$F = \int_\Gamma \left[F(\kappa) + \frac{\gamma}{2} (\partial_s \kappa)^2 \right] \mathrm{d}s \qquad (3)$$

with the second term penalising gradients in curvature. The corresponding stiffness parameter γ is related to the above phenomenological parameter α through the mobility, $\alpha = \mu \cdot \gamma$. The function $F(\kappa) \propto \int \mathrm{d}\kappa f(\kappa)$ may be interpreted as an effective curvature potential. Since we model line tension only effectively

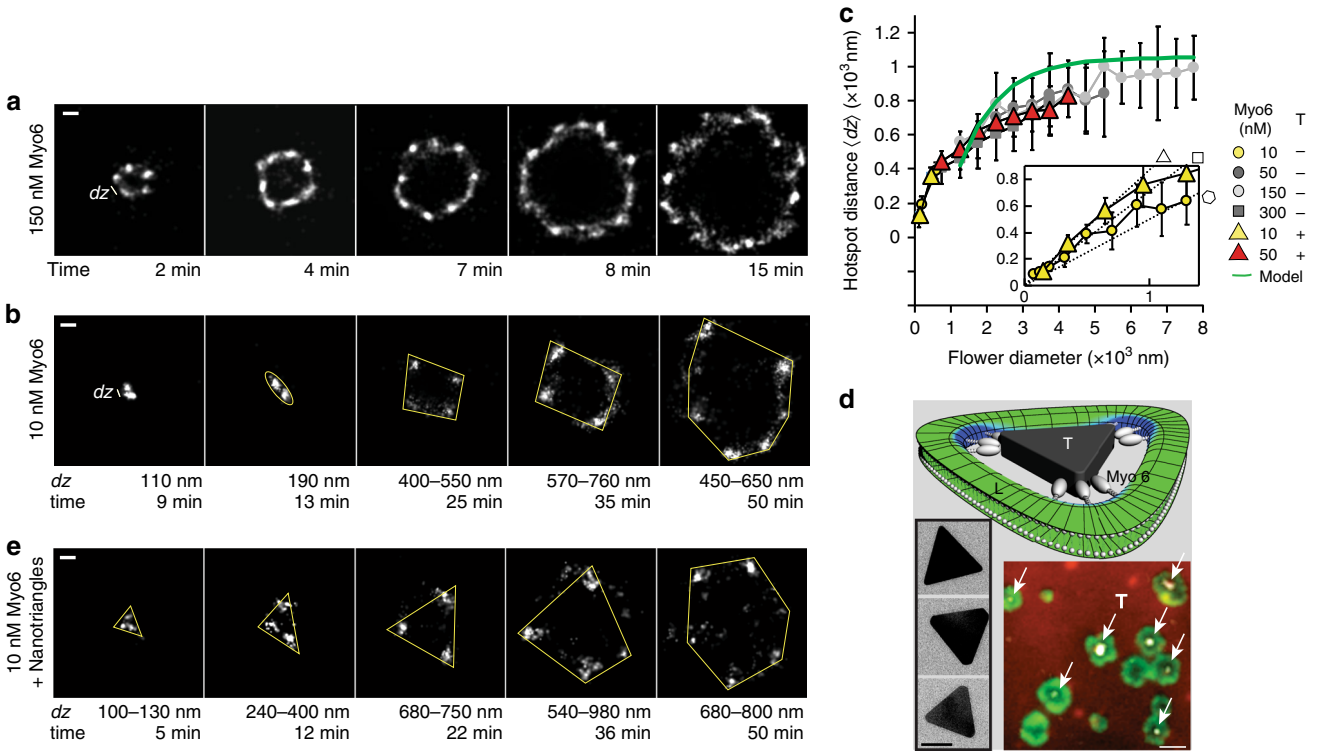

Fig. 3 Myo6 lipid binding favours a saddle-shaped membrane geometry. Representative super-resolution microscopic (SRM) images at **a** 150 nM and **b** 10 nM myo6, integrated over 1 min; scale bar **a** 400 nm and **b** 200 nm. Distance *dz* marks distances between GFP-myo6 hotspots. **c** Distances ⟨dz⟩ (mean ± s.d.) from 10 to 36 measurements in the absence or presence of nano-triangles T (0.3 pM), respectively. Green line, theoretical model. Inset: dotted lines show the side lengths of an equilateral triangular, quadrangular and hexagonal shape with increasing diameter of 0–1 µm. **d** Transmission electron microscopic images of gold nano-triangles T (side length 60–80 nm, height 8 nm), scale bar 40 nm; cartoon of a lipid bilayer surrounding a T (L = lipid, green; saddle-shaped curvature, blue); cartoon illustrates that, in contrast to a circular-shaped membrane pore, triangular-shaped pores have saddle-shaped curvatures only at the corners of the triangular pore (blue). This is where we found the curvature-sensitive myo6 to bind (see **e**); gap between lipid and nano-triangle not to scale and enlarged for clarity. Co-localisation of the TRITC-labelled T (white, arrows) and GFP-myo6 (green) on a DOPC:DOPE-Cy5 bilayer (red), scale bar 2 µm. **e** SRM of a flower growing at 10 nM myo6 in the presence of 0.3 pM T; scale bar 200 nm. Source data are provided as a Source Data file

via the term $-\alpha\partial_s^2\kappa$, the parameter α is proportional but not equal to a classical line tension parameter[35–37]. This is also evident from the units of the parameter α (length^4 time^{-1}), which is different from a classical line tension (energy length^{-1}).

After validating the model parameters for the growth term ('Methods', Supplementary Fig. 6, Fig. 4e) (see above), we performed an extensive set of simulations in order to explore whether the model can qualitatively as well as quantitatively explain the dynamic morphology of the protein–lipid interface observed experimentally (Fig. 4a, b). In fact, it correctly reproduces the key qualitative features of the experimentally determined protein–lipid interface (Fig. 4a–d, 'Methods', Supplementary Fig. 6): flower-shaped morphology, memory effects for triangle-shaped pores, spontaneous emergence of new hotspots, and tip-splitting. To quantiatively match the average distance dz between the experimentally observed hotspots of myo6 attachment (Fig. 3c), we fitted the value of the effective line tension parameter: $\alpha = 10^{-6}\,\mu m^4\,s^{-1}$ ('Methods'). Taken together, we conclude that the basic mechanisms included in the model, feedback between binding kinetics of myo6, interface growth and surface smoothing mediated by myo6 rearrangement and line tension of the bilayer, explain the observed dynamics of the membrane sculpting process.

Discussion

Combining experimental approaches and theoretical modelling, our study addresses a fundamental problem of molecular cell biology, which is to reveal mechanisms used by cells to produce and remodel membrane shape. The sequence of events during membrane reshaping in various cell biological contexts remains controversial. Molecular motors are thought to get involved at the later stages of membrane trafficking or endocytosis, while other, specialised proteins are responsible for initial local membrane reshaping. Our results challenge the classical view of the role of motor proteins and introduce an innovative function of membrane sculpting by direct protein–lipid interaction, indicating that motor proteins can get involved in the initial stages of membrane remodelling.

Using a fluid supported lipid bilayer, we found that the molecular motor myo6 on its own remarkably remodels the membrane into dynamic spatial patterns. The motor protein–lipid interaction generates a heretofore unknown system of feedback and instability, so that dynamic membrane patterns self-organise on the nanometre to micrometre length scale. The process starts with myo6 binding to spontaneously and transiently forming membrane pores. Subsequently, these pores grow into rugged flower shapes, reaching several microns in diameter. We have developed a theory that quantitatively explains the membrane sculpting process leading to the dynamic morphology of the growing protein–lipid interface, including the spontaneous emergence of new myo6-binding hotspots and tip splitting. The basic idea underlying our theory is a reduction of the complex and interlinked chemo-mechanical problem of protein (myo6) binding kinetics and dynamics of the protein–lipid interface to an

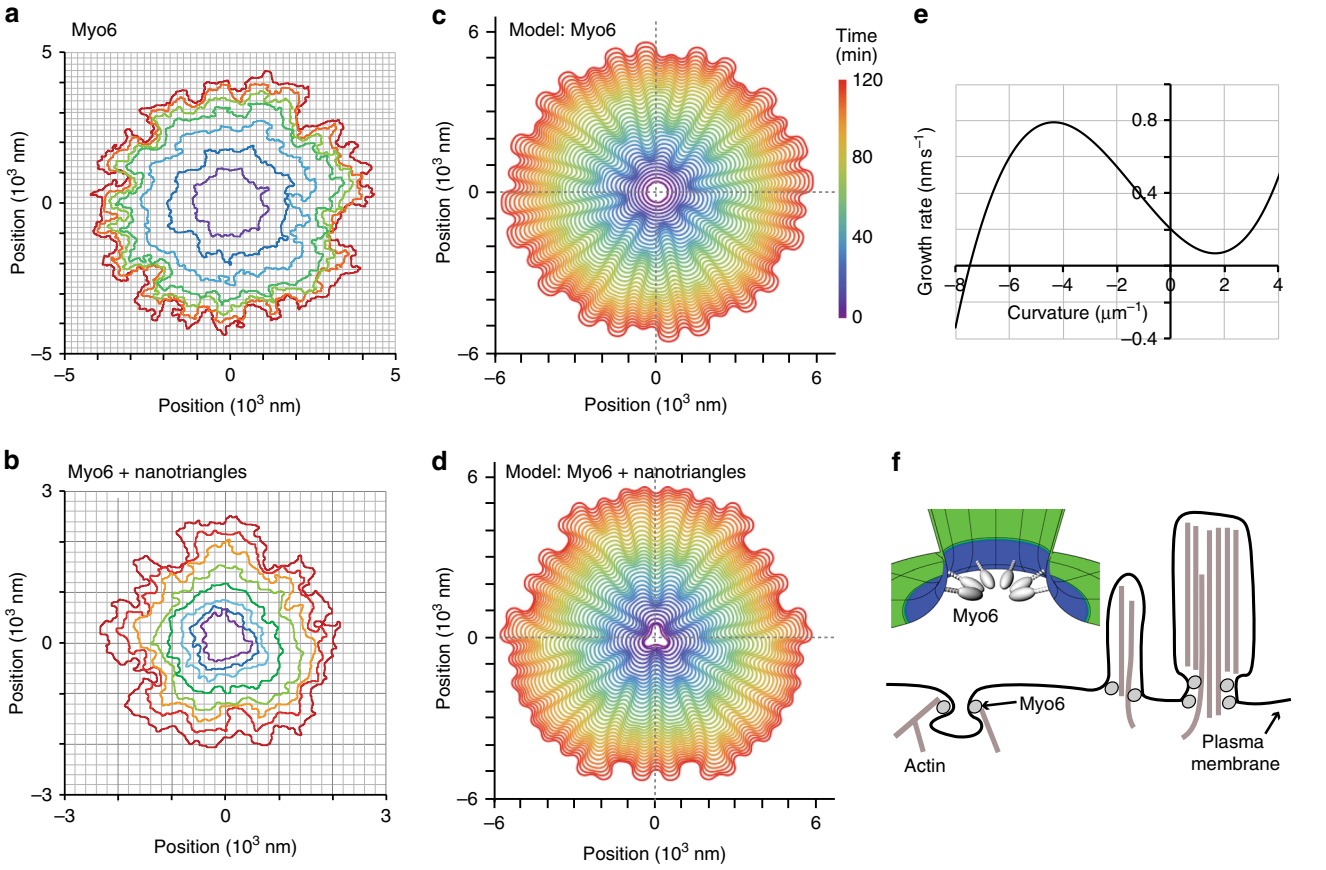

Fig. 4 A quantitative model explains the dynamic membrane sculpting. **a** Representative examples of the flower perimeter determined by super-resolution microscopy at different time stamps in the absence and **b** presence of a nano-triangle inserted into the membrane as a seed (50 nM myo6, colour code as in Fig. 2). **c** The model reproduces the time evolution of the flower perimeter for different starting geometries in the absence and **d** presence of nano-triangles. **e** Profile of the curvature-dependent myo6-binding rate used in the model. **f** Localisation of myo6 at cellular sites with saddle-shaped membrane geometry[13]

effective description in terms of an evolving line characterised by its local curvature and gradients in that curvature. The nonlinear coupling between the morphology of the protein–lipid interface and biochemical processes facilitating binding and unbinding of proteins is encoded in a curvature-dependent growth term that is inferred from the experimental data. In addition to being computationally efficient, this theoretical approach provides innovative insights: It shows that local curvature-dependent interactions between myo6 and lipids are sufficient to remodel the membrane, explaining the dynamic membrane sculpting. The theory also reveals that the pattern forming process is mainly controlled by material parameters like the effective line tension and membrane stiffness. This suggests that length scale selection in the membrane pattern depends crucially on the lipid composition and the molecular interactions of myo6 with the lipids, which to date are not fully understood. Moreover, our theoretical approach is quite general and can easily be extended to include nonlocal interactions and coupling to other dynamic variables, such as the myo6 bulk density. Therefore, we expect that the theoretical concepts and methods developed here may be broadly applicable to biological processes dynamically coupling membrane morphology and biochemical pattern formation. This may serve as a basis for future studies addressing general pattern forming processes on evolving geometries in biological systems.

Our results also show that membrane remodelling by myo6 does not require nucleotide as an energy source nor interactions with actin. The tail domain of the motor was sufficient to induce growing membrane pores, indicating that the catalytic activity of the motor domain is not necessary for myo6 to induce the remodelling effect on the membrane shape. Furthermore, the time course of pore growth and the characteristic myo6binding patterns were similar in the absence or presence of apyrase treatment of the motor protein to remove residuals of ATP or ADP (Supplementary Fig. 1f–h). These results are consistent with the binding energy of the myo6–lipid interaction to be sufficient for the remodelling of the membrane.

The densities of the motor protein obtained by self-organisation at the protein–lipid interface was high, with an average distance between myosin motors of only ~3.74 ± 0.64 nm, independent of the actual perimeter of the growing protein–lipid interface. These densities, which appear to be at the limit for spacing if all myosin molecules in the flower are bound to the membrane, might well indicate interaction between the lipid-bound motors, affecting their orientation on the bilayer, so that the mechanical output of the motor protein is optimised when interacting with actin filaments. In fact, the native myo6 motors, bound to the pores of the DOPC lipid bilayer, translocated actin filaments at ~365 ± 125 nm s^{-1} (22 °C) at saturating ATP concentrations (2 mM ATP). These velocities exceed the range of speeds previously reported for monomeric and enforced dimeric myo6 constructs[18,27,29,39]. The variations in speed might be related to the variability of motors partly back-folded and/or contributing with a range of lever arm lengths to the gliding velocity in these studies. The details of the molecular

conformation of myo6 when bound at high density to the lipid bilayer in our study, which produced these high actin-gliding velocities, remain unclear and will be addressed in future experiments.

Our study also revealed the unexpected result that myo6–lipid binding does not require the presence of PIP2 lipids[9]. Instead, the myo6–lipid interaction depended on the shape of the bilayer and was highly selective for saddle-shaped membrane geometries (Fig. 4f). The assay of triangular-shaped gold nano-particles combined with SRM has now provided the opportunity to explore the geometric preference of the (motor-)protein–lipid interaction at the nanometre scale. The strong preference of myo6 for saddle-shaped membrane geometries is consistent with its intracellular locations at the base of microvilli, stereocilia and sites of endocytosis (Fig. 4f)[13].

In conclusion, our results broaden the classical view of the role of motor proteins and introduce the function of membrane sculpting by direct protein–lipid interaction. In addition to the currently known distinct mechanisms that allow proteins to sense, stabilize or generate high local membrane curvature, we believe that we have identified a hitherto unknown mechanism of dynamic membrane sculpting by (motor-)protein–lipid interaction. Consistent with the generality of the already identified mechanisms of membrane reshaping within eukaryotic cells, our original assay and modelling approach might help to uncover additional mechanisms underlying membrane shaping in the near future and contribute towards revealing the universal role of membrane curvature in cellular functions.

Methods

Molecular biology. Myosin-VI (myo6) from human cells (accession number XP_005248783.1, residues 1–1253) was cloned into pFastbacHtB (Invitrogen) via EcoRI/SalI sites using primers HVIEcoRIF (GAATTCAAATGGAGGATGGA AAGCCCG) and HVISalR (GTCGACTTATTTCAACAGGTTCTGC). Two full-length constructs were expressed, one native full-length myo6 and a fusion full-length myo6 with an N-terminal eGFP cloned between the BamHI site using primers GFPBamF (GGATTCATGGTGAGCAAGGGCGAG) and GFPBamR (GAATCCCTTGTACAGCTCGTCCATG); furthermore, a Head construct (aa1–913) was cloned into the pFastbacHTb vector via EcoRI/SalI sites using primers HVIEcoRIF and HVI913SalR (GTCGACTTACATGGACGAGCTGTACA AGGGATTC), note HVIEcoRIF has a stop codon added. A Tail construct was cloned into pET28a vector via EcoRI/SalI (aa1037–1253) using primers HVI1037EcoRIF (GAATTCCCTGCTGTACTAGCCACC) and HVISalR (with an N-terminal GFP cloned BamHI using primers GFPBamF and GFPBamR; Supplementary Fig. 1a). The myo6 heavy chain was co-expressed with human calmodulin and purified as described in detail in our previous work[18,39]. In brief, myo6 full-length and the Head construct were expressed in a 500-ml culture of SF21 cells (ThermoFisher Scientific B82101) and infected with a combination of baculovirus motor protein (multiplicity of infection (MOI) 3) and calmodulin (MOI 2) and grown at 27 °C for 72 h. Cells were pelleted and resuspended in phosphate-buffered saline (PBS) plus protease inhibitors (Roche cOmplete EDTA free). This was then sonicated for 3 min and spun at 70,000 × *g* (RCF) for 30 min at 4 °C. The supernatant was immediately loaded onto a 5-ml HisFF column (GE Healthcare). An AKTA programme was used with PBS and His high (50 mM Tris-HCl pH 7.5, 400 mM Imidazole, 300 mM NaCl) using 2 steps, the 5% step removed non-specific proteins and a 50% step eluted the myo6. The peak fraction collections were pooled, 20% glycerol added and snap frozen and stored at −80 °C. The Tail construct was expressed in BL21 one shot (DE3) cells (Invitrogen C600003). Two litres of cells grown in 2 × TY media at 37 °C to an OD600 of 0.6 were induced with 1 mM IPTG and grown overnight at 24 °C. Cells were pelleted at 8000 × *g* (RCF). The cell pellet was resuspended in His low (50 mM Tris-HCl (pH 7.5), 40 mM Imidazole, 300 mM NaCl) and sonicated for 5 min. This was then clarified at 70,000 × *g* (RCF) for 30 min and the supernatant was loaded onto the AKTA. Using His low and His high, a 5, 10 and 50% step programme was used to elute the protein. The 50% fraction peak was snap frozen and stored at −80 °C.

Lipid bilayer on mica. A few monolayer thick, freshly cleaved mica sheet was deposited onto a glass coverslip using an index matching immersion oil and the coverslip made into a 300-µl flow cell. A supported lipid bilayer was formed using single unilamellar vesicle fusion as described[40]. The vesicles were made from DOPC (Sigma Aldrich™) and 1,2-dioleoyl-sn-glycero-phosphoethanolamine-*N*-Cyanine 5 (DOPE-Cy5, Avanti Polar Lipids™) at a 4000:1 ratio. In short, the vesicles (~1.7 mg ml^{-1} DOPC) in lipid buffer (LB; 20 mM Hepes pH 7.5 and 150 mM NaCl) were applied to the mica surface and allowed to fuse for 10 min at room temperature (RT) by adjusting the buffer to contain (in mM): 3.3 $CaCl_2$, 100 Tris (pH 7.5), and 50 NaCl. Unfused vesicles were removed from the bilayer by washing with assay buffer (AB) containing (in mM): 25 Imidazole pH 7.4, 25 KCl, 4 $MgCl_2$, and 1 EGTA. The formation of a continuous and fluid bilayer on the mica surface was confirmed by FRAP.

Fluorescence microscopy in TIRF mode. The flowers were recorded using a Nikon Ti-Eclipse combining TIRFM including an EMCCD (Andor iXon3) camera and an A1 confocal module with a ×100 oil immersion objective, NA 1.49. A 10:1 ratio of myo6:GFP-myo6 was used and the 488-nm excitation laser set to 60 mW. To determine the density of myo6 along the perimeter of the flower (Fig. 1b), the perimeter of individual flowers, the total fluorescence intensity of individual flowers (I_{total}) and the fluorescence signal of single GFP-myo6 molecules bound to the lipid bilayer ($I_{single\ GFP}$) were measured in TIRF mode (Supplementary Fig. 1c, d). Here the flower perimeter was determined as the closed line connecting the pixels with maximum fluorescence intensity of a given flower (Supplementary Fig. 1c, yellow line). This closed line was enlarged radially by 400 nm in order to measure I_{total} of the individual flower (Supplementary Fig. 1c, area within green line). To reduce the effect of bleaching, only the first image acquired after activation of the excitation laser was used. $I_{single\ GFP}$ was determined from binding events followed by single-step photo-bleaching (Supplementary Fig. 1d, fluorescence signal 18,917 ± 5523 (mean ± s.d., $n = 288$). The maximum I_{total} measured for each flower was within the linear range of the camera. Using I_{total} of individual flowers, $I_{single\ GFP}$, the flower perimeter, and taking the 1:10 labelling ratio of GFP-myo6: myo6 into account, we estimated the average distance 3.74 ± 0.64 nm (mean ± s.d., $n = 48$) between neighbouring myo6 molecules along the flower perimeter.

Fluorescence recovery after photobleaching. To test the fluidity of the bilayer, a circular area of ~40 µm in diameter was bleached in confocal mode using a 647-nm laser at 30 mW and FRAP was monitored using the same laser at 4 mW and an image sampling rate of 12 images per minute. All bilayers used in this study were tested using FRAP to ensure a full fluorescence recovery (FR) within <5 min. The diffusion coefficient D for DOPC in the absence and presence of myosin was estimated from the FR of a small area of ~4 µm in diameter in the centre of the bleached area. Single exponential fitting of the FR in the absence of myosin yielded a time constant τ consistent with $D \sim 1.15-1.8\ \mu m^2\ s^{-1}$ and in agreement with the literature for a supported and fluid DOPC bilayer[23,41].

Motility assay. A fluid DOPC bilayer was generated as described above. The formation of flowers was induced by incubation with 50 nM unlabelled myo6 and the flowers allowed to grow for 15 min. The buffer in the flow cell was replaced by AB buffer including 50 µg ml^{-1} bovine serum albumin (BSA, Sigma) and incubated for 5 min to prevent F-actin from binding to mica exposed at the membrane pores. Finally, the solution was replaced by AB buffer including 2 mM ATP, an oxygen scavenger system (50 mM dithiothreitol (DTT) and (in mg ml^{-1}) 0.25 glucose oxidase, 7.5 glucose, 0.05 catalase) and ~17 nM Alexa488-phalloidin labelled F-actin (labelled at a 1:1 molar ratio). The motility of F-actin was recorded and analysed using TIRF microscopy as described in detail in our previous work[18,42]. In brief, time-lapse microscopy was performed and the movement of the actin filaments recorded at a frame rate of 0.1 Hz (for 600 s) using a ×100 TIRF microscope objective. The gliding velocity of F-actin was calculated using the analysis software GMimPro (www.mashanov.uk). The motility assays were all performed at 2 mM ATP and at 22 °C.

Giant unilamellar vesicles. The GUVs are produced using electroformation as described in detail in our previous work[43]. In brief, 2 mg ml^{-1} DOPC, 2 µg ml^{-1} DOPE-Cy5 and 2 µg ml^{-1} Biotin-DHPE, dissolved in chloroform, were applied to a platinum wire and vesicle formation was induced in AB buffer supplemented with 100 mM sucrose to reach a total osmolarity of 200 mOsmol. The detaching vesicles were harvested and transferred to a streptavidin-coated flow cell using AB-buffer supplemented with 150 mM glucose to reach 250 mOsmol. Finally, the buffer was replaced by either 50 nM GFP-myo6 or 50 nM GFP alone in AB buffer including 150 mM glucose, and the change in fluorescence inside the tethered vesicle was monitored using confocal microscopy (Supplementary Fig. 1e). The time constant $\tau = 78 \pm 19$ s (mean ± s.d., $R^2 = 0.94 \pm 0.04$; $n = 5$), derived from the time course of the fluorescence increase inside the vesicles (11.24 ± 3.35 µm diameter, mean ± s.d., $n = 5$), and the application of Fick's law allowed us to estimate the combined radius of the pores (~10 ± 5 nm, mean ± s.d.) introduced into the GUV vesicle membrane by membrane binding of GFP-myo6.

Super resolution microscopy. The fluorescence images recorded on a Nikon Ti-Eclipse in TIRF mode were analysed using a combination of the proprietary N-STORM plugin and ImageJ. Our approach is related to the STORM/PALM techniques, e.g. ref. [44] in the sense that wide-field microscopy is used and the position of individual fluorophores is estimated by a two-dimensional (2D) Gaussian fit to the detected fluorescence signal. In contrast to these techniques, however, which involve individual fluorophores to be activated by a laser pulse, the fluorophores in our study are all activated, but only those GFP-myo6 molecules that are binding to

the membrane are detected. This approach is related to the PAINT technique[45]. In brief, the algorithm automatically detected the centre position of local fluorescence intensity maxima by fitting a 2D Gaussian. Single GFP-myo6 molecules could be localised with a resolution of ~25 nm (full width at half maximum of the fitted Gaussian), at distances below the diffraction limit of ~200 nm. The resulting image consisted of a set of discs each centred according to the Gaussian fits. The SRM image consisted of the position of all fluorophores detected within given time intervals. The time intervals were encoded by different colours (Fig.2). A 10:1 ratio of myo6:GFP-myo6 was used for all myo6 concentrations we applied. Images were recorded at a frame rate of 1.6 images per second using an Andor iXon 3, EM gain 300x.

Perimeter and area of the flowers measured using SRM. To determine the perimeter and area of individual flowers at time point t_x in SRM, we developed an algorithm based on the Nikon N-STORM plugin to analyse the SRM images. The detected fluorophores were fitted by a 2D Gaussian (15–20 nm radius). SRM images of 'filled-in' flowers were generated by overlaying all GFP-myo6-binding events detected from the beginning of the data acquisition until the time point t_x. The 'filled-in' flowers formed an enclosed area of Gaussian spots (Supplementary Fig. 1f). The outline of this area was used to determine the perimeter of the flower at time point t_x. Gaussian spots not connected to the enclosed area were ignored. The perimeter of the flowers in SRM was determined by connecting the centre positions of the Gaussian spots at the outline of the enclosed area. The procedure corresponds to low pass filtering (Gaussian spots 15–20 nm radius) and thresholding (eliminating Gaussian spots not connected to the enclosed flower area). To compensate for the delayed start of some flowers relative to others, each temporal evolution of a given flower was timeshifted to achieve synchronisation. The statistics are plotted for different concentrations of GFP-myo6 (50, 150, 300 nM; 19, 42, 55 flowers analysed, respectively). Owing to the higher numbers of flowers forming per field of view at higher myo6 concentrations in solution, the confluence of flowers became the limiting factor when measuring the perimeter of the flowers over time (Fig. 2c, 300 nM myo6).

Gold nano-triangles. Gold nanoparticles were produced in a two-step reaction as described in detail in our previous work[30,46]. In brief, the reaction of $HAuCl_4$ mixed with Na_2S was followed spectroscopically to obtain triangles (equilateral prisms) with ~60–80 nm side length and ~8 nm thickness and stopped by the addition of an excess of Na_2S. Following precipitation in 0.6 M cetyl trimethyl ammonium chloride and purification using 3 centrifugation cycles, the nano-triangle stock solution was centrifuged and the pellet resuspended in destilled water. Unless stated otherwise, the particles were applied to the mica surface at ~0.3 pM concentration, which led to ~50 particles on a $80 \times 80\ \mu m^2$ surface. When applied to the mica surface together with the DOPC bilayer in our experiments, the smallest distance of ~100 nm between the earliest myo6 hotspots (Fig. 3e) indicated that initially the proximity between bilayer and nano-triangle (60–80 nm side length) must have been ≤10–20 nm.

In situ labelling of the gold nano-triangles using TRITC. TRITC-maleimide (Sigma) was dissolved in dimethylsulfoxide (Sigma) to a concentration of 470 µM. The solution was reacted with 10 mM DTT (Sigma) for 10 min at RT and diluted in LB to obtain a 100-µM thiolated dye solution. Gold nano-triangles diluted to 0.07–1.2 pM in LB buffer were added to a flow cell and left to sediment on the mica surface for 5 min before DOPC vesicles were added to form a bilayer as described above. After 10 min, the bilayer was washed three times with AB buffer supplemented with scavenger. The solution was exchanged by 100 µM thiolated dye in AB buffer and incubated for 10 min. Finally, the flow cell was washed ten times to ensure that all unbound dye was removed.

Gold nano-particle effect on bilayer formation. The nano-triangles deposited on the mica surface in the absence of (white bars) or before a lipid bilayer was formed (grey bars) (Supplementary Fig. 3a). The number of detected triangles per field of view scaled roughly with the concentration of triangles applied. No significant difference was found between the number of triangles detected in the absence and presence of a lipid bilayer, indicating that the triangles were not covered but surrounded by the lipids. The relatively broad fluorescence intensity distribution from the labelled triangles was consistent with multiple dye molecules binding to a single triangle. Photobleaching of the spots was rarely observed in a single step. To probe the proximity of the lipid bilayer to the triangles, a line scan across an area with three detected triangles in the TRITC-channel (blue curve) was compared with the signal of the lipid Cy5-channel (red curve) (Supplementary Fig. 3b). No signal change within the resolution limit was found at the position of the nano-triangles, consistent with a proximity between lipid and triangles of ≤160 nm (one pixel). FRAP studies confirmed the fluidity of the bilayer in the presence of 0.3 pM nano-triangles, with $D \sim 1.29 \pm 0.1\ \mu m^2\ s^{-1}$ (mean ± s.d., $n = 2$, $R^2 = 0.97 \pm 0.005$; Supplementary Fig. 3c). The nano-triangles acted as seeds for the formation of myo6-induced flowers. The number of flowers increased with the number of triangles applied and reached a ten-fold increase at 0.3 pM nano-triangles (Supplementary Fig. 3d).

Geometric curve evolution. As discussed earlier, the time evolution of the planar curve $\Gamma(t)$ is solely determined by the normal velocity (Eq. (1)). This mesoscale approach is used in many other disciplines, including geometry[47–49], crystal growth[35–38,50,51], combustion[52–54] and fluid dynamics[37,55,56]. The basic idea is to model the dynamics through a semi-phenomenological growth law, i.e. by the dependence of the normal velocity on the position along the curve and the conformation of the curve. Before specifying this growth law, we need to introduce some basic concepts from the differential geometry of planar curves[57]. The local conformation of a planar curve Γ is determined by the curvature $\kappa(\sigma)$:

$$\hat{\mathbf{n}}\kappa(\sigma) = \frac{1}{\sqrt{g(\sigma)}}\partial_\sigma\left(\frac{\vec{\tau}(\sigma)}{\sqrt{g(\sigma)}}\right) \tag{4}$$

Here $\vec{\boldsymbol{\tau}} = \partial_\sigma\vec{\mathbf{x}}$ denotes the tangent vector to the curve Γ, and the metric is given by $g(\sigma) = \partial_\sigma\vec{\mathbf{x}}\cdot\partial_\sigma\vec{\mathbf{x}} = (\partial_\sigma x)^2 + (\partial_\sigma y)^2$. The unit tangent vector is then given by $\hat{\boldsymbol{\tau}} = \vec{\boldsymbol{\tau}}/\sqrt{g(\sigma)}$. We use the convention that $\kappa < 0$ for convex portions of Γ, i.e. outward bulges along the front (Supplementary Fig. 4). The arc length s is defined as the length along the curve:

$$s(t,\sigma) = \int_0^\sigma \sqrt{g(\sigma')}\mathrm{d}\sigma' = \int_0^\sigma \sqrt{(\partial_\sigma x)^2 + (\partial_\sigma y)^2}\mathrm{d}\sigma' \tag{5}$$

In the following, we use a parametrisation of the curve in terms of arc length. We assume that the membrane is spatially uniform in its properties and hence the normal growth velocity does not explicitly depend on the position $\vec{\mathbf{x}}$ of the curve but only on the curvature, κ, and gradients thereof, $\partial_s\kappa$. Moreover, we assume that there is no chirality, i.e. the system is invariant under the transformation $s \to -s$. Then the growth velocity must be of the form:

$$V_\mathrm{n} = V_\mathrm{n}\left(\kappa, \partial_s^2\kappa, \ldots\right) \tag{6}$$

We perform a gradient expansion keeping terms up to third order (note that κ has the dimension of an inverse length):

$$V_\mathrm{n} = \epsilon_0 - \epsilon_1(\kappa - \kappa_0) + \epsilon_2(\kappa - \kappa_0)^2 + \epsilon_3(\kappa - \kappa_0)^3 - \alpha\partial_s^2\kappa$$
$$\equiv f(\kappa) - \alpha\partial_s^2\kappa, \tag{7}$$

where ϵ_i, κ_0 and α are phenomenological parameters with a sign convention that will become clear later as we discuss the physical significance of each term; we chose to expand with respect to κ_0 for convenience as it allows us to shift the growth curve without changing its overall shape. Note that a term proportional to $(\partial_s\kappa)^2$ is subleading compared to the terms contained in Eq. (7).

The first term, $\epsilon_0 > 0$, describes the basal curvature-independent growth speed due to the average rate of attachment of myo6 and the resulting displacement of lipid molecules. From the experimental data, we know that myo6 strongly favours saddle-shaped membrane geometry, i.e. negative curvature ($\kappa < 0$); see Fig. 3d, e. This tendency is reflected in the combined effect of the curvature-dependent terms (second to third term) that lead to a growth speed asymmetry favouring growth of convex interface regions with negative curvature. Without the third-order term, $\epsilon_3(\kappa - \kappa_0)^3$, the growth law, V_n, would have a parabolic shape implying that the growth velocity diverges as $\kappa \to -\infty$. This would lead to unphysical instabilities that create needle-like protrusions. The third-order term corrects for this and gives the N-shaped growth law shown in Fig. 4e where strong negative curvatures are attenuated. Taken together, the phenomenological parameters ϵ_1, ϵ_2 and ϵ_3 characterise myo6 recruitment to saddle-shaped regions giving rise to the phenomenological growth law (Fig. 4e).

Finally, the last term, $-\alpha\partial_s^2\kappa$, penalises changes in the interface curvature, i.e. acts as a surface tension that smoothes the interface.

The physical motivation of this term was, to the best of our knowledge, first discussed in ref. [58] where the author studied the development of surface grooves at grain boundaries of polycrystalline materials. In these studies, it is assumed that newly deposited atoms from solution bind preferentially to valleys in the surface profile and the term $\alpha\partial_s^2\kappa$ is hence, on a microscopic level, interpreted as surface diffusion (Supplementary Fig. 5a). Similarly, in our system, smoothing of the interface is mediated by myo6 rearrangement along the protein–lipid interface and line tension of the lipid bilayer (Supplementary Fig. 5b). In ref. [37], the authors demonstrate that a term $\alpha\partial_s^2\kappa$ in phenomenological models of crystal growth acts as a short wavelength cut-off, analogous to surface tension in solidification processes. Furthermore, they show by a linear stability analysis that the dispersion relation of the growth rate of perturbations for crystal growth, pattern formation in multiphase fluid flow and phenomenological models equivalent to Eq. (7) share the same form: A morphological instability is induced by a driving force, which is counteracted by surface/line tension. In this analogy, one could interpret myo6 attachment and recruitment to saddle-shaped regions as the (chemical) driving force (the terms proportional to ϵ_0, ϵ_1, ϵ_2 and ϵ_3 in Eq. (7)), which is counteracted by the effective line tension term $\alpha\partial_s^2\kappa$.

Parameters to describe the curvature-dependent growth rate. In order to determine the phenomenological parameters (ϵ_0, ϵ_1, ϵ_2, ϵ_3 and κ_0) in the curvature-dependent growth rate, $f(\kappa)$, we used the following approach: We measured the average radius, $R_\mathrm{exp}(t)$, of a growing flower as a function of time and compared it to the theoretical results obtained for a growing spherical interface in the absence of shape fluctuations, i.e. we set $\partial_s^2\kappa = 0$ and $\kappa = -1/R$ in Eq. (7) and

solved the ordinary differential equation for the radius R:

$$\partial_t R = \epsilon_0 + \epsilon_1\left(\tfrac{1}{R}+\kappa_0\right) + \epsilon_2\left(\tfrac{1}{R}+\kappa_0\right)^2 - \epsilon_3\left(\tfrac{1}{R}+\kappa_0\right)^3 \quad (8)$$

The initial condition, which we obtained from experimental data, was always set to $R(0) = 0.3\,\mu$m. Supplementary Fig. 6 shows the average radius $R_{\rm exp}$ obtained from an ensemble of $n = 253$ growing flowers for a bulk concentration of $c = 50$ nM for myo6. The best fit of the data was obtained for the following parameter set: $\epsilon_0 = (0.0171 \pm 0.0005)\,\mu\text{m min}^{-1}$, $\epsilon_1 = (0.0102 \pm 0.0012)\,\mu\text{m}^2\,\text{min}^{-1}$, $\epsilon_2 = (0.0010 \pm 0.0001)\,\mu\text{m}^3\,\text{min}^{-1}$, $\epsilon_3 = (0.000403 \pm 0.000051)\,\mu\text{m}^4\,\text{min}^{-1}$, and $\kappa_0 = (0.52 \pm 0.05)\,\mu\text{m}^{-1}$.

Parameter to describe the stiffness. The stiffness parameter α, as introduced in Eq. (7), is used as a fitting parameter such that the computational results for the wavelength in the flower pattern (see Fig. 3c) matches with the experimental results. We obtain

$$\alpha = (1.00 \pm 0.25) \times 10^{-6}\,\mu\text{m}^4\text{s}^{-1} \quad (9)$$

Numerical implementation of the model. To numerically solve for the time evolution of the closed planar curve, as described by Eq. (1), we chose the following algorithm following refs. [36,37,51,55,56,59]. We discretise the curve Γ by a set of points (marker particles) and evaluate the velocity at each point. In order to prevent numerical instability[52,53], it is important to choose a parametrisation in terms of arc length s, as it guarantees that points along the curve remain evenly distributed as the curve expands and deforms.

In detail, we adopt the following approach to solve the equations numerically. First, we decompose the local velocity into its component tangential and normal to the curve,

$$\partial_t \vec{\mathbf{x}} = V_{\rm n}\hat{\mathbf{n}} + T\hat{\boldsymbol{\tau}}, \quad (10)$$

where $T = \partial_t\vec{\mathbf{x}}\cdot\hat{\boldsymbol{\tau}}$ and $V_{\rm n} = \partial_t\vec{\mathbf{x}}\cdot\hat{\mathbf{n}}$ are the tangential and normal components, respectively, with $\hat{\boldsymbol{\tau}} = \partial_s\vec{\mathbf{x}}$ the unit tangent vector and $\hat{\mathbf{n}}$ the unit normal vector to the curve Γ. As the time evolution and hence the shape of the interface is determined solely by the normal velocity $V_{\rm n}$ (cf. Eq. (1)), only the normal component of the velocity $\partial_t\vec{\mathbf{x}}$ is fixed. Hence, we can freely choose the velocity tangential to Γ without affecting the shape of the curve. For reasons that will become clear below, we require the following property to hold:

$$\partial_t\vec{\mathbf{x}}(t,s)\cdot\partial_s\vec{\mathbf{x}}(t,s)|_{s=0} = 0 \quad (11)$$

Geometrically, this condition means that we demand that the point at $s = 0$ moves along the normal to the curve for all times.

Now consider the arc length $s(t,\sigma) = \int_0^\sigma\sqrt{g}\,\mathrm{d}\sigma'$ in terms of an arbitrary curve parametrisation σ, where $g = \partial_\sigma\vec{\mathbf{x}}\cdot\partial_\sigma\vec{\mathbf{x}}$ is the metric. Recalling that $\hat{\boldsymbol{\tau}} = \partial_s\vec{\mathbf{x}}$, $\partial_s\hat{\boldsymbol{\tau}} = \kappa\hat{\mathbf{n}}$ and $\partial_s\hat{\mathbf{n}} = -\kappa\hat{\boldsymbol{\tau}}$, the time derivative of the arc length can be rewritten as

$$\partial_t s(t,\sigma) = \int_0^\sigma(\partial_t\partial_\sigma\vec{\mathbf{x}})\cdot\frac{\partial_\sigma\vec{\mathbf{x}}}{\sqrt{g}}\mathrm{d}\sigma' = \int_0^\sigma(\partial_\sigma(\partial_t\vec{\mathbf{x}}))\cdot\hat{\boldsymbol{\tau}}\mathrm{d}\sigma' = \int_0^\sigma(-V_{\rm n}\kappa + \partial_s T)\mathrm{d}s' \quad (12)$$

Hence, the time evolution of the total length L (perimeter) of the curve can be written in the form

$$\partial_t L(t) = \int_0^L(-V_{\rm n}\kappa + \partial_s T)\mathrm{d}s = -\int_0^L V_{\rm n}\kappa\mathrm{d}s, \quad (13)$$

where for the last equality in Eq. (13) we used the periodicity of T along the curve Γ. We now choose a parametrisation of the curve relative to the full arc length, $\rho = s/L$ that is time invariant: $\partial_t(s/L) = 0$; as the curve expands (L changes), the internal distance (ρ) between the points along the curve remains the same. In other words, the points on $\Gamma(t)$ will be evenly distributed as the interface grows. With Eqs. (12) and (13), this condition translates into

$$T(t,s) - T(t,0) = \int_0^s V_{\rm n}\kappa\mathrm{d}s' - \tfrac{s}{L}\int_0^L V_{\rm n}\kappa\mathrm{d}s \quad (14)$$

Since the choice, Eq. (11), amounts to $T(t,0) = 0$, we have

$$T(t,s) = \int_0^s V_{\rm n}\kappa\mathrm{d}s' - \tfrac{s}{L}\int_0^L V_{\rm n}\kappa\mathrm{d}s \quad (15)$$

The evolution equation for the Cartesian coordinates x and y then follow from Eqs. (10) and (15) as

$$\partial_t x(t,s) = V_{\rm n}\partial_s y + \partial_s x\left(\int_0^s V_{\rm n}\kappa\mathrm{d}s' - \tfrac{s}{L}\int_0^L V_{\rm n}\kappa\mathrm{d}s\right), \quad (16)$$

$$\partial_t y(t,s) = -V_{\rm n}\partial_s x + \partial_s y\left(\int_0^s V_{\rm n}\kappa\mathrm{d}s' - \frac{s}{L}\int_0^L V_{\rm n}\kappa\mathrm{d}s\right) \quad (17)$$

To proceed, we derive an equation of motion for the angle θ between the tangent to the curve and the positive x axis, defined as

$$\partial_s x = \cos\theta, \quad (18)$$

$$\partial_s y = \sin\theta \quad (19)$$

To this end, we will need the following identity

$$\partial_t\partial_s = \partial_t\left(\frac{1}{\sqrt{g}}\partial_\sigma\right) = \frac{1}{\sqrt{g}}\partial_t\partial_\sigma - \frac{1}{2}\frac{\partial_t g}{g^{\frac{3}{2}}} = \partial_s\partial_t - (-V_{\rm n}\kappa + \partial_s T)\partial_s, = \partial_s\partial_t - \tfrac{\partial_t L}{L}\partial_s, \quad (20)$$

where in the first line we used that $\partial_t g = 2g(-V_{\rm n}\kappa + \partial_s T)$, which follows from Eq. (12) together with the definition $\partial_t s = \int_0^\sigma\frac{1}{2}\frac{\partial_t g}{\sqrt{g}}\mathrm{d}\sigma'$. Using Eq. (15) for $\partial_s T$, we arrive at Eq. (20). Furthermore, note that by definition $\partial_t\hat{\boldsymbol{\tau}} = \partial_t\partial_s\vec{\mathbf{x}} = -\partial_t\theta\cdot\hat{\mathbf{n}}$. Applying Eq. (20) to $\partial_t\partial_s\vec{\mathbf{x}}$ and using the fact that the curvature κ can be written in the form $\kappa = \partial_s^2 x\partial_s y - \partial_s x\partial_s^2 y = -\partial_s\theta$, we find:

$$\partial_t\theta(t,s) = -\partial_s V_{\rm n} - \partial_s\theta\left(\tfrac{s}{L}\int_0^L V_{\rm n}\partial_s\theta\mathrm{d}s - \int_0^s V_{\rm n}\partial_s\theta\mathrm{d}s'\right) \quad (21)$$

The position vector $\vec{\mathbf{x}}$ can be obtained from the definition $\partial_s\vec{\mathbf{x}} = \hat{\boldsymbol{\tau}}$ by integration: $\vec{\mathbf{x}} = \vec{\mathbf{x}}(t,0) + \int_0^s\hat{\boldsymbol{\tau}}\,ds'$. The time-dependent integration constant $\vec{\mathbf{x}}(t,0)$ follows from Eq. (11): $\partial_t\vec{\mathbf{x}}(t,0) = V_{\rm n}(t,0)\cdot\hat{\mathbf{n}}(t,0)$, and hence $\vec{\mathbf{x}}(t,0) = \vec{\mathbf{x}}(0,0) + \int_0^t V_{\rm n}(t',0)\cdot\hat{\mathbf{n}}(t',0)dt'$. The solution of Eq. (21) can then be used to reconstruct the position vector:

$$x(t,s) = x(0,0) + \int_0^t V_{\rm n}(t',0)\sin\theta(t',0)\mathrm{d}t' + \int_0^s\cos\theta(t,s')\mathrm{d}s', \quad (22)$$

$$y(t,s) = y(0,0) - \int_0^t V_{\rm n}(t',0)\cos\theta(t',0)\mathrm{d}t' + \int_0^s\sin\theta(t,s')\mathrm{d}s' \quad (23)$$

Finally, using the rescaled curve parameter $\rho = s/L$, the set of equations read in summary:

$$\partial_t\theta(t,\rho) = -\tfrac{1}{L}\partial_\rho V_{\rm n} - \tfrac{1}{L}\partial_\rho\theta\left(\rho\int_0^1 V_{\rm n}\partial_\rho\theta\mathrm{d}\rho - \int_0^\rho V_{\rm n}\partial_\rho\theta\mathrm{d}\rho'\right), \quad (24)$$

$$\partial_t L(t) = \int_0^1 V_{\rm n}\partial_\rho\theta\mathrm{d}\rho, \quad (25)$$

$$x(t,\rho) = x(0,0) + \int_0^t V_{\rm n}(t',0)\sin\theta(t',0)\mathrm{d}t' + L\int_0^\rho\cos\theta(t,\rho')\mathrm{d}\rho', \quad (26)$$

$$y(t,\rho) = y(0,0) - \int_0^t V_{\rm n}(t',0)\cos\theta(t',0)\mathrm{d}t' + L\int_0^\rho\sin\theta(t,\rho')\mathrm{d}\rho'. \quad (27)$$

We solve the partial integro-differential equation Eq. (24) and the ordinary differential equation Eq. (25) using the Finite-Element software *COMSOL 5.3a*. The coupled system of equations is solved on a line $\rho \in [0,1]$ with boundary and initial conditions as follows: For the θ equation, Eq. (24), we impose Dirichlet boundary condition at the end of the interval $\theta(t,1) = \theta(t,0) + 2\pi$ since the angle θ must rotate by 2π when traversing the closed curve.

As the initial condition for the curve, we take a circle that is perturbed by a finite number of Fourier modes

$$\theta(0,\rho) = 2\pi\rho + \delta\sum_{n=1}^{N} g(n)\sin(2\pi n\rho + u(n)), \quad (28)$$

where $\delta = 0.03$ is a parameter for the amplitude of perturbations. The functions $g(n)$ and $u(n)$ are random numbers drawn from a Gaussian distribution with mean zero and standard deviation of 1 and a uniform distribution on the interval $[0,\pi]$, respectively. This way we generate circular seeds with some initial random surface roughness.

To simulate the time evolution of a triangular seed, we only need to select the corresponding mode, hence giving $\theta(0,\rho) = 2\pi\rho + \delta\sin(6\pi\rho)$ where we set $\delta = 0.8$ in this case (see Supplementary Fig. 7a, b for an illustration). The initial condition for the perimeter $L(t)$ was set to $L(0) = 2\pi R_0$, where $R_0 = 0.4\,\mu$m is the initial seed radius. The origin is located at $(0,0)$ and we therefore set $x(0,0) = 0$ and $y(0,0) = -R_0$ (Supplementary Fig. 7b). Finally, we obtain the cartesian position, $\vec{\mathbf{x}}$, using Eqs. (26) and (27) from the solutions of θ and L in *COMSOL 5.3a*.

Hotspot distance determined from the numerical simulation. The wavelength (average hotspot distance) $\langle\mathrm{d}z\rangle$ of a growing flower (Fig. 3c) was obtained as follows: Given the numerical solutions of Eqs. (24)–(27), we calculated the average Euclidean distance between two neighbouring outward bulges (peak-to-peak distance) along the curve at a time (Supplementary Fig. 8a). In addition, we calculated the average flower radius R at each time step:

$$R(t) = \int_0^1\sqrt{x(t,\rho')^2 + y(t,\rho')^2}\mathrm{d}\rho'. \quad (29)$$

The result for $\langle\mathrm{d}z\rangle$ as a function of the average flower diameter is shown in Supplementary Fig. 8b (blue curve). As can be inferred from this Figure, the curve shows some irregularities but saturates (on average) at a value of $\langle\mathrm{d}z\rangle$ around 1 μm. The irregularities originate from two sources: (i) Tip splitting, which leads to an abrupt decrease of $\langle\mathrm{d}z\rangle$ as one peak splits into two peaks, which have (initially) a smaller distance (see Supplementary Fig. 8a for an illustration). (ii) Averaging of the peak-to-peak distance along the curve, which produces minor irregularities between time steps.

To obtain a smooth curve and for better comparison with our experiments, we fitted the blue curve in Supplementary Fig. 8b using a fit function with four parameters of the form $p(x) = a\left(1 - \exp\left(-\frac{x-b}{c}\right)\right) + d$ (Supplementary Fig. 8b, green curve).

The theoretical curve for ⟨dz⟩ appears to be shifted relative to the experimentally obtained hotspot distance (see Fig. 3c). The reason for this lies in the assumption of our model: The gradient expansion of the normal velocity Eq. (7) sets the smallest length scale, which can be resolved. More precisely, regions of too large negative curvature (or a too small initial seed) cannot grow but decay to a point as indicated from the shape of the growth function in Fig. 4e. In the experiments, however, we are able to measure distances between only two hotspots, which are roughly 100 nm apart (Fig. 3a, b). This stage cannot be captured by the model since the model is only valid around the onset of pattern formation, i.e. for large enough seeds that exhibit a wavelength. This leads to a slight shift of the theoretical curve for ⟨dz⟩.

We could, however, shift this length scale penalty in the model to smaller values by including higher-order terms in the gradient expansion Eq. (7), but this would also add more parameters to the model without gaining additional insight.

Reporting summary. Further information on research design is available in the Nature Research Reporting Summary linked to this article.

Data availability

Data supporting the findings of this manuscript are available from the corresponding authors upon reasonable request. A reporting summary for this article is available as a Supplementary Information file. The source data underlying Figs. 1b, c, 2c and 3c and Supplementary Figs. 1e, 3a and 6 are provided as a Source Data file.

Received: 1 February 2019 Accepted: 24 June 2019
Published online: 24 July 2019

References

1. McMahon, H. T. & Gallop, J. L. Membrane curvature and mechanisms of dynamic cell membrane remodelling. *Nature* **438**, 590–596 (2005).
2. Simunovic, M., Voth, G. A., Callan-Jones, A. & Bassereau, P. When physics takes over: BAR proteins and membrane curvature. *Trends Cell Biol.* **25**, 780–792 (2015).
3. Leduc, C., Campas, O., Joanny, J. F., Prost, J. & Bassereau, P. Mechanism of membrane nanotube formation by molecular motors. *Biochim. Et. Biophys. Acta-Biomembr.* **1798**, 1418–1426 (2010).
4. McMahon, H. T. & Boucrot, E. Membrane curvature at a glance. *J. Cell Sci.* **128**, 1065–1070 (2015).
5. Zimmerberg, J. & Kozlov, M. M. How proteins produce cellular membrane curvature. *Nat. Rev. Mol. Cell Biol.* **7**, 9–19 (2006).
6. Gebhardt, C., Gruler, H. & Sackmann, E. Domain structure and local curvature in lipid bilayers and biological membranes. *Z. Naturforsch. C* **32**, 581–596 (1977).
7. Sheetz, M. P. & Singer, S. J. Biological membranes as bilayer couples - molecular mechanism of drug-erythrocyte interactions. *Proc. Natl Acad. Sci. USA* **71**, 4457–4461 (1974).
8. Blanchoin, L., Boujemaa-Paterski, R., Sykes, C. & Plastino, J. Actin dynamics, architecture, and mechanics in cell motility. *Physiol. Rev.* **94**, 235–263 (2014).
9. Spudich, G. et al. Myosin VI targeting to clathrin-coated structures and dimerization is mediated by binding to disabled-2 and PtdIns(4,5)P-2. *Nat. Cell Biol.* **9**, 176–183 (2007).
10. Pyrpassopoulos, S., Shuman, H. & Ostap, E. M. Adhesion force and attachment lifetime of the KIF16B-PX domain interaction with lipid membranes. *Mol. Biol. Cell* **28**, 3315–3322 (2017).
11. Phillips, M. J. & Voeltz, G. K. Structure and function of ER membrane contact sites with other organelles. *Nat. Rev. Mol. Cell Biol.* **17**, 69–82 (2016).
12. Sahlender, D. A. et al. Optineurin links myosin VI to the Golgi complex and is involved in Golgi organization and exocytosis. *J. Cell Biol.* **169**, 285–295 (2005).
13. Tumbarello, D. A., Kendrick-Jones, J. & Buss, F. Myosin VI and its cargo adaptors - linking endocytosis and autophagy. *J. Cell Sci.* **126**, 2561–2570 (2013).
14. Wong, Y. C. & Holzbaur, E. L. F. Optineurin is an autophagy receptor for damaged mitochondria in parkin-mediated mitophagy that is disrupted by an ALS-linked mutation. *Proc. Natl Acad. Sci. USA* **111**, E4439–E4448 (2014).
15. Dunn, T. A. et al. A novel role of myosin VI in human prostate cancer. *Am. J. Pathol.* **169**, 1843–1854 (2006).
16. Al Olama, A. A. et al. A meta-analysis of 87,040 individuals identifies 23 new susceptibility loci for prostate cancer. *Nat. Genet.* **46**, 1103–1109 (2014).
17. Naora, H. & Montell, D. J. Ovarian cancer metastasis: Integrating insights from disparate model organisms. *Nat. Rev. Cancer* **5**, 355–366 (2005).
18. Batters, C., Brack, D., Ellrich, H., Averbeck, B. & Veigel, C. Calcium can mobilize and activate myosin-VI. *Proc. Natl Acad. Sci. USA* **113**, E1162–E1169 (2016).
19. van Meer, G., Voelker, D. R. & Feigenson, G. W. Membrane lipids: where they are and how they behave. *Nat. Rev. Mol. Cell Biol.* **9**, 112–124 (2008).
20. van Meer, G. & de Kroon, A. Lipid map of the mammalian cell. *J. Cell Sci.* **124**, 5–8 (2011).
21. Monticelli, L. et al. The MARTINI coarse-grained force field: extension to proteins. *J. Chem. Theory Comput.* **4**, 819–834 (2008).
22. Frolov, V. A., Shnyrova, A. V. & Zimmerberg, J. Lipid polymorphisms and membrane shape. *Cold Spring Harb. Perspect. Biol.* **3**, 1–14 (2011).
23. Pincet, F. et al. FRAP to characterize molecular diffusion and interaction in various membrane environments. *PLoS ONE* **11**, 1–19 (2016).
24. Marrink, S. J., de Vries, A. H. & Tieleman, D. P. Lipids on the move: Simulations of membrane pores, domains, stalks and curves. *Biochim. Biophys. Acta* **1788**, 149–168 (2009).
25. Akimov, S. A. et al. Pore formation in lipid membrane I: continuous reversible trajectory from intact bilayer through hydrophobic defect to transversal pore. *Sci. Rep.* **7**, 1–20 (2017).
26. Menetrey, J. et al. The structure of the myosin VI motor reveals the mechanism of directionality reversal. *Nature* **435**, 779–785 (2005).
27. Rock, R. S. et al. Myosin VI is a processive motor with a large step size. *Proc. Natl Acad. Sci. USA* **98**, 13655–13659 (2001).
28. Brawley, C. M. & Rock, R. S. Unconventional myosin traffic in cells reveals a selective actin cytoskeleton. *Proc. Natl Acad. Sci. USA* **106**, 9685–9690 (2009).
29. Park, H. et al. The unique insert at the end of the myosin VI motor is the sole determinant of directionality. *Proc. Natl Acad. Sci. USA* **104**, 778–783 (2007).
30. Huergo, M. A. et al. Optical nanoparticle sorting elucidates synthesis of plasmonic nanotriangles. *ACS Nano* **10**, 3614–3621 (2016).
31. Roiter, Y. et al. Interaction of nanoparticles with lipid membrane. *Nano Lett.* **8**, 941–944 (2008).
32. Sandre, O., Moreaux, L. & Brochard-Wyart, F. Dynamics of transient pores in stretched vesicles. *Proc. Natl Acad. Sci. USA* **96**, 10591–10596 (1999).
33. Brochard-Wyart, F., de Gennes, P. G. & Sandre, O. Transient pores in stretched vesicles: role of leak-out. *Phys. A* **278**, 32–51 (2000).
34. Karatekin, E., Sandre, O. & Brochard-Wyart, F. Transient pores in vesicles. *Polym. Int.* **52**, 486–493 (2003).
35. Kaplan, C. N. et al. Controlled growth and form of precipitating microsculptures. *Science* **355**, 1395–1398 (2017).
36. Kessler, D. A., Koplik, J. & Levine, H. Geometrical models of interface evolution. 2. *Numer. Simul. Phys. Rev. A* **30**, 3161–3174 (1984).
37. Kessler, D. A., Koplik, J. & Levine, H. Pattern selection in fingered growth phenomena. *Adv. Phys.* **37**, 255–339 (1988).
38. Mullins, W. W. & Sekerka, R. F. Stability of planar interface during solidification of dilute binary alloy. *J. Appl. Phys.* **35**, 444–451 (1964).
39. Lister, I. et al. A monomeric myosin VI with a large working stroke. *Embo J.* **23**, 1729–1738 (2004).
40. Brian, A. A. & McConnell, H. M. Allogeneic stimulation of cyto-toxic T-cells by supported planar membranes. *Proc. Natl Acad. Sci. USA* **81**, 6159–6163 (1984).
41. Axelrod, D., Koppel, D. E., Schlessinger, J., Elson, E. & Webb, W. W. Mobility measurements by analysis of fluorescence photobleaching recovery kinetics. *Biophys. J.* **16**, 1055–1069 (1976).
42. Saczko-Brack, D. et al. Self-organization of actin networks by a monomeric myosin. *Proc. Natl Acad. Sci. USA* **113**, E8387–E8395 (2016).
43. Garcia-Saez, A. J., Carrer, D. C. & Schwille, P. Fluorescence correlation spectroscopy for the study of membrane dynamics and organization in giant unilamellar vesicles. *Methods Mol. Biol.* **606**, 493–508 (2010).
44. Manley, S. et al. High-density mapping of single-molecule trajectories with photoactivated localization microscopy. *Nat. Methods* **5**, 155–157 (2008).
45. Sharonov, A. & Hochstrasser, R. M. Wide-field subdiffraction imaging by accumulated binding of diffusing probes. *Proc. Natl Acad. Sci. USA* **103**, 18911–18916 (2006).
46. Zhou, H. S., Honma, I., Komiyama, H. & Haus, J. W. Controlled synthesis and quantum-size effect in gold-coated nanoparticles. *Phys. Rev. B* **50**, 12052–12056 (1994).
47. Deckelnick, K., Dziuk, G. & Elliott, C. M. Computation of geometric partial differential equations and mean curvature flow. *Acta Numer.* **14**, 139–232 (2005).
48. Elliott, C. M. & Fritz, H. On approximations of the curve shortening flow and of the mean curvature flow based on the DeTurck trick. *IMA J. Numer. Anal.* **37**, 543–603 (2017).
49. Huisken, G. Flow by mean curvature of convex surfaces into spheres. *J. Differ. Geom.* **20**, 237–266 (1984).
50. Ben-Jacob, E., Goldenfeld, N., Langer, J. S. & Schon, G. Boundary-Layer model of pattern formation in solidification. *Phys. Rev. A* **29**, 330–340 (1984).
51. Strain, J. A boundary intergral approach to unstable solidification. *J. Comput. Phys.* **85**, 342–389 (1989).
52. Sethian, J. A. Curvature and the evolution of fronts. *Commun. Math. Phys.* **101**, 487–499 (1985).

53. Sethian, J. A. Numerical algorithms for propagating interfaces - Hamilton - Jacobi equations and conservation - laws. *J. Differ. Geom.* **31**, 131–161 (1990).
54. van Saarloos, W. Front propagation into unstable states. *Phys. Rep.* **386**, 29–222 (2003).
55. Hou, T. Y., Lowengrub, J. S. & Shelley, M. J. Removing the stiffness from interfacial flows with surface - tension. *J. Comput. Phys.* **114**, 312–338 (1994).
56. Langer, S. A., Goldstein, R. E. & Jackson, D. P. Dynamics of labyrinthine pattern - formation in magnetic fluids. *Phys. Rev. A* **46**, 4894–4904 (1992).
57. Berger, M. *A Panoramic View of Riemannian Geometry* (Springer Verlag, Berlin, Heidelberg, 2003).
58. Mullins, W. W. TTheory of thermal grooving. *J. Appl. Phys.* **28**, 333–339 (1957).
59. Goldstein, R. E. & Petrich, D. M. The Korteweg - de Vries hierarchy as dynamics of closed curves in the plane. *Phys. Rev. Lett.* **67**, 3203–3206 (1991).

Acknowledgements

This research was supported by the German Excellence Initiative via the programme 'NanoSystems Initiative Munich' (NIM) and the Deutsche Forschungsgemeinschaft (DFG) via projects B02 (to E.F.) and B06 (to C.V.) within the Collaborative Research Center (SFB 863) 'Forces in Biomolecular Systems'. Moreover, we acknowledge Friedrich-Baur-Stiftung for financial support. We thank Florian Gartner for useful discussions on the theoretical model.

Author contributions

C.V. and C.B. designed the project. B.R., A.B.P., F.B.Z, D.S.-B. and C.B. generated the protein and performed the fluorescence experiments, C.V. guided and performed fluorescence data analysis, M.A.H. produced the gold nano-triangles, L.W. and E.F. developed the theoretical model and performed the mathematical analysis. E.F. and C.V. wrote the paper.

Additional information

Supplementary Information accompanies this paper at https://doi.org/10.1038/s41467-019-11268-9.

Competing interests: The authors declare no competing interests.

Peer review information: *Nature Communications* thanks the anonymous reviewers for their contribution to the peer review of this work.

Supplementary Information

Reconstitution reveals how myosin-VI self-organises to generate a dynamic mechanism of membrane sculpting

Rogez *et al.*

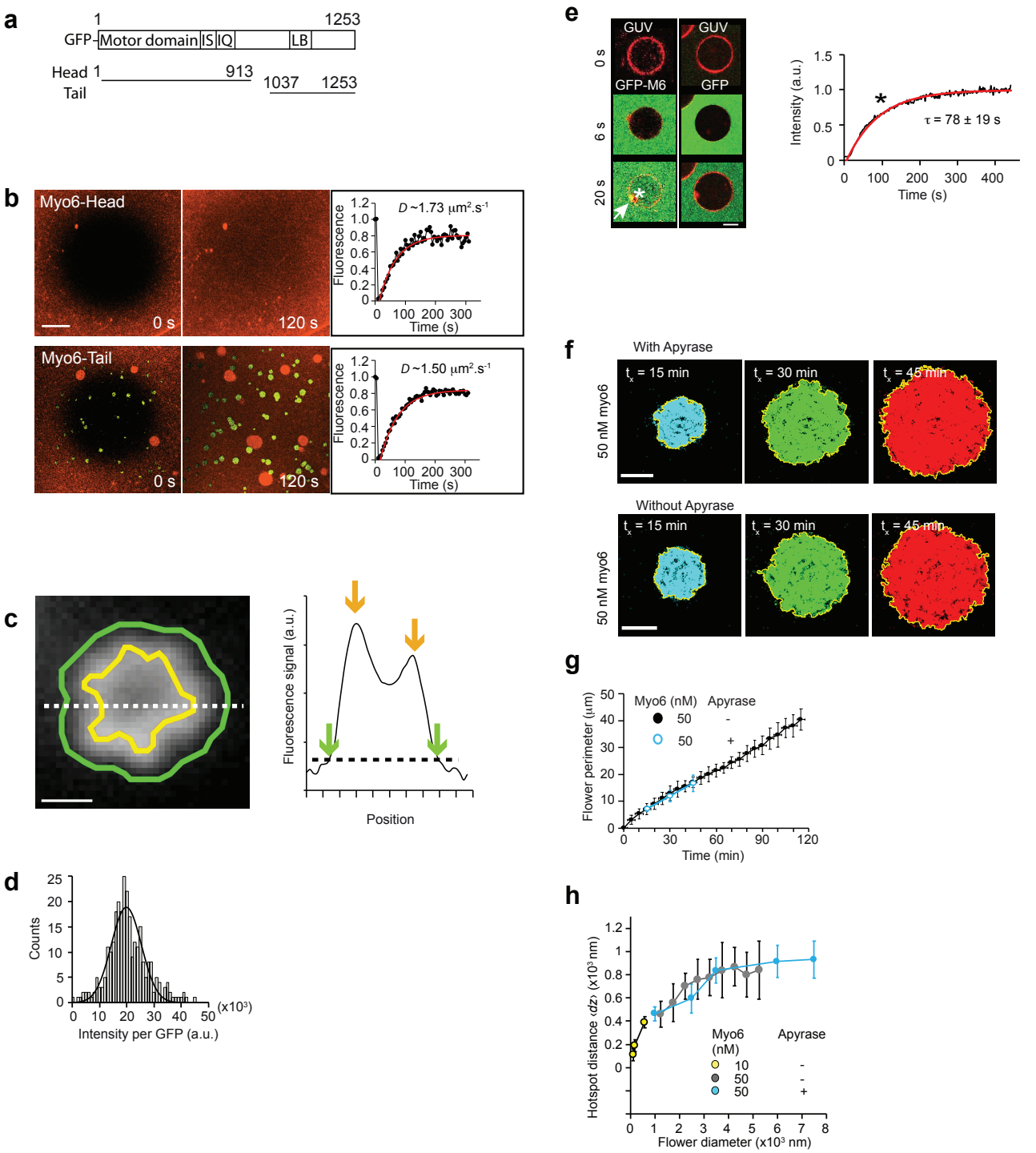

Supplementary Figure 1. The myo6 tail domain is responsible for membrane binding. a, Sequence and domain structure of human full-length myo6, myo6-head and tail constructs; IS (53-residue insert), IQ (calmodulin-binding motif) and LB (lipid-binding site aa1084-1099) (Ref (9)). **b**, Myo6-Head construct did not, while the Tail construct did bind to the DOPC bilayer (50 nM myo6 (Head/Tail), 10% GFP-myo6). FRAP experiments (DOPC:DOPE-Cy5, 4000:1) to determine the lipid diffusion coefficient D; with Myo6-Head (no binding) $\tau = 57.8$ s ($R^2 = 0.92$), $D \sim 1.73$ μm².s^{-1}; $D_{av} \sim 1.66 \pm 0.22$ μm².s^{-1} (mean ± s.d., $n = 3$). With Myo6-Tail (binding) $\tau = 66.6$ s ($R^2 = 0.98$), $D \sim 1.50$ μm².s^{-1}; $D_{av} \sim 1.41 \pm 0.26$ μm².s^{-1} (mean ± s.d., $n = 3$). **c**, TIRFM of a myo6 induced flower-shaped membrane pore (150 nM myo6,10% GFP-myo6). Pixels with local maximum fluorescence intensity were connected to form a closed line (yellow); total fluorescence intensity obtained from area within green line; scale bar 1 μm. **d**, Emission signal of single GFP-myo6; mean ± s.d. 18,917 ± 5,523 ($R^2 = 0.88$) for 288 GFP molecules photobleaching in a single step. **e**, Confocal microscopy of GUV vesicles (DOPC:DOPE-Cy5 (red), 4000:1) in the presence of 50 nM GFP-myo6 (GFP-M6, green) or 50 nM GFP (GFP, green; control experiment). The time constant τ for fluorescence increase inside the vesicles in the presence of 50 nM GFP-myo6, $\tau = 78 \pm 19$ s (mean ± s.d., $n = 5$, $R^2 = 0.94 \pm 0.04$; diameter of the vesicles 11.24 ± 3.35 μm). **f**, Determination of the perimeter of flowers in SRM; the signal is integrated fom the start of flower growth until time t_x; the detected fluorophores are plotted as Gaussian discs (20 nm radius). The perimeter is obtained by connecting the centre of the peripheral Gaussian spots of the enclosed area (yellow line). Representative examples of 50 nM myo6 (10% GFP-myo6) induced flower growth, with and without apyrase treatment of myo6 to remove residual nucleotide bound to the myo6 catalytic domain. **g**, The perimeter growth is not affected by myo6 apyrase treatment (data without apyrase from Fig. 2c; myo6 with apyrase treatment (blue unfilled circles) mean ± s.d., $n = 4$). **h**, The average hostpot distance $\langle dz \rangle$ is also not affected by myo6 apyrase treatment (data without apyrase from Fig. 3c; myo6 with apyrase treatment (blue filled circles) mean ± s.d., $n = 9$-19). Source data are provided as a Source Data file.

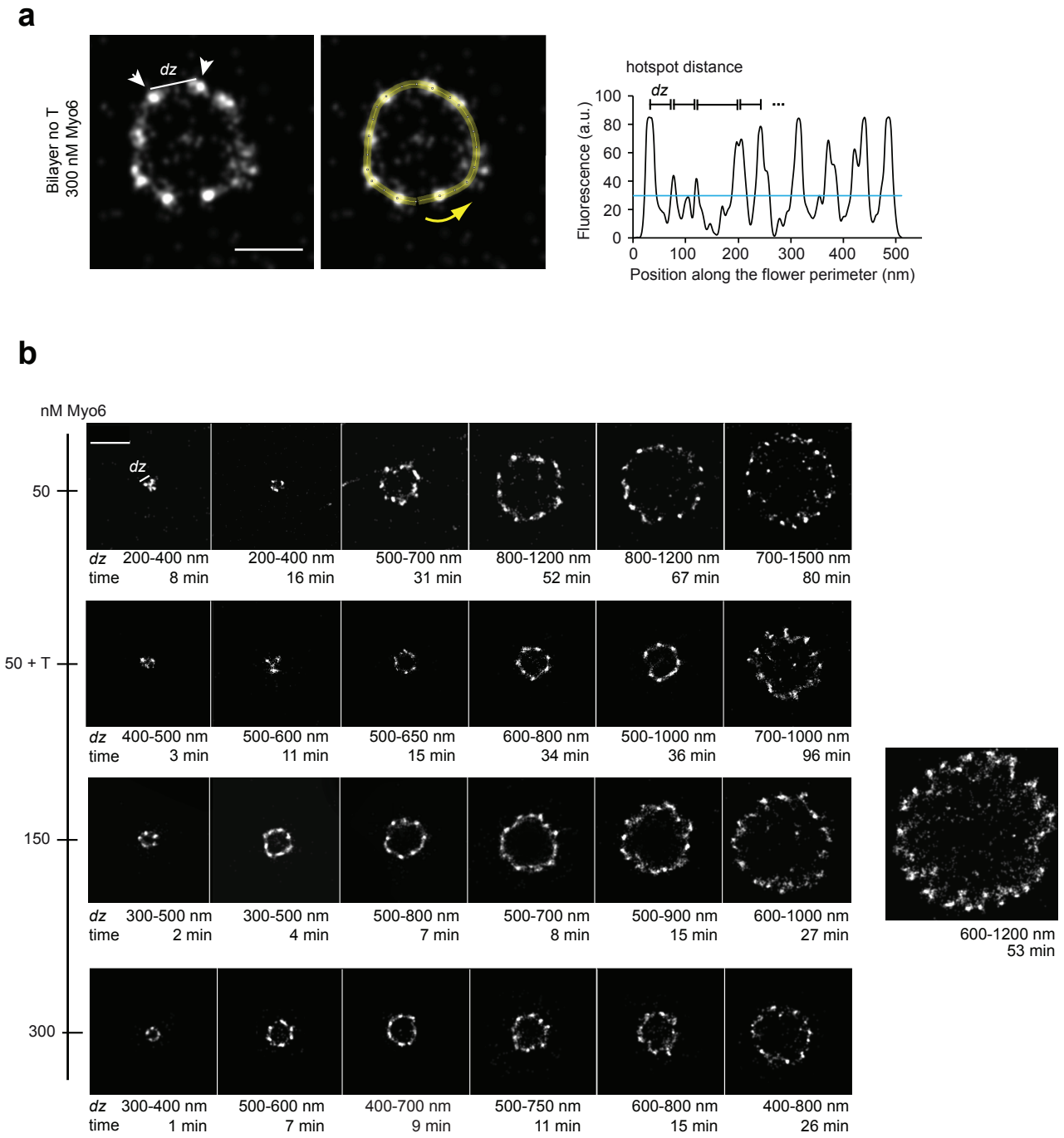

Supplementary Figure 2. Membrane pores formed at different myo6 concentrations. a, Analysis of the super resolution images; scale bar 10 μm. The distances *dz* between the hotspots were determined by thresholding the fluorescence intensity (blue line); the threshold was set at ~3 times the background fluorescence noise level. SRM integration time 1 min. **b**, Representative examples of super resolution images at different time points after addition of myo6; scale bar 2 μm; for the condition 50 + T we applied 0.3 pM triangles (T) to the surface before forming a lipid bilayer. SRM integration time 1 min, except for 300 nM myo6 (30s).

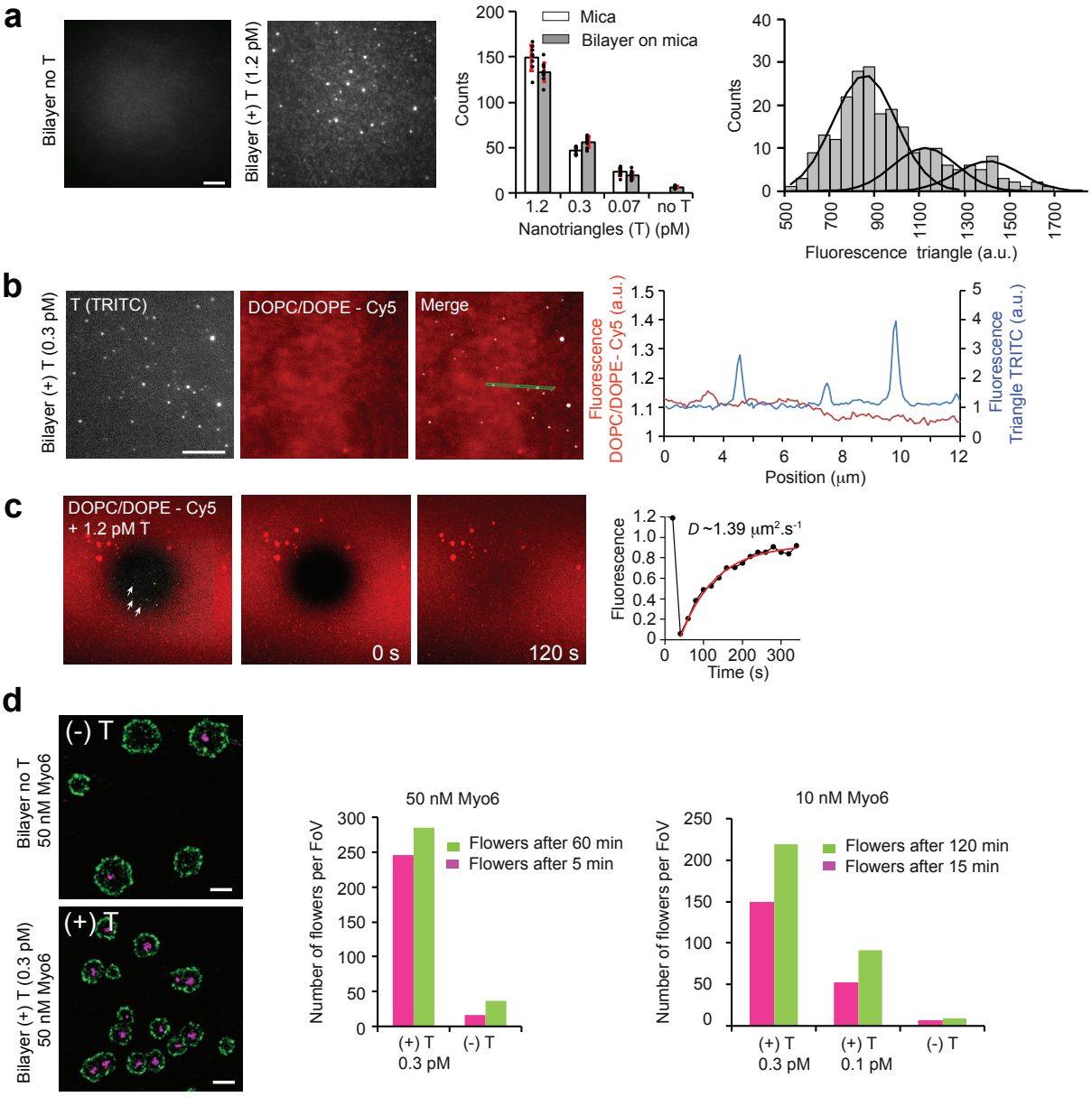

Supplementary Figure 3. Effect of nano-triangles on the bilayer and on myo6-induced flowers. a, TIRFM to detect gold nano-triangles deposited on a mica surface, labelled using TRITC-maleimide (Sigma); scale bar 10 μm. Nano-triangles labelled in the absence of (white bars), or after a lipid bilayer was formed (grey bars) and detected in the TRITC channel. Number of triangles detected (mean ± s.d. and raw data points) in 8 -14 fields of view (FoV) in each condition. No significant difference was found between *N* of detected triangles in the presence and absence of the bilayer (*p*-value 0.01, 0.002 and 0.02 for 1.2, 0.3 and 0.07 pM triangles respectively, two-tailed t-test). Fluorescence intensity (a.u.) of TRITC-labelled triangles; scale bar 10 μm. Intensity maxima at 825 ± 139, 1160 ± 140 and 1388 ± 122 (mean ± s.d.) consistent with one, two and three dye molecules respectively. Source data are provided as a Source Data file. **b**, Signal of a line scan (merged image, green box) across an area with 3 detected triangles in the TRITC-channel (blue curve) compared with the signal of the lipid Cy5-channel (red curve). **c**, FRAP studies (DOPC:DOPE-Cy5, 4000:1) to confirm the fluidity of the bilayer in the presence of the 1.2 pM nano-triangles (green, white arrows); for a bleached circle of 45 μm diameter τ = 95 s (R^2 = 0.98), corresponding to $D \sim 1.39$ $\mu m^2.s^{-1}$. **d**, Number of flowers per FoV at different times after addition of myo6 with and without nano-triangles inserted into the bilayer; scale bars 2 μm.

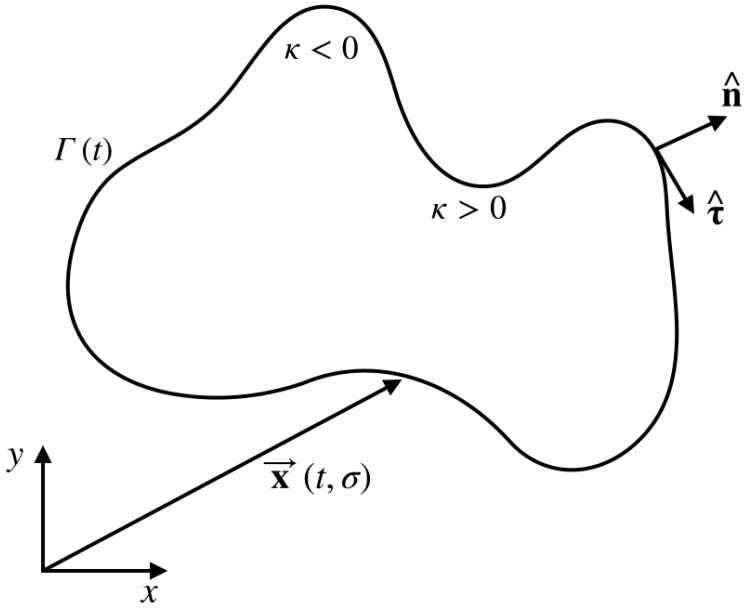

Supplementary Figure 4. Mathematical description of a closed planar curve. The curve $\Gamma(t)$ is parametrized by the Cartesian position vector $\vec{\mathbf{x}}(t, \sigma)$. The conformation of $\Gamma(t)$ is characterized by the curvature κ and we use the convention that κ is negative for convex portions of the curve.

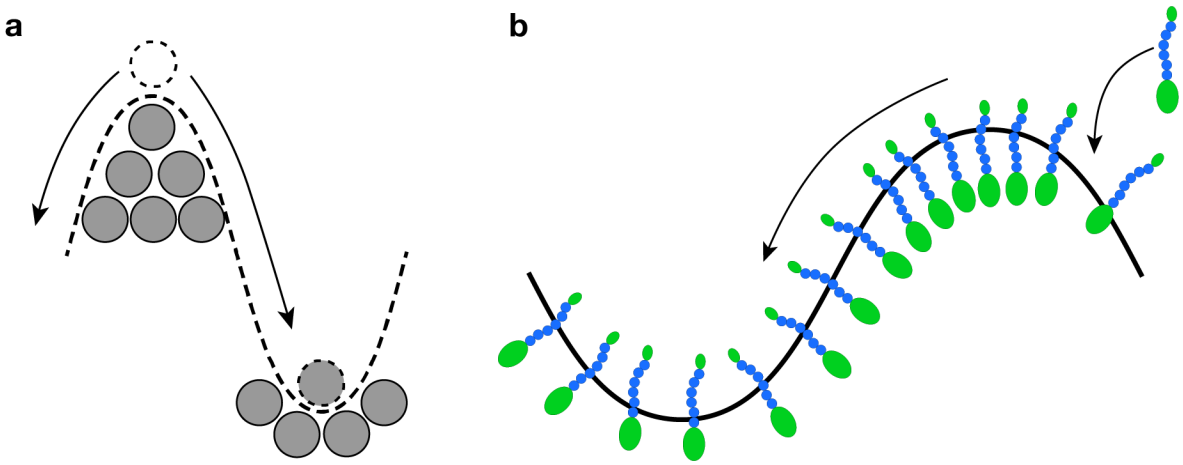

Supplementary Figure 5. Microscopic origin of the effective line tension term in the model. a, Surface diffusion of atoms (grey circle) along grain boundaries (dashed line) as introduced in Ref.[58]. Atoms from solution (dashed circle) bind and diffuse along the interface until they reach a valley where the free energy is minimized (dashed grey circle). This process leads naturally to smoothing of an irregular surface profile. **b**, Myosin6 binds to the protein-lipid interface (black solid line) and thereby increases the interface perimeter. The increase of the perimeter is counteracted by myosin6 rearrangement along the interface and line tension of the lipid. This also leads to smoothing of the surface profile analogous to surface growth models (**a)**.

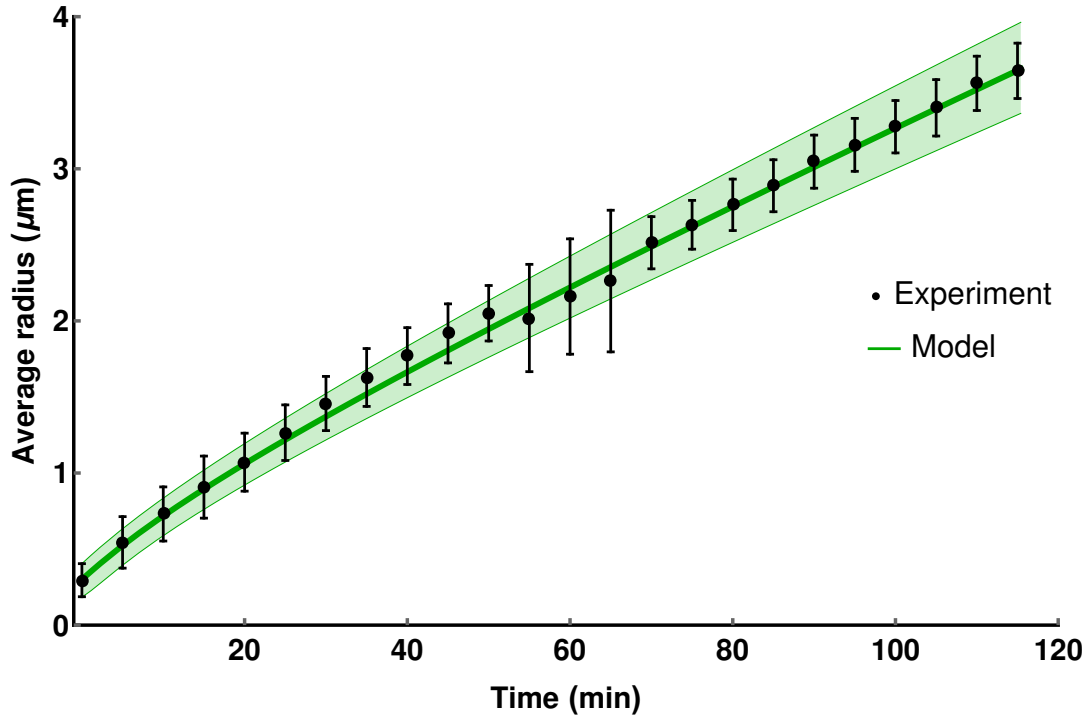

Supplementary Figure 6. Fit of the phenomenological parameters. Average radius $\langle R_{\mathrm{exp}} \rangle$ obtained for a bulk concentration $c = 50\ nM$ for myo6 from an ensemble of $N = 253$ measurements of the flower radius (black filled symbols). The (green) solid line shows the best theoretical result obtained from solving Eq.8. Source Data are provided as a Source Data file.

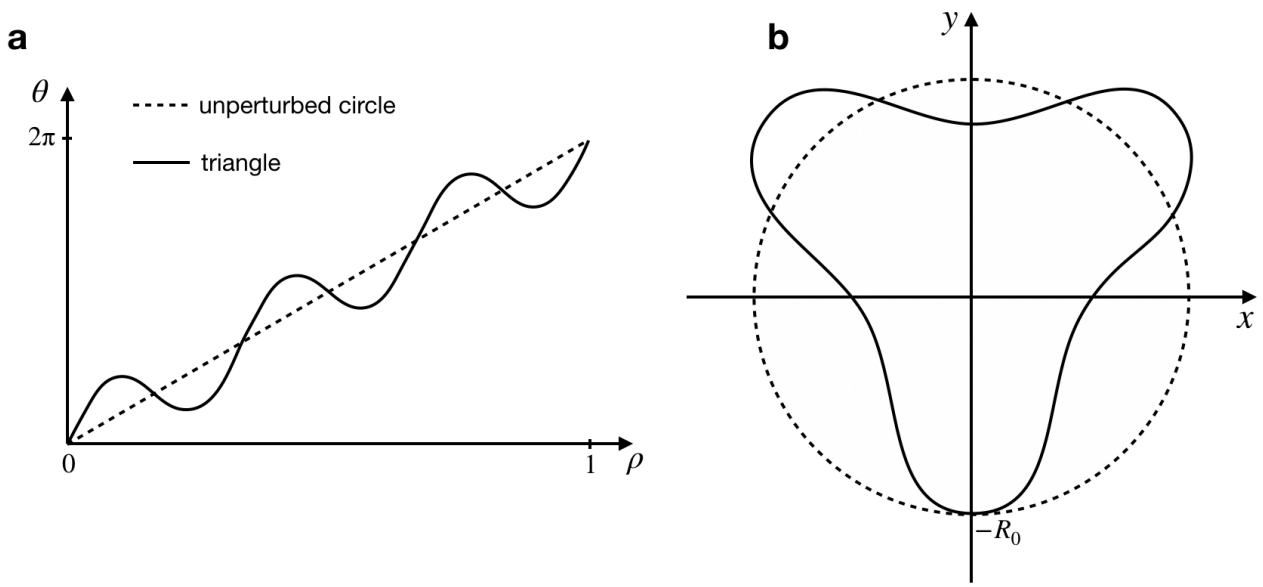

Supplementary Figure 7. Illustration of the initial configuration for the angle θ. a, Initial configuration of θ for an unperturbed circle (dotted line) and a triangle (solid line), respectively. **b**, The corresponding shapes in Cartesian coordinates for the initial conditions of θ as shown in panel **a**.

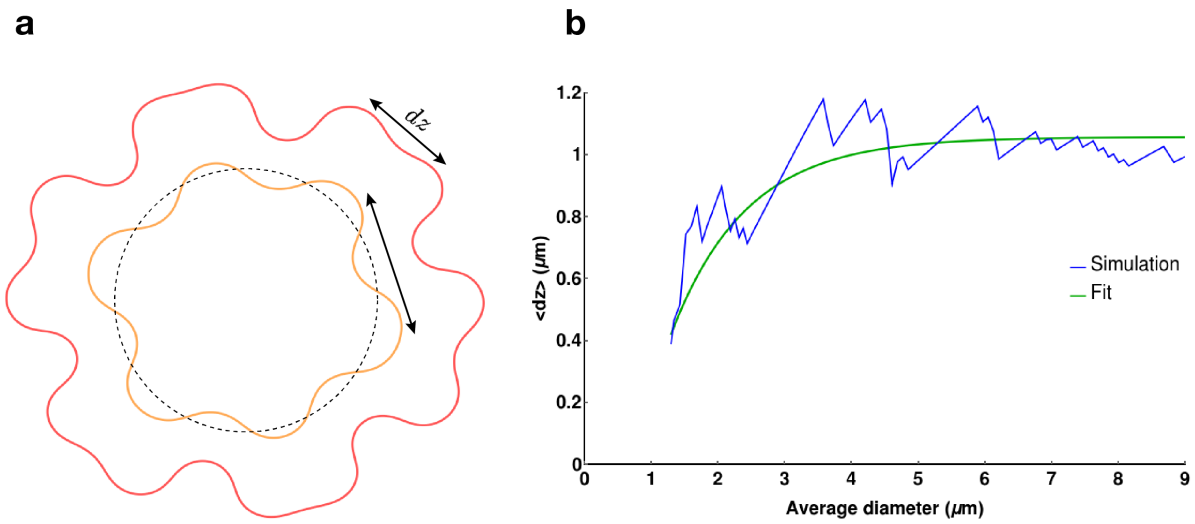

Supplementary Figure 8. Determination of the average hotspot distance. a, Shown is the simulated flower shape at two successive time points (orange and red curve, respectively). The hotspot distance $\langle dz \rangle$ is obtained from the average Euclidean distance between neighbouring outward bulges (black double arrow). The dotted circle represents the average diameter of the orange curve. **b**, Hotspot distance $\langle dz \rangle$ plotted as a function of the average flower diameter. The blue curve shows the result as obtained from the simulation data and the green graph is a smooth fit to this curve.

2 Anomalous roughening of growing protein-lipid interfaces

The joint experimental and theoretical study presented in section 1 inspired us to theoretically investigate general interface growth models, with a special focus on the interplay between interface morphology and biochemical dynamics. As we will show in the following, the coupling between interface morphology and chemical dynamics leads to turbulence, which we did not expect. Moreover, the turbulent dynamics leads to a number of interesting consequences, including kinetic roughening of the growing protein-lipid interface, which is produced by the deterministic dynamics and thus independent of noise supply.

2.1 Background: The KPZ equation

The dynamics of growing interfaces is relevant for a broad range of physical systems, including epitaxial growth [194], solidification processes [177], bacterial biofilms [195], combustion and flame propagation [196], and protein-lipid interfaces [34, 197–199]. As such, the theoretical understanding of interface growth phenomena and the pursuit of underlying universal principles in such systems are of great interest.

One of the most important theoretical considerations in this context is the popular *Kardar-Parisi-Zhang* equation (KPZ equation) [200], which is a stochastic partial differential equation that describes the growth of dynamic interfaces

$$\frac{\partial}{\partial t}h(x,t) = \nu\nabla^2 h + \frac{\lambda}{2}(\nabla h)^2 + \eta(x,t)\,, \tag{IV.8}$$

where the height field $h(x,t)$ denotes the vertical position of the interface. The KPZ equation basically describes the growth of *Eden clusters* [201] with diffusive relaxation and so-called "lateral growth" (local growth along the normal direction of the interface). These two processes are captured by the first and second term in Eq. (IV.8), respectively (note that the KPZ equation is invariant under vertical translations $h \to h + \text{const}$). The last term in Eq. (IV.8) describes space-time Gaussian white noise and hence obeys the usual properties

$$\langle \eta(x,t)\rangle = 0\,, \tag{IV.9a}$$

$$\langle \eta(x,t)\eta(x',t')\rangle = 2\Gamma\delta(x-x')\delta(t-t')\,, \tag{IV.9b}$$

where Γ is the noise amplitude and $\langle\cdot\rangle$ is to be understood as the ensemble average. Interestingly, the two deterministic terms in Eq. (IV.8) are the only *relevant* terms at large scales, which has been demonstrated by the dynamic renormalization group

(RG) theory [200, 202]. In other words, higher-order terms in Eq. (IV.8) do not change the behaviour at large scales as they become irrelevant in the RG procedure. As a result, the KPZ equation describes a broad class of physical systems and actually defines a "universality class". The KPZ universality class is characterized by critical exponents, which can be, for example, defined via the *Family–Vicsek scaling relations* [203] for the interface width $W(L,t)$

$$W(L,t) = L^{\alpha} g\left(\frac{t}{L^{z}}\right), \tag{IV.10}$$

where the width of the interface is defined as

$$W(L,t) = \sqrt{\left\langle \frac{1}{L}\int_{0}^{L} \left(h(x,t) - \langle h\rangle_{x}(t)\right)^{2} dx \right\rangle}. \tag{IV.11}$$

The scaling exponent α in Eq. (IV.10) is referred to as the *roughness exponent*, and can be interpreted as a measure for the roughness of the interface profile for long times [204]. Typically, the width evolves as $W(L,t) \sim t^{\beta}$ for small times, where the exponent β characterizes the transient dynamics of the roughening process (before saturation), and is hence called the *growth exponent*. After a critical time τ, the interface width saturates (on average), and this transition point depends on how fast lateral correlations spread on the interface. This can be characterized by a third exponent z which relates the critical time and the system size $\tau \sim L^{z}$ [204]. These exponents are not independent, but are related via the properties of the scaling function $g(t/L^{z})$ in Eq. (IV.10), from which one concludes that $z = \alpha/\beta$. For the one-dimensonal KPZ equation, the critical exponents have been determined exactly via RG calculations, where it was found that $\alpha = 1/2$, $\beta = 1/3$, and hence $z = 3/2$ [69, 200, 202]. These results are consistent with the exact solution of the one-dimensional KPZ equation obtained from random matrix theory, where it was shown that the statistics follows the *Tracy-Widom distribution* [205–207]. The roughening transition predicted by the KPZ equation, as well as the Tracy-Widom statistics, has also been confirmed by very impressive experimental studies with nematic liquid crystals [208, 209].

The KPZ equation is characterized by a constant growth velocity along the normal direction (given by the parameter λ in the second term of Eq. (IV.8)). However, the velocity of growing interfaces is generally not constant, but may depend on a number of variables. For example, the growth velocity of solidification fronts depends on how well the solid is able to radiate latent heat, which is most efficient for negatively curved regions [177, 181, 183]. The same principle remarkably holds for the growth of bacterial colonies [210, 211]. These examples illustrate that the normal growth velocity is generally inhomogeneous along the interface and that it depends on geometric features as well as other field variables,

such as nutrient concentration distribution for bacterial populations, or temperature gradients in the case of solidification processes. One may therefore wonder whether such inhomogeneities are relevant at large scales, or whether they can be "integrated out" and are therefore irrelevant for the large scale dynamics of the system. There are a growing number of studies examining the KPZ equation coupled to other field variables. For example, it has been shown that the equations describing active growth of interfaces (where local growth is stimulated by active agents) take a similar form as the KPZ equation, but with inhomogeneous growth velocities dictated by an additional field describing the density profile of agents along the interface [212]. The dynamics of such a system does not fall into the KPZ universality class and leads to additional phenomenology, such as traveling wave patterns or microphase separation [212]. In general, no unique universality class can be assigned to systems with inhomogeneous growth rates, but they may exhibit different large scale behaviour depending on control parameters [213].

The motorprotein-lipid interface introduced in section 1 is an ideal model system for investigating non-uniformly growing interfaces, since it combines geometric features (curvature-dependent growth) and biochemistry (chemical dynamics of proteins along the interface). In this section, we will derive a generic model that describes the dynamics of a protein system on a dynamic membrane, similar as the system discussed in section 2 of chapter II. We assume that the normal velocity of the interface depends on the local protein density, and that the binding kinetics of proteins to the membrane strictly depends on the morphology of the interface. To gain some intuition, and to see to what extent such systems deviate from the KPZ dynamics, we will first consider minimal models and then successively increase the model complexity. We show that inhomogeneous growth and morphological coupling results in non-trivial dynamics, including large-scale mode selection and the emergence of turbulence. In the latter case, we show that the chaotic dynamics drives kinetic roughening of the protein-lipid interface. The roughening transition does not fall into the KPZ universality class, and is, in contrast to stochastic interface growth models, solely driven by the deterministic dynamics of the system.

2.2 General interface growth model

Following the approach presented in section 2 of chapter II, the dynamics of an arbitrary reaction-diffusion equation (for the protein density ϱ) on a dynamic one-dimensional manifold take the following form in local coordinates σ:

$$\frac{\partial}{\partial t}\varrho(\sigma,t) = D\nabla_s^2\varrho + f(\varrho,\kappa) + v_n\,\kappa\,\varrho + v_\tau\,\nabla_s\varrho\,, \tag{IV.12a}$$

$$\frac{\partial}{\partial t}\boldsymbol{r}(\sigma,t)\cdot\hat{\boldsymbol{n}} = v_n(\varrho,\kappa)\,. \tag{IV.12b}$$

Using the Monge gauge $\boldsymbol{r} = \big(x, h(x,t)\big)^T$, we can rewrite the equation for the position vector in a more convenient form:

$$\frac{\partial}{\partial t}\varrho(\sigma,t) = D\nabla_s^2\varrho + f\,(\varrho,\kappa) + v_n\,\kappa\,\varrho + v_\tau\,\nabla_s\varrho\,, \tag{IV.13a}$$

$$\frac{\partial}{\partial t}h(x,t) = v_n\,\sqrt{g}\,, \tag{IV.13b}$$

where $\sqrt{g} = \sqrt{1+(\partial h/\partial x)^2}$ denotes the metric. Note that we assume here that the reaction kinetics $f\,(\varrho,\kappa)$, as well as the normal velocity $v_n(\varrho,\kappa)$, may be explicitly dependent on the local protein density and the interface morphology via the curvature κ. The reaction term includes curvature-sensitive binding kinetics, and inhomogeneous growth is accounted for by the dependency of the normal velocity v_n on the local protein density (see Fig. IV.2 for an illustration). Consistent with the fact that the KPZ equation assumes a constant growth velocity along the normal direction, note that the dynamics of the height field $h(x,t)$ in Eq. (IV.13b) reduces (to leading order) to the KPZ equation if we choose the particular form $v_n = \lambda + \mu\kappa$, where it is straightforward to show that the second term proportional to curvature translates to the surface tension term in Eq. (IV.8).

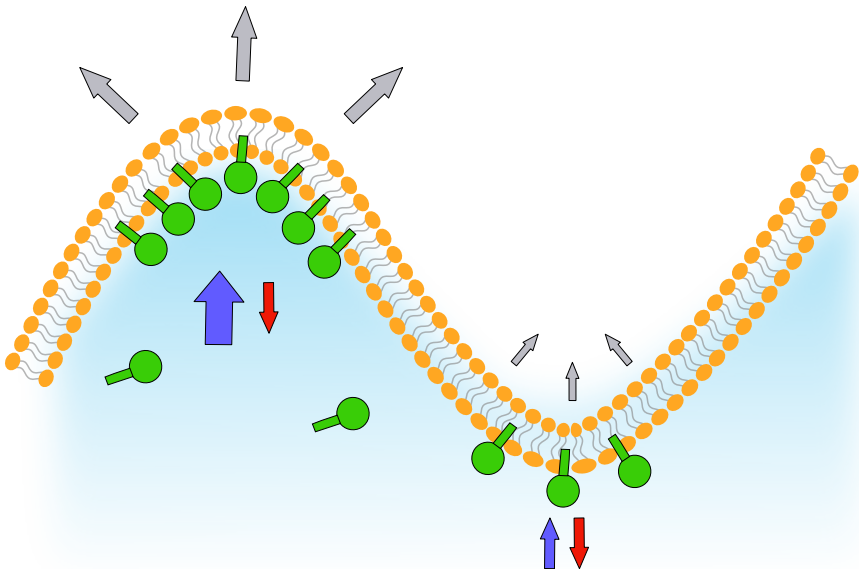

Figure IV.2 Schematic illustration of the interface growth model for protein-lipid interfaces. Proteins (green symbols) can bind to and detach from the lipid membrane (orange symbols). Membrane-bound proteins locally induce growth along the normal direction of the membrane (gray arrows). The binding kinetics is curvature-sensitive and therefore depends on the local morphology of the membrane, preferring membrane binding to negatively curved regions (illustrated by different sizes of the purple and red arrows).

2.3 Minimal conceptual model without lateral growth

To understand how inhomogeneities affect the interface growth dynamics, we start with investigating a very simple model. The model that we consider here can be interpreted as an extension of the *Edwards–Wilkinson model* (EW) [214], where we replace the constant growth rate in the EW model by an inhomogeneous growth rate that is dictated by a separate (density) field ϕ. The governing equations can be derived from the general expression Eq. (IV.13b) and by assuming weakly varying variations of the interface $(\partial h/\partial x)^2 \ll 1$:

$$\frac{\partial}{\partial t}\phi(x,t) = D\frac{\partial^2}{\partial x^2}\phi - \vartheta\phi + \sqrt{\Gamma}\eta(x,t)\,, \tag{IV.14a}$$

$$\frac{\partial}{\partial t}h(x,t) = \nu\frac{\partial^2}{\partial x^2}h + \mu\phi\,. \tag{IV.14b}$$

The density field is a simple (fluctuating) diffusion equation with a linear degradation term (second term). This field locally stimulates growth of the interface via the term $\nu\phi$, where the parameter ν is the coupling strength. Note that we assume here that the dynamics of the density field is not affected by fluctuations of the interface, which is a crucial simplification of the problem as we will see later. The detachment rate ϑ is a control parameter and can be interpreted as a "reduced temperature". Depending on this parameter, one may draw two interesting consequences: First, for $\vartheta > 0$ the dynamics reduces to the EW model, since correlations in ϕ decay exponentially in this case, such that the coupling term $\mu\phi$ effectively acts as a white noise term in the equation for the height field. Therefore, the scaling exponents in this case are $\alpha = 1/2$, $\beta = 1/4$, and $z = 2$. However, the dynamics at the "critical temperature" $\vartheta = 0$ is not immediately clear, and can be best investigated by analytically solving the linear set of equations using Fourier modes. We start with the solution of the density field, since it can be solved independently of $h(x,t)$. We define the Fourier series

$$\phi(x,t) = \frac{1}{L}\sum_{n=-\infty}^{\infty}\hat{\phi}_n e^{-iq_n x}\,, \tag{IV.15}$$

where $\hat{\phi}_n$ denotes the Fourier components of ϕ. The dynamics for the Fourier components are then given by *Langevin equations*

$$\frac{\partial}{\partial t}\hat{\phi}(t) = -Dq_n^2\hat{\phi}_n + \sqrt{\Gamma}\hat{\eta}_n(t)\,, \tag{IV.16}$$

where the correlation function of Fourier components of the noise term $\hat{\eta}_n$ obeys the usual relationship

$$\left\langle \hat{\eta}_n(t)\hat{\eta}_m(t')\right\rangle = 2L\delta_{n,-m}\delta(t-t')\,. \tag{IV.17}$$

The solution in Fourier space is therefore

$$\hat{\phi}(t) = \hat{\phi}_{n,0}e^{-Dq_n^2 t} + \sqrt{\Gamma}\int_0^t e^{-Dq_n^2(t-t')}\hat{\eta}_n(t')\,dt'\,, \tag{IV.18}$$

where the homogenous solution (first term) can be disregarded for sufficiently long times. Using the general solution, we then determine the correlation function of Fourier components

$$\left\langle \hat{\phi}_n(t)\hat{\phi}_m(t')\right\rangle = 2\Gamma L\delta_{n,-m}\frac{e^{-Dq_n^2|t-t'|} - e^{-Dq_n^2 t - Dq_m^2 t'}}{D(q_n^2+q_m^2)}\,. \tag{IV.19}$$

From the above solution, it is clear that correlations are no longer delta-peaked in time (as is the case for white noise), but rather decay mode-dependent over a characteristic time scale $\xi = 1/Dq_n^2$, which indicates that large-scale modes decay much slower than modes with small wavelengths. In other words, the dynamics of the density field effectively alters the white noise statistics and generates correlated (colored) noise.

This altered noise statistics feeds back to the dynamics of the height field via the coupling term $\mu\phi$, and therefore causes interesting effects. To investigate the dynamics of the interface $h(x,t)$, we proceed analogously as before and first determine the correlation function between Fourier modes

$$\left\langle \hat{h}_n(t)\hat{h}_m(t')\right\rangle = 2\mu^2\Gamma L\delta_{n,-m}\int_0^{t'}\frac{e^{-\mu q_n^2|t-t''|} - e^{-Dq_n^2|t-t''|}}{(D-\mu)q_n^2} \times \frac{e^{-\mu q_m^2|t'-t''|} - e^{-Dq_m^2|t'-t''|}}{(D-\mu)q_m^2}\,dt''\,, \tag{IV.20}$$

where we assume that $D \neq \mu$. Using the correlation function above, and transforming back to real space, we obtain a closed expression for the mean square

displacement of the interface profile:

$$\begin{aligned}\left\langle h(x,t)^2\right\rangle &= \frac{1}{L}\sum_n\sum_m e^{-i(q_n+q_m)x}\left\langle \hat{h}_n(t)\hat{h}_m(t)\right\rangle \\ &= \frac{2\mu^2\Gamma}{L(D-\mu)}\sum_n \frac{1-e^{-2\mu q_n^2 t}}{2\mu q_n^6} - 2\frac{1-e^{-(\mu+D)q_n^2 t}}{(\mu+D)q_n^6} + \frac{1-e^{-2Dq_n^2 t}}{2Dq_n^6}\,, \end{aligned} \tag{IV.21}$$

and then consider the saturation of the mean square displacement for $t->\infty$

$$\langle h^2\rangle = \frac{2\mu^2\Gamma}{(D-\mu)}\frac{((\mu+D)^2+4\mu D)L^5}{2^4 945\mu D(\mu+D)} := const\times L^5\,, \tag{IV.22}$$

where we used the fact that $q_n = 2\pi n/L$ (periodic boundaries) and the result

$$\sum_{n=1}^{\infty}\frac{1}{n^6} = \frac{\pi^6}{945}\,. \tag{IV.23}$$

We therefore find that the width scales as $\sim L^{5/2}$. In contrast to the case where $\vartheta > 0$, this result clearly does not indicate a roughening transition (since $\alpha > 1$), but rather shows that the interface is correlated over very large distances. One also sees from Eq. (IV.21) that the system selects the largest mode in the system (which is the first mode), while all other modes with short wavelengths decay rapidly $\sim 1/q_n^6$. Hence, the dynamics of the density field induces large-scale mode selection of the interface width, leading to a pattern of the interface.

2.4 Minimal conceptual model with lateral growth

A natural extension of the previous minimal model is to include the KPZ nonlinearity in the height field and thus accounting for growth along the normal direction (again, under the assumption that $(\partial h/\partial x)^2 \ll 1$)

$$\frac{\partial}{\partial t}h(x,t) = \mu\frac{\partial^2}{\partial x^2}h + \mu\phi + \frac{\mu\phi}{2}\left(\frac{\partial h}{\partial x}\right)^2\,. \tag{IV.24}$$

Unfortunately, one cannot determine an analytical solution in this case, since modes do not decouple, i.e. the system cannot be "diagonalized". This becomes evident by transforming the equations using Fourier modes

$$\frac{\partial}{\partial t}\hat{h}_n(t) = -\mu q_n^2\hat{h}_n + \mu\hat{\phi}_n - \frac{\mu}{2}\sum_m\sum_l \hat{\phi}_{n-l-m}\hat{h}_m\hat{h}_l q_m q_l\,. \tag{IV.25}$$

However, we can numerically solve these equations. As before, we find that small wavelength modes decay rapidly $\sim 1/q_n^6$, while large-scale modes dominate the dynamics. Thus, for $\vartheta = 0$, the system, again, does not undergo a roughening transition, but the interface rather forms a "pattern" by selecting the largest mode. For $\vartheta > 0$, one recovers – due to identical reasons as before – the KPZ equation.

2.5 Interface growth with morphological coupling

We now turn to a more realistic model for growing protein-lipid interfaces and assume that the morphology of the interface influences the chemical dynamics along the interface. We start with Eq. (IV.13b) and define the reaction function

$$f(\varrho, \kappa) := \gamma_0 - \gamma_1 \varrho \kappa - \vartheta \varrho , \tag{IV.26}$$

and the normal velocity

$$v_n(\varrho, \kappa) := \mu \varrho + \nu \kappa . \tag{IV.27}$$

The reaction function is chosen such that proteins preferentially bind to negatively curved regions (accounted for by the term proportional to curvature κ, see also Fig. IV.2). As before, we assume that proteins locally stimulate growth, and further assume that this is counteracted by surface tension (second term in the normal velocity proportional to curvature). Supposing once again that the interface dynamics is weakly varying in space $(\partial h/\partial x)^2 \ll 1$, we obtain the following set of equations

$$\frac{\partial}{\partial t}\varrho(x,t) = D\frac{\partial^2}{\partial x^2}\varrho + \gamma_0 - \gamma_1 \varrho \frac{\partial^2}{\partial x^2}h - \vartheta\varrho + \mu\varrho^2\frac{\partial^2}{\partial x^2}h + \mu\varrho\frac{\partial}{\partial x}h\frac{\partial}{\partial x}\varrho , \tag{IV.28a}$$

$$\frac{\partial}{\partial t}h(x,t) = \nu\frac{\partial^2}{\partial x^2}h + \mu\varrho + \frac{\mu\varrho}{2}\left(\frac{\partial}{\partial x}h\right)^2 , \tag{IV.28b}$$

and we see that the interface growth law corresponds to the (deterministic) KPZ equation with inhomogeneous growth dictated by the protein density field ϱ. In contrast to the simplified models considered before, any changes in the interface shape will feed back to the protein dynamics, and this interplay can lead to a complex phenomenology as we will see. We can reduce the number of free parameters by non-dimensionalization of the equations above.

To this end, we define dimensionless parameters $\tilde{\vartheta} := \vartheta\gamma_1/\gamma_0\mu$, $\tilde{\nu} := \nu/D$, and $\tilde{\mu} := \gamma_1^3/\gamma_0\mu D$, and rewrite the equations in terms of these parameters

$$\frac{\partial}{\partial t}\varrho(x,t) = \frac{\partial^2}{\partial x^2}\varrho + 1 - \varrho\frac{\partial^2}{\partial x^2}h - \tilde{\vartheta}\varrho + \varrho^2\frac{\partial^2}{\partial x^2}h + \varrho\frac{\partial}{\partial x}h\frac{\partial}{\partial x}\varrho, \tag{IV.29a}$$

$$\frac{\partial}{\partial t}h(x,t) = \tilde{\nu}\frac{\partial^2}{\partial x^2}h + \tilde{\mu}\varrho + \frac{\varrho}{2}\left(\frac{\partial}{\partial x}h\right)^2. \tag{IV.29b}$$

A more convenient form of Eq. (IV.29) can be obtained by recasting the system into "conservative form". This can be done by rewriting Eq. (IV.29) in terms of the "velocity" $u := \partial h/\partial x$, which yields

$$\frac{\partial}{\partial t}\varrho(x,t) = \frac{\partial^2}{\partial x^2}\varrho + 1 - \tilde{\vartheta}\varrho + \varrho(\varrho-1)\frac{\partial}{\partial x}u + \varrho u\frac{\partial}{\partial x}\varrho, \tag{IV.30a}$$

$$\frac{\partial}{\partial t}u(x,t) = \frac{\partial}{\partial x}\left[\tilde{\nu}\frac{\partial}{\partial x}u + \tilde{\mu}\varrho + \frac{\varrho^2}{2}\right]. \tag{IV.30b}$$

Equation (IV.30) is equivalent to the *Burgers equation* [215] with a conservative (and inhomogeneous) driving force given by $\tilde{\mu}\varrho$.

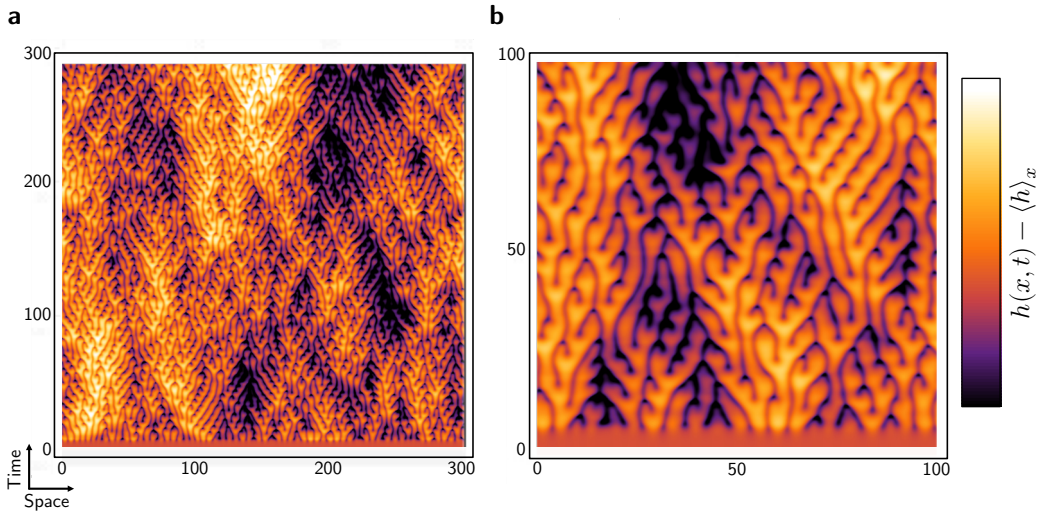

Figure IV.3 Space-time plots (kymographs), obtained by numerically solving Eq. (IV.30). a) Shown is the interface fluctuation in the co-moving frame $h(x,t) - \langle h\rangle_x$, where the amplitude is color coded according to the color bar shown on the very right (brighter colors indicate larger amplitude values). b) Simulation result for identical parameters as in a), but for a smaller system size $L = 100$, where one clearly observes the cascade of tip-splitting that drives the chaotic dynamics.

By numerically solving the governing equations, we find that the system produces chaotic dynamics for sufficiently large system sizes (Fig. IV.3). One characteristic feature of this turbulent dynamics is a never-ending sequence of tip-splitting: regions of negative curvature growth and expand laterally, eventually splitting into two new peaks, and this process then begins a new. Heuristically, tip-splitting is caused by curvature-sensitive binding of proteins, since regions with negative curvature growth faster because proteins accumulate in those portions of the interface. The phenomena of lateral growth and tip-splitting is actually very similar to the Mullins-Sekerka instability of solidification fronts [179]. Moreover, the dynamics we observe here is quite reminiscent to the well-known *Kuramoto-Sivashinsky* equation [216, 217], which is a paradigmatic and simple model for turbulence that produces a very similar phenomenology.

2.6 Finite-time Lyapunov exponents

Chaotic systems can be investigated by determining their respective spectrum of *Lyapunov exponents*, which basically characterize whether two (initially) nearby trajectories in phase-space approach each other or diverge as time progresses. In the former case, the Lyapunov exponent λ_i (of the $i-$th direction) is negative, whereas in the latter it is positive, hence indicating the onset of chaotic dynamics. Generally, one positive Lyapunov exponent is sufficient to drive the system into chaos.

Moreover, Lyapunov exponents also inform about how the phase-space volume of the attractor evolves over time [218, 219]. For Hamiltonian systems, for example, the sum of Lyapunov exponents must be exactly zero due to Liouville's theorem. For dissipative systems, on the other hand, one usually finds mixed positive and negative Lyapunov exponents, such that the sum over all exponents can become negative, thus implying that the dimension of the attractor collapses to a (finite) subspace in phase-space.

For an $N-$dimensional ODE system of the form

$$\frac{d}{dt}\mathbf{\Phi}(t) = \boldsymbol{F}(\mathbf{\Phi}(\boldsymbol{t}))\,, \tag{IV.31}$$

the Lyapunov exponents are formally defined as

$$\lambda_i = \lim_{t\to\infty} \frac{1}{t} \ln\left(\frac{\| \delta\mathbf{\Phi}_i(t) \|}{\| \delta\mathbf{\Phi}_i(0) \|}\right), \tag{IV.32}$$

and the existence of such a limit has been indeed mathematically proven [220]. In numerical simulations, however, the definition above is of course evaluated for a finite time period T, where it is important to make sure that this time range

is fine-tuned in a way such that one approximately recovers the true value. The time-evolution of perturbations $\delta\mathbf{\Phi}(t)$ are obtained by linearizing Eq. (IV.31) around the trajectories $\mathbf{\Phi}(t)$:

$$\frac{d}{dt}\delta\mathbf{\Phi}(t) = \boldsymbol{J}[\mathbf{\Phi}(t)]\delta\mathbf{\Phi}(t)\,, \tag{IV.33}$$

where $\boldsymbol{J}[\mathbf{\Phi}(t)]$ denotes the Jacobian evaluated at $\mathbf{\Phi}(t)$, i.e. $\boldsymbol{J}[\mathbf{\Phi}(t)] = dF/d\mathbf{\Phi}\big|_{\mathbf{\Phi}}$. Therefore, to determine the Lyapunov exponents, one needs to solve the fully nonlinear system Eq. (IV.31) and the linearized system Eq. (IV.33) simultaneously.

Lyapunov exponents can be also determined for partial differential equations. This can be done by discretizing all spatial operators, e.g, by a finite-difference approximation. By doing so, the resulting equations can be written as an ODE system of the form shown in Eq. (IV.31), where the main difference is that partial differential equations are infinite-dimensional systems. This then implies that there are in general infinitely many Lyapunov exponents for PDEs. However, the attractor of PDE systems is often restricted to a finite-dimensional subspace that is characterized by a finite number of positive Lyapunov exponents.

To numerically determine the Lyapunov exponents for the interface growth model Eq. (IV.30), we first perturb the solutions $\varrho \to \varrho+\delta\varrho(x,t)$, $u \to u+\delta u(x,t)$ and then linearize the equations, which read in semi-discrete form (note that $\delta\varrho$ and δu are now $N-$ dimensional vectors):

$$\begin{aligned}\frac{\partial}{\partial t}\delta\varrho(x,t) = \frac{\partial^2}{\partial x^2}\delta\varrho + 1 - \tilde{\vartheta}\delta\varrho + 2\varrho\frac{\partial}{\partial x}u\delta\varrho - \frac{\partial}{\partial x}u\delta\varrho + \varrho(\varrho-1)\frac{\partial}{\partial x}\delta u \\ + u\frac{\partial}{\partial x}\varrho\delta\varrho + u\varrho\frac{\partial}{\partial x}\delta\varrho + \varrho\frac{\partial}{\partial x}\varrho\delta u\,,\end{aligned} \tag{IV.34a}$$

$$\begin{aligned}\frac{\partial}{\partial t}\delta u(x,t) = \tilde{\nu}\frac{\partial^2}{\partial x^2}\delta u + \tilde{\mu}\frac{\partial}{\partial x}\delta\varrho + \frac{1}{2}u^2\frac{\partial}{\partial x}\delta\varrho + \frac{\partial}{\partial x}\varrho u\delta u + u\frac{\partial}{\partial x}u\delta\varrho \\ + \varrho\frac{\partial}{\partial x}u\delta u + \varrho u\frac{\partial}{\partial x}\delta u\,.\end{aligned} \tag{IV.34b}$$

As outlined above, we can now determine the Lyapunov spectrum by solving Eqs. (IV.30) and (IV.34) simultaneously. However, there is one serious issue with the numerics here that we must resolve first. Unfortunately, the numerical estimation of the Lyapunov spectrum via Eq. (IV.32) is not possible. The reason for this is that, after a finite time, all directions in phase-space will eventually align with the dominant direction associated with the largest Lyapunov exponent, and thereby render the problem ill-conditioned (because the initial orthogonal basis in phase-space collapses as the vectors become linearly dependent, see Fig. IV.4a for

an illustration). To resolve this issue, we split the time interval T into n pieces of size Δt, and perform a *Gram-Schmidt orthonormalization* after each interval Δt in order to reforce orthogonality of the phase-space basis (Fig. IV.4b). By doing so, the following approximation of Eq. (IV.32) should give us a reliable result of the Lyapunov exponent if n is chosen large enough:

$$\lambda_i = \frac{1}{n\Delta t} \sum_{k=0}^{k=n} \ln \left(\| \, \delta \mathbf{\Phi}_i^{(k)}(t) \, \| \right) . \tag{IV.35}$$

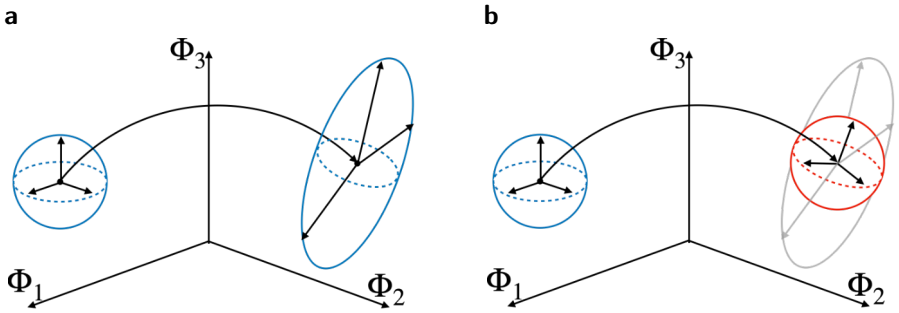

Figure IV.4 Illustration of why the naive numerical approach to determine the Lyapunov exponents via Eq. (IV.32) does not work. a) Suppose the initial condition of the system are chosen uniformly in a unit sphere in phase-space, spanned by an initially orthonormal basis. The unit sphere will be deformed by the flow in phase-space, as directions associated with positive Lyapunov exponents will stretch the volume and directions associated with negative Lyapunov exponents will squeeze the volume, respectively. Notably, the initially orthonormal basis vectors will eventually align with the fastest growing direction associated with the largest positive Lyapunov exponents. b) To prevent this, we perform an orientation-preserving Gram-Schmidt procedure after a small time interval Δt, which produces again an orthonormal basis. This procedure is repeated n times up to an end time T.

The typical form of the Lyapunov spectrum of our model is shown in Fig. IV.5a. Consistent with our numerical simulations of the full system, we find that the system exhibits positive Lyapunov exponents, and this result underscores that the dynamics is indeed chaotic. Interestingly, even though the PDE system is infinite-dimensional, we only find a small number of positive Lyapunov exponents, while most Lyapunov exponents are negative (see Fig. IV.5a). This suggests that the attractor in phase-space is constrained to a finite-dimensional subspace. Furthermore, by evaluating the sum of all Lyapunov exponents we find that $\sum_i \lambda_i < 0$ (Fig. IV.5b), implying that the system is dissipative. This is actually to be expected, because curvature-dependent growth destabilizes the system on all length scales, while line tension "dissipates" short wavelength perturbations by trying to keep

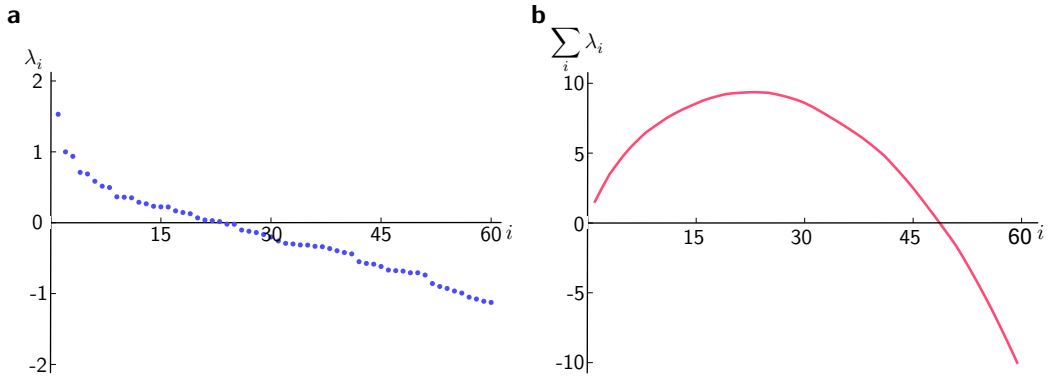

Figure IV.5 Lyapunov spectrum of the interface growth model with morphological coupling. a) Typical shape of the Lyapunov spectrum, determined numerically from Eq. (IV.35). The Lyapunov exponents are ordered from largest to smallest value. b) The sum of all Lyapunov exponents becomes eventually negative, indicating that the system is dissipative.

the interface flat, very similar to the energy cascade that underlies turbulent fluid flow [221].

2.7 Dimension of the chaotic attractor

What is the interpretation of the threshold value where $\sum_i \lambda_i \approx 0$ (see Fig. IV.5b)? Intuitively, one may interpret this point as a volume in phase-space (in which the attractor is embedded) that remains invariant by the dynamics, i.e. the volume does not expand or shrink. In addition, one generally expects that this point is not fixed, but should be dependent on parameters, such as the system size, because increasing the total length would result in more and more degrees of freedom (modes) entering the nonlinear dynamics.

Strikingly, it has been suggested that the value where $\sum_i \lambda_i \approx 0$ may be used to approximate the *fractal dimension* of the attractor [222, 223]. Extrapolating between the integer j for which $\sum_{i=1}^{j} \lambda_i \geq 0$ and $j+1$ where $\sum_{i=1}^{j+1} \lambda_i < 0$, Kaplan and Yorke [222] conjectured that the dimension of the attractor D_{KY} can be obtained from the formula

$$D_{\mathrm{KY}} = j + \frac{\sum_{i=1}^{j} \lambda_i}{|\lambda_{j+1}|} . \tag{IV.36}$$

We used Eq. (IV.36) to approximate the dimension of the attractor as a function of system size L, the result is shown in Fig. IV.6. Interestingly, we find that the chaotic attractor is extensive, i.e. its fractal dimension increases proportionally to the

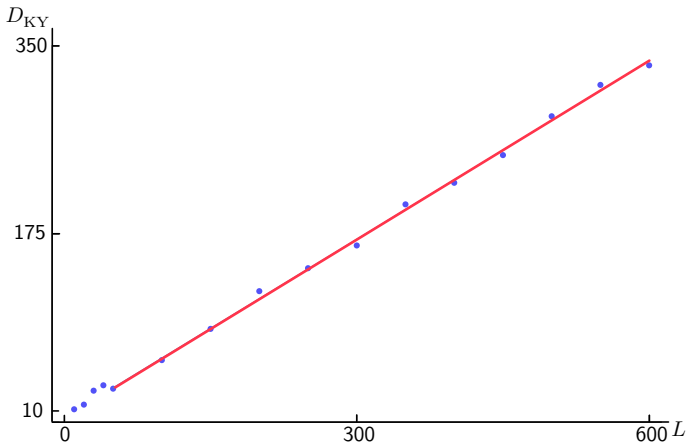

Figure IV.6 Kaplan-Yorke dimension of the interface growth model as a function of system size L. The dimension of the attractor scales linearly with the system size, which indicates that the system produces extensive chaos (except for small system sizes, where finite-size effects are present). The red line represents a linear fit to the numerically determined values (blue points).

system size $D_{KY} \sim L$ (for sufficiently large systems, where finite-size effects can be ruled out). Extensive chaos is common in many chaotic systems, such as Rayleigh-Bénard convection [224, 225], or the Kuramoto-Sivashinsky equation [226]. This result suggests that, even though the PDE system consists of infinitely many degrees of freedom, only a finite number of degrees of freedom are excited and actually participate in the chaotic dynamics.

2.8 Kinetic roughening

As we have explained in the beginning of this section, interface growth models usually exhibit a scaling law that characterizes the dynamics at large scales. The fact that the chaotic attractor here is extensive, suggests that the deterministic system may indeed exhibit a similar scaling relation, even though the system is not stochastic. However, for large enough system sizes, spatiotemporal chaos may indeed mimic noise in the system [227]. Strikingly, such an effect was shown for the (1D) Kuramoto-Sivashinsky equation, which actually falls into the KPZ universality class for sufficiently large system sizes and times. This has been shown via different techniques, such as via coarse-graining methods [228, 229], RG calculations [230], and also numerical simulations [231].

To test whether our interface growth model undergoes kinetic roughening, we performed extensive numerical simulations for a large range of system sizes, long times, and various parameter combinations. Intuitively, we expect that the system behaves identical to the KPZ equation if we choose a parameter range where

the system is laterally stable, i.e. no chaotic patterns form (Fig. IV.7). In other words, if we add white noise to the dynamics of the density field in a parameter regime where no pattern forms, then we expect that the system falls into the KPZ universality class. To verify this, we performed stochastic simulations for a range

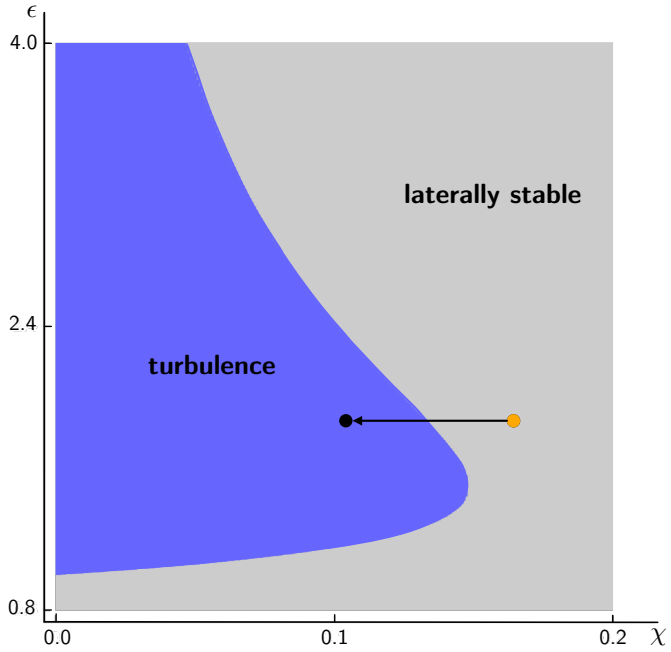

Figure IV.7 Bifurcation diagram of the deterministic model. The parameter space is spanned by the effective parameters $\epsilon = \tilde{\nu} + \tilde{\mu}$ and $\chi = \tilde{\nu}/\tilde{\mu}$. The system is laterally stable in the grey filled regime (stable homogeneous steady state), and unstable in the blue filled regime (spatiotemporal chaos). Finite-size scaling is performed for two different configurations: first, we prepare the system in a region where no lateral instabilities occur (orange dot), and then repeat the analysis in a regime where the system produces spatiotemporal chaos (black dot).

of system sizes and measured the interface width $W(L,t)$ (finite-size scaling). The result is shown in Fig. IV.8, and we find, as expected, that the system falls into the KPZ universality class. As shown in Fig. IV.8a,b, we numerically obtain the KPZ scaling exponents $\alpha = 1/2$, $\beta = 1/3$, and $z = 3/2$.

Next, we asked whether deterministic chaos alone leads to dynamic scaling, and if so, does it again belong to the KPZ universality class? To answer these questions, we again performed large-scale numerical simulations for various system sizes (Fig. IV.9a,b). Interestingly, we find that system shows dynamic scaling for sufficiently long times, i.e. once the system enters the highly nonlinear regime. Note that scaling in this case is purely driven by spatiotemporal chaos, so no extra noise terms were added to the model. The dynamic scaling is characterized by

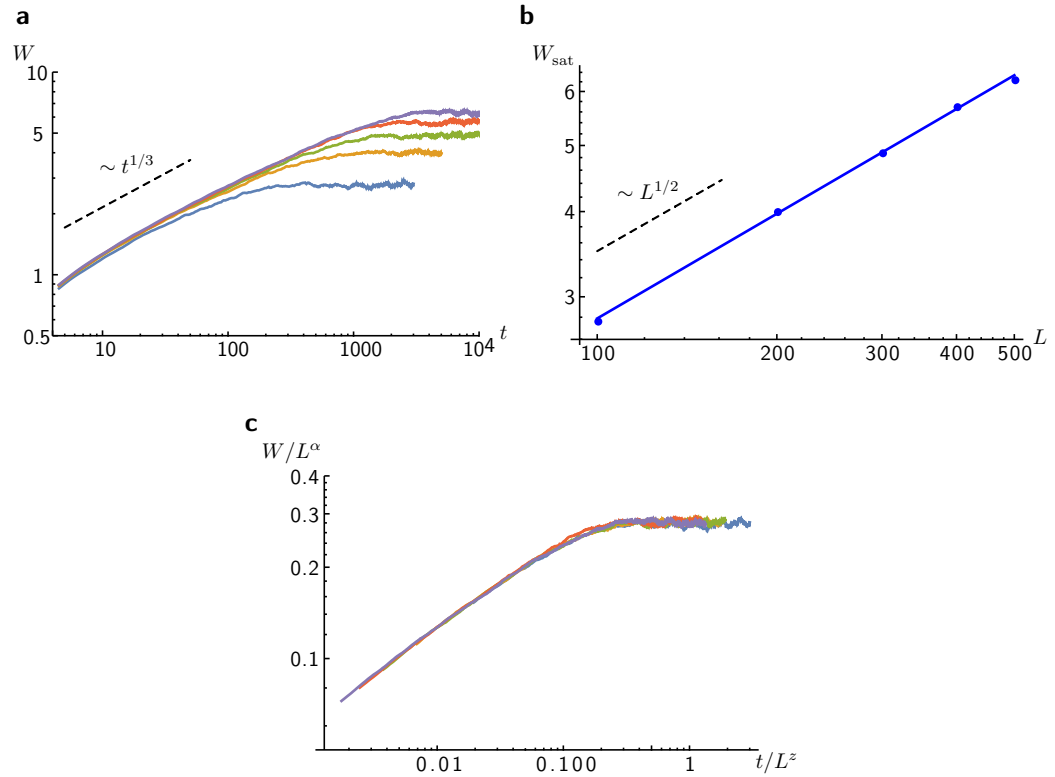

Figure IV.8 Finite-size scaling shows that the system falls into the KPZ universality class in absence of spatiotemporal chaos. a) Time-evolution of the interface width $W(L,t)$ for various system sizes L. For small times, the width increases proportionally to t^{β}, with the KPZ scaling exponent $\beta = 1/3$ (dashed line is a guide to the eye). b) The saturation value of the width for long times depends on the system size L, and scales as L^{α}, where we obtain again the KPZ exponent $\alpha = 1/2$. c) Rescaling the width by L^{α} and time by L^{z}, where $z = \alpha/\beta$, one obtains the scaling function Eq. (IV.10). In this case, all data collapse into one universal curve.

scaling exponents $\alpha \approx 0.38$, $\beta \approx 0.15$, and $z \approx 2.5$. This clearly shows that the system does not fall into the KPZ universality class.

Overall, we have shown that a feedback loop between protein binding kinetics and local morphology leads to non-trivial (deterministic) chaotic dynamics of the membrane shape. The chaotic attractor mimics noise and drives dynamic scaling of the protein-lipid interface. Beside thermal fluctuations, these results suggest that the roughness of membranes may be also driven by an intricate interplay between biochemical dynamics and membrane morphology.

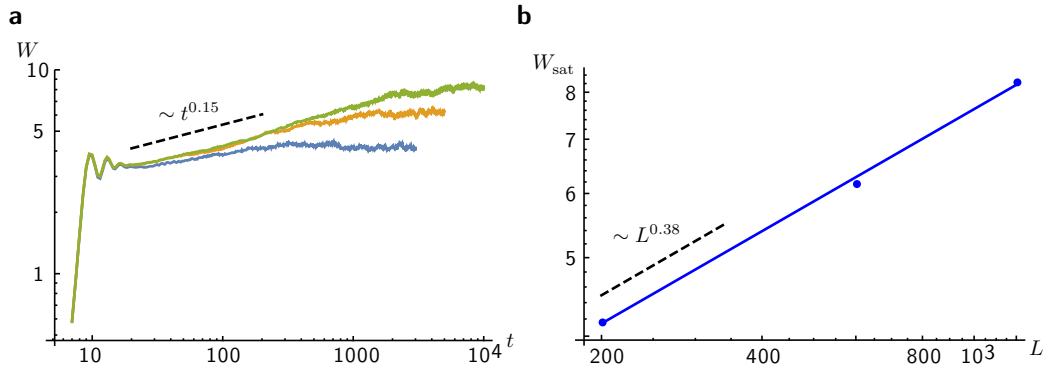

Figure IV.9 Finite-size scaling of the deterministic system in the chaotic regime. a) For sufficiently long times (after the dynamics leaves the linearly unstable regime), the chaotic attractor drives dynamic scaling, where the interface width scales as $\sim t^{\beta}$ with scaling exponent $\beta \approx 0.15$. b) The saturation width scales as $\sim L^{\alpha}$ with roughness exponent $\alpha \approx 0.38$.

2.9 Key points and outlook

In the following, we summarize the key findings of this research project and provide an outlook.

- We developed interface growth models that account for inhomogeneous growth rates along the normal direction of the interface. Such inhomogeneities occur naturally in biological systems, since the shape of cell membranes, for example, is usually controlled by proteins and other cytoskeletal components in a density dependent way.

- In simple (noisy) minimal models with linear coupling between membrane-bound proteins and the protein-lipid interface, we have shown analytically that non-uniform growth rates induce large-scale membrane deformations. We explained our findings via altered noise statistics that are induced by the protein dynamics on the membrane and which favour modes with long wavelengths. These long-wavelength modes are then further amplified by fluctuations of the protein-lipid interface, while short-wavelength modes are strongly suppressed due to surface tension.

- Inspired by previous experimental findings [34], we investigated an interface growth model in which proteins bind to the cell membrane in a strongly curvature-dependent manner. Moreover, we assumed that lateral growth of the protein-lipid interface is locally stimulated proportional to the protein density. We have shown that such a feedback loop results in spatiotemporal chaos. The existence of chaos was further supported by determining the

Lyapunov spectrum of the system. By determining the fractal dimension, we have further shown that the system exhibits extensive chaos (fractal dimension scales linearly with the system size). These results then led us to investigate dynamic scaling, where we found that the (deterministic) chaotic attractor mimics noise on large scales and thereby causes universal scaling of the interface width. We have shown that the system does not fall into the KPZ universality class.

The roughening transition in the interface growth model with morphological coupling was shown by performing extensive numerical simulations. However, one could also investigate scale-invariance by performing a systematic renormalization group analysis. Such an analysis would shed more light on the underlying principles, and would further reveal which of the terms in the model Eq. (IV.29) are relevant on large-scales, thus eventually allowing to substantially simplify the model.

We assumed here that proteins locally bind to and stimulate growth of the membrane. However, as discussed in chapters II and III, proteins usually diffuse in the cytosolic volume and only interact with the cell boundary via attachment and detachment processes (once they are close to the membrane). Hence, an interesting extension of our model would be to include non-localities by explicitly accounting for bulk-surface coupling. Since the local bulk to surface ratio is an important control parameter (see chapters II and III), such non-local effects can lead to a plethora of additional interesting patterns.

Our model can be also extended to higher dimensions, and may also be applied to circular or spherical growth. Furthermore, one may include additional membrane properties, such as bending stiffness, by adding additional terms to the normal velocity v_n. The pattern-forming dynamics, as well as dynamic scaling, can be very different in higher dimensions due to a number of reasons. In higher dimensions, one obtains additional degrees of freedom that might play an important role, such as the Gaussian curvature (which is erased in one-dimensional models). These additional features might possibly alter how correlations propagate through the system and consequently may affect both patterns and scaling exponents.

Bibliography

[1] J. Rosemeier and P. Spichtinger. Pattern Formation in Clouds via Turing Instabilities. *Mathematics of Climate and Weather Forecasting* **6**(1), 75–96, 2020. DOI: 10.1515/mcwf-2020-0104.

[2] G. Kocurek and R. C. Ewing. Aeolian Dune Field Self-Organization – Implications for the Formation of Simple versus Complex Dune-Field Patterns. *Geomorphology* **72**(1), 94–105, 2005. DOI: 10.1016/j.geomorph.2005.05.005.

[3] E. Karsenti. Self-Organization in Cell Biology: A Brief History. *Nature Reviews Molecular Cell Biology* **9**(3), 255–262, 2008. DOI: 10.1038/nrm2357.

[4] M. M. J. P. E. Sthijns, V. L. S. LaPointe and C. A. van Blitterswijk. Building Complex Life Through Self-Organization. *Tissue Engineering. Part A* **25**(19-20), 1341–1346, 2019. DOI: 10.1089/ten.TEA.2019.0208.

[5] E. Frey, J. Halatek, S. Kretschmer and P. Schwille. Protein Pattern Formation. *Physics of Biological Membranes*. Ed. by P. Bassereau and P. Sens. Springer International Publishing, Cham, 2018, pp. 229–260. DOI: 10.1007/978-3-030-00630-3_10.

[6] J. Zhu and C. B. Thompson. Metabolic Regulation of Cell Growth and Proliferation. *Nature Reviews Molecular Cell Biology* **20**(7), 436–450, 2019. DOI: 10.1038/s41580-019-0123-5.

[7] A. Satyanarayana and P. Kaldis. Mammalian Cell-Cycle Regulation: Several Cdks, Numerous Cyclins and Diverse Compensatory Mechanisms. *Oncogene* **28**(33), 2925–2939, 2009. DOI: 10.1038/onc.2009.170.

[8] C. D. Paul, P. Mistriotis and K. Konstantopoulos. Cancer Cell Motility: Lessons from Migration in Confined Spaces. *Nature Reviews Cancer* **17**(2), 131–140, 2017. DOI: 10.1038/nrc.2016.123.

[9] T. D. Pollard. Cell Motility and Cytokinesis: From Mysteries to Molecular Mechanisms in Five Decades. *Annual Review of Cell and Developmental Biology* **35**(1), 1–28, 2019. DOI: 10.1146/annurev-cellbio-100818-125427.

[10] D. A. Guertin and D. M. Sabatini. Chapter 12 - Cell Growth. *The Molecular Basis of Cancer (Third Edition)*. Ed. by J. Mendelsohn, P. M. Howley, M. A. Israel, J. W. Gray and C. B. Thompson. W.B. Saunders, Philadelphia, Jan. 2008, pp. 169–175. DOI: 10.1016/B978-141603703-3.10012-3.

[11] H. K. Matthews, C. Bertoli and R. A. M. de Bruin. Cell Cycle Control in Cancer. *Nature Reviews Molecular Cell Biology* **23**(1), 74–88, 2022. DOI: 10.1038/s41580-021-00404-3.

[12] J. Halatek, F. Brauns and E. Frey. Self-Organization Principles of Intracellular Pattern Formation. *Philosophical Transactions of the Royal Society B: Biological Sciences* **373**(1747), 2018. DOI: 10.1098/rstb.2017.0107.

[13] E. Frey and F. Brauns. Self-Organisation of Protein Patterns. *arXiv:2012.01797*, 2020. arXiv: 2012.01797.

[14] T. Burkart, M. C. Wigbers, L. Würthner and E. Frey. Control of Protein-Based Pattern Formation via Guiding Cues. *Nature Reviews Physics*, 1–17, 2022. DOI: 10.1038/s42254-022-00461-3.

[15] M. Loose, K. Kruse and P. Schwille. Protein Self-Organization: Lessons from the Min System. *Annual Review of Biophysics* **40**(1), 315–336, 2011. DOI: 10.1146/annurev-biophys-042910-155332.

[16] L. Wettmann and K. Kruse. The Min-protein Oscillations in Escherichia Coli: An Example of Self-Organized Cellular Protein Waves. *Philosophical Transactions of the Royal Society B: Biological Sciences* **373**(1747), 20170111, 2018. DOI: 10.1098/rstb.2017.0111.

[17] B. Ramm, T. Heermann and P. Schwille. The E. Coli MinCDE System in the Regulation of Protein Patterns and Gradients. *Cellular and Molecular Life Sciences* **76**(21), 4245–4273, 2019. DOI: 10.1007/s00018-019-03218-x.

[18] B. Goldstein and I. G. Macara. The PAR Proteins: Fundamental Players in Animal Cell Polarization. *Dev. Cell* **13**, 2007. DOI: 10.1016/j.devcel.2007.10.007.

[19] J. Nance and J. A. Zallen. Elaborating Polarity: PAR Proteins and the Cytoskeleton. *Development (Cambridge, England)* **138**(5), 799–809, 2011. DOI: 10.1242/dev.053538.

[20] C. Hoege and A. A. Hyman. Principles of PAR Polarity in Caenorhabditis Elegans Embryos. *Nat. Rev. Mol. Cell Biol.* **14**, 2013. DOI: 10.1038/nrm3558.

[21] W. M. Bement *et al.* Activator–Inhibitor Coupling between Rho Signalling and Actin Assembly Makes the Cell Cortex an Excitable Medium. *Nature Cell Biology* **17**(11), 1471–1483, 2015. DOI: 10.1038/ncb3251.

[22] M. C. Wigbers, T. H. Tan, F. Brauns, J. Liu, S. Z. Swartz, E. Frey and N. Fakhri. A Hierarchy of Protein Patterns Robustly Decodes Cell Shape Information. *Nature Physics*, 1–7, 2021. DOI: 10.1038/s41567-021-01164-9.

[23] J. Landino, M. Leda, A. Michaud, Z. T. Swider, M. Prom, C. M. Field, W. M. Bement, A. G. Vecchiarelli, A. B. Goryachev and A. L. Miller. Rho and F-actin Self-Organize within an Artificial Cell Cortex. *Current Biology* **31**(24), 5613–5621.e5, 2021. DOI: 10.1016/j.cub.2021.10.021.

[24] A. M. Turing. The Chemical Basis of Morphogenesis. *Philosophical Transactions of the Royal Society of London. Series B, Biological Sciences* **237**(641), 37–72, 1952. DOI: 10.1098/rstb.1952.0012.

[25] P. Gross, K. V. Kumar, N. W. Goehring, J. S. Bois, C. Hoege, F. Jülicher and S. W. Grill. Guiding Self-Organized Pattern Formation in Cell Polarity Establishment. *Nature Physics* **15**(3), 293–300, 2018. DOI: 10.1038/s41567-018-0358-7.

[26] J. B. A. Green and J. Sharpe. Positional Information and Reaction-Diffusion: Two Big Ideas in Developmental Biology Combine. *Development (Cambridge, England)* **142**(7), 1203–1211, 2015. DOI: 10.1242/dev.114991.

[27] C. A. Klausmeier. Regular and Irregular Patterns in Semiarid Vegetation. *Science (New York, N.Y.)* **284**(5421), 1826–1828, 1999. DOI: 10.1126/science.284.5421.1826.

[28] J. Halatek and E. Frey. Rethinking Pattern Formation in Reaction–Diffusion Systems. *Nature Physics* **14**(5), 507–514, 2018. DOI: 10.1038/s41567-017-0040-5.

[29] C. R. Geßele. *Cell polarisation in geometry*. PhD thesis. Ludwig-Maximilians-Universität München, May 2020.

[30] R. Geßele, J. Halatek, L. Würthner and E. Frey. Geometric Cues Stabilise Long-Axis Polarisation of PAR Protein Patterns in C. Elegans. *Nature Communications* **11**(1), 2020. DOI: 10.1038/s41467-020-14317-w.

[31] H. T. McMahon and J. L. Gallop. Membrane Curvature and Mechanisms of Dynamic Cell Membrane Remodelling. *Nature* **438**(7068), 590–596, 2005. DOI: 10.1038/nature04396.

[32] M. Simunovic, G. A. Voth, A. Callan-Jones and P. Bassereau. When Physics Takes over: BAR Proteins and Membrane Curvature. *Trends in Cell Biology* **25**(12), 780–792, 2015. DOI: 10.1016/j.tcb.2015.09.005.

[33] H. T. McMahon and E. Boucrot. Membrane Curvature at a Glance. *Journal of Cell Science* **128**(6), 1065–1070, 2015. DOI: 10.1242/jcs.114454.

[34] B. Rogez, L. Würthner, A. B. Petrova, F. B. Zierhut, D. Saczko-Brack, M.-A. Huergo, C. Batters, E. Frey and C. Veigel. Reconstitution Reveals How Myosin-VI Self-Organises to Generate a Dynamic Mechanism of Membrane Sculpting. *Nature Communications* **10**(1), 3305, 2019. DOI: 10.1038/s41467-019-11268-9.

[35] A.-L. Le Roux, C. Tozzi, N. Walani, X. Quiroga, D. Zalvidea, X. Trepat, M. Staykova, M. Arroyo and P. Roca-Cusachs. Dynamic Mechanochemical Feedback between Curved Membranes and BAR Protein Self-Organization. *Nature Communications* **12**(1), 6550, 2021. DOI: 10.1038/s41467-021-26591-3.

[36] M. Wu, X. Wu and P. De Camilli. Calcium Oscillations-Coupled Conversion of Actin Travelling Waves to Standing Oscillations. *Proceedings of the National Academy of Sciences* **110**(4), 1339–1344, 2013. DOI: 10.1073/pnas.1221538110.

[37] C. D. Lawson and A. J. Ridley. Rho GTPase Signaling Complexes in Cell Migration and Invasion. *Journal of Cell Biology* **217**(2), 447–457, 2018. DOI: 10.1083/jcb.201612069.

[38] P. Chugh and E. K. Paluch. The Actin Cortex at a Glance. *Journal of Cell Science* **131**(14), jcs186254, 2018. DOI: 10.1242/jcs.186254.

[39] M. C. Cross and P. C. Hohenberg. Pattern Formation Outside of Equilibrium. *Reviews of Modern Physics* **65**(3), 851–1112, 1993. DOI: 10.1103/RevModPhys.65.851.

[40] L. Hubatsch, F. Peglion, J. D. Reich, N. T. L. Rodrigues, N. Hirani, R. Illukkumbura and N. W. Goehring. A Cell-Size Threshold Limits Cell Polarity and Asymmetric Division Potential. *Nature Physics* **15**(10), 1078–1085, 2019. DOI: 10.1038/s41567-019-0601-x.

[41] F. Brauns, J. Halatek and E. Frey. Phase-Space Geometry of Mass-Conserving Reaction-Diffusion Dynamics. *Physical Review X* **10**(4), 2020. DOI: 10.1103/PhysRevX.10.041036.

[42] M. Loose, E. Fischer-Friedrich, J. Ries, K. Kruse and P. Schwille. Spatial Regulators for Bacterial Cell Division Self-Organize into Surface Waves in Vitro. *Science (New York, N.Y.)* **320**(5877), 789–792, 2008. DOI: doi:10.1126/science.1154413.

[43] F. Brauns, G. Pawlik, J. Halatek, J. Kerssemakers, E. Frey and C. Dekker. Bulk-Surface Coupling Identifies the Mechanistic Connection between Min-protein Patterns in Vivo and in Vitro. *Nature Communications* **12**(1), 3312, 2021. DOI: 10.1038/s41467-021-23412-5.

[44] B. J. Peter, H. M. Kent, I. G. Mills, Y. Vallis, P. J. G. Butler, P. R. Evans and H. T. McMahon. BAR Domains as Sensors of Membrane Curvature: The Amphiphysin BAR Structure. *Science* **303**(5657), 495–499, 2004. DOI: 10.1126/science.1092586.

[45] C. Mim and V. M. Unger. Membrane Curvature and Its Generation by BAR Proteins. *Trends in Biochemical Sciences* **37**(12), 526–533, 2012. DOI: 10.1016/j.tibs.2012.09.001.

[46] B. Peleg, A. Disanza, G. Scita and N. Gov. Propagating Cell-Membrane Waves Driven by Curved Activators of Actin Polymerization. *PLOS ONE* **6**(4), e18635, 2011. DOI: 10.1371/journal.pone.0018635.

[47] B. Qualmann, D. Koch and M. M. Kessels. Let's Go Bananas: Revisiting the Endocytic BAR Code. *The EMBO Journal* **30**(17), 3501–3515, 2011. DOI: 10.1038/emboj.2011.266.

[48] A. Goychuk and E. Frey. Protein Recruitment through Indirect Mechanochemical Interactions. *Physical Review Letters* **123**(17), 178101, 2019. DOI: 10.1103/PhysRevLett.123.178101.

[49] M. C. Wigbers, F. Brauns, T. Hermann and E. Frey. Pattern Localization to a Domain Edge. *Physical Review E* **101**(2), 022414, 2020. DOI: 10.1103/PhysRevE.101.022414.

[50] L. Wolpert. Positional Information and Pattern Formation in Development. *Developmental Genetics* **15**(6), 485–490, 1994. DOI: 10.1002/dvg.1020150607.

[51] M. Thanbichler and L. Shapiro. MipZ, a Spatial Regulator Coordinating Chromosome Segregation with Cell Division in Caulobacter. *Cell* **126**(1), 147–162, 2006. DOI: 10.1016/j.cell.2006.05.038.

[52] D. Kiekebusch, K. A. Michie, L.-O. Essen, J. Löwe and M. Thanbichler. Localized Dimerization and Nucleoid Binding Drive Gradient Formation by the Bacterial Cell Division Inhibitor MipZ. *Molecular Cell* **46**(3), 245–259, 2012. DOI: 10.1016/j.molcel.2012.03.004.

[53] E. Bi and H.-O. Park. Cell Polarization and Cytokinesis in Budding Yeast. *Genetics* **191**(2), 347–387, 2012. DOI: 10.1534/genetics.111.132886.

[54] F. Meitinger, A. Khmelinskii, S. Morlot, B. Kurtulmus, S. Palani, A. Andres-Pons, B. Hub, M. Knop, G. Charvin and G. Pereira. A Memory System of Negative Polarity Cues Prevents Replicative Aging. *Cell* **159**(5), 1056–1069, 2014. DOI: 10.1016/j.cell.2014.10.014.

[55] J. O. Magliozzi, J. Sears, L. Cressey, M. Brady, H. E. Opalko, A. N. Kettenbach and J. B. Moseley. Fission Yeast Pak1 Phosphorylates Anillin-like Mid1 for Spatial Control of Cytokinesis. *The Journal of Cell Biology* **219**(8), e201908017, 2020. DOI: 10.1083/jcb.201908017.

[56] B. E. Walker, J. Männik and J. Männik. Transient Membrane-Linked FtsZ Assemblies Precede Z-Ring Formation in Escherichia Coli. *Current biology: CB* **30**(3), 499–508.e6, 2020. DOI: 10.1016/j.cub.2019.12.023.

[57] M. Bauer, M. D. Petkova, T. Gregor, E. F. Wieschaus and W. Bialek. Trading Bits in the Readout from a Genetic Network. *Proceedings of the National Academy of Sciences* **118**(46), e2109011118, 2021. DOI: 10.1073/pnas.2109011118.

[58] Y.-L. Shih *et al.* Active Transport of Membrane Components by Self-Organization of the Min Proteins. *Biophysical Journal* **116**(8), 1469–1482, 2019. DOI: 10.1016/j.bpj.2019.03.011.

[59] B. Ramm, A. Goychuk, A. Khmelinskaia, P. Blumhardt, H. Eto, K. A. Ganzinger, E. Frey and P. Schwille. A Diffusiophoretic Mechanism for ATP-driven Transport without Motor Proteins. *Nature Physics* **17**(7), 850–858, 2021. DOI: 10.1038/s41567-021-01213-3.

[60] B. V. Derjaguin, S. S. Dukhin and A. A. Korotkova. Diffusiophoresis in Electrolyte Solutions and Its Role in the Mechanism of the Formation of Films from Caoutchouc Latexes by the Ionic Deposition Method. *Progress in Surface Science* **43**(1), 153–158, 1993. DOI: 10.1016/0079-6816(93)90024-P.

[61] S. Iacopini and R. Piazza. Thermophoresis in Protein Solutions. *Europhysics Letters* **63**(2), 247, 2003. DOI: 10.1209/epl/i2003-00520-y.

[62] T. Sugawara and K. Kaneko. Chemophoresis as a Driving Force for Intracellular Organization: Theory and Application to Plasmid Partitioning. *Biophysics* **7**, 77–88, 2011. DOI: 10.2142/biophysics.7.77.

[63] G. M. Allen, A. Mogilner and J. A. Theriot. Electrophoresis of Cellular Membrane Components Creates the Directional Cue Guiding Keratocyte Galvanotaxis. *Current biology: CB* **23**(7), 560–568, 2013. DOI: 10.1016/j.cub.2013.02.047.

[64] A. G. Vecchiarelli, K. C. Neuman and K. Mizuuchi. A Propagating ATPase Gradient Drives Transport of Surface-Confined Cellular Cargo. *Proceedings of the National Academy of Sciences* **111**(13), 4880–4885, 2014. DOI: 10.1073/pnas.1401025111.

[65] N. Klughammer, J. Bischof, N. D. Schnellbächer, A. Callegari, P. Lénárt and U. S. Schwarz. Cytoplasmic Flows in Starfish Oocytes Are Fully Determined by Cortical Contractions. *PLOS Computational Biology* **14**(11), e1006588, 2018. DOI: 10.1371/journal.pcbi.1006588.

[66] M. Mayer, M. Depken, J. S. Bois, F. Jülicher and S. W. Grill. Anisotropies in Cortical Tension Reveal the Physical Basis of Polarizing Cortical Flows. *Nature* **467**(7315), 617–621, 2010. DOI: 10.1038/nature09376.

[67] L. Würthner, F. Brauns, G. Pawlik, J. Halatek, J. Kerssemakers, C. Dekker and E. Frey. Bridging Scales in a Multiscale Pattern-Forming System. *arXiv:2111.12043v2*, 2021. arXiv: 2111.12043v2.

[68] K. G. Wilson. The Renormalization Group: Critical Phenomena and the Kondo Problem. *Reviews of Modern Physics* **47**(4), 773–840, 1975. DOI: 10.1103/RevModPhys.47.773.

[69] U. C. Täuber. *Critical Dynamics: A Field Theory Approach to Equilibrium and Non-Equilibrium Scaling Behavior*. 2014.

[70] S. H. Strogatz. *Nonlinear Dynamics and Chaos*. Second edition. CRC Press, Boca Raton, 2015.

[71] I. S. Aranson and L. Kramer. The World of the Complex Ginzburg-Landau Equation. *Reviews of Modern Physics* **74**(1), 99–143, 2002. DOI: 10.1103/RevModPhys.74.99.

[72] P. C. Matthews and S. M. Cox. Pattern Formation with a Conservation Law. *Nonlinearity* **13**(4), 1293–1320, 2000. DOI: 10.1088/0951-7715/13/4/317.

[73] S. M. Cox and P. C. Matthews. Instability and Localisation of Patterns Due to a Conserved Quantity. *Physica D: Nonlinear Phenomena* **175**(3-4), 196–219, 2003. DOI: 10.1016/s0167-2789(02)00733-9.

[74] D. M. Winterbottom, P. C. Matthews and S. M. Cox. Oscillatory Pattern Formation with a Conserved Quantity. *Nonlinearity* **18**(3), 1031–1056, 2005. DOI: 10.1088/0951-7715/18/3/006.

[75] D. M. Winterbottom, S. M. Cox and P. C. Matthews. Pattern Formation in a Model of a Vibrated Granular Layer. *SIAM Journal on Applied Dynamical Systems* **7**(1), 63–78, 2008. DOI: 10.1137/06067540x.

[76] F. Brauns, H. Weyer, J. Halatek, J. Yoon and E. Frey. Wavelength Selection by Interrupted Coarsening in Reaction-Diffusion Systems. *Physical Review Letters* **126**(10), 2021. DOI: 10.1103/PhysRevLett.126.104101.

[77] J. Halatek and E. Frey. Highly Canalized MinD Transfer and MinE Sequestration Explain the Origin of Robust MinCDE-Protein Dynamics. *Cell Reports* **1**(6), 741–752, 2012. DOI: 10.1016/j.celrep.2012.04.005.

[78] J. Denk, S. Kretschmer, J. Halatek, C. Hartl, P. Schwille and E. Frey. MinE Conformational Switching Confers Robustness on Self-Organized Min Protein Patterns. *Proceedings of the National Academy of Sciences* **115**(18), 4553–4558, 2018. DOI: 10.1073/pnas.1719801115.

[79] M. Raissi, P. Perdikaris and G. E. Karniadakis. Physics Informed Deep Learning (Part I): Data-driven Solutions of Nonlinear Partial Differential Equations. *arXiv:1711.10561 [cs, math, stat]*, 2017. arXiv: 1711.10561 [cs, math, stat].

[80] T. Kadeethum, T. M. Jørgensen and H. M. Nick. Physics-Informed Neural Networks for Solving Nonlinear Diffusivity and Biot's Equations. *Plos One* **15**(5), 2020. DOI: 10.1371/journal.pone.0232683.

[81] R. Supekar, B. Song, A. Hastewell, A. Mietke and J. Dunkel. Learning Hydrodynamic Equations for Active Matter from Particle Simulations and Experiments. *arXiv:2101.06568 [cond-mat, physics:physics]*, 2021. arXiv: 2101.06568 [cond-mat, physics:physics].

[82] L. Würthner, A. Goychuk and E. Frey. *Geometry-Induced Patterns through Mechanochemical Coupling*. May 2022. DOI: 10.48550/arXiv.2205.02820. arXiv: 2205.02820 [nlin].

[83] T. D. Pollard and G. G. Borisy. Cellular Motility Driven by Assembly and Disassembly of Actin Filaments. *Cell* **112**(4), 453–465, 2003. DOI: 10.1016/S0092-8674(03)00120-X.

[84] T. D. Pollard and J. A. Cooper. Actin, a Central Player in Cell Shape and Movement. *Science (New York, N.Y.)* **326**(5957), 1208–1212, 2009. DOI: doi:10.1126/science.1175862.

[85] M. D. Welch and R. D. Mullins. Cellular Control of Actin Nucleation. *Annual Review of Cell and Developmental Biology* **18**(1), 247–288, 2002. DOI: 10.1146/annurev.cellbio.18.040202.112133.

[86] Y.-L. Shih and L. Rothfield. The Bacterial Cytoskeleton. *Microbiology and Molecular Biology Reviews* **70**(3), 729–754, 2006. DOI: 10.1128/MMBR.00017-06.

[87] J. Zimmerberg and M. M. Kozlov. How Proteins Produce Cellular Membrane Curvature. *Nature Reviews Molecular Cell Biology* **7**(1), 9–19, 2006. DOI: 10.1038/nrm1784.

[88] W. A. Prinz and J. E. Hinshaw. Membrane-Bending Proteins. *Critical Reviews in Biochemistry and Molecular Biology* **44**(5), 278–291, 2009. DOI: 10.1080/10409230903183472.

[89] N. S. Gov. Guided by Curvature: Shaping Cells by Coupling Curved Membrane Proteins and Cytoskeletal Forces. *Philosophical Transactions of the Royal Society B: Biological Sciences* **373**(1747), 20170115, 2018. DOI: 10.1098/rstb.2017.0115.

[90] T. Litschel, B. Ramm, R. Maas, M. Heymann and P. Schwille. Beating Vesicles: Encapsulated Protein Oscillations Cause Dynamic Membrane Deformations. *Angewandte Chemie International Edition* **57**(50), 16286–16290, 2018. DOI: 10.1002/anie.201808750.

[91] S. Christ, T. Litschel, P. Schwille and R. Lipowsky. Active Shape Oscillations of Giant Vesicles with Cyclic Closure and Opening of Membrane Necks. *Soft Matter* **17**(2), 319–330, 2021. DOI: 10.1039/d0sm00790k.

[92] M. Fu, H. G. Franquelim, S. Kretschmer and P. Schwille. Non-Equilibrium Large-Scale Membrane Transformations Driven by MinDE Biochemical Reaction Cycles. *Angewandte Chemie International Edition* **60**(12), 6496–6502, 2021. DOI: 10.1002/anie.202015184.

[93] J. Howard, S. W. Grill and J. S. Bois. Turing's next Steps: The Mechanochemical Basis of Morphogenesis. *Nature Reviews Molecular Cell Biology* **12**(6), 392–398, 2011. DOI: 10.1038/nrm3120.

[94] H. Alimohamadi and P. Rangamani. Modeling Membrane Curvature Generation Due to Membrane–Protein Interactions. *Biomolecules* **8**(4), 2018. DOI: 10.3390/biom8040120.

[95] F. Frey and T. Idema. More than Just a Barrier: Using Physical Models to Couple Membrane Shape to Cell Function. *Soft Matter* **17**(13), 3533–3549, 2021. DOI: 10.1039/D0SM01758B.

[96] A. Mietke, F. Jülicher and I. F. Sbalzarini. Self-Organized Shape Dynamics of Active Surfaces. *Proceedings of the National Academy of Sciences* **116**(1), 29–34, 2019. DOI: 10.1073/pnas.1810896115.

[97] P. W. Miller, N. Stoop and J. Dunkel. Geometry of Wave Propagation on Active Deformable Surfaces. *Physical Review Letters* **120**(26), 268001, 2018. DOI: 10.1103/PhysRevLett.120.268001.

[98] N. Tamemoto and H. Noguchi. Pattern Formation in Reaction–Diffusion System on Membrane with Mechanochemical Feedback. *Scientific Reports* **10**(1), 19582, 2020. DOI: 10.1038/s41598-020-76695-x.

[99] A. Mahapatra, D. Saintillan and P. Rangamani. Curvature-Driven Feedback on Aggregation–Diffusion of Proteins in Lipid Bilayers. *Soft Matter* **17**(36), 8373–8386, 2021. DOI: 10.1039/d1sm00502b.

[100] C. Tozzi, N. Walani and M. Arroyo. Out-of-Equilibrium Mechanochemistry and Self-Organization of Fluid Membranes Interacting with Curved Proteins. *New Journal of Physics* **21**(9), 093004, 2019. DOI: 10.1088/1367-2630/ab3ad6.

[101] M. Mercker, F. Brinkmann, A. Marciniak-Czochra and T. Richter. Beyond Turing: Mechanochemical Pattern Formation in Biological Tissues. *Biology Direct* **11**(1), 2016. DOI: 10.1186/s13062-016-0124-7.

[102] Y. Mori, A. Jilkine and L. Edelstein-Keshet. Asymptotic and Bifurcation Analysis of Wave-Pinning in a Reaction-Diffusion Model for Cell Polarization. *SIAM Journal on Applied Mathematics* **71**(4), 1401–1427, 2011. DOI: 10.1137/10079118x.

[103] A. Mietke, V. Jemseena, K. V. Kumar, I. F. Sbalzarini and F. Jülicher. Minimal Model of Cellular Symmetry Breaking. *Physical Review Letters* **123**(18), 2019. DOI: 10.1103/PhysRevLett.123.188101.

[104] B. B. Kimia, A. Tannenbaum and S. W. Zucker. On the Evolution of Curves via a Function of Curvature. I. The Classical Case. *Journal of Mathematical Analysis and Applications* **163**(2), 438–458, 1992. DOI: 10.1016/0022-247X(92)90260-K.

[105] P. Grinfeld. *Introduction to Tensor Analysis and the Calculus of Moving Surfaces*. Springer New York, New York, NY, 2013. DOI: 10.1007/978-1-4614-7867-6.

[106] P. Grinfeld. *Exact Nonlinear Equations for Fluid Films and Proper Adaptations of Conservation Theorems from Classical Hydrodynamics*. Conference Paper. 2009.

[107] P. Grinfeld. *A Better Calculus of Moving Surfaces*. Conference Paper. 2012.

[108] Y. J. Liu, S. Mukherjee, N. Nishimura, M. Schanz, W. Ye, A. Sutradhar, E. Pan, N. A. Dumont, A. Frangi and A. Saez. Recent Advances and Emerging Applications of the Boundary Element Method. *Applied Mechanics Reviews* **64**(3), 030802, 2011. DOI: 10.1115/1.4005491.

[109] Kirkup. The Boundary Element Method in Acoustics: A Survey. *Applied Sciences* **9**(8), 1642, 2019. DOI: 10.3390/app9081642.

[110] J. P. Campanale, T. Y. Sun and D. J. Montell. Development and Dynamics of Cell Polarity at a Glance. *J. Cell Sci.* **130**, 2017. DOI: 10.1242/jcs.188599.

[111] B. Klünder, T. Freisinger, R. Wedlich-Söldner and E. Frey. GDI-Mediated Cell Polarization in Yeast Provides Precise Spatial and Temporal Control of Cdc42 Signaling. *PLOS Computational Biology* **9**(12), e1003396, 2013. DOI: 10.1371/journal.pcbi.1003396.

[112] J.-G. Chiou, M. K. Balasubramanian and D. J. Lew. Cell Polarity in Yeast. *Annu. Rev. Cell Dev. Biol.* **15**, 2017.

[113] Q. Nie, J.-G. Chiou, S. A. Ramirez, T. C. Elston, T. P. Witelski, D. G. Schaeffer and D. J. Lew. Principles That Govern Competition or Co-Existence in Rho-GTPase Driven Polarization. *PLOS Computational Biology* **14**(4), 2018. DOI: 10.1371/journal.pcbi.1006095.

[114] B. Etemad-Moghadam, S. Guo and K. Kemphues. Asymmetrically Distributed PAR-3 Protein Contributes to Cell Polarity and Spindle Alignment in Early C. Elegans Embryos. *Cell* **83**, 1995. DOI: 10.1016/0092-8674(95)90187-6.

[115] P. Gönczy. Asymmetric Cell Division and Axis Formation in the Embryo. *WormBook* **15**, 2005. DOI: 10.1895/wormbook.1.30.1.

[116] N. W. Goehring. PAR Polarity: From Complexity to Design Principles. *Exp. Cell Res.* **328**, 2014. DOI: 10.1016/j.yexcr.2014.08.009.

[117] Y. Hao, L. Boyd and G. Seydoux. Stabilization of Cell Polarity by the C. Elegans Ring Protein Par-2. *Dev. Cell* **10**, 2006. DOI: 10.1016/j.devcel.2005.12.015.

[118] S. Zonies, F. Motegi, Y. Hao and G. Seydoux. Symmetry Breaking and Polarization of the C. Elegans Zygote by the Polarity Protein PAR-2. *Development* **137**, 2010. DOI: 10.1242/dev.045823.

[119] F. Motegi. Microtubules Induce Self-Organization of Polarized PAR Domains in Caenorhabditis Elegans Zygotes. *Nat. Cell Biol.* **13**, 2011. DOI: 10.1038/ncb2354.

[120] N. W. Goehring, P. K. Trong, J. S. Bois, D. Chowdhury, E. M. Nicola, A. A. Hyman and S. W. Grill. Polarization of PAR Proteins by Advective Triggering of a Pattern-Forming System. *Science (New York, N.Y.)* **334**(6059), 1137–1141, 2011. DOI: 10.1126/science.1208619.

[121] N. W. Goehring and S. W. Grill. Cell Polarity: Mechanochemical Patterning. *Trends in Cell Biology* **23**(2), 72–80, 2013. DOI: 10.1016/j.tcb.2012.10.009.

[122] D. P. Hill and S. Strome. An Analysis of the Role of Microfilaments in the Establishment and Maintenance of Asymmetry in Caenorhabditis Elegans Zygotes. *Dev. Biol.* **125**, 1988. DOI: 10.1016/0012-1606(88)90060-7.

[123] A. A. Cuenca, A. Schetter, D. Aceto, K. Kemphues and G. Seydoux. Polarization of the C. Elegans Zygote Proceeds via Distinct Establishment and Maintenance Phases. *Development* **130**, 2003. DOI: 10.1242/dev.00284.

[124] C. R. Cowan and A. A. Cowan. Centrosomes Direct Cell Polarity Independently of Microtubule Assembly in C. Elegans Embryos. *Nature* **431**, 2004. DOI: 10.1038/nature02825.

[125] Z. Petrásek. Characterization of Protein Dynamics in Asymmetric Cell Division by Scanning Fluorescence Correlation Spectroscopy. *Biophys. J.* **95**, 2008. DOI: 10.1529/biophysj.108.135152.

[126] C. Schenk, H. Bringmann, A. A. Hyman and C. R. Cowan. Cortical Domain Correction Repositions the Polarity Boundary to Match the Cytokinesis Furrow in C. Elegans Embryos. *Development* **137**, 2010. DOI: 10.1242/dev.040436.

[127] F. Motegi and G. Seydoux. The PAR Network: Redundancy and Robustness in a Symmetry-Breaking System. *Philos. Trans. R Soc. Lond. B Biol. Sci.* **368**, 2013. DOI: 10.1098/rstb.2013.0010.

[128] A. T. Dawes and E. M. Munro. PAR-3 Oligomerization May Provide an Actin-Independent Mechanism to Maintain Distinct Par Protein Domains in the Early Caenorhabditis Elegans Embryo. *Biophys. J.* **101**, 2011. DOI: 10.1016/j.bpj.2011.07.030.

[129] N. W. Goehring, C. Hoege, S. W. Grill and A. Hyman. PAR Proteins Diffuse Freely across the Anterior-Posterior Boundary in Polarized C. Elegans Embryos. *J. Cell Biol.* **193**, 2011. DOI: 10.1083/jcb.201011094.

[130] D. Thalmeier, J. Halatek and E. Frey. Geometry-Induced Protein Pattern Formation. *Proceedings of the National Academy of Sciences* **113**(3), 548–553, 2016. DOI: 10.1073/pnas.1515191113.

[131] H. Feddersen, L. Würthner, E. Frey and M. Bramkamp. Dynamics of the Bacillus Subtilis Min System. *mBio* **12**(2), e00296–21, 2021. DOI: doi: 10.1128/mBio.00296-21.

[132] J. L. Watts. Par-6, a Gene Involved in the Establishment of Asymmetry in Early C. Elegans Embryos, Mediates the Asymmetric Localization of PAR-3. *Development* **122**, 1996.

[133] Y. Tabuse. Atypical Protein Kinase C Cooperates with PAR-3 to Establish Embryonic Polarity in Caenorhabditis Elegans. *Development* **125**, 1998.

[134] T. .-. J. Hung and K. J. Kemphues. PAR-6 Is a Conserved PDZ Domain-Containing Protein That Colocalizes with PAR-3 in Caenorhabditis Elegans Embryos. *Development* **126**, 1999.

[135] J. Li. Binding to PKC-3, but Not to PAR-3 or to a Conventional PDZ Domain Ligand, Is Required for PAR-6 Function in C. Elegans. *Dev. Biol.* **340**, 2010. DOI: 10.1016/j.ydbio.2010.01.023.

[136] J. Rodriguez. aPKC Cycles between Functionally Distinct PAR Protein Assemblies to Drive Cell Polarity. *Dev. Cell* **42**, 2017. DOI: 10.1016/j.devcel.2017.07.007.

[137] C. Brimacombe, R. M. Corless and M. Zamir. Computation and Applications of Mathieu Functions: A Historical Perspective. *SIAM Review* **63**(4), 653–720, 2021. DOI: 10.1137/20M135786X.

[138] J. R. Frank, J. Guven, M. Kardar and H. Shackleton. Pinning of Diffusional Patterns by Non-Uniform Curvature. *EPL (Europhysics Letters)* **127**(4), 48001, 2019. DOI: 10.1209/0295-5075/127/48001.

[139] T. Colding, W. Minicozzi and E. Pedersen. Mean Curvature Flow. *Bulletin of the American Mathematical Society* **52**(2), 297–333, 2015. DOI: 10.1090/S0273-0979-2015-01468-0.

[140] J. W. Cahn and J. E. Hilliard. Free Energy of a Nonuniform System. I. Interfacial Free Energy. *The Journal of Chemical Physics* **28**(2), 258–267, 1958. DOI: 10.1063/1.1744102.

[141] M. Burger, S.-Y. Chu, P. A. Markowich and C.-B. Schonlieb. The Willmore Functional and Instabilities in the Cahn-Hilliard Equation. *Communications in Mathematical Sciences* **6**(2), 309–329, 2008. DOI: 10.4310/CMS.2008.v6.n2.a3.

[142] J. Errington and L. J. Wu. Cell Cycle Machinery in Bacillus Subtilis. *Sub-Cellular Biochemistry* **84**, 67–101, 2017. DOI: 10.1007/978-3-319-53047-5_3.

[143] D. P. Haeusser and W. Margolin. Splitsville: Structural and Functional Insights into the Dynamic Bacterial Z Ring. *Nature Reviews. Microbiology* **14**(5), 305–319, 2016. DOI: 10.1038/nrmicro.2016.26.

[144] V. W. Rowlett and W. Margolin. The Min System and Other Nucleoid-Independent Regulators of Z Ring Positioning. *Frontiers in Microbiology* **6**, 478, 2015. DOI: 10.3389/fmicb.2015.00478.

[145] A. Dajkovic, G. Lan, S. X. Sun, D. Wirtz and J. Lutkenhaus. MinC Spatially Controls Bacterial Cytokinesis by Antagonizing the Scaffolding Function of FtsZ. *Current biology: CB* **18**(4), 235–244, 2008. DOI: 10.1016/j.cub.2008.01.042.

[146] V. Blasios, A. W. Bisson-Filho, P. Castellen, M. L. C. Nogueira, J. Bettini, R. V. Portugal, A. C. M. Zeri and F. J. Gueiros-Filho. Genetic and Biochemical Characterization of the MinC-FtsZ Interaction in Bacillus Subtilis. *PloS One* **8**(4), e60690, 2013. DOI: 10.1371/journal.pone.0060690.

[147] Z. Hu, A. Mukherjee, S. Pichoff and J. Lutkenhaus. The MinC Component of the Division Site Selection System in Escherichia Coli Interacts with FtsZ to Prevent Polymerization. *Proceedings of the National Academy of Sciences of the United States of America* **96**(26), 14819–14824, 1999. DOI: 10.1073/pnas.96.26.14819.

[148] B. Shen and J. Lutkenhaus. Examination of the Interaction between FtsZ and MinCN in E. Coli Suggests How MinC Disrupts Z Rings. *Molecular Microbiology* **75**(5), 1285–1298, 2010. DOI: 10.1111/j.1365-2958.2010.07055.x.

[149] D. H. Edwards and J. Errington. The Bacillus Subtilis DivIVA Protein Targets to the Division Septum and Controls the Site Specificity of Cell Division. *Molecular Microbiology* **24**(5), 905–915, 1997. DOI: 10.1046/j.1365-2958.1997.3811764.x.

[150] R. Lenarcic, S. Halbedel, L. Visser, M. Shaw, L. J. Wu, J. Errington, D. Marenduzzo and L. W. Hamoen. Localisation of DivIVA by Targeting to Negatively Curved Membranes. *The EMBO journal* **28**(15), 2272–2282, 2009. DOI: 10.1038/emboj.2009.129.

[151] H. Stahlberg, E. Kutejová, K. Muchová, M. Gregorini, A. Lustig, S. A. Müller, V. Olivieri, A. Engel, A. J. Wilkinson and I. Barák. Oligomeric Structure of the Bacillus Subtilis Cell Division Protein DivIVA Determined by Transmission Electron Microscopy. *Molecular Microbiology* **52**(5), 1281–1290, 2004. DOI: 10.1111/j.1365-2958.2004.04074.x.

[152] S.-B. Wang, S. Cantlay, N. Nordberg, M. Letek, J. A. Gil and K. Flärdh. Domains Involved in the in Vivo Function and Oligomerization of Apical Growth Determinant DivIVA in Streptomyces Coelicolor. *FEMS Microbiology Letters* **297**(1), 101–109, 2009. DOI: 10.1111/j.1574-6968.2009.01678.x.

[153] M. Bramkamp, R. Emmins, L. Weston, C. Donovan, R. A. Daniel and J. Errington. A Novel Component of the Division-Site Selection System of Bacillus Subtilis and a New Mode of Action for the Division Inhibitor MinCD. *Molecular Microbiology* **70**(6), 1556–1569, 2008. DOI: 10.1111/j.1365-2958.2008.06501.x.

[154] J. E. Patrick and D. B. Kearns. MinJ (YvjD) Is a Topological Determinant of Cell Division in Bacillus Subtilis. *Molecular Microbiology* **70**(5), 1166–1179, 2008. DOI: 10.1111/j.1365-2958.2008.06469.x.

[155] S. van Baarle and M. Bramkamp. The MinCDJ System in Bacillus Subtilis Prevents Minicell Formation by Promoting Divisome Disassembly. *PLOS ONE* **5**(3), e9850, 2010. DOI: 10.1371/journal.pone.0009850.

[156] A. L. Marston, H. B. Thomaides, D. H. Edwards, M. E. Sharpe and J. Errington. Polar Localization of the MinD Protein of Bacillus Subtilis and Its Role in Selection of the Mid-Cell Division Site. *Genes & Development* **12**(21), 3419–3430, 1998. DOI: 10.1101/gad.12.21.3419.

[157] A. L. Marston and J. Errington. Selection of the Midcell Division Site in Bacillus Subtilis through MinD-dependent Polar Localization and Activation of MinC. *Molecular Microbiology* **33**(1), 84–96, 1999. DOI: 10.1046/j.1365-2958.1999.01450.x.

[158] J. N. Bach, N. Albrecht and M. Bramkamp. Imaging DivIVA Dynamics Using Photo-Convertible and Activatable Fluorophores in Bacillus Subtilis. *Frontiers in Microbiology* **5**, 59, 2014. DOI: 10.3389/fmicb.2014.00059.

[159] M. Howard. A Mechanism for Polar Protein Localization in Bacteria. *Journal of Molecular Biology* **335**(2), 655–663, 2004. DOI: 10.1016/j.jmb.2003.10.058.

[160] P. A. de Boer, R. E. Crossley, A. R. Hand and L. I. Rothfield. The MinD Protein Is a Membrane ATPase Required for the Correct Placement of the Escherichia Coli Division Site. *The EMBO Journal* **10**(13), 4371–4380, 1991.

[161] I. Hayashi, T. Oyama and K. Morikawa. Structural and Functional Studies of MinD ATPase: Implications for the Molecular Recognition of the Bacterial Cell Division Apparatus. *The EMBO Journal* **20**(8), 1819–1828, 2001. DOI: 10.1093/emboj/20.8.1819.

[162] L. Blanchoin, R. Boujemaa-Paterski, C. Sykes and J. Plastino. Actin Dynamics, Architecture, and Mechanics in Cell Motility. *Physiological Reviews* **94**(1), 235–263, 2014. DOI: 10.1152/physrev.00018.2013.

[163] C. Gebhardt, H. Gruler and E. Sackmann. On Domain Structure and Local Curvature in Lipid Bilayers and Biological Membranes. *Zeitschrift für Naturforschung C* **32**(7-8), 581–596, 1977. DOI: 10.1515/znc-1977-7-817.

[164] M. P. Sheetz and S. J. Singer. Biological Membranes as Bilayer Couples. A Molecular Mechanism of Drug-Erythrocyte Interactions. *Proceedings of the National Academy of Sciences* **71**(11), 4457–4461, 1974. DOI: 10.1073/pnas.71.11.4457.

[165] W. Helfrich. Elastic Properties of Lipid Bilayers: Theory and Possible Experiments. *Zeitschrift für Naturforschung C* **28**(11-12), 693–703, 1973. DOI: doi:10.1515/znc-1973-11-1209.

[166] U. Seifert, L. Miao, H. G. Döbereiner and M. Wortis. Budding Transition for Bilayer Fluid Vesicles with Area-Difference Elasticity. *The Structure and Conformation of Amphiphilic Membranes*. Ed. by R. Lipowsky, D. Richter and K. Kremer. Springer Berlin Heidelberg, pp. 93–96.

[167] L. Miao, U. Seifert, M. Wortis and H.-G. Döbereiner. Budding Transitions of Fluid-Bilayer Vesicles: The Effect of Area-Difference Elasticity. *Physical Review E* **49**(6), 5389–5407, 1994. DOI: 10.1103/PhysRevE.49.5389.

[168] U. Seifert. Configurations of Fluid Membranes and Vesicles. *Advances in Physics* **46**(1), 13–137, 1997. DOI: 10.1080/00018739700101488.

[169] B. Antonny. Mechanisms of Membrane Curvature Sensing. *Annual Review of Biochemistry* **80**, 101–123, 2011. DOI: 10.1146/annurev-biochem-052809-155121.

[170] D. A. Sahlender, R. C. Roberts, S. D. Arden, G. Spudich, M. J. Taylor, J. P. Luzio, J. Kendrick-Jones and F. Buss. Optineurin Links Myosin VI to the Golgi Complex and Is Involved in Golgi Organization and Exocytosis. *Journal of Cell Biology* **169**(2), 285–295, 2005. DOI: 10.1083/jcb.200501162.

[171] G. Spudich, M. V. Chibalina, J. S.-Y. Au, S. D. Arden, F. Buss and J. Kendrick-Jones. Myosin VI Targeting to Clathrin-Coated Structures and Dimerization Is Mediated by Binding to Disabled-2 and PtdIns(4,5)P2. *Nature Cell Biology* **9**(2), 176–183, 2007. DOI: 10.1038/ncb1531.

[172] M. J. Phillips and G. K. Voeltz. Structure and Function of ER Membrane Contact Sites with Other Organelles. *Nature Reviews Molecular Cell Biology* **17**(2), 69–82, 2016. DOI: 10.1038/nrm.2015.8.

[173] S. Pyrpassopoulos, H. Shuman and E. M. Ostap. Adhesion Force and Attachment Lifetime of the KIF16B-PX Domain Interaction with Lipid Membranes. *Molecular Biology of the Cell* **28**(23), 3315–3322, 2017. DOI: 10.1091/mbc.e17-05-0324.

[174] F. Buss, J. P. Luzio and J. Kendrick-Jones. Myosin VI, a New Force in Clathrin Mediated Endocytosis. *FEBS letters* **508**(3), 295–299, 2001. DOI: 10.1016/s0014-5793(01)03065-4.

[175] F. Buss and J. Kendrick-Jones. Myosin VI: A Multifunctional Motor Protein. *Myosins: A Superfamily of Molecular Motors*. Ed. by L. M. Coluccio. Proteins and Cell Regulation. Springer Netherlands, Dordrecht, 2008, pp. 325–352. DOI: 10.1007/978-1-4020-6519-4_10.

[176] S. Manley, J. M. Gillette, G. H. Patterson, H. Shroff, H. F. Hess, E. Betzig and J. Lippincott-Schwartz. High-Density Mapping of Single-Molecule Trajectories with Photoactivated Localization Microscopy. *Nature Methods* **5**(2), 155–157, 2008. DOI: 10.1038/nmeth.1176.

[177] D. A. Kessler, J. Koplik and H. Levine. Pattern Selection in Fingered Growth Phenomena. *Advances in Physics* **37**(3), 255–339, 1988. DOI: 10.1080/00018738800101379.

[178] C. A. Weber, D. Zwicker, F. Jülicher and C. F. Lee. Physics of Active Emulsions. *Reports on Progress in Physics* **82**(6), 064601, 2019. DOI: 10.1088/1361-6633/ab052b.

[179] W. W. Mullins and R. F. Sekerka. Stability of a Planar Interface During Solidification of a Dilute Binary Alloy. *Journal of Applied Physics* **35**(2), 444–451, 1964. DOI: 10.1063/1.1713333.

[180] R. C. Brower, D. A. Kessler, J. Koplik and H. Levine. Geometrical Models of Interface Evolution. *Physical Review A* **29**(3), 1335–1342, 1984. DOI: 10.1103/PhysRevA.29.1335.

[181] D. A. Kessler, J. Koplik and H. Levine. Geometrical Models of Interface Evolution. II. Numerical Simulation. *Physical Review A* **30**(6), 3161–3174, 1984. DOI: 10.1103/PhysRevA.30.3161.

[182] E. Ben-Jacob, N. Goldenfeld, J. S. Langer and G. Schön. Boundary-Layer Model of Pattern Formation in Solidification. *Physical Review A* **29**(1), 330–340, 1984. DOI: 10.1103/PhysRevA.29.330.

[183] J. Strain. A Boundary Integral Approach to Unstable Solidification. *Journal of Computational Physics* **85**(2), 342–389, 1989. DOI: 10.1016/0021-9991(89)90155-1.

[184] Kaplan C. Nadir, Noorduin Wim L., Li Ling, Sadza Roel, Folkertsma Laura, Aizenberg Joanna and Mahadevan L. Controlled Growth and Form of Precipitating Microsculptures. *Science* **355**(6332), 1395–1399, 2017. DOI: 10.1126/science.aah6350.

[185] J. A. Sethian. Curvature and the Evolution of Fronts. *Communications in Mathematical Physics* **101**(4), 487–499, 1985. DOI: 10.1007/BF01210742.

[186] J. A. Sethian. Numerical Algorithms for Propagating Interfaces: Hamilton-Jacobi Equations and Conservation Laws. *Journal of Differential Geometry* **31**(1), 131–161, 1990. DOI: 10.4310/jdg/1214444092.

[187] W. van Saarloos. Front Propagation into Unstable States. *Physics Reports* **386**(2), 29–222, 2003. DOI: 10.1016/j.physrep.2003.08.001.

[188] T. Y. Hou, J. S. Lowengrub and M. J. Shelley. Removing the Stiffness from Interfacial Flows with Surface Tension. *Journal of Computational Physics* **114**(2), 312–338, 1994. DOI: 10.1006/jcph.1994.1170.

[189] D. A. Tumbarello, J. Kendrick-Jones and F. Buss. Myosin VI and Its Cargo Adaptors – Linking Endocytosis and Autophagy. *Journal of Cell Science* **126**(12), 2561–2570, 2013. DOI: 10.1242/jcs.095554.

[190] G. Koster, M. VanDuijn, B. Hofs and M. Dogterom. Membrane Tube Formation from Giant Vesicles by Dynamic Association of Motor Proteins. *Proceedings of the National Academy of Sciences* **100**(26), 15583–15588, 2003. DOI: 10.1073/pnas.2531786100.

[191] A. Roux, G. Koster, M. Lenz, B. Sorre, J.-B. Manneville, P. Nassoy and P. Bassereau. Membrane Curvature Controls Dynamin Polymerization. *Proceedings of the National Academy of Sciences* **107**(9), 4141–4146, 2010. DOI: 10.1073/pnas.0913734107.

[192] R. Dasgupta and R. Dimova. Inward and Outward Membrane Tubes Pulled from Giant Vesicles. *Journal of Physics D: Applied Physics* **47**(28), 282001, 2014. DOI: 10.1088/0022-3727/47/28/282001.

[193] P. Blanco Dorca. *A Computational Model for the Cooperative Binding and Self-Organization of Myosin-VI in Membrane Reshaping*. Bachelor Thesis. Universitat Politècnica de Catalunya, June 2020.

[194] L. Miglio and A. Sassella. Epitaxy. *Encyclopedia of Condensed Matter Physics*. Ed. by F. Bassani, G. L. Liedl and P. Wyder. Elsevier, Oxford, Jan. 2005, pp. 157–166. DOI: 10.1016/B0-12-369401-9/00692-6.

[195] H.-C. Flemming, J. Wingender, U. Szewzyk, P. Steinberg, S. A. Rice and S. Kjelleberg. Biofilms: An Emergent Form of Bacterial Life. *Nature Reviews Microbiology* **14**(9), 563–575, 2016. DOI: 10.1038/nrmicro.2016.94.

[196] R. H. Essenhigh. Combustion and Flame Propagation in Coal Systems: A Review. *Symposium (International) on Combustion* **16**(1), 353–374, 1977. DOI: 10.1016/S0082-0784(77)80337-8.

[197] O. Sandre, L. Moreaux and F. Brochard-Wyart. Dynamics of Transient Pores in Stretched Vesicles. *Proceedings of the National Academy of Sciences* **96**(19), 10591–10596, 1999. DOI: 10.1073/pnas.96.19.10591.

[198] F. Brochard-Wyart, P. G. de Gennes and O. Sandre. Transient Pores in Stretched Vesicles: Role of Leak-Out. *Physica A: Statistical Mechanics and its Applications* **278**(1), 32–51, 2000. DOI: 10.1016/S0378-4371(99)00559-2.

[199] E. Karatekin, O. Sandre and F. Brochard-Wyart. Transient Pores in Vesicles. *Polymer International* **52**(4), 486–493, 2003. DOI: 10.1002/pi.1007.

[200] M. Kardar, G. Parisi and Y.-C. Zhang. Dynamic Scaling of Growing Interfaces. *Physical Review Letters* **56**(9), 889–892, 1986. DOI: 10.1103/PhysRevLett.56.889.

[201] M. Eden. A Two-dimensional Growth Process. *Proceedings of the Fourth Berkeley Symposium on Mathematical Statistics and Probability, Volume 4: Contributions to Biology and Problems of Medicine* **4.4**, 223–240, 1961.

[202] E. Frey and U. C. Täuber. Two-Loop Renormalization-Group Analysis of the Burgers–Kardar-Parisi-Zhang Equation. *Physical Review E* **50**(2), 1024–1045, 1994. DOI: 10.1103/PhysRevE.50.1024.

[203] F. Family and T. Vicsek. Scaling of the Active Zone in the Eden Process on Percolation Networks and the Ballistic Deposition Model. *Journal of Physics A: Mathematical and General* **18**(2), L75–L81, 1985. DOI: 10.1088/0305-4470/18/2/005.

[204] A. L. Barabási and H. E. Stanley. *Fractal Concepts in Surface Growth*. Cambridge University Press, Cambridge, 1995. DOI: 10.1017/CBO9780511599798.

[205] C. A. Tracy and H. Widom. Level-Spacing Distributions and the Airy Kernel. *Communications in Mathematical Physics* **159**(1), 151–174, 1994. DOI: 10.1007/BF02100489.

[206] C. A. Tracy and H. Widom. Distribution Functions for Largest Eigenvalues and Their Applications. *Proceedings of the International Congress of Mathematicians, Vol. I (Beijing, 2002)*. Higher Ed. Press, Beijing, 2002, pp. 587–596.

[207] T. Sasamoto and H. Spohn. One-Dimensional Kardar-Parisi-Zhang Equation: An Exact Solution and Its Universality. *Physical Review Letters* **104**(23), 230602, 2010. DOI: 10.1103/PhysRevLett.104.230602.

[208] K. A. Takeuchi and M. Sano. Universal Fluctuations of Growing Interfaces: Evidence in Turbulent Liquid Crystals. *Physical Review Letters* **104**(23), 230601, 2010. DOI: 10.1103/PhysRevLett.104.230601.

[209] K. A. Takeuchi, M. Sano, T. Sasamoto and H. Spohn. Growing Interfaces Uncover Universal Fluctuations behind Scale Invariance. *Scientific Reports* **1**(1), 34, 2011. DOI: 10.1038/srep00034.

[210] M. R. Warren, H. Sun, Y. Yan, J. Cremer, B. Li and T. Hwa. Spatiotemporal Establishment of Dense Bacterial Colonies Growing on Hard Agar. *eLife* **8**, e41093, 2019. DOI: 10.7554/eLife.41093.

[211] A. Martínez-Calvo, T. Bhattacharjee, R. K. Bay, H. N. Luu, A. M. Hancock, N. S. Wingreen and S. S. Datta. Roughening Instability of Growing 3D Bacterial Colonies. *bioRxiv:2022.02.11.480095*, 2022. DOI: 10.1101/2022.05.09.491177.

[212] F. Cagnetta, M. R. Evans and D. Marenduzzo. Active Growth and Pattern Formation in Membrane-Protein Systems. *Physical Review Letters* **120**(25), 258001, 2018. DOI: 10.1103/PhysRevLett.120.258001.

[213] F. Cagnetta, V. Škultéty, M. R. Evans and D. Marenduzzo. Renormalization Group Study of the Dynamics of Active Membranes: Universality Classes and Scaling Laws. *Physical Review E* **105**(1), 014610, 2022. DOI: 10.1103/PhysRevE.105.014610.

[214] S. F. Edwards and D. R. Wilkinson. The Surface Statistics of a Granular Aggregate. *Proceedings of the Royal Society of London. A. Mathematical and Physical Sciences* **381**(1780), 17–31, 1982. DOI: 10.1098/rspa.1982.0056.

[215] J. M. Burgers. A Mathematical Model Illustrating the Theory of Turbulence. *Advances in Applied Mechanics*. Ed. by R. Von Mises and T. Von Kármán. Vol. 1. Elsevier, Jan. 1948, pp. 171–199. DOI: 10.1016/S0065-2156(08)70100-5.

[216] G. I. Sivashinsky. Nonlinear Analysis of Hydrodynamic Instability in Laminar Flames—I. Derivation of Basic Equations. *Acta Astronautica* **4**(11), 1177–1206, 1977. DOI: 10.1016/0094-5765(77)90096-0.

[217] Y. Kuramoto. Diffusion-Induced Chaos in Reaction Systems. *Progress of Theoretical Physics Supplement* **64**, 346–367, 1978. DOI: 10.1143/PTPS.64.346.

[218] G. Benettin, L. Galgani, A. Giorgilli and J.-M. Strelcyn. Lyapunov Characteristic Exponents for Smooth Dynamical Systems and for Hamiltonian Systems; a Method for Computing All of Them. Part 1: Theory. *Meccanica* **15**(1), 9–20, 1980. DOI: 10.1007/BF02128236.

[219] A. Wolf, J. B. Swift, H. L. Swinney and J. A. Vastano. Determining Lyapunov Exponents from a Time Series. *Physica D: Nonlinear Phenomena* **16**(3), 285–317, 1985. DOI: 10.1016/0167-2789(85)90011-9.

[220] V. I. Oseledets. A Multiplicative Ergodic Theorem. Lyapunov Characteristic Numbers for Dynamical Systems. *Trans. Moscow Math. Soc.* **19**, 197–231, 1968.

[221] S. B. Pope. *Turbulent Flows*. Cambridge University Press, Cambridge, 2000. DOI: 10.1017/CBO9780511840531.

[222] J. L. Kaplan and J. A. Yorke. Chaotic Behavior of Multidimensional Difference Equations. *Functional Differential Equations and Approximation of Fixed Points*. Ed. by H.-O. Peitgen and H.-O. Walther. Lecture Notes in Mathematics. Springer, Berlin, Heidelberg, 1979, pp. 204–227. DOI: 10.1007/BFb0064319.

[223] J. D. Farmer, E. Ott and J. A. Yorke. The Dimension of Chaotic Attractors. *Physica D: Nonlinear Phenomena* **7**(1), 153–180, 1983. DOI: 10.1016/0167-2789(83)90125-2.

[224] M. R. Paul, M. I. Einarsson, P. F. Fischer and M. C. Cross. Extensive Chaos in Rayleigh-Bénard Convection. *Physical Review E* **75**(4), 045203, 2007. DOI: 10.1103/PhysRevE.75.045203.

[225] A. Karimi and M. R. Paul. Quantifying Spatiotemporal Chaos in Rayleigh-Bénard Convection. *Physical Review E* **85**(4), 046201, 2012. DOI: 10.1103/PhysRevE.85.046201.

[226] R. A. Edson, J. E. Bunder, T. W. Mattner and A. J. Roberts. Lyapunov Exponents of the Kuramoto-Sivashinsky PDE. *The ANZIAM Journal* **61**(3), 270–285, 2019. DOI: 10.1017/S1446181119000105.

[227] J. Krug and H. Spohn. Universality Classes for Deterministic Surface Growth. *Physical Review A* **38**(8), 4271–4283, 1988. DOI: 10.1103/PhysRevA.38.4271.

[228] S. Zaleski. A Stochastic Model for the Large Scale Dynamics of Some Fluctuating Interfaces. *Physica D: Nonlinear Phenomena* **34**(3), 427–438, 1989. DOI: 10.1016/0167-2789(89)90266-2.

[229] F. Hayot, C. Jayaprakash and C. Josserand. Long-Wavelength Properties of the Kuramoto-Sivashinsky Equation. *Physical Review E* **47**(2), 911–915, 1993. DOI: 10.1103/PhysRevE.47.911.

[230] L. Zhang, G. Tang, Z. Xun, K. Han, H. Chen and B. Hu. Dynamic Renormalization-Group Analysis of the D + 1 dimensionalKuramoto-Sivashinsky Equation with Both Conservative and Nonconservative Noises. *The European Physical Journal B* **63**(2), 227–234, 2008. DOI: 10.1140/epjb/e2008-00228-4.

[231] K. Sneppen, J. Krug, M. H. Jensen, C. Jayaprakash and T. Bohr. Dynamic Scaling and Crossover Analysis for the Kuramoto-Sivashinsky Equation. *Physical Review A* **46**(12), R7351–R7354, 1992. DOI: 10.1103/PhysRevA.46.R7351.

Acknowledgements

Zuerst gilt mein tiefster Dank meinem Doktorvater Erwin Frey für die Möglichkeit, dass ich in seiner Gruppe diese äußerst lehrreiche und spannende Lebenserfahrung machen durfte. Es war mir stets eine große Freude und Ehre, mit Dir zusammen Ideen zu entwickeln und diese erfolgreich umzusetzen. Ich habe von Dir nicht nur sehr viel über Physik gelernt, sondern auch viele andere nützliche Fähigkeiten, wie z.B. das Vortragen von wissenschaftlichen Arbeiten und insbesondere das schreiben von Publikationen. Vor allem aber möchte ich mich dafür bedanken, dass Du solch eine einzigartige und angenehme Arbeitsatmosphäre in deiner Gruppe geschaffen hast.

Ich möchte mich des Weiteren bei Claudia Veigel und Benoit Rogez für die wundervolle Zusammenarbeit und den Experimenten für das Myosin-VI-Projekt bedanken. Claudia, dein Enthusiasmus und dein exzellentes Verständnis der Theorie haben mich sehr beeindruckt. In gleicher Weise möchte ich mich bei Marc Bramkamp, Helge Feddersen, Grzegorz Pawlik und Cees Dekker für die fantastische Kollaboration und den beeindruckenden experimentellen Daten zur Min-Protein-Dynamik bedanken.

Selbstverständlich möchte ich mich auch bei meinen Kollegen bedanken, mit denen ich das Vergnügen hatte, an vielen der Forschungsprojekte zusammenzuarbeiten. Mein Dank gilt Fridtjof Brauns und Jacob Halatek für die großartige Zusammenarbeit am "Wedge-Projekt". Insbesondere möchte ich mich bei Fridtjof für die vielen Inspirierenden Diskussionen bedanken – es hat mir eine große Freude bereitet und ich konnte dabei sehr viel von Dir lernen. Ein besonderer Dank gilt meinem Kollegen und guten Freund Andriy Goychuk. Die Zusammenarbeit mit Dir hat mir besonders viel Spaß gemacht, und ich freue mich sehr darauf, auch weiterhin in Zukunft mit Dir an Forschungsprojekte zu arbeiten. Ich möchte mich des Weiteren bei Tom Burkart und Manon Wigbers für die tolle Zusammenarbeit bedanken. Ein besonderer Dank gilt hier vor allem Tom für die zahlreichen Diskussionen sowie sein stets offenes Ohr für diverse Anliegen – vielen Dank für deine Geduld! Ich möchte mich außerdem besonders bei Henrik Weyer für die wundervolle und interessante Zusammenarbeit zur in vivo Min-Dynamik bedanken. Außerdem möchte ich mich bei Raphaela Geßele für die Zusammenarbeit am PAR-Projekt bedanken. Vielen Dank, dass ich daran teilhaben durfte!

Als Nächstes möchte ich allen Weiteren lieben Kollegen am Lehrstuhl für die wunderschöne Zeit danken. Vielen Dank an Severin Angerpointner, Timo Krüger, Ching Yee Leung, Ivan Maryshev, Florian Raßhofer, Moritz Striebel,

Richard Swiderski, David Muramatsu, Florian Gartner und Alexander Ziepke. Ein besonderer Dank geht hier an David Muramatsu, der sich stets dafür eingesetzt hat, dass unsere Arbeitsverträge rechtzeitig verlängert werden – vielen Dank für Deine Bemühungen! Besonders hervorheben möchte ich meinen Dank an meinem Kollegen und "Bro", Florian Gartner. Vielen Dank, dass Du mir seit so vielen Jahren ein treuer und guter Freund bist. Besonders dankbar bin ich Dir für die ganzen hilfreichen Gespräche und Tipps. Außerdem freue ich mehr sehr auf unsere zukünftigen gemeinsamen Forschungsprojekte bzw. "brojects".

Mein Dank gilt auch besonders meiner Familie, ohne die das Ganze nicht möglich gewesen wäre. Zunächst bin ich meinen Eltern Lamiha und Lukman Hassan zu tiefstem Dank verpflichtet. Ohne eure mutige Entscheidung, einfach alles aufzugeben und einen großen Schritt in eine ungewisse Zukunft zu wagen, wäre ich niemals da, wo ich jetzt stehe. Mein Dank gilt hier auch meinen Geschwistern Lauko, Lana, Larissa und Lehat für die Unterstützung und dem Vertrauen in meinen Fähigkeiten. Ich möchte mich auch herzlichst bei Stefanie Braun für das Korrekturlesen dieser Arbeit bedanken. Ein besonderer Dank gilt meinem Schwiegervater Klaus Würthner. Vielen Dank für dein großes Interesse an meinen Forschungsarbeiten, und für die ganzen schönen und inspirierenden Diskussionen. Ich möchte mich auch bei meiner Schwiegermutter Petra Würthner für Ihren Zuspruch bedanken. Und auch vielen Dank dafür, dass Du mich gelegentlich mit Essen versorgst.

Zu guter Schluss gilt mein tiefster Dank meiner liebevollen Frau Freyja. Ohne deine bedingungslose Liebe, stetige Unterstützung, die zahlreichen aufmunternden Gespräche und deine helfenden Hände wäre das niemals möglich gewesen. Vielen Dank für dein Verständnis und deine bewundernswerte Geduld! Ein besonderer Dank gilt auch unserer süßen Tochter Victoria, auch wenn sie mir im Homeoffice die meiste Zeit auf den Kopf krabbeln wollte.